

NASA Conference Publication 3328

408P.

# 30th Aerospace Mechanisms Symposium

---

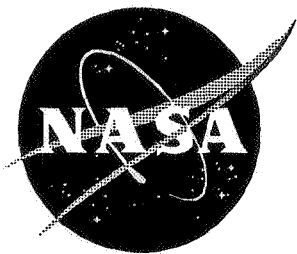
*Compiled by  
Obie H. Bradley, Jr. and John F. Rogers*

Proceedings of a symposium sponsored by the  
National Aeronautics and Space Administration,  
Washington, D.C., and Lockheed Martin Missiles and  
Space Company, Inc., Sunnyvale, California,  
and held in Hampton, Virginia  
May 15-17, 1996

---

May 1996





NASA Conference Publication 3328

# 30th Aerospace Mechanisms Symposium

---

*Compiled by  
Obie H. Bradley, Jr. and John F. Rogers  
Langley Research Center • Hampton, Virginia*

Proceedings of a symposium sponsored by the  
National Aeronautics and Space Administration,  
Washington, D.C., and Lockheed Martin Missiles and  
Space Company, Inc., Sunnyvale, California,  
and held in Hampton, Virginia  
May 15-17, 1996

National Aeronautics and Space Administration  
Langley Research Center • Hampton, Virginia 23681-0001

---

May 1996



## **PREFACE**

The Aerospace Mechanisms Symposium (AMS) provides a unique forum for those active in the design, production and use of aerospace mechanisms. A major focus is the reporting of problems and solutions associated with the development and flight certification of new mechanisms. The National Aeronautics and Space Administration and Lockheed Martin Missiles & Space share responsibility for organizing the AMS. Now in its 30th year, the AMS continues to be well attended, attracting participants from both the U.S. and abroad.

The 30th AMS, hosted by the NASA Langley Research Center, was held in Hampton, VA on May 15, 16 and 17, 1995. During these three days, 23 papers and 8 posters were presented. Topics included robotics, deployment mechanisms, bearings, actuators, scanners, boom and antenna release, and test equipment. Hardware displays during the poster session gave attendees an opportunity to meet with developers of current and future mechanism components.

The high quality of this symposium is due the efforts of many people and their efforts are gratefully acknowledged. This extends to the voluntary members of the symposium organizing committee representing the 8 NASA field centers, LMMS, and members from the European Space Agency. Also to be thanked are the session chairs, the authors, and particularly the personnel at NASA LaRC responsible for the symposium arrangements and the publication of these proceedings. Thank you also goes to the symposium executive committee at LMMS who are responsible for the year-to-year management of the AMS, including paper processing and preparation of the program.

The use of trade names of manufacturers in this publication does not constitute an official endorsement of such products or manufacturers, either expressed or implied, by the National Aeronautics and Space Administration.



## CONTENTS

<b>Preface.....</b>	<b>iii</b>
<b>Symposium Schedule.....</b>	<b>ix</b>
<b>Symposium Organizing Committee.....</b>	<b>xiv</b>
<b>Life Test Results for the Advanced Very High Resolution Radiometer Scanner.....</b>	<b>1-1</b>
James Lenz	
<b>Space Telescope Fine Guidance Sensor Bearing Anomaly.....</b>	<b>13 -2</b>
Stuart Loewenthal, Jaime Esper, J. Pan, and J. Decker	
<b>The Thermal Conductance of Solid-Lubricated Bearings at Cryogenic Temperatures in a Vacuum.....</b>	<b>31 -3</b>
Mike Anderson	
<b>Tape Recorder Failure Investigation.....</b>	<b>47 4</b>
Mark Higgins, Stuart Loewenthal, C.C. Carnahan, and G.L. Snyder	
<b>New Antenna Deployment, Pointing and Supporting Mechanism.....</b>	<b>65 -5</b>
Vincenzo Costabile, Francesco Lumaca, P. Marsili, G. Noni, and C. Portelli	
<b>Development of a Scan Mirror Assembly for an Extreme Ultraviolet Atmospheric Scanner.....</b>	<b>77 -6</b>
Thomas R. McBirney	
<b>Coarse Pointing Mechanism Assembly for Satellite Interlink.....</b>	<b>91 -7</b>
Pierre-Alain Mäusli, M.-T. Ivorra, Volker Gass, and J.-F. Berthoud	
<b>A Nitinol-Based Solar Array Deployment Mechanism.....</b>	<b>103 -8</b>
Shin-John Choi, Chia-Ao Lu, and John Feland	
<b>The ARA Mark3 Solar Array Design and Development.....</b>	<b>119 9</b>
Rob H.A. van Hassel	
<b>SCARLET I: Mechanization Solutions for Deployable Concentrator Optics Integrated with Rigid Array Technology.....</b>	<b>135 -10</b>
James J. Wachholz and David M. Murphy	
<b>A Revolute Joint with Linear Load-Displacement Response for a Deployable Lidar Telescope.....</b>	<b>145 -11</b>
Mark S. Lake, Peter A. Warren, and Lee D. Peterson	

<b>Antenna Pointing Mechanism for ESA ENVISAT Polar Platform.....</b>	<b>161</b>	<b>-12</b>
Javier Serrano, J. San Millán, and R. Santiago		
<b>Development of a Gimballed, Dual Frequency, Space-Based, Microwave Antenna for Volume Production.....</b>	<b>177</b>	<b>-13</b>
Martin Leckie and Dave Laidig		
<b>Design and Development of the Cassini Main Engine Assembly Gimbel Mechanism.....</b>	<b>191</b>	<b>-14</b>
Dale Rudolph		
<b>Advances in the Analysis and Design of Constant-Torque Springs.....</b>	<b>205</b>	<b>-15</b>
John R. McGuire and Joseph A. Yura		
<b>Jettison Mechanism for a Large Inflatable Antenna.....</b>	<b>221</b>	<b>-16</b>
Don Jarosz, Steven Hendricks, Dave Landis, Craig Tooley, and Greg Martins		
<b>Mars Pathfinder Rover Egress Deployable Ramp Assembly.....</b>	<b>239</b>	<b>-17</b>
Brian R. Spence and Lee F. Sword		
<b>Mars Pathfinder Lander Deployment Mechanisms.....</b>	<b>255</b>	<b>-18</b>
Greg Gillis-Smith		
<b>Reliability and Testing.....</b>	<b>273</b>	<b>-19</b>
Werner Auer		
<b>Development of a Hermetically Sealed Brushless DC Motor for a J-T Cryocooler.....</b>	<b>285</b>	<b>-20</b>
Edwin Joscelyn, Irwin Hochler, Andrew Ferri, Heinz Rott, and Ted Soukaris		
<b>The Design, Development and Qualification of a Lightweight Antenna Pointing Mechanism.....</b>	<b>291</b>	<b>-21</b>
M. Shmulevitz and A. Halsband		
<b>EVA Assembly and Release of Highly Loaded Bolts.....</b>	<b>299</b>	<b>-22</b>
Jim Olmstead and Paul Barker		
<b>Remote Manual Operator for Space Station Intermodule Ventilation Valve.....</b>	<b>305</b>	<b>-23</b>
James R. Guyaux		
<b>Miniature Rotary Actuator.....</b>	<b>311</b>	<b>-24</b>
Richard Fink and Robert Ellis		
<b>Mir Environmental Effects Payload Handrail Clamp/Pointing Device.....</b>	<b>317</b>	<b>-25</b>
Stephen J. Hughes		

<b>A Computer Controlled Power Tool for the Servicing of the Hubble Space Telescope.....</b>	<b>323</b>	<b>26</b>
Paul W. Richards, Carl Konkell, Chris Smith, Lee Brown, and Ken Wagner		
<b>Umbilical Mechanisms Assembly for the International Space Station.....</b>	<b>329</b>	<b>27</b>
A. Ali Mandvi		
<b>Magnetic Docking Aid for Orbiter to ISS Docking.....</b>	<b>345</b>	<b>28</b>
William C. Schneider, Kornel Nagy, and John A Schliesing		
<b>The Micro Conical System: Lessons Learned from a Successful EVA/Robot-Compatible Mechanism.....</b>	<b>361</b>	<b>29</b>
Mark Gittleman and Alistair Johnston		
<b>NASA Space Shuttle Lightweight Seat.....</b>	<b>377</b>	<b>30</b>
Chris Hansen, Wayne Jermstad, James Lewis, and Todd Colangelo		





## SYMPOSIUM SCHEDULE

### TUESDAY, 14 MAY 1995

7:00-9:00 EARLY REGISTRATION AND/OR CHECK-IN

### WEDNESDAY, 15 MAY 1995

8:00 Wednesday Authors' Breakfast - Peninsula Ballroom

8:30 REGISTRATION AND REFRESHMENTS  
Pre-Function Area

9:30 INTRODUCTORY REMARKS  
Obie H. Bradley, Host Chairman  
NASA Langley Research Center, Hampton, VA  
Stuart H. Loewenthal, General Chairman  
Lockheed Martin Missiles & Space, Sunnyvale, CA

CENTER WELCOME  
Paul F. Holloway, Center Director  
NASA Langley Research Center, Hampton, VA

10:00 **SESSION I - BEARINGS & TRIBOLOGY**  
Cliff E. Willey, Session Chair  
Applied Physics Lab, Johns Hopkins University, Laurel, MD

- *Life Test Results for the Advanced Very High Resolution Radiometer Scanner*  
James Lenz, ITT Aerospace/Communications Division, Ft. Wayne, IN
- *Space Telescope Fine Guidance Sensor Bearing Anomaly*  
Stuart Loewenthal, Lockheed Martin Missiles & Space, Sunnyvale, CA;  
Jaime Esper, AlliedSignal Technical Services Corp., Columbia, MD; J. Pan, Space Telescope Science Institute, Baltimore, MD; J. Decker, NASA Goddard Space Flight Center, Greenbelt, MD
- *The Thermal Conductance of Solid-Lubricated Bearings at Cryogenic Temperatures in Vacuum*  
Mike Anderson, European Space Tribology Laboratory, Warrington, England
- *Tape Recorder Failure Investigation*  
Mark Higgins, Stuart Loewenthal, C. C. Carnahan & G. L. Snyder, Lockheed Martin Missiles & Space, Sunnyvale, CA

12:00 LUNCH

- 1:15      **SESSION II - POINTING MECHANISMS I**  
J. Blake Sathoff, Session Chair  
TRW, Inc., Redondo Beach, CA
- *New Antenna Deployment, Pointing and Supporting Mechanism*  
Vincenzo Costabile, Francesco Lumaca, P. Marsili & G. Noni, Alenia Spazio, Rome, Italy; C. Portelli, Agenzia Spaziale Italiana, Rome, Italy
  - *Development of a Scan Mirror Assembly for an Extreme Ultraviolet Atmospheric Scanner*  
Thomas R. McBirney, Swales & Associates, Beltsville, MD
  - *Coarse Pointing Mechanism Assembly for Satellite Interlink Experiment*  
Pierre-Alain Mausli, M.-T. Ivorra, Volker Gass & J.-F. Berthoud, Mecanex S. A., Nyon, Switzerland

2:45      **BREAK**

- 3:00      **SESSION III - SOLAR ARRAY MECHANISMS**  
John Cox, Session Chair  
NASA Langley Research Center, Hampton, VA
- *A Nitinol-Based Solar Array Deployment Mechanism*  
Shin-John Choi, Chia-Ao Lu & John Feland, Stanford University, Palo Alto, CA
  - *The ARA Mark3 Solar Array Design and Development*  
Rob H. A. van Hassel, Fokker Space & Systems B. V., Leiden, The Netherlands
  - *SCARLET I: Mechanization Solutions for Deployable Concentrator Optics Integrated with Rigid Array Technology*  
James J. Wachholz & David M. Murphy, AEC-Able Engineering Co., Goleta, CA

- 5:30-10:00    **BANQUET AT SHIELDS TAVERN, WILLIAMSBURG, VA**
- 5:30            Buses depart from Radisson Hotel
  - 6:15-7:00     Social Hour/Self-Guided tour of Duke of Gloucester Street
  - 7:00-9:45     Colonial Dinner and Gambols
  - 10:00          Buses depart from Shields Tavern

**THURSDAY, 16 MAY 1995**

7:00      Thursday Authors' Breakfast - Peninsula Ballroom

- 8:00      **SESSION IV - POINTING MECHANISMS II**  
Ken Lorell, Session Chair  
Lockheed Martin Missiles & Space, Sunnyvale, CA
- *A Revolute Joint with Linear Load-Displacement Response for a Deployable Lidar Telescope*  
Mark S. Lake, NASA Langley Research Center, Hampton, VA; Peter A. Warren & Lee D. Peterson, University of Colorado, Boulder, CO

- *Antenna Pointing Mechanism for ESA ENVISAT Polar Platform*  
Javier Serrano, J. San Millan & R. Santiago, Instituto Nacional de  
Tecnica Aeroespacial, Madrid, Spain
  - *Development of a Gimballed, Dual Frequency, Space-Based,  
Microwave Antenna for Volume Production*  
Martin Leckie, COM DEV, Cambridge, Canada; Dave Laidig,  
Motorola, Chandler, AZ
  - *Design and Development of the Cassini Main Engine Assembly  
Gimbal Mechanism*  
Dale Rudolph, Lockheed Martin Astronautics, Denver, CO
- 10:00 BREAK
- 10:15 **SESSION V - DEPLOYMENT MECHANISMS**  
Bill Purdy, Session Chair  
Naval Research Laboratory, Washington, DC
- *Advances in the Analysis and Design of Constant-Torque Springs*  
John R. McGuire, NASA Goddard Space Flight Center, Greenbelt,  
MD; Joseph A. Yura, University of Texas, Austin, TX
  - *Jettison Mechanism for a Large Inflatable Antenna*  
Don Jarosz, Steven Hendricks & Dave Landis, Swales &  
Associates, Inc., Beltsville, MD; Craig Tooley & Greg Martins,  
NASA Goddard Space Flight Center, Greenbelt, MD
  - *Mars Pathfinder Rover Egress Deployable Ramp Assembly*  
Brian R. Spence, Astro Aerospace Corp, Carpinteria, CA; Lee F.  
Sword, Jet Propulsion Lab, Pasadena, CA
  - *Mars Pathfinder Lander Deployment Mechanisms*  
Greg Gillis-Smith, Jet Propulsion Lab, Pasadena, CA
- 12:15 LUNCH
- 1:30 **SPECIAL TOPIC FOR DISCUSSION**
- *Reliability and Testing*  
Werner Auer, TWB Wiesenbach/Heidelberg, Heidelberg, Germany
- 2:15 **SPECIAL PRESENTATION**  
Michael Petters, Program Director  
Aircraft Carriers Construction and Overhaul
- *Ships of the Line*  
A unique perspective on the similarities of designing mechanisms  
that have to survive the rigors of the oceans and designing  
mechanisms for space.
- 2:45 BREAK

**3:00-4:30 SESSION VI - POSTER PREVIEWS**

Dana Mitchell, Session Chair

Space Telescope Science Institute, Baltimore, MD

- *Development of a Hermetically Sealed Brushless DC Motor for a J-T Cryocooler*

Edwin Joscelyn, Irwin Hochler, Andrew Ferri, Heinz Rott & Ted Soukaris, Aeroflex Laboratories, Farmingdale, NY

- *The Design, Development and Qualification of a Lightweight Antenna Pointing Mechanism*

M. Shmulevitz & A. Halsband, Israeli Aircraft Industries, Yehud, Israel

- *EVA Assembly and Release of Highly Loaded Bolts*

Jim Olmstead & Paul Barker, Spar Space Systems, Brampton, Canada

- *Remote Manual Operator for Space Station Intermodule Ventilation Valve*

James R. Guyaux, AlliedSignal Aerospace, Tempe, AZ

- *Miniature Rotary Actuator*

Richard Fink & Robert Ellis, Honeywell Electro Components, Durham, NC

- *Mir Environmental Effects Payload Handrail Clamp/Pointing Device*

Stephen J. Hughes, NASA Langley Research Center, Hampton, VA

- *A Computer Controlled Power Tool for the Servicing of the Hubble Space Telescope*

Paul W. Richards & Ken Wagner, NASA Goddard Space Flight Center, Greenbelt, MD; Carl Konkel & Chris Smith, Orbital Sciences Corporation, Greenbelt, MD; Lee Brown, Swales and Associates, Inc., Beltsville, MD

**5:00-6:30 VIRGINIA AIR AND SPACE CENTER - Self-guided tour**

**6:30-8:30 RECEPTION**

Oyster Alley, Radisson Hotel

**FRIDAY, 17 MAY 1995**

**7:00 Friday Authors' Breakfast - Peninsula Ballroom**

**8:00 SESSION VII - ORBITER/SPACE STATION**

Charles Johnson, Session Chair

Boeing Defense & Space Group, Seattle, WA

- *Umbilical Mechanisms Assembly for the International Space Station*

A. Ali Mandvi, McDonnell Douglas Aerospace, Huntington Beach, CA

- *Magnetic Docking Aid for Orbiter to ISS Docking*

William C. Schneider, Kornel Nagy & John A. Schliesing, NASA Johnson Space Center, Houston, TX

- *The Micro Conical System: Lessons Learned from a Successful EVA/Robot-Compatible Mechanism*

Mark Gittleman & Alistair Johnston, Oceaneering Space Systems, Houston, TX

- *NASA Space Shuttle Lightweight Seat*  
Chris Hansen, Wayne Jermstad, James Lewis, NASA Johnson Space Center, Houston, TX; Todd Colangelo, Lockheed Martin Engineering & Sciences, Houston, TX

10:00 BREAK

10:15 NASA LANGLEY RESEARCH CENTER OVERVIEW

10:45 PRESENTATION OF THE HERZL AWARD

CLOSING REMARKS

Edward A. Boesiger, Operations Chairman  
Lockheed Martin Missiles & Space

11:00 LUNCH AND CHECK-OUT

12:30 BUS LEAVES HOTEL FOR TOUR

1:00-3:00 NASA LANGLEY RESEARCH CENTER FACILITY TOUR  
Aircraft Landing Dynamics Facility, an operational wind tunnel, Impact Dynamics Research Facility

## SYMPOSIUM ORGANIZING COMMITTEE

Obie H. Bradley, Jr., Host Chairman, NASA LaRC  
John F. Rogers, Co-Host Chairman, NASA LaRC

Stuart H. Loewenthal	General Chairman	Lockheed Martin
Edward A. Boesiger	Operations Chairman	Lockheed Martin
Charles W. Coale	Organizational Chairman	Lockheed Martin (ret)
Michael J. Eiden	ESA/ESTeC	
David F. Engelbert	NASA ARC	
Carlton L. Foster	NASA MSFC	
Claef F. Hakun	NASA GSFC	
John E. Harbison	NASA MSFC	
Alan C. Littlefield	NASA KSC	
Edward C. Litty	JPL	
Ronald E. Mancini	NASA ARC	
Fred G. Martwick	NASA ARC	
Stewart C. Meyers	NASA GSFC	
Douglas A. Rohn	NASA LeRC	
William C. Schneider	NASA JSC	
Donald R. Sevilla	JPL	
Sterling W. Walker	NASA KSC	
Bowden W. Ward, Jr.	NASA GSFC	
Edward A. Wegner	Lockheed Martin (ret)	

## SYMPOSIUM ADVISORY COMMITTEE

Aleck C. Bond	NASA JSC (ret)
H. Mervyn Briscoe	ESA/ESTeC (ret)
Otto H. Fedor	Lockheed Martin (ret)
Angelo Giovannetti	NASA ARC (ret)
Harvey H. Horiuchi	JPL
Frank T. Martin	NASA GSFC (ret)
John W. Redmon, Sr.	NASA MSFC (ret)
Alfred L. Rinaldo	Lockheed Martin (ret)
Nathan D. Watson	NASA LaRC (ret)

51-19  
50429  
125115

# Life Test Results for the Advanced Very High Resolution Radiometer Scanner

James Lenz\*

## Abstract

The following paper reports the results obtained during a 3.33-year life test on the TIROS Advanced Very High Resolution Radiometer/3 (AVHRR/3) Scanner. The bearing drag torque and lubricant loss over life will be compared to predicted values developed through modeling. The condition of the lubricant at the end of the test will be described and a theory presented to explain the results obtained. The differences (if any) in the predicted and measured values of drag torque and lubricant loss will be discussed and possible reasons for these examined. The life test was funded under NASA contract number NAS5-30384.

## Introduction

The AVHRR/3 Scanner, designed and developed by ITT-A/CD of Fort Wayne, IN, is the meteorological imaging system on the TIROS polar orbiting satellites (Figure 1). The AVHRR/3 is a six-channel scanning radiometer providing three solar channels in the visible-near infrared region and three channels in the thermal infrared range. It scans the earth surface twice a day with 1.1-km resolution at a low earth orbit of 834 km (450 nautical miles) [1].

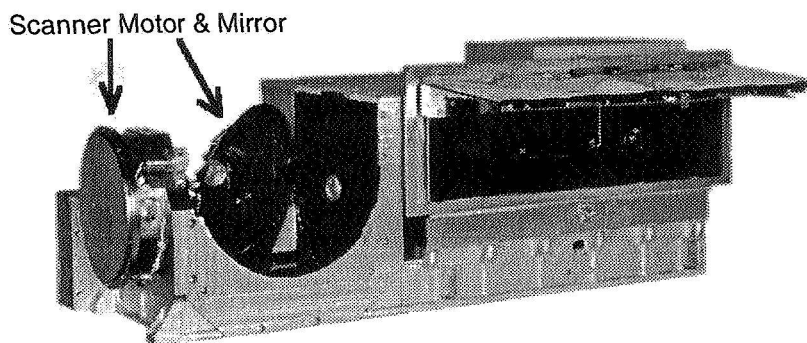


Figure 1. AVHRR/3 Instrument

The earth scanning is achieved through the use of a continuously rotating scan mirror that produces scan lines normal to the spacecraft orbital track. The scan mirror rotates at 360 rpm, thus making the adjacent scan lines contiguous at the sub-satellite position. The scan mirror is driven by an 80-pole, two-phase hysteresis synchronous

---

\* ITT Aerospace/Communications Division, Fort Wayne, IN

motor, which provides torque at a low level, thus making minimum drag torque a must. As a result of this particular motor, bearing torque and torque disturbances are a significant source of concern in the build up and operation of the instrument. Every effort is made to accurately predict the nominal torque and the torque jitter associated with its variation. In order to get a low running torque with almost no variation, a minimal amount of free lubricant must be used. The prediction of lubricant loss over the life of the bearing becomes an important analysis, since the loss of all the bearing lubricant can result in a catastrophic failure of the instrument. A life test unit, representative of a flight configuration, was built and tested. The lubricant loss and bearing evaluation after disassembly were the two main purposes of this test.

## Discussion

### Bearing System Description

The bearing system tested in the life test unit was identical in every way to the flight configuration. Angular-contact, back-to-back duplex pair bearings, lightly preloaded to 18-26 N (4-6 lb) with a contact angle of  $23^\circ$ , were installed onto the scanner shaft with a slight clearance fit. The tested bearing consisted of 440C races (double-honed), titanium-carbide-coated (TiC) 440C balls (24 per ball row), a porous polyimide retainer, fully impregnated with KRYTOX-143 AB oil (vacuum-baked in the oil for a minimum of 12 hours), and lubricated with 14 mg of KRYTOX 143-AB perfluorinated oil as the free lube. Figure 2 shows how the bearings are mounted in a scanner. The cover side bearing is mounted onto the shaft flush against the shoulder of the shaft. Two concentric cylindrical spacers are placed between the bearings with one acting on the set of inner rings and the other on the set of outer rings. The length of the spacers is honed to achieve the desired bearing preload. The mirror side bearing inner ring is secured by tightening a shaft nut to the desired torque (a spacer is used between the bearing and the nut). A retainer is bolted to the housing on both the mirror and cover sides to restrain the outer rings. All spacers, nuts, and retainers are coated with a barrier film to help prevent the migration of oil out of the bearing.

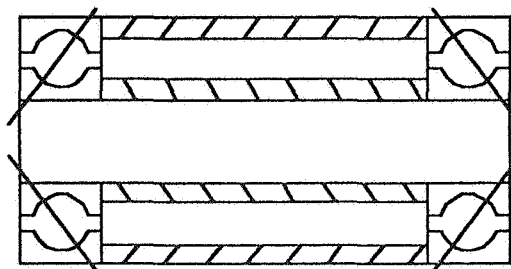


Figure 2. Bearing Configuration



## Drag Torque Modeling

One of the two main concerns in this bearing system, as previously mentioned, is the drag torque. The hysteresis synchronous motor used to operate the life test scanner had a torque capability of 35.3 mN-m (5.0 in-oz) with a bearing torque of 7.1 mN-m (1.0 in-oz). This combination gives a small torque margin of 28.2 mN-m (3.0 in-oz) until end of life.

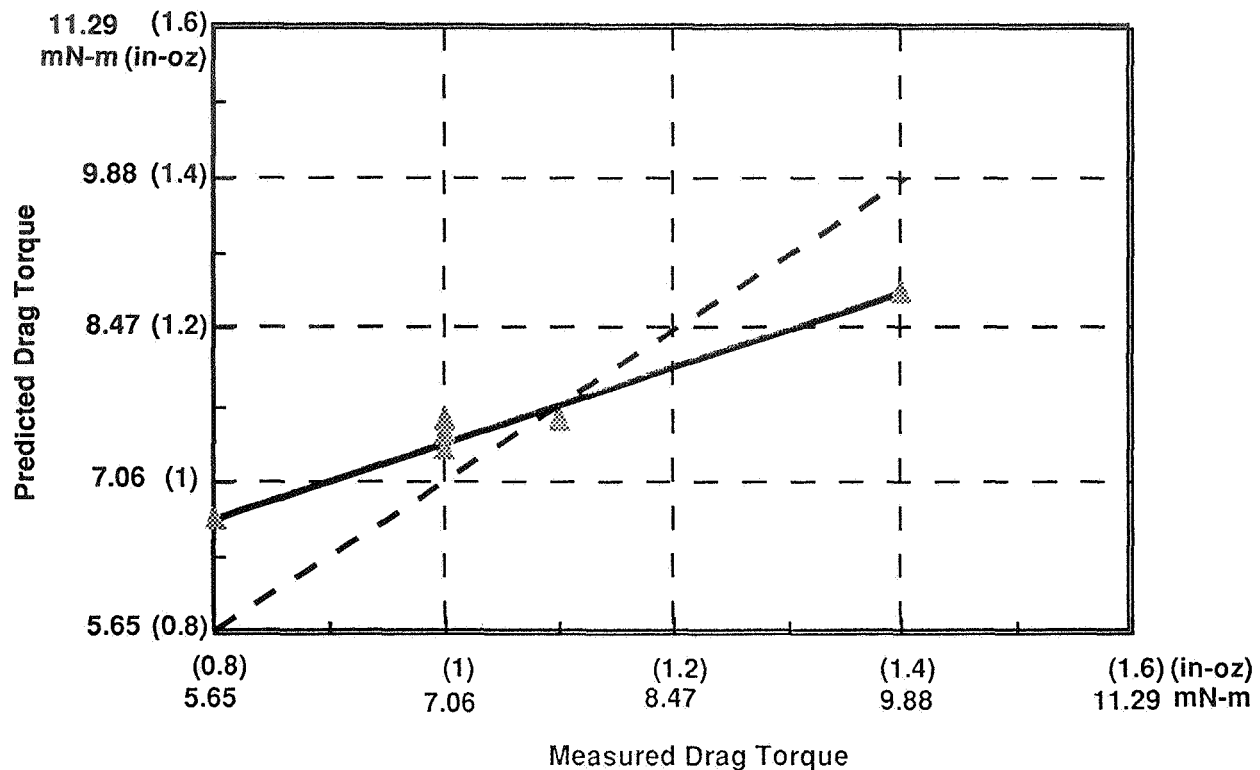
The model used to predict the drag torque was "BEARINGS9", developed by Al Leveille of the Aerospace Corporation [2]. The program analyzes the effects of the bearing configuration and external loads (including thermal loads) on the behavior of the ball bearing. The bearing, housing and shaft geometries, along with temperatures, surface finishes, lubricant and material properties are entered into the program. A lubricant quantity factor, which differs for each lubricant and the amount of lubricant used, needs to be determined prior to use of the program.

Several flight bearings (same type as life test) were tracked, as the actual drag torque during build up and amount of free lube used (same amount of KRYTOX-143AB oil as the life test) during processing were recorded. Several runs of the program were made by entering the bearing geometries and assuming a lubricant quantity factor (the lubricant quantity factor is a constant which helps define the operating condition based on the amount of lubricant used, i.e., for flooded systems the value could be ~3-4, for minimal systems it could be ~0.01).

The predicted drag torques were compared to the measured drag torques, and the lubricant quantity factor was adjusted for each bearing until an exact match was made. The lubricant quantity factors for each of the bearings examined were then averaged to arrive at a single value. Using this value, the program was re-run for each bearing and the predicted vs. measured values of drag torque are shown in Figure 3. The dashed line represents a perfect match based on the quantity factor of 0.343 (average of all other factors). The solid line is the best fit curve through the predicted values. The equation of the best fit line is

$$\text{Actual Torque} = 2 * \text{Predicted} - 1.1$$

Using the lube quantity factor of 0.343 in the "BEARINGS9" model gives a predicted drag torque for the life test unit of 7.6 mN-m (1.07 in-oz). If the best fit curve were the 45° line, this would be our result. Since the data shows a different relationship, we must input this value into the equation of the solid line. Inputting this predicted value of 7.6 mN-m (1.07 in-oz) into the equation for the best fit curve yields a torque value of 7.3 mN-m (1.04 in-oz). The measured torque was 7.1 mN-m (1.00 in-oz), a difference of 4.0%.



**Figure 3. Drag Torque Modeling Results**

### **Lube Loss Modeling**

In an effort to reduce the drag torque, a minimal amount of free lubricant needs to be used in the bearings. The more accurate the prediction of the lube loss, the less lubricant will be required by the bearings to make up for any uncertainty in the prediction. The lube loss for the life test configuration was modeled using the theory established in Scientific Foundation of Vacuum Techniques by S. Dushman [3].

#### Background

The following is a brief overview of the vacuum technique theory employed in this analysis.

The amount of lubricant lost in a bearing system is dependent on three major influences. The first influence is the physical characteristics of the lubricant used. The molecular weight, density and vapor pressure play major roles in determining what quantity of lubricant will vaporize and at what speed it will travel after vaporization. The second major influence is the environment in which the system operates. Temperature and pressure directly influence the speed of lubricant vapor molecules (in the same manner as the molecular weight) and the quantity in which it will vaporize (similar to the lubricant vapor pressure). The final influence that controls the amount of lubricant lost from the bearing system is the mechanism labyrinth system.

The labyrinths need to be designed small enough to restrict the flow of the lubricant vapor and still allow for free rotation of the parts. In the AVHRR design, there are two

types of labyrinths: an axial labyrinth (volume between two concentric cylinders, Figure 4) and a radial labyrinth (volume between two flat discs with flow from the center outward, Figure 5). The ratio of the length of a labyrinth to its gap has a direct relationship to how well the labyrinth will work. For instance, if the length to gap ratio is very large ( $>100$ ), the labyrinth will retard most of the vapor flow through it. Conversely, if the ratio is very small ( $<0.1$ ), most of the vapor will pass without interference.

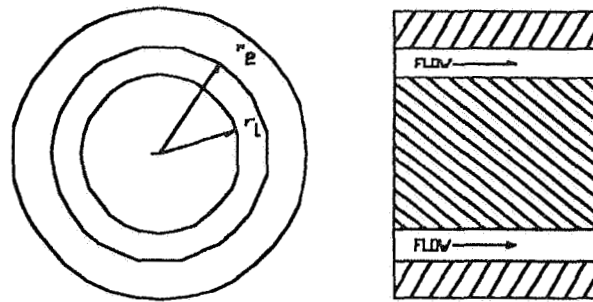


Figure 4. Axial Labyrinth

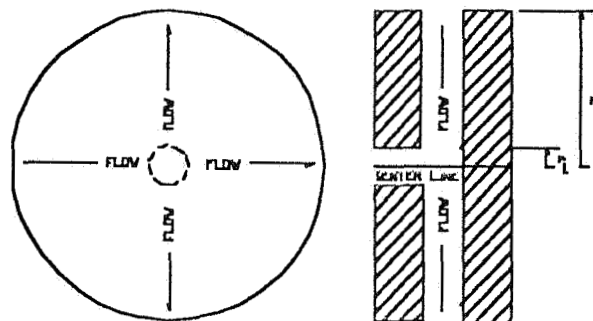


Figure 5. Radial Labyrinth

#### Derivation

A flow rate,  $Q$ , is used to define the amount of lubricant vapor per unit time that escapes from the labyrinth seal of the system. It is defined as:

$$Q = F(P_2 - P_1) \quad \text{where: } P_2 = \text{Pressure at channel entrance}$$

$$P_1 = \text{Pressure at channel exit}$$

$$F = \text{Conductance}$$

The quantity F (conductance) corresponds to the rate of flow per unit difference in pressure between the upstream and downstream ends of the channel. Each gap between the rotating and stationary parts in the system from the bearing through to the outside of the mechanism will be evaluated and a conductance calculated for it. All the conductances for a given bearing will then be added together to arrive at a total conductance for that bearing. The lubricant loss rate can then be predicted based on the conductance and the vapor density.

The conductance for an axial labyrinth (volume between concentric cylinders) is found by following the steps outlined in Dushman. First, the arithmetic mean velocity,  $V_a$ , is found. This is the average speed at which a molecule of a certain vapor will travel.

$$v_a = \left( \frac{8 \cdot R_o \cdot T}{\pi \cdot M} \right)^{\frac{1}{2}} \quad v_a = 1.4551 \cdot 10^4 \left( \frac{T}{M} \right)^{\frac{1}{2}}$$

Where:  $R_o$  = universal gas constant ( $8.3146 \times 10^7 \text{ cm}^2/\text{K} \cdot \text{S}^2$ )  
 $T$  = lubricant temperature in Kelvin  
 $M$  = lubricant molecular weight

The conductance is defined as follows:

$$F = \frac{\frac{4}{3} V_a}{\int_0^L \frac{H_A}{(A_A)^2} dL}$$

Where:  $V_a$  = arithmetic mean velocity (cm/s)  
 $H_A$  = sum of inner and outer labyrinth perimeters (cm)  
 $= 2\pi r_1 + 2\pi r_2 = 2\pi(r_1 + r_2)$   
 Where:  $r_1$  and  $r_2$  are the inner and outer radii  
 $A_A$  = Axial labyrinth cross-sectional area ( $\text{cm}^2$ )  
 $= \pi r_2^2 - \pi r_1^2 = \pi(r_2^2 - r_1^2)$

Which gives:

$$F = \frac{\frac{4}{3} \cdot V_a \cdot \pi \cdot [(r_2)^2 - (r_1)^2] \cdot (r_2 - r_1)}{L}$$

for an infinitely long labyrinth. Since our case is not infinitely long, a correction factor is required.

Clausing deduced a relationship between actual and theoretical conductances.

$$\frac{F_{Theo}}{F_{Act}} = \frac{8 \cdot a}{3 \cdot K \cdot L}$$

Where:  $F_{Theo}$  = theoretical conductance (cm<sup>3</sup>/s)  
 $F_{Act}$  = actual measured conductance (cm<sup>3</sup>/s)  
 $a$  = annular opening, gap ( $r_2 - r_1$ ) (cm)  
 $L$  = length of labyrinth (cm)  
 $K$  = Clausing's factor (based on  $L/a$ )

Substituting the above relationship into the derived conductance (for infinite length) gives an actual conductance based on the length to gap ratio.

$$F_{Act} = \frac{\pi}{4} \cdot V_a \cdot \left[ (r_2)^2 - (r_1)^2 \right] \cdot K$$

Following the same process, a conductance for a radially expanding or contracting labyrinth can be found. The new Perimeter ( $H_R$ ) and Area ( $A_R$ ) values are:

$$H_R = 2\pi r \quad \text{and} \quad A_R = 2\pi r L$$

as  $r$  goes from  $r_1$  to  $r_2$

Since there is a change in the cross-sectional area and perimeter with respect to the radius and not to  $L$ , a new integral must be evaluated.

$$F = \frac{\frac{4}{3} \cdot V_a}{\int_{r_1}^{r_2} \frac{4 \cdot \pi \cdot \rho}{(2 \cdot \pi \cdot \rho \cdot L)^2} dr} = \frac{\frac{4}{3} \cdot V_a \cdot \pi \cdot L^2}{\int_{r_1}^{r_2} \frac{1}{r} dr} = \frac{\frac{4}{3} \cdot V_a \cdot \pi \cdot L^2}{\ln \frac{r_2}{r_1}}$$

The correction factor derived previously also requires modification for the radial change. If we assume that the correction factor will work for a radially changing labyrinth as it does for an axial labyrinth, changes to the gap and length definitions need to be made. The distance,  $a$ , is now equal to  $L$  and not  $r_2 - r_1$ . The length of the labyrinth also changes from  $L$  to  $r_2 - r_1$ .

This changes the Clausing relationship to:

$$F_{Act} = \frac{F_{Theo} \cdot 3 \cdot K \cdot (r_2 - r_1)}{8 \cdot L}$$

Substituting back into the derived equation gives:

$$F_{Act} = \frac{\pi}{2} \cdot V_a \cdot (r_2 - r_1) \cdot L \cdot K \cdot \left( \ln \frac{r_2}{r_1} \right)^2$$

Now that the bearing geometric considerations are determined, the properties of the lubricant need to be examined.

The temperature of the lubricant vapor, the lubricant molecular weight, and the vapor pressure of the lubricant at that temperature define the density ( $\rho$ ) of the vapor:

$$\rho = 1.6035 \times 10^{-5} (M \cdot P) / T \quad \text{g/cm}^3$$

Where: M = molecular weight of lubricant  
T = temperature of lubricant in Kelvin  
P = pressure differential in Torr

The mass loss rate ( $m$ ) is then defined as the density multiplied by the conductance as shown below:

$$m = F \rho \quad \text{g/s}$$

Knowing the initial amount of lubricant in the bearings, a time to complete depletion ( $t$ ) is calculated:

$$t = (\text{initial lube mass}) / m$$

or the amount of lubricant lost over a period of time can be calculated:

$$\text{mass loss} = (\text{time in operation}) (m)$$

#### Empirical Lube Loss Data

The AVHRR life test concluded after 3.3 years of operation in a vacuum environment with no signs of performance degradation (drag torque was ~7.7 mN-m (1.1 in-oz)). The bearings were removed, weighed, and examined. The weights were compared to the original weights, and the lubricant loss was found to be 8 mg for the cover side bearing and 9 mg for the mirror side. The measured results are much different from the predicted values of 3.9 and 18.8 mg for the cover and mirror rows, respectively, using the previously derived equations. An examination into the differences was performed.

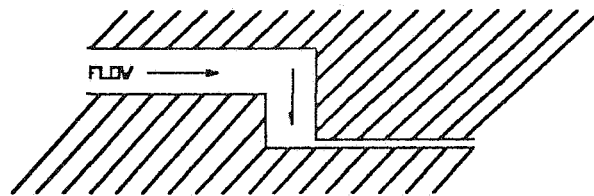
#### Data Comparison

The analytical prediction of oil loss for the life test unit considered each bearing as a separate entity and not as a single system. If the bearings were considered to be a single system, the total measured loss would be 17 mg over the 3.3-year life, compared to the predicted value of 23 mg. This predicted value is closer than the original prediction, but still not close enough to be useful.

The reasons for the difference between the predicted and measured lube loss values is most likely a function of one or more of the following:

1. Vapor pressure of KRYTOX is not correct
2. Sticking factor plays larger role than thought
3. Bearing temperatures are not known
4. Barrier film has a vapor pressure that adds to the system
5. Conductances are not modeled correctly

The vapor pressure value published by the vendor of KRYTOX-143AB ( $2 \cdot 10^{-10}$  kPa or  $1.5 \cdot 10^{-9}$  Torr) [4] was questioned in an earlier analysis performed at ITT and was shown to be different in tests performed at NASA ( $3.3 \cdot 10^{-11}$  kPa or  $2.5 \cdot 10^{-10}$  Torr) [5]. The NASA value was the one used in the analysis, so it should be considered correct. The parts were inspected after disassembly, and no lubricant film was observed on any of the labyrinth parts, thus ruling out that the lube was adhering to the walls of the unit and increasing the local vapor pressure enough to inhibit new vapor from forming. The temperature of the bearings (not measured directly but through thermocouples on the cover and housing) should not increase enough from the thermal model to warrant a doubling of the evaporation. The barrier film is also an area that could help the lubricant remain in the bearings by raising the local pressure high enough to decrease the evaporation rate of the lubricant. The barrier film vendor was contacted about the vapor pressure of the film used and they stated that it was negligible. The conductances were modeled from the works of Dushman and Clausing for straight labyrinths. Our configuration has a straight axial labyrinth making a  $90^\circ$  turn into a radially contracting labyrinth. This is an area that requires another correction factor to account for the bend. The flow from the mirror side labyrinth is a good example of this configuration. Figure 6 shows the configuration and relative sizes of the labyrinths in question.



**Figure 6. Relative Size of Labyrinths**

By taking 75% of the flow through the axial labyrinth and assuming that it makes the turn into the radial labyrinth at any given time, the mirror side conductance prediction gives a lube loss of 14 mg, compared to the 9-mg actual loss. The cover side would not be affected by this factor and has a predicted loss of 4 mg, compared to an actual loss of 8 mg. The sum of these predicted losses is 18 mg, which is close to the measured loss of 17 mg. This observation lends credence to the belief that the two bearings act as a single source. It can be theorized that the two concentric spacers

used between the bearings allow an unobstructed path for the oil vapor to travel from one bearing to the other. The straight path of the oil vapor allows the bearings to act as reservoirs for each other. When one bearing loses too much oil, a pressure drop occurs and pulls vapor from the other bearing of the pair to replenish the bearing that lost the oil (in this situation, it would flow from the cover side bearing to the mirror side).

### **Blackened Lubricant**

An inspection of the AVHRR motor bearings under a microscope (30X magnification) was performed at the end of the life test. The bearing row near the cover end (away from the opening to vacuum) had a continuous band of blackened debris around the inner race and large clumps (~2 mm diameter) on the outer race and retainer. The debris was later identified as polymerized KRYTOX oil. When the polymerized KRYTOX was removed from the races, there was no sign of wear on either of the races or the balls.

The bearing row on the mirror side (near the labyrinth to vacuum) did not show blackened debris but had a thin film that resembled KRYTOX grease. The cloudy, thickened oil could possibly be the initial stage in the degradation of the oil. The inner race had a large wear mark all the way around, and the outer race had a smaller, variable wear mark. The difference in lubricant degradation between the two ball rows could be attributed to either the difference in radial loads as a result of the 17.8-N (4-lb) weight (used to simulate the mirror) or the easier flow path that the oil vapor has from the mirror side bearing to vacuum. The loads caused by the weight were not much different (19.6 and 37.4 N (4.4 and 8.4 lb) for the cover and mirror side rows, respectively), and a 17.8-N (4-lb) difference in a bearing rated for 543 N (122 lb) (3.3%) should not cause degradation to occur in one bearing and not the other.

The other difference, the conductance out to vacuum, has more merit as a possible explanation. The conductance out of the mirror side bearings is calculated to be 25.6 cm<sup>3</sup>/s, while the cover row is 7.5 cm<sup>3</sup>/s. This means that more oil vapor will travel out the mirror side row than the cover side row. If this is the case, and the bearings remain in a state of equilibrium, the loss from both sides must be the same. Meaning, that vapor from the cover side replenishes the vapor from the mirror side after it leaves the system. Since the loss rate is greater on the mirror side, the oil does not remain in the bearing as long as it would on the cover side, thus not accumulating the number of cycles required to become degraded. The cover side oil, however, does not easily leave the system (except to replenish the mirror side) and has much more time to become degraded.

### **Conclusions**

The life test was terminated after 3.33 years of operation and showed no signs of performance degradation or impending failure. The jitter performance at end of life was identical to the beginning value (100% within 16 microseconds). Two measurements that were different from the initial testing were the coast down time (increasing from 32 sec to 76 sec) and the break-away torque (increasing from 2.65 mN-m to 7.94 mN-m (0.375 in-oz to 1.125 in-oz)). The 7.94-mN-m (1.125 in-oz) break-



away torque exceeds the test limit of 3.53 mN-m (0.50 in-oz) and can be attributed to the debris found in the bearing. The increase in coast down time is related to the decrease in free lube in the bearing.

The drag torque model used shows good correlation to empirical data once a satisfactory number of runs are accumulated to get the lubricant quantity factor required for the input. For an initial estimate on the drag torque, where precision is not required, the program is also very good. As with other tools, the more the program is used and the more familiar one becomes with it, the more useful it becomes.

The lubricant loss analysis correlates very well with the measured values once the correction factor for the 90° bend is used. The 75% factor should only be used for this labyrinth combination. Further testing and analyses would be required to get a relationship between labyrinth sizes (at a 90° bend) vs. conductance. A search of published results is being conducted to obtain further information. Based on the results obtained, a time to complete oil depletion will be 6 years, much longer than the 3.33 year requirement.

The blackened lubricant has been shown in many papers to be degraded KRYTOX. The interesting part is that only one of the two bearing rows showed signs of degraded lubricant. The conductance of the mirror side bearing row is much greater than the cover side row, yet they both lost about the same amount of lubricant. This shows that they act as a single source and that one bearing row will act as a reservoir for the other. The difference in the appearance of the lubricant from one row to the other also makes sense, knowing that the lubricant is more prone to leave the mirror side bearing and does not remain there long enough to accumulate the cycles required to degrade.

## References

1. Molisani, J. "TIROS KLM-HIRS/3 Filter/Chopper & AVHRR/3 Scanner Life Test Final Report." Prepared under NASA Contract No. NAS5-30384, June 1995.
2. Leveille, A. "BEARINGS9." Computer Program.
3. Dushman, S. and J. Lafferty. Scientific Foundations of Vacuum Techniques, Wiley and Sons, 1962.
4. "KRYTOX Product Information." Distributed by Dupont Corporation.
5. Zurmehly, E. "Correction of HIRS Bearing Lube Calculations." ITT Technical Memorandum, March 1989.



52-37  
50430  
125116

## Space Telescope Fine Guidance Sensor Bearing Anomaly

S. Loewenthal\*, J. Esper\*\*, J. Pan+ and J. Decker++

### Abstract

Early in 1993, a servo motor within one of three Fine Guidance Sensors (FGS) aboard the Hubble Space Telescope (HST) reached stall torque levels on several occasions. Little time was left to plan replacement during the first servicing mission, scheduled at the end of '93. Accelerated bearing life tests confirmed that a small angle rocking motion, known as Coarse Track (CT), accelerated bearing degradation. Saturation torque levels were reached after approximately 20 million test cycles, similar to the flight bearings. Reduction in CT operation, implemented in flight software, extended FGS life well beyond the first servicing mission. However in recent years, bearing torques have resumed upward trends and together with a second, recent bearing torque anomaly has necessitated a scheduled FGS replacement during the upcoming second servicing mission in '97. The results from two series of life tests to quantify FGS bearing remaining life, discussion of bearing on-orbit performance, and future plans to service the FGS servos are presented in this paper.

### Background

In April of 1990, the HST was launched into Low Earth Orbit (LEO) aboard the space shuttle Endeavor. Soon after launch, it became apparent that the required HST pointing precision could not be achieved due to the presence of thermally-induced jitter originating from the large, flexible HST solar arrays. In addition to the jitter problem, HST operations were compromised by spherical aberration in the HST primary mirror, the presence of which was confirmed several months after HST deployment. Plans were drawn up to conduct a servicing mission to remedy these problems. Periodic servicing of the HST using the space shuttle is necessary, and is possible because the HST is in LEO and designed to facilitate such on orbit servicing. The HST First Servicing Mission (FSM) occurred in December of 1993, and achieved the goals of correcting the solar array jitter and spherical aberration.

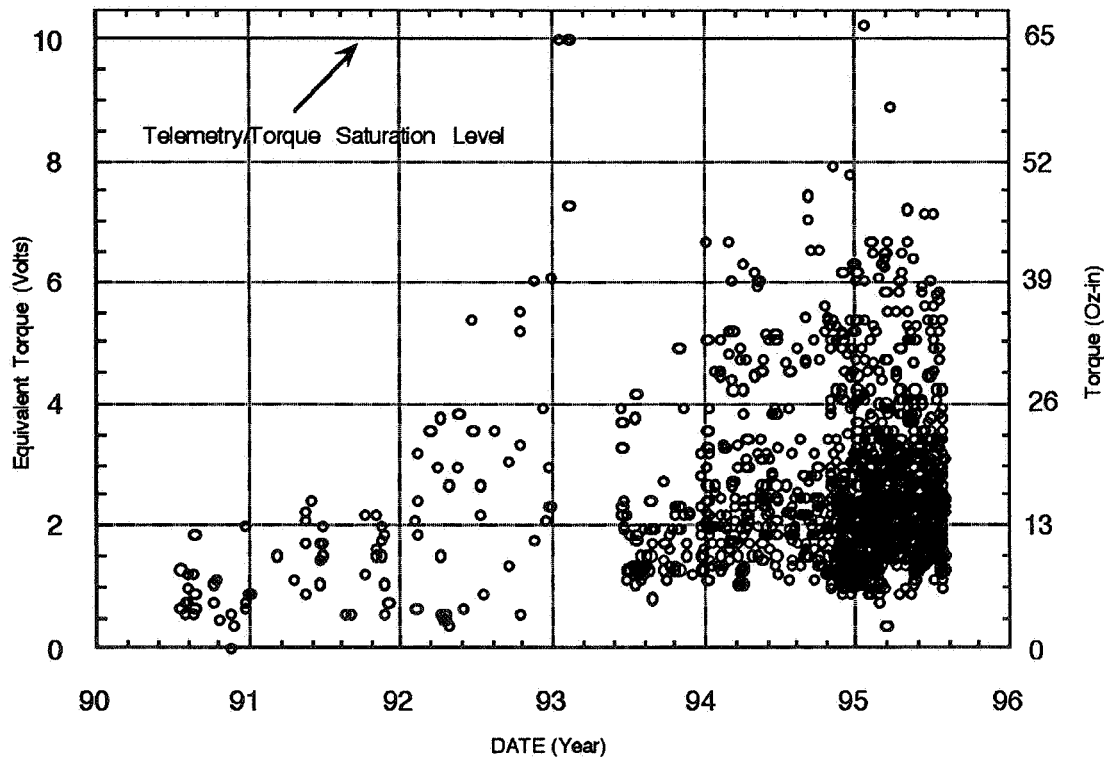
In the period prior to the FSM, HST operations were tailored to achieve the best possible science in spite of the operational problems noted above. To that end, the FGS's aboard the HST were operated in a manner which helped improve the HST pointing performance, but did so at the cost of incurring degradation within the Star Selector Servo (SSS) ball bearings. As will be presented, FGS bearing degradation in general has been strongly correlated with a "Coarse Track" mode. During the first three years of HST orbital activities, this mode was implemented due to its robustness in maintaining star lock during strong disturbance periods caused by the thermal "snapping" of the now replaced solar arrays. In CT, the servo bearings rock back and forth  $\pm 0.75$  degree or less for extended periods, causing depletion of the oil under the

---

\* Lockheed Martin Missiles and Space Co., Sunnyvale, CA  
\*\* Allied Signal Technical Services Corp., Columbia, MD  
+ Space Telescope Science Institute, Baltimore, MD  
++ NASA Goddard Space Flight Center, Greenbelt, MD

ball contact and inhibiting oil replenishment. At a frequency of 1 Hz, tens of millions of CT cycles were accumulated causing degradation of the Bray 815Z oil in the contact and the formation of lubricant debris (friction polymer).

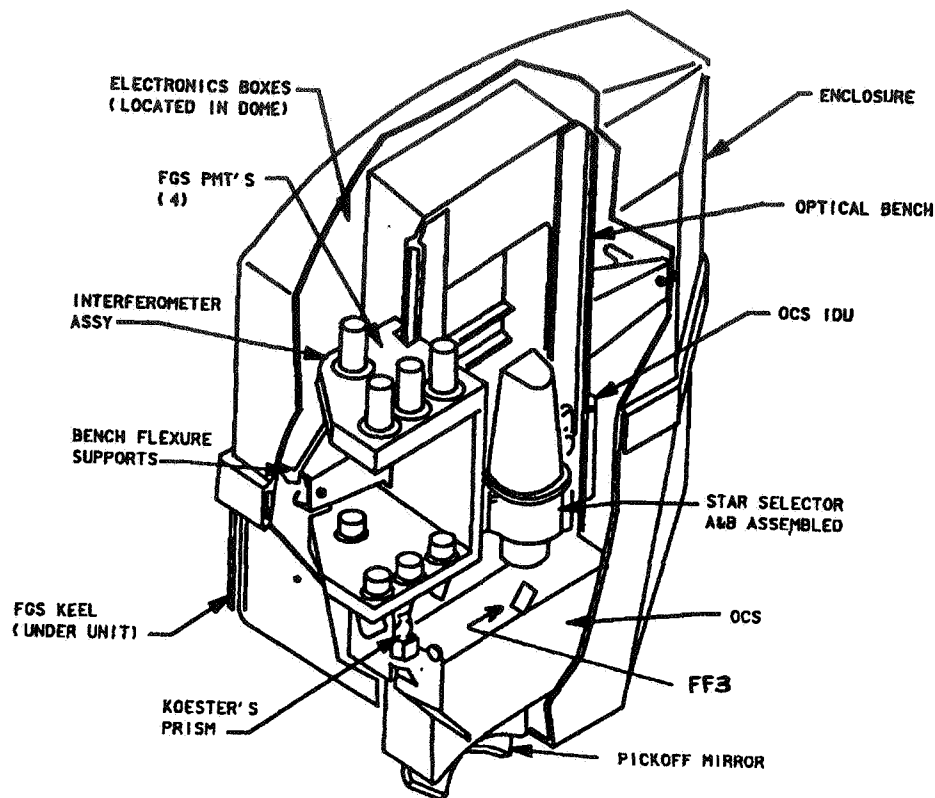
The presence of this degradation became apparent early in 1993, when HST telemetry revealed instances of high torque in one of the FGS bearings. In fact, the excessive torque occurrences resulted in operational interruptions and some loss of HST science observations. Torque levels of the bearings in one of three FGS's on-board HST, reached motor saturation levels of approximately 10 volts equivalent servo torque (1 volt  $\approx$  46 N-mm or 6.5 oz-in) as shown in Fig. 1 (see early '93 time frame). Although temporarily stuck, subsequent operations freed it. This anomalous bearing behavior led to the investigation outlined in this paper.



**Figure 1 - FGS 2A Torque history from launch. Note motor torque saturation in early '93 and then temporarily recovers with change to Fine Lock operation.**

### **Fine Guidance Sensor Description**

The Fine Guidance Sensors are electro-optical, interferometric instruments used to lock and track target stars. About the size of baby grand piano (Fig. 2), the FGS is perhaps the most precise pointing system ever built. It is capable of holding 0.007 arc secs of pointing accuracy over a 24 hour period; equivalent of targeting a dime over 400 km. At the heart of the FGS is the bearing-motor-encoder system which positions optics inside the SSS assemblies (Fig. 2).



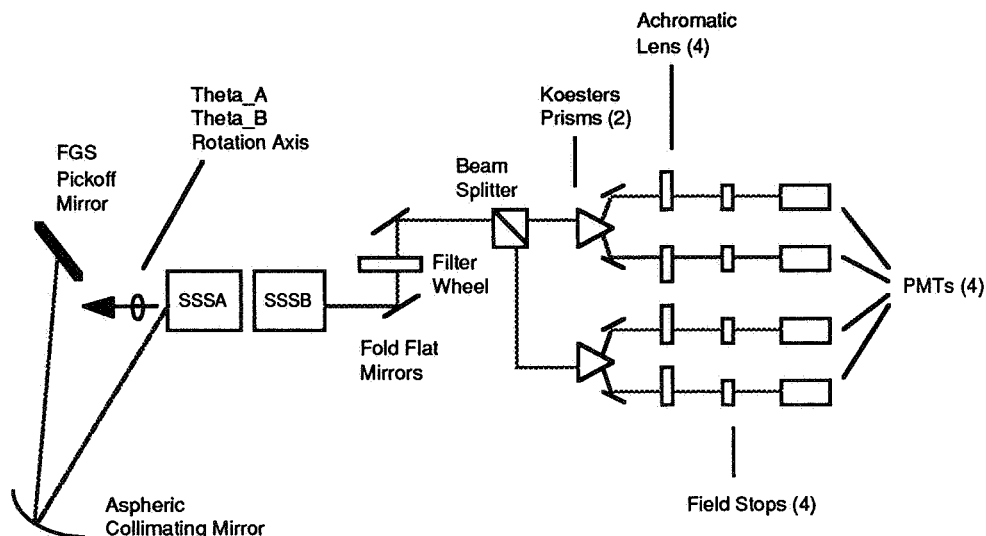
**Figure 2 - FGS optical and mechanical arrangement showing Star Selector Servo location.**

**Operation** - The FGS operation consists of comparing guide star intensity measurements so as to achieve a prescribed amplitude level at each of four Photo Multiplier Tubes (PMT). The intensity at each PMT is in turn dependent on the amount of wave front tilt falling onto the Koesters prisms within the FGS optical train, illustrated in Fig. 3. Initially, a combination of spacecraft and FGS optical element motion will set the intensity levels within a range for which "lock" is defined. Once the FGS is locked onto the target, any deviations will be quickly corrected by repositioning the spacecraft in order to maintain the target on axis (zero wave front tilt).

As shown in Fig. 3, the light from the HST primary mirror is intercepted by the FGS pickoff mirror and channeled through the Star Selector Servo "A" and "B" assemblies. These SSS assemblies can be moved independently of each other to affect the tilt of the wave front onto the Koesters prisms. The centerpiece of each SSS assembly is a 21-bit encoder, brushless DC motor supported in large, thin section angular contact ball bearings.

**Target Star Acquisition** - In order to achieve lock in the first place, the FGS must go through a target star acquisition process. The SSS assemblies optically positions a 5 arc-second-squared, Instantaneous Field of View (IFOV) onto a 60 arc-minute-squared, Total Field of View (TFOV) (see Fig. 4). Hence, by moving the SSS

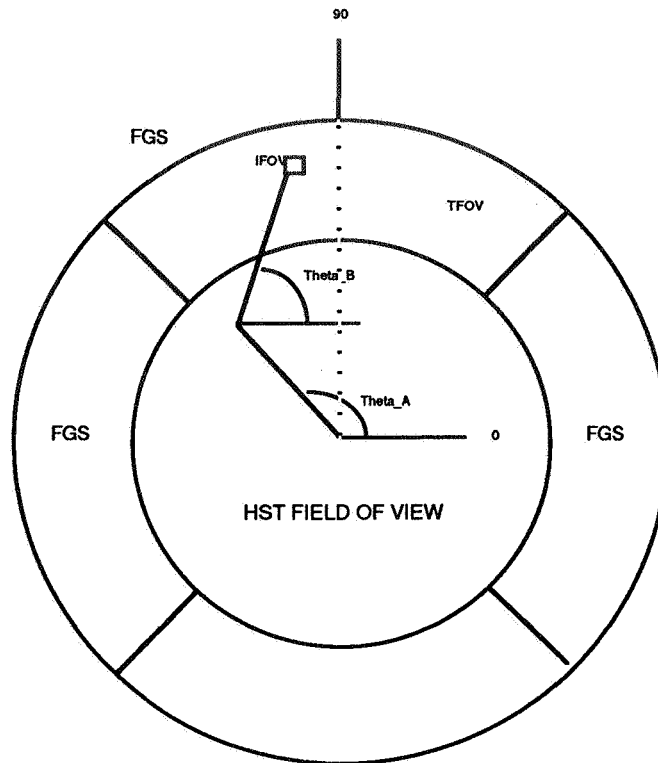
assemblies about their rotation axes, the IFOV can be maneuvered anywhere in the TFOV. Briefly, the SSS is slewed (*#58 command*) to the start of a *spiral search* pattern, where the angles oscillate at increasing amplitudes, reaching a maximum amplitude of about 2 degrees (4 degrees full stroke). Following this is a brief period of Coarse Track (CT) oscillations, where the target is initially acquired prior to transitions to either Fine Lock (FL) or CT operations (described next). In the case when the system transitions into FL, a second slew (*vehicle offset*) is carried out to position the astronomical target at the science aperture. To provide a realistic ground test, these modes of operation were emulated during the second of two series of bearing life tests.



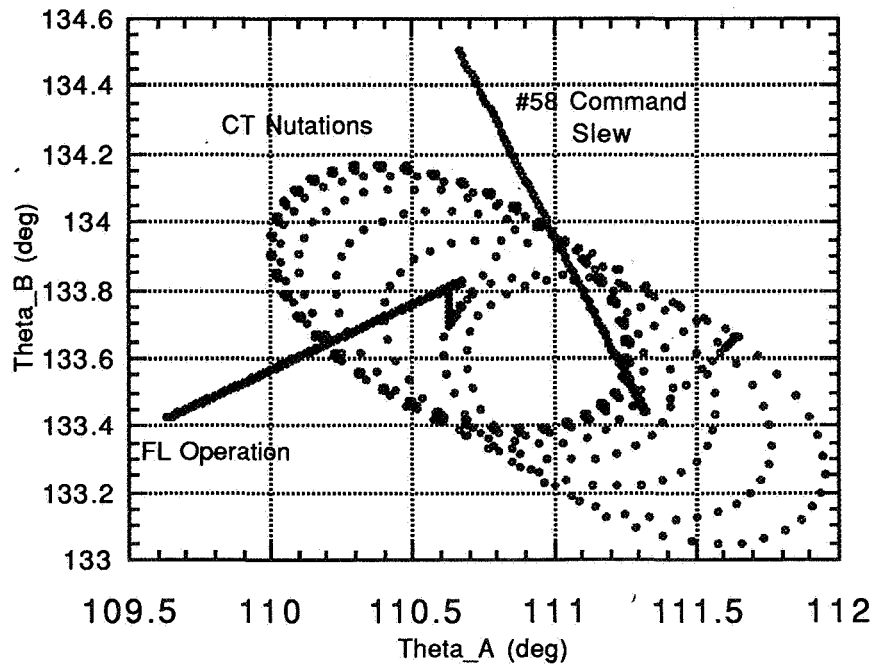
**Figure 3 - FGS optical train showing optical path through SSS A & B assemblies and Koesters prisms to PMT's**

Coarse Track and Fine Lock - The tracking operation begins once the target star has been locked on. There are two different tracking modes: Coarse Track (CT), and Fine Lock (FL). These two operational modes have the greatest impact on long term FGS bearing life. During CT operation, the IFOV is made to nutate about the center of light of the target star. This nutation cycle is accomplished by oscillating each SSS about their rotation axes with an amplitude of approximately  $\pm 0.75^\circ$  or less, forming the elliptical pattern appearing in Fig. 5. The life tests were geared toward simulating the CT mode of operation, the suspected cause of SSS bearing degradation.

On the other hand, FL operation does not involve any SSS nutation, but rather the IFOV is held relatively fixed at the target star. The only motion is the result of spacecraft jitter, generally less than  $\pm 10$  arc-seconds of SSS rotation. FL operation with its microscopic SSS motions were not considered to contribute to bearing degradation, since the resulting bearing ball motions were believed within the elastic (Dahl friction) regime. This too was to be proven by the bearing ground test.



**Figure 4 - FGS Field of View showing both SSS “lever arms” (A and B) in terms of corresponding servo (rotation) angles, Theta\_A and Theta\_B**

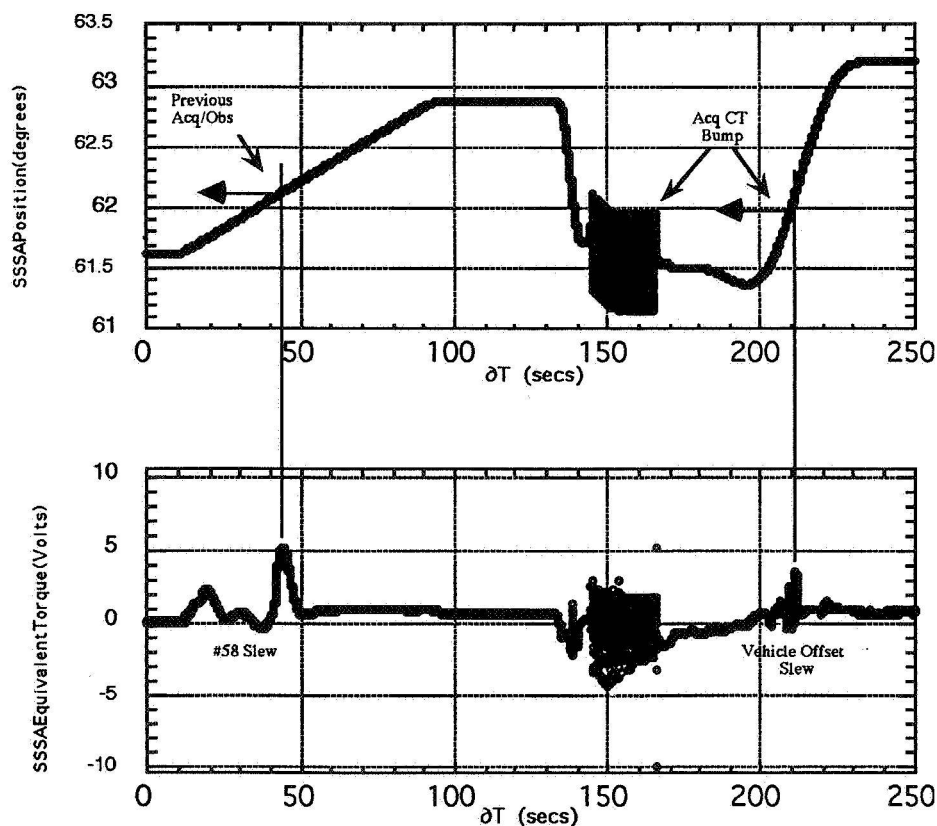


**Figure 5 - Coarse Track nutations during a guide star acquisition (spiral search is negligible in this case)**

## Anomalous Flight Data

As a result of the millions of CT cycles accumulated, all FGS bearings exhibited anomalous torque spikes or bumps at various times during their operational use. However, only the bearings from the FGS 2A servo showed serious degraded performance. Although such events may occur at other times, there are three occasions where their appearance have been trended over time to monitor bearing health: during a #58 slew, during a vehicle offset, and during "rate reversals". The latter is a "target acquisition" maneuver in the reverse direction during a vehicle offset slew. This reversal maneuver has recently shown to be a problem for FGS 1B.

As illustrated in Fig. 6, high torque is consistently observed in FGS on-orbit data when a FGS bearing slews past the its end of CT stroke position. Of the 6 SSS's, the CT bumps appear largest in Servo 2A and smallest in Servo 2B. The torque magnitude of a CT bump is, on average, proportional to the duration of CT operations. The longer a CT operation lasts, the bigger a resultant CT bump until some limit is reached. This limit value grew with mission time, causing the anomalous torque observed in Fig. 1.



**Figure 6 - Correlation of torque bumps with bearing operations.**  
Notice that torque bumps (bottom) correspond to end of CT stroke at  $\approx 62$  deg (upper)

From telemetry data it appeared that the CT bump heights (torque) were sequentially reduced as balls compressed them during a slew. Rather than hard impediments, it suggested that a CT bump resulted from the balls running over some kind of debris



ridges that had accumulated along the bearing races and perhaps the sides of the balls during the limited back-and-forth motion of each ball in CT operation.

### **First Bearing Life Tests**

Two series of accelerated bearing life tests were conducted to investigate the problems observed on orbit. The first of these was conducted shortly before the first servicing mission in December of 1993. It was crucial to have results as soon as possible to support a replacement decision for FGS 2A, the most degraded servo. The previously unplanned replacement of this FGS represented a major addition to the servicing mission, which was already pushing the limits for EVA time and little training time remained for the SSTS crew to practice such a replacement. The key goals of the test were to: (a) determine the likely remaining life of the FGS bearings, (b) assess life benefits from minimizing CT operation in favor of FL operation, believed more benign and (c) identify the likely failure mechanism.

Test Conditions - The first life tests consisted mainly of Coarse Track motion, the primary suspected cause of accelerated lubricant degradation and subsequent debris related torque bumps. While long periods of dithering motion over the same spot on the bearing is difficult for any oil, it is particularly troublesome for the Bray 815Z, a perfluorinated ether oil, which contains no protective boundary lubricant additives.

It was estimated that approximately 21 million  $\pm 0.75$  deg CT cycles were accumulated at the time of FGS 2A failure, some 33 months after launch. To obtain test data quickly, the first 3 years of the FGSs' primarily CT operation were compressed into 13 test weeks by accelerating the CT frequency from 1 Hz to 3.5 Hz and eliminating idle time. This acceleration factor still maintained the bearing's boundary mode of lubrication and expected wear out failure mode. Also to save test time, the test excluded other FGS slew modes, which contributed little to the bearing problem. However, periodic 0 to 40 to 0 deg #58 command slews were simulated every 19,000 cycles, since these help redistribute the debris and re-wet the contact.

The second phase of the tests were to evaluate the expected life that could be obtained with FL operation. Hopefully, the primary use of FL would enable FGS 2A to operate until the second servicing mission, scheduled some 3 years later. During FL, the bearings "strain" through a very small angle ( $< 10$  arcsec) to compensate for the small amount of spacecraft jitter caused by the reaction wheels, solar arrays and any other contributing sources. This small motion was expected to be primarily in the elastic range of the bearing before breakaway (so-called Dahl regime) and below that resulting in fretting damage. It was estimated that  $\pm 12$  asec stroke would envelope the worst case displacement observed during the first 3 years of service. Projected usage indicated that an additional 160 million cycles of FL would be accumulated before the second servicing mission. A FL cycle rate of 16 Hz would permit completing the test in less than 20 weeks.

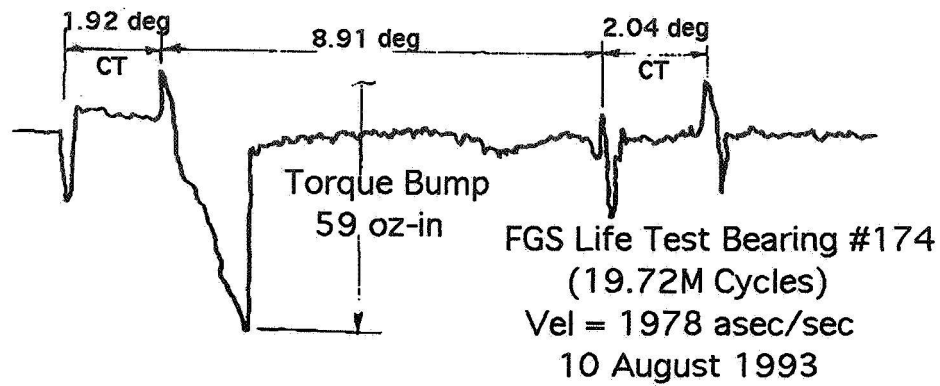
Test Bearings - In the flight servos, each bearing assembly consisted of a pair of class 7+, thin-sectioned, 25 deg angular contact ball bearings mounted in Beryllium structure, separated by 3.6 cm long, inner and outer preload spacers and hard

preloaded in a back-to-back configuration. These bearings were designed to provide maximum stiffness and precision in supporting the servo's 21-bit encoder and, as a consequence, were unusually torque sensitive to lubricant debris and thermal gradients.

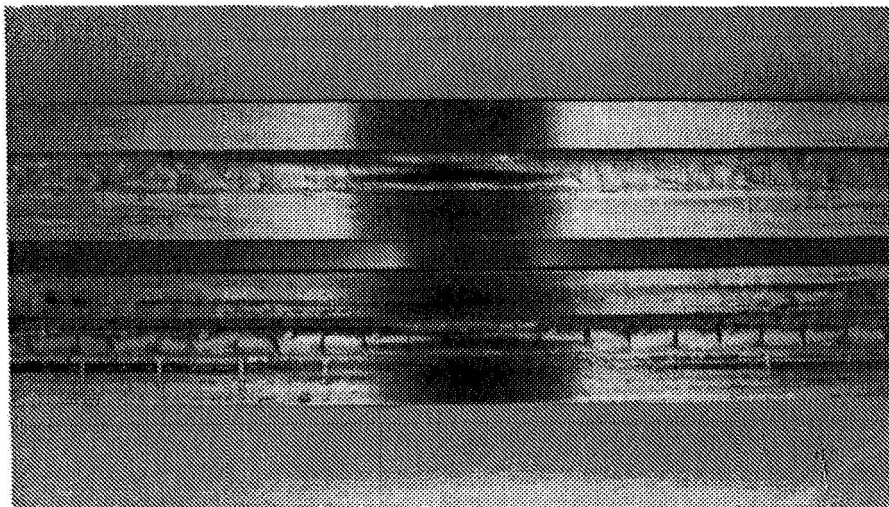
Off-the-shelf angular contact ball bearings were fortunately available that closely matched the flight bearings' geometry, except that the test bearing's contact angle was 30 instead of 25 deg and the PTFE alternating ball toroids were about 2/3 the thickness of the flight bearings' toroids. To assure a conservative test, an oil charge of 100 mg of Bray 815Z oil was used, instead of the flight's 375 mg, in order to help compensate for the flight bearings' losses during the 7 years of storage and 3 years of orbital time. A trycrystalline phosphate (TCP) pre-coating on the races was used in keeping with the flight bearings. The flight and test bearings were both made from 440-C steel, had bore diameters of 165mm (6.5 in), outside diameters of 190 mm (7.5 in) and contained 88 balls of 4.8 mm (3/16 in diameter per row. The bearings were hard-preloaded to 670 N (150 lb), producing a relatively low, maximum Hertz stress of 0.83 GPa (120 Ksi).

Test Rigs - Lockheed's computer controlled, turbo-vacuum pump bearing life test rigs were used for the CT life tests. Vacuum levels of  $10^{-6}$  to  $10^{-7}$  torr and temperatures of 20 to 22°C were maintained to simulate on orbit conditions. The FL tests required the construction of a special 4-bar, bell-crank mechanism that could accurately impose the desired  $\pm 12$  arc sec motion. The motorized bell crank reciprocated a linkage attached via flex pivots (no dead band) attached to a crank arm coupled to the inner race of the test bearing. A proximity probe measured bearing rotation angle while a load cell monitored bearing torque.

CT Results - Both test bearings showed evidence of high torque after CT cycling near the 20 million cycle point. This, coincidentally, was about the same number of CT cycles accumulated by the FGS 2A bearing when it began to get stuck and of similar torque magnitudes. Torque levels of 424 N-mm (60 oz-in) or greater were recorded when the bearing was slewed past the end of CT motion, designated by torque bump spacing on the order of 2 degs in Fig. 7. Debris primarily from degraded lubricant, piles up at the end of the CT stroke creating a barrier for the ball to roll over. This end-of-stroke debris location closely corresponds to the theoretical ball spacing of 8.9 degs, labeled between the start of the large torque bump and the following one in Fig. 7. Careful disassembly of the bearing clearly show debris ridges at regular ball spacing as shown in Fig. 8. Telemetry data from the flight bearings also showed similar end-of-CT stroke spacing for the torque irregularities.



**Figure 7 Torque Bump Trace for Test Bearing at 19.7M Cycle, showing Bump Spacing at CT End-of-Stroke Locations**



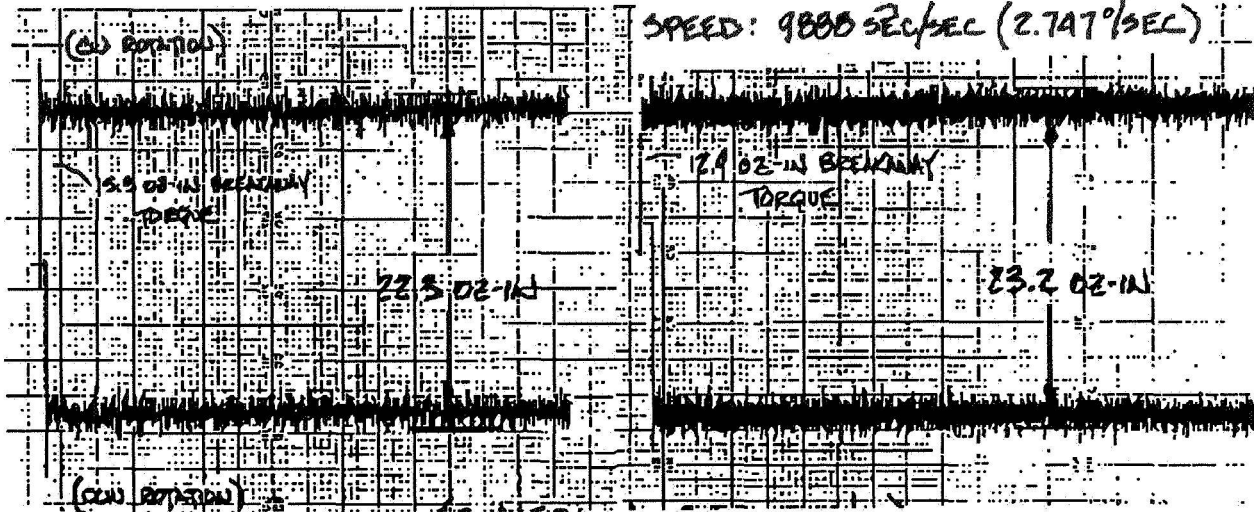
**Figure 8 - Debris Ridges Observed at Ball Spacing Intervals on Post Test Disassembled Bearings**

FL Results - No noticeable change in torque signature was observed for the test bearing receiving 178 M cycles of FL after it had already been exposed to nearly 35 M CT cycles as shown in Fig. 9. To confirm these results, a second, but virgin, test bearing was tested to 105M cycles of FL and it too exhibited no detectable degradation.

COURSE TRACK TO 24.5 M CYCLES

E.D.L. COURSE TRACK (24.5 M CYCLES) +  
ADDITIONAL 178 M CYCLES FINE LOCK

SPEED: 9888 SEC/SEC (2.747%/SEC)



**Figure 9 - Bearing torque signature showed little change after 178M cycles of Fine Lock dithering after previously receiving 35M cycles of CT.**

## **Second Bearing Life Tests**

On the basis of the results from the first set of tests, a change in operation to primarily FL operation (>90%) was uploaded to the flight FGSs in the April 93 time frame. A marked decrease in FGS 2A torque was observed (Fig. 1) and a decision not to replace the servo for the December repair mission was made. However, the question remained as to how long this and the other servos would continue to last with the normal modes of operation which still include some CT operation. Furthermore, could replacement be avoided again during the second servicing mission, scheduled for in the spring of '97.

A second set of life tests were planned. These tests had greater fidelity in emulating the various modes of on-orbit operation and simulating bearing life far into the future, up to the 4th potential service mission in the year 2002. Unlike the first set of tests conducted in only a few months, the acceleration factor would be reduced to nearly unity and the test bearings would be "identical" to the flight ones in all aspects. Another objective was to evaluate the effectiveness of current on-orbit trending techniques and to establish the benefits, if any, of periodic maintenance slews on the recurrence of torque bumps. A final goal was to quantify life improvements with an "improved" bearing design for a future FGS replacement. This bearing maintained the same geometry as the flight bearings to facilitate replacement, but a more wear resistant Neopentyl Ester (NPE) oil containing a boundary lubricant additive (TCP) was substituted for the Bray 815Z. Also the ball toroid thickness was slightly reduced to provide a little more clearance than the flight unit. This time all test bearings were lubricated with the flight charge of 375 mg of oil.

**Duty Cycle** - The test duty cycle was divided into two parts. The first part "aged" the two "flight" bearings using the same CT intensive operation that was in effect for the first 37 months of flight (23 million cycles). The 4 FGS motion modes (vehicle offset, #58 command, spiral search and coarse track), as described earlier and defined in Table I, became part of the test profile.

The second part of the test exposed the test bearings to the current Fine Lock (FL) intensive operation for the next 8 years (to 2002). During this period another 7 million additional CT cycles was expected to be accumulated, representing just 10% of the past CT usage rate. Actual Fine Lock operation was eliminated from the test profile since it produced no detectable degradation of the two test bearings during the first life test. This saved extra schedule time and the potential bias to the test from switching between different test rigs for FL and CT operation.

In addition to the life test profile, a special on-orbit diagnostic test, referred to as the "4-Rev Test" (see Table I), was periodically performed. This was to evaluate the effectiveness of this on orbit trending technique used to forecast flight bearing degradation.

**Results** - The torque time histories of the test bearings (see Fig 10) showed that one of the flight test bearings showed significant signs of degradation after about 20 million CT cycles. This was similar to that observed in the first test and the observed on-orbit anomalies of FGS 2A. Somewhat surprisingly, the torque of the second "flight" bearing showed little change through 30 million cycles, beyond the mission equivalent of 2002. This paralleled the large scatter observed with the on orbit bearings in that the bearings in FGS 2A were clearly more degraded than the others in the remaining 5 Star Selector Servos (see CT bump flight data in Fig. 13). The bearing with the NPE oil showed relatively stable performance, despite the harshness associated with 30 million CT cycles.

Like FGS 2A, the torque of the degraded test bearing also approach the equivalent 10 volt torque saturation level ( $\approx 460$  N-mm (65 oz-in)) after slewing past debris left from prior CT cycling as shown in Fig. 11. To generate such large torque bumps, it generally required more than 20 or 30 minutes of CT cycling. In this figure, the effect of subsequent ball roll overs in "flattening" the debris can be seen.

**Table I - Test Profile**

First 37 months of Flight 4/90 - 6/93 (23M CT Cycles)

Motion Type	Direction	Angle deg	Rate deg/sec	Cycles
Continuous (Veh Offset)	CCW	8	1.112	1
Continuous (#58 com)	CW	30	1.868	1
Gimbal (Spiral)		$\pm 1.92$		10
Gimbal (CT)		$\pm 0.65$		2301

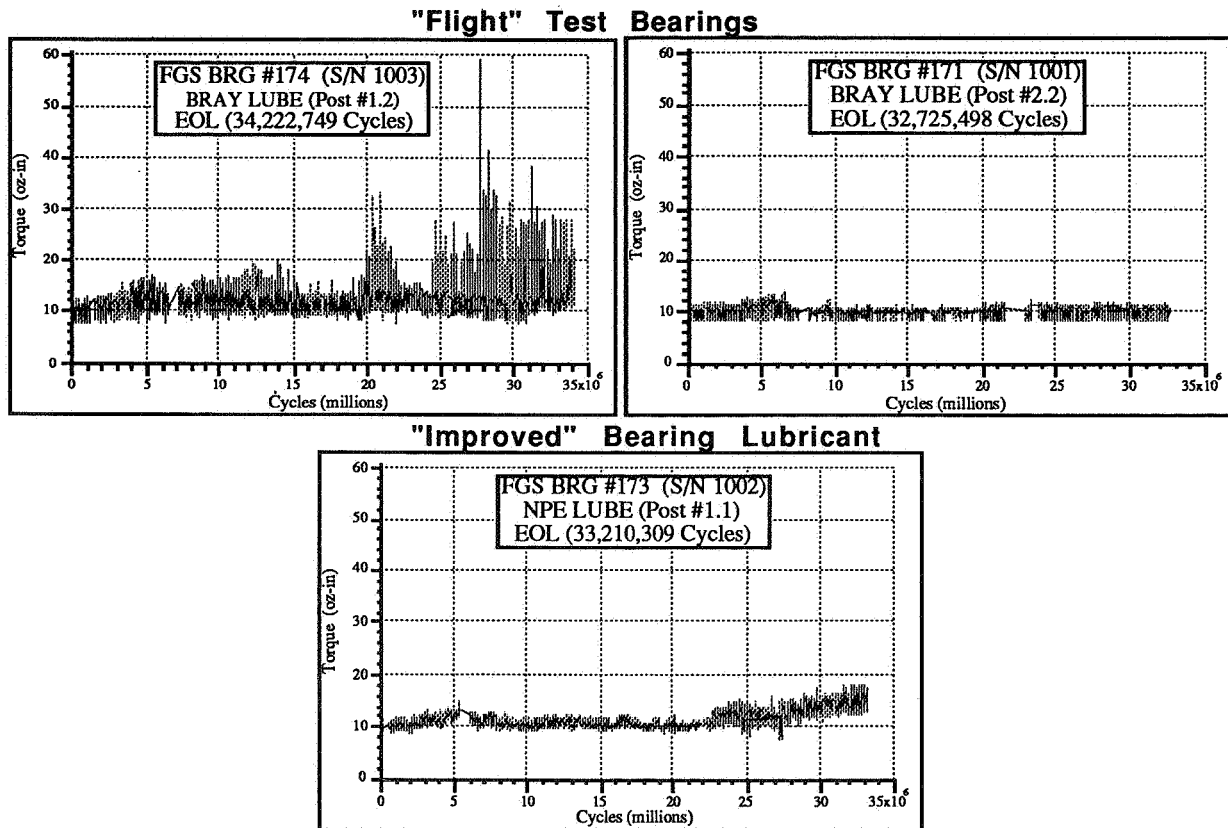
Next 110 months of Flight 6/93 - 9/02 (30M CT Cycles)

Motion Type	Direction	Angle deg	Rate deg/sec	Cycles
Continuous (Veh Offset)	CCW	11	1.11	1
Continuous (#58 com)	CW	42	1.43	1
Gimbal (Spiral)		$\pm 1.16$		4
Gimbal (CT)		$\pm 0.44$		249

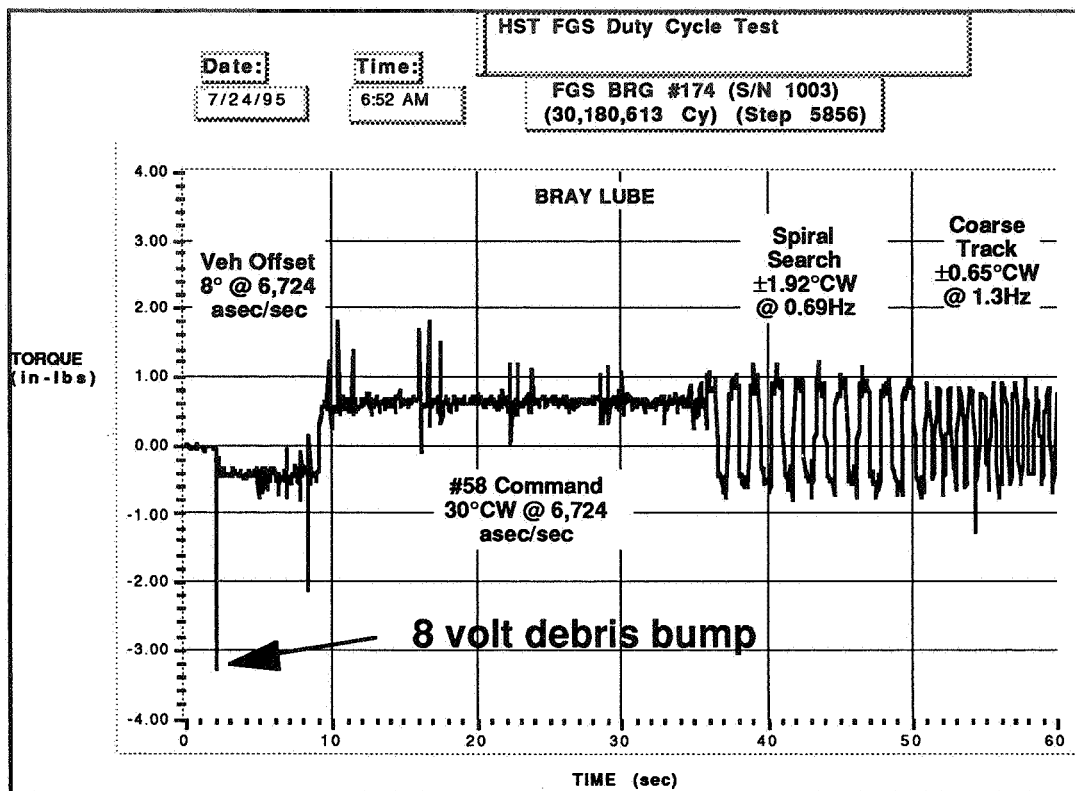
**Special Profile (4-Rev Test)**

Speed deg/sec	Direction	Revs deg
1.87	CW	1
1.87	CCW	2
0.55	CCW	1

The 4-Rev diagnostic test followed the flight experience in that it was sensitive to DC level shifts in running torque and not transient torque bumps. As such it was used mainly for long term health monitoring of more permanent changes to bearing condition.



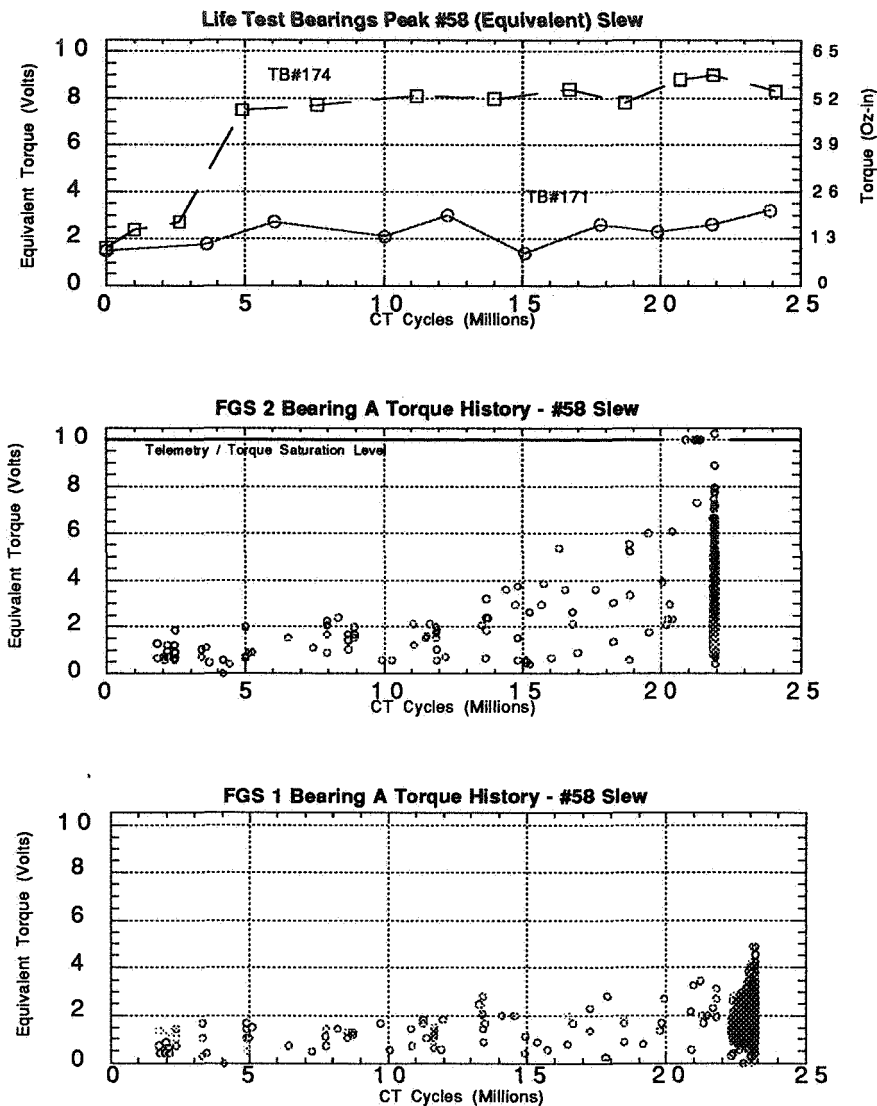
**Figure 10 - Running torque time histories of test bearings showing degradation of one Flight bearing at 20 M Cycles. Torque levels of the other test bearings were relatively stable despite the harshness of CT cycling.**



**Figure 11 - Ground test bearing at 30 million Coarse Track cycles showing large torque bump due to piled up debris at end of CT stroke. Note the reduction in bump height in subsequent roll overs at ball spacing intervals.**

Comparison with Flight Data - It is instructive to note that torque levels much higher than 10 volts was rarely observed, as if there was an equivalent yield strength to the lubricant debris. This is illustrated in Fig. 12 which shows a comparison between ground and on-orbit bearing peak torque bumps during Command #58 slews. Note that the torque of test bearing # 174 seems to limit out between 8 and 9 volts after 5 million CT cycles. Similarly, on-orbit bearing FGS 2A has gotten stuck and then freed around the 10 volt saturation level on numerous occasions in early '93, suggesting that it too reached some limit torque level.

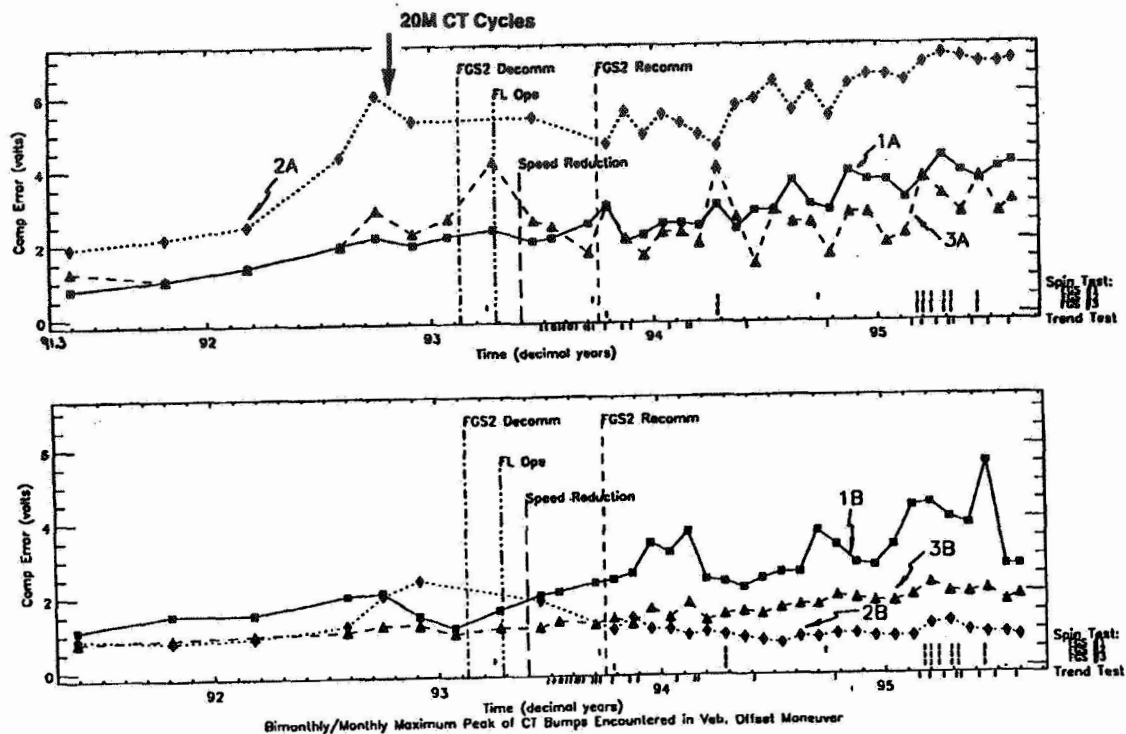
Fig. 12 shows that peak equivalent torque from test bearing #171 seems to correlate well with that from a typical flight FGS bearing 1A. Although test bearing #174 appears to reach about the same torque saturation limit of flight FGS 2A, it does so at considerably fewer CT cycles.



**Figure 12 - Comparison of ground and flight bearing torque data. Test bearing #171 correlates with a typical FGS 1A but #174 reaches torque saturation sooner than FGS 2A.**

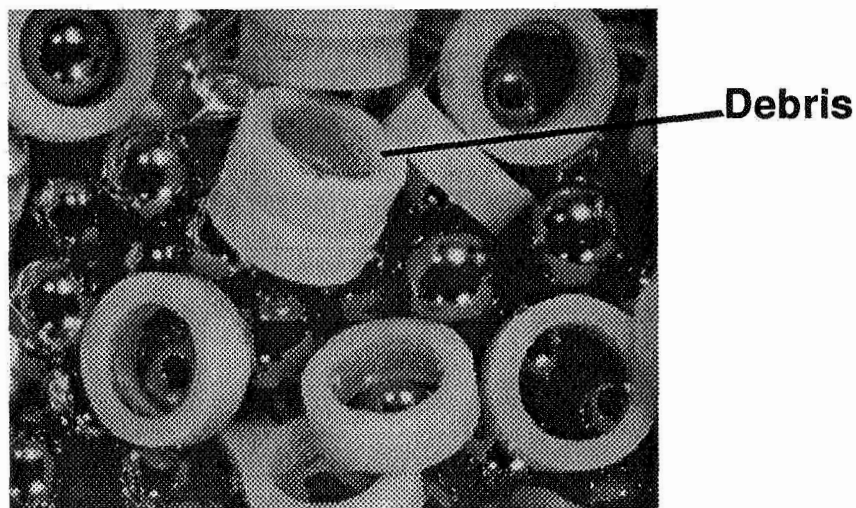
The relative on-orbit health of the 6 sets of FGS bearings can be judged from Fig. 13. In this figure, the peak CT bump equivalent torque is recorded after a brief period (< 30 sec) of CT cycling during star acquisition. While the switch to primarily FL operation in early '93 help to stabilize FGS 2A's performance as well as that of 3A throughout '93, the torque started upward again about a year later. Also, the torque levels of the remaining FGS servos, although considerably lower than 2A, are also trending upward. Apparently, the lubricant chemical degradation process initiated by many millions of CT cycles is still continuing with time, even though the bearing duty cycle is considerably less damaging than before.





**Figure 13 Peak CT bumps of on-orbit bearings during acquisition showing upward torque trends despite minimizing CT cycling.**

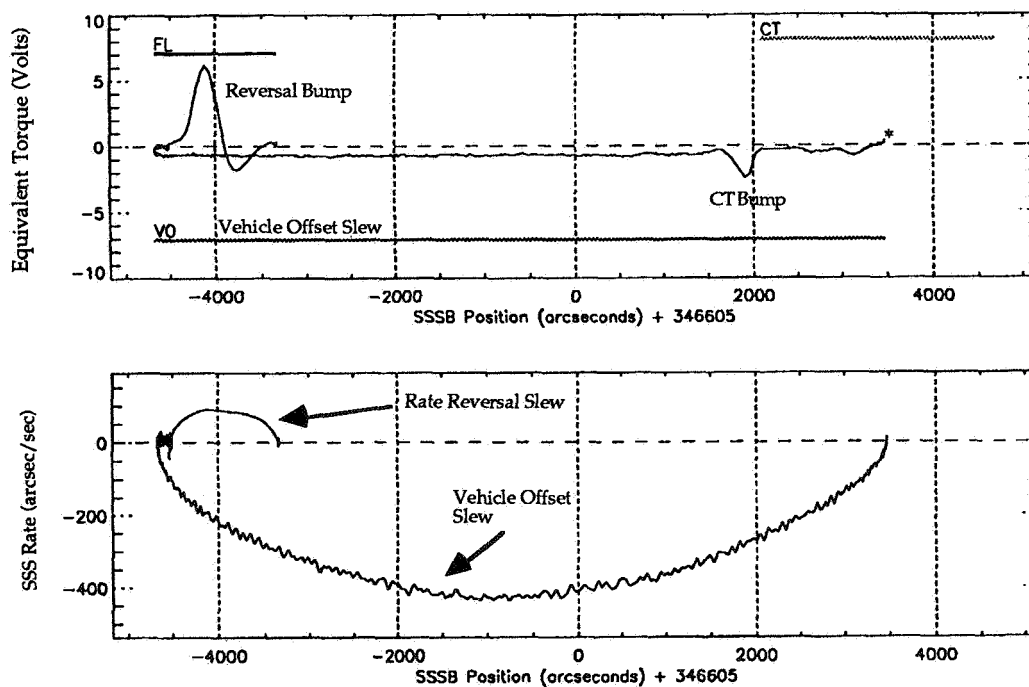
Teardown Inspection - Post-test teardown inspection showed surprisingly little damage to the test bearings. All bearings were still wet with free oil and, unlike the first test bearing set, showed a relatively small amount of lubricant debris most noticeable against the white background of the ball toroids (Fig. 14).



**Figure 14 Test bearings were in remarkably good condition with free oil and small amounts of debris as shown here on the toroids of the worst test bearing #174.**

## Reversal Bump

Within the last year, an unusual type of torque anomaly was observed with one of the FGS servos causing disruption to HST science. Although not completely diagnosed at the time of this writing, a comprehensive evaluation of on-orbit data suggests that FGS bearings are the only likely cause of the anomaly which only occurs when the servo reverses direction. Typically, the bearing must reach a minimum slew rate of 300 arcseconds/sec in one direction before reversing direction. Also it must travel through at least 400 arcseconds in the opposite direction before the "reversal bump" is generated (Fig. 15). Another unusual characteristic of the reversal bump is that its peak torque is consistently located approximately 460 arcseconds from its point of turn around, no matter at which position the bearing changes direction. The equivalent driving torque of FGS 1 SSSB (solid line) is plotted in the upper panel of Fig. 15 and the associated slew rates are presented in the bottom panel. Note that a 6.1 volt reversal bump occurs after an initial 2.3 deg slew having a maximum rate of 430 arcseconds/sec in the negative direction.



**Figure 15 - Example of FGS 1 SSSB Reversal Bump. Initial direction of motion is right to left. Note CT bump at end of CT stroke (bar, upper panel). Direction reverses at a position of about -4,700 arcseconds and a 6.1 volt reversal bump forms.**

Although two out of the 6 FGS SSS exhibit reversal bumps, only FGS 1 SSSB has reached torque levels that have caused acquisition failures. Currently, revisions to operating software are being implemented to minimize or eliminate this problem. The choice of which FGS to replace during the next servicing mission will depend on the effectiveness of this software workaround.

### **Concluding Remarks / Next Servicing Mission**

The investigation has led to an appreciation of the need for a systematic approach to managing the operation of the pointing system of an observatory like HST. In particular, the value of systematic, on-orbit performance trending along with comprehensive, flight-like life testing of ball bearings on the ground has been validated. Correlation of flight and ground test data is not always achievable, but a comprehensive body of on-orbit and ground test observations can afford insight to beneficial operational workarounds and appropriate responses to operational anomalies.

Long duration, small angle CT gimbaling motion was found to hasten the degradation of the FGS bearings lubricant. Rolling over debris generated at the end of stroke caused torque levels to reach motor saturation levels. In contrast, significant improvements in torque performance were realized with a switch to FL operation. As verified by the ground test, this small motion within the ball/race elastic regime before the starting of rolling was found to be completely benign after hundreds of millions of cycles. This finding permitted unimpeded operation of HST without the burden of FGS 2 replacement during the first servicing mission.

Periodic, scheduled servicing of the HST affords a unique opportunity to implement the lessons learned from on-orbit and ground tests, and to remedy problems such as the observed FGS SSS ball bearing anomalies. Based on the current understanding of the compromised condition of the FGS ball bearings, replacement of an FGS is planned during the HST Second Servicing Mission, scheduled for February of 1997. If necessary, another replacement of an FGS can occur during the Third Servicing Mission, planned for December, 1999. Once a new FGS is installed in the HST, it will be operated in a manner which will avoid the type of SSS ball bearing degradation seen in the original units. Implementation of these learned lessons will help to assure that the HST continues to produce extraordinary astronomical discoveries well into the twenty-first century.

### **Acknowledgement**

The authors would like to acknowledge the valuable contribution by Mr. George Damas to the FGS trending data presented in this study.



53-37 ✓  
50431  
125117

# The Thermal Conductance of Solid-Lubricated Bearings at Cryogenic Temperatures in Vacuum

M. J. Anderson\*

## Abstract

The thermal conductance of Hertzian contacts is of great importance to cryogenic spacecraft mechanisms such as the Infra-Red Space Observatory (ISO) and the Far Infra-Red Space Telescope (FIRST). At cryogenic temperatures, cooling of mechanism shafts and associated components occurs via conduction through the bearings. When fluid lubricants are cooled below their pour points, they no longer lubricate effectively, and it is necessary to use low shear strength solid lubricants. Currently, only very limited low temperature data exists on the thermal conductance of Hertzian contacts in both unlubricated and lubricated conditions. This paper reports on measurements of thermal conductance made on stationary ball bearings under cryo-vacuum conditions. Quantitative data is provided to support the development of computer models predicting the thermal conductance of Hertzian contacts and solid lubricants at cryogenic temperatures.

## Introduction

The thermal conductance of Hertzian contacts is important in cryogenic spacecraft applications. For example, cryogenically cooled mechanisms are integral components of the ISO and the FIRST. At cryogenic temperatures, the Hertzian contacts in ball bearings are often the only route by which heat can be extracted and thus enable the cooling of mechanism shafts and associated components to take place. Although extensive research has been carried out [1, 2] to measure the thermal conductances of metallic and non-metallic materials, often in loaded configurations, only very limited low temperature data exists on the thermal conductance of Hertzian contacts. In this work, the Hertzian contacts in a stationary ball bearing were investigated. Initially measurements were performed using an unlubricated bearing to confirm that the temperature dependence of the thermal conductance of Hertzian contacts was consistent with the bearing steel's thermal properties.

The unlubricated bearing measurements were followed by investigating the influence of solid lubricants on the thermal conductance of Hertzian contacts at room and at cryogenic temperatures. When fluid lubricants are cooled below their pour points, they no longer lubricate effectively and it is necessary to use low shear strength solid lubricants.

Research has shown that low shear strength solids are effective lubricants at both room and at cryogenic temperatures [4]. Two of the most widely used ball bearing solid lubricants, i.e. MoS<sub>2</sub> applied by RF magnetron sputtering, and lead applied by ion-plating, were studied. In addition to lubricant films, other coatings are frequently

---

\* European Space Tribology Laboratory, AEA Technology, Warrington, Cheshire, UK

F7476346

applied, such as thin TiC coatings, which are used as adhesion barriers between contacting metallic surfaces.

This paper reports measurements of the radial thermal conductance made on ball bearings under cryo-vacuum conditions. Quantitative data is provided to support the development of computer models predicting the thermal conductance of Hertzian contacts, and solid lubricants, at cryogenic temperatures.

### Basic Concept

A steady-state axial heat flow method was used to measure the radial thermal conductance across a bearing. Figure 1 illustrates the basic concept. Heat is supplied, at a constant rate, along a 304 stainless steel rod of uniform cross-section and known thermal conductivity and then across the test specimen to a heat sink. Temperature sensors enable measurements of the temperature gradients along the rod and across the test specimen to be made. Under steady-state conditions, the heat flow rate through the rod, known as the heat flux meter (HFM), equals that through the test specimen, provided there are no heat losses, e.g., by radiation. The mathematical expressions governing the heat flow rates through the HFM and test specimen, as functions of conductance and temperature gradient, can therefore be equated. The thermal conductance of the test specimen can then be determined by solving the resulting expression.

Under steady-state conditions, the heat flux ( $q_{\text{HFM}}$ ) through the HFM is related to the conductivity ( $k$ ) and dimensions of the HFM (cross-sectional area =  $A$ , and distance between temperature sensors =  $L$ ) by the following expression:

$$q_{\text{HFM}} = (T_u - T_l) \cdot kA/L \quad (1)$$

$T_u$  and  $T_l$  are as defined on Figure 2.

The heat flux through the bearing is determined by the bearing conductance ( $C$ ) and is equal to that through the HFM.  $T_c$  and  $T_b$  denote the temperatures of the inner and outer raceways respectively. The outer raceway temperature is also equivalent to the nominal base temperature. The following expressions are obtained.

$$q_{\text{bearing}} = C \cdot (T_c - T_b) \quad (2)$$

Equating (1) and (2) gives

$$C = (T_u - T_l) / (T_c - T_b) \cdot kA/L \quad (3)$$

By measuring the temperature gradient across the bearing and at defined points on the HFM, the bearing conductance can be obtained using the above expression.

## Experimental Details

### Apparatus Design

Figure 2 is a schematic representation of the test bearing and HFM. The test specimen is a stationary angular-contact ball bearing. The outer raceway is attached to a copper support piece secured to the base. The base, in turn, is bolted to the 20 K cryopot of the ESTL vacuum Cryogenic Facility. The inner raceway is firmly fastened to the lower end of the HFM via an Oxygen Free High Conductivity (OFHC) Cu spacer which acts as a thermal short circuit. Such a precaution is essential to minimize temperature differences between the inner raceway and the bottom end of the HFM. A wire-wound resistive heater block is located within the upper portion of the HFM. Polyimide-insulated nichrome wire (resistivity = 34.4 Ohm/m) is used for the heater windings. The heater coil is located within the HFM so that heat radiated from the heater coil will be absorbed by the HFM, minimizing heat loss to the surrounding environment. Axial loading is accomplished by tensioning a steel wire running from the HFM to a spring system linked to a tension-load cell. The load cell enables the axial load to be measured and the springs give some degree of compliance to allow for the effects of thermal expansion and contraction. It is necessary to be able to alter the applied load so that the effect of load on bearing conductance can be quantified. In order to avoid the need for breaking the vacuum or warming the cryostat to room temperature, the load can be changed in-situ by rotating a manually operated linear motion drive connected to the upper end of the load cell.

Three locating balls, manufactured from PTFE, are situated between the heater block and the 20 K structure to prevent rotation of the HFM and contact assembly. The PTFE also thermally isolates the heater block from the cooling arm.

Silicon diode temperature sensors are located at each end of the HFM and on the bearing raceways as indicated on Figure 2. Three silicon diode temperature sensors are also spaced around the circumference of each raceway, and were defined as follows:

$T_u$	located on HFM and is the sensor closest to the heater coil
$T_l$	located on HFM and situated 3.0 cm from $T_u$ .
$T_{b1}$ to $T_{b3}$	attached on the outer raceway abutment faces of the bearing. These sensors also define the base temperature.
$T_{c1}$ to $T_{c3}$	attached to the inner raceway abutment faces.

Radiative heat losses are minimized by insulating the surfaces of the HFM and by filling the space below the bearing with superinsulating material (aluminized mylar).

### Test Bearings

The test bearings are specified as RA 8220 and were manufactured by RMB, Switzerland. The bearing details are shown in Table 1.

**Table 1 Bearing Details**

Raceway Material	440C stainless steel
Ball Material	440C stainless steel
Outer Raceway Diameter	22.0 mm
Bore	8.0 mm
Width	7.0 mm
Ball Diameter	3.969 mm
Ball Complement	7
Conformity	1.14
Contact Angle	15 degrees

Table 2 summarizes the coating processes applied to the rolling elements and defines the cage materials.

**Table 2 Details of Bearing Coatings and Lubrication**

Bearing ID	Ball Coating	Raceway Coating	Cage Material
Unlubricated	None	None	303 stainless steel <sup>1</sup>
Lead	None	Ion-plated lead	Lead/bronze
MoS <sub>2</sub>	MoS <sub>2</sub>	MoS <sub>2</sub>	RT/duroid 5813 <sup>2</sup>
TiC Balls	CVD TiC	None	303 stainless steel <sup>1</sup>

<sup>1</sup> Cage unlubricated.

<sup>2</sup> RT/duroid 5813 is an MoS<sub>2</sub>/PTFE/glass fiber composite manufactured by the Rogers Corporation, USA

The lead film was deposited, at ESTL, by lead-ion plating and the MoS<sub>2</sub> films were deposited by RF magnetron sputtering, also at ESTL. Estimations of film thickness were made using an X-ray fluorescence technique and the typical MoS<sub>2</sub> film thickness on the bearing inner raceway was  $0.8 \pm 0.2$  microns and  $0.20 \pm 0.03$  microns on the balls. For the lead films, a typical thickness was  $0.7 \pm 0.1$  microns on the inner raceway.

The TiC coating (thickness = 3 microns, according to CSEM literature) was applied to the balls by CSEM, Switzerland, by their proprietary chemical vapor deposition technique.

The following Table summarizes the load and contact stress conditions under which the bearings were tested.



**Table 3 Load and Contact Stress Conditions**

Load (N)	Mean Hertzian Contact Stress	
	(Inner Raceway, MPa)	(Outer Raceway, MPa)
0	0	0
10	614	491
20	769	615
40	962	769
60	1094	875
80	1198	958

Additionally, it should be noted that the bearings were not run-in prior to testing.

#### Experimental Errors

Experimental errors arise from the errors in the measurements of thermal gradients across the bearing and along the HFM. Experimental errors are governed by the accuracy of the temperature sensors ( $\pm 0.5$  K at room temperature and  $\pm 0.2$  K at 20K). Further errors result from heat loss and in the dimensions of the HFM. A summary of experimental errors is now presented.

Room Temp: HFM calibration errors are of the order of  $\pm 25\%$ , and the dimensional tolerances give the error in  $L = \pm 2\%$ , and the error in  $A = \pm 1\%$ .

At 48 mW heater power, typical temperature differentials across the bearing were 2 to 4K. As the sensors are only accurate to  $\pm 0.5$  K, experimental errors on temperature measurements are, respectively,  $\pm 50\%$  and  $\pm 25\%$ . Combining this error with HFM calibration and dimensional errors gives a maximum experimental error of approximately  $\pm 80\%$ .

Increasing the heater power to 180 mW resulted in larger temperature gradients, and hence the measured temperature difference errors were reduced by a factor of 4 to 5, i.e., errors are of the order of  $\pm 10\%$ . The resulting experimental errors, including HFM calibration and dimensional errors, were of the order of  $\pm 40\%$  to  $\pm 50\%$ .

Cryogenic Temperatures: The improved sensitivities of the temperature sensors, at cryogenic temperatures, resulted in HFM calibration errors of  $\pm 10\%$ . Combining these with the dimensional errors and the measured temperature gradients give typical experimental errors of less than  $\pm 30\%$ . At 20 K baseplate temperatures, maximum errors can be as great as  $\pm 70\%$  if the temperature differentials are less than 1 K.

## **Results**

### HFM Calibration

The HFM was manufactured from 304 stainless steel and it was calibrated by applying a known quantity of power to the HFM heater, and measuring the temperature gradient along the HFM. Equation (1) was used to obtain the thermal conductivity,  $k$ , of the HFM material. Figure 3 shows the temperature dependence of the HFM material's

thermal conductivity. The conductivity varied non-linearly, from 6 W/m/K at 35 K, to 22 W/m/K at room temperature. The values plotted on this graph were used for the subsequent calculations of the bearing thermal conductance at a given temperature.

### Results

The graphs of thermal conductance, at cryogenic temperatures, show data for baseplate temperatures of, nominally, 20 K and 50 K. At each baseplate temperature, two levels of power (48 mW, denoted by (1) in Tables 4 to 7, and 180 mW, denoted by (2)) were applied to the HFM heater, which varied the thermal gradients along the HFM and across the bearing. This resulted in two different values of the mean bearing temperature for a given baseplate temperature. The mean bearing temperatures are given in Tables 4 to 7. For cryogenic temperatures, the first two columns relate to a baseplate temperature of 20 K, and the following two columns to a baseplate temperature of 50 K.

The thermal conductance results, for zero applied axial load and for an 80 N axial load, are summarized in the Tables 4 to 7. The Tables summarize data from tests conducted at 293 K and at cryogenic temperatures.

**Table 4 Thermal Conductance ( $\times 10^{-3}$  W/K) of an Unlubricated Brg**

Load (N)	Temp (K)	Cryogenic Temp (K)				Room Temp (293 K)	
		25	45	55	65	(1)	(2)
0		0.19	0.21	0.88	0.65	5.88	4.11
80		2.00	5.28	5.64	6.42	31.5	23.2

**Table 5 Thermal Conductance ( $\times 10^{-3}$  W/K) of a Lead lubricated Brg**

Load (N)	Temp (K)	Cryogenic Temp (K)				Room Temp (293 K)	
		27	40	46	57	(1)	(2)
0		1.41	-	1.44	3.77	-	12.1
80		3.27	4.32	6.42	8.43	35.1	29.4

**Table 6 Thermal Conductance ( $\times 10^{-3}$  W/K) of an MoS<sub>2</sub> lubricated Brg**

Load (N)	Temp (K)	Cryogenic Temp (K)				Room Temp (293 K)	
		35	50	55	65	(1)	(2)
0		0.35	0.59	1.41	1.18	4.38	6.47
80		1.92	5.02	3.76	-	18.1	18.1

**Table 7 Thermal Conductance ( $\times 10^{-3}$  W/K) of a Brg fitted with TiC-coated Balls**

Load (N)	Temp (K)	Cryogenic Temp (K)				Room Temp (293 K)	
		35	52	65	75	(1)	(2)
0		0.87	1.76	1.25	2.5	10.9	-
80		4.65	6.40	7.51	7.51	13.9	24.5

Examination of the data showed that, at room temperature, the thermal conductance of the unlubricated bearing was 0.03 W/K at an 80 N axial load. A decrease of approximately an order of magnitude was measured over the temperature range from room temperature to 20 K (baseplate temperature) and the 50 K results were intermediate. At all test temperatures, the effect of the lead film was to increase the thermal conductance of a bearing by up to 30%. An MoS<sub>2</sub> film caused the thermal conductance to be up to 20% less than that for an unlubricated bearing. The thermal conductance of the bearing fitted with TiC-coated balls was comparable, at room and at cryogenic temperatures, with the thermal conductance of the unlubricated bearing containing steel balls.

The bearing thermal conductance varied non-linearly with applied axial load. A typical example of Thermal Conductance vs Axial Load is shown in Figure 4. Note that the thermal conductance was not zero when no axial load is applied.

## Discussion

### General Comments

The bearing conductance at zero applied axial load is not zero as heat transfer occurs across the bearing by radiation at room temperature and, at room and cryogenic temperatures, via the thermal path presented by ball raceway contacts due to the finite cage weight.

The thermal conductances for the bearings have been plotted against the Hertzian contact area per ball at the ball/inner raceway (Figures 5 to 9). Figure 5 shows the room temperature data for all bearing/coating combinations tested. In the graphs, at cryogenic temperatures, a correction has been made for the change in Young's Modulus (assumed to increase by 10%[2]). In general, Figures 6 to 9 are linear within experimental error, thus indicating that the thermal conductance of a solid lubricated or unlubricated bearing is proportional to the Hertzian contact area, and hence proportional to  $\text{load}^{2/3}$ .

Some anomalous points were found, in which the measured conductance values deviated from the best fit line through the points, and the values are also outside the experimental errors predicted. This additional error is consistent with errors arising from ball load distribution. Assuming 6 balls were loaded, the error is of the order of between 10% and 20%, as corresponding reductions, in the Hertzian contact areas, also occur at the outer raceway contacts.

### Unlubricated Bearing

At cryogenic temperatures, the bearing thermal conductance is less than it is at ambient temperatures as a consequence of the reduced thermal conductivity of the bearing steel, as discussed in References 1 and 2. A similar decrease was obtained in the material used to fabricate the HFM.

### Lead Lubricated Bearing

The thermal conductance for the lead-lubricated bearing exceeds that of the unlubricated bearing. In the unlubricated bearing, conduction takes place only through the asperities of the Hertzian contacts at the ball/race interfaces. In the lead-lubricated bearing, thermal conduction can now occur via the Hertzian contact and through any additional thermal paths created by the contact asperity gap-filling properties of the lead film.

### MoS<sub>2</sub>-Lubricated Bearing

Typically, non-metallic materials exhibit relatively low thermal conductivities in comparison with metals [2]. A thin film of MoS<sub>2</sub> applied between contacting asperities would therefore act as an insulating layer and reduce the thermal conductance of the bearing. The results, at ambient and at cryogenic temperatures, confirm that the thermal conductance of an MoS<sub>2</sub>-lubricated bearing is less than that of an unlubricated bearing.

### Unlubricated Bearing Fitted with TiC-Coated Balls

The thermal conductance results obtained at cryogenic temperatures for the bearing fitted with TiC-coated balls are comparable to the corresponding data obtained for the unlubricated bearing. Such a result is expected, as the thermal conductivity of TiC is similar to that of steel [5].

### Effect of Bearing Rotation

Although the experimental technique described in this report focuses on a stationary bearing, the results can be applied to slowly rotating bearings. It was shown theoretically by Holm [3], and also experimentally by Stevens and Todd [6] that the heat flow path is essentially unchanged between a stationary and a slow moving contact. In a stationary bearing, the heat flow path is dependent on the geometries of the Hertzian contacts. The regions of the bearing raceways between contacts only play a minor role in the heat flow process. As a bearing rotates, the heat flow path will be altered by thermal dissipation in the inter-contact regions. At slow speeds the change is not significant, but at higher speeds, the heat generated at a contact will not have dissipated before the arrival of the next contact. The heat flow characteristics will therefore change and alter the thermal conductance of the bearing. Stevens and Todd found that the heat flow characteristics, and thus the thermal conductance, of their test bearings remained unchanged below rotation rates of 100 rpm. The time taken for heat to dissipate is dependent on the rotation rate, the specific heat capacity and inversely proportional to the thermal conductivity (Reference 7 contains details of the calculation). As temperature is decreased from room temperature to 20 K, the heat capacity of steels decreases by at least an order of magnitude more than the thermal conductivity. Heat can therefore be expected to dissipate more rapidly with

decreasing temperature. The thermal conductance measurements carried out on stationary bearings are thus representative of slowly rotating bearings.

#### Extrapolation of Thermal Conductance Data

Changes in thermal conductance, due to applying solid lubricants, are of the order of  $\pm 20\%$ . In applications requiring the thermal conductance of a bearing to be maximized, then lead lubrication provides an improvement over  $\text{MoS}_2$  lubrication. Fitting with TiC balls and applying an  $\text{MoS}_2$  coating to the bearing is unlikely to reduce the thermal conductance to a limit which is far below that of  $\text{MoS}_2$  lubrication alone. It must be noted, however, that in any application, the benefits gained by any particular method of solid lubrication to the thermal conductance must be considered along with the torque and duty requirements of the bearings.

Figure 10 can be used to predict the thermal conductance for a given coating/temperature combination. Extrapolation of the results to bearings of differing dimensions must be performed with caution, although any deduced data may be sufficient for a first approximation.

#### **Conclusions**

The measured changes in the thermal conductances of Hertzian contacts in ball bearings, as a function of temperature, is primarily related to the changes in bulk material properties. The influence of lubricant and TiC coatings is a secondary effect.

Ion-plated lead, applied to the raceways of a 440C bearing, increased the thermal conductance by 20%, at room temperature and 20 K. The increase was attributed to the gap-filling properties and the relatively high thermal conductivity of the lead film.

Sputtered  $\text{MoS}_2$  films, applied to the balls and raceways, reduced the thermal conductance of the bearing by up to 35%, and was due to the  $\text{MoS}_2$  film acting as an insulating layer.

TiC coatings, on the balls, did not change the bearing thermal conductance as the thermal conductivity of TiC is similar to that of steel.

The thermal conductance, in all test cases, increased non-linearly with applied axial load, and was found to be directly proportional to the Hertzian contact area.

The finite thermal conductance values, measured at zero applied axial load, were due to the thermal path through the ball/raceway contacts under the weight of the cage and, at room temperature, radiative heat transfer.

## References

1. Gould, S. G. "The Thermal Conductance of Solids and Pressed Contacts at Very Low Temperatures." ESTL/TR/80, 1988.
2. Reed, P. R. and A. F. Clark. Materials at Low Temperatures, American Society for Metals, 1983.
3. Stevens, K. T. and M. J. Todd. "Thermal Conductance Across Ball Bearings In Vacuum," ESA Tribology/1, 1979.
4. Gould, S. G. and E. W. Roberts. "The In-Vacuo Torque Performance of Dry-Lubricated Bearings at Cryogenic Temperatures," 23rd Aerospace Mechanisms Symposium, May 1989.
5. Kaye, G. W. C. and T. H. Laby. Tables of Physical and Chemical Constants, Longman, 1973.
6. Holm, R. Electrical Contacts. Springer Verlag, 4th Edition, 1967.
7. Rowntree, R. A. "Metallurgical Phase Transitions in the Rubbing of Steels," PhD Thesis, University of Leicester, UK, 1982

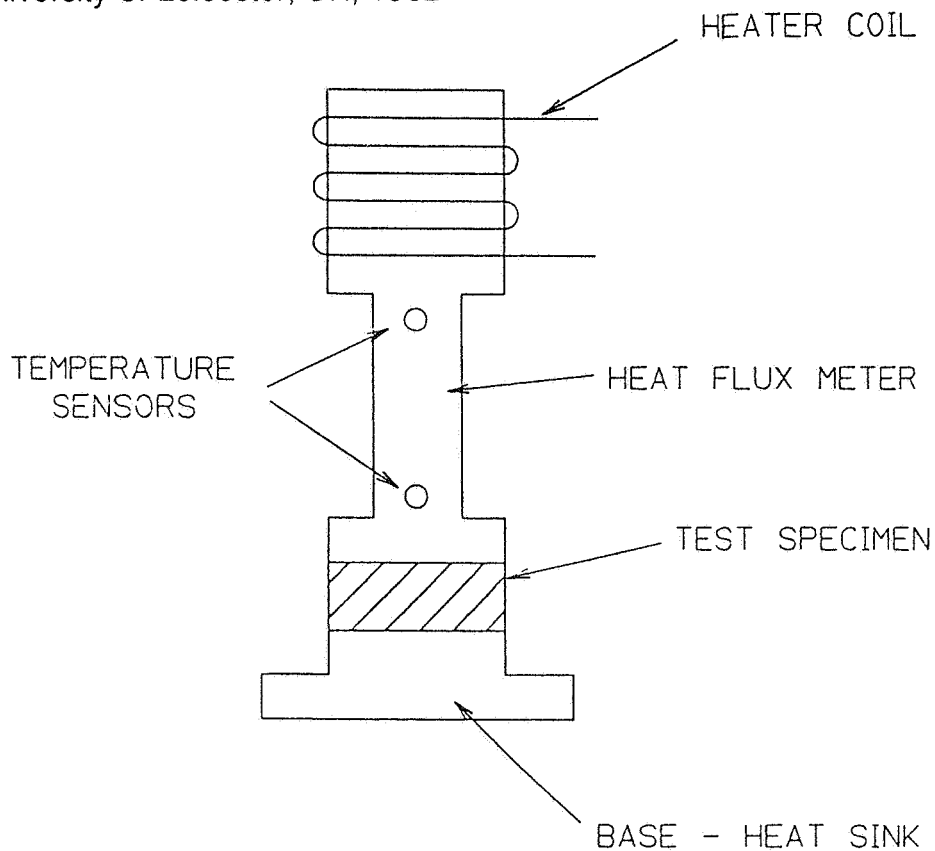


Figure 1 DESIGN CONCEPT

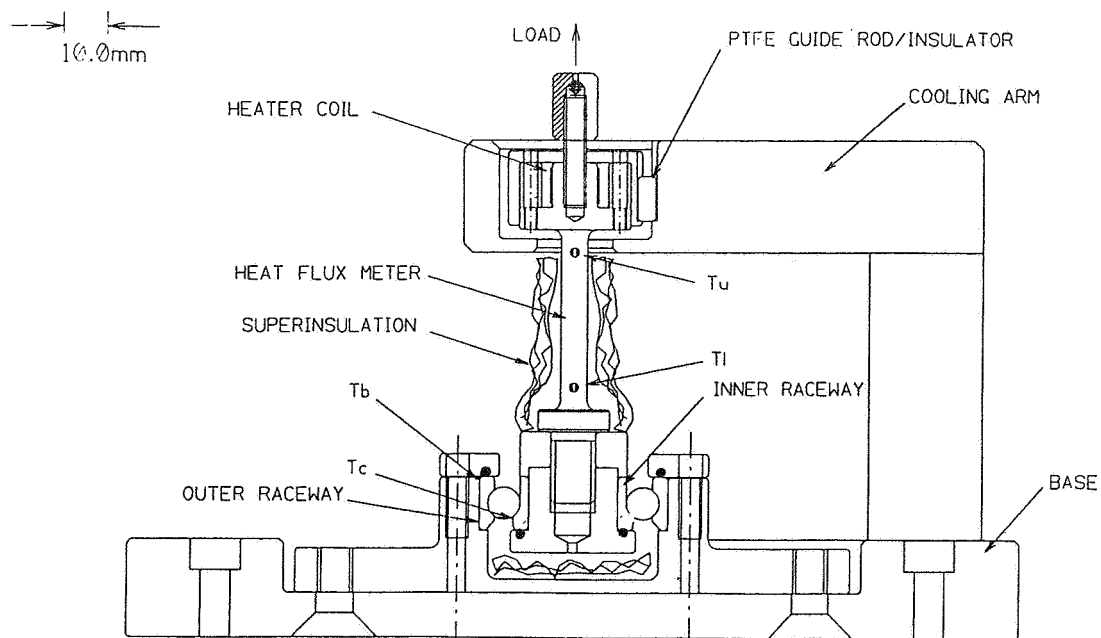
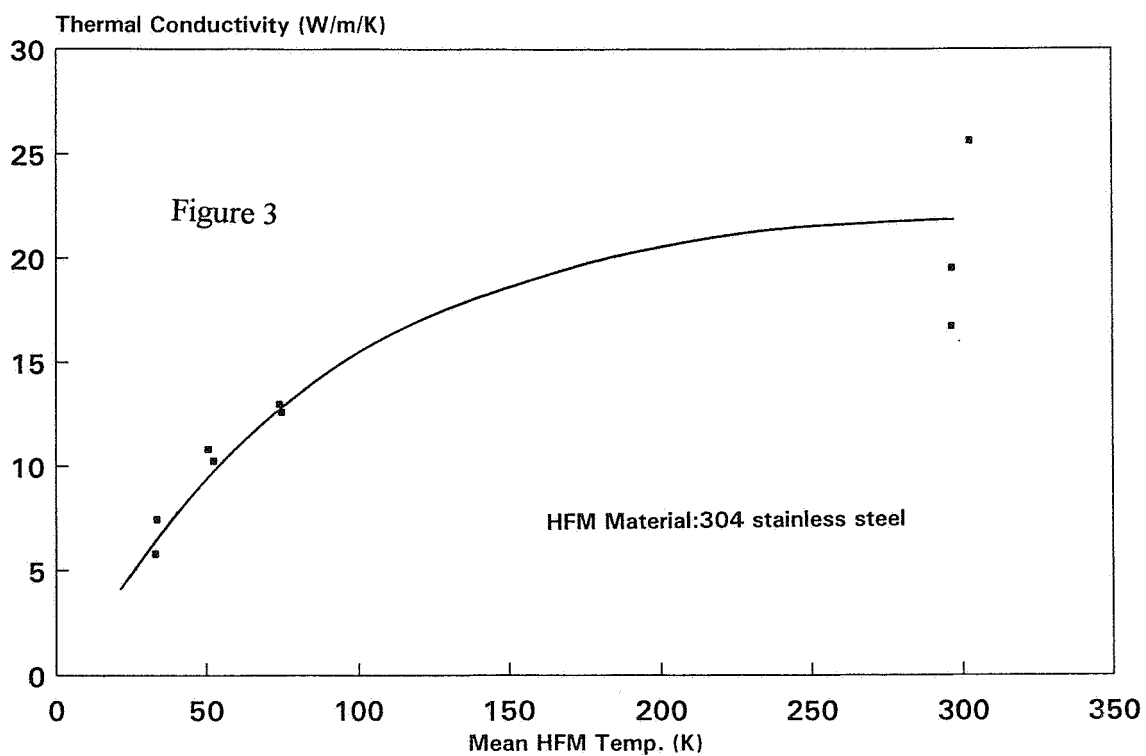


Figure 2 CRYO-THERMAL CONDUCTANCE RIG  
ED 20 BEARING TEST SET UP

### CRYOGENIC THERMAL CONDUCTANCE EXPT. Thermal Conductivity of HFM vs Temp.



**CRYOGENIC THERMAL CONDUCTANCE EXPT.**  
**Thermal Conductance vs Axial Load**  
**ED8 Bearing (440C), Cryogenic Temp.**

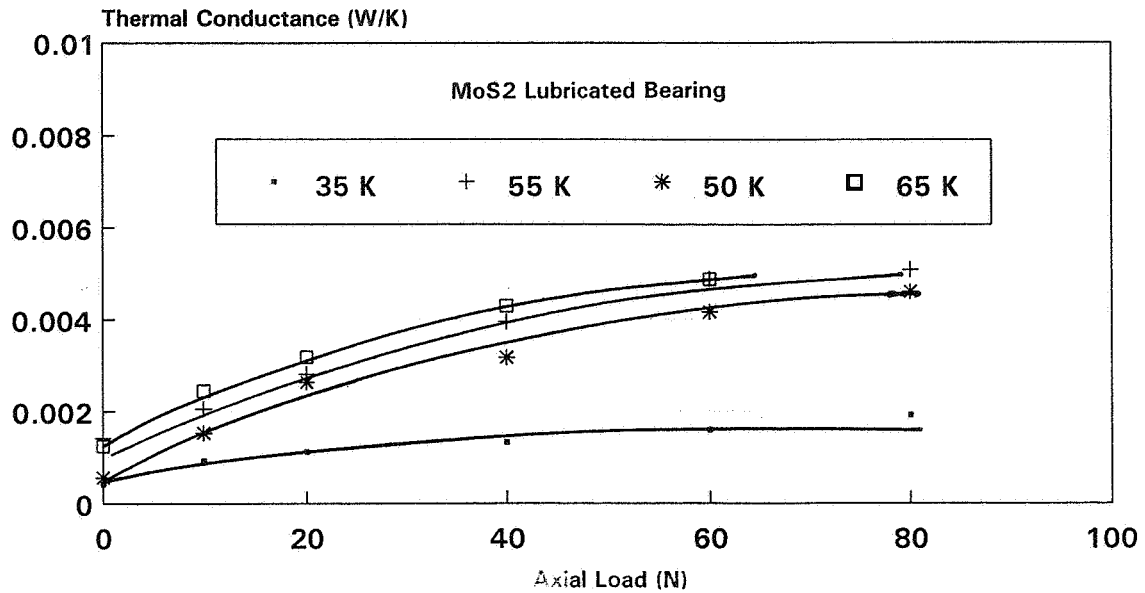


Figure 4

**CRYOGENIC THERMAL CONDUCTANCE EXPT.**  
**Thermal Conductance vs Contact Area**  
**ED8 Bearing (440C), room temp.**

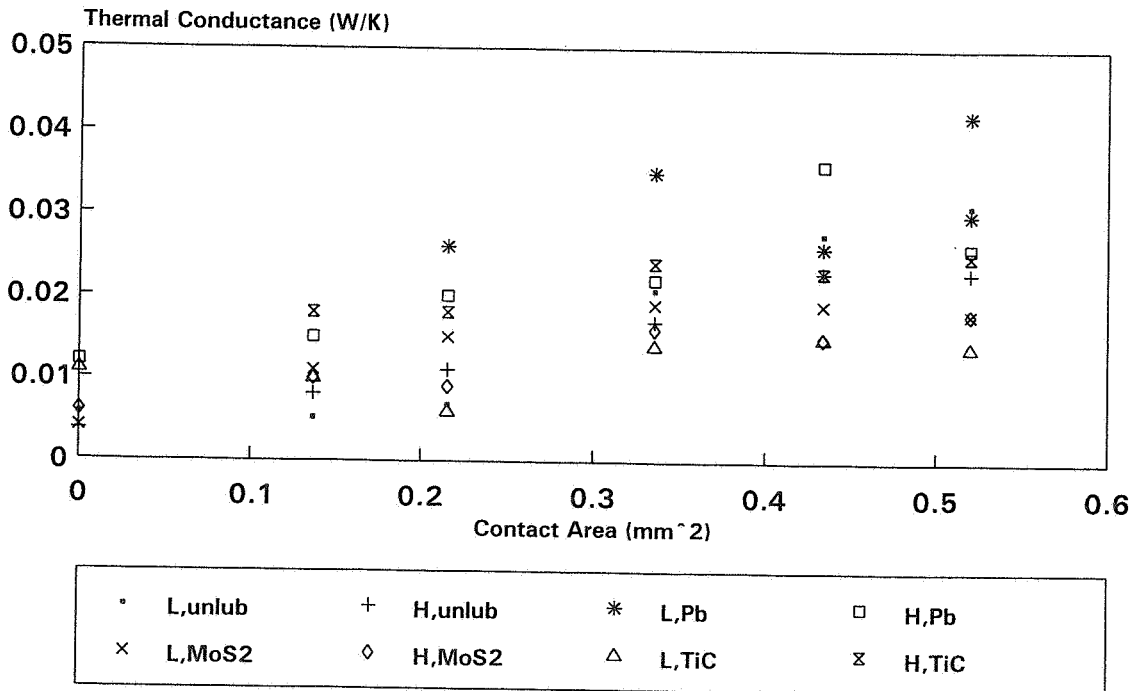


Figure 5



**CRYOGENIC THERMAL CONDUCTANCE EXPT.**  
**Thermal Conductance vs Contact Area**  
**ED8 Bearing (440C), cryogenic temp.**

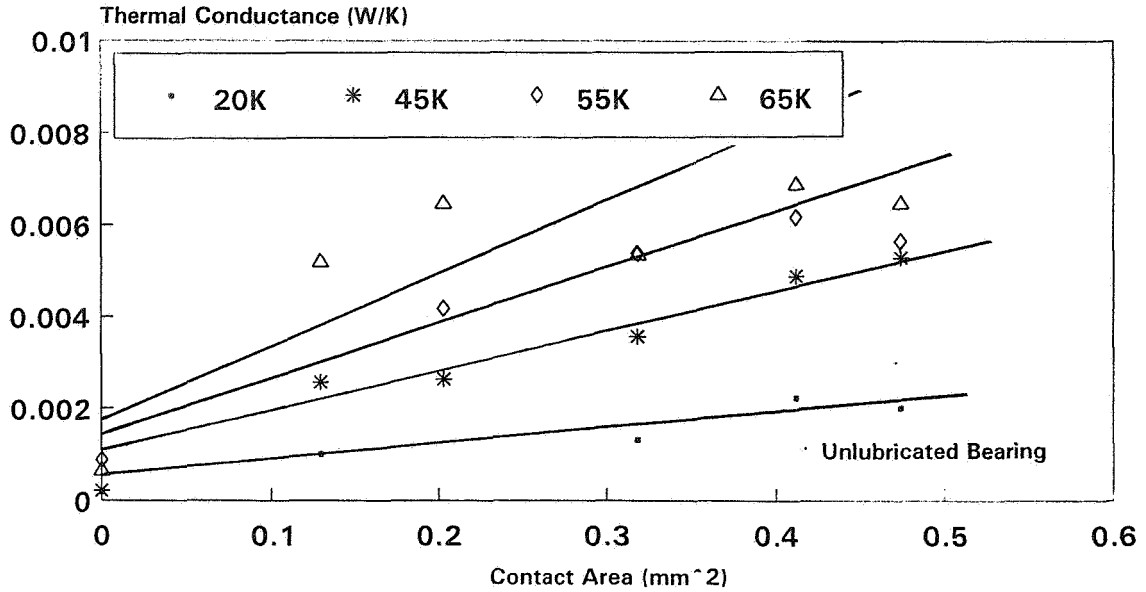


Figure 6

**CRYOGENIC THERMAL CONDUCTANCE EXPT.**  
**Thermal Conductance vs Contact Area**  
**ED8 Bearing (440C), cryogenic temp.**

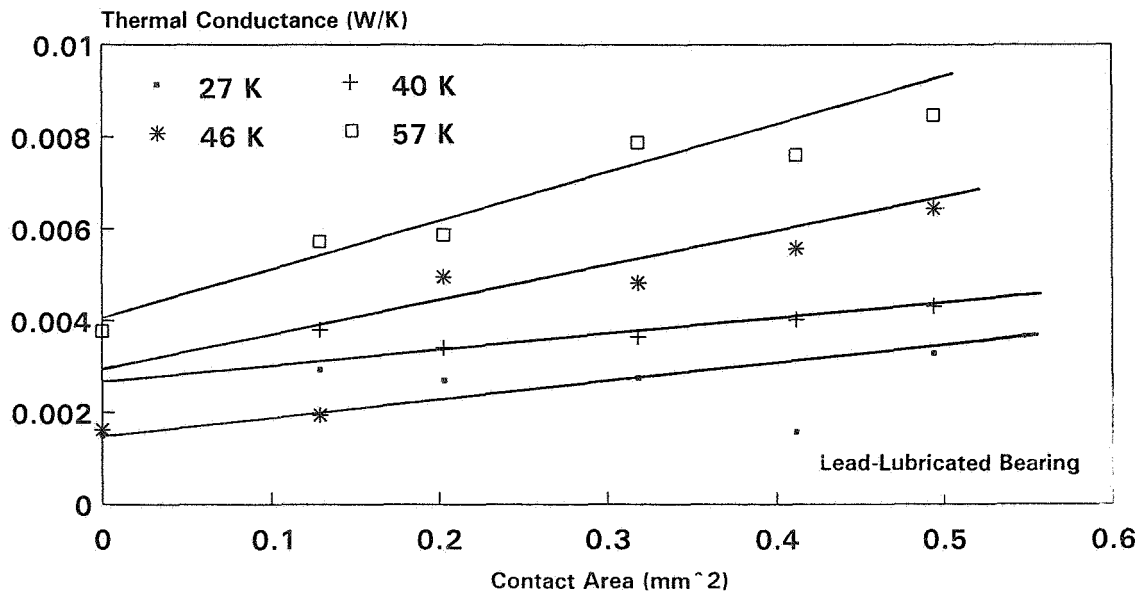


Figure 7

**CRYOGENIC THERMAL CONDUCTANCE EXPT.**  
**Thermal Conductance vs Contact Area**  
**ED8 Bearing (440C), cryogenic temp.**

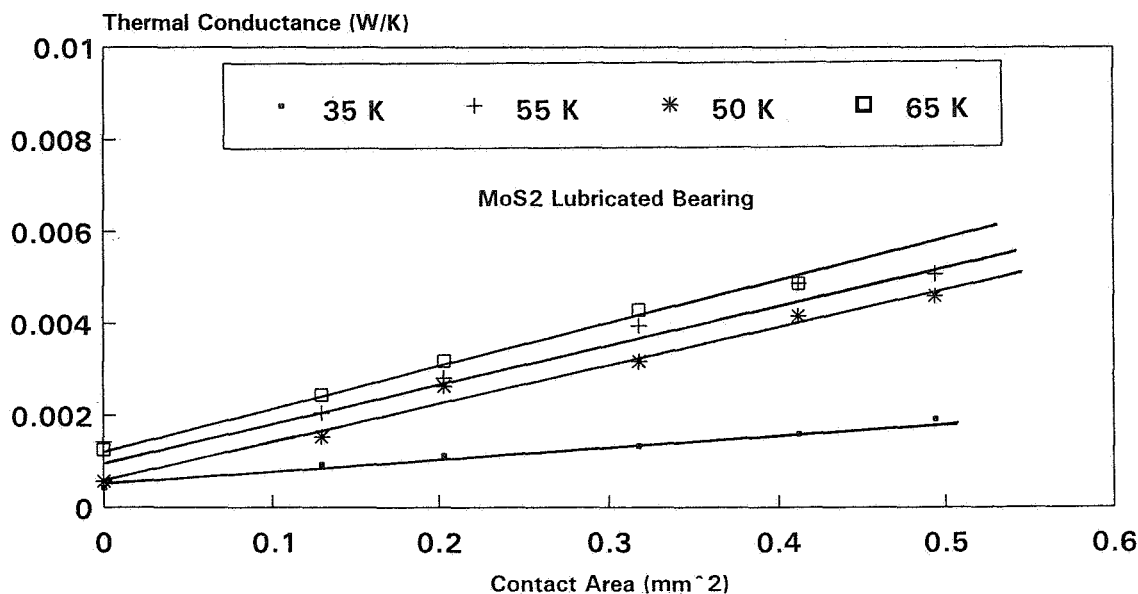


Figure 8

**CRYOGENIC THERMAL CONDUCTANCE EXPT.**  
**Thermal Conductance vs Contact Area**  
**ED8 Bearing (440C), cryogenic temp.**

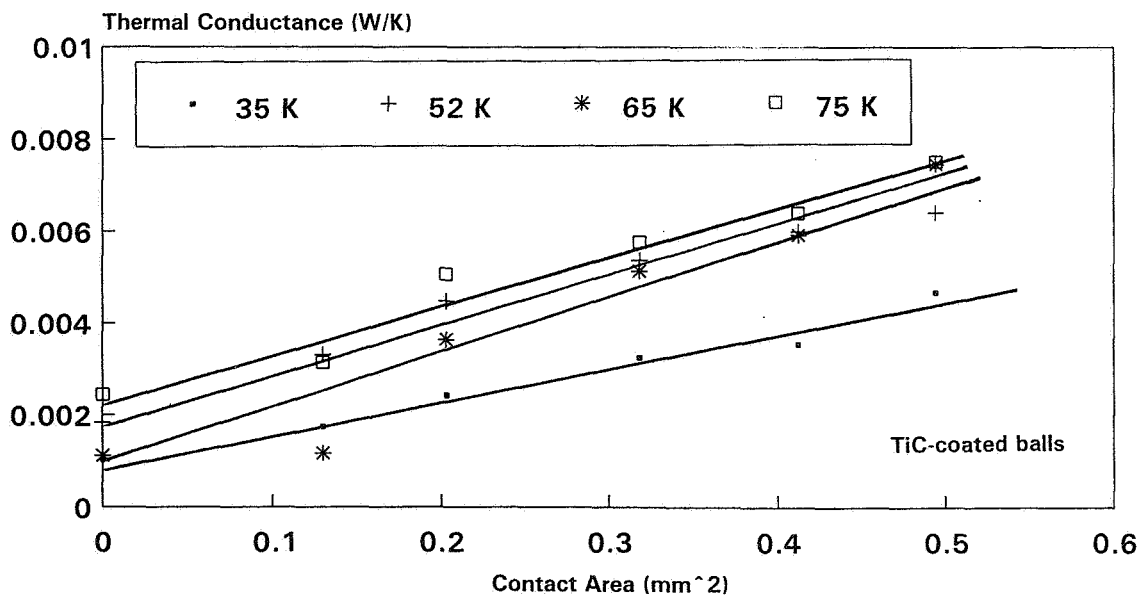


Figure 9

## BEARING THERMAL CONDUCTANCE AS FUNCTION OF TEMPERATURE (IN VACUO)

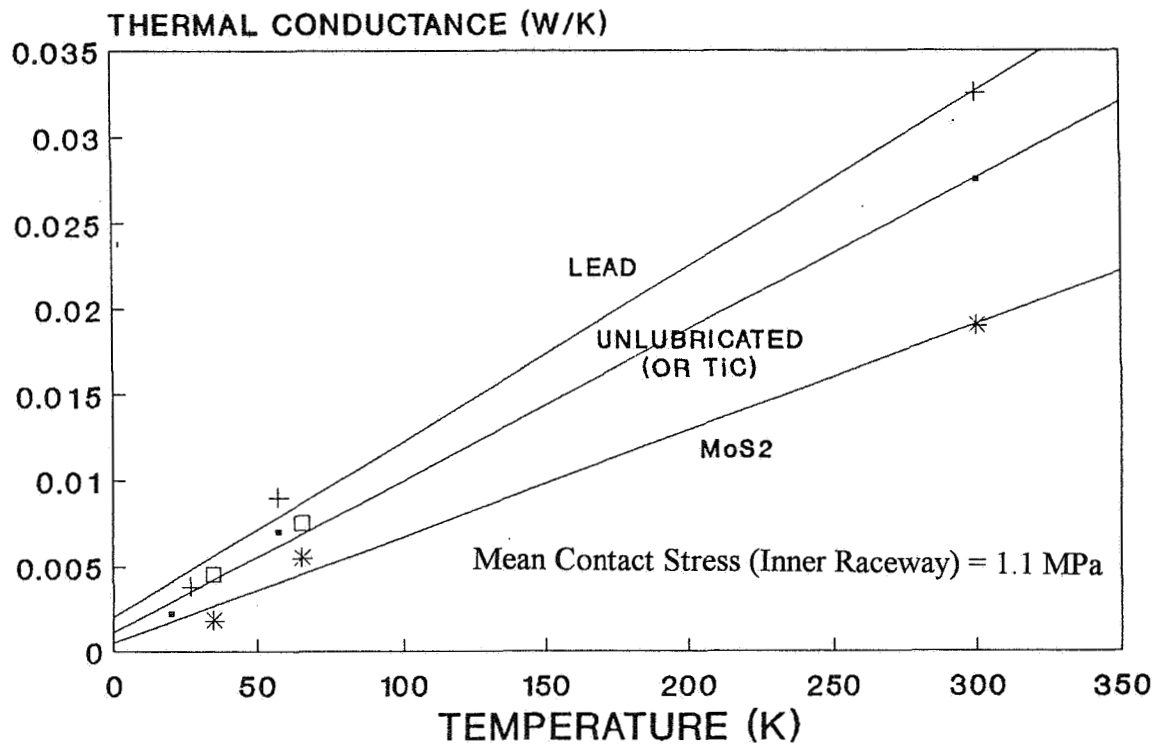


Figure 10



## Tape Recorder Failure Investigation

M.D. Higgins\*, S.H. Loewenthal\*, C.C. Carnahan\*, and G.L. Snyder\*

54-35  
50432  
125118 ✓  
2/18

### Abstract

Two end-item tape recorders lost 4:1 mode data recording mode capability at less than half of their 16,000-cycle, 4-year operating life. Subsequent life tests on two spare recorders also experienced 4:1 mode data loss at 8,000 and 11,700 cycles. Tear down inspection after completion of the life tests showed that the tape had worn through the alferil record and reproduce heads. An investigation was initiated to understand the cause of excessive tape head wear and the reasons why the 4:1 mode data rate, low-speed mode is more damaging than the 1:1 mode data rate, high-speed recording mode. The objective was to establish how operating conditions (tape speed, humidity, temperature, stop/start cycles) affects head life with the goal of extending head life on the remaining in-service tape recorders. Another interest was to explain why an earlier vendor life test showed capability beyond 16,000 cycles.

### Background

This paper addresses discrepancies between the results of tape recorder life tests performed at the vendor in 1984 and at Lockheed Martin Missiles and Space (LMMS) in 1994, as they relate to the friction and head wear. The unit tested by the vendor accumulated 19,000 cycles before the head was inspected and found to be in relatively good health. LMMS tested two units, both of which were terminated due to head failure. Unit #1 failed at 17,100 cycles, while unit #2 failed at 15,300 cycles. Post-test examinations found significant head wear in both units.

Additional tests, reported here, were performed to help determine the cause of the recorder failure. These tests dynamically measured tape tension and tape head friction of an end-item recorder by using a specially designed load cell platform. The effects of tape speed, temperature, humidity, and operation mode were investigated. The results of these tests and how they relate to the head failure are presented.

In order to identify the operating parameters that are critical to head wear, it was necessary to design a friction force/tape tension sensor with a sensitivity to a fraction of a newton and with accurate support and alignment of the read head within the confines of the tape recorder housing. The transducer has to fit within the small space left between the tape transport mechanism and the hermetically sealed case. The humidity within the case must be carefully controlled around 30%, since higher humidity is believed to be detrimental to head life, and lower humidity will increase static electricity and noise.

---

\* Lockheed Martin Missiles and Space, Sunnyvale, CA

This paper describes the development of a novel load cell platform for both measuring force and moment loads with sub-newton sensitivity and for fitting within the required package envelope. The use of the two sub-miniature load cells not only eliminated parasitic friction but also allowed a direct measurement of tape head friction and tape tension. Problems associated with load cell cross talk and initial locked-in loads (bias) are addressed.

A description and method for calculating the friction energy is also presented. Results of subsequent head wear testing and its relationship between the friction energy and the head wear are established.

## **Tape Recorder**

The end-item tape recorder contains two coaxial reels that contain 840 meters of wide-band polyester magnetic tape. The ends of the tape are designated as the Beginning of Tape (BOT) and the End of Tape (EOT). The tape transport mechanism contains three individual tape heads for recording, reproducing, and erasing operations.

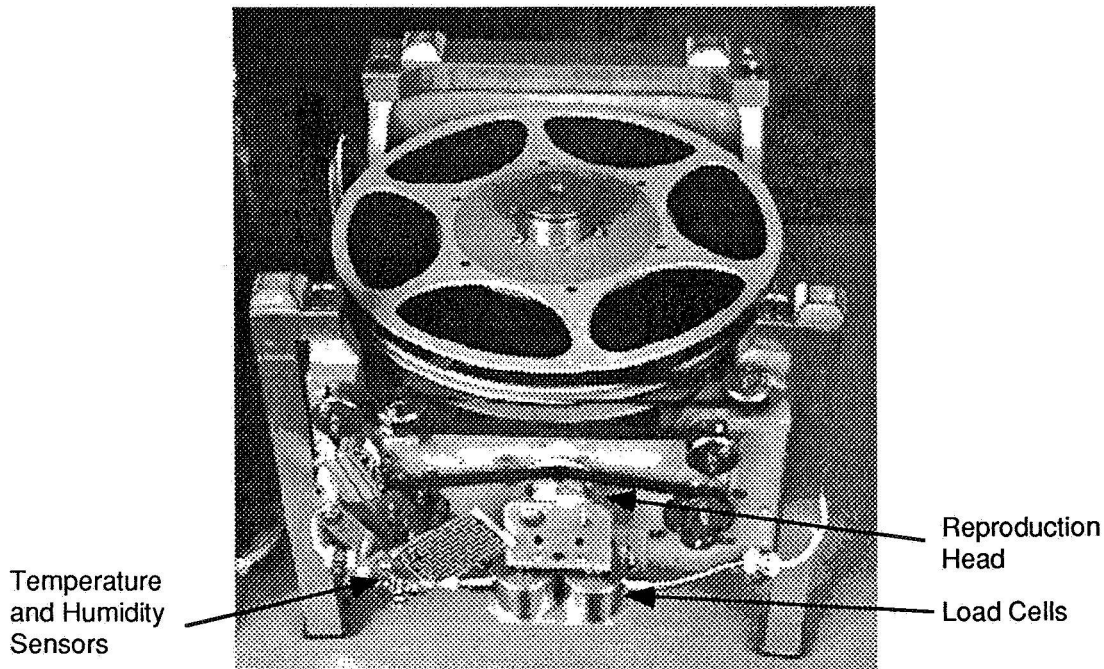
The record and reproduce heads each contain 5 alfesil cores, housed in an aluminum case. The erase head contains a single alfesil core, which is also housed in an aluminum case. The entire tape recorder is housed in a 20 x 23 x 22-cm hermetically sealed case. The case is back-filled with dry nitrogen, and distilled water is included to raise the relative humidity within the case from 27% to 40%. As mentioned above, higher humidity is detrimental to head life, while lower humidity increases static electricity and noise. The recorder typically operates at temperatures between -2°C and 35°C.

In order to determine the effects of operating conditions on tape head wear, a means to measure dynamically the contact force between the tape and the read heads, along with its friction force, needed to be developed. Furthermore, the "sensor" not only had to fit in the same location as the actual read head (5 x 5 x 2.5 cm) but also needed to incorporate an actual read head with the proper geometry.

The major design challenge was to record very small tape head load levels (1 to 1.5 N) simultaneously with dynamic friction levels on the order of 0.05 to 0.1 N. At these low levels, any form of hysteresis would significantly contaminate the results. Thus, "floating" some sort of sliding bearing system was eliminated. A "teeter totter" beam, supported by a flexure pivot at the fulcrum and reacted by a load cell, was also considered but was eliminated because it was too complicated to measure normal force and moment (friction) simultaneously. Furthermore, it required too much room to package and was thought to be too susceptible to dynamic excitation.

The force platform that was finally selected directly mounted two sub-miniature 0.5-N load cells to a bracket to which the read head is directly mounted (Figure 1). This arrangement not only provided the smallest package size with the required load sensitivity but also eliminated hysteresis through the hard mounting of the tape head directly to the load cells. Furthermore, both the tape tension and the friction force could be deduced from the normal and moment loads that were measured directly.

The drawback to this arrangement, as later found, was that the desired stiffness and load sensitivity was also accompanied by an equally high sensitivity to temperatures and thermal gradients. Using dead weights, the load cell temperature sensitivity was calibrated statistically. To account for temperature effects, a technique was developed to remove biases and thermally induced loading of the sensor. This was done by equating friction forces produced in the forward and reverse direction at points where matching measured normal loads exist. This technique allowed for the reliable in-place calibration at dynamic operating conditions within the tape recorder.



**Figure 1. The end-item tape recorder fitted with the tension/friction transducer and the temperature/humidity probe**

### **Performance Testing Setup**

A diagram of the test setup is presented in Figure 2. The tape recorder mechanism was housed in a normal end-item recorder case. The tape recorder was placed in an environmental chamber where the external temperature was controlled from  $-2^{\circ}\text{C}$  to  $35^{\circ}\text{C}$ . The recorder was fitted with the load cell platform for use during the performance testing. Internal temperature, relative humidity, and load cell readings were monitored with the Labview<sup>TM</sup> program and stored on disk.

### **Operational Modes and Recording Rates**

A description of the recording modes evaluated during performance testing is presented in Table 1. The 4:1 Interrupt mode is the primary recording mode in service. This particular mode runs at a tape speed of 0.42 m/s, records to all 840 meters of tape in a single pass, and contains 5 to 7 recording interruptions.

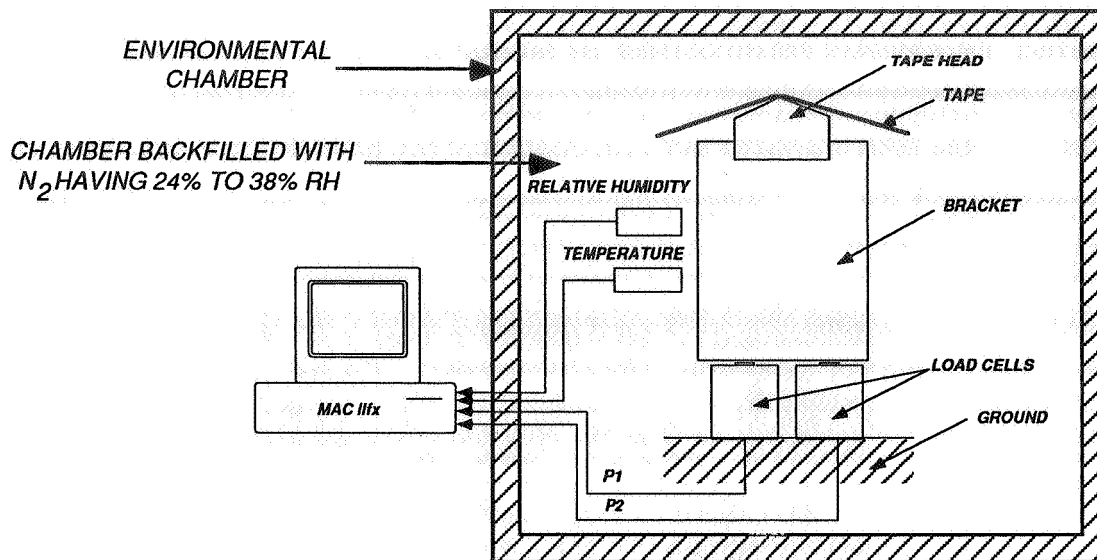


Figure 2. The test setup

Table 1. Operational Mode Definitions

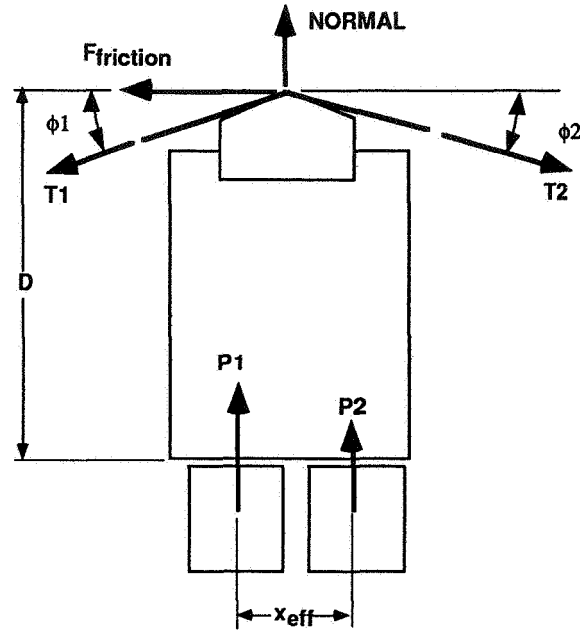
Mode	Tape Speed (m/s)	Number of Recording Interruptions	Temperature and Humidity Stabilization	Description
1:1 Clean	1.6942	NONE	Temperature and humidity is stabilized before preceding to the next cycle	Baseline recording rate used during the test. "Clean" refers to the absence of pauses (or interruptions) during the recording cycle.
4:1 Clean	0.4235	NONE	Both are stabilized before preceding to the next cycle	25% lower speed allows for 4x higher data density on tape.
1:1 Interrupt	1.6942	5 to 7	Both are stabilized before preceding to the next cycle	Baseline recording rate. Interrupt refers to the absence of pauses (or interruptions) during the recording cycle
4:1 Interrupt	0.4235	5 to 7	Both are stabilized before preceding to the next cycle	25% Lower speed allows for 4x higher data density on the tape
1:1 Multi-Cycle	1.6942	NONE	Temp is stabilized, RH is NOT stabilized before preceding to next cycle	Baseline recording rate. Temperature and humidity are not stabilized before moving to additional cycles. Represents accelerated life test operating mode.
Reproduce	1.6942	NONE	Function of recording mode	The baseline reproduce cycle. The reproduce cycle always runs at this tape speed without interruptions.

The reproduction cycle is not initiated until all 840 meters of tape have been recorded. The life tests performed at the vendor match the 1:1 multi-cycle recording mode, which is absent of any recording interruptions. No attempt was made to stabilize the relative humidity between recording cycles in this recording mode.



## Test Methodology: General Equations

A schematic of the loads acting on the system is presented in Figure 3. The schematic shows both the forces due to the tape sliding across the tape head and the reaction forces produced by the load cells.



**Figure 3. Schematic of forces acting on the tape head**

The load cells attached to the bottom of the bracket that supports the head were used to record the loads required to calculate the normal and moment loading. The normal force is a function of the sum of the load cell forces, while the moment is a function of their difference and the distance between the two load cells. The normal and moment loads are used to determine the tape tension, friction, coefficient of friction ( $\mu$ ), and the friction energy. The normal force is determined by considering the equilibrium of the forces in the vertical direction.

$$N = P_1 + P_2 \quad (1)$$

The relationship between the friction and the load cell forces was derived by considering the equilibrium of the moment acting on the bracket. The term on the left side of the equal sign represents the moment produced by the friction force, and the term on the right side represents the couple produced by the load cells:

$$DF_{friction} = x_{eff} (P_1 - P_2) \quad (2)$$

The expression for the friction force is obtained by dividing both sides of the above equation by  $D$  :

$$F_{friction} = \frac{x_{eff}(P_1 - P_2)}{D} \quad (3)$$

The coefficient of friction,  $\mu$ , is the ratio of the friction force to the normal force.

$$\mu = \frac{F_{friction}}{N} \quad (4)$$

The tape tension is calculated, once the friction and normal forces are known. The equilibrium equations in the horizontal and vertical directions produce the following two equations:

$$T_1 \sin \phi_1 + T_2 \sin \phi_2 = N \quad (5)$$

$$T_1 \cos \phi_1 + F_{friction} = T_2 \cos \phi_2 \quad (6)$$

Equations 5 and 6 reduce to two equations and two unknowns, since the normal and the friction forces are known (Equations 1 and 3).

### The Friction Force Bias Removal

Data analysis revealed the presence of a bias in the friction force. The bias was found to be a consequence of a locked-in load cell residual moment load that tends to shift the true null point with a reversal in tape direction. To account for the bias, the friction force, as well as the normal force of sequential record and reproduction runs, was required. Testing and previous experience showed that the normal force (used to derive the tape tension) tends to build steadily from start to finish (Figure 4), regardless of whether recording or reproducing tape data was being performed.

The friction force also exhibits the same increase in magnitude over the length of the recording cycle. Figure 5 shows the unbiased friction force of sequential record and reproduction runs.

Figure 4 shows that the normal force of the record cycle was found to be equal to that of the reproduction cycle at only one tape position. This position, referred to as the "normal cross over" position, provides us with a key piece of information needed to remove the bias. At the cross over position, the record and reproduction normal forces are known to be equal. Assuming that the coefficients of friction at this position in either direction are also equal leads us to the relationship that shows that the friction force, in either direction, are equal and opposite:

$$\therefore F_{repro} = -F_{record} \quad (11)$$

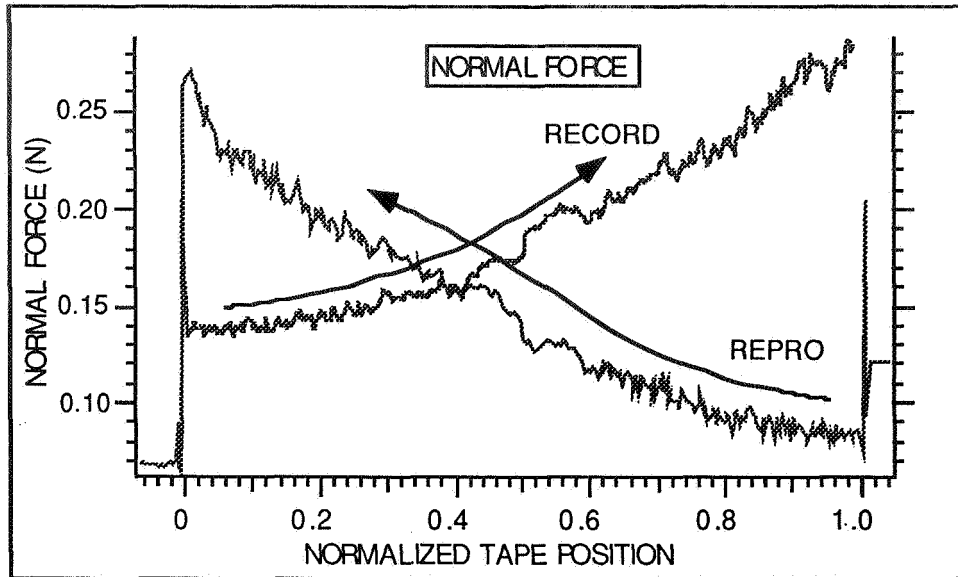


Figure 4. The typical Normal Force vs. Normalized Tape Position profile of sequential record and reproduction runs.

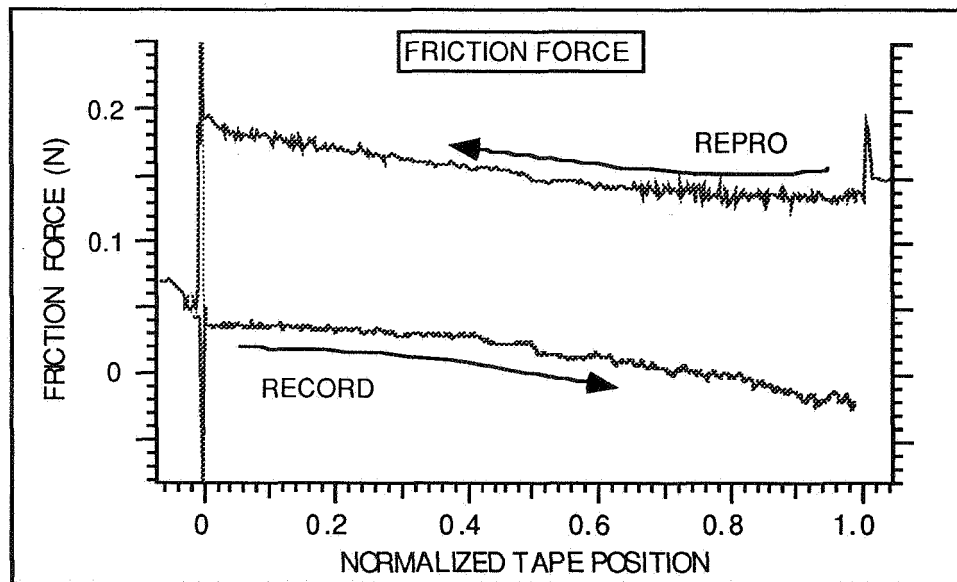


Figure 5. The biased Friction Force vs. Normalized Tape Position of sequential record and reproduction runs

Thus, to remove the bias from the friction force, the location of the cross over point and the biased friction forces formed from sequential record and reproduction cycles must be known. The relationship between the biased friction force (the uncorrected measurement), the bias, and the unbiased friction (the true friction force) becomes:

$$F_{rec}^{biased} = F_{bias}^{friction} + F_{rec}^{unbiased} \quad (12)$$

$$F_{repro}^{biased} = F_{bias}^{friction} - F_{repro}^{unbiased} \quad (13)$$

Assuming that the unbiased friction forces are equal at the cross over point results in the following relationship between the bias and the biased friction forces:

$$F_{bias}^{friction} = \frac{F_{repro}^{biased} + F_{rec}^{biased}}{2} \quad (14)$$

### Air Bearing Effects

A hydrodynamic air bearing, due to the convergent passage or "wedge" formed by the tape and tape head, begins to form at tape speeds above 1.0 m/s [1]. A schematic of the convergent passage formed by the tape and the tape head is shown in Figure 6.

Figure 7 is an approximate representation of the coefficient of friction vs. tape speed diagram presented in [1]. The diagram shows that the air bearing effect begins to form at 1.0 m/s and is strong enough to produce complete separation between the tape and head at speeds of 2.0 m/s.

As denoted in Figure 7, the 1:1 record mode operates at a tape speed of 1.6 m/s, thus which placing it in a region where the air bearing effect is significant but not strong enough to cause complete separation between the tape and the head. On the other hand, the friction is noticeably higher for the 0.4-m/s speed of the 4:1 mode. The differences in friction observed in our tests between the 4:1 and 1:1 recording modes is generally supported by this phenomenon.

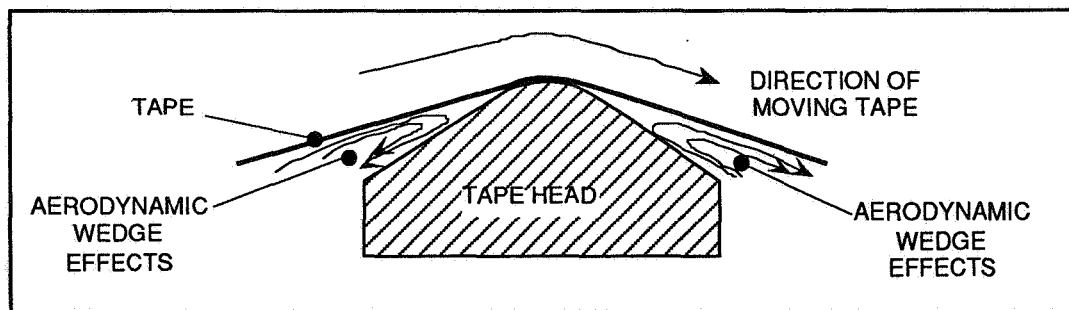


Figure 6. Schematic of air bearing effect

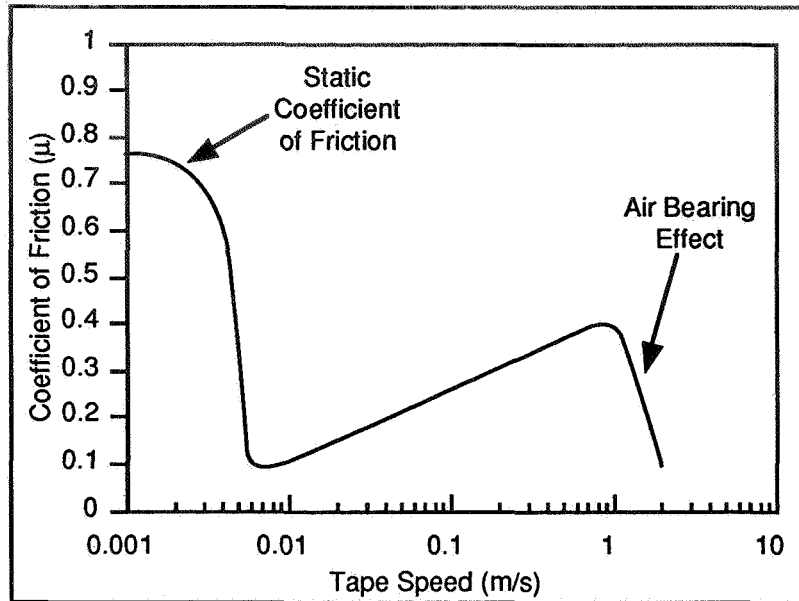


Figure 7. Coefficient of Friction vs. Tape Speed [1]

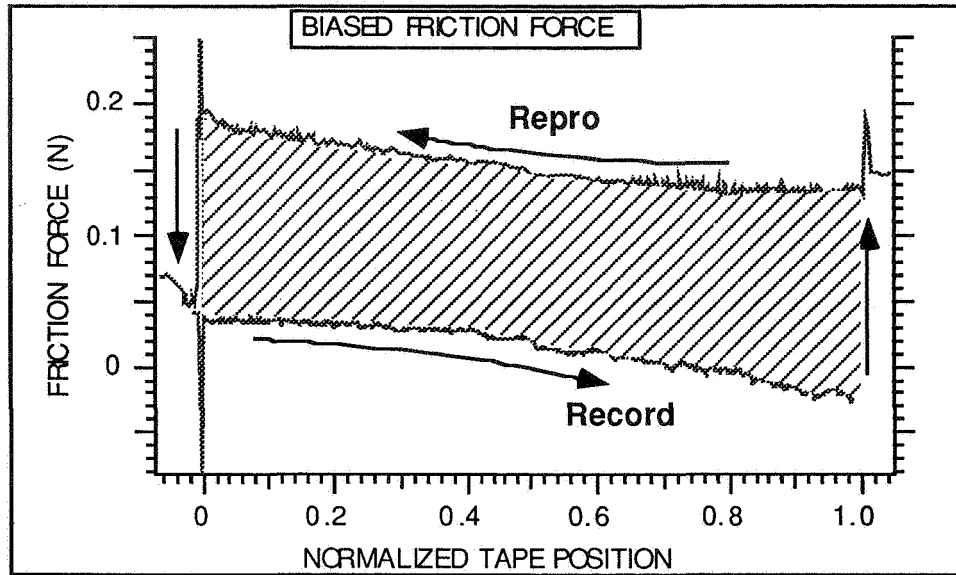
### Friction Energy Approach

The main interest of this investigation was to determine the effect of the tape recorders dynamic operating conditions (speed, temperature, humidity, etc.) on the tape head wear at a given point in time. Since running many concurrent tape head wear tests was impractical, a scalar quantity, referred to as the "Friction Energy" (FE), was formulated. To define the friction energy, we must first consider the classic wear<sup>1</sup> between two bodies. The equation used to calculate the classic wear is known to be proportional to the magnitude of the sliding friction between the two bodies in contact and the distance slid. The quantity can be expressed as the integral of the friction acting over the differential sliding distance  $dx$ .

$$Wear \propto \int_{x=0}^{x=1} F_{friction} dx \quad (15)$$

<sup>1</sup> Archard's classic wear equation states that the wear volume between two hard bodies in sliding contact is linearly proportional to the wear coefficient for the materials, the normal load, and the total distance slid and is inversely proportional to the hardness of the softer of the two bodies. Since wear data is unavailable for the magnetic tape and the tape head material in question, under the specific operating test conditions described herein, it is assumed that the wear coefficient would increase under conditions that produce an increase in friction. While this assumption is not strictly true between different material/geometry combinations, it is believed to be a reasonable way of comparing the effect of operating conditions on one specific contact material configuration.

The integral represents the energy produced by the friction force acting over the sliding distance. In the case of the tape recorder, the FE represents energy imparted by the tape to the tape head. Consideration of sequential record and reproduction runs leads to the formation of a friction hysteresis loop. A typical friction hysteresis loop is presented in Figure 8.



**Figure 8. The FE is the area inside the friction hysteresis loop created by sequential record and reproduction runs.**

The area in the enclosed loop represents the friction energy produced by one complete record and reproduction cycle. The equation for the FE for the sequential runs requires integrating over the closed path:

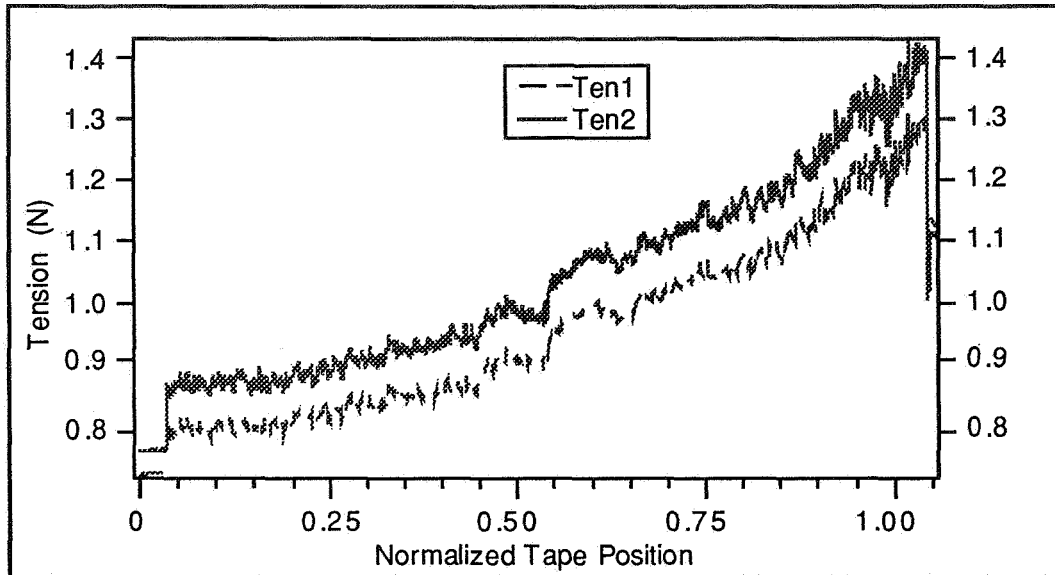
$$FE = \oint F_{friction}(x)dx = \int_{x=0}^{x=1} F_{frict}^{record} dx + \int_{x=1}^{x=0} F_{frict}^{repro} dx \quad (16)$$

By integrating over the closed path, we are able to disregard the steps required to remove the bias. It was for this reason that Equation 16 was used to calculate the FE terms presented in the preceding and forthcoming sections.

The FE is a valuable quantity for several reasons: 1) It is a scalar quantity proportional to the head wear; 2) Unlike  $\mu$ , it can easily be calculated without removal of the bias in the friction force; 3) The area inside the hysteresis loop is unaffected by the bias; 4) The FE can be used to estimate the amount of head life that a recorder has left, provided life test data and the FE of the typical record/reproduction cycles are available; 5) The FE values of different recording modes can be combined with life test data to estimate the number of cycles to failure.

## Results: Tape Tension

The load cell platform was used to gather the raw data used to calculate the tape tension, friction, and coefficient of friction vs. tape position. A typical tape tension profile is presented in Figure 9.



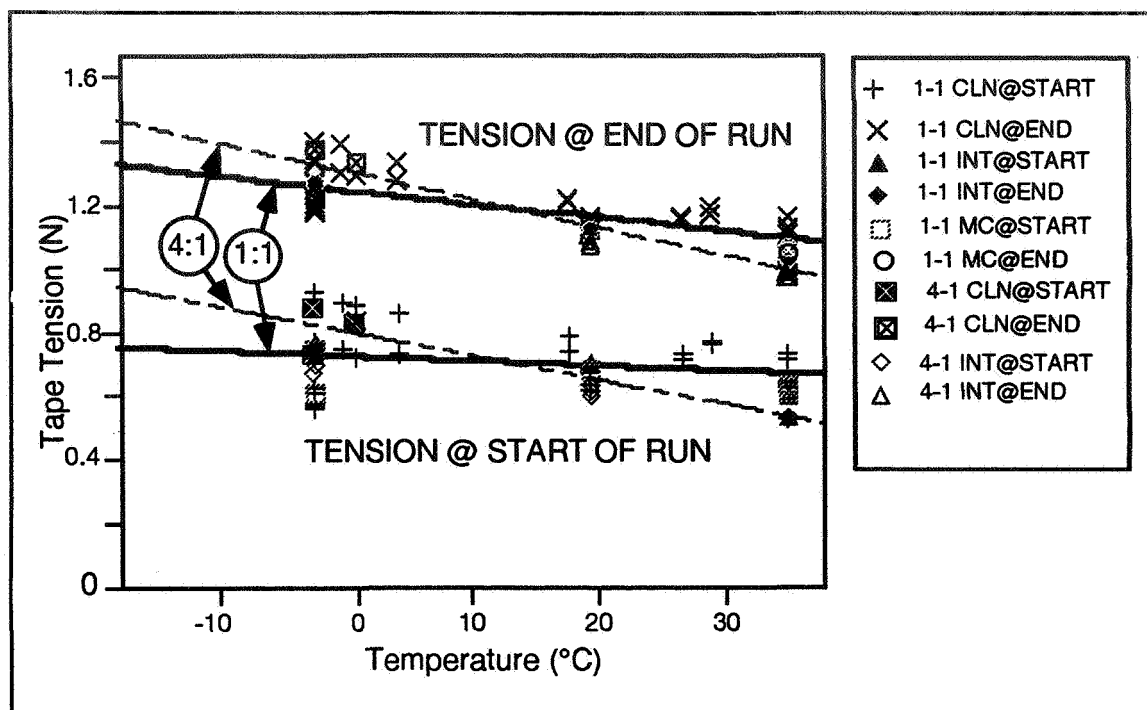
**Figure 9. Tape Tension vs. Normalized Tape Position**

The tension in all the profiles show the same increase in magnitude over the length of the tape. This is a characteristic of tape recorders that have negator spring tensioning mechanisms. These results generally agree with static measurements made by hand with a mechanical tape tension gage.

The tension at the BOT and EOT positions and its variation with recording speed and temperature is depicted in Figure 10. The tape tension profile was found to be insensitive to recording rate. The tension was found to be sensitive to temperature. The testing shows that the tension at the BOT position drops 0.278 N between -2°C and 35°C. The tension profile always shows the same increase of 0.55 N in magnitude from BOT to EOT, regardless of recording rate.

## Results: Speed Effects

Typical friction profiles, produced by the recorder operating in the 1:1 and 4:1 recording mode, are presented in Figure 11. The friction force was also found to increase in magnitude when moving from the BOT and EOT positions. The initial friction in the 4:1 recording mode is approximately twice its 1:1 counterpart. The 0.278-N difference is maintained for the duration of the recording cycle.



**Figure 10. The tape tension at BOT & EOT positions**

The reduction in friction with increased speed is generally attributed to an air bearing effect. The tape tension and friction profiles were used to derive the coefficient of friction as it varies with tape position.

The coefficient of friction variation over the length of the tape was used to calculate the mean coefficient of friction (Figure 13). At temperatures above 4°C, the friction and  $\mu$  doubled in value over its 1:1 counterpart. The temperature was found to have a comparatively small effect on the  $\mu$  associated with the 1:1 recording mode. This is also believed to be due to a more prominent air bearing effect that is present at the higher recording rates. The higher friction values of the 4:1 recording mode were found to be more strongly influenced by temperature effects in the absence of the air bearing effect. The coefficient of friction ( $\mu$ ) is consistent with values published in [1].

The Friction Energy and its variation with temperature and recording mode are presented in Figure 14. The figure shows that the FE of the 4:1 clean and 4:1 interrupt modes are sensitive to temperature. The curves fitted to the data are meant to show general trends. The sample sizes for all the recording modes, with the exception of the 1:1 clean mode, were not large enough to form any meaningful statistics. The data that are available shows that the FE produced by the 4:1 clean and 4:1 interrupt modes have three things in common: 1) both recording modes produced FE profiles that show the same general trends over the temperature range considered; 2) both recording modes produced nearly constant FE levels at temperatures above 4°C; 3) the FE drops nearly 20% at temperatures below 4°C.



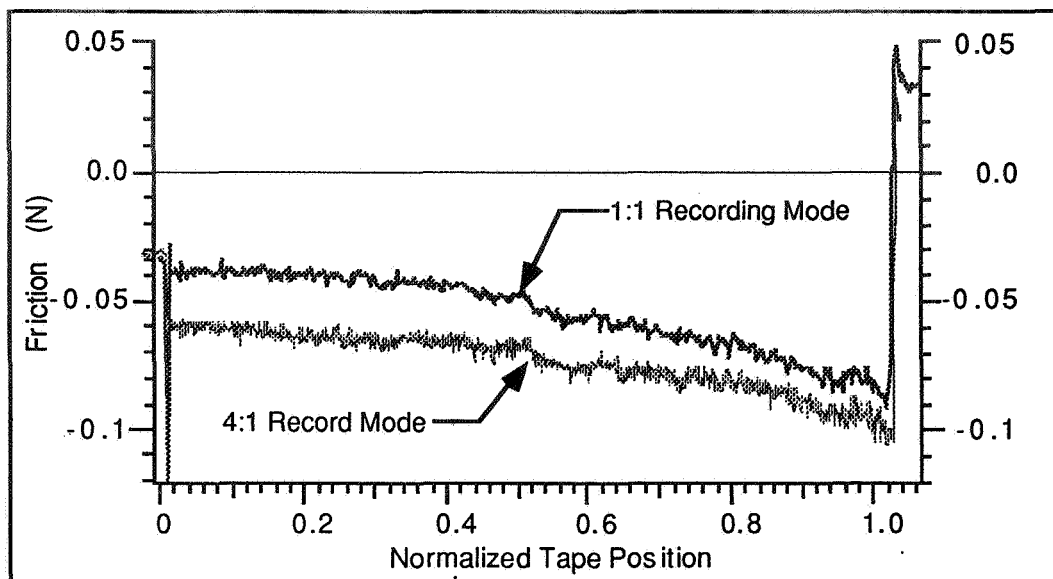


Figure 11. Friction Force vs. Tape Position

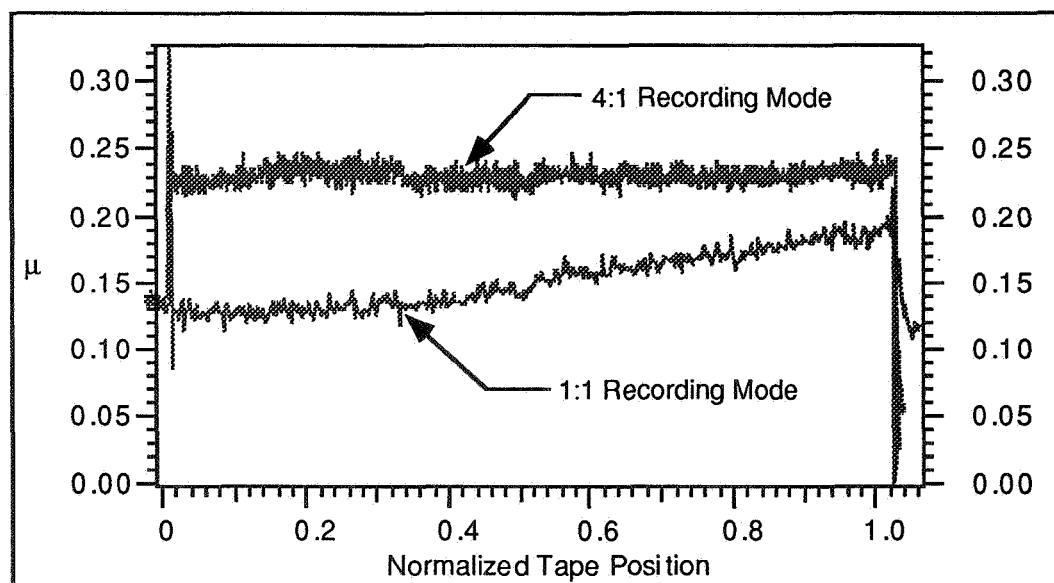


Figure 12. Coefficient of Friction vs. Tape Position

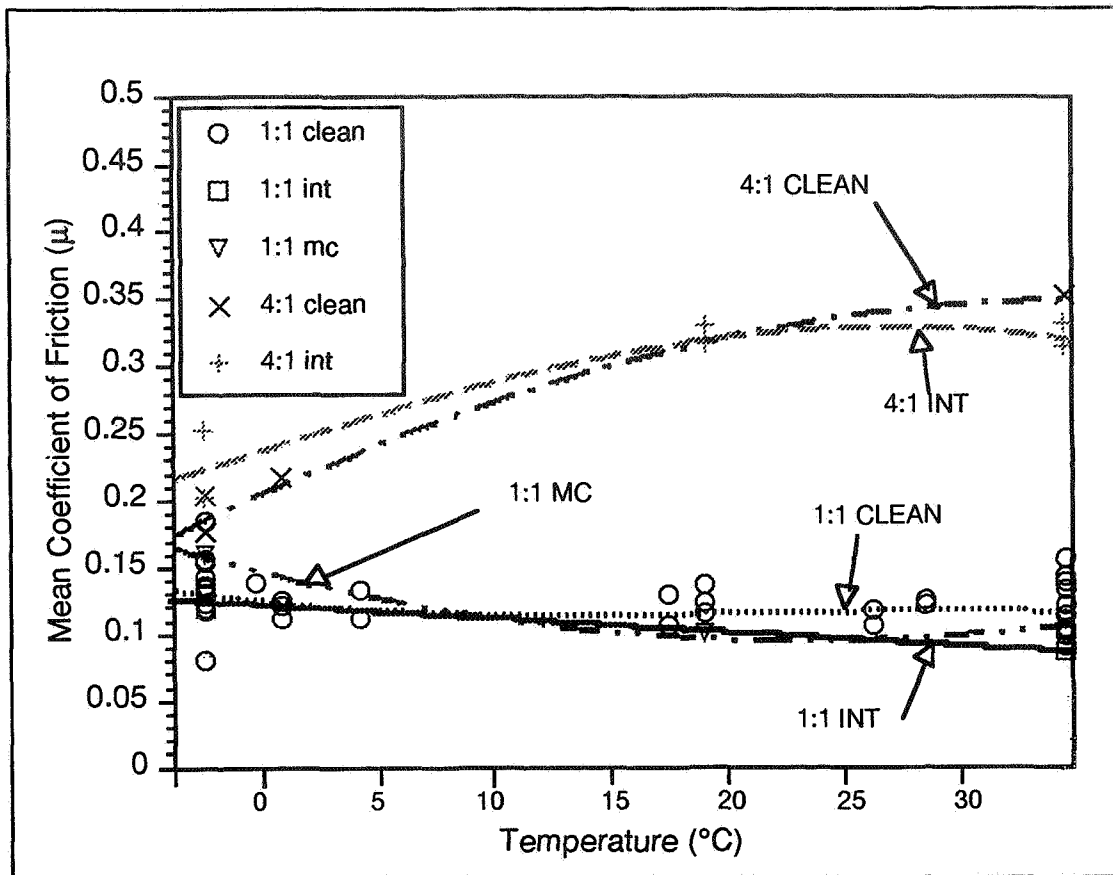
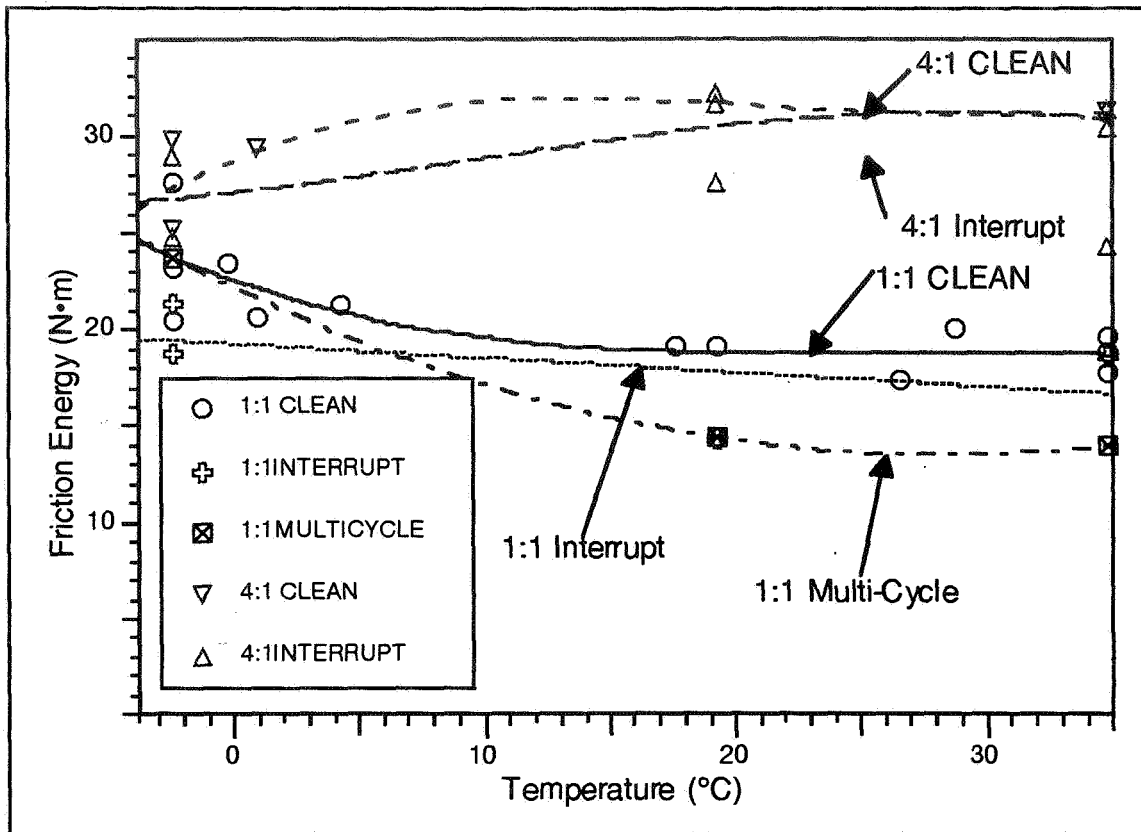


Figure 13. The mean coefficient of friction

### Friction Energy and Head Life

The FE data presented in Figure 14 provided a basis for determining the differences between the life tests performed at LMMS and the vendor. The life test performed at the vendor accumulated 19,000 cycles, all of which were performed at 19.4°C with crude control over the relative humidity. An uninterrupted "1:1 multi-cycle" recording mode was used for the duration of the vendors life test. Inspection of the recorder after accumulating 19k cycles revealed a healthy tape head that was still capable of operation.

The two recorders used for life testing at LMMS did not fair as well. The recorders, designated as the LMMS recorder #1 and #2, accumulated 17,100 and 15,300 cycles respectively. Both recorders were tested a total of 7 days per week, 5 of which were tested at -1.1°C and the remaining 2 days at 35°C. The 1:1 interrupt mode was used for the duration of the test. The life tests were terminated after the recorders had failed operation tests. Inspection of the recorders revealed significant wear in the tape heads of both recorders.



**Figure 14. FE vs. Temperature**

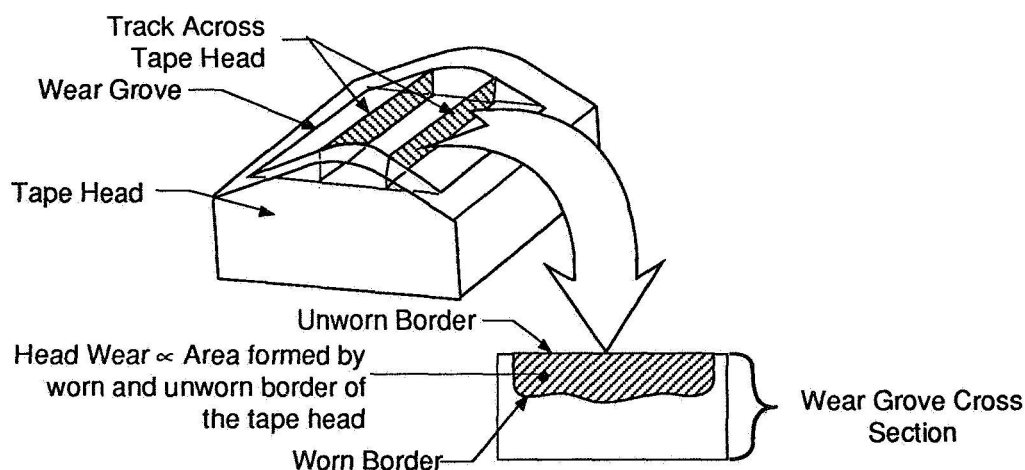
The differences between the results of the life tests performed at the vendor and LMMS are believed to be due to differences in the temperature, humidity level, and operating modes used during the life test. The duty cycle, total number cycles, and friction energy data from this investigation were used to evaluate the differences in head wear. The results presented in Table 2 support the relative test lives between tests performed at LMMS and the vendor. Table 2 shows that, while the recorder tested at the vendor accumulated the largest number of cycles, the recorders tested at LMMS were subjected to a more difficult test based on the larger amount of friction energy. The LMMS recorder #1 incurred 28% more total FE, while the #2 unit incurred 14% more total FE than its counterpart at the vendor. These differences are due to the fact that the friction energy associated with the 1:1 interrupt mode in the -1.1°C range is 50% larger than the FE associated with the multi-cycle recording mode at 19.4°C (used for testing at the vendor), and that 71% of the testing Lockheed performed was at the colder temperature (Figure 14).

**Table 2. FE Comparison of Recorders Tested at LMMS and Vendor**

Recorder Designation	Total No Of Cycles (k)	Days/Week	Days @ -1°C	Days @ 19°C	Days @ 35°C	FE per Cycle @ -1°C ( INTERRUPT)	FE per Cycle @ 19°C ( Multi-Cycle)	FE per Cycle @ 35°C ( INTERRUPT)	Total Friction Energy (N-m)
The Vendor	19	7	0	7	0		14.7		279.3 k
LMMS Recorder # 1	17.1	7	5	0	2	21.56		19.11	356.7 k
LMMS Recorder # 2	15.3	7	5	0	2	21.56		19.11	319.5 k

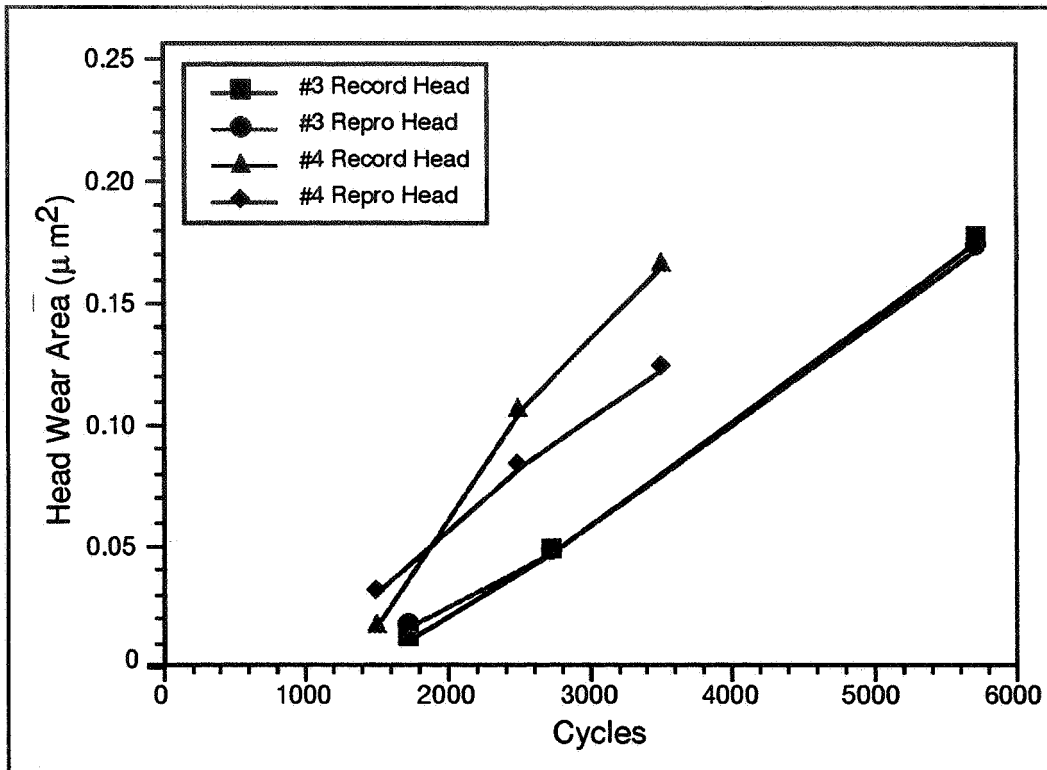
### Head Wear Testing

Head wear testing of the spare tape recorders was initiated to 1) prove or disprove the findings predicted during performance testing; 2) develop algorithms for tape head wear-out using the health of the recorder, recording speed, temperature, and humidity levels; 3) obtain data to better manage the long term use of the recorders still in the field. The head wear test consisted of two recorders operating in the same environment at different recording rates (1:1 and 4:1).



**Figure 15. Profilometer measurements used to measure head wear**

The heads of both recorders were periodically measured for wear with a profilometer. The cross-sectional area of the wear notch was evaluated at two locations across the head (Figure 15). The borders of the cross section consist of the worn and unworn sections of the head. The cross-sectional area values at the two locations were then averaged. The wear notch cross-section vs. cycle number is presented in Figure 16. The results show that the 4:1 recording mode produces twice as much head wear as its 1:1 counterpart. The results of the head wear testing support the findings and prediction formed during performance testing.



**Figure 16. Measured head wear**

## Conclusion

The investigation successfully provided dynamic friction and tape head wear measurements in an operational tape recorder. The sub-miniature load cell platform provided the necessary sensitivity but required an in-place calibration.

The friction energy provides a useful scalar quantity for evaluating relative wear without the need for frequent disassembly and head wear measurements. The larger friction energy associated with the LMMS life test appears to explain qualitatively the observed shorter life. The end-item recorder head wear test shows a strong correlation between increased head wear and lower recording speeds, as predicted by the friction energy method described in this study. This is consistent with the higher friction at low tape speeds reported in the literature [1].

## References

1. Jorgensen, F., 1988, "The Complete Handbook of Magnetic Tape Recording, 3rd Edition," Tab Professional and Reference Books, Blue Ridge Summit, PA.
2. Cuddihy, E.F, "Hygroscopic Properties of Magnetic Recording Tape," IEEE Transactions on Magnetics, Vol. Mag-12, No. 2, March 1976.



3537  
50433  
125119 ✓  
p 12

## New Antenna Deployment, Pointing and Supporting Mechanism

V. Costabile\*, F. Lumaca\*, P. Marsili\*, G. Noni\*,  
C. Portelli\*\*

### Abstract

On ITALSAT Flight 2, the Italian telecommunications satellite, the two L-Ka antennas (Tx and Rx) use two large deployable reflectors (2000-mm diameter), whose deployment and fine pointing functions are accomplished by means of an innovative mechanism concept. The Antenna Deployment & Pointing Mechanism and Supporting Structure (ADPMSS) is based on a new configuration solution, where the reflector and mechanisms are conceived as an integrated, self-contained assembly. This approach is different from the traditional configuration solution. Typically, a rigid arm is used to deploy and then support the reflector in the operating position, and an Antenna Pointing Mechanism (APM) is normally interposed between the reflector and the arm for steering operation. The main characteristics of the ADPMSS are:

- combined implementation of deployment, pointing, and reflector support;
- optimum integration of active components and interface matching with the satellite platform;
- structural link distribution to avoid hyperstatic connections;
- very light weight;
- high performance in terms of deployment torque margin and pointing range/accuracy.

After having successfully been subjected to all component-level qualification and system-level acceptance tests, two flight ADPMSS mechanisms (one for each antenna) are now integrated on ITALSAT F2 and are ready for launch. This paper deals with the design concept, development, and testing program performed to qualify the ADPMSS mechanism.

### Introduction

The deployment mechanisms for large antenna reflectors on satellites must bring the reflector from its stowed launch configuration up to the operative, in-orbit deployed one. A three-axis stabilized spacecraft, once in orbit, has to continuously adjust the fine pointing (relative to the ground stations) of its reflectors when high pointing accuracy is required.

The ITALSAT F2, an Italian satellite for domestic telecommunications service, was commissioned by the Italian Space Agency (ASI) to Alenia Spazio as follow-up to the previous ITALSAT flight unit 1. It is scheduled for launch in mid-1996. It was conceived, such that a higher payload mass (with respect to F1) was introduced; therefore, a particular effort was made to reduce the overall satellite weight as much as

---

\* Alenia Spazio, Rome, Italy

\*\* Agenzia Spaziale Italiana (ASI), Rome, Italy

### Design Criteria

The ADPMSS has been developed according to the following design criteria:

- a) use an integrated system to cover the antenna deployment, pointing, and support functions with an optimum function/hardware allocation;
- b) ensure a "load-free" condition for the ADPMSS hardware during the launch phase, such that its basic dimensioning is only enabled for the on-orbit stiffness requirement. In other words, the mechanism is not a part of the launch load path between the S/C structure and the antenna reflector when in the stowed condition (launch configuration); therefore, the ADPM parts do not carry any significant load (except for that of the masses when subjected to flight accelerations). As a positive consequence of this criterion, the use of beam elements became feasible, thus leading to the achievement of the maximum structural efficiency;
- c) tailor the structural links architecture for supporting the reflector on the spacecraft body to avoid hyperstatic connections, which could result in dangerous preloads acting on the mechanism;
- d) achieve an accurate definition of specific loads on structural elements and on kinematic couplings to get maximum strength/mass ratio;

Although all the previously described design criteria are very important for the ADPMSS functionality/efficiency, (b) represents a key design point. To meet this requirement, special I/Fs have been designed to connect the ADPM parts to the reflector. In fact, when the antenna is held down by the Pyro Release System, each ADPM-reflector I/F allows for large relative motion (several millimeters) without inducing significant loads on the matching parts. After the antenna release, the ADPM internal springs immediately restrain all the reflector degrees of freedom to the S/C body. The same springs provide the internal forces necessary to preload the I/F matching parts to avoid backlash. Therefore, this approach provides both a simple passive switching of structural links from large compliance to large stiffness and a backlash-restraining capability of the kinematic couplings.

### **Mechanisms Description**

#### Antenna Deployment Mechanism

The ADM is an articulated frame, composed of a "trapezium" and an "upper beam" that are linked together by a metallic/plastic hinged joint. All the rods are CFRP-made. The upper beam interfaces to the reflector center by a suitable gimbal, and the assembly is preloaded by a compliant spring, mounted on the terminal part of the upper beam. On the S/C side, the trapezium is fitted on two metallic, hinged supports: each consists of one propulsive rotational spring and one oil damper device. The assembly, consisting of the two rotational springs and the one mounted on the upper beam, is able to provide the motor torque necessary for the antenna deployment motion. Specifically, just after the reflector release, the upper beam spring acts as a kick-off spring. The deployment motion is made very smooth by the two dampers. Due to the deployment kinetics, the motor torque value is maximum at both the beginning and the end of the deployment run (theoretically, it tends to infinity in this case!), when the torque needs are greater. Over the entire ADM run, the minimum torque margin



value is 8. When the antenna is in the stowed configuration, the ADM is folded in the allowable volume between the reflector and the S/C side wall.

### Antenna Pointing Mechanism

The APM is a linear actuator, essentially composed of a rotating stepper motor and a screw gear, connected to the motor shaft by a lead screw coupled to the screw gear to obtain the linear motion. These components are integrated on a compact aluminum frame, which also provides the support guides for the lead screw and the housing for the electrical end-stroke limits. The linear motion of the lead screw is directly applied to the reflector arm pin-jointed I/F. The kinematic couplings, in which only sliding motion between parts is foreseen, are made of hard materials in contact with soft, self-lubricating materials. The coupling, between the screw gear and the lead screw, is made of steel (screw gear) in contact with Teflon, which constitutes an insert that is mounted inside the lead screw titanium case. This assembly has been carefully designed to ensure the maximum dimensional stability of the Teflon insert under both mechanical loads and thermal environment. This is to avoid stress concentration inside the Teflon-made part from asymmetrical contact between the matching parties. The prismatic coupling between the supporting case and the lead screw body is based on Vespel parts, which ensure a low friction coefficient. The driving unit is a dual-wound, four-phase hybrid stepping motor with a step angle of  $1.8^\circ$  and a minimum dynamic torque value of 170 N-mm. Due to the geometric characteristics of the screw gear-lead screw kinematic coupling, a single motor step provides a displacement of 0.01 mm at the reflector arm I/F level. The overall APM kinematic chain axial play is continuously recovered by the Spring Restraining System, which acts on the motor with a constant force over the entire linear actuator stroke.

### Reflector Supporting Structure

The RSS sub-assembly is a truss-shaped structure, firmly mounted on the reflector back side, and is composed of two short "arms," made of sandwich material (CFRP skins and Al core), in conjunction with six CFRP-made rods. In addition, a special rod, coincident with the actual antenna deployment axis, is interposed between the dish (bottom edge) and one actuator to prevent in-plane reflector rotations. The RSS arms are designed to provide high stiffness along the in-plane directions and low stiffness in the orthogonal one. This solution, in conjunction with a suitable gap at the APM interface, avoids induced stresses on the APM-RSS composite. The ADPMSS features are summarized in Table 1.

## **Development and Qualification Program**

The ADPMSS development and qualification phase included manufacturing and testing of three models:

- The bread-board model was used to validate the design concept and to provide high confidence of the conceptual approach. It mainly consisted of preliminary testing on critical parts — the coupling between the lead screw and screw gear of the APM — to verify ADM kinematics for accomplishing correct reflector deployment function.

- The engineering model (EM) was mainly used for development purposes, to define the main design choices, and to detect, in advance, any major criticality before starting the subsequent formal qualification test program. It was built, as close as possible, to flight standards to be quite representative of the final Flight Model. At the end of the activity on the EM, a high level of design maturity was obtained.
- The qualification model (QM) was the hardware built at full flight standard and used to formally qualify the ADPMSS. It was submitted to a complete test campaign. After successful completion of the first testing phase at the component level (i.e., the APM and ADM were tested alone as single components), the QM underwent a sub-system level (i.e., at antenna level) test program.

#### Component Level Test Program

Due to the differences in the functional aims, the duty cycle characteristics, and the design of each component, the ADM, APM, and RSS qualification models were qualified according to different test plans and modalities to cover all the environmental, functional, and reliability aspects.

The ADM alone was submitted to the following component-level qualification test program:

- Deployment functional check at ambient conditions (torque margin, deployment time, deployment angle repeatability);
- Vibration along three axes (sine, random, quasi-static loads applied on each axis);
- Deployment functional check at ambient conditions (torque margin, deployment time, deployment angle repeatability);
- Deployment functional check at extreme temperatures (deployment time at +55°C hot and at -25°C cold conditions).

Furthermore, before starting the test on the ADM, a special test program was performed to qualify the damper alone, whose design was based on the fluid viscosity effect principle. The damper test sequence included:

- Reference functional test at ambient conditions (50 mechanical cycles of extension/retraction, followed by fluid leak check)
- Thermal vacuum (4 thermal cycles, -26°C/+50°C range, including 6 cycles of extension/retraction at cold and 20 cycles of extension/retraction at hot)
- Final functional test at ambient conditions (50 mechanical cycles of extension/retraction, followed by fluid leak check).

Similarly to the ADM tests, the APM alone was also submitted to a dedicated component-level qualification test program. It included the following:

- Performance test:
  - motor pull-in minimum voltage measurement
  - electrical/mechanical stops check
  - step size check and its reproducibility
  - step response
  - actuator torque margin
  - backlash verification
- Vibration along three axes  
(sine, random, quasi-static loads applied on each axis)
- Performance test  
(short form);
- Thermal vacuum with short form performance test  
(temperature range: -21°C/+58°C, four cycles);
- Life test  
( $5 \times 10^6$  triangle wave cycles with 50 steps peak-to-peak; i.e., 100 steps each cycle).

All the measured parameters fulfilled the requirements, and an excellent repeatability, both before and after environmental exposure, of the main functional parameters were found.

The RSS was not submitted to a dedicated test campaign because it was not a "stand-alone component"; but by a mechanical point of view, it could be considered a part of the reflector structure. Therefore, its qualification was achieved in the frame of the subsequent ADPMSS sub-system level test program.

#### Sub-system Level Testing

The sub-system testing was carried out at the antenna level using a complete QM ADPMSS integrated on a QM reflector and mounted on a satellite structural panel simulator. The purpose of the antenna-level test program was to validate the integration procedure of the "reflector-ADPMSS" composite on the satellite and to verify that the mechanisms meet the performance requirements after exposure to the qualification load. To perform this test program, a typical off-loading set-up was used: the reflector was placed with the hinge line vertical and suspended on swing-arm test equipment ("opening door" concept).

The test plan, at the sub-system level, included the following verifications:

- functional deployment with reflector manual release in ambient conditions
- deployment angle repeatability
- deployment time
- ADM torque margin
- environmental exposure: vibration (sine and acoustic), thermal vacuum cycling

- functional deployment with reflector pyro release in ambient conditions
- deployment angle repeatability
- deployment time
- ADM torque margin
- antenna steering test (APM stepping)
- first mode frequency of deployed reflector (dynamic response).

The tests were successfully performed, and all the obtained results met the requirements. In particular, the torque margin, measured by applying a zero kinetic energy test methodology, was always 8, at the minimum, and the deployment time was 22 seconds average, with a maximum delta variation of  $\pm 0.5$  second. These values were produced very consistently when the same parameters were measured during the ADM component qualification.

During the test program, two anomalies occurred and resulted in design changes, as described later.

#### Radio Frequency Compatibility Check

The qualification activity at subsystem level also included a radio frequency compatibility check to verify and quantify any effect of the ADM on the antenna electrical performance, since the mechanism is located between the antenna feed cluster and the reflector.

The test was performed throughout the antenna test range with two antenna configurations: one without the ADM (i.e. "clean" area between feeds and reflector), and one with the mounted ADM (corresponding to the antenna on-orbit configuration). For both conditions, the radiation patterns in azimuth and elevation were measured and then compared, also taking into account the test range measurement errors and repeatability.

The test results showed a negligible influence of the ADM on the first side lobe level of co-polar radiation patterns along the azimuth plane. This degradation corresponds to a worst-case interference contribution on communication channels of -34 dB in transmit and -30 dB in receive. These values were largely acceptable because the impact on the antenna performance along the azimuth plane was always well within electrical requirements.

On the other hand, the test demonstrated that the ADM did not degrade on the first side lobe along the orthogonal plane (i.e., elevation plane). Furthermore, all the other antenna parameters (e.g., beam pointing, gain slope, first null shift) were not significantly influenced by the presence of the mechanism.

Finally, mutual coupling verifications were performed between the Ka and L-band functions by transmitting a Ka signal and measuring the received level in L-band. In this case, the impact of the ADM was also quite negligible because the measured values were well within the antenna noise behavior requirements (i.e., about -55/-60 dB).

## **Satellite Level Testing**

After the successful completion of ADPMSS qualification, the mechanism was declared ready for space application. Therefore, the ADPMSS was selected for use on the ITALSAT Flight Model 2 satellite for on-orbit deployment and steering of the two large L-Ka antenna reflectors. To optimize the Assembly, Integration and Test (AIT) operations sequence at satellite level, testing of antenna reflector integration/alignment and deployment/pointing was planned to occur just after the satellite alignment phase. Instead of using the traditional test set-up approach (based on testing configuration with spacecraft z-axis parallel to the floor and reflector hinge line vertical), as previously used during the sub-system test campaign, the spacecraft is in a vertical position (alignment set-up), with the satellite z-axis orthogonal to the floor. To perform the AIT operations on the "reflector-ADPMSS" assembly in this condition, an innovative test set-up concept was developed because the reflector had to be deployed with the hinge line horizontal ("lowering draw bridges" concept).

The AIT operations were performed by special off-loading test equipment, aimed to compensate for the gravity effect on the "reflector-ADPMSS" assembly during both the integration and testing phases. This equipment is based on a counterweight concept with the reflector suspended on a steel wire at its center of gravity.

The test plan, at satellite level, included the same verifications previously performed during the antenna-level testing and aimed to verify that the "reflector-ADPMSS" assembly integration on the satellite was correctly done.

All the test results at satellite level were well within performance requirements and always consistent with the same parameters that were previously measured during the qualification test programs at both component and sub-system level. No anomalies or problems occurred.

## **Development Problems and Solutions**

During the development/qualification program, some problems were encountered and then solved. Among them, the most significant anomalies (by engineering point of view) occurred during the APM life test and during the sine vibration testing, performed at sub-system (antenna) level. Two major anomalies were detected:

- Modest pollution of Teflon particles was generated due to wear phenomenon in the kinematic coupling between the steel gear screw and the Teflon-made internal insert of the lead screw. This fact created concern, not for the APM integrity risk, since the thread thickness was large enough to guarantee a long lifetime, but because the Teflon particles escaping from the mechanism could pollute the satellite components (e.g., mechanisms, optical sensors). The problem was solved by modifying the internal thread profile of the Teflon insert (i.e., a sort of race, placed at base of the thread, was added to act as a "reservoir" for Teflon particles). Furthermore, tighter manufacturing tolerances of the gear/lead screw assembly and improved surface finishing of the gear screw thread were also introduced;

- Friction torque of the electric motor ball bearing increased due to a lubrication fault, induced by a sum of causes. The bearing is fitted with a Duroid cage (PTFE/MoS<sub>2</sub>/glass fiber composite). After a thorough investigation, involving the bearing supplier and the European Space Tribology Laboratory, the findings were:
  - Due to the limited motor shaft rotation (90°), each ball path did not overlap the adjacent ones;
  - The high peak friction torque was caused by an accumulation (on the raceways) of heavily compacted Duroid debris from the cage at the ends of ball motion profile. No steel wear was found;
  - The relatively high peak contact Hertzian stress (about 1.4 GPa) due to the motor internal preload (45 N) and the air humidity (life test in a thermal chamber at ambient pressure) caused the cage anomalous wearing phenomena and the Duroid cage debris compression in the raceway "dead zones."

To overcome this problem, a series of improvements have been introduced in the motor design: internal preload reduction and more accurate evaluation of its actual value after motor assembly, tighter tolerances applied to the bearing-shaft fitting, etc.

The lessons learned were that, except for the specific design optimization need, this problem mainly occurred as consequence of attempting to carry out a very accelerated life test aimed at saving testing time. This led to unrealistic worst-case mechanical cycling. Therefore, a subsequent, more realistic, life test program was performed on the APM, and the qualification was then fulfilled.

Two other anomalies occurred in the frame of the sub-system level testing. The first problem, concerning the APM, was the breakage of one internal joint between the motor and the gear screw. The subsequent investigation showed that an operator mistake, during the APM integration phase, caused pre-stress conditions in the joint. Therefore, a more accurate step-by-step integration procedure was generated. In addition, improvements on the joint design, such as material change (from Vespel to aluminum) and tighter manufacturing tolerances, were also introduced.

The second anomaly occurred during the dynamic response test. The first resonance frequency (10.13 Hz) of the reflector in the deployed configuration was too close to the first sub-harmonic of the antenna closed-loop tracking system (i.e., 9.125 Hz). This could create instability of the control loop system during antenna pointing operation, thus leading to a long steering operation time. Therefore, the RSS design was improved by adding two additional struts, so that the structural stiffness improved and the deployed reflector frequency increased up to 11.1 Hz.

## Conclusions

The extensive development program and subsequent testing campaign — at component, sub-system, and system level — demonstrated the validity of the ADPMSS innovative design concept and its suitability for space application. All the problems during the qualification process were solved by suitable changes that definitively eliminated the malfunctions and improved the mechanism performance.

The launch of the ITALSAT 2 satellite is currently scheduled for Summer, 1996. ASI and Alenia Spazio are now waiting for the in-orbit ADPM behavior confirmation and are looking forward to possible new future applications of the presented mechanism concept for other spacecraft.

**TABLE 1    ADPMSS MAIN TECHNICAL FEATURES AND PERFORMANCE**

DESCRIPTION	VALUE
MASS	5.2 KG
REFLECTOR DEPL. ANGLE ADJUSTMENT CAPAB. (on ground)	$\Delta\alpha = \pm 0.3^\circ$
REFLECTOR DEPLOYMENT ANGLE ACCURACY	$\Delta\alpha = \pm 0.001^\circ$
DEPLOYMENT TORQUE MARGIN	M = 8 (minimum)
REFLECTOR POINTING ANGULAR RANGES	Az.: $\pm 2.1^\circ$ , El. : $\pm 3.1^\circ$
POINTING ANGULAR RESOLUTION	Az.: $\Delta\alpha = 0.0006^\circ$ El. : $\Delta\epsilon = 0.001^\circ$
STEADY STATE POINTING MODE ACCURACY (thermal and mechanical errors contribution)	$\Delta\alpha = 0.05^\circ$
REFLECTOR SLEW RATE	$\omega = 0.11 \text{ deg/sec}$
ON ORBIT STIFFNESS	1st mode at 11.1 Hz
OPERATIONAL LIFE	10 Years
RELIABILITY	P = 0.9966

# ADPMSS GENERAL ARCHITECTURE

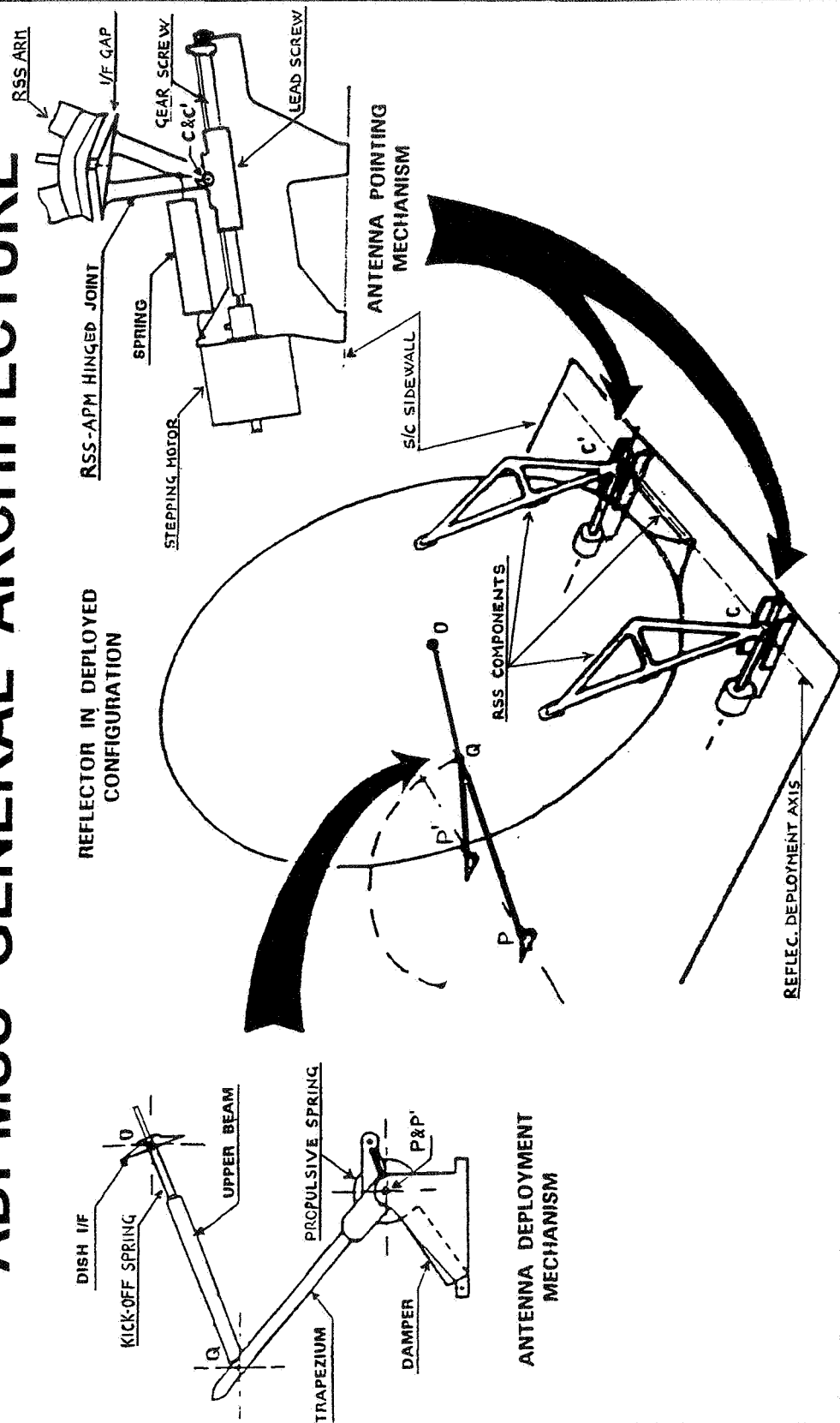
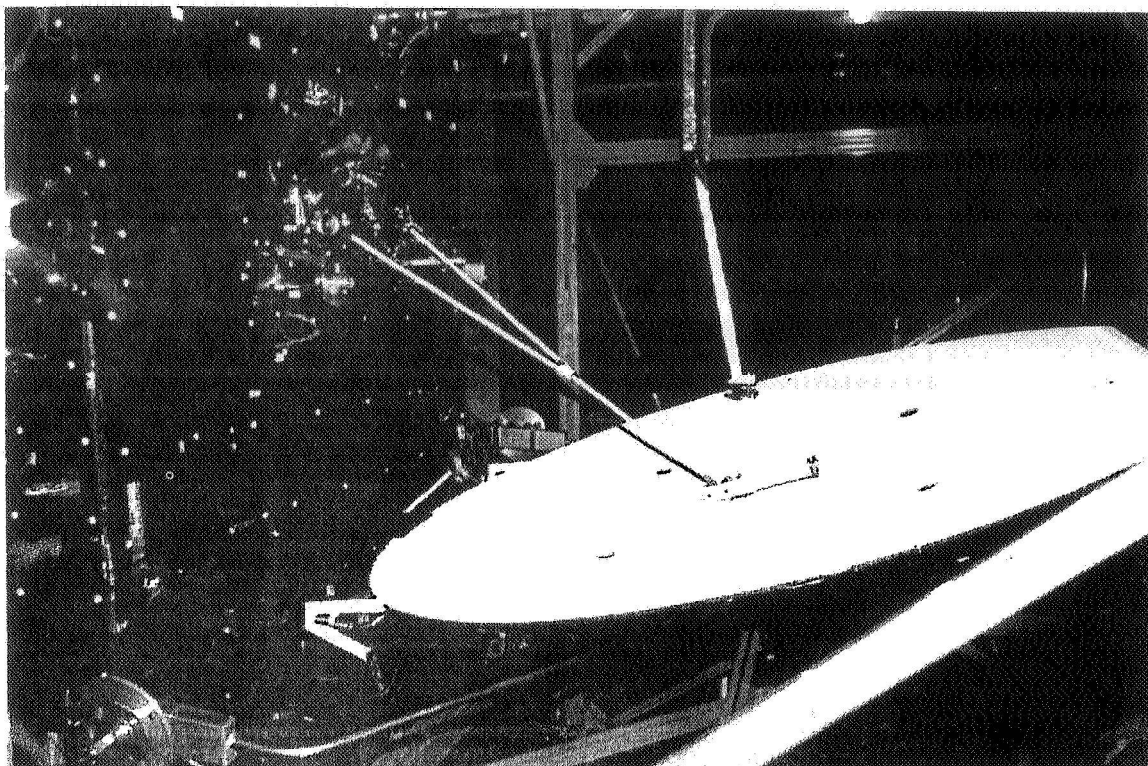
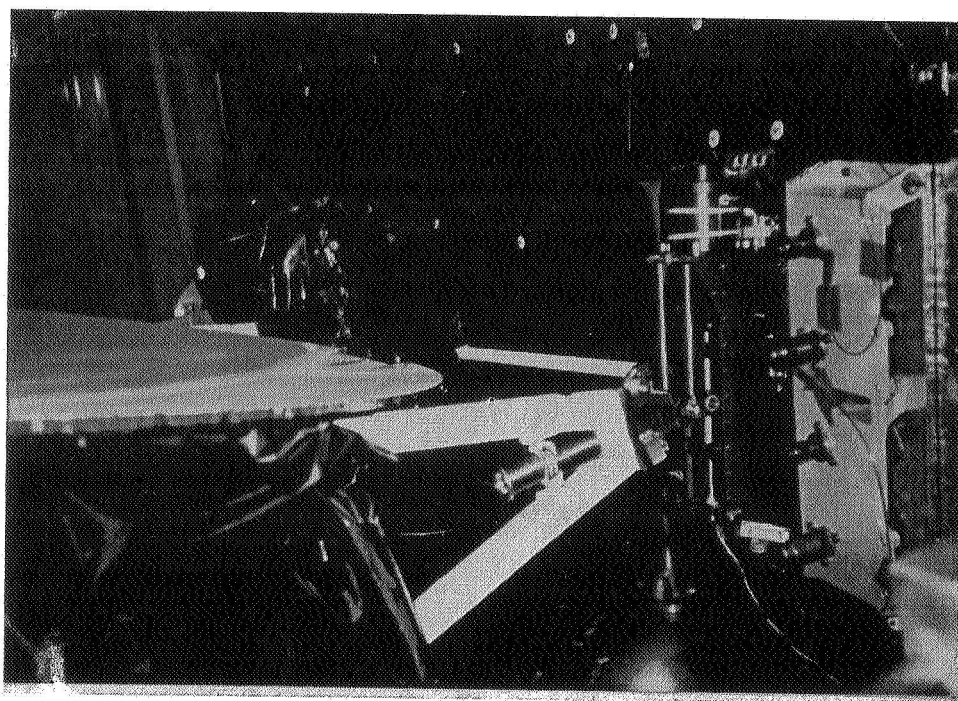


FIGURE 1 ADPMSS GENERAL ARCHITECTURE

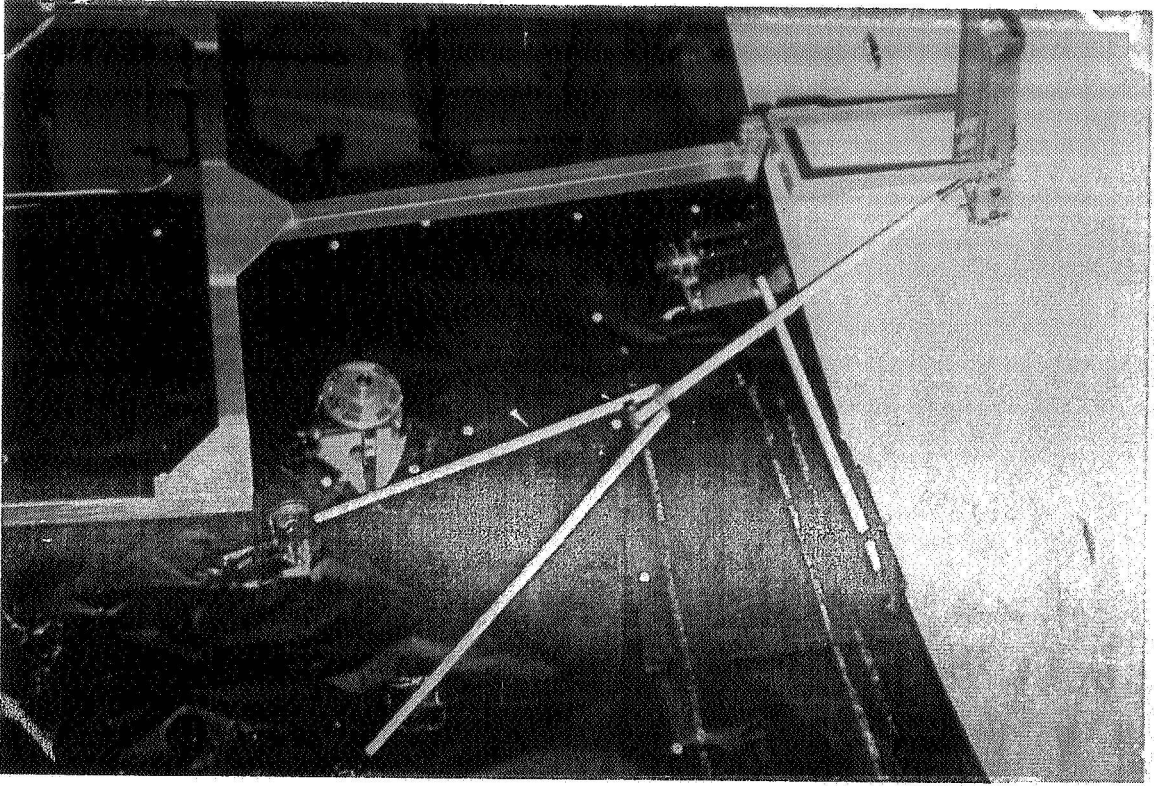




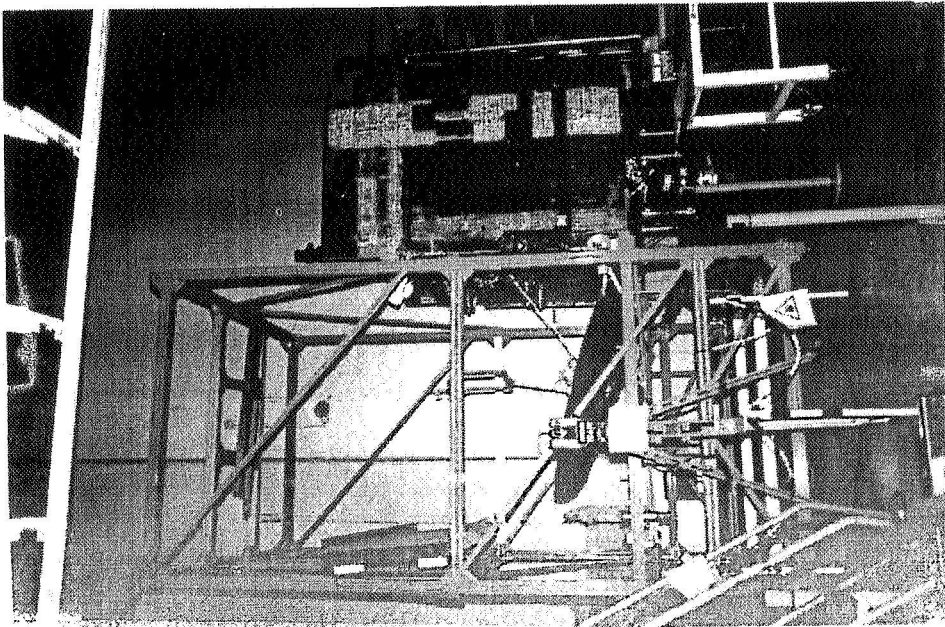
REFLECTOR AND ADPMSS ON THE ITALSAT SATELLITE



APM ACTUATOR DETAILS



ADM DETAILS



SYSTEM LEVEL TESTING

56-74  
56434  
125120 ✓

Development of a Scan Mirror Assembly  
for an Extreme Ultraviolet Atmospheric Scanner

Thomas R. McBirney\*

p 14

## Abstract

A Scan Mirror Assembly (SMA) was created to rotate its SiC mirror through 8.5° in 90 seconds, then to return in 2 seconds, and repeating this motion continuously for at least three years.

Unique design features are:

- **Lightly preloaded, large angular-contact bearings.**
- Bearing preload using a **convoluted diaphragm.**
- Launch locks avoided by **static balancing.**
- Limited-scan rotation so **ball travel does not overlap.**
- **Silicon carbide mirror** on semi-kinematic mounts.

## Introduction

Swales & Associates, Inc. was asked by the Naval Center for Space Technology to design and fabricate a Scan Mirror Assembly (SMA) for the Special Sensor/Ultraviolet Limb Imager (SSULI) Instrument for launch on the DMSP spacecraft. The SMA is expected to rotate its mirror through 8.5° in 90 seconds, then return in 2 seconds, repeating this motion continuously for at least three years with occasional excursion to 15° for cross calibration with other instruments. Figure 1 is a cross-section view of the SMA.

The SMA development program has resulted in the delivery of six flight articles. It also taught some lessons in spacecraft mechanism design, and these should be shared. Unique design features of the SMA are:

- **Lightly preloaded** (less than peak launch load), **angular-contact bearings** that are sized **larger** than the bearing loads would normally require.
- Bearing preload using a **convoluted diaphragm.**
- Launch locks avoided by **static balancing.**
- Limited scan rotation so **ball travel does not overlap.**
- A solid **silicon carbide mirror** on semi-kinematic mounts.

After design changes were made to eliminate failures of the diaphragm and mirror mounting, the SMA has successfully passed all system-level functional and environmental tests.

---

\* Swales & Associates, Inc., Beltsville, MD

56059606 USI

## Description

The SMA consists of an aluminum housing that supports several components:

- A 16-speed resolver stator.
- A DC torque motor stator.
- Two angular-contact ball bearings, which support a titanium shaft, which, in turn, supports the resolver and torque motor rotors and a mirror.

## Description of Noted Features

### Ball Bearings

The angular-contact Barden bearings are made with 440C races and TiC-coated 440C balls plated with "Demnum" grease. The retainer, made of Meldin 9000, is vacuum-impregnated with "Demnum" oil.

### *Lubrication*

"Demnum" oil is a perfluoropolyether, low-outgassing lubricant made by Daiken Industries, Ltd. (Osaka, Japan). In recent NASA outgassing tests, its outgassing was measured at 0.00% CVCM (Collected Volatile Condensable Material) and 0.01% TML (Total Mass Loss), which is lower than any other known lubricant. (NASA Reference Publication 1124<sup>1</sup> lists Demnum L200 grease at 0.05% TML/0.00% CVCM and lists Demnum S200 oil at 0.12% TML/0.03% CVCM).

This lubricant was chosen as the best way to protect the delicate, far-ultraviolet reflecting surface of the mirror from molecular contamination.

There were considerable discussion and controversy regarding the use of this lubricant, since it is well-known that the perfluoropolyether lubricant family is known to suffer long-term chemical breakdown in the presence of iron/iron asperity contact that occurs in the boundary layer regime, and (since the scan speed is extremely slow) the bearings will operate continuously in that regime. This chemical breakdown is accelerated by the breakdown products themselves.

The proposed alternate lubricant was "Pennzane 2000" with 5% lead naphthanate added to provide boundary layer lubrication. Pennzane 2000 is listed in NASA Reference Publication 1124<sup>1</sup> as 0.42% TML/0.21% CVCM, and Pennzane 2000 with 5% Lead naphthanate is listed as 1.64% TML/0.19% CVCM, which raised concerns about mirror contamination. However, contemporary work at the Aerospace Corporation indicated that it was the solvent vehicle used to render lead naphthanate soluble in Pennzane 2000 (and not the lead naphthanate itself) that outgassed. This may well be correct, but no other solvent vehicle was proposed. In any event, the use of TiC-coated balls in our bearings eliminates the iron/iron asperity contact that causes Demnum to break down.

---

<sup>1</sup> Rev 2, dated November 1990, "Outgassing Data for Selecting Spacecraft Materials"

### *Preload*

The bearing axial preload is set between 8 and 12 lbf to minimize rolling friction and power consumption during on-orbit operation. This very light preload is insufficient to withstand the inertial forces generated during launch vibration, so the bearing balls lose their preload at that time. To minimize impact loads, the maximum allowable axial travel is limited to between 0.008 and 0.012 in by a stainless steel spacer that bottoms out on a Titanium bearing bulkhead. Figure 2 depicts a typical force/deflection curve, and Figure 3 depicts the test setup used to measure it.

The bearing preload is provided by a convoluted diaphragm described below.

### *Convoluted Diaphragm*

To control the very light axial bearing preload during operation, the outboard bearing is contained in a bearing carrier that is axially preloaded by the controlled deflection of a convoluted diaphragm.

The first design used a convoluted diaphragm formed from 304 CRES sheet that was electron beam welded to 304 CRES inner and outer machined rings. Unfortunately, I placed the welds in a high stress concentration area, so they cracked during vibration testing of the first SMA. This failure led to a re-design that used a CRES 17-7PH H900 convoluted diaphragm mechanically clamped at its inner and outer edges. I still feel a properly welded design that moved the welds to a lower stress area would save considerable weight, cost, and complexity.

The normal practice of using a slip fit at the outer bearing race to allow it to move axially in a fixed bulkhead was rejected due to the possibility of losing all control of the preload due to radial binding with thermal changes.

Flat diaphragms have also been used in spacecraft mechanisms to avoid thermal binding, but the limited OD/ID ratio available to the diaphragm in the SMA envelope would have severely limited their low spring rate travel range or would have required an unacceptably thin diaphragm. Adding a single shallow convolution to the diaphragm greatly increased the low spring rate travel range. The diaphragm is preloaded with a machined shim.

To measure the preload and the axial travel, the test setup shown in Figure 3 was used. A load cell, attached to a machine slide, imposed a bi-directional axial force on the SMA shaft, and an LVDT measured the resulting deflection. Both the load cell and LVDT outputs were recorded by a PC-based data acquisition system.

Figure 2 plots the deflection vs. force data recorded for a typical SMA. The spring rate of the diaphragm, the travel limits, and the bearing preload can be seen. The force level, which succeeds in starting motion by moving the shaft away from its preloaded position, is the bearing preload. Since the preload decreases as the spacer is made thinner, the initial preload is higher than the desired value, so the data of Figure 2 is taken several times as the spacer is gradually machined to its final thickness. This iterative process is accelerated by calculating the thickness to be removed based on the measured diaphragm stiffness and the desired change in preload. A suitable margin is inserted, since spacer thinning is obviously an irreversible act for a given spacer.

#### Optical/Electronic Alignment

To tag on-orbit scientific data from the SSULI Far Infrared Detector with the correct elevation angle, the angular relationship between the electrical resolver and the mirror must be accurately known. Although this correlation is finally performed on-orbit with known stars, the relationship must be set accurately enough during SMA assembly to preclude resolver rollover.

The electro-optical alignment jig shown in Figure 4 is used to locate the mirror in relation to the SMA housing, then null the resolver stator at the mid-position of the mirror travel. This jig is also used to set the spring-loaded travel stops.

To align the SMA housing with the alignment jig, a gauge block (used as a test mirror) is clamped to one side of the housing. A dowel pin is inserted into position 1 in the jig, then the SMA is centered in a pilot hole in the jig, and rotated until the test mirror autocollimates with a laser beam. The SMA is then clamped to the jig. The dowel pin is now removed, the jig rotated, and the pin placed in position 2.

Using an auxiliary clamp with twin adjustment screws (not shown in Figure 4), the SMA mirror is rotated until it is autocollimated with the laser beam. The resolver stator is rotated to electrically null the resolver output, then the stator is clamped.

Finally, the SMA and Jig are rotated to positions 3 and 4 in turn, and, at each position, the threaded, spring-loaded stops are adjusted to limit the maximum travel of the SMA shaft.

#### Static Balancing

Vibration, imposed along one axis during testing, will invariably couple into the other axes. In addition, flight vibration exists simultaneously along all three axes. Consequently, there is a possibility that, during vibration, the rotating parts of the SMA would rotate violently into the mechanical travel stops. To eliminate that possibility, many spacecraft scanners employ launch locks that are remotely released once on orbit.

To avoid the complexity of launch locks, the rotating parts of the SMA are statically balanced. The SMA also has four resolver rotor flex leads (redundant windings) and five mirror flex leads (three thermistor flex leads and 2 heater flex leads) that resist the rotational motion of the moving parts. Although it is desirable to minimize the angular



spring rate of these flex leads, they do perform a vital service during launch vibration. By forming the leads so that they exert zero torque near the center of mirror travel, they should tend to center the moving parts between the travel stops during vibration, thus preventing the SMA rotating parts from angular impact into those stops.

#### Limited Ball Travel

There was some concern that the very limited rotation of the scan motion would not allow the ball travel paths to overlap. This could lead to lubricant buildup in the races at the ends of the ball travel.

#### Silicon Carbide Mirror

The mirror is fabricated of solid silicon carbide for good reflectivity in the extreme ultraviolet and is mounted on three semi-kinematic supports to minimize mirror distortion due to differential thermal expansion between the SiC mirror and the titanium shaft. Figure 5 shows a schematic view of the three supports, which are designated flexures A, B, and C and simulate the kinematics of a ball in a socket, a ball in a groove, and a ball on a flat surface, respectively:

- Flexure A is a cruciform beam to allow 2 axis pivoting while restraining translations normal to and parallel to the mirror surface.
- Flexure B is a long small pin to allow 2 axis translation while restraining translation normal to the mirror surface.
- Flexure C is a long flat blade to allow single axis translation parallel to the mirror surface while restraining translation normal to the mirror surface.

The dimensions of the three flexural elements were selected by using an FEA model of the mirror, the flexures, and the shaft.

### **Test Results**

#### Vibration Testing

As expected, the bearings did move freely during vibration testing. However, no damage to balls or races was experienced at any time.

There was one anomaly that was repeatedly observed, and is worth noting. Before and after each vibration test run, the SMA was functionally tested by scanning the mirror over its travel range, operating in a closed-position loop using its torque motor and resolver. The motor current was recorded versus scan position, thus providing a very sensitive indication of bearing friction and flex lead spring torque. Each pre-vibration functional test created a skewed rectangle with a motor current hysteresis of about 50 mA peak-to-peak (due to bearing friction of  $\pm 0.005$  N-m ( $\pm 0.35$  in-lbf)) and a slope of 0.040 N-m/rad (5.7 in-lbf/rad) due to the flex lead spring rate.

However, every time we ran a post-vibration functional test, the motor current hysteresis increased to about 250 mA peak-to-peak *for only the first cycle of motion*. After a particular position had been passed once, the hysteresis loop up to that position returned to its pre-vibration level. Manually moving the mirror after the vibration table was turned off, *but before any other mirror motion had occurred*,

confirmed what the instrumentation told us — it was as if we had to push a barely noticeable “obstruction” out of the way. This phenomenon is currently unexplained but does not affect the SMA operation, since the torque motor has adequate margin to overcome it (maximum motor current can be 1,000 mA, which produces a torque of 1.6 N-m (14 in-lbf), and it disappears after the first scan motion.

#### Static Balancing

The static balancing, combined with the cable spring rate, successfully prevented stop contact during vibration testing. There was some initial concern that the flex leads would have to be carefully formed to bring the initial position to the center of travel, but this concern has diminished; contact during vibration has never been experienced.

#### Limited Ball Travel

Another phenomenon (not completely unexpected) was actually observed: When the scan angle was increased after many short scans had been performed, small “bumps” about 20 mA ( $\approx 0.002$  N-m or 0.3 in-oz) high in the motor current were observed as the mirror moved past the end of travel of the short scans. These are currently attributed to a buildup of grease at the end of each ball track. However, after as few as 50 scan cycles that move past a bump, it gradually flattens out and disappears.

#### Silicon Carbide Mirror

The mirror was originally mounted on three semi-kinematic flexures that were attached to the mirror through three mounting holes in pockets at the edges of the mirror. However, after experiencing mirror pocket failures at flexure A during vibration, two parallel efforts were initiated to understand the problem:

1. several static load tests were performed that defined the static strength of the flexure A pocket, and
2. an analytical study was conducted to define the dynamic loads around that mirror pocket.

As a result of these efforts, two design changes were incorporated:

1. The flexure “A” mirror pocket was fitted with an Invar block retained by epoxy to spread the bending loads out as much as possible.
2. A “collar” was added to the original flexure “A” design, thus forming a second load bearing point against the shaft to reduce bending moments applied to the mirror by about a factor of 10 (Figure 6). Since this collar effectively provided the two-axis lateral restraint that was the function of the cruciform cross-section, that cross-section was changed to circular and reduced in size.

With these two changes, no further failures were experienced. In particular, the observed fracture pattern during a subsequent breakout test on a mirror pocket indicated excellent load coupling into the mirror.

It should be noted that the UTS of the SiC material was originally stated as 52 ksi, but later information indicated an actual average UTS of 20 ksi and a 3- $\sigma$  low value of 9 ksi. In addition, subsurface defects were detected in one mirror by ultrasonic



scanning. However, as noted above, the Invar reinforcing block very effectively distributes the applied load into the mirror, so even this defect was acceptable. Table 1 is summary of the static load tests on the mirror pockets. Note that an intermediate design, using soft components to eliminate metal-to-SiC contact, also provided some improvement but was rendered unnecessary by the Invar block.

**Table 1 - Mirror Static Load Test Summary**

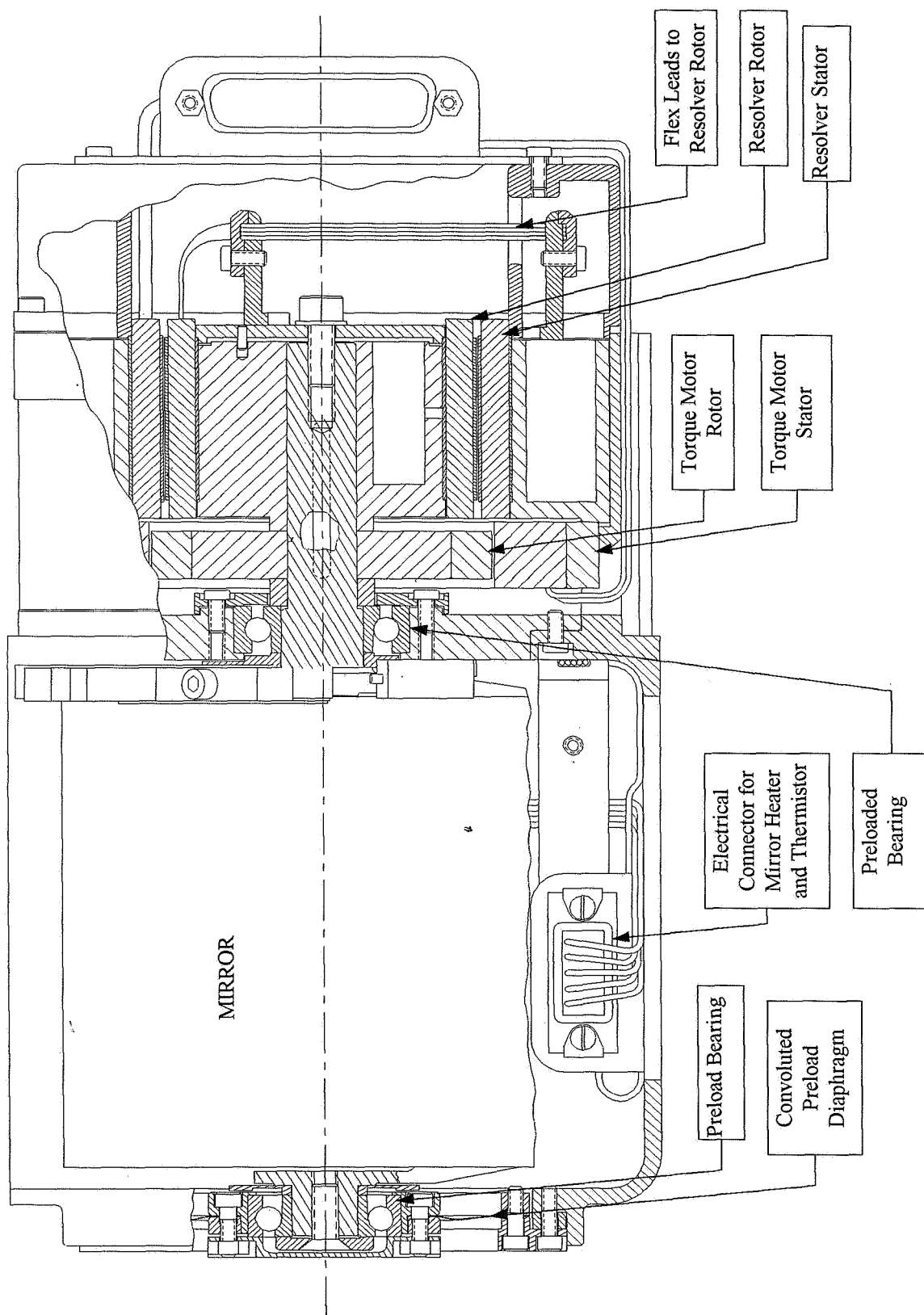
Mirror #	Original design	Original design with flexure A-to-mirror interface cushioned with Vespel sleeve and soft aluminum washers	Flexure A with collar with Invar block
#4-2		On 24 Feb 95, Pocket B broke at 75 lb On 1 Mar 95, Pocket C broke at 120 lb under pseudo-cyclic loading	
#2	On 2 Feb 95, Pocket A broke at 45.18 lb, then Pocket C broke at 46.48 lb		On 21 Apr 95, Pocket B broke at 194.40 lb
#1			On 21 Apr 95, Pocket B did not break at 483.1 lb

### Lessons Learned

- Lightly preloaded, oversized ball bearings can survive space launch vehicle vibration levels to provide low-friction levels, thus minimizing on-orbit power consumption.
- Slightly anomalous ball bearing operation can be experienced immediately after vibration, but no long term effect is seen.
- Static balancing of rotating assemblies can be sufficient to eliminate launch locks.
- Structural attachments to silicon carbide mirrors must minimize and spread vibration-induced bending loads to avoid fracture.
- Convolute diaphragms, which provide a desirable combination of low axial and high radial spring rates, can be used successfully to provide precision support to scan mirror rotating shafts.

### Acknowledgments

This work was sponsored by the Naval Research Laboratory, Washington, D.C. I want to thank Mr. Ed Devine of Swales for his invaluable guidance during this effort.



**Figure 1 - Scan Mirror Assembly**

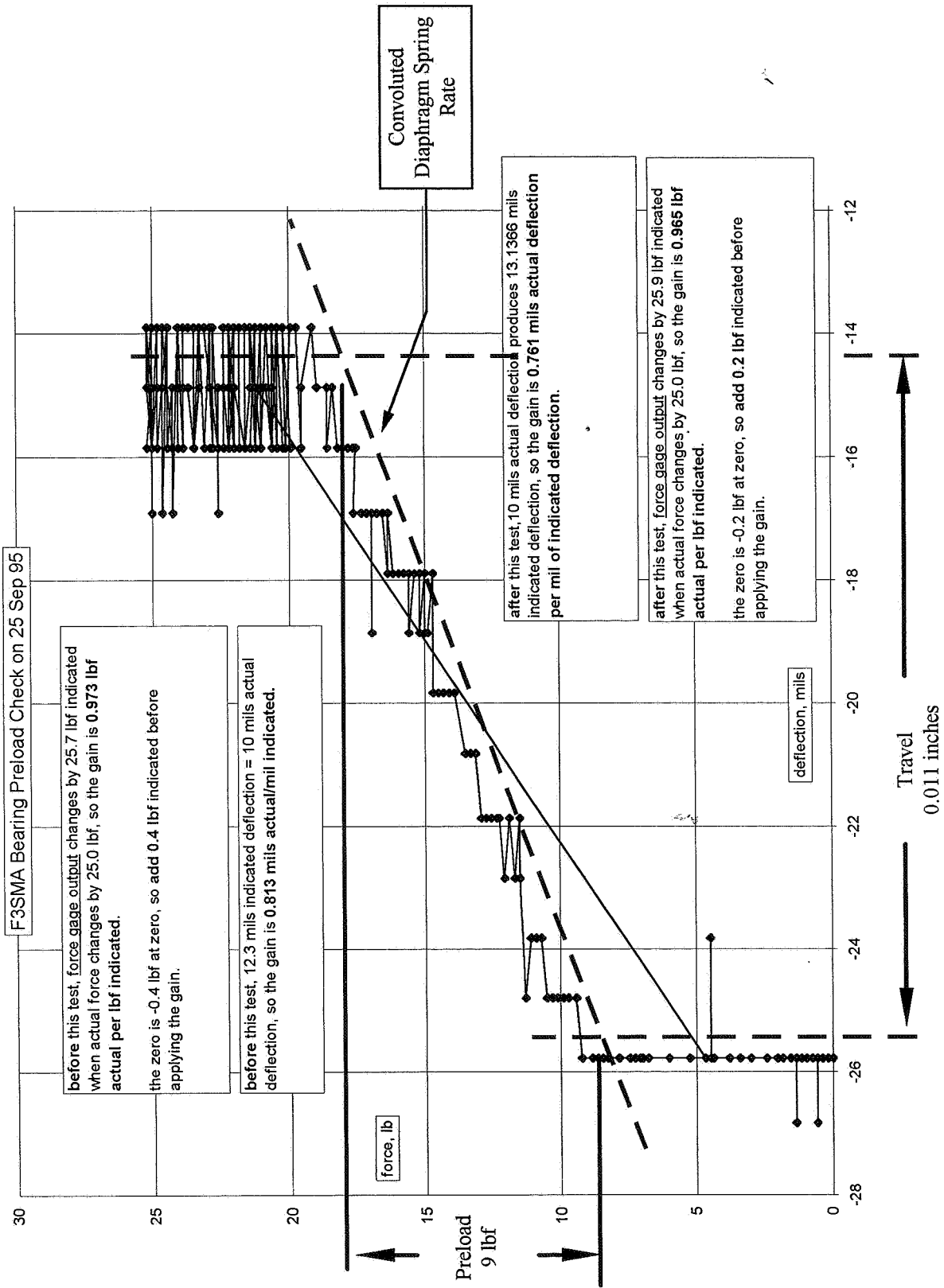
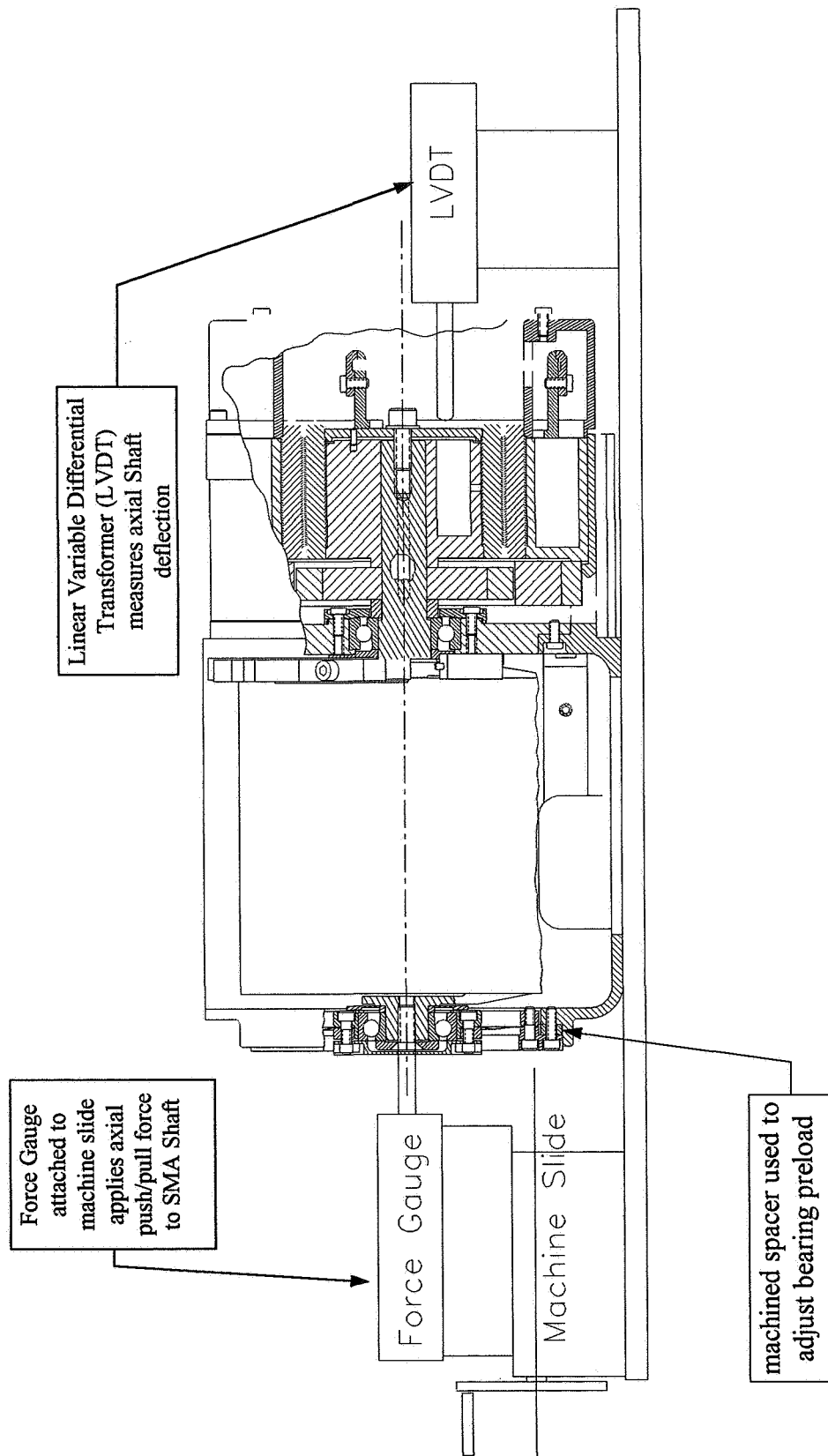
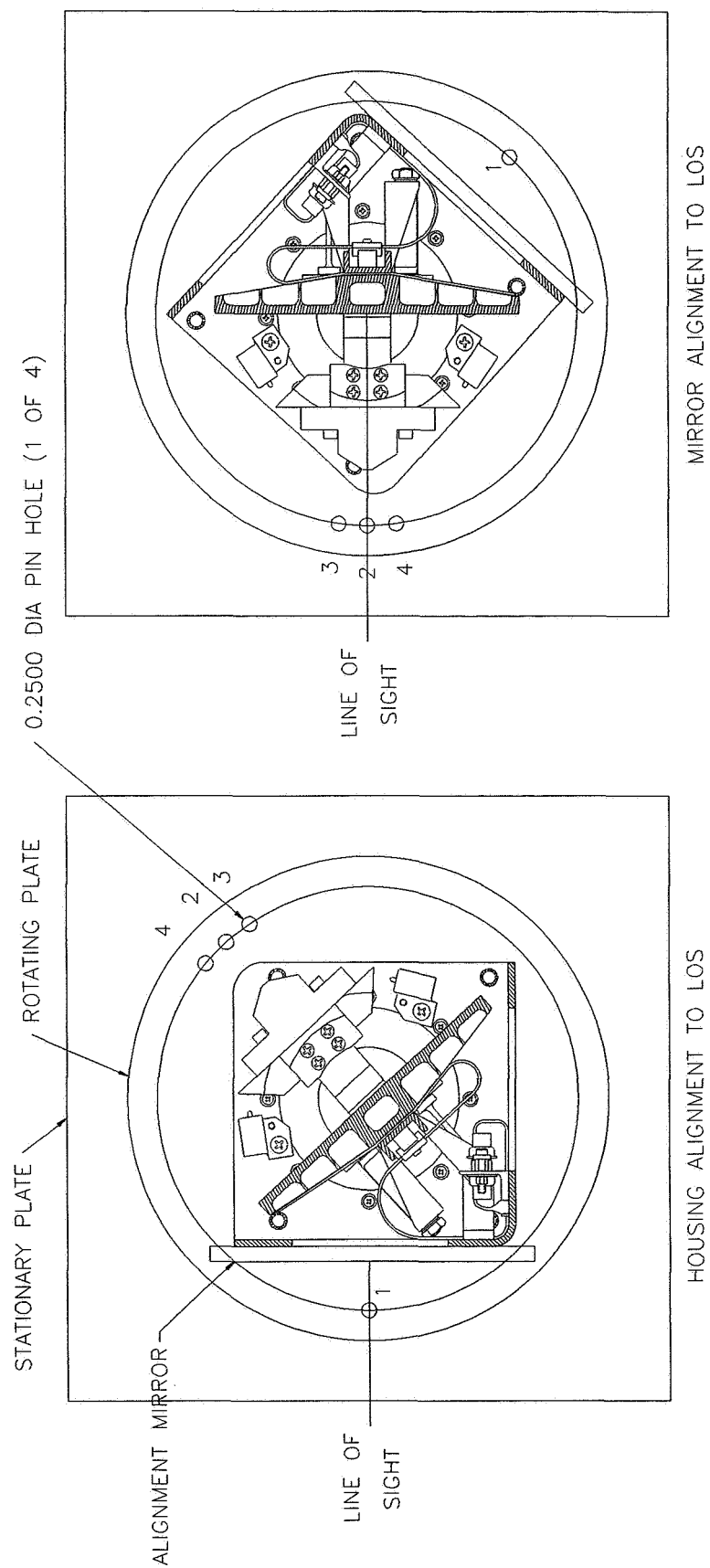


Figure 2 - Bearing Force/Deflection Curve



**Figure 3 - SMA Bearing Test Setup**



**Figure 4 - Optoelec Alignment Jig**

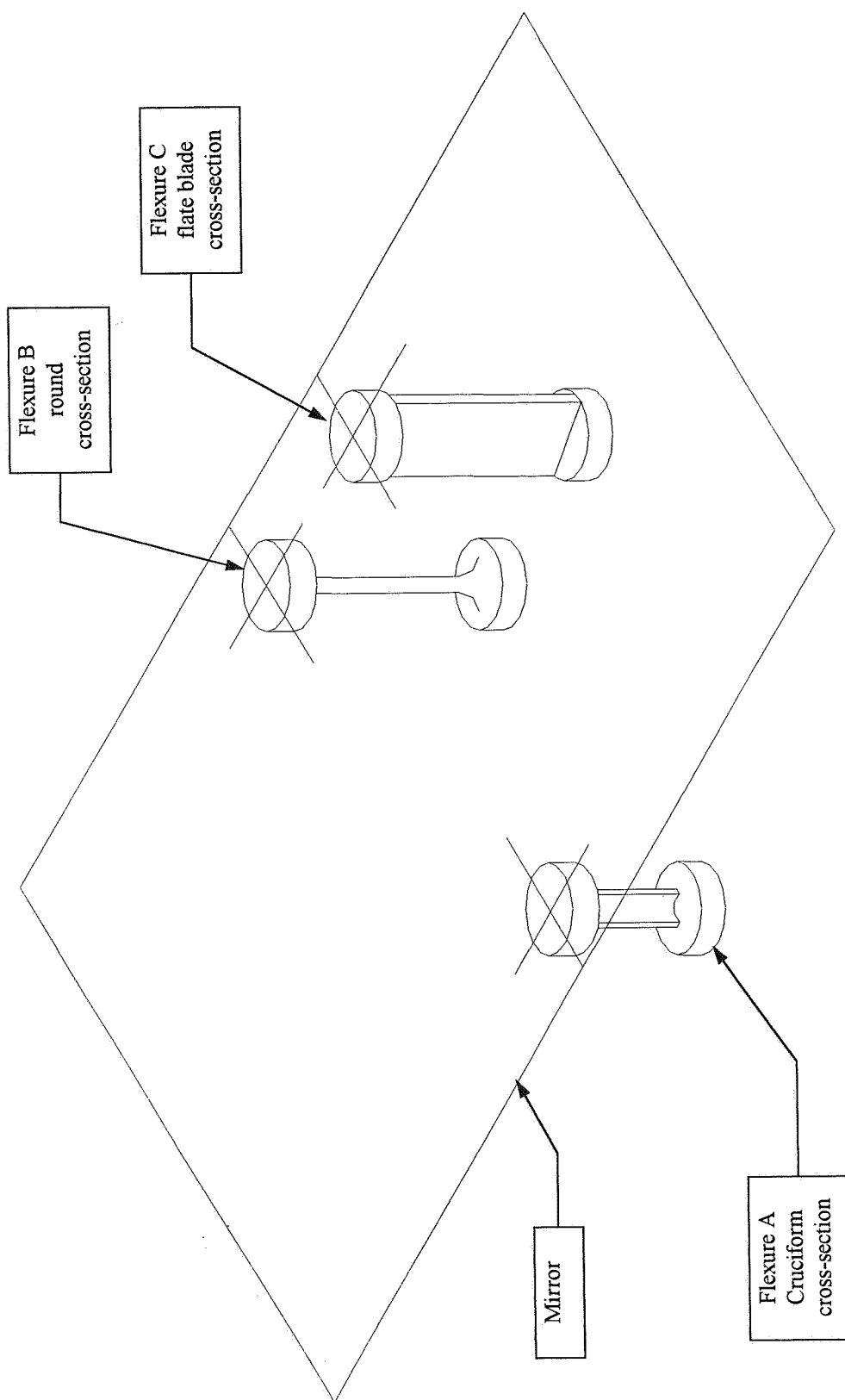


Figure 5 - Mirror Mount

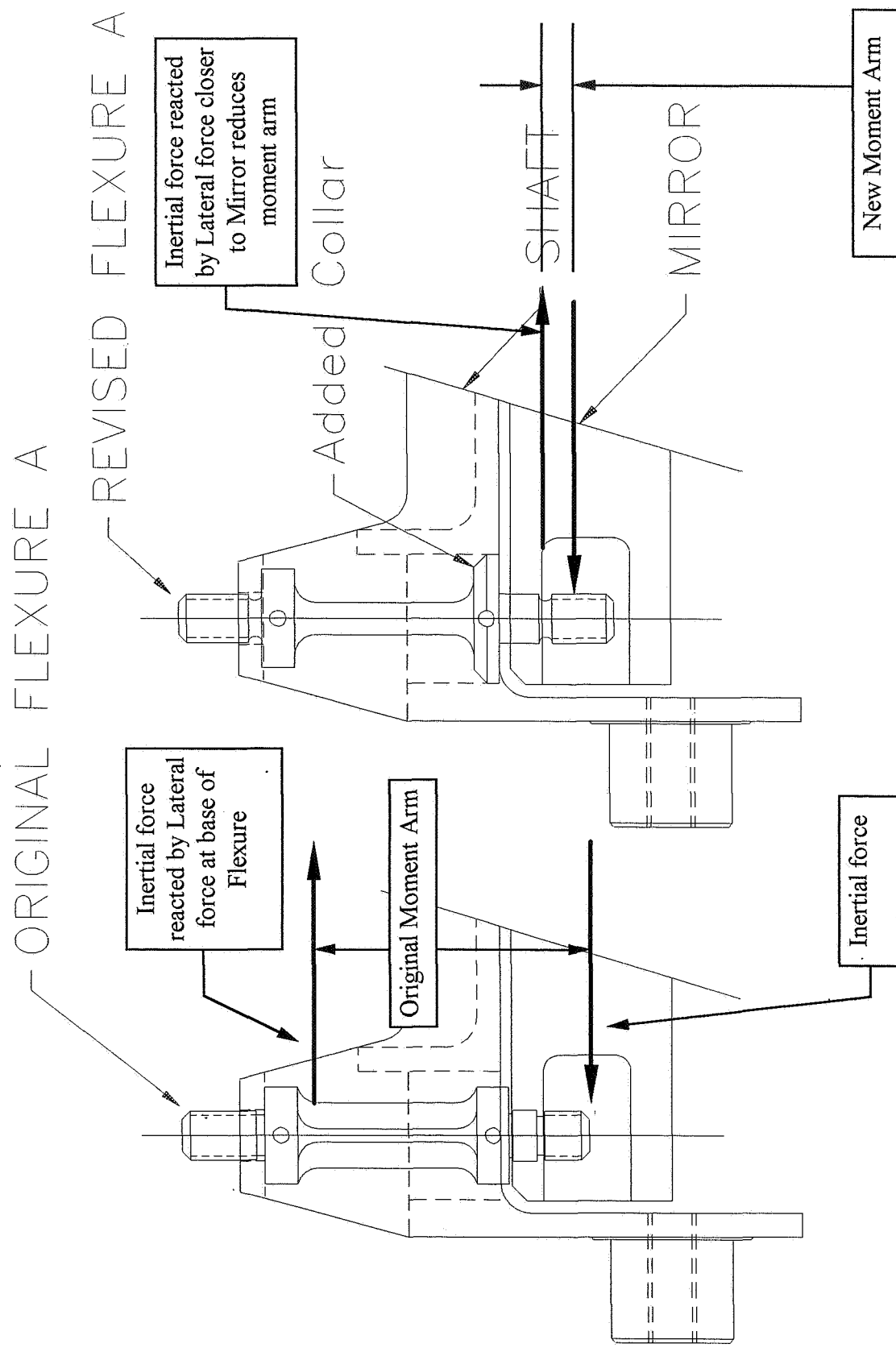


Figure 6 - Revised Flexure A





57-37 ✓  
50435  
125121

## Coarse Pointing Mechanism Assembly for Satellite Interlink Experiment

P.-A. Mäusli, M.-T. Ivorra, V. Gass & J.-F. Berthoud \*

### Abstract

Since 1975, MECANEX S.A. has been manufacturing components for solar array drives and mechanisms used in space applications [1]. In 1991, work was started in an early phase C (Engineering Model) on a Coarse Pointing Mechanism Assembly (CPMA) for the Semiconductor-laser Inter-satellite Link EXperiment (SILEX).

This paper deals with the history, the evolution, and the lessons learned from taking over a pre-design in 1991 to the delivery of last flight models (FM 5 & 6) in 1995.

### Introduction

The objective of the SILEX project is to establish an optical link between a low earth orbit satellite (LEO) and a geostationary satellite (GEO), or two GEO satellites. The core of this system, developed by MATRA MARCONI SPACE (MMS) in Toulouse, France, is a very narrow laser beam ( $\pm 4 \mu\text{rad}$  divergence) mounted in a 250-mm-diameter telescope [2].

The pointing, acquisition & tracking sub-systems, having extreme accuracy, are integrated close to the telescope in the terminal. For the purpose of the present paper, the terminal shall be called the payload. The payload characteristics have been presented earlier [1] and will not be addressed in this paper.

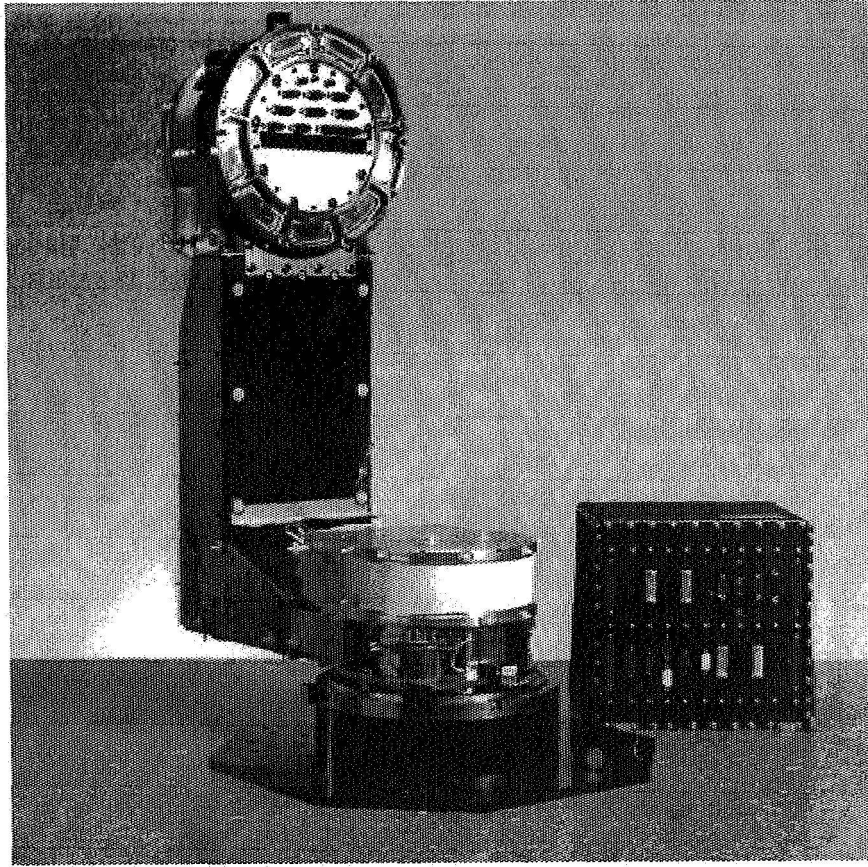
The payload is supported by a two-axis mechanism, the Coarse Pointing Assembly (CPA). The articulations allowing movement about the elevation and the azimuth axis are the Coarse Pointing Mechanism Assembly (CPMA), developed, manufactured, assembled and tested by MECANEX. These two articulations of very high structural stiffness, are bound together with an L-shaped bracket represented on Figure 1.

The global coarse pointing performances are as follows:

- |              |  |
|--------------|--|
| - Kinematics | - Angular coverage up to $200^\circ$   |
|              | - Angular velocity $< 2^\circ/\text{s}$ ( $< 0.2^\circ/\text{s}$ for full performance) |
|              | - Angular acceleration $< 0.02^\circ/\text{s}^2$                                       |
| - Pointing   | - Two axis bias $< 0.03^\circ$   |
|              | - Two axis random $< 0.01^\circ$ ( $1 \sigma$ )  |
|              | - Stability over 60 s (one axis) $< 0.007^\circ$ (p.p.)                                |
| - Torque     | - Noise $< 6 \cdot 10^{-3} \text{ N}\cdot\text{m}$ ( $1 \sigma$ )                      |

---

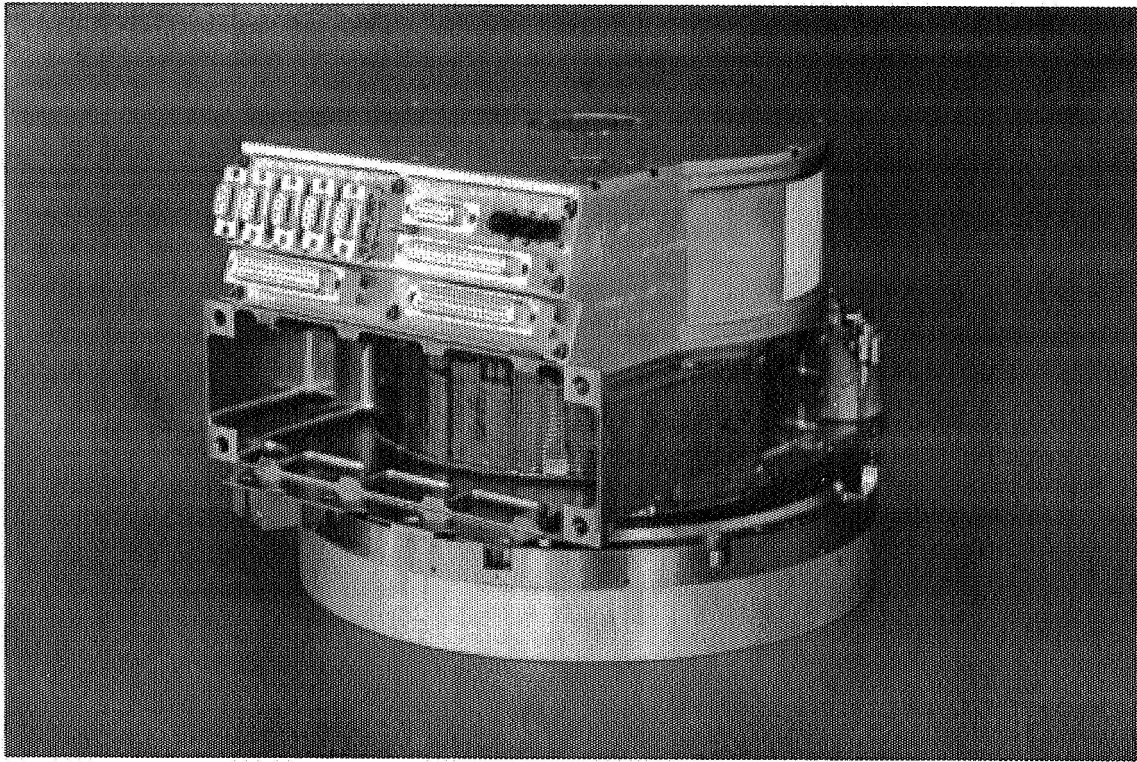
\* MECANEX S.A., Nyon, Switzerland



**Figure 1: CPA: The two articulations (CPMA) are supported by the L-Bracket.**

This paper presents details of the CPMA designed by MECANEX S.A. under a collaboration contract from MMS. The CPM Assembly is shown in Figure 2.

The characteristics listed above can only be achieved with a compact, rigid design. The torque and electrical stiffness of the motors must be high enough to guarantee not only the static stability in the satellite micro-vibration environment, but also the angular position reproducibility of an open-loop tracking, in spite of the torque disturbances generated by the ball bearing and the cable-wrap.



**Figure 2: Assembled CPMA (Azimuth type): The connectors on the Overshielding box next to the Cable-Wrap are placed on the Housing structure. The Base-Plate is visible below.**

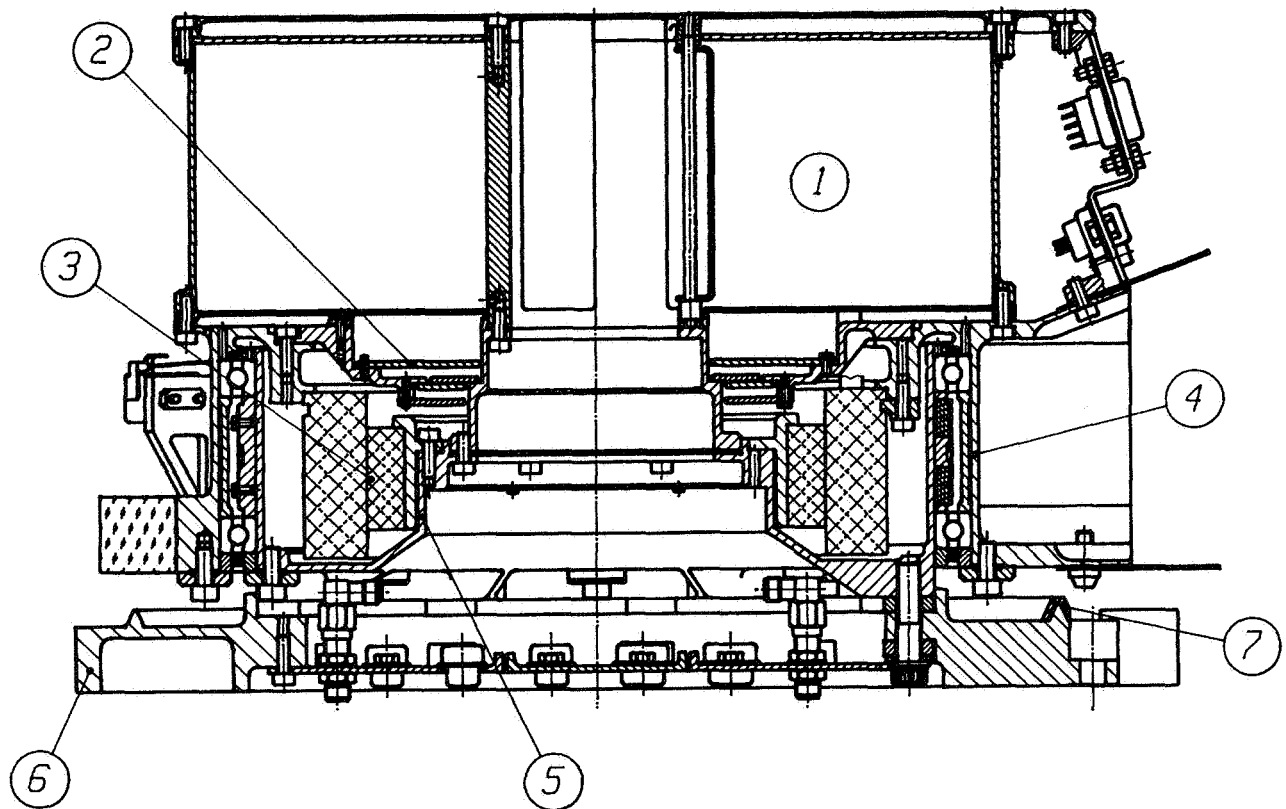
The functions required for each CPMA unit are:

- Rotation actuation (motor)
- Blocking device braking capability
- Angular position sensing (encoder)
- Electrical status (position sensitive switches, thermistors, thermoswitches)
- End stops
- Electrical transfer to the terminal (Cable-Wrap)
- Temperature control (heaters).

### **Historical Evolution of the CPMA Design**

The CPA concept is based on the IOC (Inter Orbital Communication) mechanism flown on EURECA, developed by MMS for an RF antenna pointing system. The direct application of the IOC device to SILEX requirements proved to be unsatisfactory. Important design modification had to be brought in the early C/D phase to take into account the new specifications. These are much more demanding with respect to pointing accuracy, electrical connection capacity, mass handling capability, mechanism mass and volume allowance, mechanical noise generation allowance, and thermal insulation with payload allowance.

The basic IOC architecture was preserved. An increase in the dimensions was necessary, however, with the corollary that the IOC concept, with respect to ball-bearing and Cable-Wrap torque, thermal behavior, mass, and volume had to follow this evolution. A complete analysis of the performance had to be undertaken, leading firstly to the complete re-design of the structure, secondly to the introduction of an improved thermal control, thirdly to the design of a new Blocking device concept, and finally deep re-work of the Cable-Wrap with all the connection scheme. The development of a representative bread-board model was decided late in phase C/D. This proved to be extremely beneficial to the overall model refinements. Numerous performance and model verifications, as well as design adjustments could therefore be done before the final design was frozen.



**Figure 3: CPMA cross-section:**

- |                       |                    |
|-----------------------|--------------------|
| 1: Cable-Wrap Housing | 4: Housing         |
| 2: Encoder            | 5: Body            |
| 3: Motor              | 6: Base-Plate      |
|                       | 7: Blocking-Device |
|                       | Castellated track  |

The carved walls (1.5-mm thickness) of the adapter are visible on the photograph.

A number of specific difficulties had to be overcome during the design and manufacturing of the parts. The most relevant aspects are discussed below.

Figure 3 shows a cross-section of the articulation. The main body, called Housing, is mounted on a Base-Plate with a pair of preloaded thin section ball bearings. The hollow shaft, called Body, allows the electrical wiring between connectors situated on the Base-Plate and connectors on the Housing side, through the Cable-Wrap. The wire connections and distribution to the connectors are in an Overshielding box. The motor and encoder are mounted inside the Housing. A lateral Housing adapter provides for the articulation fixation capability to the L-Bracket.

The main structural parts are made of beryllium, secondary parts of titanium alloy (Grade 5), while the non-structural elements are essentially aluminum alloy.

The mechanical design is particularly compact, thus favoring a stiff structure. The direct drive (without gear) imposes that an extremely accurate angular positioning is achievable by the motor. The coupling to the L-Bracket is also a point of concern with respect to the global stability of the CPA [2].

The compactness of the design leaves little room for additional features like the Blocking-Device, End Stops and Micro-switches. These elements are fixed on the lateral external part of the Housing, in the narrow groove between the fixed and rotating parts. The heaters surround the Housing at the level of the bearing. A white-painted radiator allows heat evacuation from the Cable-Wrap shield box.

### **Structure**

The necessity for a very low weight imposed the use of beryllium for the structural parts. The high Young's modulus of this material is also favorable with respect to the stiffness requirements. These two advantages, though essential, cannot override the many disadvantages attached to the practical application of this metal in complex structures, i.e.:

- The metal although innocuous in simple handling, presents toxicity when inhaled in small particle or vapor form; this prevents all possibility of in-house machining. Very few equipped workshops with the capacity to produce complex accurate mechanics are available. In this project, the company SAGEM (France) was selected. The sub-contracting of machining implies complete definition of the design, which is not necessarily possible at a prototype level. The procedure for modification is complex.
- The metal production is based on sintered powder technology. The raw material quality is strongly process dependent, and irregular machinability has been encountered in different material batches, even though the material mechanical properties were within the specification.
- Most of the Housing and body structure was carved to leave walls of only 1.5 mm in thickness as can be seen on a detail photograph of the Housing on Figure 3. The brittleness of the material associated to such dimensions makes the structures sensitive to local shocks. Fractures of the walls may likely happen, leading to the discarding of the piece as reparation is not recommended on structural area.

Some difficulties have also been encountered in adhesive application on beryllium. Though excellent adhesion may be achieved when the surface is properly treated followed by quick application of the adhesive, inappropriate bonding was also obtained when the application was done on freshly cleaned surfaces having formerly experienced several months of exposition to air. The type of adhesive may also be a sensitive element for bonding on beryllium.

The above drawbacks of this material makes its use extremely expensive and penalizing with respect to planning. We would recommend to use it only when its unequaled mechanical and physical properties are unavoidable; simple shapes with as little machining as possible should be a design driver.

The Aluminum-Lithium alloy could be an interesting alternative to light structural materials. The scarcity of application in space applications makes its availability somewhat problematic, however, more interest should be given to this material of high technological potential.

### **Ball Bearing assembly**

A very sensitive element with respect to stiffness lies in the ball bearing assembly. A large diameter (o.d. about 200 mm) and separation (about 30 mm) was adopted here. The two spacers' relative lengths should be adjusted with an accuracy better than 1  $\mu\text{m}$  to control the rigid preload within 10 %. The thermal constraints implies that the spacers, Housing and shaft must be of the same material, i.e. beryllium. The preload adjustment was thus realized by the manufacturer (ADR, France) on a tool on which the bearings were assembled with the dedicated spacers. Integration in the CPMA was later done at MECANEX.

The pointing performance is particularly sensitive to torque noise. Very special care had to be given to the track grinding finish and to the dust control. A dedicated tooling had to be devised to record torque noise under nominal preload in production, before integration.

Fluid lubrication was adopted here to help achieve the low mechanical noise requirement. Oil impregnated reservoirs placed on the spacer between the two ball bearings assure that the lubricant will last over the full life of the articulation. Anti-creep barriers was also applied to prevent oil depletion and pollution towards the optics of the terminal.

The handling of lubricated parts implied the participation of 5 contractors, which made the cleanliness control of the bearing a perilous task.

### **Motor**

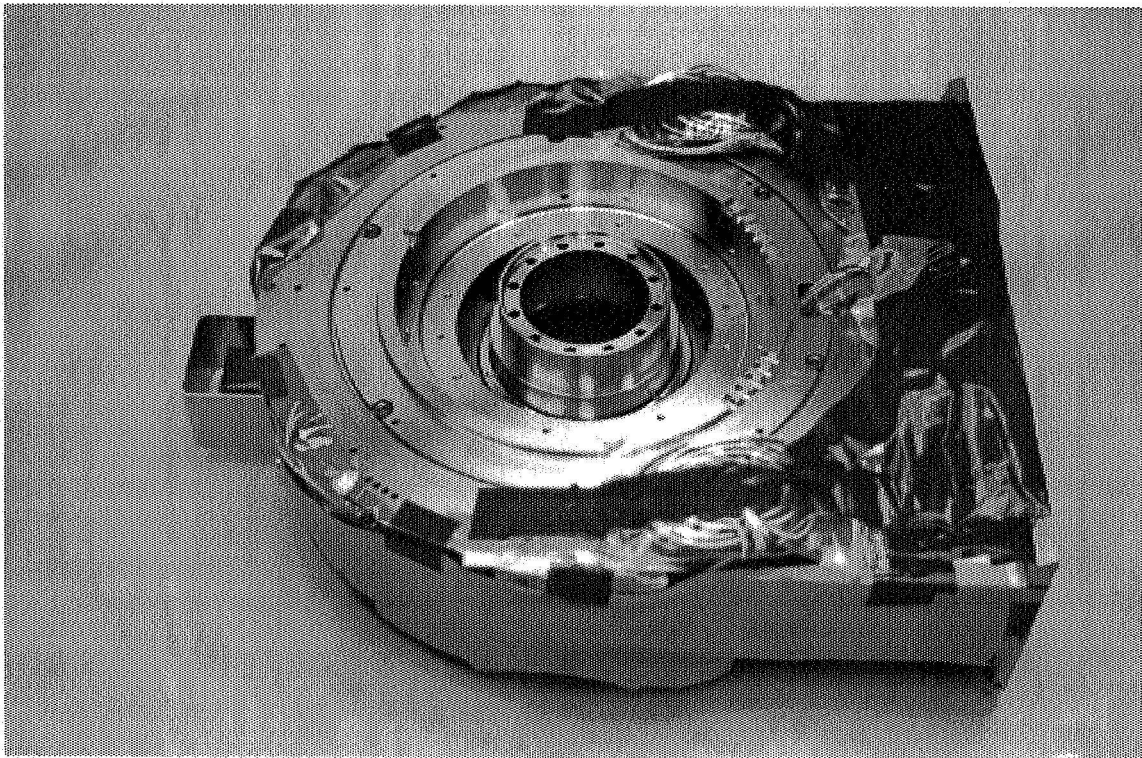
The CPMA is equipped with a SAGEM motor of the series 57 PPP. The record of micro-step angular deviation was recorded over a full revolution to allow the necessary pointing compensations.



The rotor and stator were assembled by MECANEX at the same time as the ball bearing. No particular difficulty was encountered during this integration thanks to an adequate tooling providing a rigid guidance to the concentric elements.

### **Encoder**

The 10-bit optical encoder was developed and produced by CODECHAMP (France). It includes the optical masks, the opto-electronic elements, and the drive electronics all mounted within the CPMA. The criticality of parts alignment and availability of tooling imposed that the mounting, adjustment and control be done at the producer's site. Although this procedure was technically the best suited, it was cumbersome administratively (custom, transports).



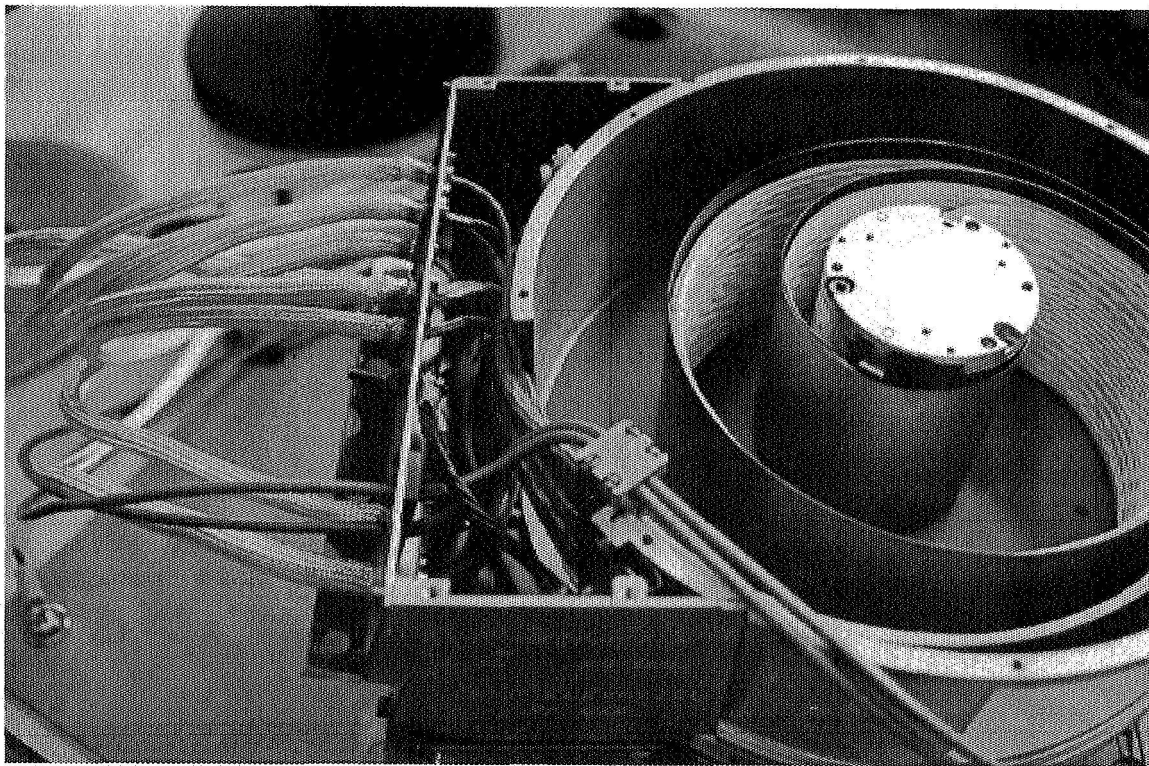
**Figure 4: Top view of the Housing sub-assembly prior to encoder integration**

Figure 5 shows a top view of the Housing sub-assembly prior to encoder integration. The motor and encoder wires, routed to the Housing adapter (lower part of the picture), become completely covered by the Cable-Wrap in further assembling steps. The high integration level of this design prevents any easy access to internal parts after integration. Servicing being generally not part of space requirements, this configuration is acceptable here; preference has been given to compactness.

The main difficulty of a totally integrated concept arises on sub-system control level as wire routings cannot be traced from beginning to end. A special testing procedure of the encoder at first power-up following final integration has to be set-up to make sure that no overload would be applied on the electronic parts, should a wiring mistake be present.

### **Cable-Wrap**

Over 60 twisted pairs of wires (shielded and unshielded), two coax and 1 bonding strap were concerned in one Cable-Wrap execution. An angular coverage of nearly 200° was necessary (Figure 5).

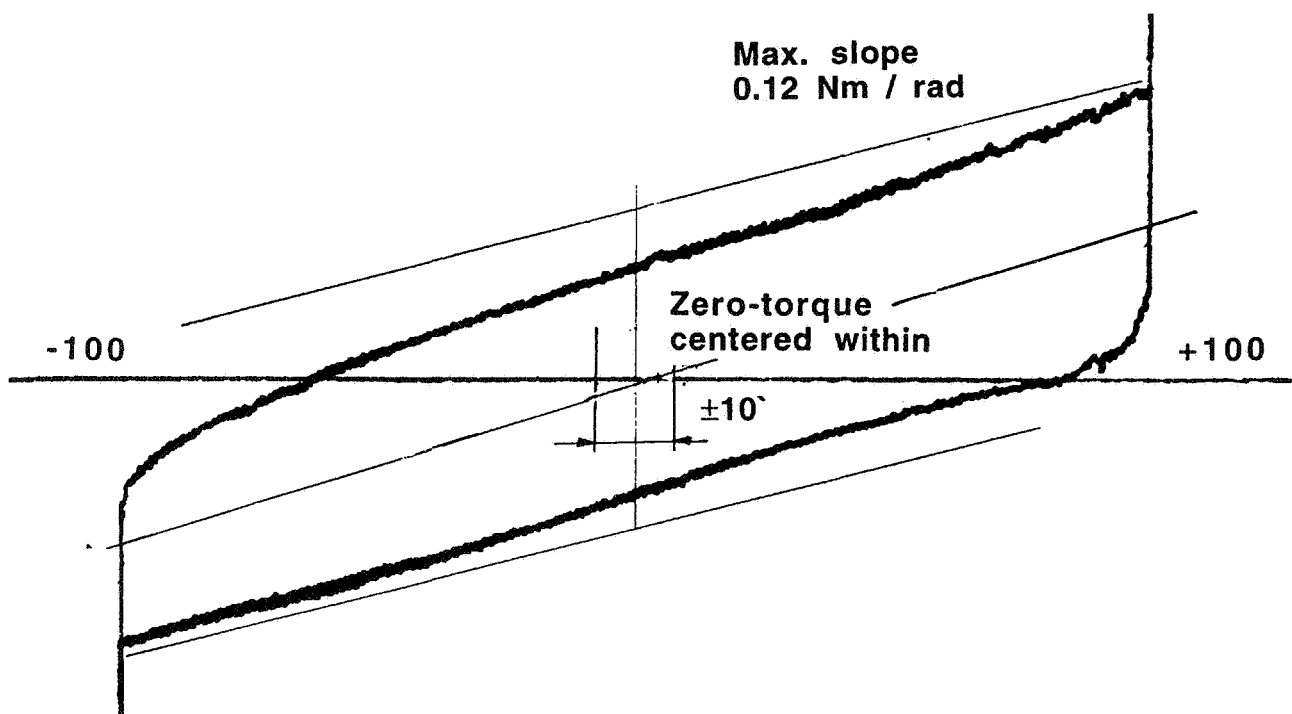


**Figure 5: Top view of the CPMA without its cover. The flex cable and bonding sheets fixed on the central rotating drum are visible.**

The action of a torque on the rotor generates de-pointing. The maximum acceptable resistive torque from the Cable-Wrap, ball bearings and motor resistance is of the order of  $\pm 0.25 \text{ N}\cdot\text{m}$ . The soft nature of the Cable-Wrap does not allow rotation without generating friction under 1-"g" conditions. A special low-friction coating was applied for this reason on the upper and lower plates imprisoning the cables.



Furthermore, the presence of insulation material around the wires also favors friction losses. The development of a multi-layered spiral made of flat cable and bonding metal sheet assembly enabled meeting the requirements of minimum absolute torque (i.e., to control the zero-torque equilibrium position within a range of  $\pm 10^\circ$ ) and to limit the hysteresis under 1-"g" to an acceptable value. Careful cable and cable sheet stiffness evaluation gave inputs to a model we developed from a theory of springs in watches, and implemented it to take into account the specific nature of the "soft" elastic element. A careful choice of the cable sheet length in the definition phase, and the adjustment of the spiral tension was done for each model (Figure 6).



**Figure 6: Record of a full articulation cycle over the maximum range of 200°.**

### **Blocking Device**

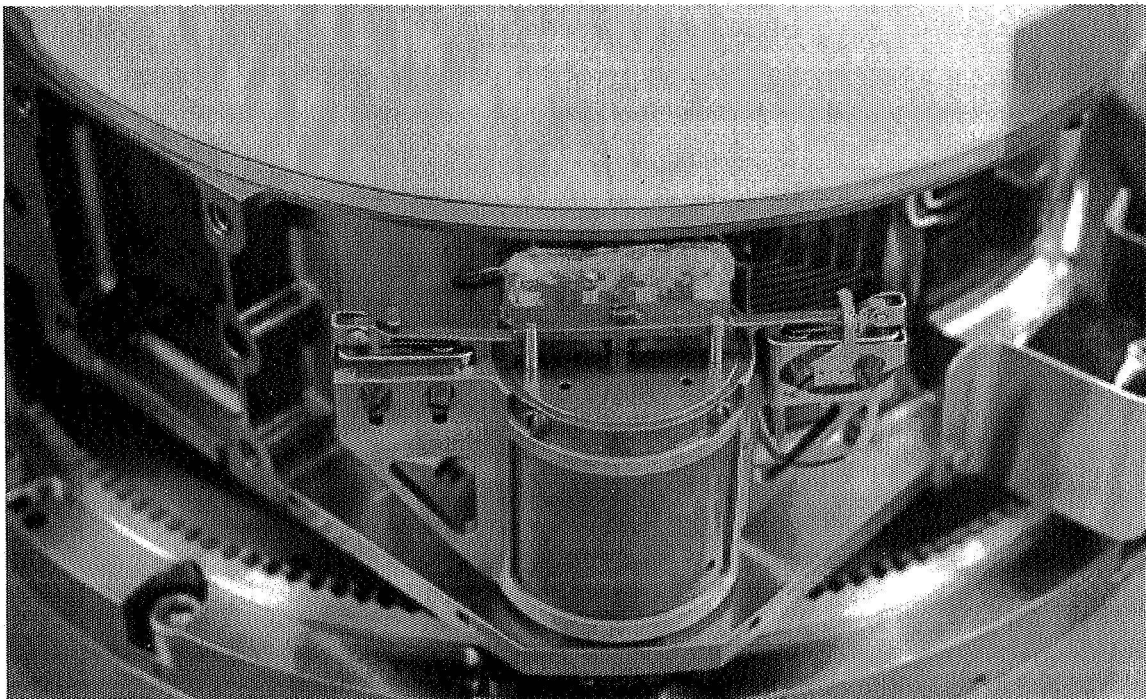
Immobilization of the payload in case of power interruption is guaranteed by a Blocking Device which has to provide a braking torque of at least 1.35 N·m. A reluctant electromagnetic actuator, developed and produced by ETEL, Switzerland, is used to hold a brake block against its counterpart without energy consumption, and to release the movement when powered (Figure 7).

Initially, the blocked position had to be achieved at any angular position; it is also in this state during the launch vibration period.

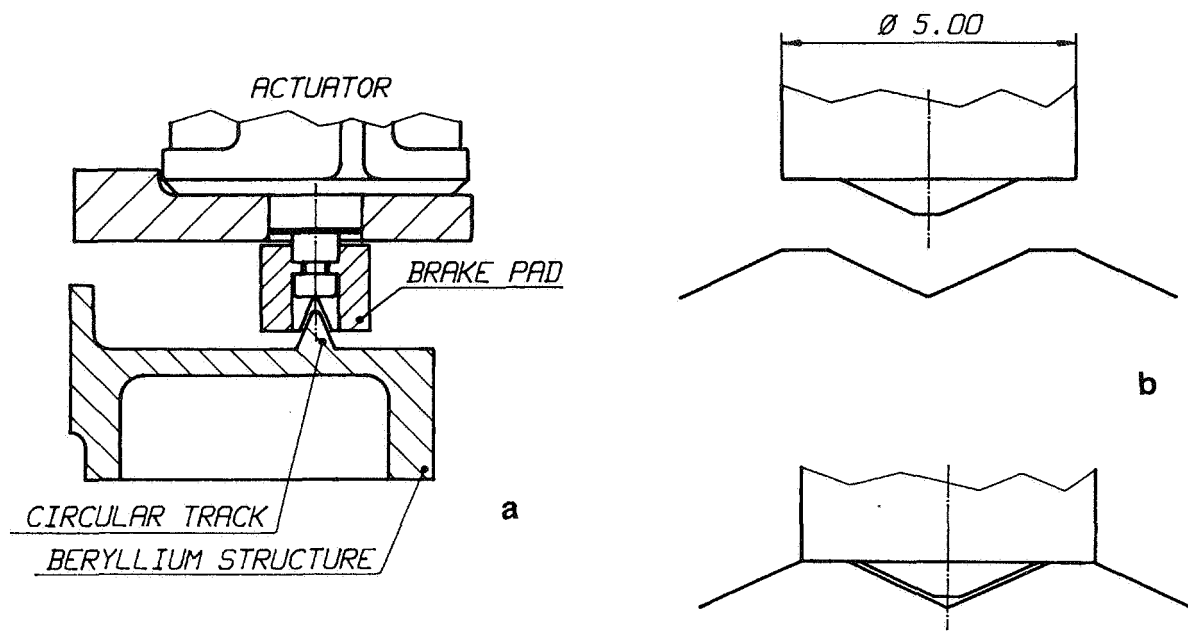
The first proposition to solve this question was to wind a belt around the mobile part; the brake action was done with an actuator pulling the belt. This solution was ruled out in the initial trade-off for lack of available room, difficulty to avoid any friction contact in the released state, and finally because of the relative low reliability figure of this solution which is a potential single point failure.

The first brake was designed as a VESPEL friction pad pressed on a toroidal track of beryllium with a triangular cross-section as shown by Figure 8a. Very satisfactory results were obtained in air where sufficient braking capacity was obtained and no jamming was observed. High vacuum tests however, showed a deficiency in braking capacity due to the collapse of the friction coefficient under vacuum. This material pair had to be rejected; the replacement of VESPEL by a harder material (hard anodic oxidation of aluminum) tended to jam in micro-vibration in spite of the increase of the triangular cross-section angle (formerly adapted to VESPEL friction coefficient); it was caused by the generation of beryllium dust in the friction zone (beryllium is not adapted to friction!).

The requirement of continuous blocking position was relaxed to a discrete one later in the project, allowing the replacement of the friction brake by a castellated track of titanium alloy, the blocking action being assured by a VESPEL diving core driven between the teeth; this last design has been successfully qualified. Figure 8b shows the principle.



**Figure 7: Blocking-Device actuator with a part of the castellated track.**



**Figure 8: Blocking-Device braking elements:**  
**a) initial design,      b) final principle.**

## Conclusions

The search for solutions in the development of this articulation with very demanding specifications led to a number of lessons summarized below:

- Tribological phenomena, especially with non-conventional materials, are unpredictable. When the mechanism requires the friction coefficient working range to be bound by lower and upper limits, considerable care is necessary to assure a sufficient stability on this parameter.

It is recommended to avoid this situation by creating mechanisms whose function does not depend on friction, or, if not possible, to have only one limit (upper or lower) on the friction coefficient.

- The problems generated by material shipment (clean and shock-proof packages, customs handling, reliable transports), and by manipulation by well trained and competent people, but belonging to different laboratories obeying to different rules, imply important impacts on price and planning.

It is most advantageous to consider the mechanism as a unit sub-system, which should, in the largest possible extend, be completely assembled without transfer.

- The price increases drastically and planning is badly affected by late design verification and modifications. Analytical investigation cannot replace experimental verifications of the designed principles, especially when the effect of environment must be predicted for extreme accuracy conditions.

The early production of a bread-board model is highly recommended. Its definition should be as close as possible to the final one, though differences may advantageously be accepted to avoid impact of long lead item procurement and reduce the price of some parts. Testing of the breadboard must not be neglected particularly with respect to environmental constraints.

## Acknowledgments

The authors wish to thank the SILEX team at MATRA MARCONI SPACE for the fruitful collaboration in this project, and especially A. Brunschvig and Ph. Faucheux whose close contribution to our work was essential and appreciated.

## References

- [1] Atlas, G. and Thomin, G. "Experiences of CNES and SEP on Space Mechanisms Rotating at Low Speed." 21st Aerospace Mechanism Symposium, NASA Conf. Publ. 2470, 1987, p. 131-144.
- [2] Di Jesu F. and Brunschvig A. "SILEX Mechanisms: Which lessons after qualification?" Proc. Sixth European Space Mechanisms & Tribology Symp., Zürich, 4-6 October 1995., (ESA SP-374, August 1995), p. 235-243.

# A Nitinol-Based Solar Array Deployment Mechanism

Shin John Choi\*, Chia-Ao (Bill) Lu\*, and John Feland\*

58-37 ✓

50436

125122

## Abstract

This document describes a simple, light weight, and scalable mechanism capable of deploying flexible or rigid substrate solar arrays that have been configured in an accordion-like folding scheme. This mechanism is unique in that it incorporates a Shape Memory Alloy (SMA) actuator made of Nitinol. This paper documents the design of the mechanism in full detail while offering to designers a foundation of knowledge by which they can develop future applications with SMAs.

## Introduction

Solar array deployment technology has reached a high level of sophistication via the use of traditional mechanical means such as linkages, motors, springs, and dampers. Although proven reliable and effective, many deployment means have been found to have high weight penalties. In an effort to reduce the weight and complexity of deployment mechanisms, a simple, Nitinol-driven deployment means was developed.

The mechanism described in this paper is the result of a 25 week collaborative effort between Stanford University and Lockheed Martin Missiles and Space. The development effort took place within the context of a graduate level, project based design course called Cross Functional Systems Design (ME210). The objective of the project was not to deliver a flight-ready mechanism, but rather to explore the possibility of applying shape memory technology to solar array deployment.

## Shape Memory Alloys and Nitinol

### Background

Shape Memory Alloys are a class of materials with the peculiar property of being able to "remember" a specific shape. SMAs can be deformed and then returned to their original shape when heated beyond a specific temperature known as its transition temperature. The two most common types of SMAs are NiTi and CuZnAl. Nitinol is a trade name for Nickel Titanium (NiTi) alloy.

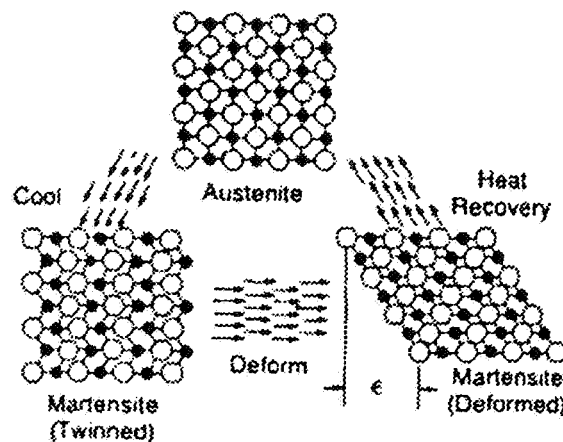
### The Shape Memory Effect

The key to the shape memory effect is a change in the crystalline structure of the material. Above its transition temperature, it is an ordered cubic structure known as Austenite. Below the transition temperature, it is in a monoclinic phase called Martensite. The crystals in the monoclinic phase are tilted in opposing bands so that the structure appears as a "squashed" cubic structure. When it is deformed, the material does not act like a normal metal. Rather than deform through dislocation movement, the crystal bands bend and align themselves in one direction or the other.

---

\* Mechanical Engineering Design Division, Stanford University, Stanford, CA

When the crystalline structure is heated beyond its transition temperature, the “squashed” monoclinic crystals expand back into the ordered cubic state, thereby reversing any deformation done in the martensitic state. When heat reverses the deformation, it returns to the austenitic form set during the training process. This phenomenon is known as one-way memory. Figure 1 shows what happens between the two states. The material can, under specific conditions, be trained to have shape memory in both the austenitic and martensitic states. This is referred to as two-way memory. Discussion on two-way memory is beyond the scope of this paper.



**Figure 1. Representation of the changes in the crystalline form of Shape Memory Alloys that give it the memory characteristic.**

#### Properties of Nitinol (NiTi)

Table 1 summarizes the physical, mechanical, and transformation properties of the material. Note in particular the wide range in the yield strength of the material. The wide range in the mechanical properties is explained by the strong dependence of the material composition to temperature. The ratio of martensite to austenite in the material at temperatures close to its transformation determines its exact properties. Figure 2 shows stress-strain curves for Nitinol at its fully austenitic (T1) and fully martensitic (T2) states.

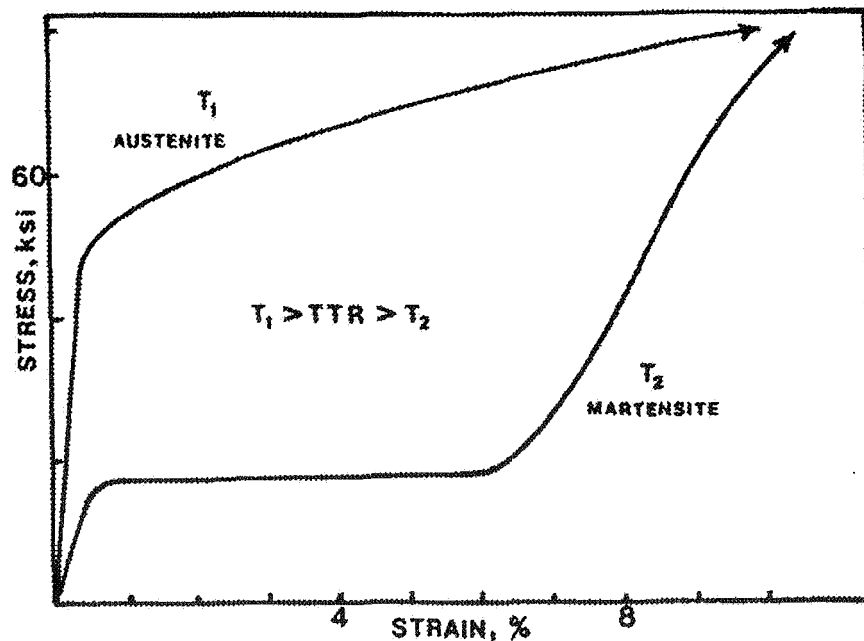
#### Stress-Induced Martensite: Obtaining More Travel

There is a unique and subtle change in the behavior of SMAs when they cool and transition from the austenitic to martensitic state. The transition between these states during cooling is marked by a dramatic change in material properties. This change in material properties is very important in that it allows much easier and effective use of the material as an actuator.

As the material cools from martensite to austenite, the material's yield strength and elastic modulus do not merely change in a smooth, linear fashion. It was found that both of these properties drop far below their martensitic material values when loaded

**Table 1. The physical, mechanical, and transformation properties of NiTi, the most commonly used Shape Memory Alloy.<sup>a</sup>**

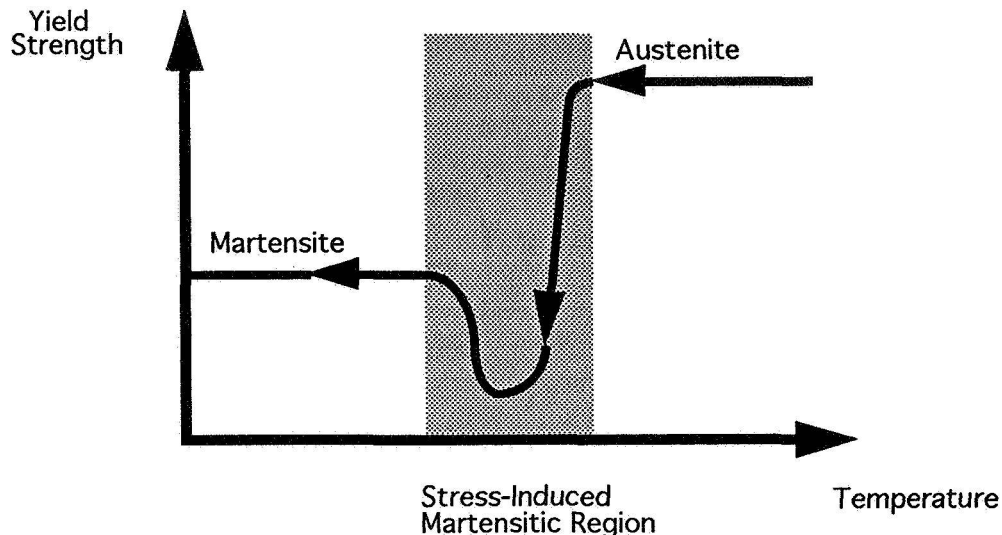
Melting Point	1300°C
Density	$6.45 \times 10^3 \text{ kg/m}^3$
Electrical Resistivity (austenite)	$\sim 100 \mu\Omega\cdot\text{cm}$
Electrical Resistivity (martensite)	$\sim 70 \mu\Omega\cdot\text{cm}$
Thermal Conductivity (austenite)	$0.18 \text{ W/cm}\cdot^\circ\text{C}$
Thermal Conductivity (martensite)	$0.085 \text{ W/cm}\cdot^\circ\text{C}$
Corrosion Resistance	Similar to 300 series Stainless or Ti Alloys
Specific Heat	$0.20 \text{ cal/g}\cdot^\circ\text{C}$
Young's Modulus (austenite)	$8.27 \times 10^7 \text{ kPa}$
Young's Modulus (martensite)	$2.76\text{-}4.14 \times 10^7 \text{ kPa}$
Yield Strength (austenite)	$1.93 \times 10^5 \text{ kPa}$
Yield Strength (martensite)	$6.89 \times 10^5 \text{ kPa}$
Ultimate Strength	$8.96 \times 10^5 \text{ kPa}$
Elongation at Failure	20-40%
Transformation Temperature	-200 to 110°C
Latent Heat of Transformation	$5.78 \text{ cal/g}$
Shape Memory Strain	8.5% maximum



**Figure 2. The stress-strain relations for NiTi, a common shape memory alloy. Notice the differences in properties between the two crystalline phases, the Austenite or “memory” phase, and the Martensite or “deformable” phase.<sup>a</sup>**

<sup>a</sup> “Using Shape Memory Alloys,” Darel E. Hodgson, Ph.D. Shape Memory Applications, Inc., CA, 1988.

during cooling (The martensitic properties of SMAs in steady state are approximately a half to a third lower than the austenitic properties.) The elastic modulus and yield strength drop by almost an order of magnitude from the austenitic properties **ONLY WHEN COOLED**, eventually rising back up to the martensitic material properties when it has finished cooling. Figure 3 shows an approximate relationship between material yield strength and temperature as it cools.



**Figure 3. Material yield strength (approximate) for Nitinol vs. temperature during cooling from austenite to martensite. The stress-induced martensitic region is highlighted, showing how the material “gives” when cooled.**

When the material is at its transition temperature, a bias stress can be used to induce the early formation of martensite, thus creating a soft, malleable state in the material. This property can be exploited to obtain larger material deformation without overstraining (damaging) the material. The net effect is that large deformations of the material can be obtained using relatively small forces for deformation.

This unique property of the material is exploited by simply heating the material above its transition temperature, and then applying a bias stress on it as it cools. As the material cools, it will “give” quite dramatically, thus allowing approximately twice as much material deformation than possible when trying to deform the steady state martensitic structure.

#### Why Use SMAs?

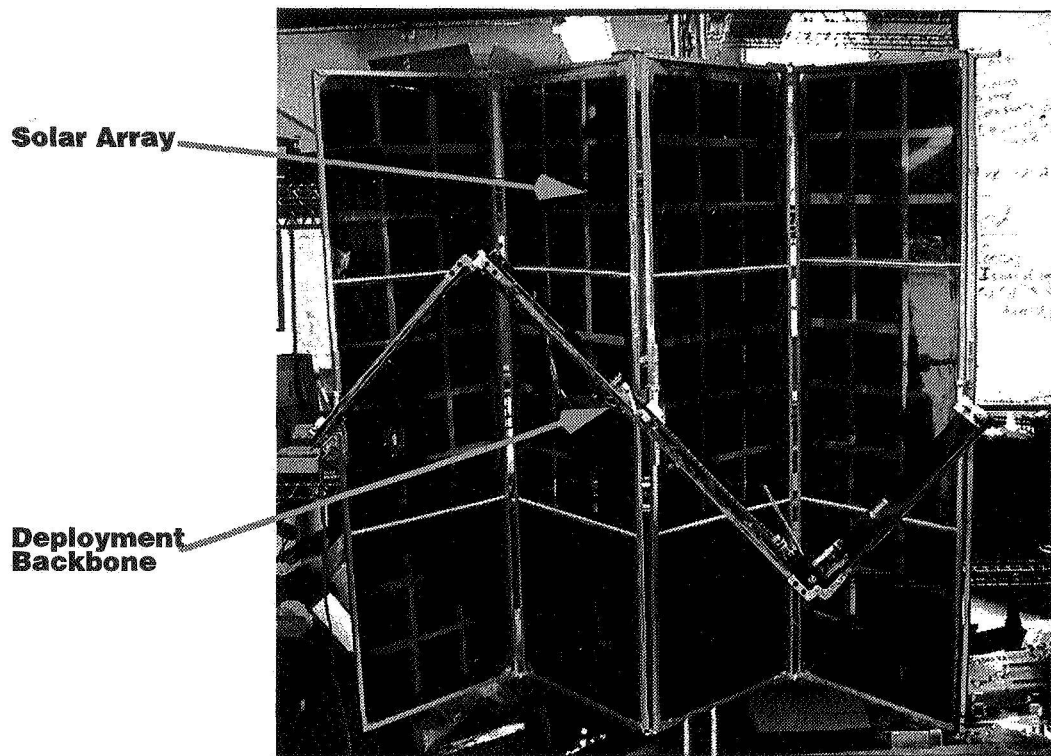
Nitinol was selected for use as the driver for the mechanism, due to its ability to accomplish a large amount of work per weight of material. By heating the material above its transition temperatures to induce its shape memory transformation, useful work was accomplished to deploy solar panels. The material was able to produce very high forces/torques under testing while the material’s inherent damping properties provided very smooth motion, thus removing the necessity of incorporating dampers in the system.



## System Description

### Overview

The Nitinol deployment mechanism uses a backbone of accordion folded members to both deploy and stiffen the satellite solar array. The backbone members rotate orthogonal to the solar array, deploying the panels and locking them flat as the backbone straightens. Figure 4 shows a picture of the deployment prototype, showing the array of four solar panels and the three member backbone.



**Figure 4. The Nitinol Deployment Mechanism prototype halfway through deployment. The unfolding of the backbone pulls apart and deploys the solar array.**

Two Nitinol torsion bars (only one is needed to deploy, as the actuators are redundant) are mounted to the backbone and transmit torque through a right-angle drive system, applying torque to unfold the backbone and deploy the array. A flexible, electrical heating system is used to actuate the torsion bars while a simple, semi-lenticular lockup system is employed, utilizing sections of a tape measure to keep the backbone locked straight.

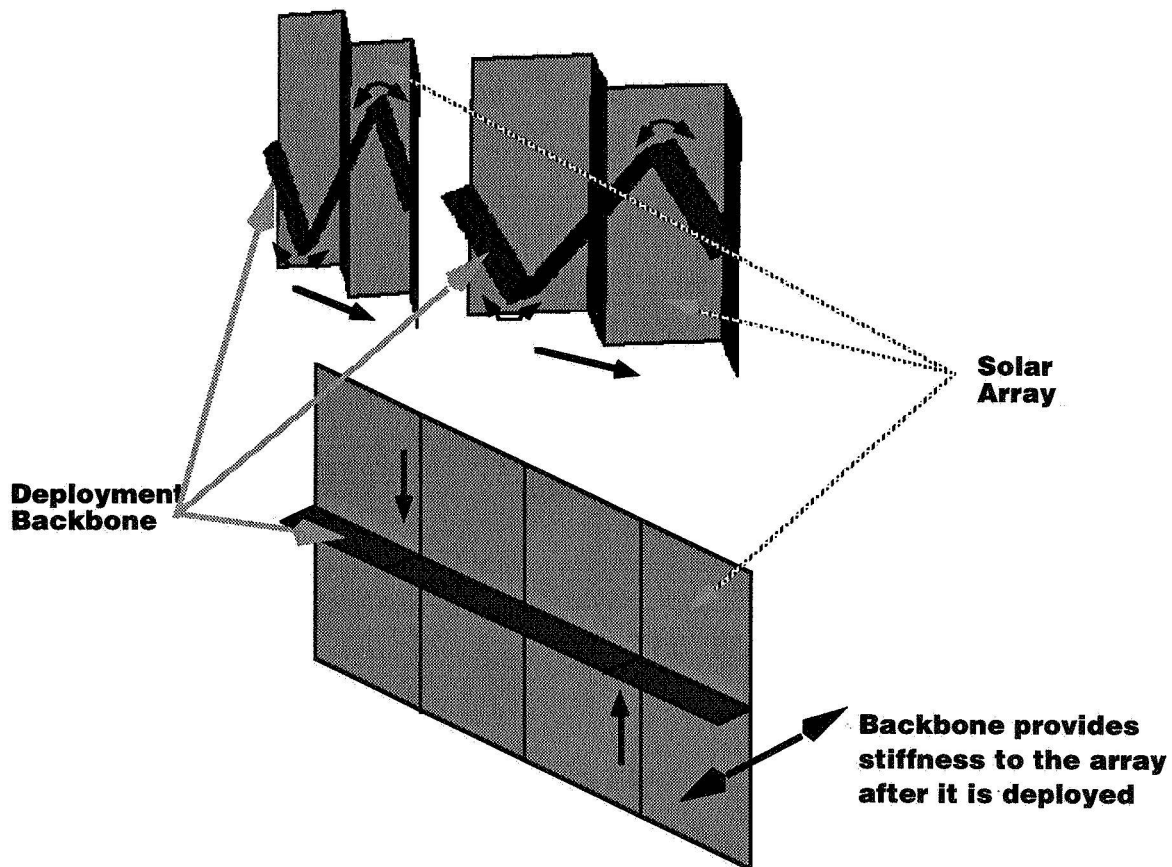
### Deployment Backbone

The deployment backbone is the cornerstone of the Nitinol deployment mechanism. It serves dual functions in that it is used to deploy the solar array, and then stiffen it once it is deployed. Figure 5 shows a schematic diagram of how the backbone unfolds and pulls apart the solar panels to deploy the array. The backbone is mounted orthogonal

to the solar array, thus providing outstanding stiffness when deployed. The backbone is also used as the support structure for all of the other components in the mechanism.

The deployment backbone is constructed of three fiber-reinforced composite laminate members. For the sake of this prototype, poplar wood was the chosen material due to its workability, extreme light weight and high stiffness. In a final space application, graphite epoxy composites could be used.

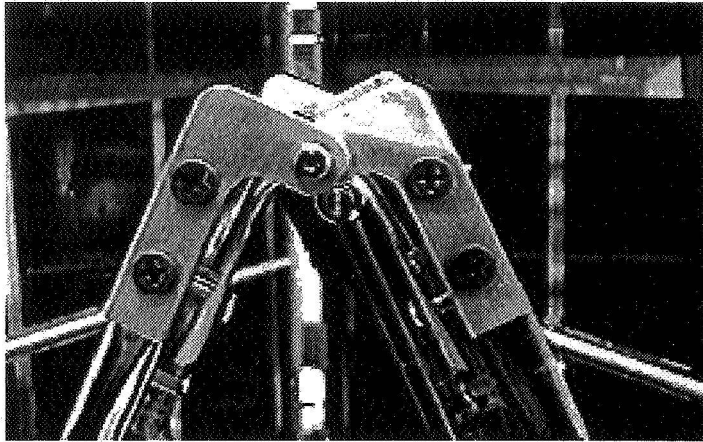
The three backbone members are 1.3 cm (0.5") thick and 14 cm (5.5") wide. The center member is 76 cm (30") long, while the other two members are 40 cm (16") in length. The width and thickness of the backbone were determined by the stiffness requirements of the array.



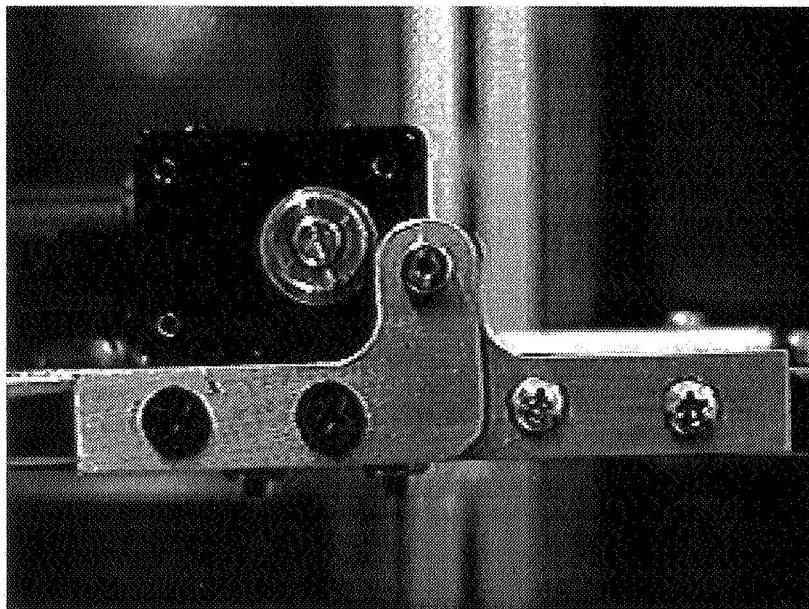
**Figure 5. The deployment backbone deploys the solar array by pulling apart the solar panels as it straightens or unfolds. Notice how the backbone's orthogonal orientation stiffens the array after deployment.**

The backbone members are connected together by simple, discrete, single pivot hinges. These hinges were designed to allow for the 2.5 cm (1") gap required when fully folded (stowed). The hinges also prevent the backbone from over rotating during deployment, by constraining the backbone to a maximum 180° of rotation in the fully flat (and open) position. When the backbone is folded and stowed, a 2.5 cm (1") gap is required between the members to allow for mechanism component clearance. Once

the backbone is unfolded, it must not rotate past  $180^\circ$  since the backbone must be flat to be an effective stiffener. Rotation of the backbone members is limited by having them meet end to end when unfolded. Figures 6 and 7 show the hinge detail when fully stowed and unfolded.



**Figure 6. Backbone hinge detail when stowed. The simple hinges provide a one inch gap between the members for mechanism component clearance.**



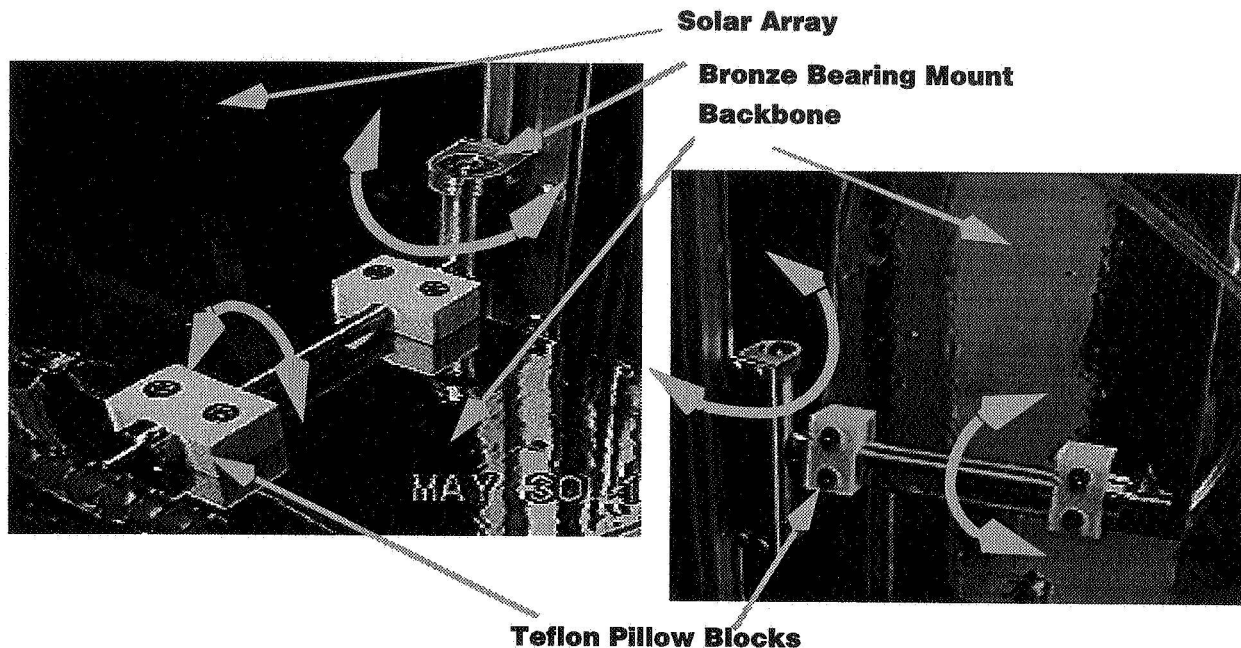
**Figure 7. Hinge detail of the backbone when unfolded. The hinges cause the backbone members to meet end to end, thus assuring that the backbone will not rotate beyond flat.**

#### Solar Array-to-Backbone Coupling

Since the solar array panels fold in one plane and the backbone members fold in yet another, a special two degree of freedom rotational joint is required to couple the two

subsystems together. The solar array-to-backbone coupling provides this function while maintaining very low friction pivot points.

Figure 8 shows a picture of the coupling system. A T-shaped bar is allowed to pivot through bronze bushings in one degree of freedom (axis of the panel rotation) while the other degree of freedom (axis of the backbone rotation) rotates within Teflon pillow blocks. By attaching the bronze bushings (via a bearing mount) to the solar array and the Teflon pillow blocks to the backbone, a rigid two degree of freedom rotational joint is formed.



**Figure 8. The Solar Array-to-Backbone Coupling allows two degree of freedom rotation, thus acting as an effective joint between the solar array and the deployment backbone.**

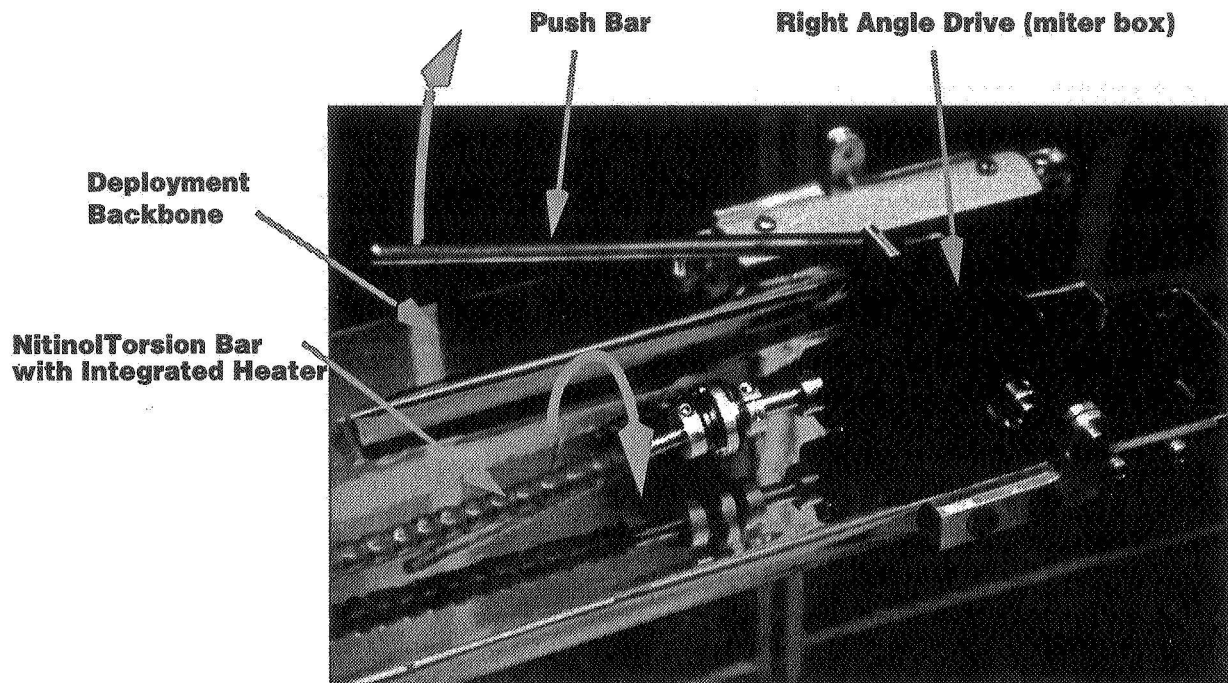
The T-shaped bar is constructed from 1.3 cm (0.5") aluminum shaft and 6.4 mm (0.25") stainless shaft. The aluminum shaft is tapped through the middle of its length and the stainless shaft is screwed in orthogonally through the entire thickness of the aluminum.

#### Actuation Subsystem

The actuation subsystem applies the motive force required to unfold the backbone and thus deploy the array. This subsystem integrates a Nitinol torsion bar, a flexible heater system, a right angle drive, and a push bar. Figure 9 shows an overview of the actuation subsystem.

The actuation subsystem utilizes the untwisting of a Nitinol torsion bar to apply the torque necessary to unfold the backbone. The torque from the Nitinol driver is transmitted through the right angle drive, thus rotating the push bar against an adjacent backbone member.

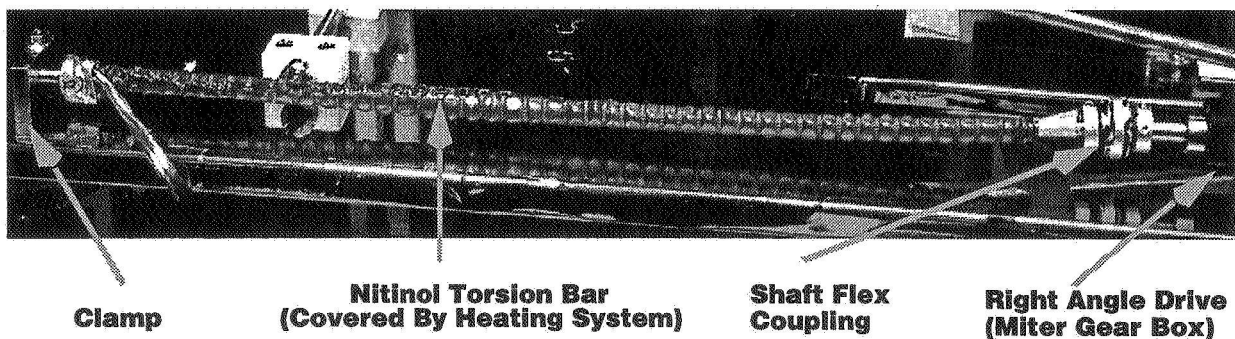




**Figure 9. The actuation subsystem. A Nitinol torsion bar untwists when heated, thus applying torque through the right angle drive and push bar to unfold the backbone and therefore deploy the solar array.**

#### *SMA Torsion Bar Actuators*

Two 0.48 cm (3/16") diameter, 38 cm (15") long Nitinol rods are used as torsion bars to apply the torque required to unfold the backbone and thus deploy the array. Each torsion bar actuator is constrained (clamped) on one end, while the other end is coupled to a right angle drive via a flexible shaft coupling. This allows the untwisting of the Nitinol actuator to apply a useful torque to the right angle drive. Figure 10 shows a picture of the Nitinol torsion bar mounted in the actuation system.



**Figure 10. Nitinol torsion bar used to apply torque to deploy the array. The torsion bar is clamped on the left end and coupled to the right angle drive through a flexible shaft coupling on the right.**

The Nitinol torsion bars are implemented using one-way memory, thus implying a very simple training process for the material (see section on Nitinol Torsion Bar Training). Due to the high actuation torques and large rotations required by the deployment system, the stress-induced martensitic transformation of the material is exploited. This means that the torsion bars are first heated above their transition temperature and then slightly stressed during the cooling of the material back to its martensitic state when set for deployment. This bias stress, applied as a torque of approximately 2 N•m (18 in-lb), allows the material to be deformed well beyond 270° of rotation. Since the actuator has no force at the end of its travel, it is preset with 90° of rotation to assure full deployment of the array. At start-up, the actuation torque of the torsion bars has been measured to be greater than 11.3 N•m (100 in-lb)!

The transition temperature of the actuators is set at 79°C (175°F), as requested by Lockheed for Nitinol actuators used in space applications. Heating of the material higher than this temperature is required to obtain full recovery of the material strain.

#### *Flexible Heating Systems*

Integrated, flexible, electrical heater systems are used to heat the Nitinol torsion bars above their 79°C (175°F) transition temperature. These heaters are constructed by impregnating resistive heating elements into a silicone RTV matrix and bonding them to the surface of the actuators. The heaters keep the material heated until the array has fully deployed and locked up. Since the Nitinol actuators deform during deployment, the heating systems must be able to flex and move with the actuator. This is to assure that intimate surface contact is maintained during heating. (essential for conduction, since convection does not occur in space)

#### *Right Angle Drives: Miter Gear Boxes*

The right angle drives are used to transmit the torque from the Nitinol torsion bars, around a 90° angle to the axis of rotation of the backbone members. These drives must be very smooth and must have very low friction to insure proper operation of the actuators.

The drives are merely 90° miter gear boxes that were purchased off the shelf from W. M. Berg, Inc. The particular units applied have no gear reduction, and were chosen by virtue of the fact that they were the smallest gear boxes capable of transmitting the high torques supplied by the SMA torsion bars.

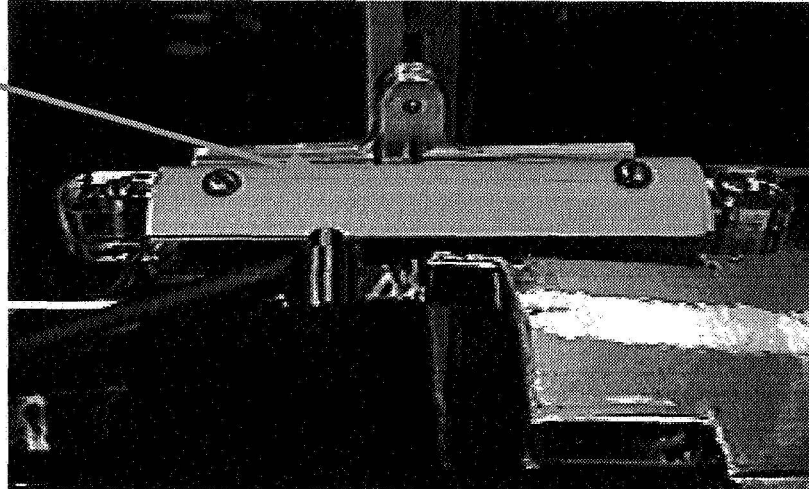
#### *Push Bar*

The function of the push bar is merely to apply a force on the backbone to make it unfold during actuation. Due to its configuration, it is only capable of applying force to deploy the array. Even if the push bar rotated all the way back (for example, in the case of two way memory) no force could be applied to the backbone by the push bar. This is due to the fact that the push bar is not rigidly connected to the adjacent backbone member that it pushes against. It is allowed to retract from contact with the adjacent member, and actually rotate through the member that it is mounted on (a hole has been cut out of the member it is mounted on specifically for this purpose). The actuator bar is shown in the actuation subsystem overview, Figure 9.

### *Semi-Lenticular Lockup Mechanism*

Lock-up of the backbone members is necessary to maintain the integrity and stiffness of the solar array. A semi-lenticular structure (provided by sections of an actual tape measure) is used to provide lock-up rigidity to the backbone in the prototype. Figure 11 shows a picture of the lenticular lockup mechanism as implemented in the prototype.

Sections of  
a tape measure



**Figure 11. Sections of an actual tape measure used to lock up the deployed backbone. The curvature of the tape measure provides high stiffness when straight, but provides little resistance when folded.**

A lenticular structure (named after the lentil) is a structure with a slight curvature along its length. This curved cross section creates high stiffness due to the increased section properties produced by the curvature. However, when a lenticular structure is bent, it loses its section and provides little resistance to bending. This unique property of tape measures was exploited to provide a simple, passive lockup means for the deployment mechanism.

### Nitinol Torsion Bar Training

The behavior of the Nitinol actuators was predetermined by the process used to “train” them. In this particular application, the rods were trained to have one-way memory. The training process for the torsion bars was extremely simple. The 0.48-cm (3/16")-diameter drawn, Nitinol stock was cut down to two 38 cm (15") lengths and then placed into a fixture that constrained them in a straight position. The rods were then heated to a temperature of approximately 815°C (1500°F) for ten minutes. The heating of the rods annealed the material, thus releasing all residual stresses. The net effect of the annealing process was to set the trained or remembered shape to the straight configuration.

After training, the material can be twisted and deformed when in the martensitic (low temperature) state. When heated above 79°C (175°F), the rod returns to its straight shape (assuming that it was stressed less than 8%). If stress induced martensite is used, then material can be deformed a great deal more without overstraining the material.

Some two way memory was trained in the material, although somewhat by accident. Two way memory is trained into the material by intentionally OVERSTRAINING the material over a repeated set of load cycles.

#### Deployment System Stiffness Analysis

The solar array needs to have its first bending normal mode at a frequency greater than 0.1 Hz to assure that it does not interfere with the attitude control system of the satellite. The following calculations are based on the prototype as designed, extrapolated to a 6 m (20') full-sized array.

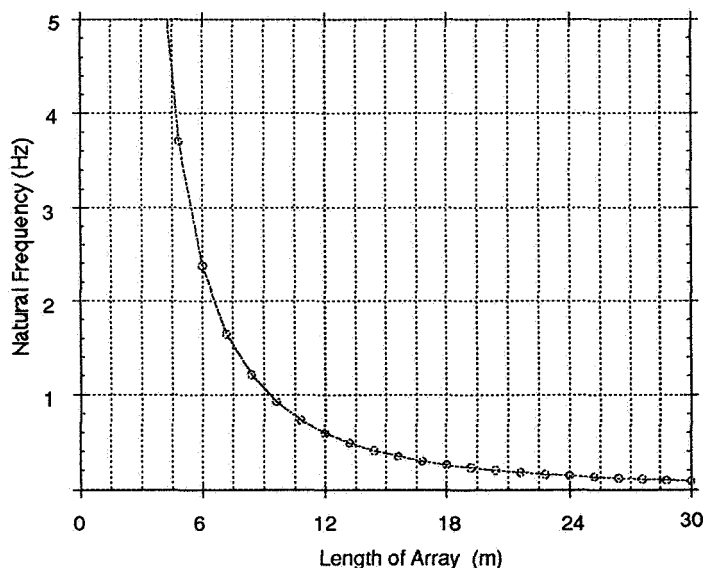
The extended solar array wing was modeled as a beam, with the moment of inertia calculated from the backbone and mass calculated from the entire system. The following equation was used to calculate the natural frequency of the system.:

$$\omega_n = \sqrt{\frac{3EI}{(0.23m)l^3}} \quad (1)$$

Where  $E \approx 17$  GPa (2500 ksi),  $I = 113 \text{ cm}^3$  (6.9 in<sup>3</sup>), and  $m = 24$  kg (52 lb) for the solar array.

The natural frequency,  $\omega_n$  is calculated as 3.7 Hz.

Figure 12 shows the relationship between the length of the array and its 1st natural frequency. It was analytically determined that the current design could be extended up to 30 m (100 ft.) without violating the 0.1 Hz first bending requirement.



**Figure 12. Natural Frequency of the Solar Array vs. the Length of the Array. Notice that the Backbone design could be scaled to a 30 m (100 ft) array without falling below the 0.1 Hz 1st bending requirement.**



## Concept Development

Initially the design space of possible solutions was tremendous, with concepts varying from simplistic concepts such as using Nitinol helical springs at hinge joints to "blue sky" ideas like Nitinol actuated solar sails to pull out the arrays. The Morphological Matrix in the figure below shows a cross section of the concepts developed for specific requirements.


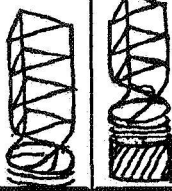







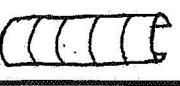

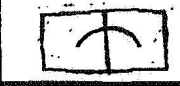
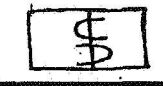
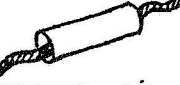


Deploy						
						
Lockup/ Rigidity					Latching cam snap fit	Locking hinge: ratcheting over center
Heating						
Panel/Panel Connection	piano hinge	flexure bearing	discreet hinge	strings/ cables	SMA hinge	
Cell Support	Frame	Rigid Substrate				

Figure 13: Morphological Chart was used by the design team to generate ideas for sub-systems within the design project.

From this vast array of ideas three concepts were chosen as superior concepts because they provided both deployment and lockup/stiffness. Each of these concepts was prototyped to confirm feasibility. These three concepts were the Nitinol Semi-lenticular Spring, the Nitinol Mast, and the Nitinol Backbone Deployment System, which has already been described.

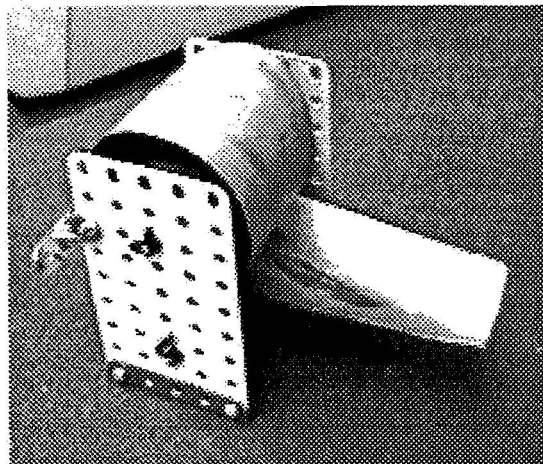
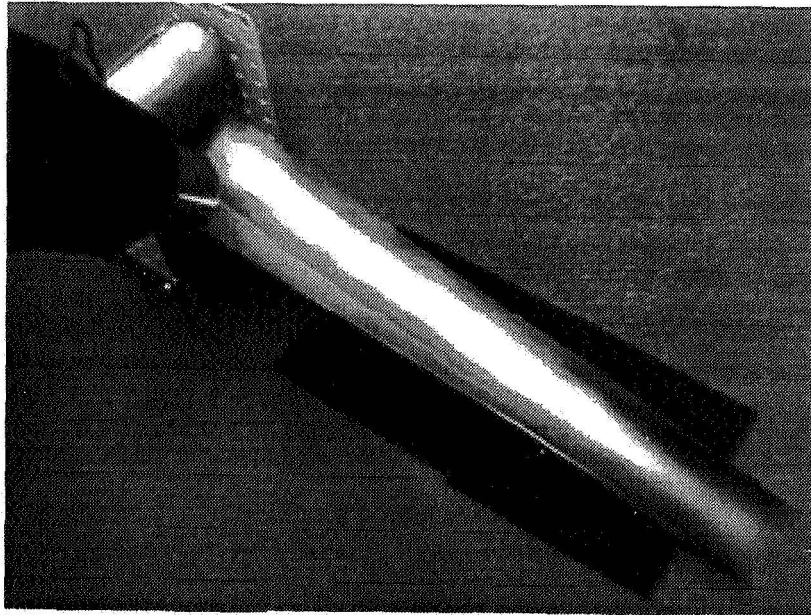
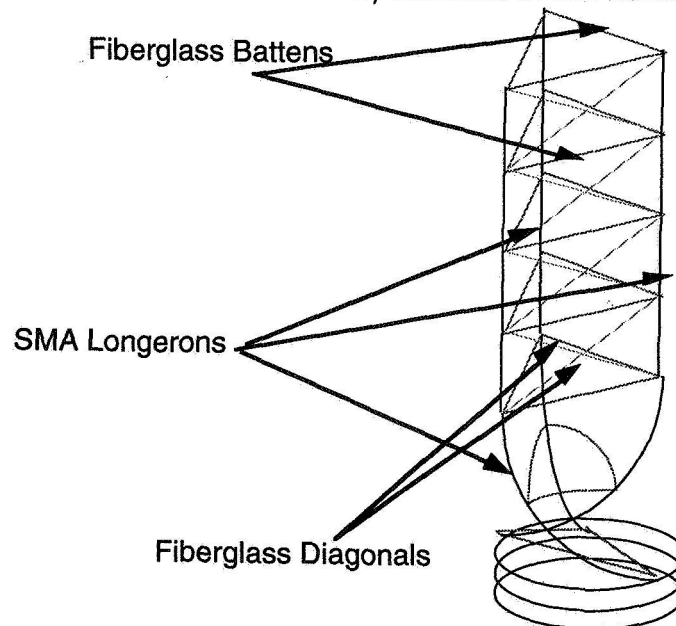


Figure 14: Nitinol Semi-lenticular prototype before heating.



**Figure 15: Nitinol Semi-lenticular prototype after the application of heat.**

The semi-lenticular spring concept is a thin strip of Nitinol that is trained into a semi-circular cross section. The element is flattened and rolled onto a drum in the stored position, and it can be extended by heating the Nitinol strip to return it to the trained, curved shape. As the strip tries to regain its curvature, it pushes on itself, extending very much like a tape measure does. The semi-lenticular structure is also called a STEM (Storable Tubular Extendible Member) element in the aerospace industry.



**Figure 16: Nitinol Mast.**

The motion of the Nitinol mast is similar to the current masts used by Lockheed made by Astro Aerospace or AEC-Able Engineering. Instead of being driven by a motor, the vertical members are replaced by Nitinol to provide recovery forces.

From these promising concepts, the Nitinol Backbone was chosen as the concept for further development. Although all could be applied effectively to solar array deployment, the Backbone was deemed to be more unique and exploited the properties of Nitinol better than the other concepts. The other concepts were also problematic due to the fact that they rely on the Nitinol to provide lockup stiffness. Nitinol exhibits a severe dip in stiffness as it cools from the austenitic to the martensitic state, thus leaving these concepts unsuitable for the combination of deployment and lockup.

### Prototype Performance Results

The Nitinol Backbone deployment met and exceeded all the requirements set by the project constraints. The most poignant results are the comparisons between the Nitinol Backbone and the current state-of-the-art, the Astromast from Astro Aerospace. The table below makes direct comparisons for major performance criteria.

**Table 2: Comparison of key performance characteristics between the Astromast and the Nitinol Backbone mechanism. Weight, volume, and part count are for a 6 m (20 ft) long solar array.**

	<b>Astromast</b>	<b>Nitinol Backbone</b>
Mass	91 kg (200 lb)	5.4 kg (12 lb)
Stow Volume	0.041 m <sup>3</sup> (2,500 in <sup>3</sup> )	0.023 m <sup>3</sup> (1,400 in <sup>3</sup> )
Deployment Time	≈3 minutes	≈2-3 minutes
Power Required	100 Watts	100 Watts
Part Count	many(intricate parts to build mast)	120 total, 15 distinct

The table clearly indicates the advantages of using Nitinol over current technologies. It also achieves the required stiffness with a natural frequency of 3.7 Hz at 6 m and above 0.1 Hz at 30 m. The kinematic constraints create a natural redundancy in the actuation. If one actuator moves, the entire array will deploy. Should one of the many actuators fail, the remaining actuators are sufficient to deploy the array, increasing the reliability of the design. The deployment can be easily controlled for smooth motion by varying the heating rate of the torsion bars. As a result, no additional dampers are necessary. This further reduces the cost of the system.

### Conclusion

Using a 207 g (1.5 oz) piece of Nitinol, it is possible to deploy a 1.5 m (5 ft) wing with actuation torques up to 11.3 N•m (100 in-lb) over 180° of travel. Such performance is only possible with Nitinol. The backbone system exploits Nitinol in many different ways, including utilizing the natural damping of Nitinol, the little known Stress Induced Martensitic transformation, and the simplicity of one way memory. In this 25 week

study, a prototype was successfully developed to apply the use of Nitinol to solar array deployment. Although still in the prototype stage, significant improvements in weight, stow volumes, complexity, efficiency, and system cost are foreseen through the use of Nitinol. The development of this prototype has not only seen the creation of a better, lighter, and cheaper deployment system when compared to the current state of the art, but also the conceptualization of many possible "spin-off" ideas using Nitinol that can be applied to other mechanisms. This work has shown the development of a superior deployment technology, providing the rationale and analysis necessary to foster further development of other mechanisms exploiting the unique properties of Nitinol.

## References

1. T. R. Cawsey, "A Deployment Mechanism for the Double Roll-Out Flexible Solar Array on the Space Telescope," British Aerospace P.L.C., England.
2. C. M. Friend, "Shape-Strain Degradation in Reversible Shape-Memory Actuators," Scripta Metallurgica, Pergamon Journals, Ltd., 1987.
3. H. Funakubo, Shape Memory Alloys, Gordon and Breach Science Publishers, Tokyo, 1984.
4. Handbook of Satellite Array Design, JPL, CA
5. R. Haviland, C. M. House, Handbook of Satellites and Space Vehicles, D. Van Nostrand Co., Inc., Princeton, New Jersey, 1965.
6. D. Hodgson, "Shape Memory Alloys," Santa Clara, 1992.
7. D. Hodgson, "Using Shape Memory Alloys," Shape Memory Applications, Inc., CA, 1988.
8. K. Honer, A. Santoso, "Mass Positioning System," Professor Larry Leifer, instructor, for Lockheed, June 1991.
9. C. Liu, H. Kunsmann, K. Osuka, M. Wuttig, Shape-Memory Materials and Phenomena-Fundamental Aspects and Applications, Materials Research Society, Pennsylvania, 1992.
10. D. Packard, M. Benton, "The Galileo Spacecraft Magnetometer Boom," Jet Propulsion Laboratory, Pasadena, CA.
11. R. Warden, "Folding, Articulated, Square Truss," AEC-Able Engineering Co., Goleta, CA.
12. R. Warden, P. A. Jones, "Carousel Deployment Mechanism for Coilable Lattice Truss," AEC-Able Engineering Company, Inc., Goleta, CA.

# The ARA Mark 3 Solar Array Design and Development

Rob H.A. van Hassel\*

59-44  
30437  
125123V

## Abstract

The ARA (Advanced Rigid Array) Mark3 solar array of Fokker Space BV is currently in its final stages of qualification (wing tests to be completed in March, 1996; unit/part tests in April, 1996). With regard to its predecessor, the ARA Mark2, the design has not only been improved in terms of mechanical and electrical performance, but also with regard to production cost and throughput time. This 'state of the art' array is designed to fit the needs of a wide variety of geostationary telecommunications satellites and is qualified for launch on the complete range of medium/large size commercial launchers (Ariane IV & V, Atlas, Delta, Proton, Long March, H2).

The first mission to fly the new ARA Mk3 array is Hot Bird 2 (customer: Eutelsat, prime contractor: Matra Marconi Space; launch: mid-1996). In this configuration, its end of life (EOL) power-to-mass ratio is 42 W/kg, with an operational life of more than 12 years.

The main mechanisms on a solar array are typically found in the deployment system and in the hold down and release system. During the design and development phase of these mechanisms, extensive engineering and qualification tests have been performed.

This paper presents the key design features of these mechanisms and the improvements that were made with regard to their predecessors. It also describes the qualification philosophy on unit/part and wing level. Finally, some of the development items that turned out to be critical, as well as the lessons learned from them, are discussed.

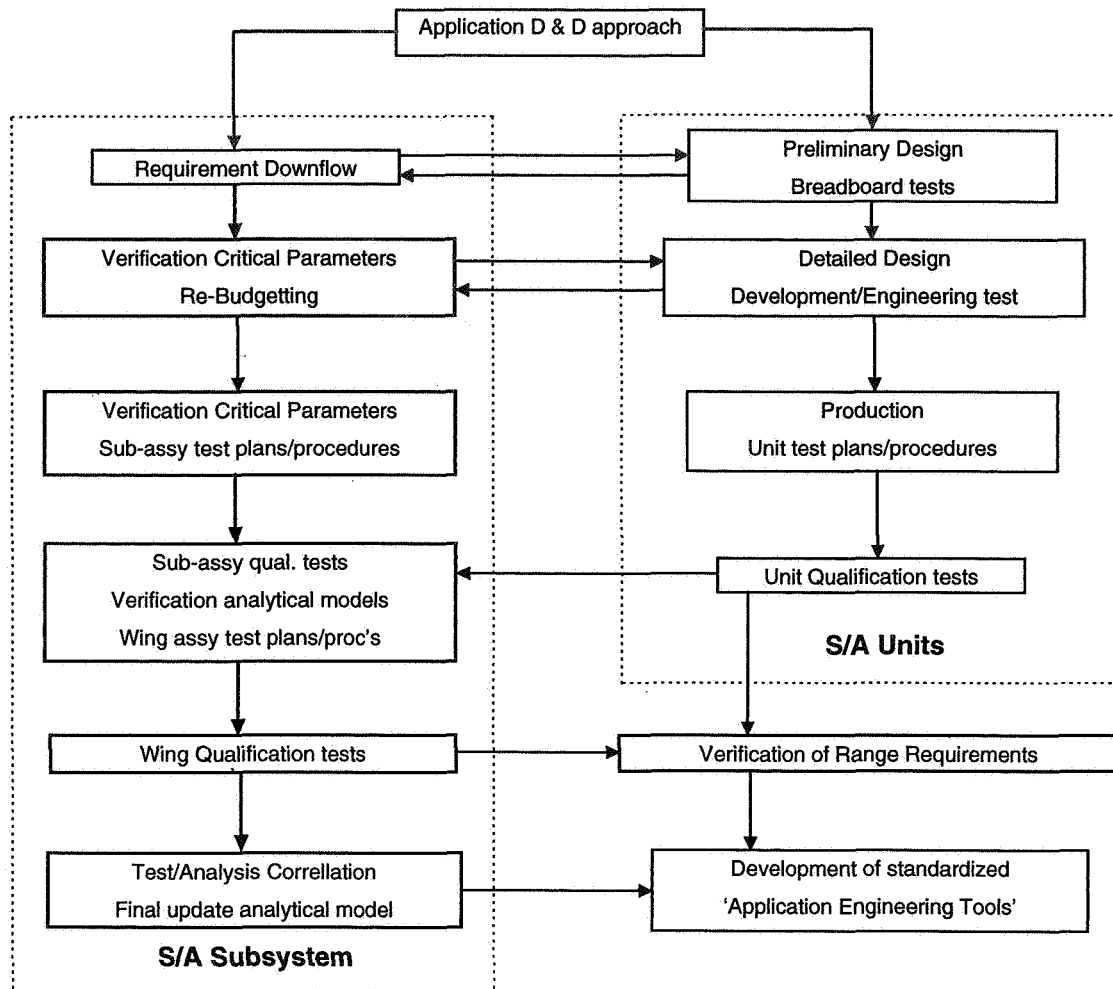
## Introduction

At the start of the development program, an extensive study was carried out to identify the advantages and disadvantages of the previous ARA Mk2 design, based on the current and future solar array market demands. For this purpose, a range of possible applications was identified, such that the newly designed solar array family would be usable without any delta qualification being required on unit or wing level.

With this in mind, key requirements were defined at subsystem (solar array) level and were carefully translated and budgeted down to unit and part level. This resulted in the definition of critical design parameters that were to be monitored throughout the design process. This process is described in Figure 1, which shows the flow from detailed unit design to production and further on to unit qualification testing. Also, the connection with the activities on subsystem level, such as analytical modeling, qualification testing and correlation, is given.

---

\* Fokker Space BV, Leiden, The Netherlands



**Figure 1 The ARA Mark3 requirement downflow process**

## Design Factors

Throughout the development program, we have tried to maximize the margins of the various units. This would allow us to use 'coarse' engineering and analysis tools, which would ensure that the non-recurring costs for a solar array application would be as low as possible.

However, the solar array market currently sees a trend towards increased system requirements in combination with reduced mass budgets. Therefore, frequent interaction between the unit and subsystem requirement definitions was mandatory in order to balance the criticality and margin of key parameters.

At wing level, the definition of applicable environments was rather straightforward: they should simply envelop the requirements of the desired range of spacecraft and launchers, including qualification margins and a safety factor against yield.

On unit level, however, this definition was more complex. Environments and boundary conditions had to be defined in such a way that they would ensure qualification of the unit for the full application range.

For the thermal environment definition, a qualification range that would envelop all desired applications was chosen. This was done by careful study of all thermal analyses of previous ARA Mark2 solar array designs and by increasing margins to allow for uncertainties.

For the mechanical loads, a set of factors was defined, as found from subsystem analyses. The definition of these factors is given below. For each individual unit, these factors were quantified by analyzing the criticality of the design, the sensitivity to parameter changes, and the uncertainties in the design.

Growth Factor [GF]:

- The design of the solar array shall allow for an approximate 50-mm shift of the hold down locations without any effect on the overall qualification status. This is based on our experience with spacecraft layouts changes at a late stage in the program. The consequences of such a shift are normally a change of the natural frequencies and mode shapes and a change of the load pattern in the panels.
- Furthermore, the design shall allow for power growth of an existing solar array geometry by changing from silicon to gallium arsenide solar cells. The latter have a considerably higher mass, thus causing higher stresses in the substrate and higher loads on the hold downs.

Parameter Inaccuracy Factor [PIF]:

- Although all design parameters are well known after completion of the development and qualification program, inaccuracies must be taken into account for variations in both stiffness and mass properties (panels, hold down stacks, hinges, yoke, etc.) that were yet unknown.

Analysis Inaccuracy Factor [AIF]:

- The analytical models that we used for load predictions, of course, do not have a complete 1:1 relationship with the hardware.

General Reserve Factor [GRF]:

- Boundary conditions (Ground Support Equipment, test setups, supports etc.) for unit tests will very often not be identical to those on wing level.

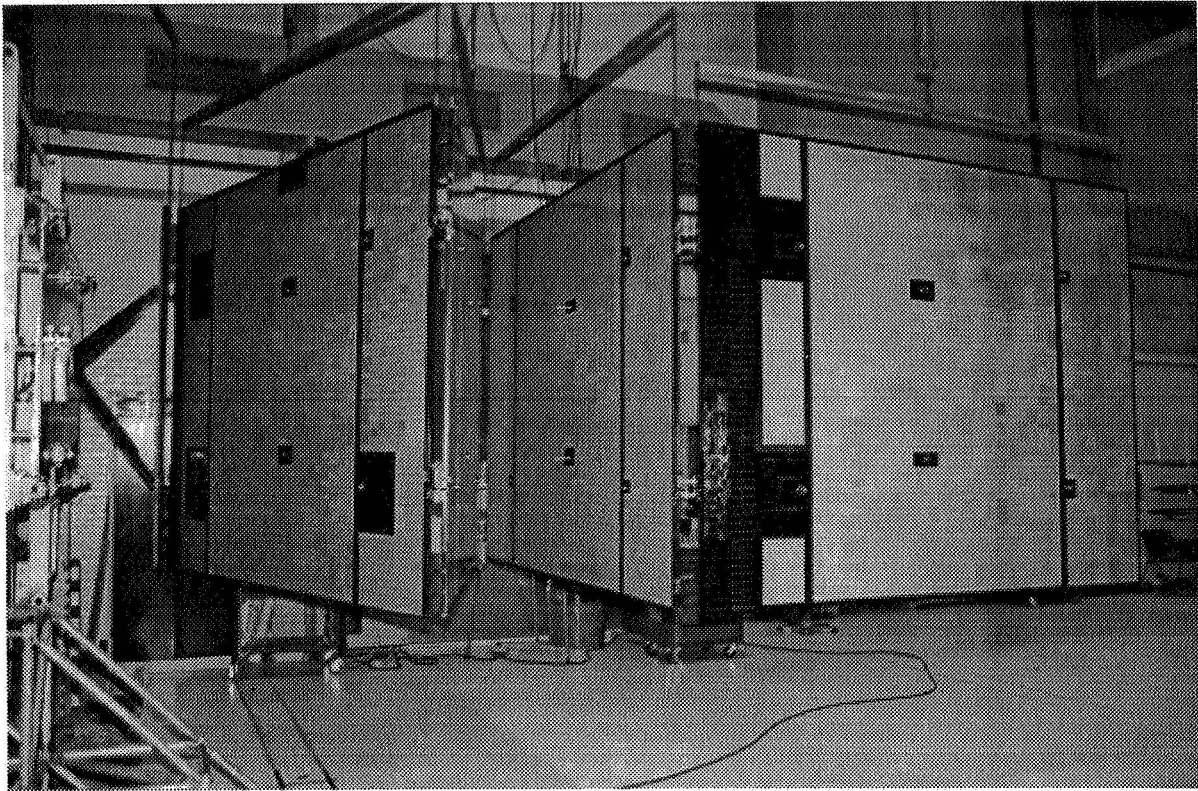
Thus, the overall safety factor for a unit (on top of the regular factor against yield) is:

$$\text{Overall Unit Factor} = [GF] \times [PIF] \times [AIF] \times [GRF]$$



## Key Design Features

The solar array design features that were chosen to meet the desired application range are described below.



**Figure 2 The ARA Mark3 solar array qualification model**

- An array typically consists of two identical wings, mounted on the north and south side walls of the spacecraft. Figure 2 shows an overview of the ARA Mark3 Qualification Model (QM) wing during one of its deployment tests (4 panels of more than 6 m<sup>2</sup> each; total wing span of more than 13 m).
- Each wing is composed of a maximum of 5 sandwich panels with aluminum honeycomb core and CFRP face sheets, covered by solar cells (cell type is project specific).
- During launch, the wings are stowed in folded positions against the side walls of the satellite by means of 4 to 6 (inboard) hold downs per wing.
- The deployment system is equipped with an eddy current damper. Thus, the deployment shocks on the Solar Array Drive Mechanism (SADM) hinge and the interpanel hinges can be limited.



- In transfer orbit, two configurations are possible: either the satellite is spinning and the wings are kept folded, or it is 3-axis stabilized, such that the outer panel of each wing is deployed over 90° to a partially deployed position. The remaining stowed panels are kept folded to the side walls by means of 1 or 2 hold downs. After arrival in its final orbit, the wing is deployed to its fully deployed position.
- The solar array wings are released for partial and full deployment by cutting aramid restraint cables by means of thermal knives (identical principle to ARA Mk2).
- The adverse effects of shadowing are countered by:
  - the yoke length; maximum yoke length without extra hold down provisions is 1.80 m
  - shunt diodes
- Each wing can be equipped with:
  - thermal fins for thermal shielding of the spacecraft radiator panels and to prevent sun trapping between the solar array wings and the satellite side wall
  - plume shields to avoid thruster plume impingement on the wing
  - an AOCS flap (solar sail) to save fuel by assisting satellite attitude control
  - solar array-mounted sun sensors

## Design Description

In the following paragraphs, the design of the various components is described in detail.

### Solar Panel Substrates

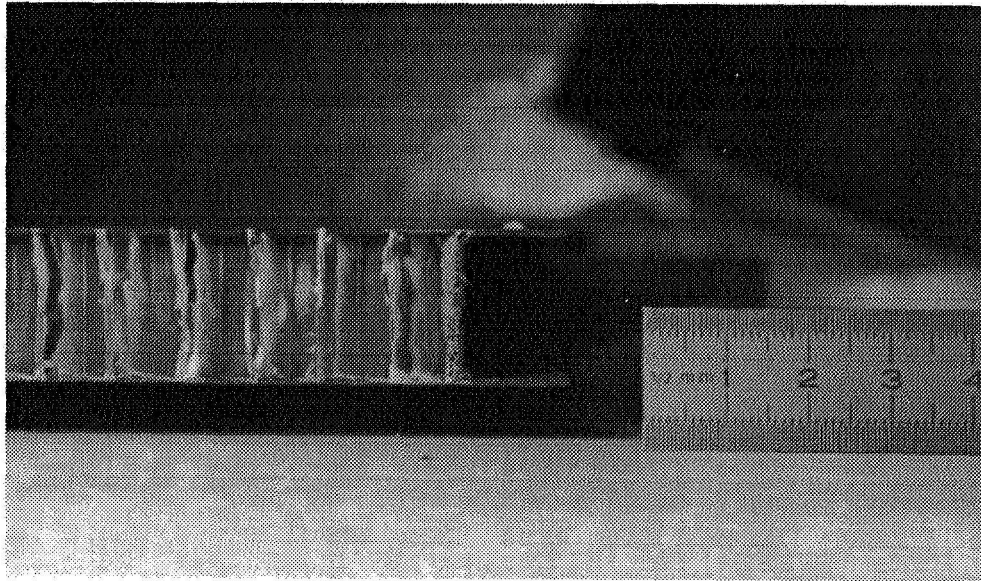
The panel design is based on “standardized” components (skins, honeycomb, subassembly panels for hold down areas, edge members), such that it fits the stiffness and strength requirements, while keeping the mass to a minimum.

For each application, the panel loading, which depends on the spacecraft/launcher combination, must be checked to ensure that it is within the qualification spectrum. The nominal substrate covers the application range of solar arrays from 3 minimum sized panels ( $\sim 1.2 \times 1.7 \text{ m}^2$ ) up to 5 panels with maximum sizes ( $\sim 2.25 \times 2.75 \text{ m}^2$ ) per wing. Outside this range, it is of course still possible and justifiable to apply the ARA Mark3 design components. However, one must realize that the performance parameters (such as power-to-mass ratio) then start to deteriorate.

The skins of all panels of each solar array are kept identical and consist of M55 CFRP prepreg in closed lay-up. Reinforcement patches are located between each pair of opposite hinges to provide extra stiffness and skin strength. Since mass budgets are invariably tight, the skin layout is mass-optimized.

The panel core consists of low density aluminum honeycomb (height of 22 mm). Edge members ('C-sections') of CFRP weave are applied in the hingeline edges along the full length of the panel edge. Figure 3 shows a cross-section of a substrate at the panel edge.

Local reinforcement plugs ('subassembly panels') are used to give extra strength and stiffness to the hold down areas. These are circular and consist of relatively dense aluminum honeycomb and several layers M55 CFRP. They provide margin against yield and fatigue of the nominal honeycomb and reinforce the skin at the hold down locations.



**Figure 3 Detail of panel substrate with edge member**

#### Photovoltaic Assembly

The solar cells and their cover glasses are typically project specific. The solar cell isolation is provided by a layer of Kapton on the front CFRP skin. Isolation with regard to the power subsystem, if required, can be obtained with flat blocking diodes mounted on the panel rear side.

Shadow protection in the fully deployed configuration is provided by shunt diodes (flat, mounted on the panel front and/or rear side).

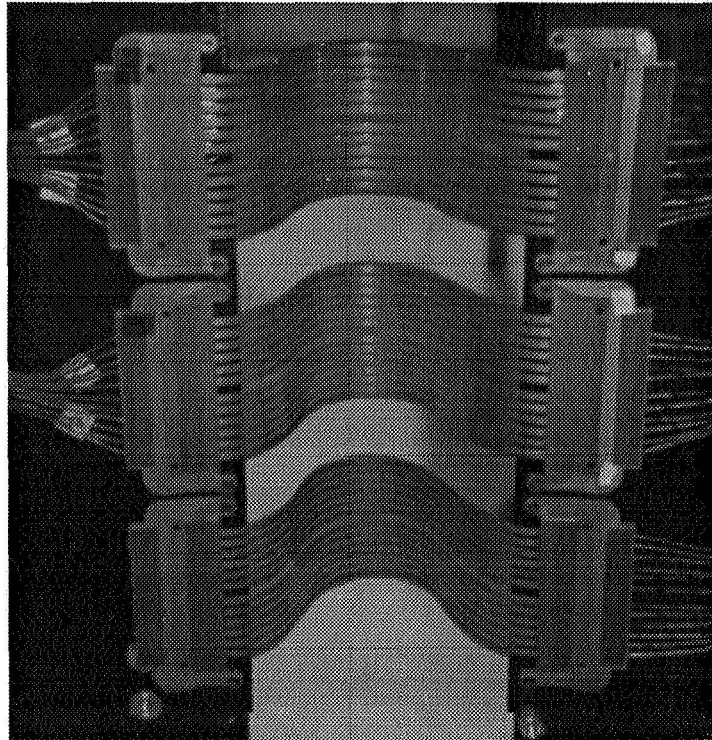
The panel wiring and solar cell string design are positioned, such that the string ends and feedthrough holes are all located at the same panel edge for each panel.

#### Transfer Harness

The transfer harness is lightweight and modular. The panel wiring from the solar cell string ends, as well as the harness coming from the more outer panels, is routed to dedicated female 'flexprint connector' parts. These connector parts are attached to the

edge members along the panel hingeline edges. Therefore, the harness can be installed on the panel rear side completely by the cell supplier, thus resulting in a decrease of assembly cost and throughput time.

The hingelines are then crossed by flexible flat wiring, so called 'flexprints' (Figure 4), with male connector parts attached to them and are inserted into the female connector parts on the panel edges. The flexprints are made of two Kapton front and rear sheets, with 12 etched copper tracks sandwiched between them. They are designed, such that they ensure low electrical resistance and minimum retarding torque under extreme thermal conditions.



**Figure 4 Flexprint/Connector assembly on panel edge**

#### Deployment Mechanism

The deployment mechanism consists of the following items:

- Yoke
- SADM ('root') hinge
- Deployment damper
- Interpanel hinges
- Synchronization system
- Partial Deployment Mechanism (PDM)

### Yoke

The V-shaped yoke ranges in length from 1.0 to 1.8 m. The length of the yoke pipes may vary, as well as the angle between them. As a consequence, the interfacing parts of the root hinge and the hinge attachment brackets will then also have a different angle.

The arms of the V-shaped yoke consist of CFRP filament wound tubes with a circular cross-section. The thermal expansion coefficient is kept as close to zero as possible in order to be able to meet the alignment requirements for the complete range.

Flexprints can be attached to the dedicated yoke flexprint panel (standard M55 CFRP skin with edge members for flexprint and hinge attachment and nominal honeycomb), running parallel to the panel hingeline edge.

### SADM Hinge

The SADM hinge interfaces with the satellite mechanically, thermally, and electrically and consists of two hinged brackets providing attachment points for the SADM hinge torsion spring, the deployment damper, the yoke tubes, the SADM interface plate, and the I/F connector bracket. One hinge axis serves as the input shaft for the damper gearbox, while the other is used as feedthrough for the yoke harness.

### Deployment Damper

A deployment damper is included in the ARA Mark3 design baseline in order to reduce deployment shocks, while maintaining ample margins with respect to retarding torques. The damper is of the eddy current type, in combination with a gearbox mechanism, manufactured by Honeywell. Its performance can serve the full ARA Mark3 range.

The damper/gearbox combination is mounted on one of the two axes of the SADM hinge. In order to enable this configuration, the gap between the inner panel and the satellite side wall was increased with regard to the ARA Mk2 design.

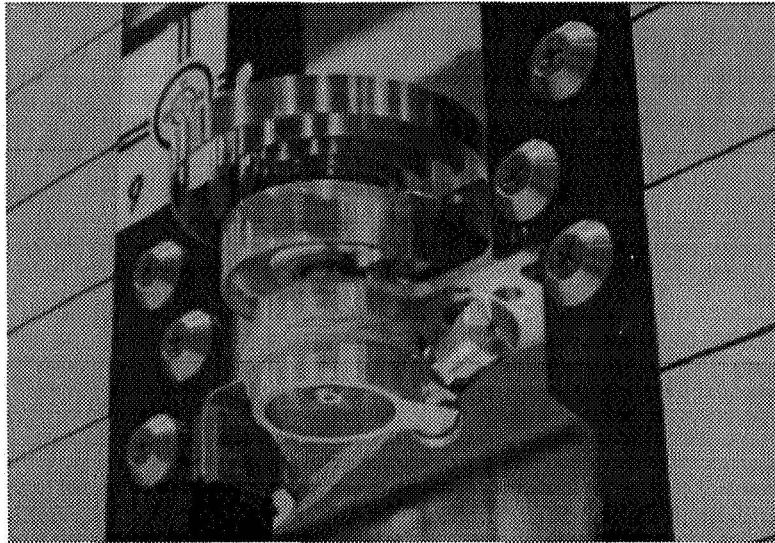
The use of a damper allows for relaxation of the strength requirements from deployment shock of the SADM and the panel hinges after secondary, full deployment. The load case of the deployment shock at the end of the primary, partial deployment of the outer panel still requires a higher allowable bending moment of the hinges because this deployment is not damped.

The damper can cover the range of applications up to 5 maximum size panels per wing, enveloping the complete range of thermal environments. For each application, the damping coefficient must be determined, while considering the applicable thermal environments and the deployment safety factors.

### Interpanel Hinge

Each interpanel hingeline consists of with two co-axial hinges (Figure 5). These are equipped with dedicated 'clock' springs to counter the retarding torque of the Power Transfer Harness, the friction of the synchronization system, and the internal friction of the hinge bearing itself.

The required torque is strongly dependent on the number and size of panels and will vary per hingeline. Therefore, the actuating torque that has to be produced by the hinges will also deviate over a large range. From both a mass and a strength point of view, one type of spring to cover the complete torque range is not acceptable, so the hinge design accommodates several different spring types.



**Figure 5 Interpanel hinge**

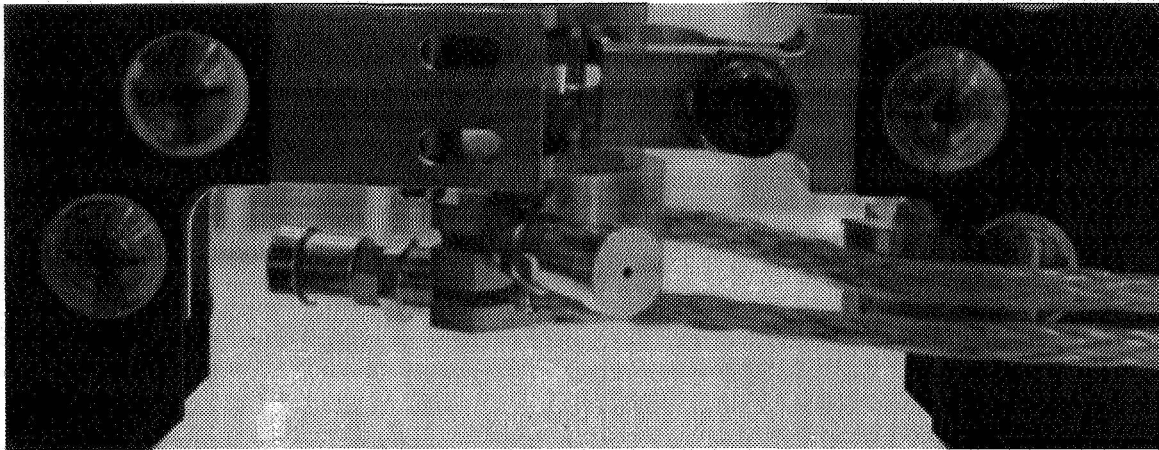
The interface with the panel substrate for each hinge bracket is provided by three titanium pins. The I/F holes are not in line in order to reduce hysteresis effects under bending loads. The brackets are mounted internally in the edge member, and shear webs in the brackets provide the necessary stiffness.

#### Synchronization Mechanism

The synchronization of the deploying panels is ensured by braided aramid cables, running from hingeline to hingeline. To accommodate this, each hinge is equipped with a dedicated pulley.

Because of the deployment damper, the stiffness of these synchro cables is very high. Without this, the combination of high hinge actuation torques (driven by the high deployment safety factor) and a high damping coefficient (for cold temperatures) would cause an asynchronous deployment, thus resulting in unpredictable high deployment latch-up shocks at the interpanel hinges.

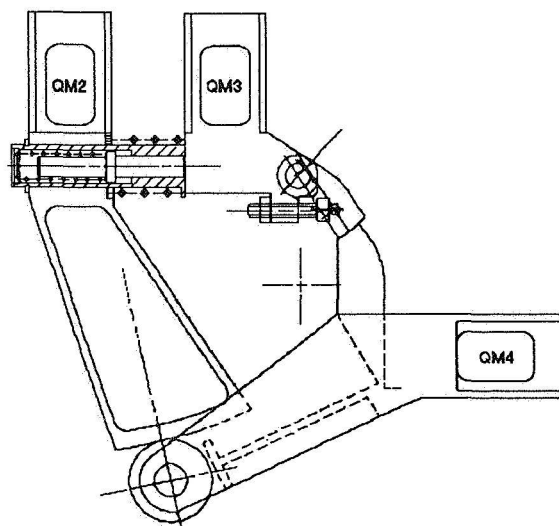
A slack compensator spring is attached internally in the braided cables in order to maintain a minimum cable tension and to prevent the cables from running off their pulleys under dynamic loading during launch.



**Figure 6 Synchro cable/pulley system**

#### Partial Deployment Mechanism

The bracketry for the PDM is shown in Figure 7. The various brackets are in 'closed form' configuration, as long as the inner panels are kept stowed, thus providing the required stiffness and load path. The rotation axes are provided by the interpanel hinges between panels 3 and 4. A bracket with a titanium wheel is attached to the outer panel. In a partially deployed position, the wheel is pressed against the flange of the bracket on panel 2.



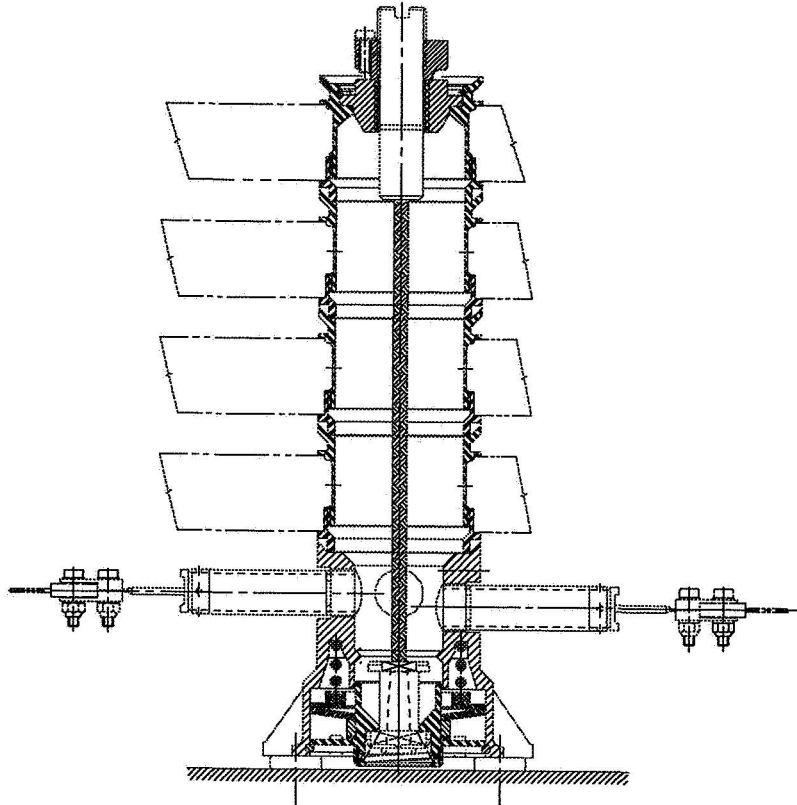
**Figure 7 Partial Deployment Mechanism (PDM)**

Positive locking of the PDM assembly is provided by the latch and cam combination on the brackets of panels 3 and 4. As soon as the secondary, full deployment starts, the wheel and flange, as well as the latch and cam, will start to move away from each other. All attachments to the panels are identical to the panel/hinge interface.



### Hold Down and Release System

Functionally, the same basic concept as for ARA Mk2, using a flexible tie-down element (aramid cable) under high preload, is applied. The stack height can vary between 2 panels (in case of a partially deployed 3-panel wing) and 5 panels (completely stowed 5-panel wing). The hold down points are located inboard on the panels, thus allowing optimization of the mechanical interface location with the satellite side wall. Figure 8 shows a typical hold down stack.



**Figure 8 Typical hold down and release stack**

The first row of honeycomb cells around the cylinder are filled with a potting compound in order to create a good shear connection between the honeycomb and the cylinder. The cups and cones are also bonded to the skin.

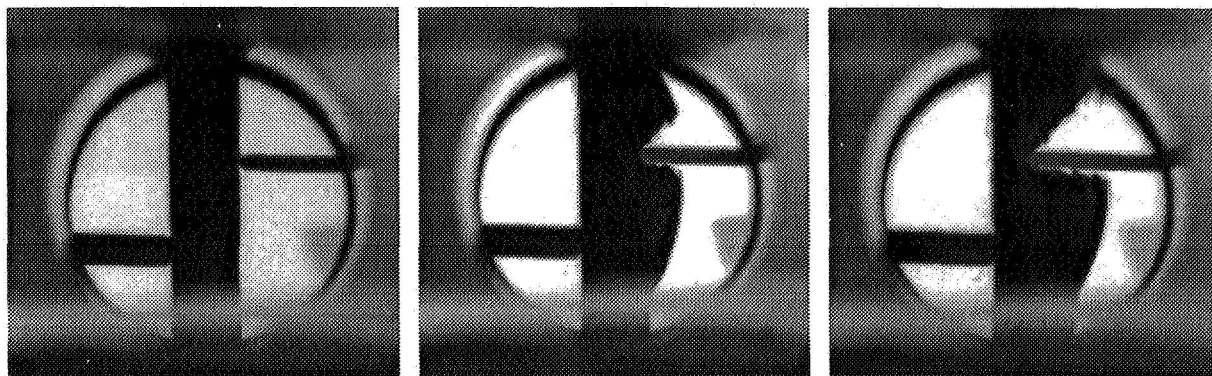
### Cup/Cone

The hold down points in the panel consist of a cup and a cone part. Both parts consist of a threaded titanium (good compatibility with the thermal expansion of the aramid restraint cable) cylinder. The conical shape is chosen to ensure that they do not start to cant or to gap relative to each other under the severe launch loads. In order to prevent fretting and/or cold welding of the cups and cones under those same loads, the contact surfaces on the cone side are covered by a surface coating.

### Thermal Knife

The aramid restraint cable is cut by means of a thermal knife. The knife consists of a ceramic plate that is heated to approximately 1000°C, while being pressed against the cable. At that temperature, the cable is gradually degraded at the location of the plate/cable interface until it is completely cut (Figure 9).

The thermal knife has proven to be very reliable in numerous applications. Furthermore, it avoids shocks at the moment of wing release.



**Figure 9 Thermal knife, cutting through restraint cable**

### Restraint Cable

As already mentioned, the cable is made of aramid. It is braided and equipped with end fittings. The bottom end fitting of the restraint cable is bayonet-shaped to ensure simple installation and traction of the cable in the stack in the stowed wing configuration. The upper end fitting is threaded to enable tensioning of the restraint cable. Both end fittings are attached to the cable by means of a conical wedge, or 'spike'.

### Hold Down Bracket

The hold down bracket interfaces with the satellite side wall. In the hold down bracket, a bayonet bus is located, constraining a package of belville springs. The bayonet bus contains the lower end fitting of the restraint cables. During the cutting process, the tension in the restraint cable decreases. The belville washers ensure a minimum pretension level in the hold down cable.

### **The Wing Qualification Test Program**

The qualification tests for ARA Mark3 are performed both on wing level and on unit/part level. Since the wing and unit/part level qual tests have been scheduled in parallel in order to enable delivery for the first flight program, both test flows still have tests in progress or not yet performed.



### Wing Qualification Tests

Wing level dynamic tests (acoustic and sine vibration) have been performed successfully at the test facility of IABG, Germany. The output of these tests was helpful in ensuring that the mechanical load levels for the unit/part tests indeed envelop the wing levels. Table 10 shows the total wing qualification test program.

**Table 10 Overall QM wing qualification test program**

Configuration / Item	Feature / Requirement to be verified	Verification method
Solar Array	Mass	Mass analysis
QM wing	Mass	Weighing of hardware
Stowed QM wing	Stiffness, Strength, fatigue	NASTRAN analysis
		Vibration test
		Acoustic test
Partially deployed array	Deployment shock strength	Deployment analysis
		Shock test
	Stiffness	NASTRAN analysis
		Stiffness test
	Alignment	Alignment test
Fully deployed array	Deployment shock strength	Deployment analysis
		Shock test
	Stiffness	NASTRAN analysis
		Stiffness test
	Alignment	Alignment test
QM wing	Deployment torque margin	Deployment analysis
		Energy surplus test
QM wing	Functional partial deployment	Deployments, including thermal knife firing
QM wing	Functional full deployment	Deployments, including thermal knife firing
QM wing	Electrical performance	Electrical health checks
		Flasher tests

### **Key Performance Parameters**

Based on the 'Hot Bird 2' solar array configuration (2 x 4 panels of 2.736 x 2.250 m; 6 hold downs per wing; yoke length of 1.8 m; 10-Wcm Si cells), the following key performance parameters have been established:

#### Mechanical Subsystem

- 133-kg total mass
- 52-Hz first stowed global natural frequency
- 0.6-Hz partially deployed frequency
- 0.05-Hz deployed frequency
- minimum out-of-plane input at natural frequencies  $\geq 2.0$  g
- acoustic input 148.7 dB overall sound pressure level

### Electrical Subsystem

- 44-V I/F voltage
- at autumn equinox, EOL power of 5.5 kW

## **Critical Design Items And Lessons Learned**

### Deployment Hinge Development Issues

Although several parts for the hinges had already been manufactured, assembled, and tested before the Critical Design Review of the development program, there was one design feature that was not tested on the engineering level simply because it was not considered critical: the stiffness and backlash properties of the deployed hinge.

However, after technical discussions with ESA experts, we had decided to increase the angular play in the hinges to allow for a larger build misalignment budget in the hinge assemblies. This would then result in very low friction during the deployment which would lead to a favorable reduction of the total required deployment energy budget.

At that time, it was not realized that this also introduced a considerable amount of backlash in the hinges in deployed configuration. Thus, the deployed stiffness was almost nil for low disturbance loads (Figure 11). For large solar arrays, this feature is unacceptable, and it was only found during hardware acceptance testing, just before installation in the qualification wing.

The solution that we found was as elegant as it was simple: The male hinge bracket rotates around a bearing. This bearing was originally cylindrical, but the design was updated to a conical one. Now it allowed for relatively large angular rotations, while keeping lateral play to the minimum. Figure 11 shows both stiffness curves.

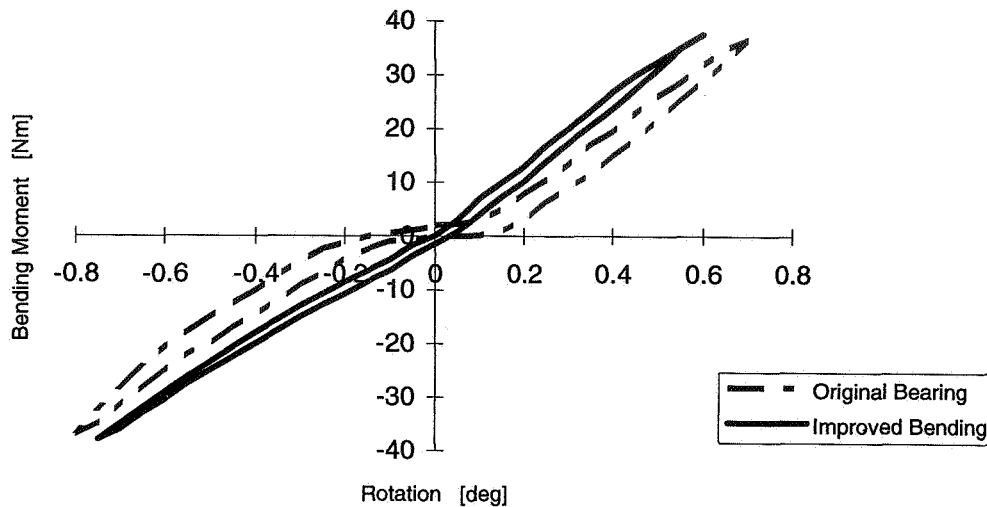
### Hinge Lessons Learned

- A change of one design parameter does not necessarily affect only one aspect of the performance. Track down all the possible effects, both positive and negative, of the design change.
- ARA Mark 3 has succeeded in developing a low friction hinge with positive locking and no backlash in deployed position.

### Partial Deployment Mechanism Development Issues

At the start of the program, in-house development and qualification tests on a PDM design for another project had just finished. It was decided, given the success of these tests, to keep the design 'as is' for ARA Mark3 and concentrate on more urgent matters.

At the end of the QM wing program, at the start of the deployment shock qualification tests, a flaw in the design was found. Under low loads, the mechanisms behaved perfectly. However, under increasing load levels (e.g., the undamped shocks at latch-up after deployment), the stiffness dropped sharply, while the adjacent brackets showed large relative displacements.

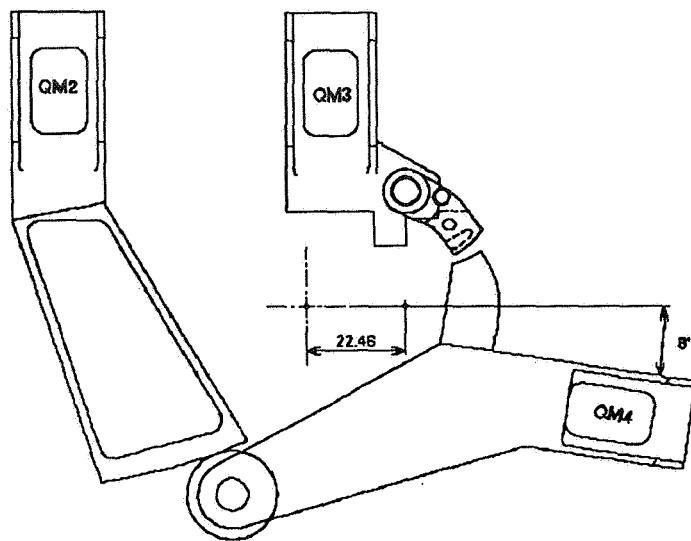


**Figure 11 Deployed stiffness of the 'old' & 'new' bearing design**

Detailed investigation of the stresses and displacements, as found by test and by analysis in the partially deployed wing, revealed the following causes. At the end of partial deployment, outboard panel QM4 tends to rotate further due to its inertia. Furthermore, the out-of-plane flexibility of panel QM3 (outermost stowed panel) allows a displacement in the outboard direction of the hinges that connect panel QM3 and QM4 at the same time. This resulted in the combination of large relative displacements and low stiffness.

The re-design had to be, as usual, a compromise between stiffness (required to meet the needs of the Attitude & Orbit Control System of the Hot Bird 2 spacecraft) and strength (as a consequence of increasing the stiffness, the shock loads after deployment would increase).

The new brackets (Figure 7 shows the unloaded situation, and Figure 12 shows the deformed configuration) have been installed, and the tests for alignment, stiffness, and deployment shock are currently under way, with the bracketry behaving flawlessly. After this, the test program is to be resumed in order to conclude the ARA Mark3 qualification program at wing level.



**Figure 12 Deformed Partial Deployment Mechanism (e.g., shock load)**

#### PDM Lessons Learned

- A unit/part that functions correctly in a system is designed using a certain set of boundary conditions. Check if these conditions also apply to your system. Try to find killer requirements/conditions before they kill you!
- ARA Mark 3 has succeeded in developing a Partial Deployment Mechanism that is insensitive to panel size and to location of hold down points.

#### **Conclusions**

- The ARA Mark3 solar array combines high performance with low mass, low cost, and short schedule time.
- The development philosophy successfully concentrated the efforts on two fields:
  - requirement derivation from system level down to unit/part level to cover the complete application range.
  - extensive breadboard/engineering tests to correct design flaws before the actual qualification tests (the PDM being the exception that proves the rule).

#### **Acknowledgment**

The author would like to thank the members of the ARAFOM solar array project team for their comments and their never-wavering enthusiasm and devotion throughout the project.

# SCARLET I: Mechanization Solutions for Deployable Concentrator Optics Integrated with Rigid Array Technology

James J. Wachholz\* and David M. Murphy\*

516-74  
50438✓  
125124

## Abstract

The SCARLET I (Solar Concentrator Array with Refractive Linear Element Technology) solar array wing was designed and built to demonstrate, in flight, the feasibility of integrating deployable concentrator optics within the design envelope of typical rigid array technology. Innovative mechanism designs were used throughout the array, and a full series of qualification tests were successfully performed in anticipation of a flight on the Multiple Experiment Transporter to Earth Orbit and Return (METEOR) spacecraft.

Even though the Conestoga launch vehicle was unable to place the spacecraft in orbit, the program effort was successful in achieving the milestones of analytical and design development, functional validation, and flight qualification, thus leading to a future flight evaluation for the SCARLET technology.

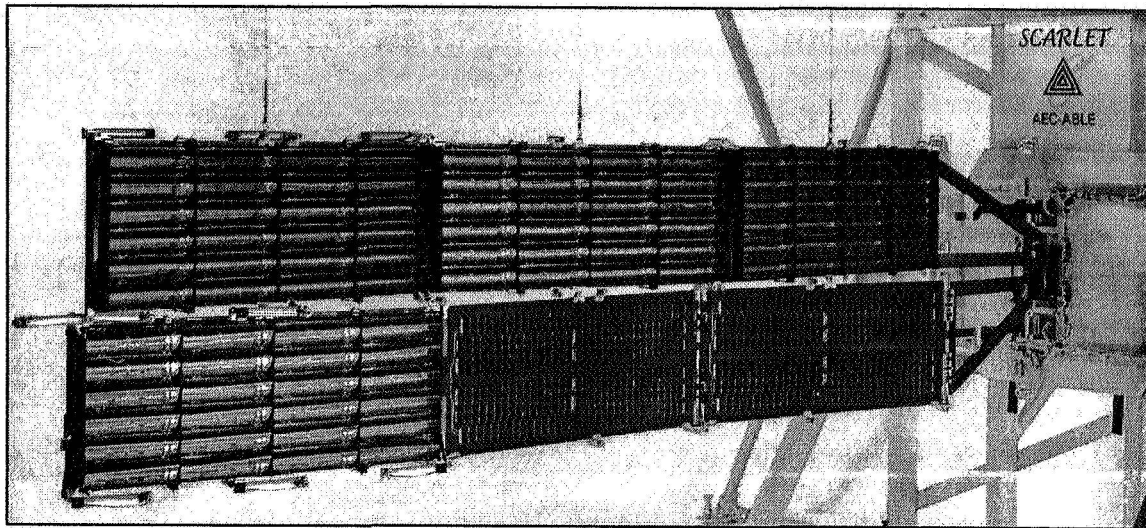
## Introduction

The rigid array structural approach chosen for this application was ABLE's flight-qualified PUMA (Pantographically Unfolding Modular Array) design, which is briefly reviewed. The array construction is a hybrid of concentrator (four panels) and planar (two panels) technology so that the non-tracked array functions as both a concentrator flight demonstration experiment and a mission power source at large solar off angles for the nadir-pointing spacecraft. The SCARLET I solar array wing, in the deployed position, is shown in Figure 1.

The main design objective was to integrate the curved Fresnel lens primary optics into the PUMA structure by using simple, controlled deployment mechanisms with accurate optics adjustment features while maintaining the standards of high reliability, small stowed volume, light weight, structural strength, and stiffness. This paper presents the details of the mechanisms designed to accomplish these objectives. The features covered include ABLE's rigid array design, the solar concentrator system, integration of the optics with the deployment system, and the launch restraint system.

---

\* AEC-Able Engineering Company, Inc., Goleta, California



**Figure 1. SCARLET I Concentrator Solar Array Wing**

### **Rigid Array Design**

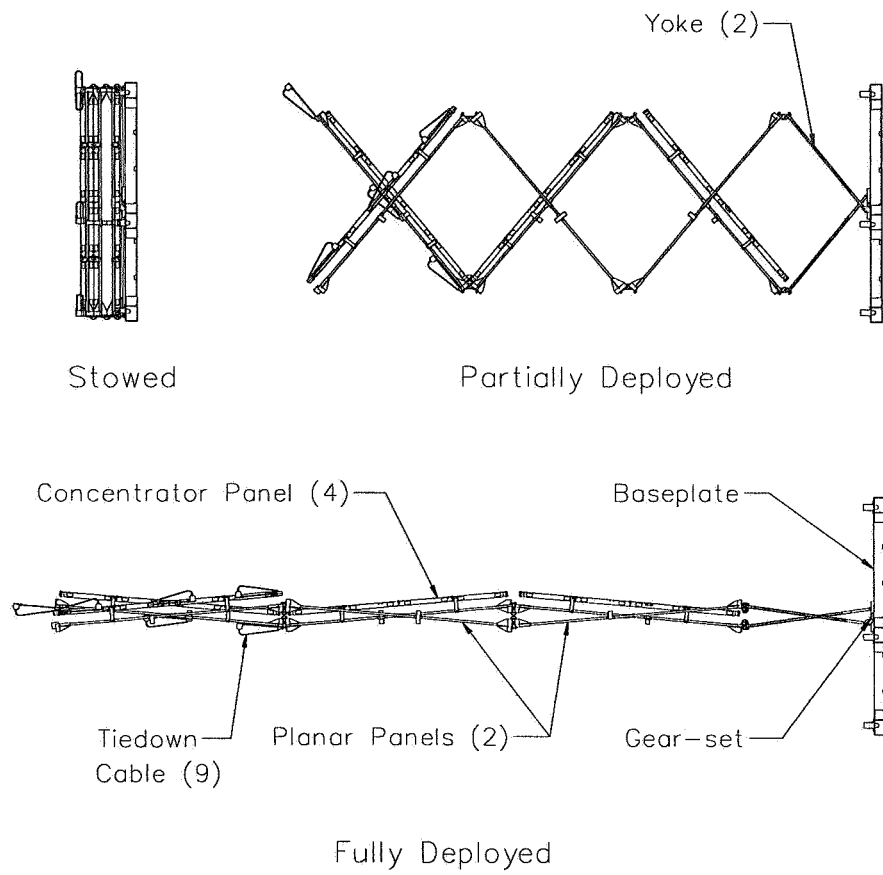
Key features of the PUMA rigid array design include pantographic deployment geometry, panels composed of honeycomb substrates with graphite/epoxy face sheets, intrinsic deployment synchronization, redundant deployment springs, small stowed volume, modular design, and high specific power.

Scissors-like array deployment occurs pantographically as the redundantly hinged panels, which are linked in pairs by pivots, unfold until the panels stop 5° short of flat, as shown in Figure 2. By stopping the deployment here, the array retains “depth” to provide substantial gains in structural efficiency with a minimal loss in solar cell power production (Figure 3). Compared to a flat panel array, this technique typically yields a 7.5-times increase in first mode out-of-plane frequency with a small power loss (<0.4%). Structurally efficient panels, composed of aluminum honeycomb with graphite/epoxy face sheets, were used to reduce panel thickness with the added benefit of reducing stowed volume and weight.

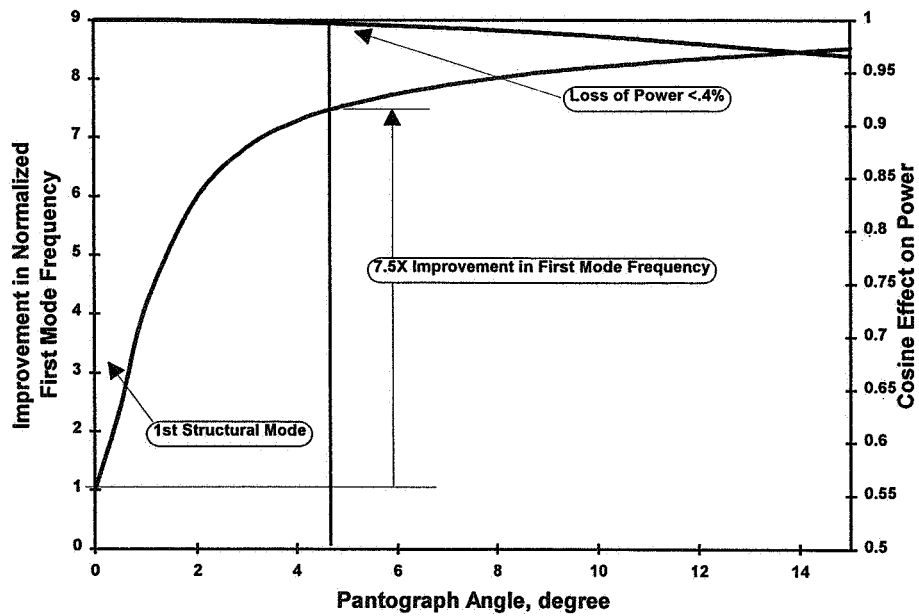
Reducing the complexity and increasing the reliability over other rigid panel designs was achieved with the intrinsic self-synchronization of the PUMA pantographic system, which requires no auxiliary timing mechanisms. To complete synchronization down to the root, two stand-off yokes and the panels are hinged together to form a linkage. The timing of the linkage is synchronized with a gear-set at the root.

Multiple redundant torsion springs at each hinge line increase reliability and allow fine tuning of the deployment rate. A viscous damper is also used to control the deployment rate.

This modular rigid array design allows easy addition of panel pairs as needed to meet specific mission requirements during the early design phase.



**Figure 2. Array Deployment Sequence**

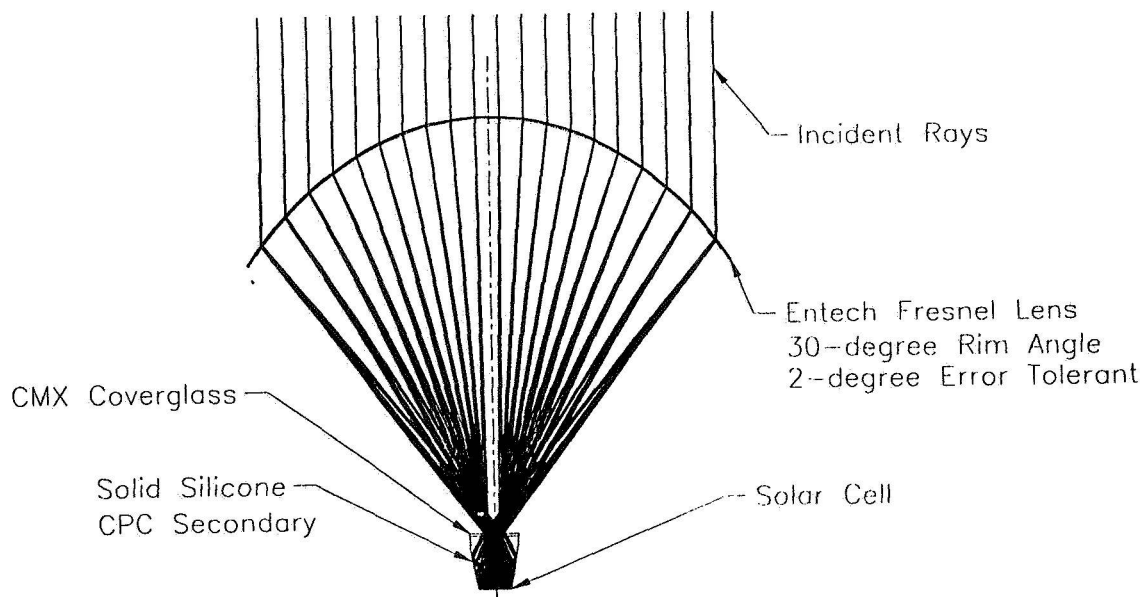


**Figure 3. Structural Efficiency Advantage**

## Solar Concentrator System

The solar concentrating system consists of two optical elements, as shown schematically with ray traces in Figure 4. The primary element is a Fresnel lens composed of 0.006-inch-thick, space-grade silicone bonded to 0.0024-inch-thick, ceria-doped borosilicate glass. The glass, which protects and stiffens the lens, has been thermally shaped as a cylinder to facilitate lamination and to minimize stresses. The refractive Fresnel design yields much better shape error tolerance than reflective concentrating systems.

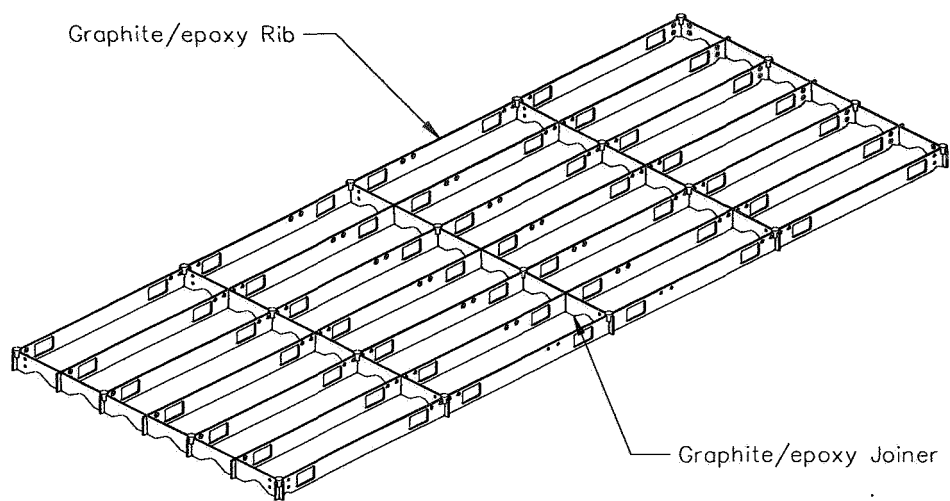
The compound parabolic concentrator secondary element is made of silicone and is shaped to produce additional concentration by the principle of total internal reflection. The optical system is configured with a tolerance to 2° pointing errors. A detailed description of the optical concentrator system can be found in Reference 1.



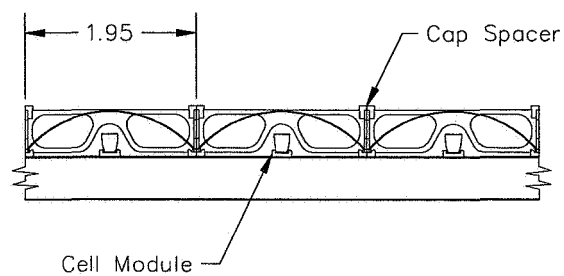
**Figure 4. Optical Components**

The task of properly supporting and providing for individual adjustability of 24 primary lens assemblies per panel was made challenging by the fact that maintaining a high packing factor is critical to specific power performance. A stiff, lightweight graphite/epoxy frame is used as the primary structure to hold the lenses, as shown in Figure 5. Lenses were bonded with silicone along their long edges into thin-formed steel edge supports. These supports were independently adjustable within the frame, thus allowing the lens to be properly aligned above the secondary optics.

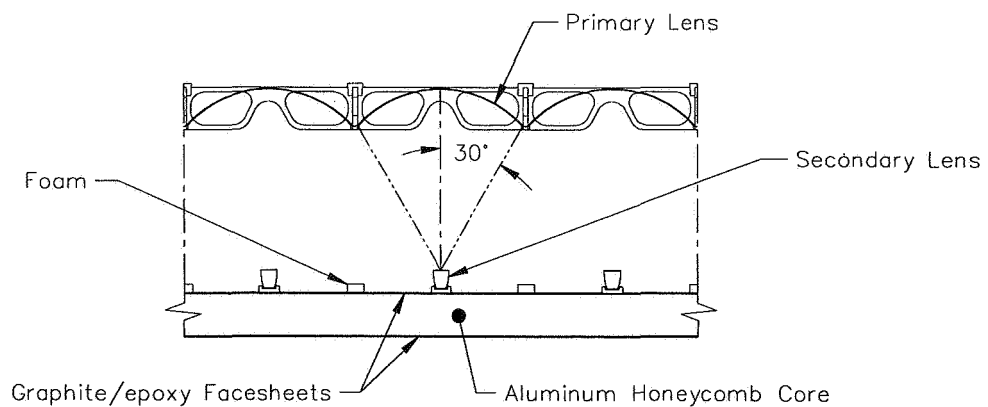




Primary Lens Frame



Stowed View

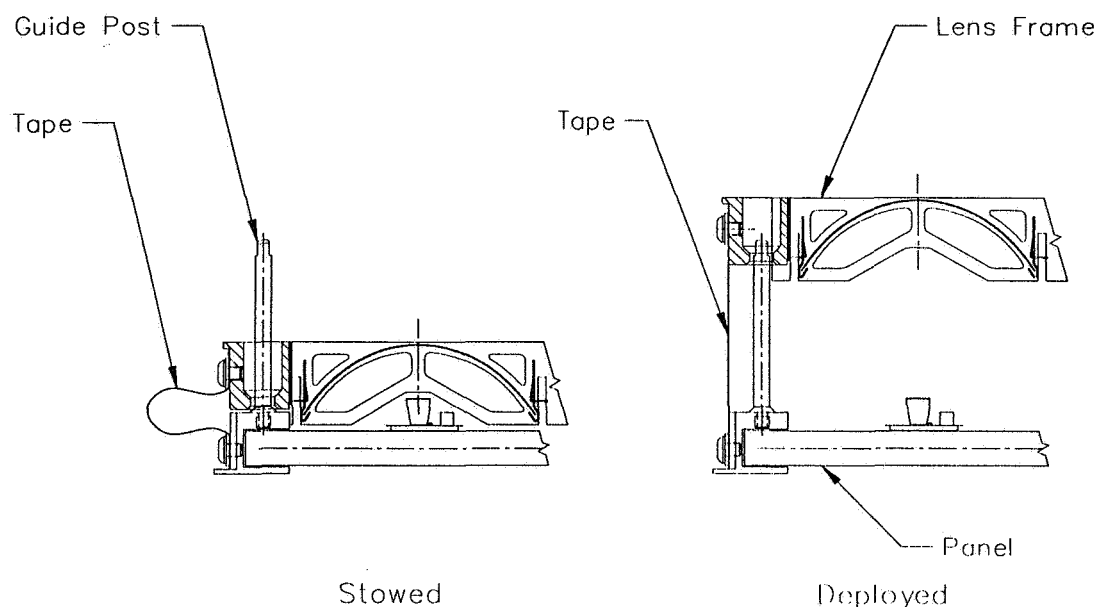


Deployed View

**Figure 5. Lens Frame Components**

## Integration of the Optics with the Deployment System

To maintain low stowed volume, it was determined that the 2.5-inch focal length offset of the primary optics would need to be stowable by collapsing the lens panel down to the structural panel. A trade study was used to determine the optimal method to extend the lens frame assemblies during deployment. Beryllium copper lenticular tapes were chosen because they yield high alignment accuracy, are frictionless, have low stored energy, are lightweight, and have flight history. Figure 6 shows the lenticular tapes deploying the lens frame.

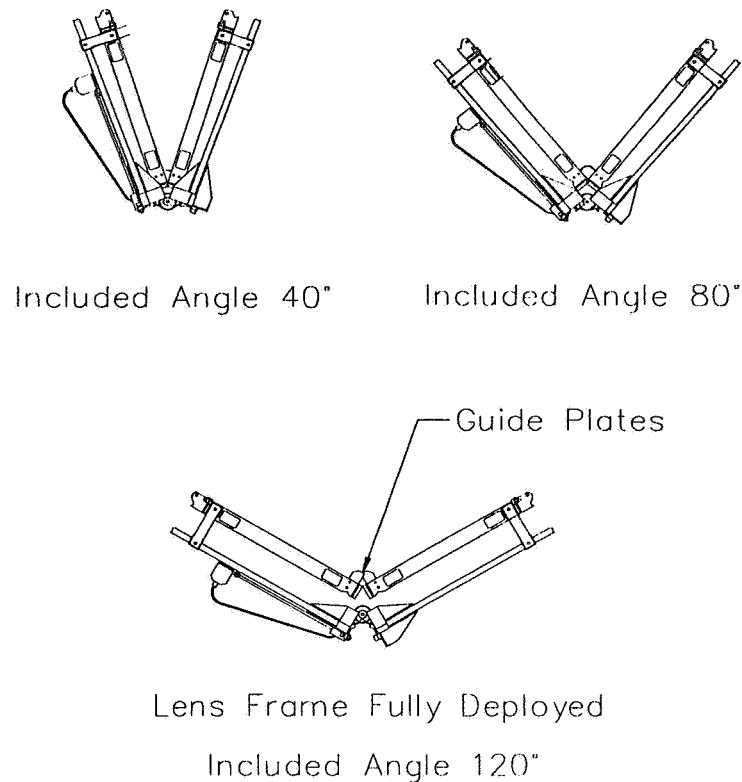


**Figure 6. Lens Frame Deployment System**

Proper synchronization of the pantographic array panels with their pop-out lens frames was a critical design concern. During preliminary functional testing, interference was noted between neighboring lens frames at a point halfway through the deployment sequence. Mounting small aluminum guide plate pairs to the two interfering lens frames proved to be a simple solution to the interference problem. Figure 7 shows how the guide plates interact with the lens frames during deployment.

## Launch Restraint System

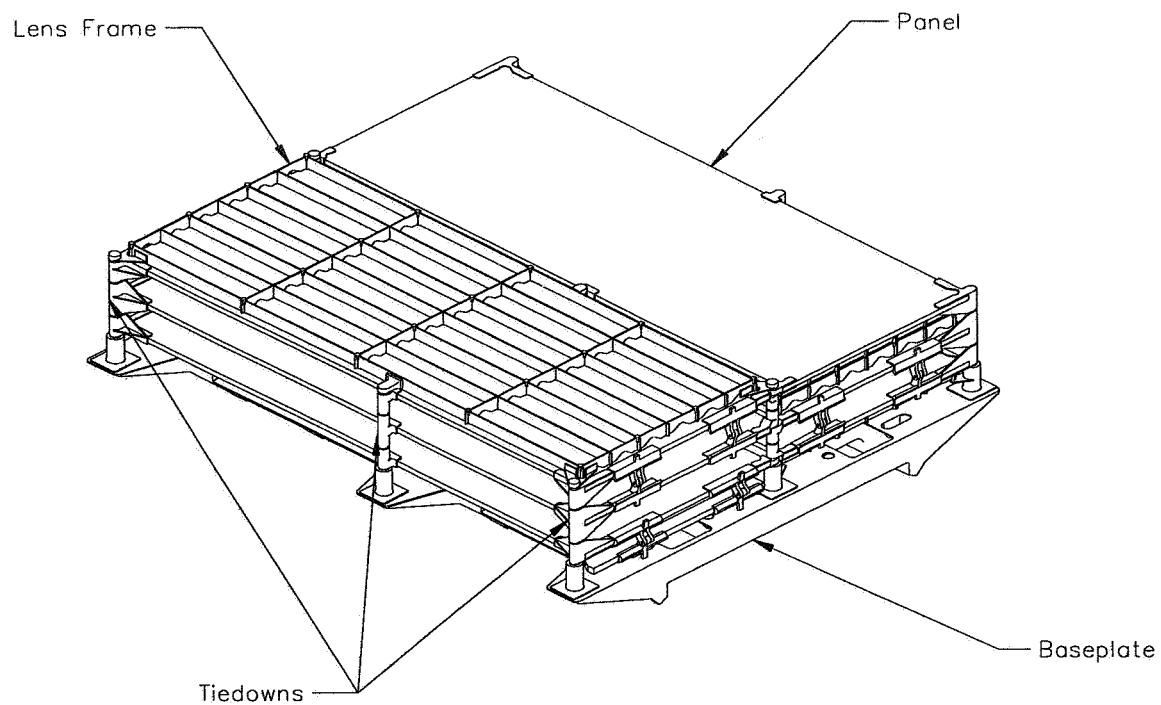
Nine cup-cone stackup assemblies are used on the stowed array to transfer launch loads that develop in the panels down to the baseplate via launch cables. The deployable lens panels are sandwiched between their stowed structural panels, which are themselves restrained by the cup-cones. Due to the bilateral geometry of the PUMA, one outboard lens panel and one inboard lens panel are left unrestrained. The inboard lens frame is sandwiched between the structural panel that it is mounted



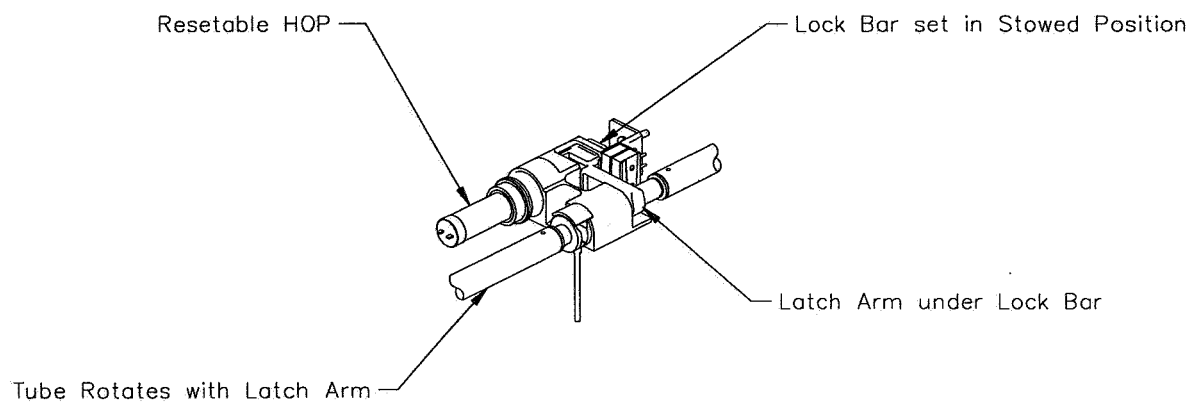
**Figure 7. Frame Guide Plate Interaction**

to small brackets on the tiedown anchor posts. The outboard lens frame is held in place by cup-cones, contacting the cup-cones of the neighboring panel. Details of the sandwich stack are shown in Figure 8. To compress and preload the stackup, the stainless steel cables of the launch hold-down system are tensioned.

The launch-hold down system consists of three tiedown mechanism assemblies (Figure 9) that each use three cables to secure, in a total of nine places, the panel stack to the baseplate, which is mounted to the spacecraft. The three assemblies are passively staged to release in sequence when given a single command for initiation. In each of the identical assemblies, a highly reliable and resettable high-output paraffin linear motor pushes a notched bar that releases a detent, which then allows a torsion shaft to rotate, thus releasing the three cables from capture fittings. This mechanism has proved to be highly reliable and has been qualified on previous array programs.

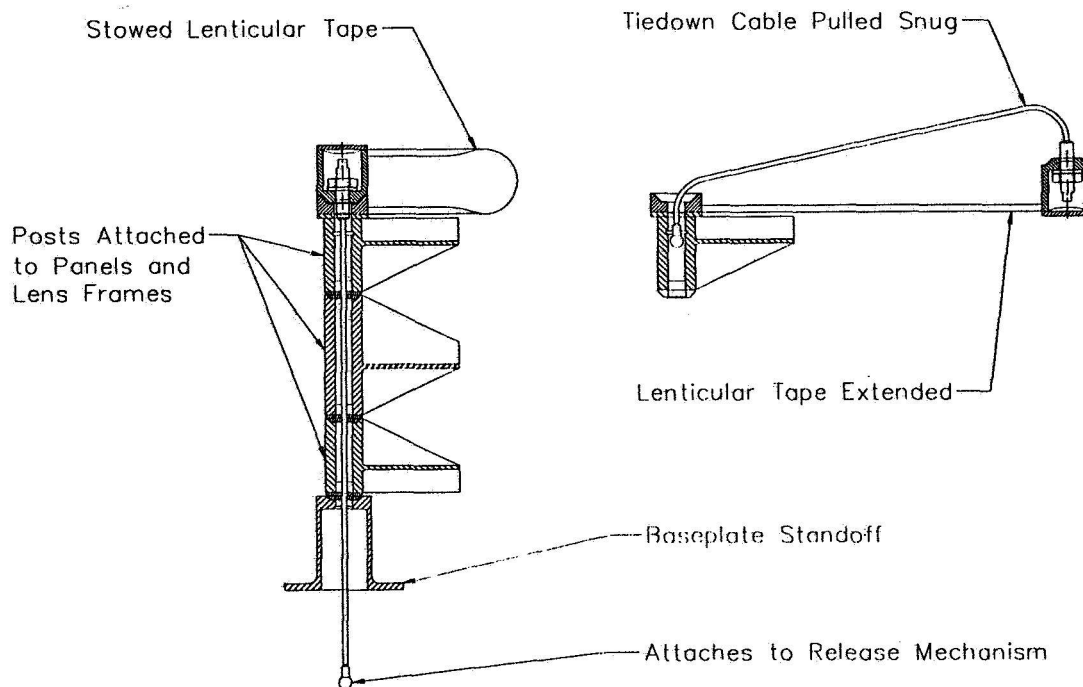


**Figure 8. Panel and Lens Frame Stackup to Baseplate**



**Figure 9. Launch Tiedown Mechanism**

To prevent tiedown cables from impacting or shadowing solar cells after deployment, a take-up mechanism is used. This mechanism consists of a lenticular tape folded in half, with one end attached to the top end of the tiedown cable and the other to the panel. As the cable releases from its tiedown mechanism, the lenticular tape pulls the cable out of the panel stackup to a known position that does not interfere with the solar cells. This mechanism provides the added benefit of extracting the tiedown cable completely during panel kinematics, thereby eliminating any possible cable hang-up during deployment. Figure 10 shows the stowed and deployed view of the take-up mechanism.



**Figure 10. Tiedown Cable Take-up Mechanism**

## Conclusion

The SCARLET I concentrator array demonstrator program was sponsored by Ballistic Missile and Defense Organization and NASA Lewis Research Center with the ambitious goal of building a flight-ready array in six months (starting from concept) to meet a launch opportunity. SCARLET I was successful in meeting this goal. The array completed a full series of qualification tests and was installed on the NASA METEOR spacecraft.

Many design details were tested successfully for the first time on the flight hardware. Lens adjustment, pop-out panel synchronization, and tiedown integration were successfully mechanized.

Due to the schedule constraints, utilization of a proven and familiar array structure, PUMA, was necessary. In the next phase of the SCARLET program, studies will be undertaken to determine the optimal array structure approach and component design configuration for high specific power at low cost. The SCARLET II array is planned to fly on the New Millennium Deep Space I spacecraft in January, 1998.

## **References**

1. P. Alan Jones, David M. Murphy, and Michael F. Piszczor, "A Linear Refractive Photovoltaic Concentrator Solar Array Flight Experiment", IECEC paper 95-351.

## **Acknowledgments**

ABLE wishes to thank ENTECH, Spectrolab, Composite Optics, and Pilkington for their efforts in successfully delivering atypical hardware assemblies in much less than typical industry time.

ABLE appreciates the funding and support provided by BMDO's Director of Innovative Technologies and the Photovoltaic Sciences branch of NASA Lewis Research Center.

# A Revolute Joint with Linear Load-Displacement Response for a Deployable Lidar Telescope

Mark S. Lake\*, Peter A. Warren\*\*, and Lee D. Peterson\*\*

511-18  
50439  
125125

## Abstract

NASA Langley Research Center is developing concepts for an advanced spacecraft, called LidarTechSat, to demonstrate key structures and mechanisms technologies necessary to deploy a segmented telescope reflector. Achieving micron-accuracy deployment requires significant advancements in deployment mechanism design, such as the revolute joint presented herein. The joint exhibits load-cycling response that is essentially linear with less than 2% hysteresis, and the joint rotates with less than 7 mN-m (1 in-oz) of resistance. A prototype reflector metering truss incorporating the joint exhibits only a few microns of kinematic error under repeated deployment and impulse loading. No other mechanically deployable structure found in the literature has been demonstrated to be this kinematically accurate.

## Introduction

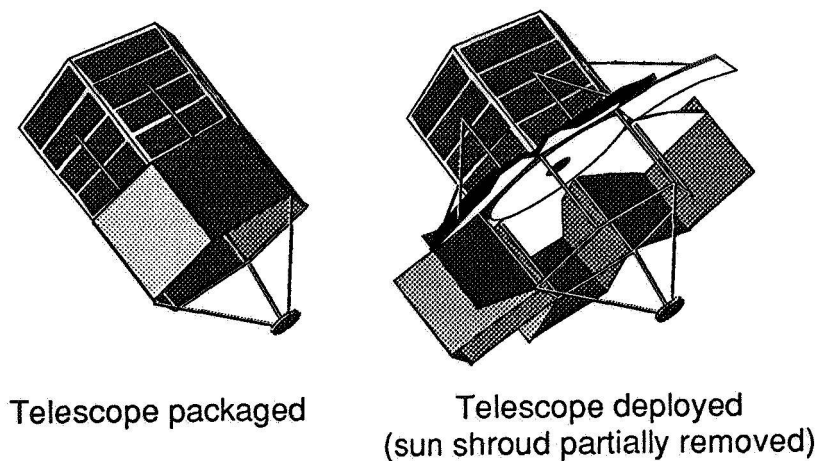
A continuing challenge for spacecraft designers and technology developers is to reduce significantly the cost of spacecraft and science instruments while increasing their performance. Recently, NASA's Office of Space Access and Technology initiated the development of a series of advanced sensor spacecraft, or "sensorcraft," which will be substantially cheaper than previous-generation science spacecraft because of aggressive use of advanced sensor and spacecraft technology. One of these sensorcraft is Lidar Technology Satellite (LidarTechSat), an Earth-observing sensorcraft for demonstrating advanced technologies in structures, mechanisms, materials, and electronics, while measuring upper atmospheric clouds and aerosols. Various concepts, one of which is shown in Figure 1, for LidarTechSat are being developed at the NASA Langley Research Center.

Lidar (light detection and ranging) is an active, remote-sensing technique first demonstrated in space on NASA Langley's Lidar In-space Technology Experiment, flown aboard the Space Shuttle in 1994 [1]. A typical lidar instrument includes a laser, which transmits laser light pulses into the atmosphere, and a telescope, which receives the reflected light from atmospheric constituents. Most lidar-science measurements are based on a comparison of the intensities of transmitted and reflected light. Thus, unlike an imaging telescope which must focus light coherently, a lidar telescope must only produce an incoherent focus. Hence, a lidar telescope can be less dimensionally accurate than an imaging telescope, thereby demanding micron-precision rather than sub-micron-precision.

---

\* NASA Langley Research Center, Hampton, VA

\*\* University of Colorado, Boulder, CO



**Figure 1. LidarTechSat Sensorcraft Concept.**

One of the key structures and mechanisms technologies being considered for LidarTechSat is micron-precision deployment of a segmented primary reflector for the lidar telescope. The mission-science benefit of precision deployment is that, for a given launch shroud diameter, an increase in telescope aperture through deployment increases the gain (i.e., sensitivity) of the instrument. Hence, deployment allows a given instrument aperture to be packaged within a smaller and less expensive launch vehicle, thus reducing mission cost for the same science return. Cost reduction through precision deployment is a desirable technology-development objective for application to many future science missions in addition to LidarTechSat.

The LidarTechSat primary reflector will consist of multiple reflector segments that must be precisely positioned using a deployable metering truss. Nonlinearities in present state-of-the-practice deployment mechanisms limit the accuracy of deployable metering trusses to approximately 100 microns [2]. Although this accuracy provides adequate reflector-panel-positioning control for low-frequency ( $\leq 20$  GHz) communication antennas, it is unacceptable for high-frequency ( $\geq 100$  GHz) science instruments. The LidarTechSat laser operates at a visible-light frequency of 564 THz, which requires a few microns of accuracy in the telescope primary reflector. Improving metering-truss-deployment accuracy by two orders of magnitude requires significant advancements to be made in the design of precision deployment mechanisms and the understanding of sub-micron structural mechanics of these mechanisms.

The revolute (i.e., hinged) joint described herein has been developed at NASA Langley Research Center for the LidarTechSat deployable telescope metering truss, but it has significant potential for application in many precision deployable structures<sup>1</sup>. The objectives of this paper are to (1) discuss the nonlinear structural response of conventional revolute joint designs and explain how these nonlinearities affect deployment accuracy; (2) describe the features designed to eliminate nonlinearities in

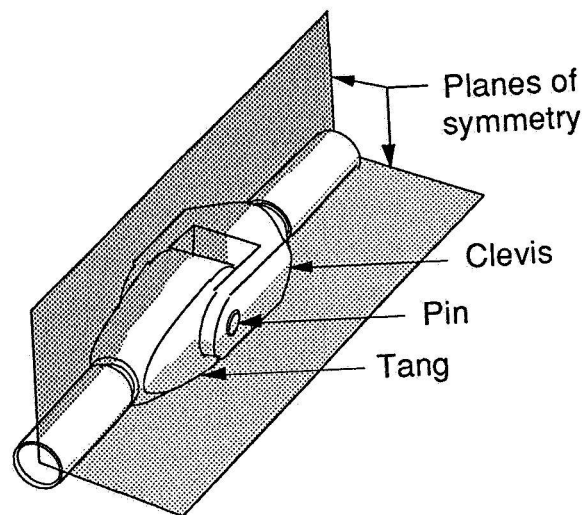
<sup>1</sup> Invention Disclosure Case No. LAR 15300-1 has been filed with the NASA Langley Patent Counsel.



the LidarTechSat metering truss revolute joint; and (3) present test results for individual joints, as well as a prototype-metering truss incorporating multiple joints.

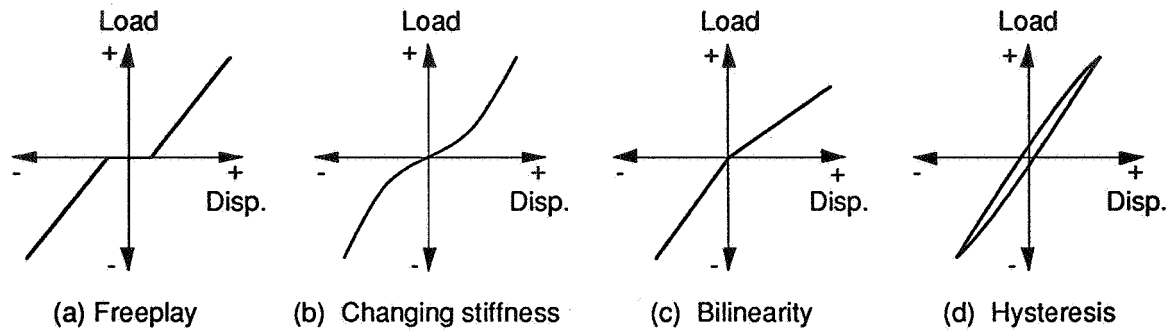
## Background

**Structural Response of Conventional Revolute Joints.** Revolute joints are necessary in all deployable structures to allow the folding and unfolding of components. Conventional revolute joints involve a tang which rotates around a clearance-fit pin and clevis assembly. As shown in Figure 2, the pin-clevis assembly surrounds the tang, resulting in a geometry that is symmetric about two perpendicular planes passing through the center of the joint: one plane is perpendicular to the pin axis, and the other plane contains the pin axis. This symmetry ensures that the joint will not bend as axial tension and compression loads are applied and places the pin in a state of double shear, thereby increasing the joint stiffness and strength.



**Figure 2. Conventional Pin-Clevis Revolute Joint.**

Under tension-compression load cycling, conventional pin-clevis joints exhibit four types of nonlinear load-displacement response (Figure 3): (a) freeplay due to clearance fit between the pin and the tang; (b) changes in stiffness due to the nonlinear, clearance-fit boundary condition of the pin; (c) bi-linearity, or unequal tension and compression stiffnesses, associated with different tension and compression load paths through the clevis and tang; and (d) hysteresis due to friction between the joint components. Numerous studies [3-6] have shown it to be essentially impossible to predict nonlinear joint response analytically. Current mathematical models of nonlinear joint phenomena involve numerous empirical parameters whose values may change significantly with changing test conditions.

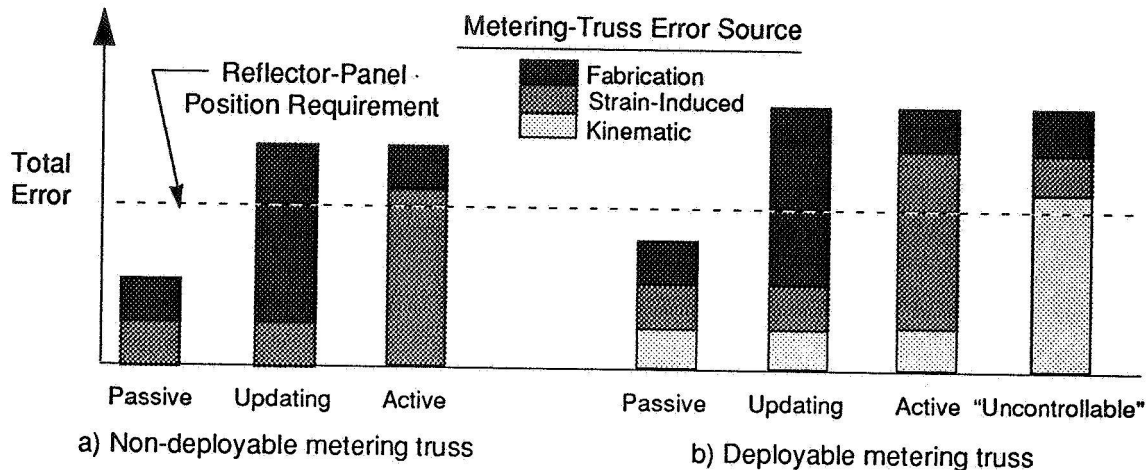


**Figure 3. Nonlinear Load-Displacement Response of Conventional Pin-Clevis Revolute Joints.**

Effect of Joint Nonlinearities on the Accuracy of a Deployable Reflector. In addition to introducing uncertainty in the response of a structure, nonlinearities in deployable joints can be a source of dimensional errors in the deployed structure. For example, a deployable structure with freeplay in its joints can be displaced within the freeplay deadband with minimal force. Hence, the geometric accuracy of a deployable structure is limited by the freeplay present in its joints. In a subsequent section, data are presented that indicate hysteresis within joints can also lead to dimensional errors in the deployed structure.

Dimensional errors in the deployed structure caused by joint freeplay and hysteresis are defined herein as “kinematic errors.” Kinematic errors represent a subset of all errors which define the structure’s “absolute accuracy,” (i.e., the deviation from the theoretical shape). Other error types are strain-induced (mechanical, thermal, and hygroscopic) and fabrication errors. If necessary, fabrication errors (and some quasi-static strain-induced errors) can be accommodated by using a variety of quasi-static or “updating” shape-adjustment techniques. In addition, dynamic strain-induced errors can be accommodated by using a variety of active shape-control techniques. However, kinematic errors are difficult to accommodate if they involve freeplay [7]. In fact, studies have shown that freeplay-induced kinematic errors can only be compensated for by using load-carrying active devices which “artificially” stiffen the joints where freeplay is present, thereby essentially eliminating the freeplay [8].

For any segmented reflector, the primary function of the metering truss is to maintain the positional accuracy of the reflector panels. Non-deployable metering trusses, such as the ground-based Keck telescope metering truss [9], exhibit no significant kinematic errors due to the absence of deployment mechanisms. Therefore, as depicted in Figure 4(a), non-deployable metering truss dimensional errors that exceed the reflector-panel positioning requirement can be accommodated by updating- or active-control systems. However, as depicted in Figure 4(b), dimensional errors in deployable metering trusses can only be offset if the reflector-panel position requirement is not exceeded by the freeplay-induced kinematic errors.



**Figure 4. Metering-Truss Error Sources and Their Effect on Reflector-Panel Position Control.**

Approach to Achieve Accurate Panel Positioning with Minimum Cost and Risk. Since the magnitude of freeplay represents a practical lower limit of the achievable panel-positioning accuracy in a deployable metering truss, it is imperative to develop deployable joint and mechanism designs which have little or no freeplay. Furthermore, to simplify the task of analytical modeling and to minimize the cost and complexity of correlating analysis and test results, it is highly desirable to minimize all sources of nonlinearity in the load-displacement response of joints and mechanisms. Finally, to minimize mechanism complexity and deployment risk, it is desirable to consider joint and mechanism concepts which can be preloaded locally rather than system concepts that are preloaded globally.

If it is assumed that freeplay-induced kinematic errors can be minimized through improved mechanism design, the accuracy of a deployable metering truss will be essentially determined by its fabrication and strain-induced errors. Therefore, as in the case for non-deployable metering trusses, achieving high accuracy at minimum cost requires a design trade between the costs of passive and active control of fabrication and strain-induced errors. To perform a meaningful trade, it is necessary to consider analysis and test verification costs in addition to hardware and software costs [10]. In general, the lowest cost and risk shape control system is passive. However, there is a precision limit below which passive shape control is not possible due to the lower bounds on fabrication tolerances and material thermal and hygroscopic stability. Although the quantitative relationship between cost or risk and absolute accuracy is different for each application, some general principles can be applied to achieve minimum cost and risk:

- Active shape control of any type is substantially less costly and risky if the structural response of the metering truss is predictable — kinematic error sources should be eliminated, and the structure should be linear.

- Panel-positioning accuracy is maximized, and cost and risk of adaptive adjustment is minimized if strain-induced errors are minimized. Thus, one should use high-stiffness, stable materials, along with efficient (high stiffness-to-mass ratio) structural architectures.
- Total cost may be reduced by relaxing fabrication tolerances and compensating for these effects with one-time shape adjustment after assembly.

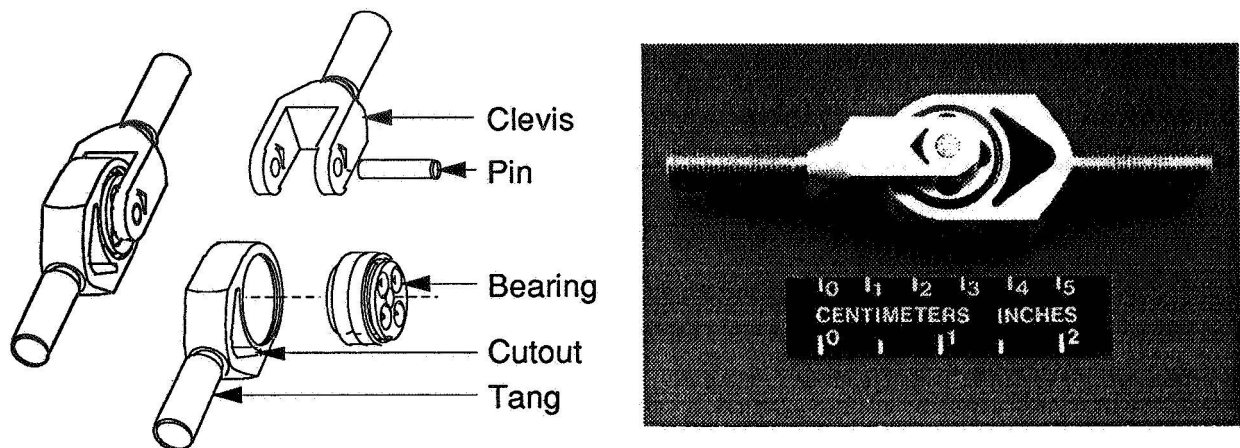
### **Design Features of the LidarTechSat Revolute Joint**

Conventional deployable structures either have significant joint freeplay and other nonlinearities, or they incorporate post-deployment preloading devices to minimize the nonlinearities. Inevitably, these devices add complexity, mass, and cost to the structure. Generally, these devices also increase deployment risk because they substantially increase deployment forces and complicate or prohibit re-stowage or re-configuration after initial deployment. In addition, post-deployment preloading induces global mechanical strains and deformations that are difficult to predict, especially if the structure is indeterminate.

The revolute joint developed at the NASA Langley Research Center for application to the LidarTechSat telescope is designed to exhibit minimal nonlinear behavior and high kinematic precision through local preloading of the joint components rather than global preloading of the assembled structure.

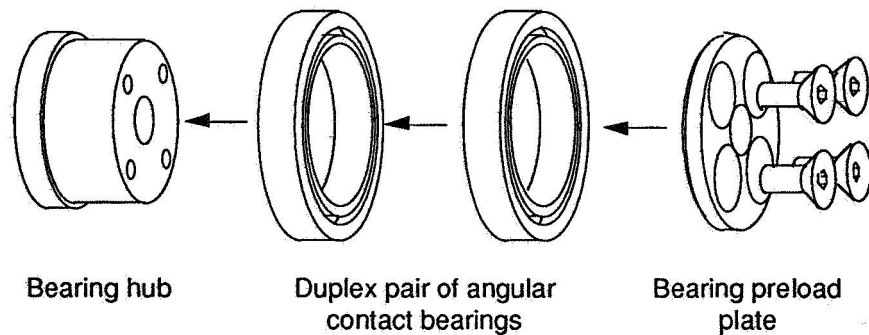
Components of the LidarTechSat Revolute Joint. The design concept, illustrated in Figure 5, represents a substantial departure from conventional pin-clevis joints, since the rotational element is a set of preloaded angular-contact bearings instead of the traditional pin. With only four fairly simple machined parts (the clevis, the tang, and two bearing-assembly pieces), the LidarTechSat revolute joint is also relatively inexpensive and easy to manufacture.

The bearing assembly, shown in Figure 6, consists of a hub and preload plate which retain and preload a commercially manufactured pair of precision angular-contact bearings. The hub is machined with an outer diameter that makes a slip-fit with the inner race of the angular-contact bearing. A raised lip is machined on the outer surface of the hub to retain the inner race of one bearing and react the preloading force applied by the preload plate, through the other bearing. The preload plate is attached to the hub using four small machine screws. As these screws are tightened,



**Figure 5. LidarTechSat Revolute Joint.**

the outer lip of the preload plate makes contact with the inner race of one angular-contact bearing. The clamping force generated by the four machine screws is applied solely to the inner races of the angular-contact bearings, thus preloading the bearings according to bearing manufacturer specifications. Prior to preloading the bearings onto the hub, a thin-film liquid adhesive is applied between the inner bearing races and the hub to ensure intimate contact and to eliminate any potential for freeplay. Once completed, the bearing assembly is bonded into the cylindrical cavity of the tang with the same thin-film liquid adhesive.



**Figure 6. Bearing Assembly.**

The tang incorporates a threaded shaft for attachment to other structural components. A cutout is provided in the body of the tang to divide the joint axial load into two paths. The load path is divided in this manner to ensure that the tension stiffness and the compression stiffness of the tang are equal. Details of the cutout design are provided in a subsequent section.

The clevis is a traditional split fork which surrounds and attaches to the bearing assembly and incorporates a threaded shaft for attachment to other structural components. The hole through the clevis arms is sized for a press-fit with the pin, and final assembly of the joint is achieved by simultaneously pressing the pin through

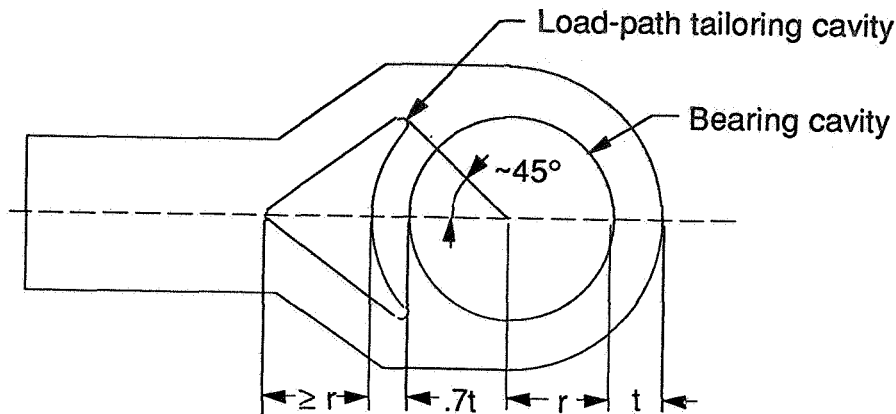
these clevis arms and the central hole of the bearing carrier. The clevis arms also incorporate cutouts that have been designed to separate the axial load through the joint and to ensure equal stiffnesses in tension and compression.

Preloaded Bearings. The source of most nonlinearities in conventional pin-clevis revolute joints is the pin and pin-clevis interface [3]. As mentioned previously, traditional pin-clevis joints require freeplay between the pin and clevis (i.e., the pin diameter is less than the clevis-hole diameter) to allow free rotation of the joint. Unfortunately, this freeplay introduces both the response deadband and the changing stiffness (Figure 3) associated with nonlinear pin-hole Hertzian contact stress. To minimize these nonlinear effects, the preloaded pair of angular-contact bearings were selected for use in the LidarTechSat revolute joint in place of a simple pin.

Angular-contact bearings are often referred to as “duplex” bearings because they are manufactured in matched pairs and installed back-to-back, so that a known preload is developed between the races and the balls as the inner races of the bearings are clamped together. Because of this preloading process, all clearance (freeplay) is eliminated between the balls and the races. However, the Hertzian contact stress between the balls and the races introduces the possibility of nonlinearity in the load-displacement response of the bearing [11]. To minimize this effect, the bearing set incorporated in the LidarTechSat revolute joint has a relatively large diameter (approximately 1.9 cm or 0.75 in), which maximizes both the size of the balls and the number of balls which carry load. Preloaded angular-contact bearings are commonly used in high-precision articulating mechanisms [12]; however, no examples of angular-contact bearing use in the design of mechanical deployable structures have been found in the literature.

Elastic Tailoring of the Tang and Clevis. In a conventional pin-clevis revolute joint, bi-linearity is caused by differences between the tension and compression load paths as a results of pin-clevis and pin-tang interfaces. In general, these joints have a more direct load path in compression than in tension and, as a result, exhibit a higher compressive stiffness than tensile stiffness.

The cutout shown in Figure 7 divides the load paths through the tang to ensure equal tension and compression stiffnesses (similar features apply to the clevis arms). The cutouts effectively reduce the compression stiffness of the joint by forcing the compression load path to divide, rather than pass in a straight line to, the bearing. To eliminate bi-linearity, the cutouts are sized such that the compression stiffness of the tang equals the tension stiffness of the tang *assuming that the bearing-tang interface carries no radial tension*. This assumption virtually ensures equal tension and compression stiffnesses, independent of the radial stiffness of the bearing-tang interface adhesive.



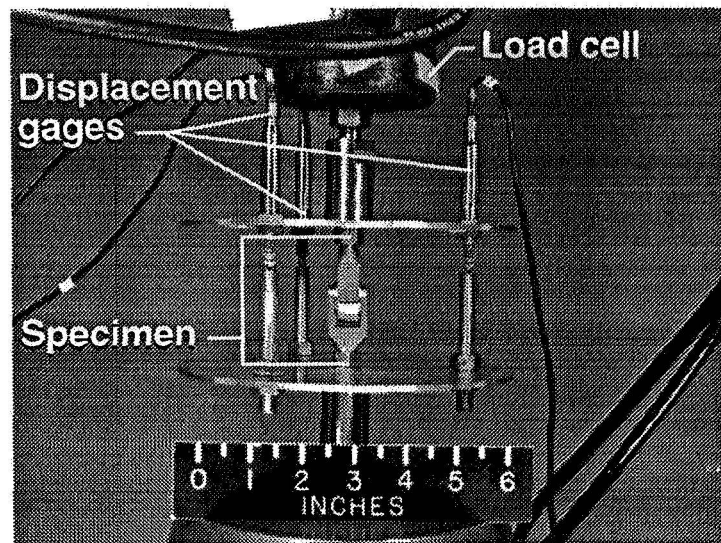
**Figure 7. Tang Cutout for Equal Tension and Compression Stiffness.**

A preliminary parametric study was conducted using a two-dimensional finite element model of a generic tang in which tension and compression loads were applied to the free end of the tang and reacted by radial *compressive* pressure on the inner boundary of the annulus. These finite element analysis results demonstrated that nearly equal tension and compression stiffnesses would result if the cutout was sized and shaped as shown in Figure 7. As indicated in Figure 7, the cutout should extend approximately 45° in each direction from the centerline of the joint, and it should be at least as deep along the axis of the joint as the inner radius of the annulus. Also, the annulus within the cutout should be thinned to approximately 70% of its nominal thickness outside of the cutout. While other cutout shapes may be tailored to eliminate bi-linearity, this cutout shape was selected because it is relatively compact.

## **Preliminary Tests and Results**

**Component-Level Joint Tests.** A few prototype joints, such as the one shown in Figure 6, were fabricated for quasi-static axial load-cycle testing. The setup used in these tests is shown in Figure 8. The joint specimen was threaded into adapter fittings and installed in a 222-kN- (50,000-lb) capacity hydraulic tension/compression test machine. A high-sensitivity 2200-N- (500-lb) capacity load cell was installed between the joint and the test-machine crosshead to measure the total axial load applied to the specimen. Centerline axial displacement within the specimen was determined by averaging displacement measurements from three high-sensitivity Linear Voltage Displacement Transducers positioned equidistantly around the specimen. Tests were performed such that the load was quasi-statically cycled between 222 N (50 lb) of tension and compression loads and between 444 N (100 lb) of tension and compression loads. Similar tests were conducted on joints incorporating two different bearing-preload values.



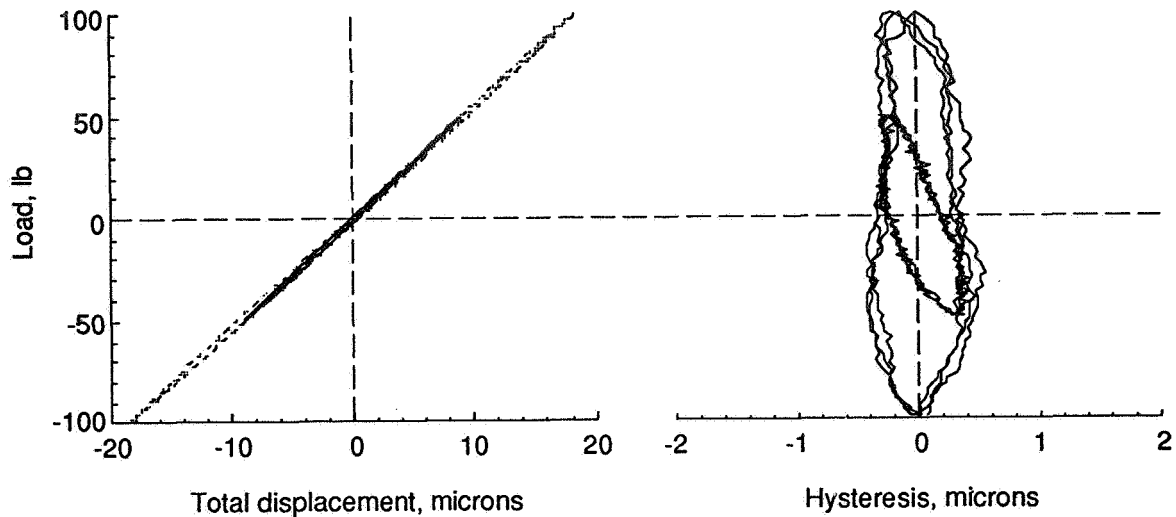


**Figure 8. Axial Load-Cycle Test Setup.**

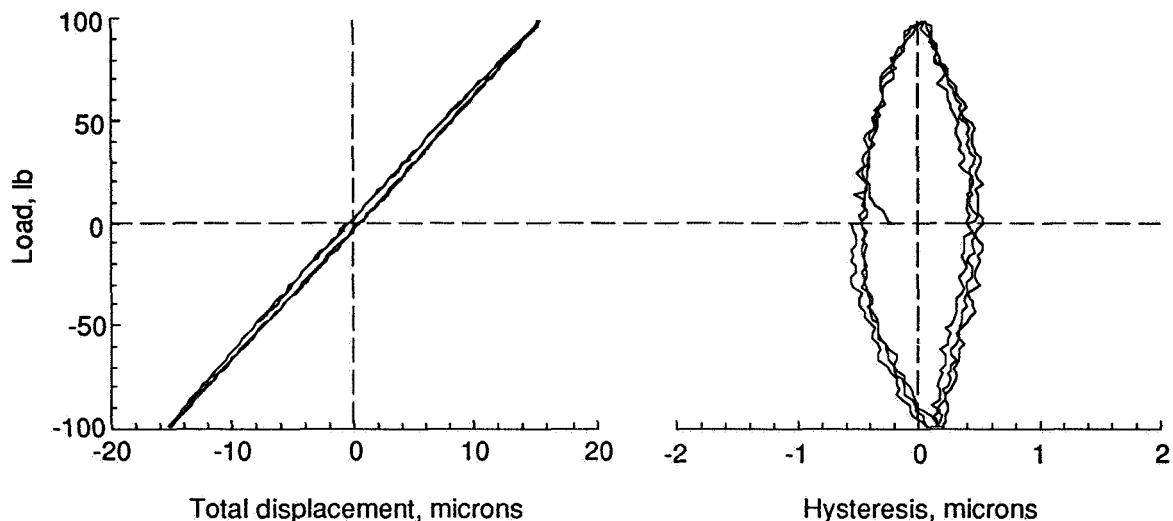
Representative load and total displacement responses for three load cycles are plotted in Figures 9 and 10 for joints with bearing preloads of 44 to 66 N (10 to 15 lb) and 111 to 142 N (25 to 32 lb), respectively (the range in the preload is a bearing manufacturer specification). Also shown in these figures are the load-displacement response after a best-fit straight line has been subtracted from the measured total displacement. The remaining displacement is the joint hysteresis. The displacement gages used are only sensitive to about 0.1 micron, hence the noise seen in the hysteresis plots of Figures 9 and 10 is likely due to instrumentation rather than to joint response.

The results in Figure 9, for the test joint with a 44- to 66-N (10- to 15-lb) preload bearing, include load cycles of  $\pm 222$  N and  $\pm 444$  N ( $\pm 50$  lb and  $\pm 100$  lb). For each load range, the joint was cycled three times, and the results from all load cycles are presented to demonstrate the load-displacement repeatability. The load-displacement response is essentially linear with less than 2% hysteresis. The hysteresis loop is approximately one micron wide for the  $\pm 444$ -N ( $\pm 100$ -lb) load cycle and somewhat narrower for the  $\pm 222$ -N ( $\pm 50$ -lb) load cycle. The shape of these hysteresis loops and their scaling with load-cycle magnitude are consistent with the occurrence of localized Coulombic micro-slippage between the balls and races as a result of the tangential load carried by the ball-race interface under load cycling [13]. Similar load-cycle tests conducted with a prismatic aluminum rod yielded approximately an order of magnitude less material-induced hysteresis. These results reinforce the assumption that the hysteresis in the load-displacement response of the joint is due to friction between the balls and races within the bearings.





**Figure 9. Load-Displacement Response and Hysteresis Loops for a Joint With 44- to 66-N (10 to 15 lb) Preload Bearings.**



**Figure 10. Load-Displacement Response and Hysteresis Loop for a Joint With 111 to 142 N (25 to 32 lb) Preload Bearings.**

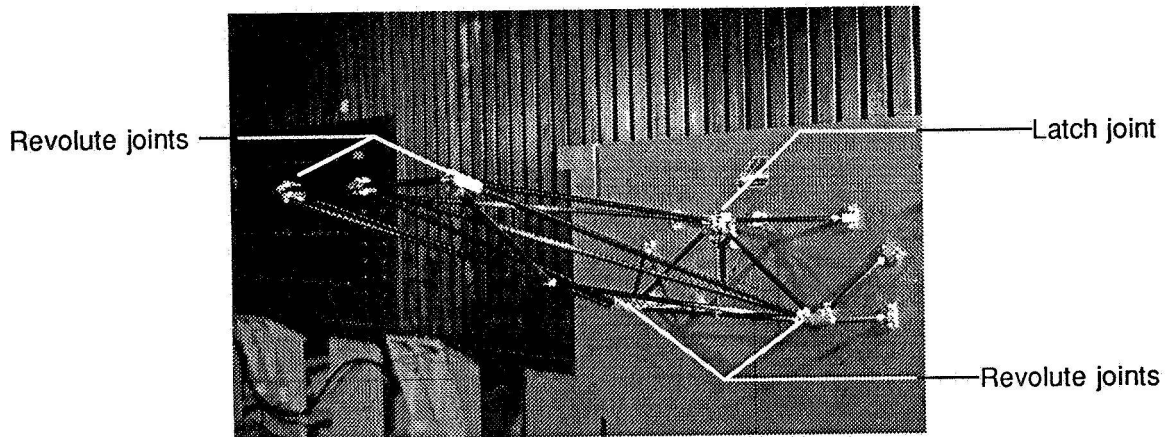
The results for the test joint with a 111- to 142-N (25- to 32-lb) preload bearing (Figure 10) also include three load cycles. Comparing the data presented in Figures 9 and 10 shows that both the stiffness and the amount of hysteresis in the joint increase slightly with increasing bearing preload. This result is consistent with the nonlinear Hertzian contact condition that exists between the balls and the races: as the normal force increases at this interface, the stiffness and tangential frictional forces increase as well.

It was noted previously that the bearing-clevis and bearing-tang interfaces within the joint have the potential to carry tensile load due to the use of a thin-film adhesive and

that this interface effect could cause the joints to exhibit a significant difference in tensile and compressive stiffnesses. However, the linearity of the results suggests that the cutouts in the tang and clevis arms are effective in eliminating bi-linearity in the linear revolute joints without regard to the tensile stiffness at the bearing-tang interface.

The angular-contact bearing incorporated in the test joints requires only about 0.5 in-oz of applied torque to overcome the operating friction, thus minimal force would be required to deploy a structure using these joints [14].

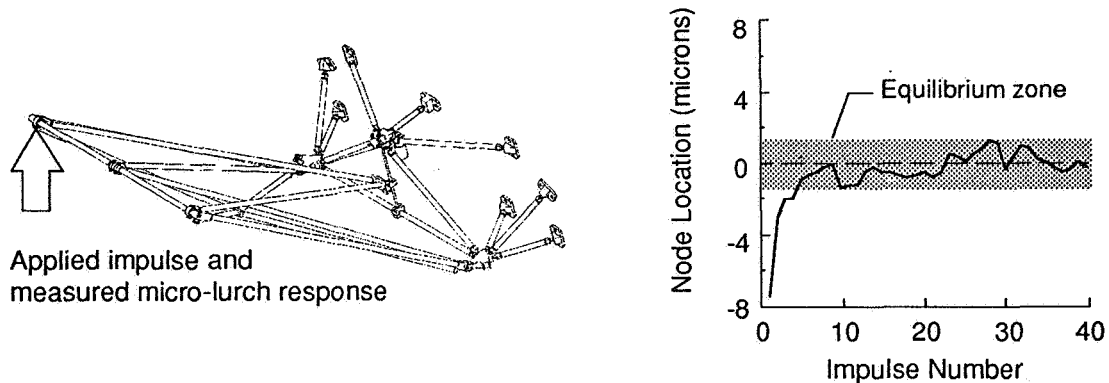
**Telescope Reflector Metering Truss Tests.** To evaluate the LidarTechSat revolute joint in a structural assembly, a portion of a deployable metering truss for a segmented reflector (like the LidarTechSat telescope primary mirror) was fabricated. A photograph of the deployable metering truss test article is shown in Figure 11. This test article represents the portion of the metering truss that supports one reflector panel (one of the six perimeter panels shown in Figure 1). The metering truss test article incorporates four of the revolute joints shown in Figure 6: two of these joints are at the base of the truss, and two are at the tip to allow the truss to fold vertically into a narrow package. The test article also incorporates a latch joint that locks the truss in position at the end of deployment. To date, no component-level testing has been performed on the end-of-deployment latch joint.



**Figure 11. Precision Reflector Metering Truss Fabricated With LidarTechSat Revolute Joints.**

A significant amount of testing has been performed to characterize the structural response and kinematic accuracy of the deployable metering truss test article. In these tests, the positions of key points on the structure were tracked under dynamic loading using an innovative new videographic metrology system with approximately 10-nm resolution [15]. Results from these tests indicate that the structural response of the test article is linear within a few microns under both static and dynamic loading, and the test article exhibits only a few microns of kinematic error after successive deployments and impulse loading.

From these tests, a new nonlinear response phenomenon, called “micro-lurching,” has been discovered. This response is a change in the equilibrium position of points on the structure following a transient disturbance. In each series of tests, the structure was deployed and then impulsed by a light tap on one of the outboard nodes, as shown in the sketch in Figure 12. The vertical location of the node was determined before impulsing and after the impulse-response decayed out. A typical set of results from these tests (Figure 12) shows the changes in node location (i.e., micro-lurches) that occur after successive impulses are applied to the test article. The first five impulses after deployment cause a total of about seven microns of micro-lurching in one direction, and the remaining impulses cause random micro-lurches of no more than a few microns each.



**Figure 12. Typical Micro-Lurching Response of Metering Truss.**

Preliminary analyses using simple two-degree-of-freedom dynamic models suggest that micro-lurching is a typical nonlinear response in structures that transmit load through Coulombic friction that is schematically parallel to the elastic deformation. Since both the revolute joints and the end-of-deployment latch joint transmit load in this manner, it is believed that these mechanisms are responsible for micro-lurching. However, additional analyses and tests are necessary to fully characterize the relationship between micro-lurching and friction-induced hysteresis in the revolute joints or nonlinearities (as of yet uncharacterized) in the end-of-deployment latch joint. Furthermore, additional analyses and tests are necessary to determine if micro-lurching is affected by gravity-induced preloading in the structure. These investigations are very important because the stochastic nature of micro-lurching might ultimately prove it to be the response parameter that defines the kinematic accuracy of a precision mechanically deployable structure.

Currently, it is believed that the initial net micro-lurch response of seven microns results from the latch and/or revolute joints which release internal strain energy and seek a lower total energy state than that present at the end of deployment. The random micro-lurches after the fifth impulse define an “equilibrium zone” within which the test article tends to remain quasi-stable over time. The width of this equilibrium zone is about 3  $\mu$ , and is a measure of the kinematic accuracy of the metering truss test article. No other mechanically deployable structure found in the literature has been demonstrated to be this kinematically accurate. This accuracy is close to the absolute

precision requirement for the LidarTechSat telescope, thus making such a concept feasible at this preliminary stage of development. However, a practical design for the telescope might require active or updating shape control to compensate for fabrication and strain-induced errors.

## **Concluding Remarks**

To date, dimensional uncertainties associated with nonlinearities in deployment mechanisms have limited the accuracy of deployable reflectors to approximately 100 microns. Although this accuracy is acceptable for low-frequency ( $\leq 20$  GHz) communication antennas, it is unacceptable for high-frequency ( $\geq 100$  GHz) science instruments. Achieving substantial improvement in deployment accuracy requires significant advancements to be made in the load-cycle linearity of precision deployment mechanisms and the understanding of sub-micron-level load-cycle nonlinearities of these mechanisms.

The revolute joint described in the present paper was designed to minimize all forms of load-cycle nonlinearity, especially freeplay, which cannot be compensated for through active control. Component-level test results prove that the concept is sound; exhibits no freeplay, bi-linearity, or changing stiffness; and has only about 2% hysteresis in the load-cycle response. These results prove the joint to be substantially more linear, as presently designed, than any joint found in the literature to date.

A deployable reflector metering truss that incorporates four of these high-precision revolute joints was fabricated and tested. These tests identified a new nonlinear response phenomenon, called "micro-lurching," which is a micron-level change in the equilibrium shape of a structure following a transient dynamic disturbance. At present, it is believed that micro-lurching is caused by load transmission through contact friction within the revolute joints and/or the end-of-deployment latch joint. However, additional analyses and tests are necessary to fully characterize these relationships as well as the effect of gravity on micro-lurching. These investigations are very important because the stochastic nature of micro-lurching might ultimately prove it to be the response parameter that defines the kinematic accuracy of a precision mechanically deployable structure. Although friction-induced hysteresis and micro-lurching in deployable structures are probably unavoidable due to the complex load paths within the mechanical joints, it may be possible to reduce these undesirable effects to an acceptable level by minimizing load transfer through friction.

The present results indicate that it is both possible and practical to design a deployable reflector metering truss that has a kinematic accuracy of a few microns for the LidarTechSat telescope. No other mechanically deployable structure found in the literature has been demonstrated to be this kinematically accurate. This accuracy is close to the absolute precision requirement for the LidarTechSat telescope, thus making such a deployable concept feasible at this preliminary stage of development. However, a practical design for the telescope might require active or updating shape control to compensate for fabrication and strain-induced errors.

## References

1. Winker, D. M., Couch, R. H., and McCormick, M. P., "An Overview of LITE: NASA's Lidar In-space Technology Experiment," Proceedings of the IEEE, February 1996.
2. Miller, Richard K., Thomson, Mark W., and Hedgepeth, John M., "Concepts and Analysis for Precision Segmented Reflector and Feed Support Structures." NASA CR 182064, December 1990.
3. Rhodes, Marvin D., "Design Considerations for Joints in Deployable Space Truss Structures," presented at the First NASA/DOD CSI Technology Conference, Norfolk, Virginia, November 18-21, 1986.
4. Belvin, W. Keith, "Modeling of Joints for the Dynamic Analysis of Truss Structures," Master's Thesis submitted to The School of Engineering and Applied Science of the George Washington University, December 1985.
5. Chapman, J. M., Shaw, F. H., and Russell, W. C., "Dynamics of Trusses Having Nonlinear Joints," presented at the Workshop on Structural Dynamics and Control Interaction of Flexible Structures, NASA Marshall Space Flight Center, Huntsville, Alabama, April 22-24, 1986.
6. Ikegami, R., Church, S. M., Keinholtz, D. A., and Fowler, B. L., "Experimental Characterization of Deployable Trusses and Joints," presented at the Workshop on Structural Dynamics and Control Interaction of Flexible Structures, NASA Marshall Space Flight Center, Huntsville, Alabama, April 22-24, 1986.
7. Salama, M., Umland, J., Bruno, R., and Garba, J., "Shape Adjustment of Precision Truss Structures: Analytical and Experimental Validation," Smart Materials and Structures, Vol. 2, 1993, pp. 240-248.
8. Tzou, H. S., "Non-Linear Joint Dynamics and Controls of Jointed Flexible Structures with Active and Viscoelastic Joint Actuators," Journal of Sound and Vibration, Vol. 143, 1990, pp. 407-422.
9. Peacock, Keith, and Long, Knox S., "Astronomical Telescopes: A New Generation," Johns Hopkins APL Technical Digest, Vol. 10, No. 1, 1989.
10. Wada, Ben K., Fanson, James L., and Chen, G.-S., "Using Adaptive Structures to Enable Future Missions by Relaxing Ground Test Requirements," Journal of Spacecraft and Rockets, Vol. 28, No. 6, November-December 1991, pp. 663-669.
11. Mindlin, R. D., "Compliance of Elastic Bodies in Contact," Journal of Applied Mechanics, Vol. 16, September 1949, pp. 259-268.
12. Brotini, M., Barbis, A., Carli, B., Fabbriizzi, F., and Spicci, V., "High Precision Double Four Bar Linkage Mechanism for Interferometric Linear Scanning," Proceedings of the Fifth European Space Mechanisms and Tribology Symposium, 1993, pp. 179-184.
13. Mindlin, R. D., Mason, W. P., Osmer, T. F., and Deresiewicz, H., "Effects of an Oscillating Tangential Force on the Contact Surfaces of Elastic Spheres," Proceedings of the National Congress of Applied Mechanics, 1951, pp. 203-208.
14. Hachkowski, M. Roman, "Friction Modeling of a Revolute Joint for a Precision Deployable Spacecraft Structure," Master's Thesis submitted to the Graduate School of the University of Colorado, August 1995.
15. Hinkle, J. D., "A Micron-Precision Metrology System for Measuring Structural Geometric Repeatability," Master's Thesis submitted to the Graduate School of the University of Colorado, August 1995.



**Antenna Pointing Mechanism for ESA ENVISAT Polar Platform**

50440

J. Serrano\*, J. San Millán\* and R. Santiago\*

125126 ✓

**Abstract**

INTA is currently developing a two-degree-of-freedom antenna pointing mechanism (APM) as part of the ESA ENVISAT POLAR PLATFORM (PPF) program. This mechanism will drive a Ka-band antenna within the Data-Relay Satellite System (DRS) on board the Polar Platform satellite. The first mission using PPF is ENVISAT, which is expected to be flown in 1998.

This paper describes the main requirements, design, and test results of this pointing system, as well as the main technical problems from customer requirements and how those have been faced to achieve a final design.

**Introduction**

The performance of the PPF Ka-band antenna requires a fine pointing device to allow linking with the DRS Ka band and ground.

The APM for PPF (APM-PPF) (Figures 1 and 2) is a two-motorgear azimuth (AZ) and elevation (EL) gimbal system, which drives the 1-m antenna with a large pointing range. The mechanism is joined to a deployable boom, and the antenna is supported by a four-bar linkage to the platform during launch (Figure 3).

The (a) absence of an off-loading device, (b) the presence of external wave guides and rotary joints, (c) the large size of the antenna and its large motion range, and (d) the large antenna-boom distance produced high loads on the mechanism and drove some aspects of the mechanism to be designed according to strength/stress criteria for a proper structure.

A first EQM (Engineering-Qualification Model) has been already delivered to the customer after qualification tests. The unit passed all tests successfully.

**Design Requirements**

Main design requirements are given below. For each field, they are listed by the degree of difficulty found by designers in meeting them (1 means top difficulty). Also listed are any complications produced in meeting another requirement.

---

\* INTA, Spanish National Center for Aerospace Research, Madrid, Spain

### Operating and performance

1. Geometrical constraints (Figure 3):
  - presence of wave guides and rotary joints
  - large size of antenna and large motion range, which create an increased interference envelope
  - antenna COG eccentricity with respect to the top of the boom
2. Large antenna pointing ranges:  $\pm 165^\circ$  (AZ),  $-30^\circ/+90^\circ$  (EL)
3. Long life: 10 years (88000 pointing cycles of  $330^\circ$ )
4. Mass limitation: 12.4 kg
5. Motorgear interchangeability
6. Overall pointing target:  $0.070^\circ$
7. High number of cables (26 main + 26 redundant = 52) to be moved along the complete AZ rotation range
8. Pointing precision of  $0.010^\circ$  per motorgear
9. Antenna mass: 13 kg
10. Maximum speed:  $4.2^\circ/\text{s}$
11. Maximum acceleration:  $1.0^\circ/\text{s}^2$
12. Others

### Environmental requirements

Key requirements are given below with the same criteria:

1. Stiffness for deployed configuration: 7 Hz
2. Random vibration levels of  $\text{PSD}_{\text{max}} = 0.125 \text{ g}^2/\text{Hz}$  on 20- to 2000-Hz range (global RMS = 11.4 g)
3. Deployable loads: APM has to withstand loads due to on-orbit pyros
4. Shock: 60g in 0.5 ms
5. Motorgear operating temperatures:  $-40^\circ\text{C}/+100^\circ\text{C}$
6. Sinusoidal vibration levels: 15-g amplitude on 10- to 100-Hz frequency range
7. Stiffness for launching configuration: 100 Hz

### **Mechanism Design**

The mechanism consists of two motorgears (AZ and EL) joined by means of an L-shaped structure. The AZ actuator is joined to a deployable boom by means of a 1-m (3-ft) bracket, while the EL unit is joined to the antenna.

Figures 1 and 2 show the complete unit with no Multilayer insulation (MLI).

The motorgear concept is shown in Figure 4.



### Bearings

The design consists of the following bearings: one preloaded output ball bearing pair that supports the encoder, the output shaft, and loads; one preloaded pair; and a deep groove, single bearing that supports the stepper motor and the gear input shaft.

All ball bearings are commercial 440C stainless steel for space applications and have vacuum oil-preimpregnated phenolic cages.

### Encoder

One 16-bit absolute encoder, manufactured by CODECHAMP (France), is located on the output shaft. The encoder was customized to the housing.

### Gear

One harmonic drive gear (type HDUC-20-BLR ratio 100), made of stainless steel, is manufactured by Harmonic Drive System (Germany). These gears were used because of their optimal reduction/mass ratio and previous in-house experience with these harmonic gears.

During the development phase, accelerated life tests were performed to assess gear performance with lubricants, as well as application procedures and controls. These tests included the application of gold coatings on contacting surfaces, but this process was decided to be excluded.

Due to the long-life requirements, the harmonic drive was customized to produce oil reservoirs (phenolic cages).

A harmonic drive (size 20) was selected to meet the torsional stiffness requirement of 7-Hz at the deployed configuration, since the 13-kg antenna COG has a considerable offset (350 mm) with respect to the AZ and EL motorgear axes.

### Motor

The motor is a 23PP stepper motor from SAGEM (France). It provides a holding torque of 0.27 N-m. The stator and rotor are bonded to the outer case and shaft.

### Motorgear Casing

The motorgear casing is made of Ti6Al4V, which provides a compromise between mass and thermal compatibility with standard elements made of stainless steel. The external case contains provisions for thermal hardware. The attachments and stop devices (mechanical and electrical) are different for AZ and EL (different motion range), so the unit was designed to contain all necessary provisions to be used as either an AZ or an EL drive.

To reduce loads on bearings due to different temperatures on motor shaft and outer case during thermal analysis, a thin membrane was used on the motorgear bottom.

### Lubrication

Lubrication was one of the key requirements because of the long-life requirement (88000 330° pointing cycles). The first baseline considered the use of solid lubricant (MoS<sub>2</sub>) for bearings and gear.

A preliminary life test showed the inadequacy of sputtered MoS<sub>2</sub> for gears and long-life applications. The test unit failed after about 7000 cycles (requirement was 88000). The backup solution, based on oil, was then considered. The oil selected was the ESA-qualified Fomblin Z25 from Montedison (Italy).

The gear oil lubrication was performed during motorgear assembly by local oil application on the contacting surfaces of the harmonic drive gears. Due to the criticality of this operation, oil reservoirs were foreseen for teeth mesh oil feeding.

The lubrication process included antispread application to avoid oil migration.

### Thermal Hardware

The design considers heaters, thermal switches, and thermistors for thermal control. Heaters and thermistors are located on the motorgears external case, on the encoders, and the stepper motors.

### Redundancy

Motors windings, encoder electronics, thermal hardware, electrical switches, and the harness are redundant.

### Structures

The motorgears are joined by an L-shaped structure of 3-mm thickness. A support fitting (2-mm thickness) joins the AZ unit to the deployable boom. A bracket was designed to support one antenna rotary joint to the wave guides. All main structures are made of Ti6Al4V. Secondary structures are made of aluminum alloy 7075.

As previously explained, the structure design was faced with three main problems from the complex physical interfaces and reduced space available: (a) the large antenna-boom distance, (b) the large antenna COG offset wrt the AZ and EL axes, and (c) the presence of wave guides, rotary joints, and antenna envelope for the motion range.

These design constraints produced quite a large main structure (L-shaped) to be as light as possible, but stiff enough to comply with the stiffness requirements. On the other hand, the effect of transverse temperature gradients across the sections during operation led the design to include an MLI and to consider a 3-mm thickness to minimize the pointing perturbances. In spite of this, this remained as the main contribution to the APM pointing errors.

### Cable Drum

Due to (a) the high number of cables coming from the antenna and EL motorgear and (b) the large motion range of the AZ motorgear, a winding device was implemented to:

- minimize the resistant torque of twisting 52 cables with thermal protection.
- control the cable motion during launch and operation to avoid possible damage to MLI or other equipment.
- control temperature of the cables.

The cable drum is made of aluminum alloy (1.5-mm thickness) to reduce mass and contains two slots for main and redundant bundles to be wound in opposite directions. This made cable resistant torque compensation possible. To allow a controlled winding, a flat cable was considered. The resistant torque was reduced to an almost constant torque of 0.150 N-m along the complete rotation range. The mass increase from the drum and cables was 1.2 kg.

Figure 5 shows the cable output from the cable drum.

### Thermal Protection

The complete unit is coated with thermal protective coatings and an MLI on an L-shaped fitting to reduce extreme temperatures for hot and cold cases.

### Structural Analysis

As mentioned before, due to the mechanism/structure duality of this equipment, a detailed strength analysis task was carried out. Along with a large amount of hand calculations, the final structural analysis of the mechanism was carried out by the Finite Element Model (FEM) technique. Figure 6 shows the APM FEM. The software used was MSC/NASTRAN, and the main analysis can be summarized:

- modal analysis
- vibration levels analysis (random, sinusoidal and pyroshocks), including a complete study of loads on the L-shaped fitting, support fitting, and motorgear cases, including bolts. Also, torques on harmonic drives and acceleration levels seen by electronic components were subjected to analysis
- deployment phase study to determine effects of antenna inertias on EL axis
- thermoelastic analysis to obtain pointing errors.

## Testing

Test performed on EQM unit (qualification levels) are grouped below:

### Functional

Motorgears were successfully tested, including the following:

- Pointing and backlash: mean values obtained were about  $0.005^\circ$  per motorgear
- Overall performance: speed, acceleration, motion ranges, and limit devices activation

Functional tests performed before and after the tests discussed below showed identical performance.

### Environmental

EQM was satisfactorily subjected to the following tests:

- Sinusoidal vibration levels: 15-g amplitude on 10- to 100-Hz frequency range
- Random vibration levels with a maximum PSD =  $0.125 \text{ g}^2/\text{Hz}$  on 20- to 2000-Hz range and global RMS level of 11.4 g
- Shock: 60 g in 0.5 ms

Figure 7 shows the mechanism and fixtures for environmental testing.

Figure 8 compares predicted (FEM) and measured natural frequencies of the APM. The average difference is about 4%.

### Life Test

One unit, including all the mechanical hardware (encoder and motors were excluded), was submitted to the following accelerated life test to check the performance of liquid lubrication on bearings and gears:

- accelerated life test, consisting of externally backdriving the unit with the following motion parameters: 10x maximum speed ( $120^\circ/\text{s}$ ), 100x maximum acceleration ( $88.5^\circ/\text{s}^2$ ), 1.25x pointing cycle ( $330^\circ$ , 88,000 cycles). The gear was inspected after the test and showed no signs of wear. The starting torque and torsional stiffness were also checked before and after testing and showed identical performance. Figure 9 shows the test setup.

### Alignment/Pointing Tests

Optical tests were carried out using laser techniques to check the following:

- motorgear axes variation along complete rotation range. Maximum orientation errors detected were about  $0.008^\circ$  for the worst axis.
- orthogonality between AZ and EL motorgears ( $0.030^\circ$  constant along motion). This error can be accommodated by software during in-orbit performance.
- angles between AZ and EL axes wrt a fixed mirror cube on support fitting to establish the APM real pointing vector after mounting.

The test setup is shown in Figure 10.

### **Lessons learned**

(a) As already mentioned, the imposition of severe geometrical constraints made the design extremely complicated because of the interference with other requirements, such as stiffness, adequate harness routing, mass, etc.:

(1) From the analysis, two local modes, at about 20 Hz, were predicted during launch due to the harmonic drive torsional stiffness, combined with the rotor inertia; the L shape (due to the presence of wave guides) of the interface fitting between both motorgears excited the AZ gear, thus producing theoretically high torques (above the gear capacity) on gear mesh due to the inertia of the gear input shaft (that tried to rotate at high speeds due to the reduction ratio). Although this phenomenon was detected during a development vibration test, and not during the formal sinusoidal test due to the existing damping, it was still an important concern.

(2) The presence of this L-shaped, thin structure (3 mm) produced the highest pointing distortions due to the temperature gradients along the cross-sections, even with an MLI as thermal protection (estimated by analysis).

The use of external wave guides and other geometrical constraints must be evaluated carefully from the beginning of the project because of the important design impacts.

(b) Interchangeability of both motorgears reduced cost and effort, but it required external location of all limit devices (electrical and mechanical) for easy mounting, since motion ranges were different for AZ and EL motorgears. However, an additional mass was necessary to locate all external provisions.

(c) The cable drum solution showed good behavior, which minimized the resistant torque of the cables. Different options were considered, and some of them tested. Inconveniences are a slightly more expensive solution and the additional mass.

(d) The liquid lubricant concept worked well. Even though a complete thermal vacuum (TV) test is pending for qualification, results until now are sufficient to eliminate lubricant concerns.

(e) Dry lubrication on gears (sputtered MoS<sub>2</sub>) was shown to be inadequate for this application. Moreover, some key parameters, such as the layer thickness, are difficult to control.

(f) The absence of an off-loading device has produced high loads on bearings, thus leading to an increase in the size of the preloaded bearings and subsequently of motorgears, thus affecting the mass and operational performance (higher friction and noise). Although implementing an off-loading device would not have been an easy task, this option should have been considered in the first program stages.

(g) The presence of an external wave guide (delivered by the customer), made of aluminum alloy and joined to the main APM structure, has doubled the pointing error due to thermal distortions (estimated by analysis).

## **Conclusions**

The results of the APM-PPF for the EQM show that the equipment satisfies the contractual technical requirements. However, formal qualification tests, as well as a TV test and TV life test, are still pending and will include the same tests that have already been completed for EQM.

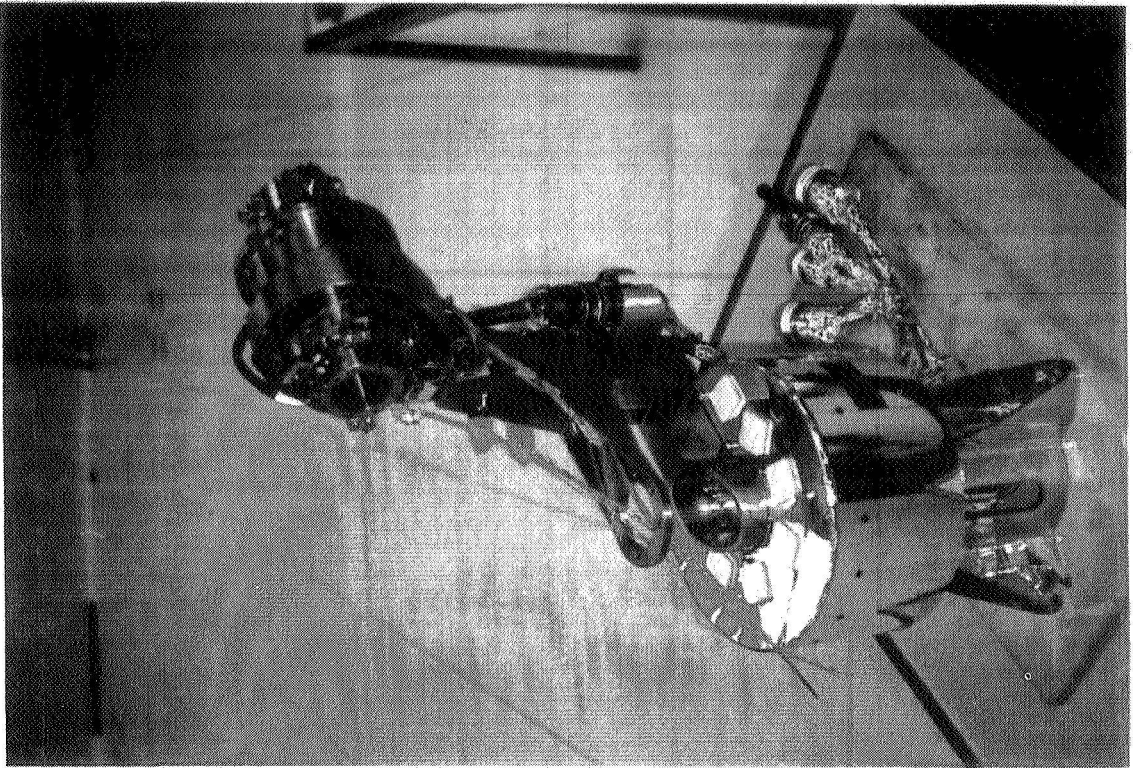
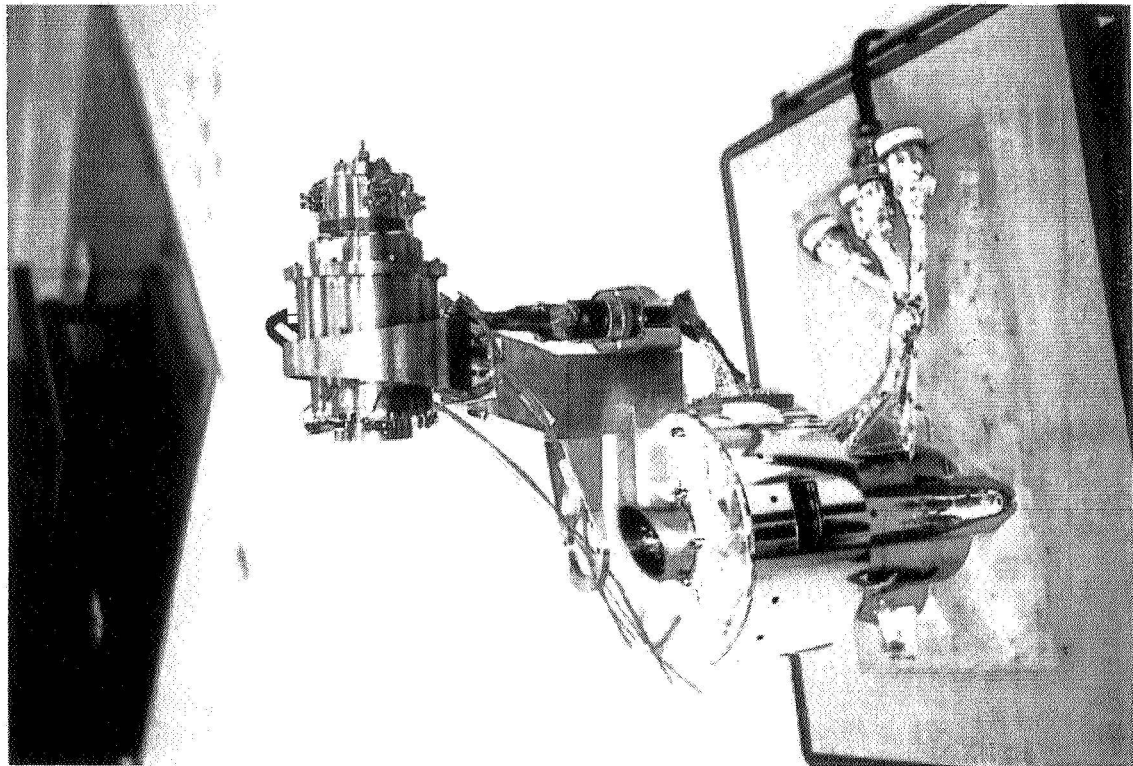


FIGURE 1: APM-PPF (EQM). Complete Assembly with no MLI

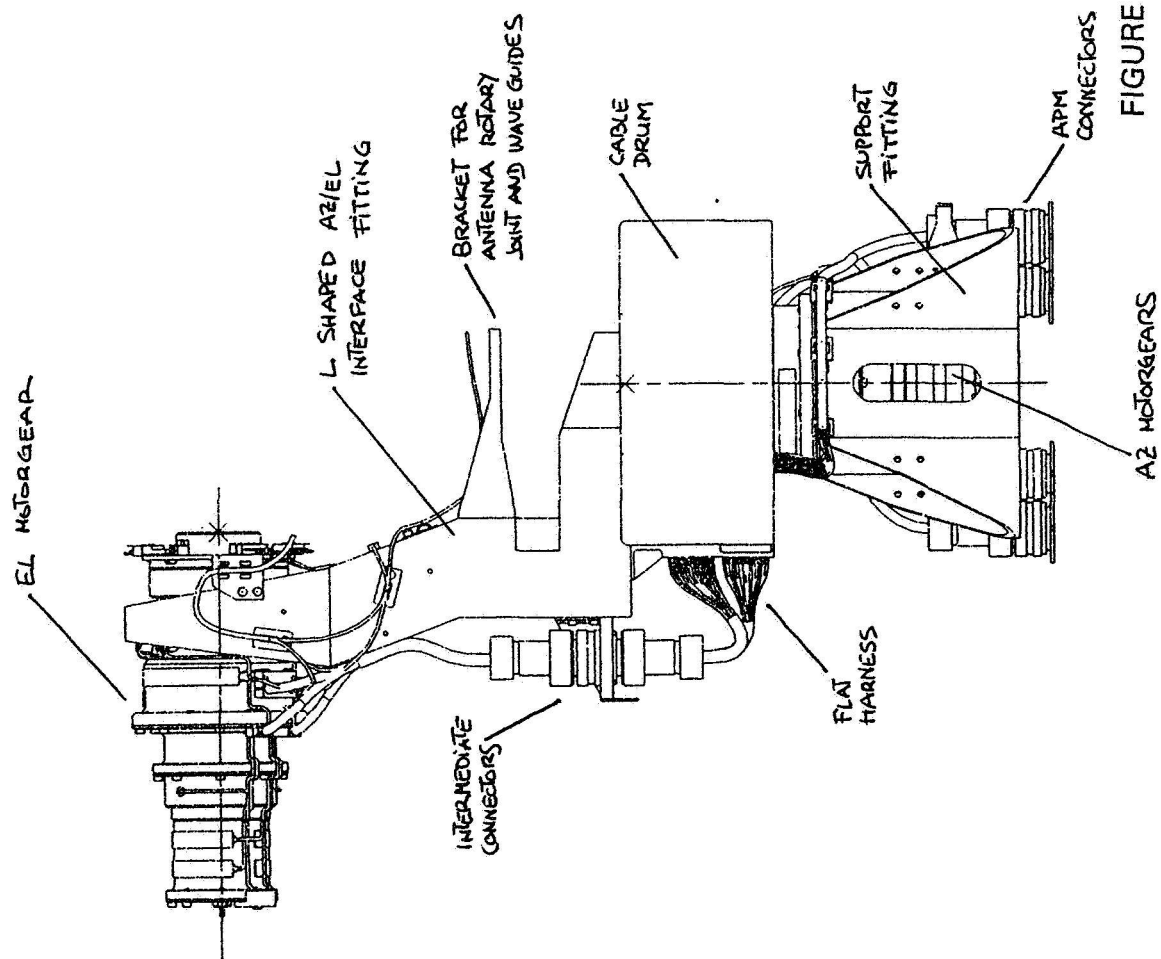
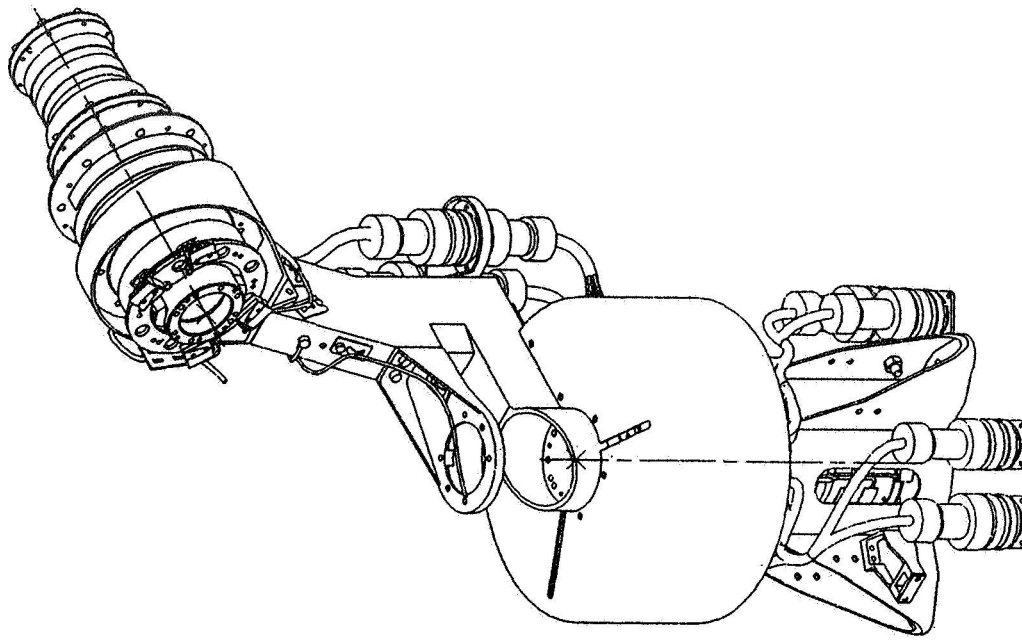


FIGURE 2: APM-PPF. Complete Assembly with no MLI

© ALTAEL ESPACIO SPAIN





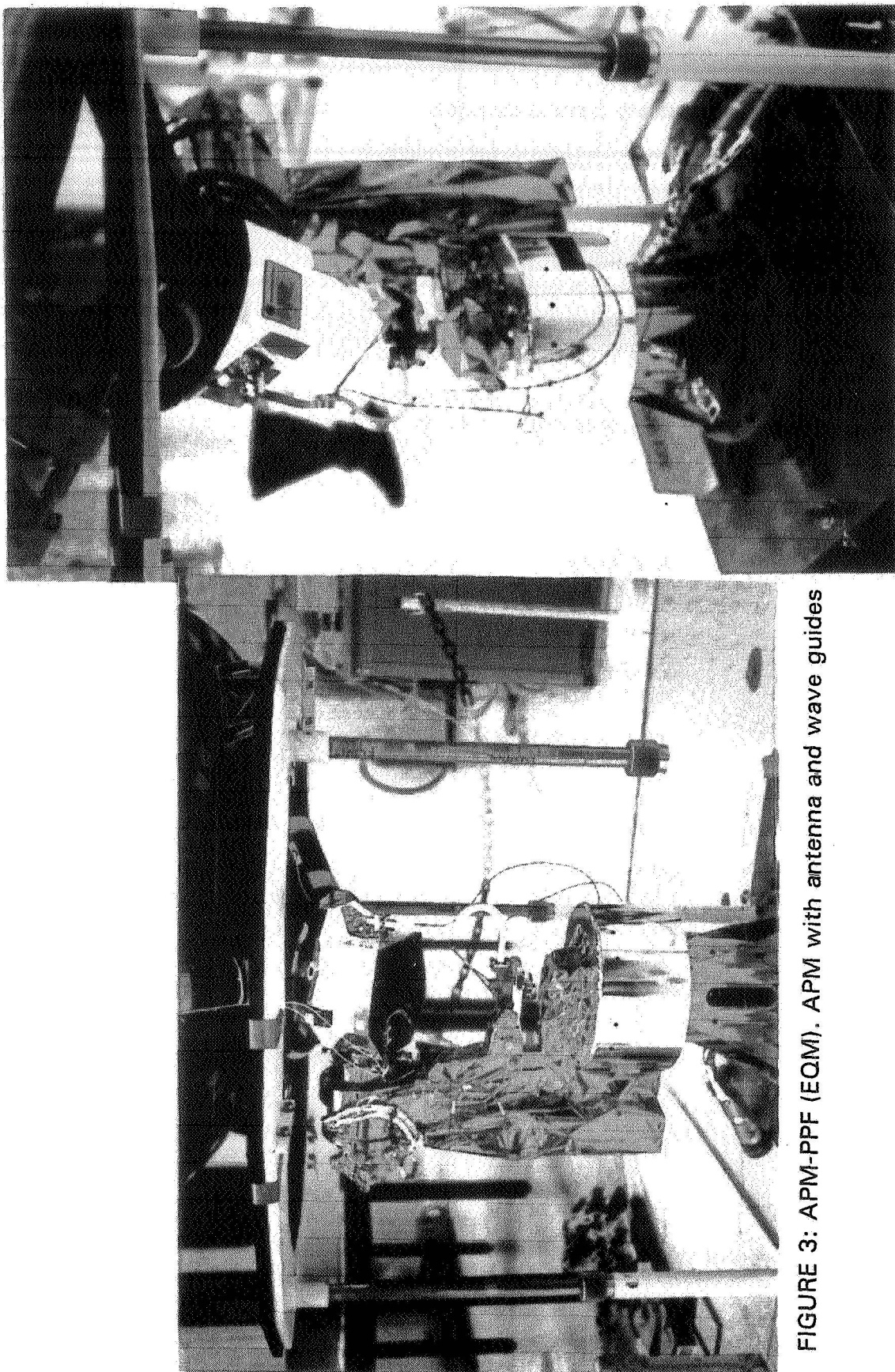


FIGURE 3: APM-PPF (EQM). APM with antenna and wave guides

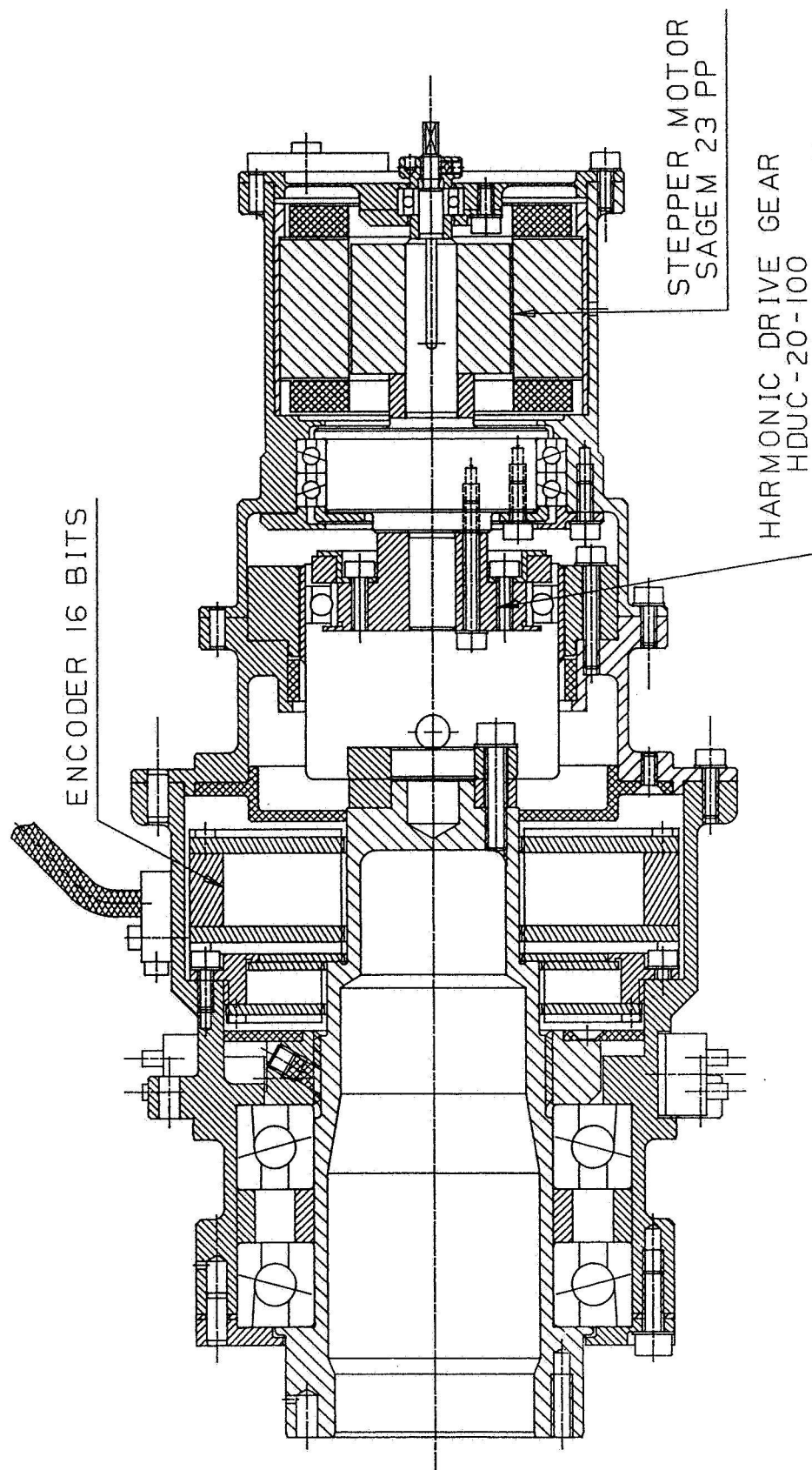


FIGURE 4: APM-PPF. Motorgear Concept

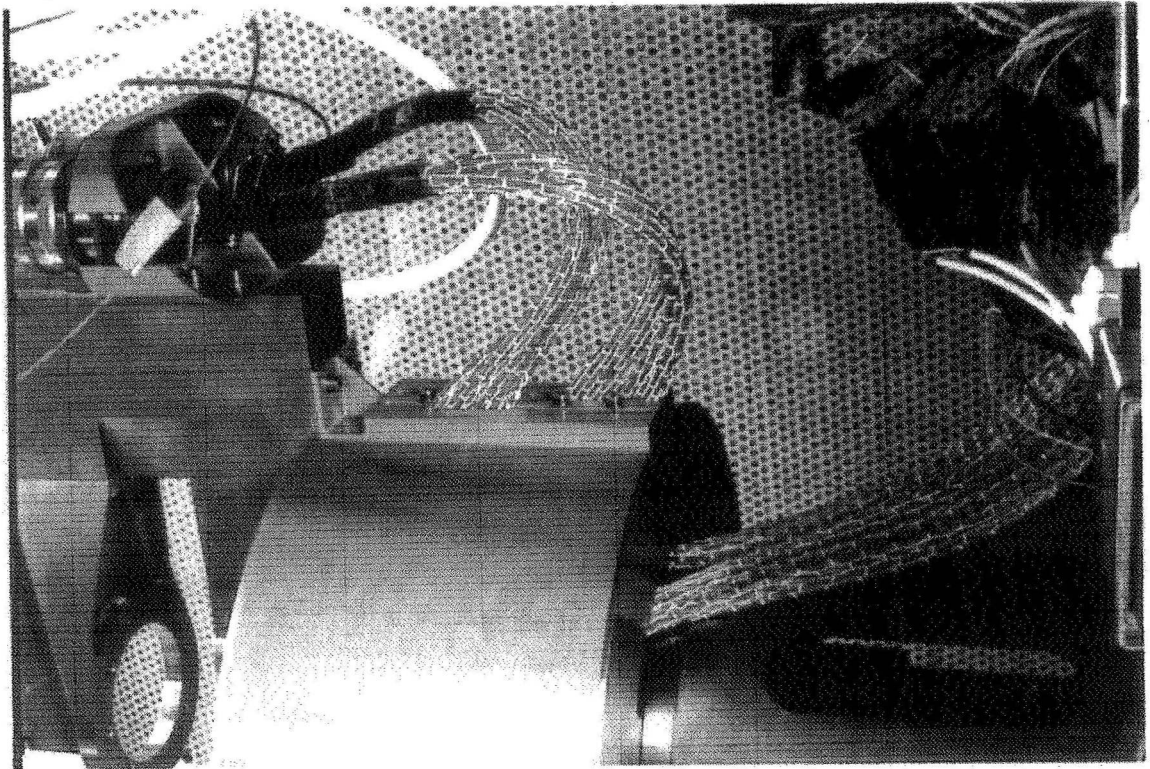


FIGURE 5: APM-PPF (EQM). Detail of Cable Drum

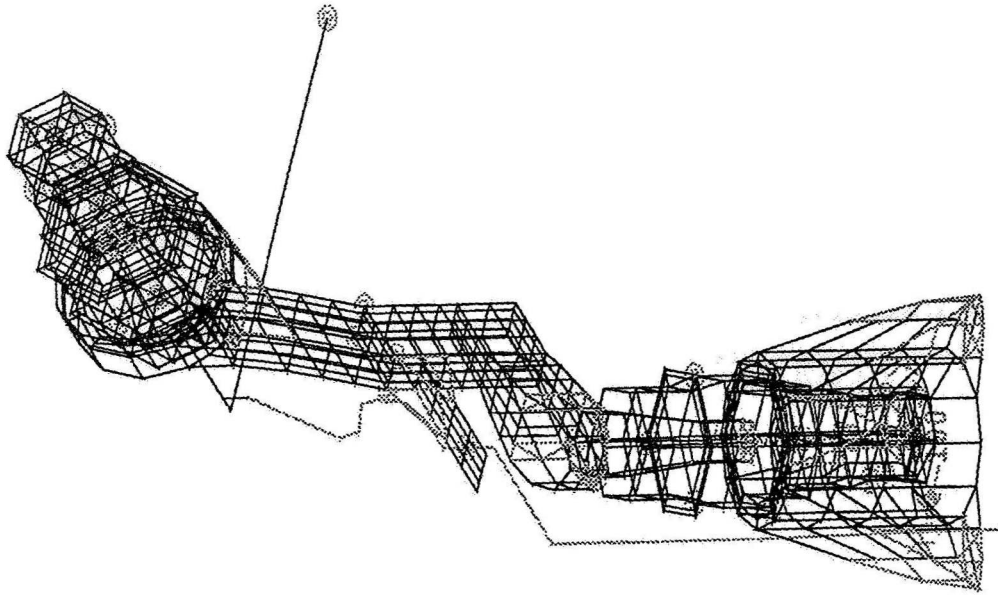


FIGURE 6: APM-PPF. Finite Element Model

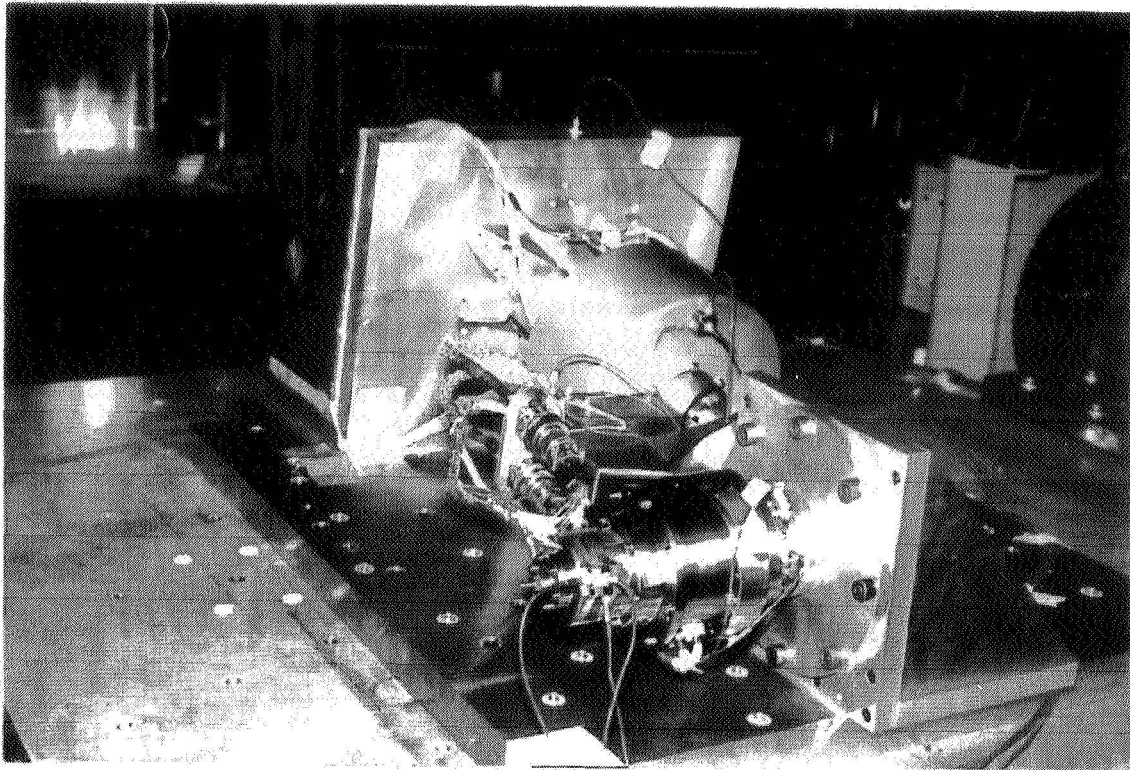


FIGURE 7: APM-PPF (EQM). Vibration Test

EQM TEST freq.	EQM FEM prediction	difference (%)
136 hz	143 hz	4.9
220 hz	205 hz	7.3
231 hz	230 hz	0.4
247 hz	246 hz	0.4
279 hz	274 hz	1.8
311 hz	329 hz	5.5
337 hz	367 hz	8.2

FIGURE 8: Frequencies Table



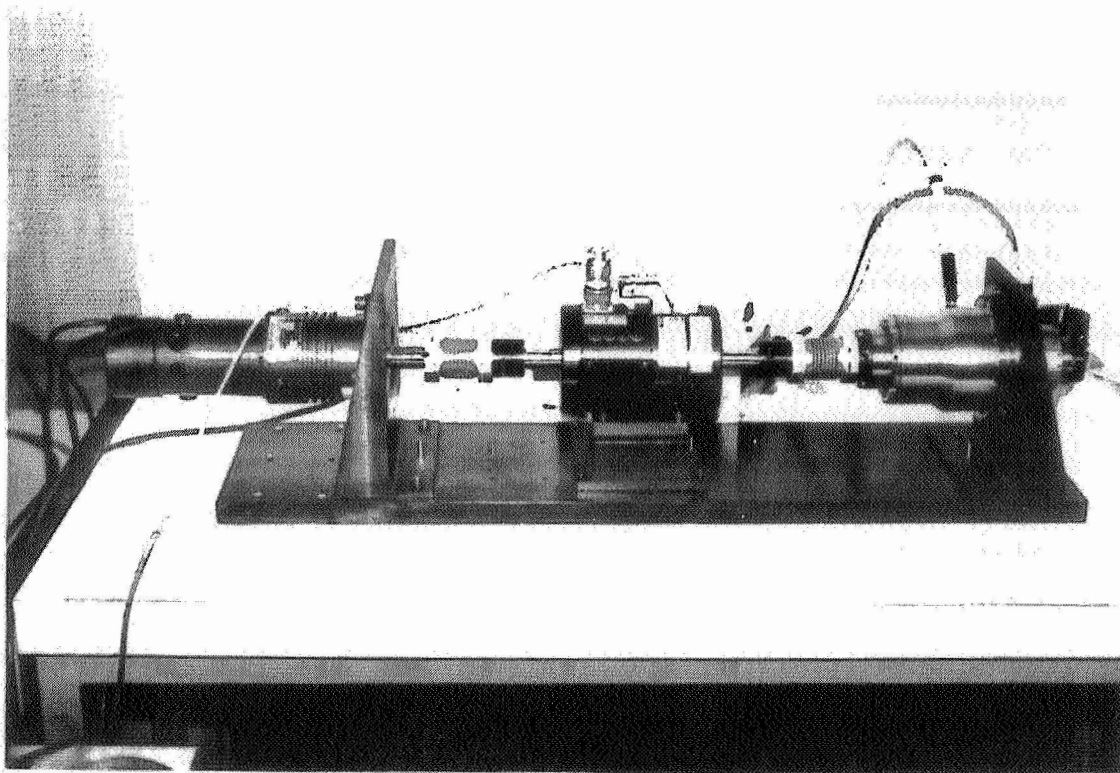


FIGURE 9: APM-PPF (EQM). Accelerated lifetest

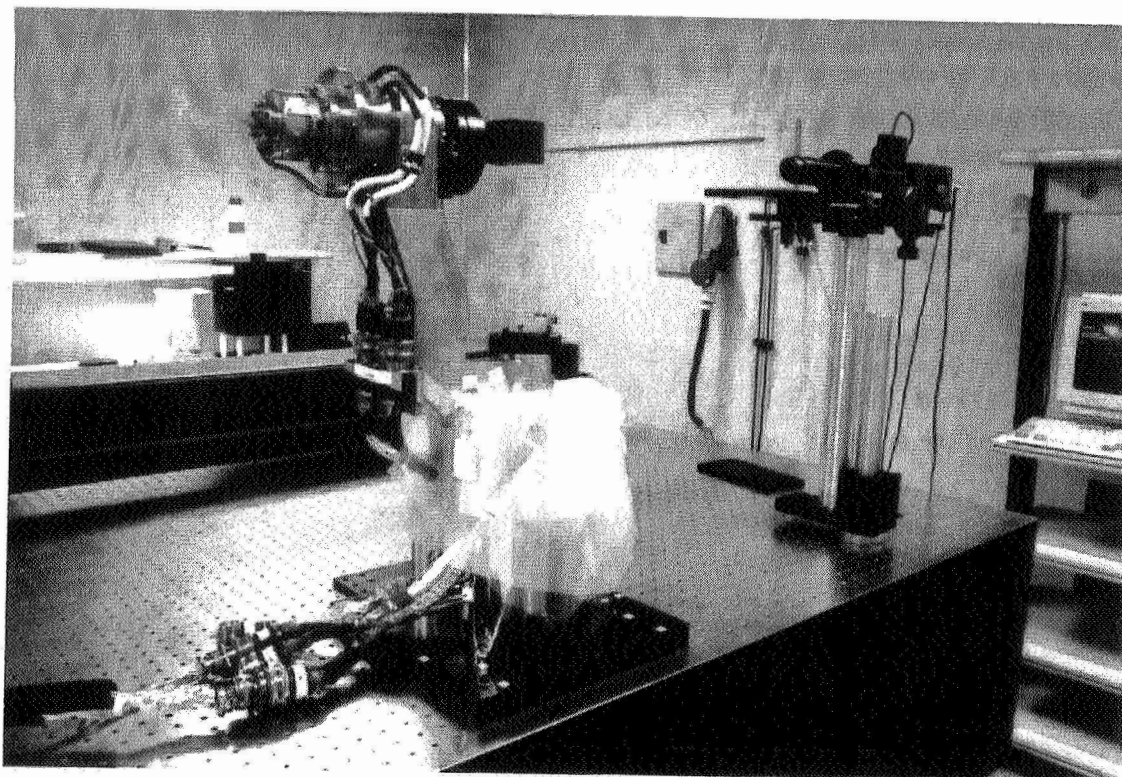


FIGURE 10: APM-PPF (EQM). Optical Measurements



513-32

50441  
125127

## Development of a Gimballed, Dual Frequency, Space-Based, Microwave Antenna for Volume Production

Martin Leckie\* and Dave Laidig\*\*

✓  
p H

### Abstract

A dual-frequency, two-axis Gimballed, Microwave Antenna (GMA) has been developed by COM DEV and Motorola for commercial satellites. The need for volume production of over three hundred antennas at a rate of four per week, a compressed development schedule, and the commercial nature of the effort necessitated a paradigm shift to an "overall" cost-driven design approach. The translation of these demands into antenna requirements, a description of the resulting GMA design, and examples of development issues are detailed herein.

### Introduction

The GMA is a gimballed, dual reflector, microwave antenna designed for use on commercial satellites. Each satellite contains four GMAs, which support communication links with Earth-based tracking terminals. The total number of GMAs to be supplied is greater than 320, including qualification models and spares, with a peak production rate of four units per week.

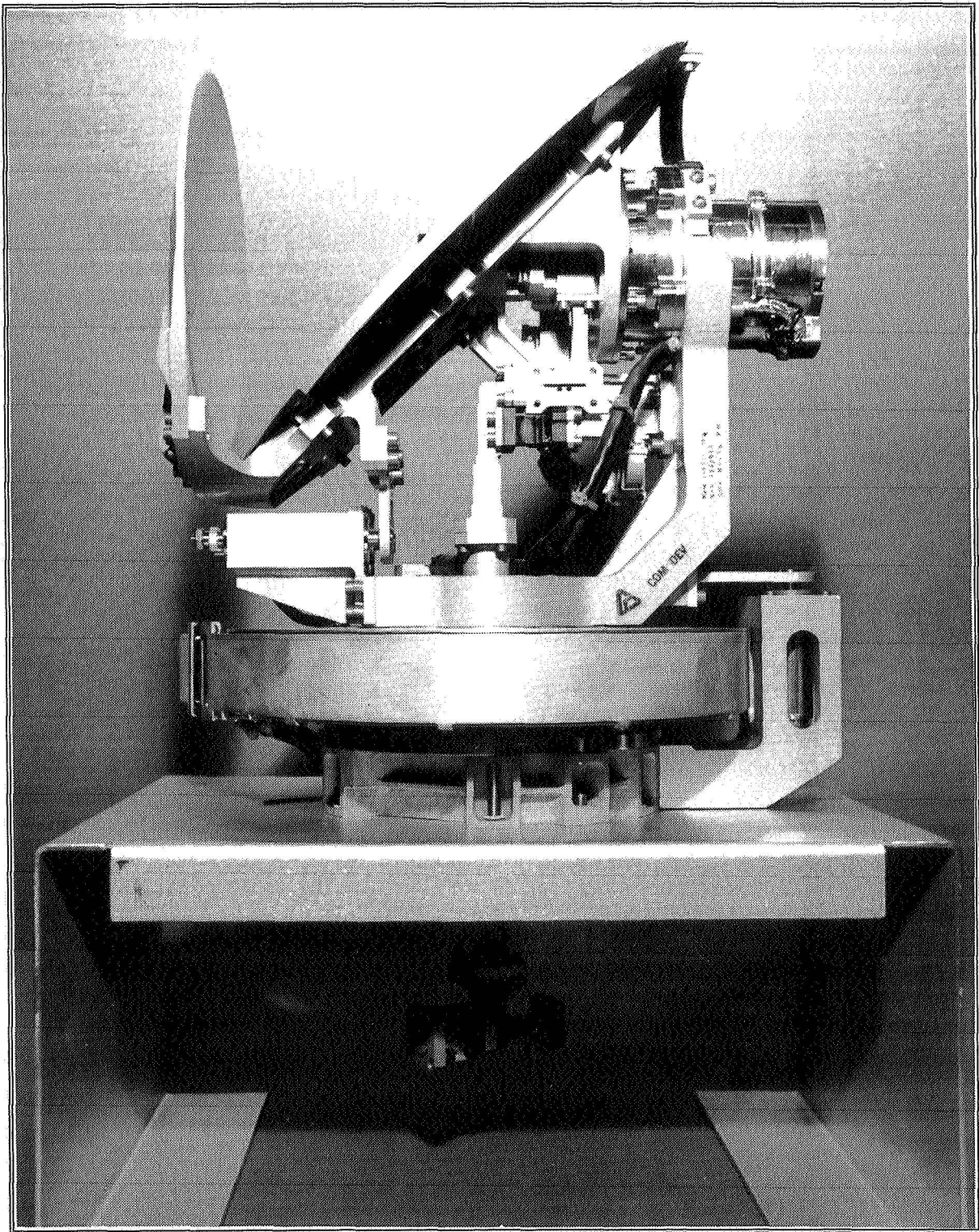
By mass production standards, neither the production quantity nor the rate is large, but by satellite equipment manufacturing standards — the primary business of the co-developers — these requirements were a quantum leap. The requirement for high-rate bulk production was just one of many development challenges for the design team. Other challenges included traditional gimballed antenna specifications — low mass, launch vibration, and pointing accuracy — as well as a short (one-year) development cycle, and low, fixed cost. How these requirements were met and the lessons learned during the development of the GMA are the focus of this paper.

Development of the GMA (Figure 1) is complete. All design issues have been resolved, and the GMA successfully passed qualification testing in July, 1995. Production shipsets have been delivered. Qualification and early production results compare favorably with specified requirements and analytical predictions.

---

\* COM DEV, Cambridge, Ontario, Canada

\*\* Motorola, Satcom Division, Chandler, AZ



**Figure 1**  
**Gimbaled Microwave Antenna (GMA)**



## Requirements and Capabilities

The design requirements of the GMA, along with its capabilities and analytical predictions, are presented in Table 1.

**Table 1**  
**GMA Requirements vs. Capabilities and Predictions**

PARAMETER	REQUIREMENT	QUAL AND PRODUCTION UNIT CAPABILITIES <sup>1</sup>	ANALYTICAL PREDICTIONS
Dual Freq. wave	20 GHz/30 GHz (Tx/Rx)	Comply	Comply
Positioning Accuracy	$\leq 0.60^\circ$	Max = $0.4^\circ$ Mean = $0.3^\circ$	$0.51^\circ$ <sup>2</sup>
Range of Motion	AZ: $\pm 185^\circ$ ; EL: $+27^\circ$ to $90^\circ$	Comply by Test	Comply
Angular Rate	AZ: 15°/sec max EL: 6°/sec max	Comply by Test	Comply
Step Size	$0.047^\circ$	Comply by Test	Comply
Motion Envelope	26.9 D X 31.1 H (cm)	Comply by Test	Comply
Lifetime Excursions	$5.9 \times 10^5$	Comply by Test	Comply
Mass	5.44 kg (12.0 lbm)	5.23 kg (11.54 lbm)	5.28 kg (11.65 lbm)
Rotational Mass	EL: 1.04 kg AZ: 2.54 kg	Comply by Design	EL: .94 kg AZ: 2.46 kg
Random Vibration	12.4 Grms	Comply by Test	Comply
Sine Vibration	5 G's From 5 Hz to 100 Hz	Comply by Test	Comply
Stowed Resonant Frequency	$\geq 100$ Hz	102 Hz; Q=7 (X-axis) 120 Hz; Q=6 (Y-axis)	108 Hz; Q=20 140 Hz; Q=15
Pyro Shock	1000 G peak	Comply by Test	Failure
Thermal Extremes: Operating	-40°C to +76°C; Low Temp Controlled by Heaters	Verified in TVAC Testing	Comply
Thermal Cycles	1020 Cycles: -50°C to +85°C	Comply by Test	Comply

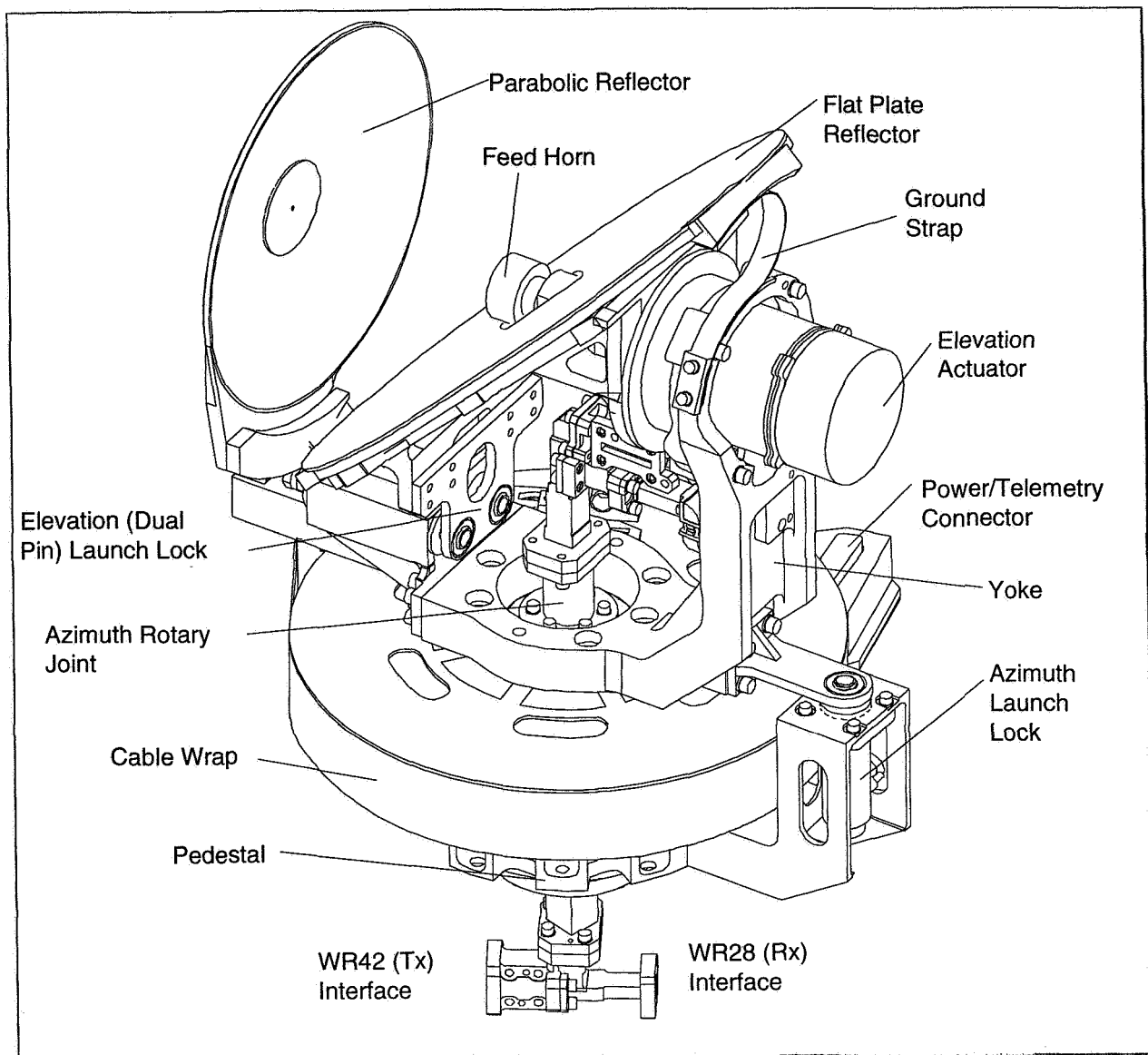
## Design Description

The GMA is a dual reflector microwave antenna driven by an elevation over azimuth gimbal system, the general layout of which is shown in Figure 2. An RF rotary joint and a flat-ribbon cable wrap are integral to the azimuth rotary actuator and pass microwave signals, power, and telemetry across the azimuth axis. The dual reflector antenna design was chosen for its compactness, and it eliminates the need for an elevation axis RF rotary joint. Paraffin actuator launch locks provide restraint of motion about the azimuth and elevation axes during launch. GMA thermal control is primarily passive, though flexible Kapton heaters are used to maintain actuator temperatures above their low-end operating extremes.

GMA azimuth motion is provided by a rotary actuator supplied by Honeywell Satellite Systems Operation (HSSO). This actuator is a three-phase,  $3.75^\circ$  stepper motor with integral 80:1 harmonic drive gear reduction, thus yielding a nominal  $0.047^\circ$  output step increment. The actuator output bearing set was sized to react expected launch loads of 283 N-m (2500 in-lbf) in bending and 4450 N (1000 lbf) in shear, while the titanium housing material was chosen to match the coefficient of thermal expansion (CTE) of the steel bearing set. A built-in, incremental encoder attached to the motor, when combined with an output shaft reference switch signal, provides both step count and actuator zero location to the GMA controller unit aboard the Space Vehicle (SV).

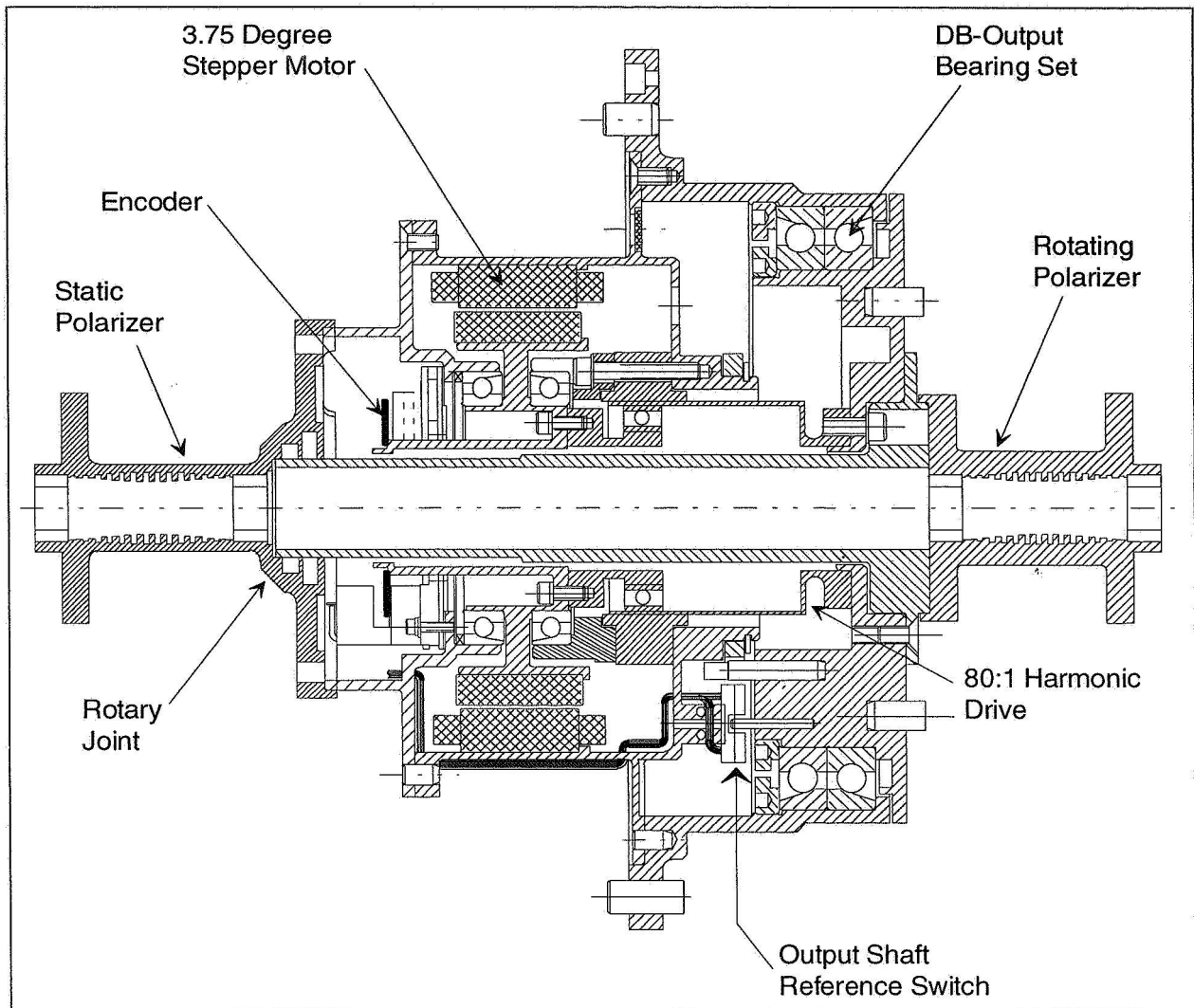
<sup>1</sup> Based on nine samples (one qual and eight production units)

<sup>2</sup>  $3\sigma$  estimate



**Figure 2**  
**GMA Layout**

To provide a transmit and receive signal path across the azimuth axis, the rotary actuator incorporates a circular waveguide along its centerline. Early teaming of mechanical and RF engineers was essential to define the interfaces between the rotary actuator and the RF signal processing components (Figure 3). The circular waveguide concept was chosen for its low signal power loss across the interface, but it required tight runout tolerances. After the concept was selected, the rotating and static components of the RF path were immediately fabricated and tested to verify performance assumptions.



**Figure 3**  
**Azimuth Actuator/Rotary Joint Cross Section**

Directly attached to the azimuth actuator is a cable wrap mechanism<sup>3</sup> which controls the motion of a 19-conductor flat-ribbon cable throughout the full 370° range of azimuth motion. The critical design feature of this mechanism is low drag torque over the operating temperature range (-40°C to +76°C). This low drag torque minimizes actuator pointing errors caused by torsional loading of the harmonic drive. Drag torque and life tests were completed early in the program to reduce risk.

The design of the azimuth actuator had to be closely coordinated between four companies in only a four-month design cycle: COM DEV defined launch loads, mass, power, pointing error, and waveguide requirements; HSSO provided detailed actuator

<sup>3</sup> Supplied as part of the azimuth rotary actuator by HSSO.

design; and Motorola and the SV bus supplier defined vehicle loads and component placement and designed the composite panel and interface to which the rotary actuator mounts.

The stator portion of the azimuth actuator is mounted to a machined titanium pedestal to raise the GMA off the SV panel enough to assure a clear field of view (FOV) for the antenna. The rotor side of the actuator is attached to an aluminum yoke which provides structural support and alignment for the elevation axis antenna components. Yoke and pedestal material selection was finalized only after completion of a detailed thermal distortion analysis of the actuator bearings. When considering use of dissimilar materials in a mechanism assembly, it is important to assure bearing performance is not adversely affected by CTE mismatch.

The GMA yoke supports the elevation actuator, antenna feedhorn, and associated RF signal paths. The elevation rotary actuator is identical to the azimuth rotary actuator in construction, except it is smaller due to lower launch loads and has no requirement for an integral RF waveguide. A more detailed description of the design of both these actuators is provided by Koehler [1].

The feedhorn of the GMA is mounted in a stationary position on the yoke, while the flat plate and parabolic reflectors are mounted to the rotor side of the elevation actuator, and thus become the rotational portion of the antenna in elevation. This configuration eliminates the need for a rotary joint through the elevation axis which, in turn, reduces the part count, cost, complexity, and mass of the assembly. The flat plate and parabolic reflectors are weight-relieved aluminum machinings with a sulfuric-acid anodized finish. The 7075-T73 aluminum was chosen over more exotic, lower mass materials for low cost and availability, and the surface finish was chosen as a compromise between thermal, RF, and cost performance.

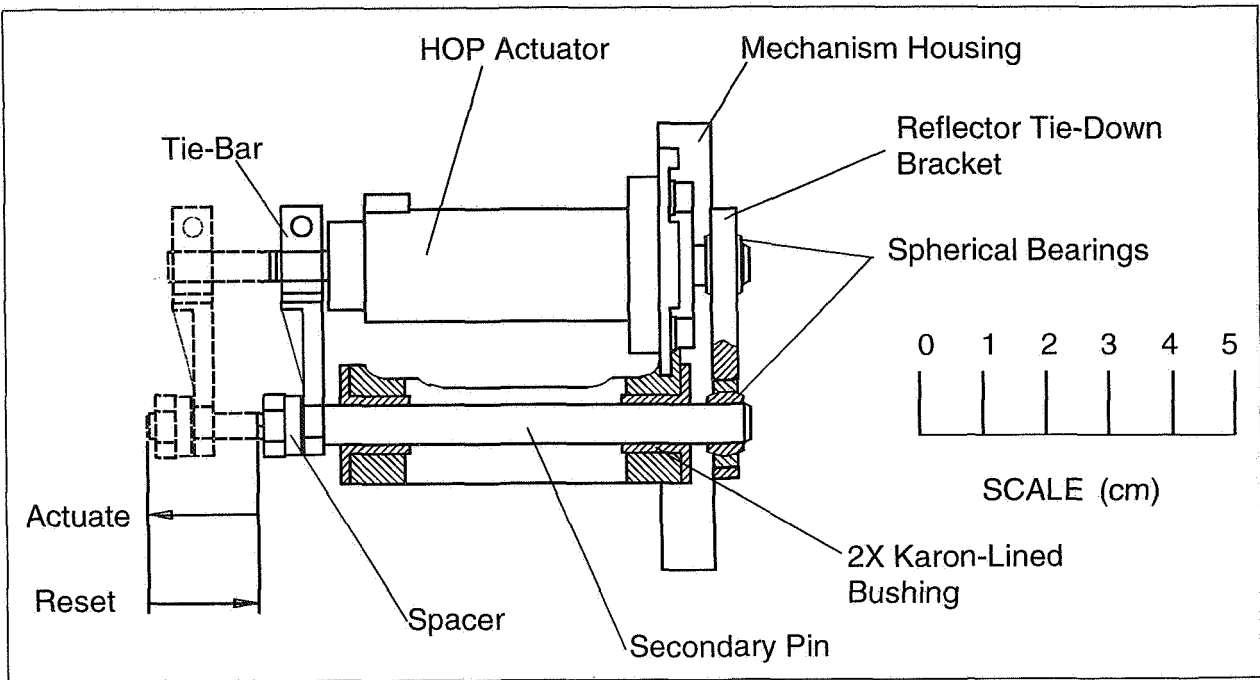
GMA pointing accuracy was specified to be within  $0.60^\circ$  of target. This accuracy had to be achieved after consideration of machined part tolerances, thermal distortion, and beam squint. Early conceptual studies concluded that the two antenna reflectors needed to be joined by a common structure so that they could be precisely aligned and rotated together about the elevation axis. This design, though volume- and RF performance-efficient, was essentially a cantilevered load suspended from the elevation rotary actuator and led to a requirement for a mechanism to offload the actuator during launch. The resulting elevation axis launch lock mechanism employs a dual-pin arrangement, using a High Output Paraffin (HOP) actuator<sup>4</sup> together with a secondary pin, joined by a tie bar (Figure 4). The secondary pin slides on Karon<sup>®5</sup>-lined, low-friction bushings, and the two pins engage Karon<sup>®</sup>-lined spherical bearings on the reflector support bracket. The spherical bearings were chosen to allow the mechanism the freedom to disengage when small misalignments are present in the assembly. The mechanism was analyzed to assure a deployment margin of at least

---

<sup>4</sup> Supplied by Starsys Research Corporation, Boulder, CO

<sup>5</sup> Karon<sup>®</sup> is a registered trademark of Kamatics, Inc., Bloomfield, CT

50% when worst-case actuation forces were compared to the worst-case combination of friction forces.



**Figure 4**  
**Elevation Axis Dual-Pin Launch Lock Mechanism**

Rotation of the GMA about the azimuth axis is prevented during launch by the azimuth launch lock, which employs a similar HOP actuator to that used in the elevation axis launch lock, but does not require a second pin.

Another important consideration in designing the GMA gimbal mechanism was electrical grounding across the rotational axes. This requirement arises from the need to bleed off charges that accumulate on the reflector surfaces in space. Rotary actuator output bearings are not suitable grounding paths for this purpose. The azimuth axis uses cable wrap conductors to provide the necessary electrical continuity, whereas the elevation axis required a ground strap to connect the flat reflector to the yoke, thus bypassing the elevation axis rotary actuator. The flat reflector rotates  $63^\circ$  in elevation relative to the yoke; therefore, the ground strap must allow for this rotation. Other ground strap requirements were (1) high flexibility to minimize drag torque; (2) shape retention during handling and launch vibration; (3) ability to survive 750,000 motion cycles; and (4) capability to withstand the external and thermal environments. After considerable testing, a 0.05-mm-thick beryllium copper strap with a black oxide finish was chosen for this purpose.

## **Design For Volume Production**

The unique aspect of the GMA spacecraft mechanism design was the requirement to design for volume production and to "Design to Unit Production Cost (DTUPC)." In this aspect, the development task took on a more commercial flavor and set it apart from the previous experience of the co-developers. Some of the design decisions that were necessitated as a result of these unique requirements are highlighted below.

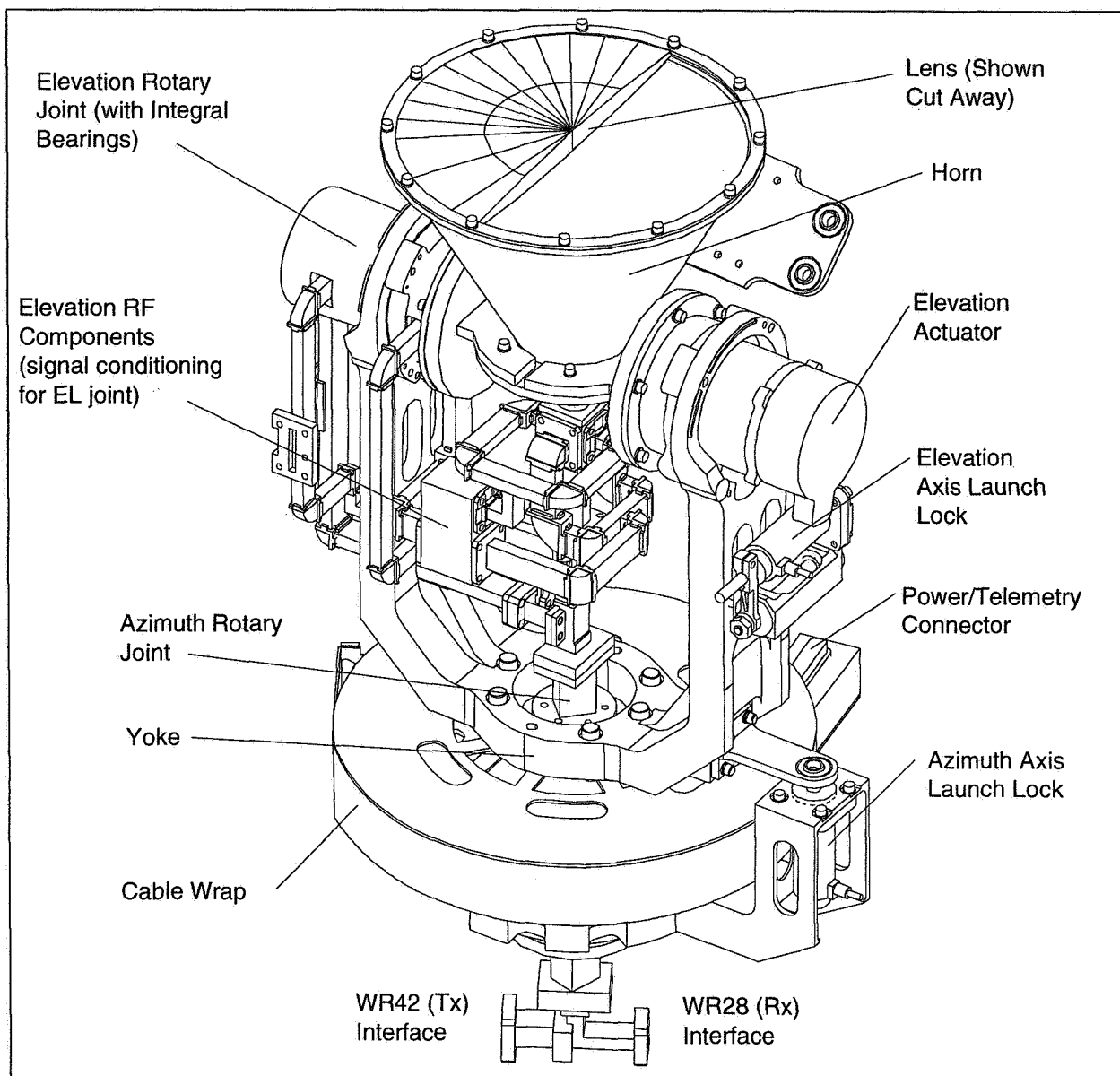
### **Antenna Configuration**

The initial GMA concept was a more traditional horn and lens design, chosen for its excellent RF parameters (Figure 5). Considerable effort was put into this design before realizing it was extremely complex, its expected cost was well over production targets, and there were significant technical issues. There were material problems with the lens (Atomic Oxygen, CTE mismatch with the horn, grounding), rotational inertia and overall mass specifications could not be met, and the assembly could not meet its volume envelope. Therefore, the design team re-opened the trade space and re-addressed the GMA design, based on manufacturability and DTUPC concepts.

Out of this joint buyer/seller re-design effort came the dual reflector design, a more compact design that allowed the GMA to meet its envelope requirements. Overall mass was lowered by 0.59 kg (1.3 lbm), thus allowing the assembly to meet its specification, CG was lowered by 1.3 cm, which lowered structural loads, and the mass imbalance of the lens was removed, thereby allowing the GMA to meet its rotational inertia specifications. These reductions made internal loads smaller, thus making launch lock design easier and cutting structural mass further. Finally, the assembly part count was reduced by half (including the removal of an elevation rotary joint which was 10% of the expected production cost), thereby increasing reliability and decreasing complexity. The slightly less efficient antenna design was offset by the decreased feed loss due to removal of the elevation rotary joint, so the only expense associated with the benefits of the dual reflector design was the addition of a pedestal to raise the assembly phase center for clear FOV.

### **Rotary Actuators**

The GMAs are not the only antennas that COM DEV and Motorola supply for commercial satellites. The four GMAs constitute just part of a K-Band antenna suite which contains two other gimbaled antenna assemblies that are quite different from the GMA design. Design of actuators, optimized for each individual gimbaled antenna assembly in the K-Band antenna suite, would have required a total of four unique actuator designs. An early program decision was made, based on DTUPC/economy of scale principles, to standardize all gimbaled antenna actuator designs, thus reducing the number of actuator designs needed to two.



**Figure 5**  
**Initial GMA Horn and Lens Design**

The use of common actuators made for a more challenging design phase, since actuator designs had to account for differences in the launch loads, waveguide dimensions, and hard stop positions of the various antenna assemblies. Possibly some volume and mass optimization were lost; however, the cost and complexity savings, as well as the tooling and overhead savings, far outweighed any losses.

#### Launch Locks

Launch locks were designed integral to the GMA instead of including them as a separate structure on the SV, thus avoiding the associated additional harnessing,

alignment problems, and higher volume. In addition, it cut assembly time and part stocking overhead at the SV level, as well as simplifying GMA testing and transporting.

The same commonality principle used in the rotary actuator design was used in the launch lock design. Each gimballed antenna assembly (six total, including GMAs) in the K-Band antenna suite needed two launch locks — a production total of 960 over the program life — so the economic benefit of standardizing launch lock designs was obvious. Design of launch locks, optimized for each gimballed antenna assembly, would have required four unique designs. Rather than use four unique designs, all efforts were made to provide a single design. In the end, however, two distinct launch lock designs had to be used: a single-pin design used in the bulk of applications, including restraint of the GMA azimuth axis, and a dual-pin design necessary to offload the GMA elevation components. The impact of accommodating two distinct launch lock designs was minimized by using the same spherical bearing in both designs and only slightly modifying the HOP actuator for use in the dual-pin design. Only one part within the HOP actuator was changed — the actuator pin was extended through the back of the actuator (Figure 4); therefore, subcontract costs were minimized.

The GMA launch locks were designed to be simple, reliable, and resettable. The HOP actuators were chosen based on these requirements, and they generate no shock on deployment. Both the azimuth and elevation launch locks were designed to be reset after actuation by using spring-loaded tools that either push (elevation dual pin) or pull (azimuth) the HOP actuators back to their locked positions. The provision to actuate and quickly reset the launch locks at both the antenna and SV level was necessary to meet both GMA and SV test cycle time requirements. Verification of flight hardware by performing multiple actuation/reset cycles during ground testing helps assure reliable on-orbit deployment. Shock-free antenna deployment helped avoid costly design and testing cycles and had the additional benefit of not requiring the handling and safety overhead associated with pyrotechnic actuators.

#### Cable Wrap Mechanism

The initial concept of the cable wrap mechanism design was based on wiring that met all military specifications for shielding and for separation of signal and power lines. The design was unacceptable from cost, volume, and mass standpoints. At this point, the design team did something that was a standard practice on the program: we got a supplier involved in the design. A cable vendor<sup>6</sup> was invited to a joint review of the design. After both reviewing the design and determining the actual requirements, the design was changed to make use of a commercial product. The final wiring configuration is based on a 19-conductor, flat-ribbon cable with internal shielding between the power lines and the encoder lines. An external shield is added using aluminized Mylar film, contacts are gang-crimped to the ends of the cable, and the contacts are batch-soldered to spaceflight connectors. All processes are highly automated, and the vendor now supplies the cable for the cable wrap mechanism as a drop-in, pre-tested assembly.

---

<sup>6</sup> W.L. Gore & Associates, Inc.



By leveraging the knowledge of a supplier and careful review of the program technical requirements, cable wrap mechanism cabling costs were reduced nearly ten-fold, assembly time was substantially decreased, and a 0.45-kg mass savings was realized.

### Manufacturability

The GMA gimbals consist of not only the azimuth and elevation rotary actuators, but also precision machined parts, such as the pedestal, yoke, and antenna support brackets. These machined parts have a large influence on the pointing accuracy of the antenna and are manufactured in quantities of 200 to 300 pieces. The use of shimming at component interfaces to assure that the pointing accuracy of any antenna would meet specification was not permitted. Therefore, the emphasis was on selecting machining tolerances that were realistic, economic, and could be controlled through statistical process control (SPC) at the machine shop level. This philosophy of manufacturing (i.e., SPC of machined parts and no shimming) had a direct impact on the next aspect of volume production — assembly.

### Assembly

The GMA design had to assure an assembly time that allowed delivery of four GMAs per week. Therefore, the assembly design was based on the following key points:

- *No Shimming Permitted:* There was simply not enough time in the production schedule to test for pointing accuracy, to disassemble, to adjust by shimming, then to retest.
- *Fully Interchangeable Parts:* Use of match drilling and pinning of parts to increase alignment accuracy was not permitted. The flexibility of allowing any rotary actuator or machined part to be used in any antenna assembly greatly increases production flow and cuts part tracking overhead.
- *Alignment features for ease of assembly:* Although the antenna gimbals are precision assemblies, the alignment of a rotary actuator to a pedestal or yoke is simply a matter of mating alignment features on one part to reciprocal features on the other part. This places minimal burden on assembly personnel, both in terms of time and elimination of alignment errors.
- *Minimal Staking:* Staking of parts was nearly eliminated, thus cutting costly assembly time and the even longer cure times during which the assembly is unavailable for further processing. This also reduces the "as required" parts count, and, therefore, assembly variation.

### Test

The time required for verification testing of each antenna was minimized through design features and testing philosophies, such as:

- *1g Holding Capability:* Rotary actuators were designed to provide unpowered detent torques large enough to maintain the antenna elements in a fixed position, regardless of antenna orientation, during ground testing. Thus, no cumbersome 1g negation devices were required.
- *Antenna Test Range Automation:* Pointing accuracy of a gimballed antenna is verified on an antenna test range. The time required to take measurements and process data is excessive, and accounts for a major portion of the GMA

acceptance test cycle. Range availability is also an issue because of the quantity of antennas which must be processed through the range during peak production. Therefore, this process has been streamlined by automating test range operations. Antenna pattern measurement and data reduction have been automated through the use of newly developed software, thereby significantly cutting test cycle time.

- *Built-in Test Ports:* RF test couplers were designed into the RF signal paths of the GMA and located for ease of access at both the antenna and SV levels. This allows for rapid test connection and end-to-end test of the SV-level RF path without cumbersome antenna-to-antenna interrogation of the system. A minimal mass penalty is paid for flying the test couplers with the GMA, but this is more than offset by minimized test set-up time and complexity.

### SV Level Assembly

Speed of assembly at the SV level is essential to achieve a peak delivery rate of one SV per week. The following features were added to the GMA to optimize SV level integration time:

- *Captive Mounting Bolts:* GMA mounting bolts are locking bolts that are captive in the pedestal. Captivity in the pedestal reduces bolt installation time and removes the possibility of bolt dropping/finding time. Locking elements in the bolts remove the need for bolt staking.
- *Single Interface Connector:* All electrical signals, excluding antenna microwave signals, enter the GMA through a single multi-pin DD interface connector. This simple interface cuts assembly time and is standard throughout the system.

The total time for GMA integration onto the SV is just 11.0 minutes and requires no further adjustment after installation.

### **Testing/Results**

The GMA successfully passed qualification testing in July, 1995. Test results correlated well with analytical predictions (Table 1).

One minor problem was encountered during the testing: the initial version of the elevation axis ground strap failed during random vibration testing. This initial design was a 0.05-mm-thick pure copper strap with a black oxide finish that was already being considered for change because it tore easily during assembly. The ground strap material was then changed to beryllium copper (BeCu), which was more durable and survived a re-qualification vibration test. The BeCu version of the ground strap was then subjected to a 750,000 motion-cycle life test, which it passed.

### **Conclusion and Keys to Success**

Development of the Gimballed, Microwave Antenna (GMA) was highly successful. The end result was a reliable, low-cost, high-performance, gimballed satellite antenna designed from a commercial, "overall cost" standpoint which allowed for volume production at the antenna assembly facility and high-rate installation and test at the

satellite level. This commercial, low-cycle time, bulk volume perspective was a paradigm shift for the contractors, who were from low volume DOD/Space backgrounds, so the development was not without difficulties. However, with these difficulties came lessons, a sample of which follow:

- *Use design heritage.* There will be enough wheels to invent.
- *Build many prototypes, especially of moving assemblies, and build them early on.* 3D models do not catch all problems. An engineering model GMA rotated into an adjacent box during SV subassembly range testing, much to our surprise. This should have been caught by the 3D model, but as the design task progressed, modelling responsibility was transferred to people less and less familiar with the design concept. Rotational operation of the GMA was not communicated accurately to the new designers; hence, the interference was not detected, thus leading to re-design which could have been prevented by building an earlier prototype.
- *Design special test equipment (STE) with an eye on all levels of assembly:* Make sure STE that might be used at higher levels of assembly is designed considering ease of access at higher levels of assembly. All launch lock resetting and optical verification tools were designed to fit both at the GMA assembly level and at the SV level. However, on another antenna assembly in the K-Band antenna suite, ease of access for a reset tool was not considered, and a new tool had to be immediately developed for use in a cramped space.
- *Account for changing requirements up front.* Requirement generation and hardware development always overlap somewhat, thus creating shifting, and entirely new, requirements during the design phase. Design in extra margin, design for easy modifications, and set aside costs for the inevitable changes.
- *Political/Cultural issues are the hardest to overcome* when jointly developing with multiple contractors. Cultural differences include
  - Direct vs. Indirect Investors
  - Military vs. Commercial Attitudes (Risk Taking)
  - Large vs. Small Corporations (Resources)
  - U.S. vs. Non-U.S. (ITAR, Customs, etc.)
  - Teaming vs. "Us Against Them"

To lessen the impact of cultural differences, create a cross-contractor team, at least at the technical level.

- *Nail down design and analytical responsibilities early to avoid arguments (about cost/resources) and delays later.* In the rush to get the GMA subcontract signed, responsibility for the GMA orbital thermal modelling was not delineated. In addition, the specification was vague. When the scope of the effort became clear, work on thermal modelling came to a halt. Many extended phone conferences were held, airline seats filled, and meetings attended. All of these efforts could have been avoided by taking the extra time to clear up "gray" areas in the contract and specification early on.
- *Synchronize work of co-contractors and suppliers.* When a team member gets ahead, the design is driven by factors other than optimal product outcome.

Rotary actuator design progressed much more rapidly than did the antenna or SV designs. Actuator envelopes were created by the actuator developer, piece part drawings were released and housings machined, all before design of the structure was complete. When the structure design was nearing completion, it was clear that either the actuator would have to change or the structure would not be optimum. An acceptable compromise was reached, but this would not have been necessary had work been better synchronized.

- *Contractor incompatibilities hinder the design process.* The different CAD systems, geographic locations, and communication systems of the various subcontractors made the design process less efficient. 3D modelling was used at only two of the four main players, so models could not be easily swapped, thus resulting in duplication of effort. Pagers were profuse at some subcontractors and virtually non-existent at others, while email, which proved to be a great time zone equalizer, was not available at one location.
- *Do not ignore small issues. Small issues become big problems later on.* The shielding concept of the actuator wires was a known issue. The desired shielding resulted in a wiring bundle that did not fit within the available routing volume. Though the desired shielding was relayed to the supplier, it was never requested in the specification, so no changes were made. Both sides thought they were getting what they wanted. When initial actuators were delivered without the shielding, the small problem transformed into a large problem. This problem was quickly solved by calling the technical team together and working the issue but could have been avoided by better communication.
- *Early supplier involvement creates better products at lower cost* by taking advantage of experts' design and capability knowledge.
- *Define interfaces as quickly as possible.* Pass on prospective changes as quickly as possible. This allows the design team to find a solution while the contractual issues are resolved as a side issue.
- *Develop a team.* "Design-in-a-vacuum" costs. Poorly communicated requirements cause huge problems. It may not seem worth it, but formalized meetings, or a process to communicate to the entire team, will solve problems more expediently and optimally. However, this requires all players' commitment to the best technical solution.

## Acknowledgments

We would like to thank our numerous colleagues at COM DEV and Motorola for contributing to the work described in this paper. We would also like to acknowledge the management of Motorola and COM DEV for their support and encouragement and Industry Canada for partial funding of the program at COM DEV.

## References

1. Koehler, David R. "Low-cost, High-reliability Rotary Actuator for a Space Satellite." Ninth Annual AIAA/USU Conference on Small Satellites, Space Dynamics Laboratory/Utah State University, Logan, UT, September 19, 1995.

# Design and Development of the Cassini Main Engine Assembly Gimbal Mechanism

Dale Rudolph\*

514-20

50442

125128

P 14

## Abstract

Cassini is an international cooperative effort between NASA, which is producing the orbiter spacecraft, the European Space Agency, which is providing the Huygens Probe, and the Italian Space Agency, which is responsible for the spacecraft radio antenna and portions of three scientific experiments. In the U.S., the mission is managed by NASA's Jet Propulsion Laboratory (JPL) in Pasadena, California. Lockheed-Martin successfully bid on the contract to build the PMS (Propulsion Module Subsystem) for this project.

The Cassini spacecraft will be launched on an expedition to Saturn in October, 1997. Its mission is to enter orbit around Saturn in July, 2004, and to explore its moons, rings, and magnetic environment for four years. Cassini will carry the Huygens probe, an instrument package equipped with a parachute, which is designed to study the atmosphere and surface of Saturn's largest moon, Titan.

## Introduction

This paper deals with some interesting aspects of the design and development of the Cassini main engine assembly (MEA) gimbal mechanism. This mechanism is a redundant, two-axis gimbal used for active thrust vector control of the main engine (or backup) during the 11-year mission to Saturn. Cone angle adjustments to the engine are necessary due to center of mass shifting as propellant is consumed and the Huygens probe releases. At the time of this writing, the Thermal Development Unit has been built and tested. The Qualification Unit has been built and successfully passed vibration testing; hot fire testing is underway. The Flight Unit has been built and passed acceptance testing.

Discussed in this paper will be interesting approaches to the design problems associated with extremely tight pointing requirements (3 milliradians) and gimbal freeplay reduction and analysis. An adjustable actuator mount and preloaded bearings were spawned from these requirements. Emphasis will be placed on the benefits of computer modeling, which was used extensively. Results, obtained from testing and analysis, demonstrate the effectiveness of these techniques.

---

\* Denver Flight Systems, Lockheed Martin, Denver, CO

## Brief Description

The Cassini main engine assembly, consisting of two 445-N (100-lbf), bi-prop engines (one as a backup) and associated hardware, is located at the bottom of the PMS.

The MEA includes all the parts suspended from eight tubular struts, which terminate at the lower ring frame of the PMS (Figure 1). In our final design, the engine assemblies are identical, except for their structural attachment parts, which are different due to an eccentric spacecraft center of mass through which the engine centerlines must point at null gimbal position. Each engine is mounted to a circular aluminum plate, which serves as the inner gimbal structure. The inner gimbal plate is supported by diametrically opposed bearings in an outer ring. The outer ring is attached to the main structural plate, called the thrust box, with another set of bearings in pillow blocks. This bearing set axis is orthogonal to the inner bearing axis. All bearings are identical precision stainless steel spherical. The bearing bore and the mating shaft are finished with an anti-friction coating to allow rotation at this interface, or the ball can rotate in its race, thus satisfying a requirement for redundant rotation surfaces. The spherical bearing was a good choice for the gimbal because of its compact size, high load capacity, small angle rotations and slow speeds, misalignment capability, and minimal freeplay.

Customer-furnished Engine Gimbal Actuators (EGAs) were specified to position the gimbal. Since the stroke and speed were pre-determined, a short moment arm was necessary to achieve the required minimum gimbal cone angle. The actuators are DC motor-driven ball screws. An LVDT resides in the hollow shaft to provide a position signal. The actuator attachment to the gimbal is a monoball and pin in a clevis. Attachment to the structure is through a universal joint and flexure. The u-joint and monoball isolate the actuator from bending moments during the angular changes of the gimbal as the actuators stroke linearly. The flexure is essentially a wide leaf spring. The thickness of this cantilever plate, and therefore the spring rate, was tuned to decouple the rocking mode of the gimbaled mass from the structural modes. Mounting the actuators in this manner provided the flexibility to change this one component if testing yielded different rocking modes than predicted analytically.

Mounted to the circular engine plate is a split tubular structure, called the tower. The tower served as the structural interface to the gimbal for the propellant lines, actuators, pressure transducers, filters, and the diode box. In addition, the tower assembly serves as a counterbalance for the rocket engine and heat shield. Through accurate solid computer models of the tower and its components, we were able to determine the center of the gimbaled mass. One of our requirements was a 890-N (200-lbf) maximum axial load on the EGAs. In order to meet this requirement, we were required to balance this assembly within a fraction of an inch of the rotation center point (RCP) of the gimbal. We achieved this goal, despite several re-designs, by iterating with incremental displacements of key components.

## Faster, Better, Cheaper

From a blank sheet of paper to a finished design, the gimbal mechanism evolved in about the time it takes to have a baby. Well, not quite a blank sheet of paper. Through the miracle of technology transfer, we inherited JPL's preliminary design. At first blush, the JPL concept appeared quite mature and perhaps just needed final polishing. But, as we systematically evaluated the design against the requirements (which, of course, had changed), we realized substantial re-design was needed. Also, many of the conceptual parts were heavy, and some presented manufacturing problems.

The first area of focus was the thrust box, the primary structural plate to which the gimbals and associated hardware were mounted. JPL's design was basically a rectangular box with the bottom machined at compound angles designed to point the rocket engines at the initial cg of the spacecraft. Assorted ribs and gussets were added for rigidity. The gimbal actuators were arranged from the hole centers, outward to the box corners (Figures 2 and 3). This plate configuration weighed approximately 20 kg and was impossible to machine due to asymmetry and complex angles required for the gimbal mounting. To simplify the design, the box bottom was made flat, and the complex angles were designed into the fittings, which now mounted and aligned the engine assemblies. Also, the actuators and attachment fittings were arranged toward the center of the box, thus eliminating the corners which were necessarily massive to react the actuator loads (Figure 4). The re-designed plate was easily machinable and weighed approximately 1/2 of the original. Just as we were about to eat our cake, we realized this approach generated much more re-design.

In order to realize the benefits of the better, cheaper box we had to tip it upside-down, literally — the actuators now had to be mounted outside, rather than inside, the box. This turned out to be a blessing, which facilitated the design of adjustable actuator mounts to precisely point the gimbals without impossible tolerancing of the parts.

The advantages of the new packaging scheme were obvious, but we needed proof that we could meet the basic requirement of a 12.5° half cone angle of gimbal travel. To accomplish this task faster and cheaper, a simplified computer model of the gimbal was constructed, using a tool called "Mechanism Design" by SDRG. This software uses an ADAMS solver but is much more user-friendly. After inputting all the appropriate joints and degrees of freedom and applying a forcing function to both actuators, one could sit back and watch the mechanism do its thing. By incrementally changing various geometric parameters and then re-running the model, the kinematics of the gimbal were quickly characterized. The parameters that could be varied were:

1. The distance above the gimbal axis at the actuator attach points
2. The actuator angle relative to the gimbal axis
3. The included angle between the actuators
4. The distance between the actuator attach points.

The actuators were GFE (government-furnished equipment), and the stroke was fixed. The results were not intuitive. Geometries that looked potentially good produced wild excursions of travel due to "togglng" of the linkage. In general, the best behaved travel patterns were produced by minimizing the offset distance between the actuator attach points and the gimbal centerline and by minimizing the actuator axis angle

relative to the gimbal null plane. In a perfect world, both actuators would lie in a plane parallel to the gimbal null plane and be attached at the same point on an axis both normal to the gimbal null plane and passing through the gimbal rotation center. Since two objects cannot occupy the same space simultaneously, this configuration is impossible.

From this exercise, the best candidate was selected, and the strawman model was replaced with a high-fidelity solid geometry model closely representing flight hardware. Running this model took much longer but was necessary to check for possible physical interferences. As it turned out, there were possible interferences, which predicated the need for hard mechanical stops. The same model was refined further with the addition of hardware, propellant lines, and cabling. This ultimate model yielded gimbal mass properties which were needed to compare with the requirement for mass moment of inertia.

Using the computer modeling and analysis techniques saved us the time and expense of creating development hardware. We were able to perform several iterations in a short time. Another benefit of the 3D computer model was a direct link to the two-dimensional line drawings of the detail parts. Fit and tolerance problems were greatly reduced.

## **Flexlines**

One of the stickiest problems that we encountered and did not anticipate was the gimbal flexible propellant lines. For this design task, development hardware took the place of computer models. The solution was more intuitive than analytical. Since the rocket engines can change orientation relative to the surrounding structure and the fuel tanks, flexible fuel lines are necessary. The routing of these flexlines seemed trivial until we built a simplified hardware model to test our ideas. The model was close to flight geometry but with much less detail. The flexhose was a vendor-supplied sample. Its configuration and material were different than our design, but it was close enough for our purposes.

The first configuration tried was the "McDonald's Arches" (Figure 5). The flexlines are side-by-side in an arch that spans between the engine mounting plate and the thrust box. This configuration was basically the same as that which we inherited from JPL. Rotating the gimbal away from the structural attach point for the flexline produced a high resisting moment; we were attempting to flatten the arch, stretch the hose, and reduce the bend radius simultaneously. Rotating the gimbal out of plane produced contortions in the flexline. We surmised that, due to offset between the gimbal rotation centerpoint and the flexline mounting point, we had introduced a torque into the flexline to which it protested vehemently. The flexline construction is a thin-walled, convoluted titanium core with stainless wire woven overbraid. Pure bending was not a problem, but torquing was forbidden.

To eliminate torque, we had a choice of either some sort of swivel joint (with necessary complexity) or aiming the flexhose end fitting through the rotation center point (RCP) of the gimbal. We took the simpler approach and moved one end of the flexline to the



tower, where it could aim through the RCP. This configuration became the "Lazy D". Symptomatic twisting disappeared. But the "Lazy D" was too short; it acted as a mechanical stop to gimbal rotation away from the fixed end. Due to packaging limitations, we could not significantly increase the length in the "real" design. In addition, vibration testing by the flexline vendor produced destructive results for the "Arch" and the "Lazy D" configurations.

A third approach was tried by moving the structural attach point from the thrust box to the lower ring frame above the gimbal. The flexline then hung downward and mounted to the tower at right angles. This was the "J" configuration. Wild contortions were produced by out-of-plane gimbal rotations. Torque reared its ugly head. This behavior was predictable, since the movable end of the hose was offset from the RCP.

Our fourth trial was the "Ess". The "J" tower fitting was revised to aim the hose through the RCP. The hose assumed the shape of a shallow letter "S". Voila, the flexline was now happy. This configuration yielded the lowest forces at the gimbal and was least stressful to the flexline.

These tests were repeated at AVICA, our English flexline vendor, to a higher degree of fidelity with similar results. Gimbal torque tests were performed on the Thermal and Qual units using the "Ess" configuration, both pressurized and unpressurized, with excellent results. These flexible propellant lines are critical to the mission, and their responses are not analytically predictable. The development testing was absolutely required. The resulting final design configuration should meet the requirements for any gimballed rocket engine.

## **Engine Pointing Accuracy**

Our initial reaction to JPL's requirement of 3 milliradians of angular pointing accuracy for the main engine gimbals was shock, but we needed some data to negotiate a relaxation in this requirement. Initially, the problem was two-fold: initial pointing inaccuracy due to part and assembly tolerance stack-up, and pointing repeatability errors due to freeplay or clearances within the system. There was no practical way to machine everything perfectly, so we were left with two options to deal with the inaccuracies resulting from tolerances: either shim or provide an adjustment. Having an aversion to shimming and its attendant complexities, I opted for an adjustable EGA mount (Figure 6). The final design is a split block with a cavity, housing an adjusting screw. Only one half of the block has threads to match the screw. As the screw is rotated, the threaded piece translates, and the stationary block half absorbs the thrust loads from the screw via thrust washers. When adjustment is complete, bolts lock the two halves together. With these adjusters, we could correct for dimensional deviations. The stationary blocks were machined to different heights and angles to compensate for the asymmetric gimbal geometry.

The adjuster idea solved the aiming problem, but we still faced the freeplay issue. There were several contributors, such as clearances between gimbal bearings and shafts, actuator backlash, and shaft-to-housing clearance. By analysis, we were able to show freeplay alone could yield a pointing error of 15.3 milliradians. By far, the

largest contributor to freeplay was the axial clearances at each gimbal axis. This was partly due to the tolerance stack-up of the parts and partly due to thermal expansion and contraction allowance. Our solution to this problem was to incorporate springs on the gimbal axes. The implementation of this idea took the form of preloaded belleville washers (Figure 7). They were chosen for their characteristic high spring rate in a small package. The preload range was high enough to prevent gimbal translation under any predicted loading conditions but still allowed rotation. The small amount of additional friction torque, which the preload created, was not even noticed by the actuators. A precision length bushing and thrust washers were used to determine the initial spring stack deflection and, therefore, the preload. Identical spring stacks were used on one bearing of each gimbal axis. The other bearing on each axis was allowed to float transversely. This gimbal bearing layout had the secondary benefit of allowing thermal growth without binding the bearings. This design has performed flawlessly in all testing, including vacuum firing of the rocket engine which reaches 1316°C (2400°F).

The only remaining source of freeplay was those which we could do nothing about: EGA ballscrew backlash, EGA universal joint clearances, and EGA monoball clearances. These parts were all GFE and were untouchable. Analysis showed that we still had a potential for 6.4 milliradians of freeplay. After much negotiation with the customer, the requirement was relaxed to this value.

## **Lessons Learned**

Our lessons learned can be summarized as follows:

### **Flexline lessons**

- 1) The hose length should be adequate for full gimbal travel in any direction, plus enough extra to allow the nominal shape of the relaxed hose to be a shallow double reverse curve, or "S".
- 2) In the null gimbal position, the entire flexline should lie in the same plane.
- 3) Under no conditions should torque be applied to the hose.
- 4) The centerline of the movable end of the flexline should intersect the rotation center point of the gimbal.
- 5) Get an early start on determining material and vendor. We had a bit of a hassle getting thin-walled titanium with the proper elongation. There is a limited number of vendors who make this product worldwide.

### **Gimbal geometry lessons (for gimbals of similar design)**

- 1) Maximize the moment arm between the actuators and the gimbal axis.
- 2) Minimize the distance between actuator attach points at the gimbal.
- 3) Keep the actuators orthogonal to each other.
- 4) Keep the actuator plane parallel to the gimbal bearing plane, if possible.

#### Gimbal kinematic lessons

- 1) Kinematic modelers, such as “Mechanism Design” by SDRC or ADAMS, can save time in the design development stage.
- 2) Start with a simplified “stick model” to use computer resources efficiently and to allow quicker iterations of geometry.
- 3) Replace with a high-fidelity model when a solution is found. Use this model for clearance studies and mass properties.

#### Pointing accuracy lessons

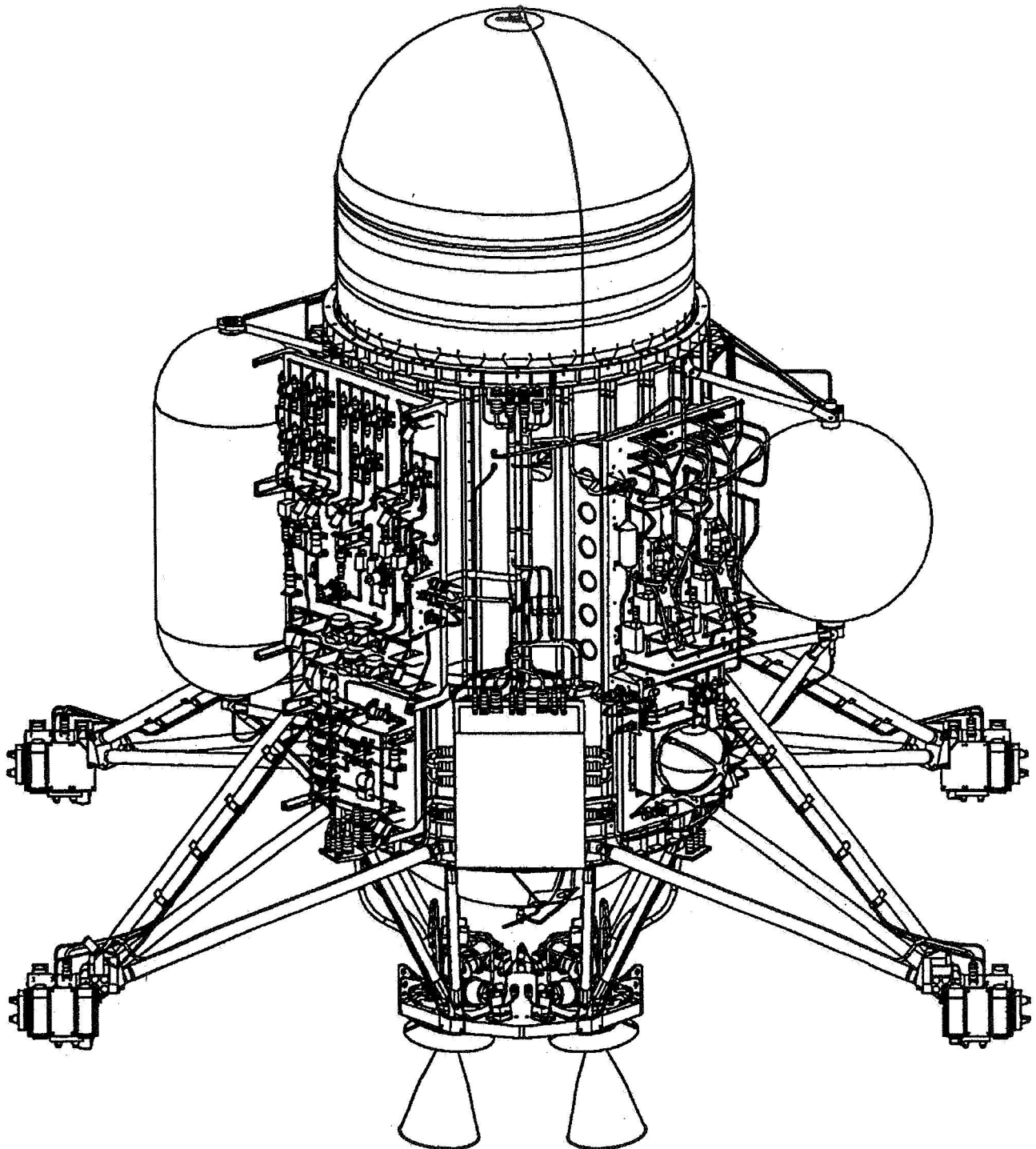
- 1) Adjustments are generally preferred to shimming.
- 2) Reduce or eliminate freeplay, where possible (preloaded bearings).

#### Computer modeling lessons

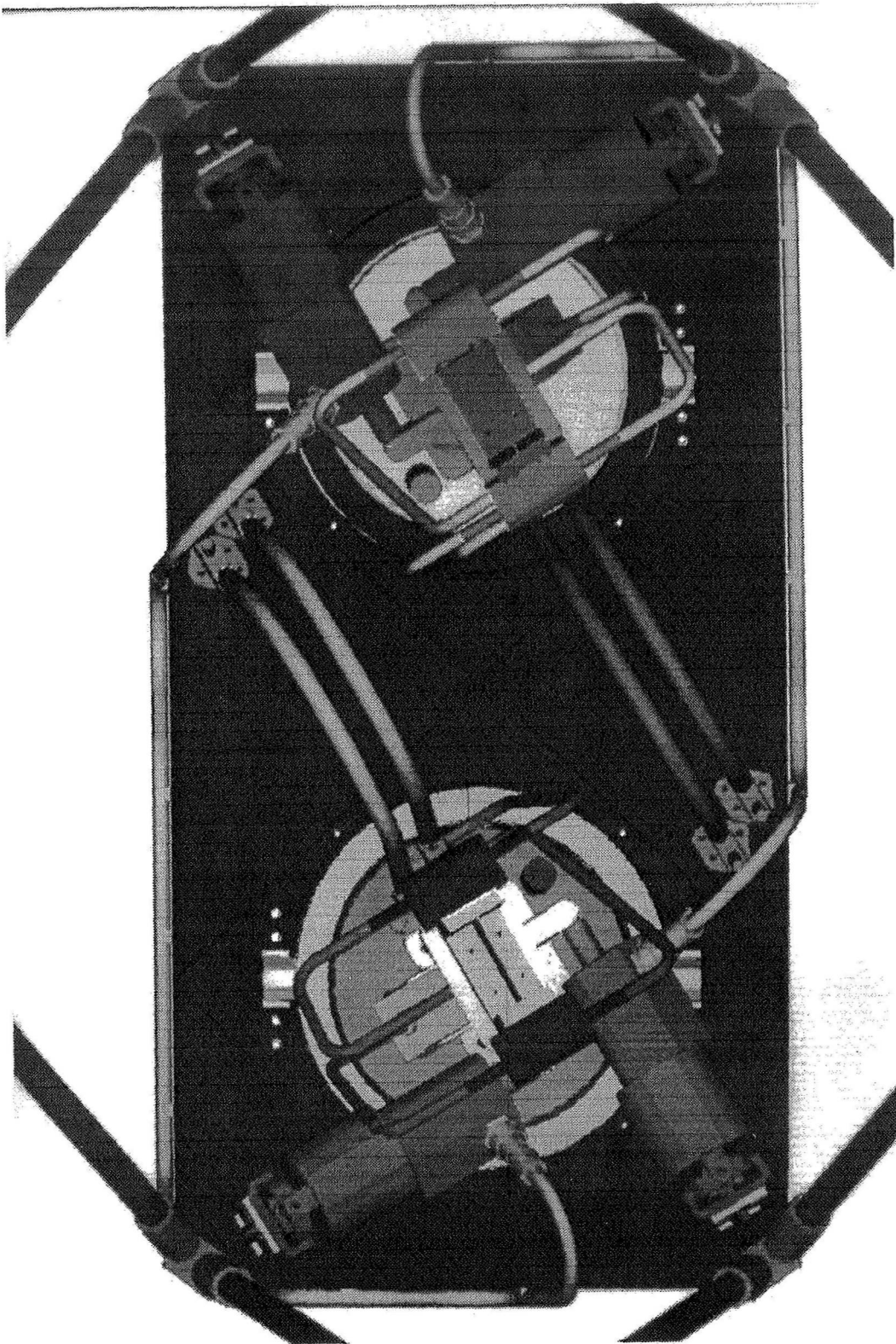
- 1) No development hardware
- 2) Kinematic verification
- 3) Clearance/fit check
- 4) Transition to detailing
- 5) CAM.

#### **“Better is the Enemy of Good Enough”**

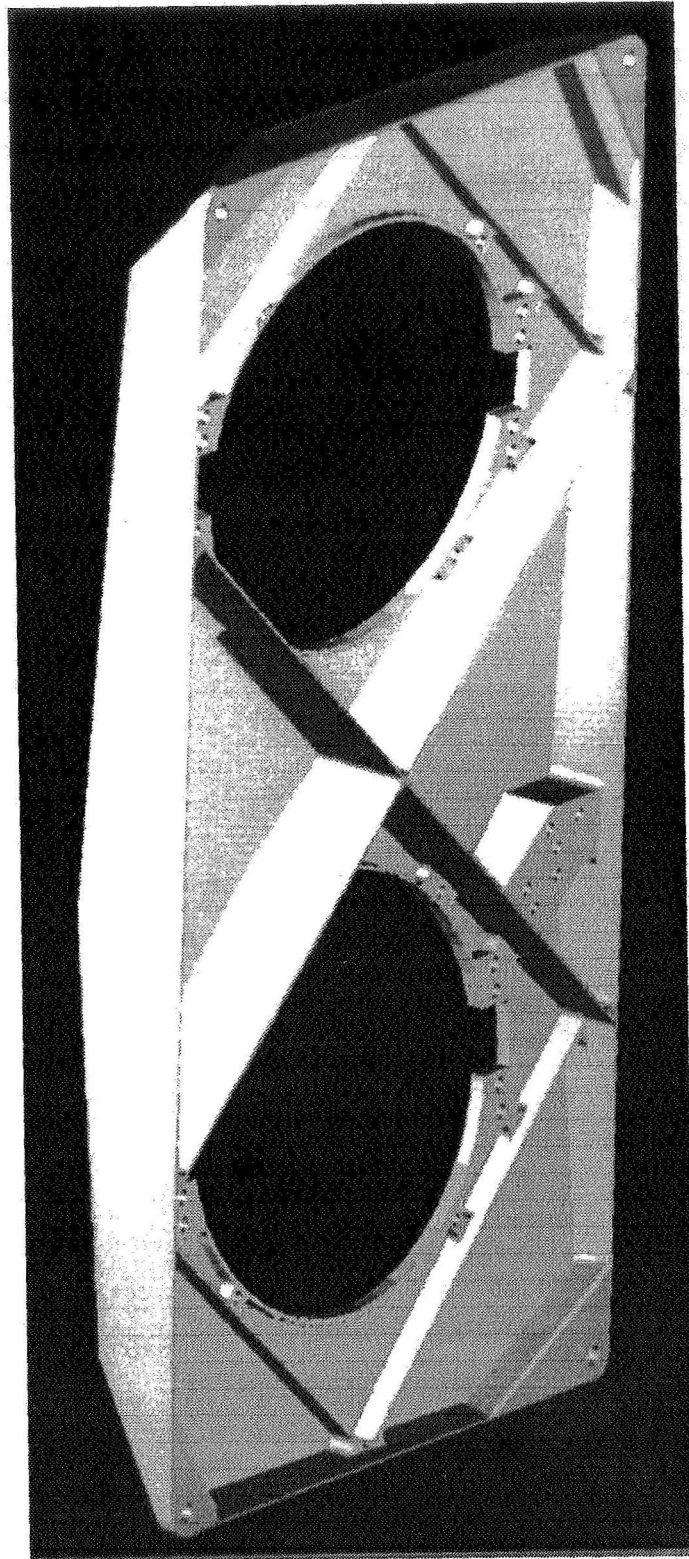
This is the message my boss constantly tried to get across during the design development process. Fortunately, with the aid of computer modeling, the CASSINI design engineers were able to evolve and refine the gimbal design through several iterations and still remain on schedule. Other than the usual number of manufacturing and procurement problems, the build of the three main engine assemblies has gone extremely well.



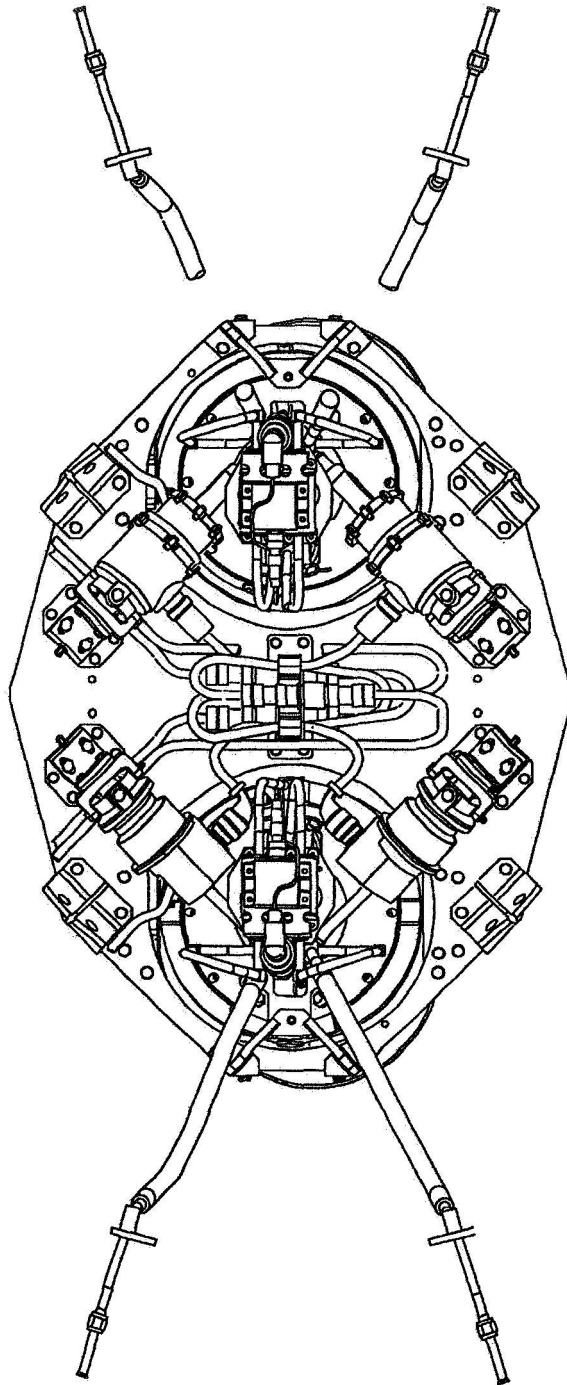
**Figure 1. Cassini PMS**



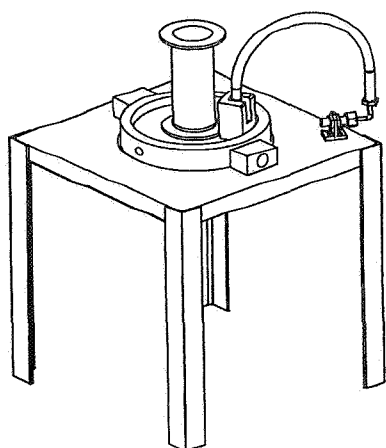
**Figure 2. JPL Layout**



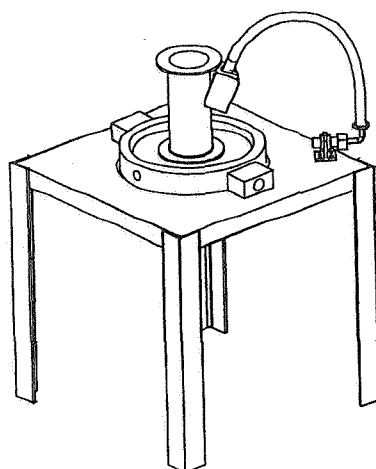
**Figure 3. JPL Thrust Box**



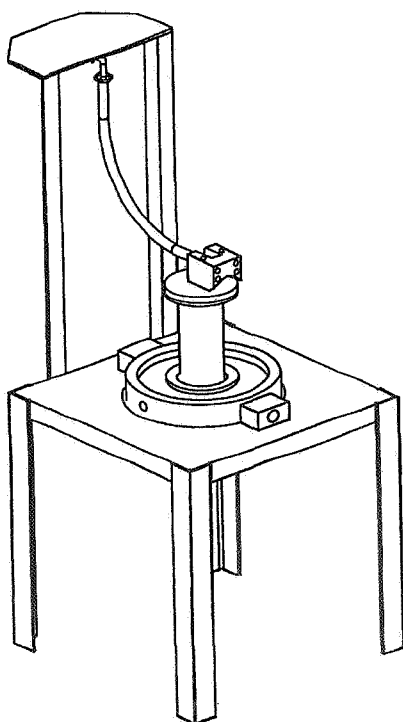
**Figure 4. Revised Layout**



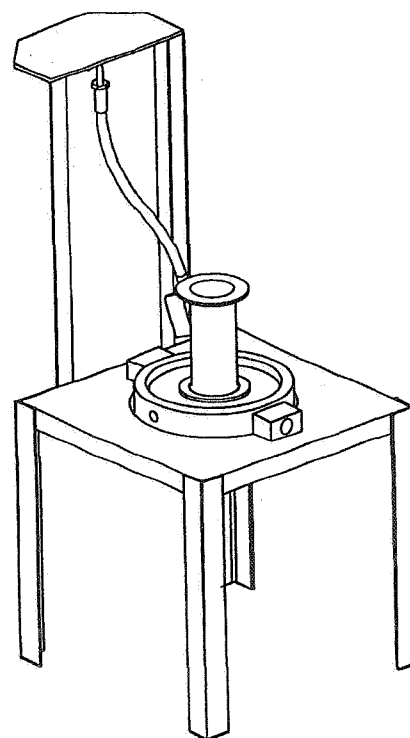
**MacDonald's Arch**



**Lazy D**



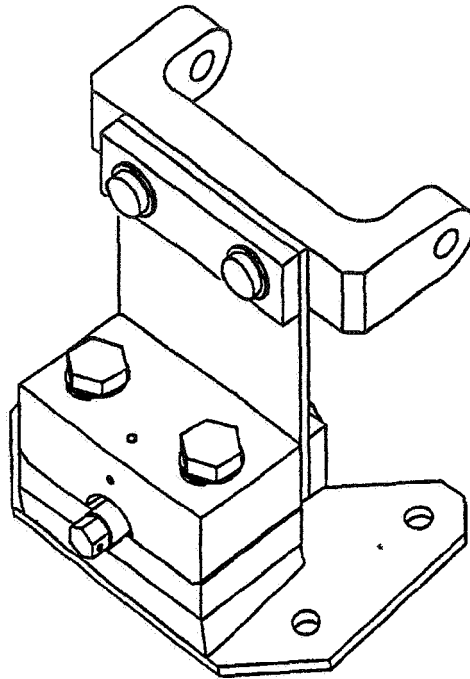
**J Configuration**



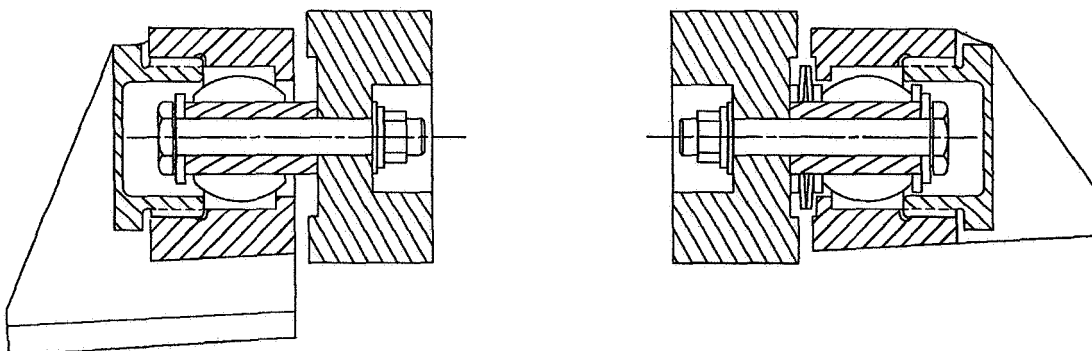
**Esse Configuration**

**Figure 5.**





**Figure 6.**



**Figure 7.**



515-39  
50443 ✓  
125129  
p.16

## Advances in the Analysis and Design of Constant-Torque Springs

John R. McGuire\* and Joseph A. Yura\*\*

### Abstract

In order to improve the design procedure of constant-torque springs used in aerospace applications, several new analysis techniques have been developed. These techniques make it possible to accurately construct a torque-rotation curve for any general constant-torque spring configuration. These new techniques allow for friction in the system to be included in the analysis, an area of analysis that has heretofore been unexplored. The new analysis techniques also include solutions for the deflected shape of the spring as well as solutions for drum and roller support reaction forces. A design procedure incorporating these new capabilities is presented.

### Introduction

Within the aerospace industry the constant-torque spring fulfills an important role. Many spacecraft, such as earth orbiting satellites and interplanetary explorers, once separated from a launch vehicle, must deploy several appendages, such as solar array panels, antennas, and sensory devices. The multi-layered constant-torque spring is often used as a power source to do this (Figures 1 and 2).

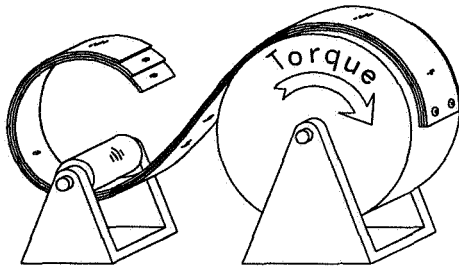


Figure 1. Layered Constant-Torque Spring

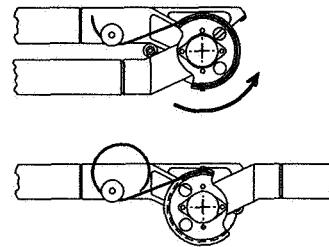


Figure 2. Typical 180° Hinge

The reason for its preference over other power sources includes the fact that the constant torque characteristic satisfies torque requirements over the entire deflection range, while at the same time minimizing the energy to be damped, also the constant-torque characteristic simplifies modeling of the system.

### Current Design Difficulties

Although the constant-torque spring is widely used, current analysis and design procedures are restrictive and inefficient. Design charts are provided by spring manufacturers for a finite number of "set" configurations. However, if the engineer

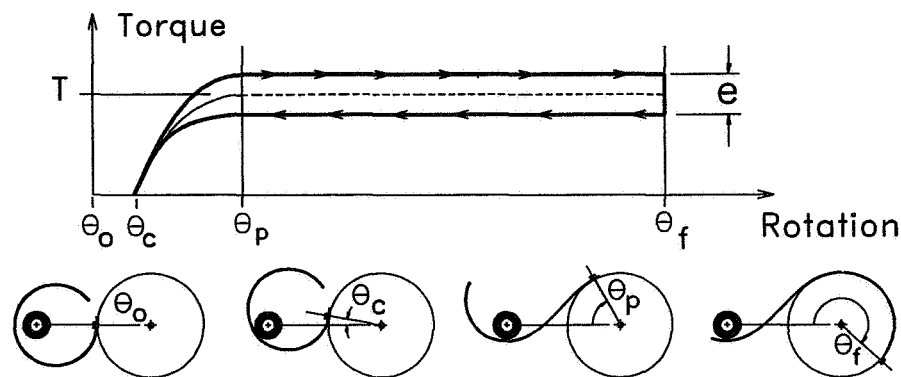
---

\*NASA - Goddard Space Flight Center, Greenbelt, MD

\*\*The University of Texas at Austin, Austin, TX

wishes to deviate from the limited selection, very little about the behavior of the spring can be predicted. Typically, adequate information about the behavior of the spring is not known until after tests are performed to determine the spring's behavior. This results in a time consuming trial and error design process.

To efficiently design a constant-torque spring, the torque-rotation response of the spring throughout the entire range of rotation must be accurately known. Figure 3 shows a typical torque-rotation response curve. The constant portion of the curve can be described using four basic parameters. The constant or average torque value  $T$ , the amount of hysteresis due to friction in the system  $e$ , the rotation required to develop the full resistance of the spring  $\theta_p$ , and the maximum or final rotation at which the spring would slip off the roller  $\theta_f$ .



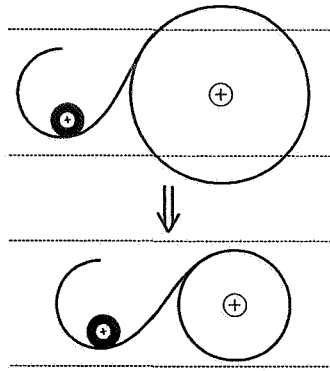
**Figure 3. Typical Torque-Rotation Curve**

In the past, the only parameter that could be accurately predicted for any general spring configuration was  $T$  (Reference 1). There were no analytical methods available for calculating  $e$ ,  $\theta_p$ , or  $\theta_f$  for the general case.

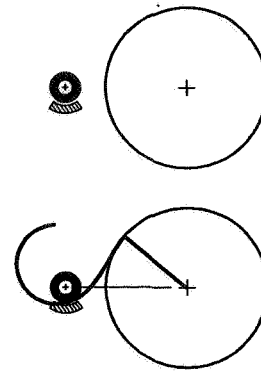
The inability to accurately predict the torque-rotation curve has led to difficulties. For example, the magnitude of the hysteresis in the system is generally unknown. If  $e$  can not be estimated analytically, a trial and error design procedure is required in order to optimize the performance of the spring.

In the case shown in Figure 4, the drum size was decreased due to operating space considerations. Since the ratio of drum size to spring size deviates from standard published design charts, no information was available as to the minimum rotation ( $\theta_p$ ) required to develop the full operating torque and could only be confirmed by testing after fabrication of the mechanism. If  $\theta_p$  could have been determined analytically the testing could have been eliminated or at least reduced.

In the past there have also been no methods available for calculating the deflected shape of the spring. In many cases it is quite advantageous to know the deflected shape and position of the spring. First, calculating the shape of the deflection curve is



**Figure 4. Non-Standard Ratio of Drum Diameter to Spring Diameter**



**Figure 5. Guard-Rail Interferes with Spring**

advantageous because the exact length of the spring can be determined; there are also other subtle advantages. Figure 5 shows a configuration that was designed with a roller-guard to protect the spring. Since the deflected shape of the spring was unknown, the roller-guard was placed in the most logical position, directly under the roller. However, after the system was assembled it became apparent that the deflected shape of the spring was different than assumed and that the roller-guard would interfere with the spring. This resulted in a trial and error design process.

### Testing Program

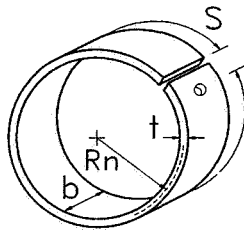
In order to develop analysis and design techniques so that problems similar to those mentioned above can be avoided an experimental program investigating several aspects of the behavior of the constant-torque spring was carried out at NASA's Goddard Space Flight Center and at The University of Texas at Austin. The results of these tests have led to the development of analysis procedures for completely defining the torque-rotation response of a constant-torque spring, including the effects of friction. Furthermore, the differential equation describing the deflected shape of the spring has been solved for, making it possible to describe the shape of the spring in the loaded configuration and possible to determine the support reaction forces created by the spring. Results will be presented herein that show that the methods developed accurately describe the deflected shape of the spring, and accurately predict the important parameters necessary for constructing the torque-rotation curve.

### Definitions and Assumptions

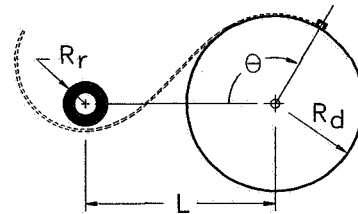
The geometry of the spring coil is uniquely defined by the following fundamental parameters: the width of the spring  $b$ , the thickness of the spring  $t$ , the natural radius of the spring  $R_n$ , the length of the spring  $S$ , and in the case of a multi-layered spring, the number of spring layers  $n$  (Figure 6). The drum-roller configuration, as shown in Figure 7, consists of the radius of the drum  $R_d$ , the radius of the roller  $R_r$ , the distance between the center of the drum and the center of the roller  $L$ , and the rotation of the

**Table 1. Summary of System Parameters and Symbols Used**

<u>Spring Fundamental Geometry</u> Spring width (b) Spring thickness (t) Spring natural radius ( $R_n$ ) Spring length (S) Number of spring layers (n)	<u>Spring Material and Section Properties</u> Young's modulus (E) Yield Strength ( $\sigma_y$ ) Bending stiffness (I) $I = bt^3/12$
<u>Drum-roller Fundamental Geometry</u> Drum radius ( $R_d$ ) Roller radius ( $R_r$ ) Drum to roller dist (L) Drum rotation ( $\theta$ )	<u>Miscellaneous Parameters</u> Roller coefficient of friction (f)
<u>Secondary Geometric Parameters</u> Spring Initial Diameter (ID) $ID = 2R_n$ Spring natural curvature ( $\phi_n$ ) $\phi_n = 1/R_n$ Spring thickness to width ratio (b/t) Spring curvature ratio ( $\beta$ ) $\beta = 2R_n/t$ Spring to drum ratio ( $\alpha$ ) $\alpha = R_d/R_n$	<u>Geometric Assumptions</u> Spring width is constant Spring thickness is constant Spring natural radius is constant All spring layers are uniformly shaped Drum is circular and rotates about its center



**Figure 6. Geometrical Parameters of the Spring Coil**



**Figure 7. Geometrical Parameters of the Drum and Roller**

drum  $\theta$ . These parameters alone uniquely define the drum roller configuration. Definitions of other parameters and symbols are summarized in Table 1.

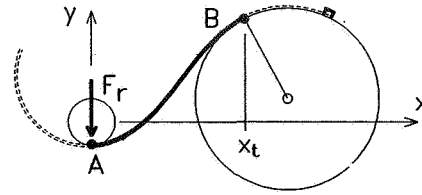
### The Deflected Shape of the Spring

In this section equations which describe the deflected shape of the spring are presented and two numerical methods for calculating the deflected shape of the spring are proposed. Results using these methods are then compared to test results from the experimental program.

The deformed shape of the loaded spring will be described as a function. Therefore it is necessary to select a coordinate system that allows for only a single value of  $y$  for each value of  $x$ . It is also advantageous to select a coordinate system that allows for as many initial and final values as possible to be defined. For this purpose the coordinate system shown in Figure 8 was selected. The portion of the spring for which the deflected shape is unknown is that segment between point A, the point where the

spring touches the roller, and point B, the point where the spring becomes tangent to the drum. This is the segment for which the deflection curve must be solved.

<u>Initial values at A</u>	<u>Final values at B</u>
$y(0) = -R_r$	$y(x_t) = \text{unknown}$
$\theta(0) = 0$	$\theta(x_t) = \text{unknown}$
$\phi(0) = 1/R_n$	$\phi(x_t) = -1/R_d$



**Figure 8. Coordinate System**

The origin of the coordinate system is the center of the roller. The angular orientation of the coordinate system is not referenced to the drum, but to the roller reaction force  $F_r$ . This means that the location of point B and the location of the center of the drum will be unknown. Since  $F_r$  must always pass through the center of the roller,  $F_r$  will always be collinear with the y axis. Therefore point A will always be at  $x = 0$ , and  $F_r$  will always be perpendicular to the spring at point A. This is advantageous because the bending moment  $M$  at any point along the spring can be simply expressed as the product of  $F_r$  and the x coordinate of the point of interest ( $M = F_r x$ ). This will be true regardless of the effects of large deflections. The change in curvature of the deflection curve is related to the magnitude of the bending moment ( $M = \Delta\phi EI$ ). Using these relationships it can be shown that the curvature, slope, and deflection at any point along the curve can be expressed using Equations 1, 2, and 3 respectively (Reference 2).

$$\text{Curvature} \quad \phi = \phi_n - \frac{F_r x}{EI} \quad (1)$$

$$\text{Slope} \quad \theta = \sin^{-1} \left[ \phi_n x - \frac{F_r x^2}{2EI} \right] \quad (2)$$

$$\text{Deflection} \quad y = \int_0^x \tan \left[ \sin^{-1} \left( \phi_n x - \frac{F_r x^2}{2EI} \right) \right] dx \quad (3)$$

It should be noted that the curvature at point B is negative and is equal in magnitude to the curvature of the surface of the drum. Therefore, substituting  $-1/R_d$  for  $\phi$  in Equation 1 results in the following expression for  $x_t$ .

$$x_t = \left( \frac{1}{R_n} + \frac{1}{R_d} \right) \frac{EI}{F_r} \quad (4)$$

Equation 3 is the expression that describes the deflected shape of the spring. Because

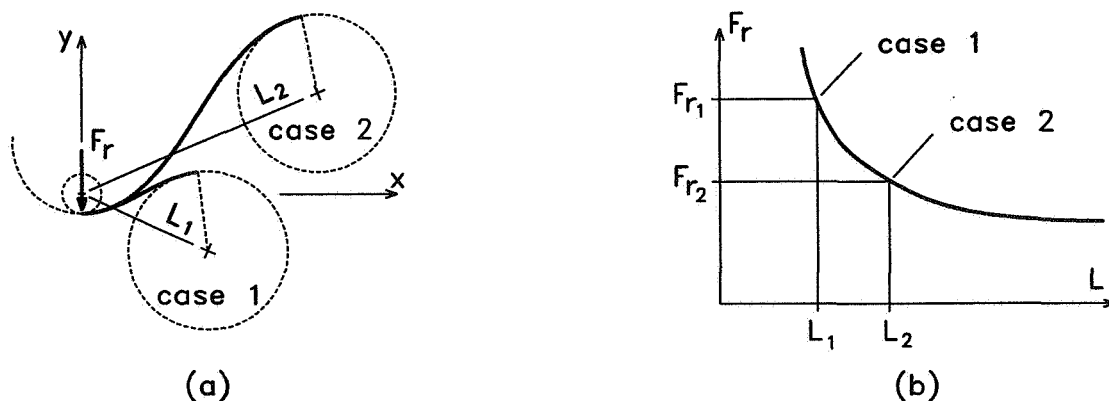
there is not a closed form solution for the integral expression, numerical calculation of the integral is required. Furthermore, because the reaction force  $F_r$  is also an unknown and is a function of the displacement, an iterative solution will be required. This, of course, is consistent with the non-linear characteristic of the problem.

Two numerical methods for calculating the deformed shape of the spring will be introduced. Theoretical results obtained using these two methods are then compared with test results of the experimental program.

**Method 1: Numerical integration.** This method uses the equations for the curvature, slope, and deflection of the spring. The values,  $\phi$ ,  $\theta$  and  $y$ , are dependent upon the magnitude of the roller reaction force  $F_r$ , but  $F_r$  is conversely dependent upon  $L$ , the distance between the roller and the drum. Therefore an iterative solution based upon the roller reaction force will be necessary. If the deformed shape calculated using Equation 4 results in a drum-roller distance ( $L$ ) that is equal to the actual drum-roller distance, then the solution is based upon the correct roller reaction force. The relation between  $L$  and the roller reaction force is shown in Figure 9. If the roller is close to the drum (i.e.  $L$  is small) the roller reaction force is large. If  $L$  is large, however, the roller reaction force approaches a minimum.

To calculate  $L$ , the position of the center of the drum must be determined. The position of the center of the drum is calculated by first determining the  $x$  and  $y$  coordinates of the tangent point B and the slope of the deflection curve at B. Since a radial of the drum will be perpendicular to the deflection curve at point B the position of the center of the drum can be calculated.

It should also be noted that it can be shown that the rotation required to develop the full strength of the spring ( $\theta_p$ ) is equal to the rotation to the tangent point B (Reference 2). This is the angle with vertex at the center of the drum, measured from the center of the roller to the tangent point B (see Figure 10).



**Figure 9. Relation Between the Roller Reaction Force  $F_r$  and  $L$**



The procedure for finding the correct solution can be summarized as follows:

- \* Assume a value for  $F_r$ .
- \* Use Equation 4 to calculate  $x_t$ .
- \* Use Equation 2 to calculate the slope of the deflection curve at point B.
- \* Solve for the y value of point B by numerically evaluating Equation 3.
- \* Now that the position and slope of the curve at point B have been determined, calculate the coordinates of the center of the drum.
- \* Calculate L and compare to the actual L.
- \* If the calculated value of L differs from the real value, adjust  $F_r$  accordingly and repeat until the value of  $F_r$  that corresponds to the real value of L is converged upon.
- \* Use true  $F_r$  to calculate deflection, rotation, or curvature for any point along the deflection curve. Since the position of point B and the center of the drum are known, the angle  $\theta_p$  can also be calculated.

**Method 2: Finite segments.** The second method for calculating the deformed shape relies only upon the expression for the curvature (Equation 2). As in the first method a value of  $F_r$  is assumed. However, in this method the driving parameter is s, the distance measured along the deformed curve from point A. Recalling that the curvature is defined as the change in slope per unit length ( $\phi = d\theta/ds$ ) the following scheme is used to calculate points along the deformed shape of the spring.

<u>Initial values</u>	<u>Differential values</u>	<u>Updated values</u>
$s = 0$	$ds = \text{small finite value}$	$s = s + ds$
$\theta = 0$	$d\theta = \phi ds$	$\theta = \theta + d\theta$
$x = 0$	$dx = ds \cos\theta$	$x = x + dx$
$y = -1/R_r$	$dy = ds \sin\theta$	$y = y + dy$
$\phi = \phi_n$		$\phi = \phi_n - F_r x/EI$

A value for the reaction force is assumed. Initial values corresponding with the actual restraint conditions at point A are set. These values are then updated using differential values for each additional segment  $ds$  along the curve. At some point along the curve the curvature will become equal to the curvature of the surface of the drum. This signifies that the spring is now tangent to the drum. The updated values at this point are for point B, the tangent point of the drum. The x, y, and slope values for that point are used to calculate the position of the center of the drum and the corresponding value of L. This calculated value of L is compared to the real value of L and then the assumed value of  $F_r$  is adjusted accordingly. This process is repeated until the correct solution is converged upon.

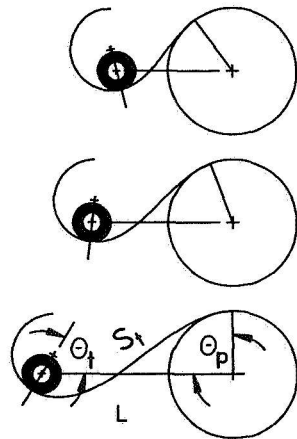
An AutoLISP algorithm which uses this method has been developed. This algorithm solves for the deflected shape of the spring and plots the spring, the drum, and the roller as an AutoCAD drawing file. Analytical results using this routine will be used in the comparison of the test results.

Comparison with test results. In solving for the displaced shape of the spring, several important characteristics of the spring have been revealed. Of particular interest are the following:

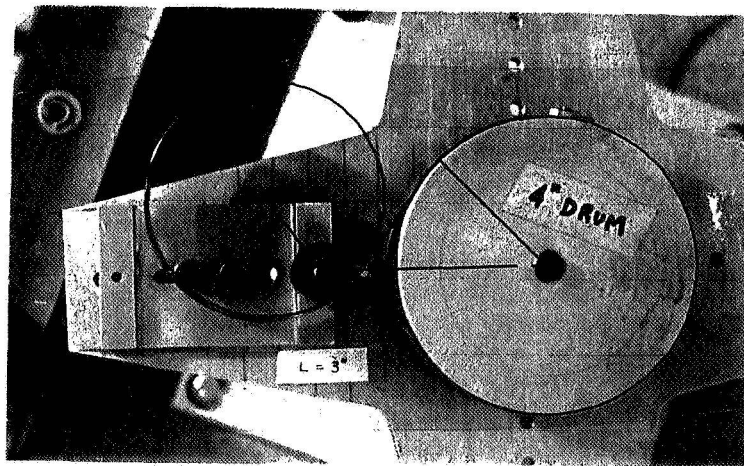
- The general shape of the spring
- The rotation required to develop the full strength of the spring  $\theta_p$
- The angle of contact between the spring and roller  $\theta_t$
- The tangent-to-tangent segment length  $s_t$

These four characteristics will be used to compare the analytical solution with test results. These values vary for each unique combination of spring size and drum-roller configuration. Figure 10 illustrates qualitatively how each of these characteristics will vary just by changing the distance between the drum and roller.

The first characteristic to be addressed is the general shape of the spring. Figure 11 shows a photograph of the deformed shape of a typical spring in the loaded position. Superposed on the photograph is a plot of the analytical solution for the deformed shape of the spring. Figure 11 is still somewhat of a qualitative comparison, but it is important because it shows that space requirements can be checked analytically rather than by building a prototype to see if the deflected spring will have clearance problems.



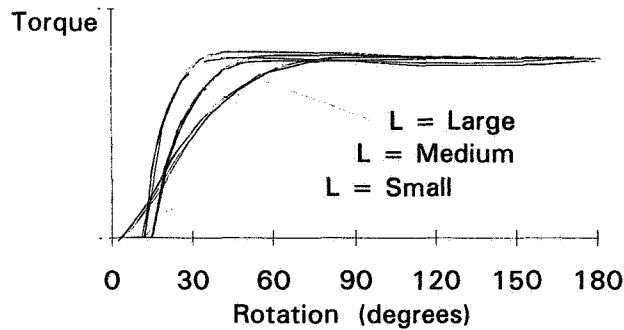
**Figure 10. Variation in the Deflected Shape of the Spring**



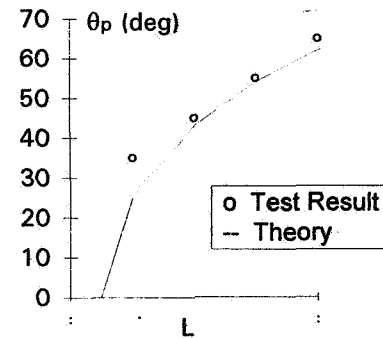
**Figure 11. Deformed Shape of a Spring**

The next characteristic to be compared is the angle  $\theta_p$ . This is the rotation at which the spring develops its full strength.  $\theta_p$  varies for different spring sizes and drum-roller configurations. Even for a given spring, drum, and roller,  $\theta_p$  will vary if the distance between the drum and roller is changed. Figure 12 shows torque-rotation curves for three different values of  $L$  using the same spring, drum, and roller. When  $L$  is small, in other words when the roller is close to the drum, it takes less rotation to develop the full torque of the spring than when  $L$  is large.  $\theta_p$  can vary by as much as 90 degrees in some cases depending upon the distance between the drum and roller. Table 2

compares values of  $\theta_p$  calculated using method 1 and method 2 with test results for a typical constant-torque spring configuration. Except for small values of  $L$  the calculated values are accurate to within 2 or 3 degrees. This is because, as illustrated in Figure 13, the slope of the curve is so steep that small errors in measuring  $L$  result in large errors for  $\theta_p$ .



**Figure 12. Torque-Rotation Curves Illustrate the Variability of  $\theta_p$**



**Figure 13.  $\theta_p$ , Comparison of Analysis with Test Results**

The other characteristics of interest are the angle of contact between the spring and the roller (this angle is called  $\theta_t$  and defines the orientation of the roller reaction force; see Figure 10), and the tangent to tangent segment length  $s_t$ .  $s_t$  is directly calculated when using the finite segment method, and can also be included in the calculation when using the numerical integration method.

Table 2 compares values calculated using method 1 and method 2 with test results for a typical constant-torque spring configuration. The results presented are for single layered springs but are also comparable to results for layered springs. The results of tests for multi-layered springs (Reference 2) demonstrate that the characteristics of the deflected shape of a layered spring do not significantly differ from the characteristics of the individual springs used to make the layered spring.

**Table 2. Comparison of Test Results to Methods 1 and 2**

L (mm)	$\theta_p$ (deg)			$\theta_t$ (deg)			$s_t$ (mm)		
	Test Result	Method 1	Method 2	Test Result	Method 1	Method 2	Test Result	Method 1	Method 2
44	35	25	25	144	145	145	20	20	20
50	45	43	43	122	120	120	36	38	38
57	55	54	54	105	104	104	48	50	50
63	65	62	62	90	92	92	58	62	62
70	70	69	69	81	83	83	72	74	74

## The Effects of Friction

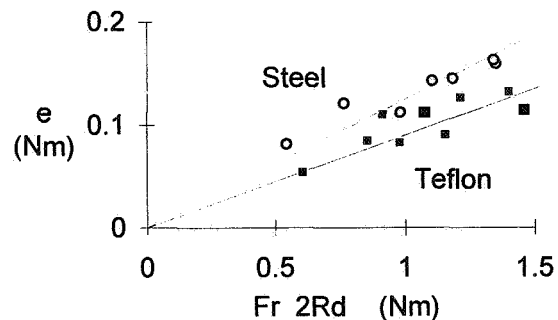
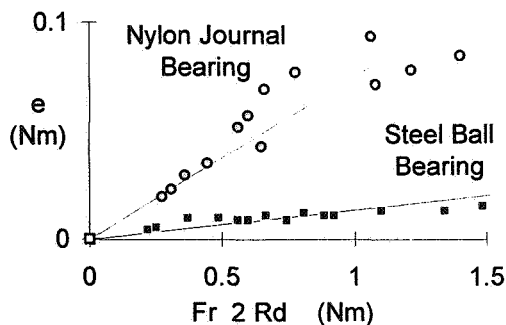
There are two sources of friction that need to be considered: the friction in the roller and the inter-laminar friction between spring layers.

Effects of friction in the roller. First it is necessary to differentiate between the two types of rollers commonly used. There are rollers that rotate and there are rollers that are just a fixed shaft. The first type of roller rotates about its center and may make use of a journal bearing, a ball bearing or some other type of bearing. This type of roller will be called a "bearing roller". This is the typical roller shown in all the previous illustrations. The second type of roller is not an actual roller, but is a fixed post or shaft that cannot rotate. Using a fixed shaft in place of a roller is not uncommon; many constant torque-spring mechanisms are designed using simply a steel pin for a roller. This type of roller will be called a "sliding roller" because when the spring is loaded or unloaded the spring slides along the surface of the fixed pin or shaft. It should be noted that if the typical bearing type roller were to bind or "freeze up" it would become a sliding roller, too. So the behavior of the sliding roller is of interest regardless of the type of roller used. In the case of a sliding roller, friction occurs when the surface of the spring actually drags across the surface of the roller. In the case of a bearing roller friction occurs within the bearing and not between the spring and the roller.

It can be shown that the hysteresis  $e$  in the torque-rotation curve due to the effects of friction in the roller can be expressed using Equation 5 (Reference 2). Where  $R_d$  is the radius of the drum,  $F_r$  is the roller reaction force obtained analytically using the methods described in the previous sections, and  $f$  is the "coefficient of friction" of the roller.

$$e = f F_r 2 R_d \quad (5)$$

Test results for a wide variety of constant-torque spring configurations demonstrate that this relationship is indeed linear (Figures 14. and 15). In Figures 14 and 15 the slope of the lines represents the coefficient of friction of the roller  $f$ . For these plots  $e$  was measured and  $F_r$  was calculated.

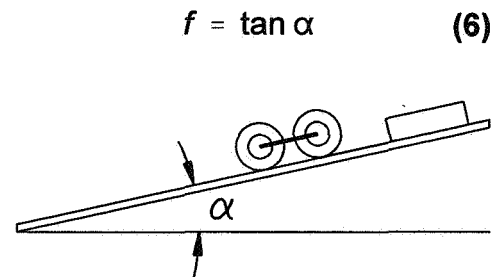


**Figure 14. Bearing Rollers:  $e$  vs  $F_r 2R_d$     Figure 15. Sliding Rollers:  $e$  vs  $F_r 2R_d$**

$f$  can also be determined experimentally using the classical technique illustrated in Figure 16. In this method a length of spring coil is secured to a flat surface. Then the roller that will be used is placed on top of the spring. (If it is a bearing roller, the two axle configuration is used; if it is a sliding roller, the roller is oriented such that it will slide down the slope rather than roll.) The flat surface is then raised to the angle at which the forces of friction are overcome by the forces of gravity. The roller coefficient of friction is calculated using Equation 6. Table 3 compares values of  $f$  obtained using the sliding test with the slope of the  $e$  vs  $F_r/2R_d$  curves shown in Figures 14 and 15.

**Table 3. Predicting Values of  $f$**

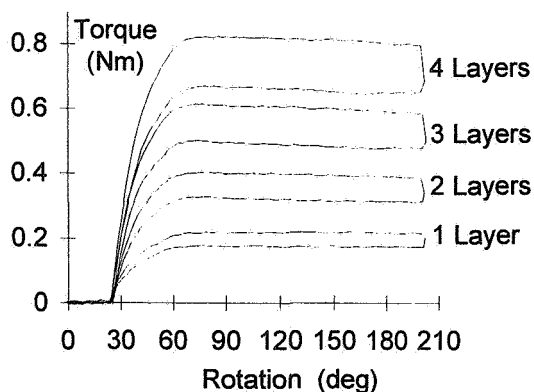
	Slope of $e$ vs $F_r/2R_d$ line	Sliding Test
Steel Sliding Roller	0.12	0.14
Teflon Sliding Roller	0.09	0.09
Nylon Journal Bearing	0.13	0.14
Steel Ball bearing	0.013	0.02



**Figure 16. Testing for  $f$**

As the values of  $f$  get small (see steel ball bearing results) it becomes difficult to accurately measure  $e$  or predict  $f$  using the sliding test. Fortunately, for values of  $f$  this small the effect of friction on the torque-rotation curve is negligible.

The effects of friction between spring layers. Test results demonstrating the effects of friction between spring layers for a four-layered spring configuration made of type 301 stainless steel are shown in Figure 17. Torque-rotation curves for a one-, two-, three-, and four-layered spring are shown. With the addition of each succeeding spring layer



**Figure 17. Torque-Rotation Curves for Multiple Layers of Springs**

**Table 4. Hysteresis by Spring Layer**

Spring Combination	$e$ (Nm) measured	$\Sigma e$	%
Layer 1 only	.035	-	-
Layer 2 only	.036	-	-
Layer 3 only	.038	-	-
Layer 4 only	.038	-	-
Layers 1, 2	.071	.071	100%
Layers 1, 2, 3	.106	.109	97%
Layers 1, 2, 3, 4	.142	.147	97%

the magnitude of the hysteresis increases. This could lead to the conclusion that the increased hysteresis is related to the friction between each additional layer. However, it must be remembered that with the addition of each additional layer the roller reaction force also increases, and hence the hysteresis due to friction in the roller increases. In order to determine how much of the hysteresis is due to relative motion of the spring layers, the increased hysteresis due to the roller must first be subtracted out. The hysteresis of each individual spring and the hysteresis of multiple spring combinations are given in Table 4. By subtracting out the hysteresis due to the roller, we find that the remaining hysteresis due to relative sliding between spring layers was smaller than the accuracy of the test. Therefore, it is concluded that hysteresis due to relative sliding of spring layers is insignificantly small compared to the effects of friction in the roller.

### Design Example

The following is a design example that incorporates the new analysis techniques. The design requirements shown in Table 6 will be used. Safety factors are examples and do not represent recommendations.

**Table 6. Example Design Requirements**

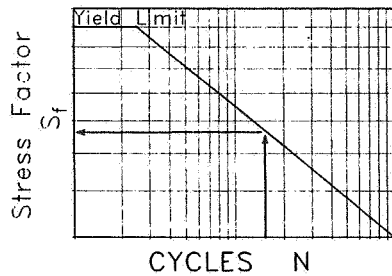
	Required Value	Safety Factor	Design Value
Torque	2.5 Nm ( $T_{REQ}$ )	4	10 Nm ( $T_{DES}$ )
Rotation	180° ( $\phi_{REQ}$ )	$\phi_{LM} = 10^\circ, \phi_{UM} = 10^\circ$	200° ( $\phi_{LM} + \phi_{REQ} + \phi_{UM}$ )
Fatigue Life	500 cycles	4	2,000 cycles
Operating Space	120 mm x 200 mm	1	120 mm x 200 mm

Upper and Lower Margins of Safety for Rotation

Determine the spring material. Spring manufacturers can help in determining the appropriate spring material to be used. Type 301 stainless steel is the most common material used and will be selected for this example.

Determine the stress factor. Using a fatigue life curve such as the one shown in Figure 18, determine the stress factor  $S_f$  corresponding to the fatigue life design value. (Spring manufacturers can provide stress factors corresponding to the fatigue life of their specific products.) The stress factor is proportional to the cyclic stress range in the spring and is equal to the product of the thickness of the spring and the change in curvature the spring will experience (Equation 7). For the material used in this example the stress factor for 2,000 cycles is 0.0275.



$$S_f = t \left( \frac{1}{R_n} + \frac{1}{R_d} \right) \quad (7)$$

**Figure 18. Fatigue Life Curve**

Estimate the drum size. The drum must fit within the 120 mm operating space. Therefore, a drum diameter of 100 mm will be chosen; hence  $R_d = 50$  mm. Minimizing the drum size can reduce the size and weight of the mechanism, so hopefully  $R_d$  can be reduced even more. But for starters we will use a diameter of 100 mm. In the case that there are no space requirements, use your best judgement to choose a “reasonable” drum diameter to start with.

Determine  $\alpha$ , the ratio of drum diameter to spring diameter. Use the recommendations in Table 7 to select  $\alpha$  ( $\alpha = R_d/R_n$ ). Most constant-torque spring design guides recommend that the drum diameter be twice the spring diameter ( $\alpha = 2$ ). However, in order to optimize mass and maximize rotation, this author recommends  $\alpha = 1.25$ .  $\alpha$  should never be less than 1.0 because instabilities can occur when the drum diameter is less than the spring diameter.

**Table 7. Recommended Values of  $\alpha$**

$\alpha$	Achievable Rotation	Comments
Less than 1	-	Causes instability
1	270° ~ 300°	Achieves maximum rotation range
1.25	200° ~ 230°	Authors recommendation
1.5	150° ~ 180°	
1.75	115° ~ 145°	
2	90° ~ 120°	Commonly used
Greater than 2	less than 90°	Small rotation ranges

Determine the natural radius of the spring coil. Based upon  $\alpha$  the natural radius of the spring coil is determined.

$$R_n = \frac{R_d}{\alpha} = \frac{50 \text{ mm}}{1.25} = 40 \text{ mm}$$

Calculate the maximum allowable spring thickness  $t_{\max}$

$$t_{\max} = \frac{S_f}{\left( \frac{1}{R_n} + \frac{1}{R_d} \right)} = \frac{S_f R_d}{(\alpha + 1)} = \frac{(0.0275) (40 \text{ mm})}{(1.25 + 1)} = 0.49 \text{ mm}$$

Select a spring. Select a spring with a thickness smaller than or equal to the maximum allowable thickness. If using stock springs, the catalog will give the width (b) of the spring and the initial diameter (ID) of the spring. The natural radius of stock springs must be modified to the design value if optimization of the mechanism is desired. If the spring is to be ordered to specifications, specify a thickness smaller than the maximum allowable thickness and specify a width approximately 60 to 100 times greater than the thickness (Reference 1). For this example the next standard thickness smaller than  $t_{\max}$  is 0.4064 mm (0.016 in).

Determine the roller diameter. The roller diameter must be smaller than the spring ID. For this example a roller diameter of 25.4 mm will be used.  $25.4 < 80$ , therefore, OK.

Determine the drum-to-roller distance L. The distance L influences the magnitude of  $\theta_p$ , the magnitude of the roller reaction force  $F_r$ , and the inclination of the roller reaction force  $\theta_t$ . In order to optimize mass, L should be small. However, if L is too small the magnitude of the roller reaction will increase, resulting in large hysteresis effects. Based upon results of the testing program the author recommends using a value of L that results in an angle of inclination of  $110^\circ$  for the roller reaction force. An analysis of the spring is carried out iteratively for various values of L until the one which results in  $\theta_t = 110^\circ$  is converged upon. Figure 19 shows the results of such a routine for this design example. Note how the appropriate value of L was selected so that  $\theta_t$  would result in a value of  $110^\circ$ .

#### DRUM-ROLLER CONFIGURATION

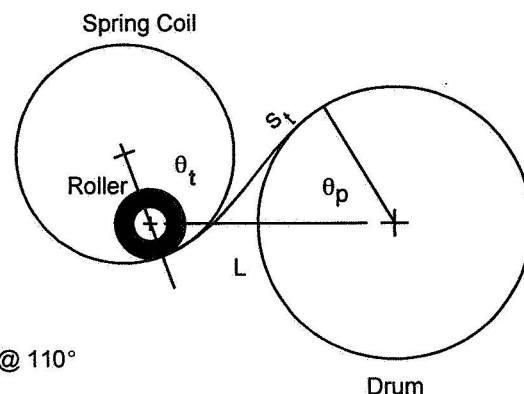
Drum diameter = 100  
 Roller diameter = 25.4  
 Center-Center dist (L) = 89.5

#### SPRING DATA

Thickness (t) = 0.4064  
 Width (w) = 25.4  
 Initial Diameter (ID) = 80  
 Young's Modulus (E) = 193,000

#### RESULTS OF ANALYSIS

Torque (T) = 1388  
 Roller reaction force ( $F_r$ ) = 16.54 @  $110^\circ$   
 Tangent to tangent length ( $s_t$ ) = 81.8  
 Minimum rotation ( $\theta_p$ ) = 59



**Figure 19. Results of Analysis (Units: Newtons, Millimeters)**



Calculate the constant-torque value T.

$$\begin{aligned}
 T &= \frac{E b t^3}{24} R_d \left( \frac{1}{R_n} + \frac{1}{R_d} \right)^2 \\
 &= \frac{(190,000 \text{ N mm}^2) (25.4 \text{ mm}) (0.4063 \text{ mm})^3}{24} (50 \text{ mm}) \left( \frac{1}{(40 \text{ mm})} + \frac{1}{(50 \text{ mm})} \right)^2 \\
 &= 1,388 \text{ Nmm} = 1.388 \text{ Nm}
 \end{aligned}$$

Calculate the magnitude of the hysteresis e. We will assume that a “sliding test” resulted in a roller coefficient of friction of 0.10.

$$e = f F_r 2 R_d = (0.1) (16.54 \text{ N}) (50 \text{ mm}) = 82.7 \text{ N mm} = 0.0827 \text{ Nm}$$

Calculate the effective torque for one layer  $T_{\text{eff}}$ . The effective torque is equal to the calculated torque less one half of the hysteresis. In this case the hysteresis resulted in a 3% loss of torque.

$$T_{\text{eff}} = T - \frac{e}{2} = 1.388 \text{ Nm} - \frac{0.0827 \text{ Nm}}{2} = 1.347 \text{ Nm}$$

Calculate the number of spring layers required n. Divide the design torque by the effective torque of one layer to determine how many spring layers are required. In order to optimize mass this author recommends using between 5 and 10 layers. If less than 5 layers are required, the drum can be made smaller and the analysis procedure repeated. If more than 10 layers are required, the drum should be made larger and the analysis procedure repeated. In the case that the drum cannot be made larger, more than 10 layers could be used, but tests to confirm stability should be performed.

$$n = \frac{T_{\text{des}}}{T_{\text{eff}}} = \frac{10 \text{ Nm}}{1.347 \text{ Nm}} = 7.4 \rightarrow 8 \text{ layers}$$

This design has 8 layers, and will therefore be accepted. The design could be fine tuned a bit by adjusting the drum diameter and repeating the procedure to this point, however, we shall accept this design and proceed.

Calculate the required length of the spring S. This calculation is for one spring layer.

$$S = s_t + R_d \left( \phi_{\text{DES}} \times \frac{\pi}{180} \right) = 81.8 + (50) \left( 200^\circ \times \frac{\pi}{180} \right) = 256 \text{ mm.}$$

Calculate the maximum and minimum rotation values. These are the rotation values between which the mechanism should operate.

$$\theta_{\min} = \theta_p + \phi_{LM} = 59^\circ + 10^\circ = 69^\circ$$

$$\theta_{\max} = \theta_p + \phi_{LM} + \phi_{REQ} = 59^\circ + 10^\circ + 180^\circ = 249^\circ$$

This completes the proposed design procedure. The torque-rotation response of the spring is completely defined, the deflected shape of the spring is known, and all the important parameters required to specify the spring, drum, and roller have been determined. This design procedure, however, is only a recommendation, the analysis capabilities presented herein can, of course, be used to enhance other design procedures as needed.

### Conclusion

In order to improve the design and analysis procedure of constant-torque springs used in aerospace applications several new analysis techniques were developed along with a design procedure which incorporates these new capabilities. The new analysis techniques include solutions for the deflected shape of the spring, the roller reaction force, and the hysteresis effects of friction. Experimental results show that these new techniques are accurate and reliable, thus allowing several new aspects to be included in the design process.

The capacity to accurately calculate the deflected shape of the spring allows for space requirements and kinematic functionality of the spring mechanism to be checked analytically rather than using the time consuming process of trial and error.

### References

1. Votta, F. A. "The theory and design of long-deflection constant-force spring elements." Transactions of the ASME, (September, 1951). Vol 74.
2. McGuire, J. Analysis and Design of Constant-Torque Springs Used in Aerospace applications. Ph.D. Dissertation, The University of Texas at Austin, December, 1994.
3. Votta, F. A. "Constant-force springs for high output at short deflection." Machine Design, January 31, 1963. 102-106.

## Jettison System for a Large Inflatable Antenna

Don Jarosz\*, Steven Hendricks\*, Dave Landis\*, Craig Tooley\*\*, Greg Martins\*\*

### Abstract

This paper describes a jettison system used to separate a large, inflatable-deployable antenna from a free-flying spacecraft. The jettison system consists of four discrete Marman band clamps, released simultaneously via pyrotechnics. The design, analysis, analytical simulation, and testing of the system are discussed. Of particular note is the correlation of test results with the Marman band design calculations.

### Introduction & Mission Overview

The Spartan Inflatable Antenna Experiment (IAE) is a Space Shuttle-borne experiment designed to test the function and performance of an inflatable-deployable antenna reflector and structure in space. Described in this paper, the jettison system is key to the mission performance, since it separates the inflated antenna structure from the Spartan carrier spacecraft, thereby allowing the Spartan carrier to be retrieved by the Shuttle. The Spartan carrier and the IAE are briefly described to provide an understanding of the jettison system design requirements and constraints.

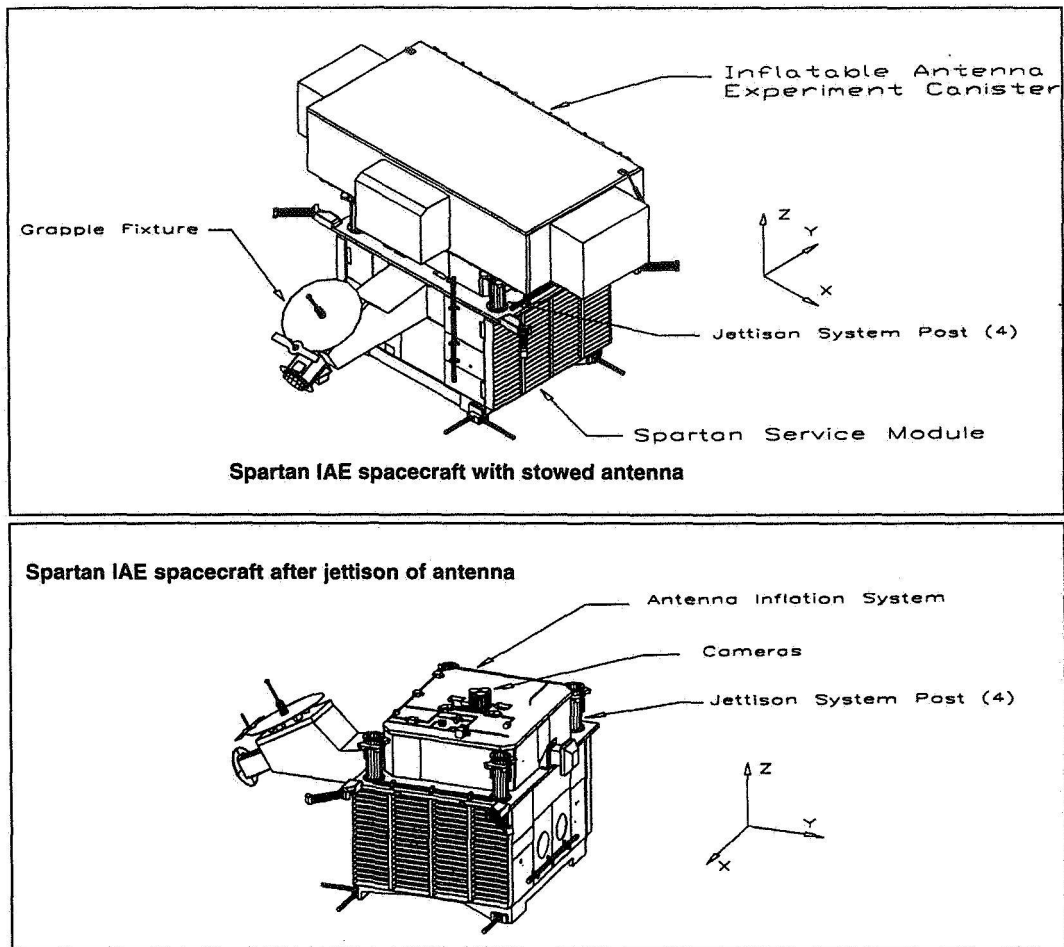
The Spartan Program provides access to low Earth orbit via the Space Shuttle and the Spartan carrier system. Spartan is an autonomous, reusable, 3-axis stabilized free flying spacecraft [1]. It is carried into orbit, deployed, and retrieved by the Shuttle. Spartan's simple, relatively generic interfaces to the Shuttle streamline and simplify both payload certification and accommodation on Shuttle missions. For each mission, the basic spacecraft system is adapted to accommodate the experiments while retaining the generic Spartan attitude control, command and data systems, thermal, and structural systems. The Spartan IAE spacecraft is shown in Figure 1.

The Inflatable Antenna Experiment [2] consists of an inflatable antenna approximately 31 m (101.7 ft) in length with a 14-meter (45.9-ft) off-axis parabolic reflector, cameras to record the antenna inflation, and optical equipment to measure the reflector surface precision. The reflector is aluminized Mylar with a clear Mylar canopy and is inflated to 0.00207 kPa (0.0003 psi). The inflatable structure consists of three struts and a torus made of neoprene-coated Kevlar and is inflated to 20.7 kPa (3 psi). The experiment objective is to demonstrate an antenna surface accuracy of 1 mm RMS. Figure 2 shows the inflated antenna, attached to the Spartan carrier. The antenna is deployed and inflated after the Shuttle crew has both released the Spartan spacecraft into autonomous free flight and maneuvered to a safe separation distance. The experiment will be completed in approximately 90 minutes after which the inflated antenna will be jettisoned from the Spartan carrier. The Spartan carrier is retrieved and re-berthed in the Shuttle bay. The overall mission scenario is shown in Figure 3.

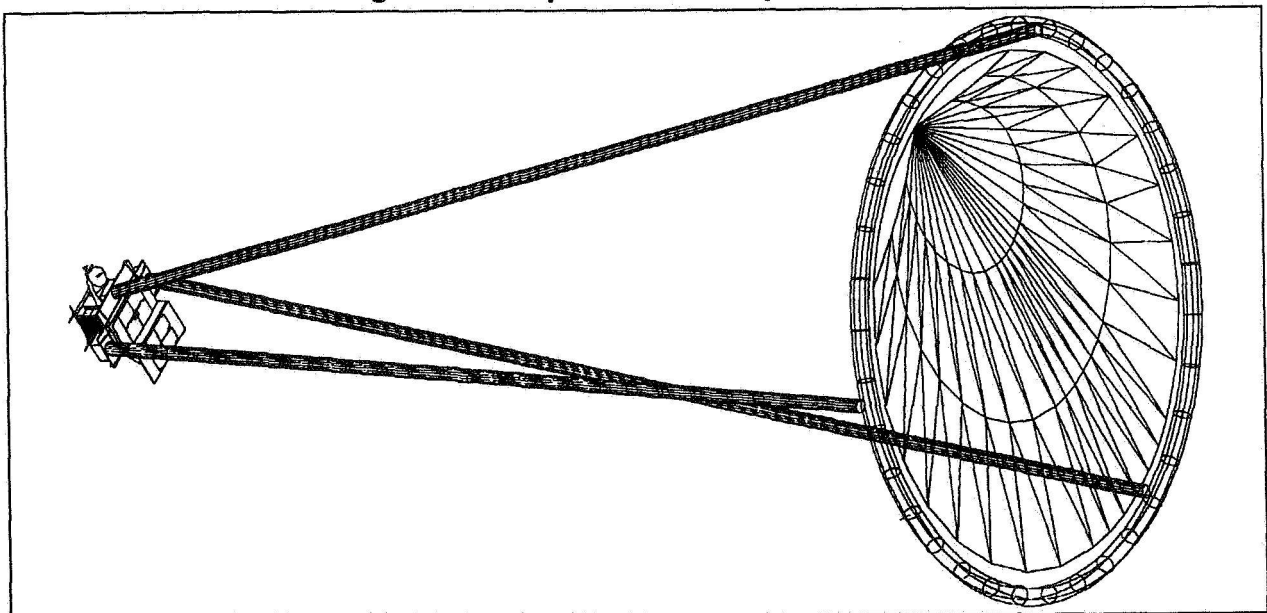
---

\* Swales & Associates Inc., Beltsville, MD

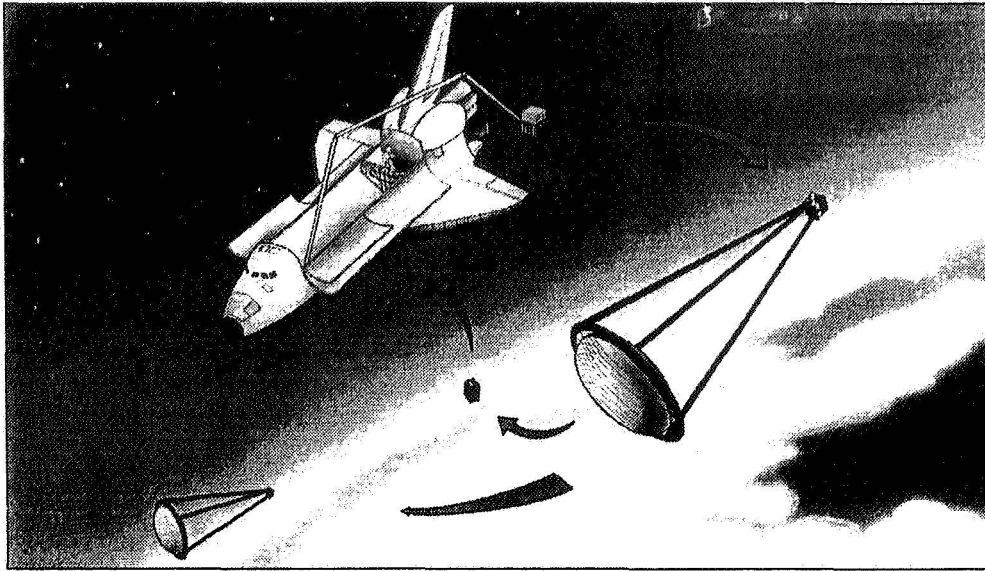
\*\* NASA Goddard Space Flight Center, Greenbelt, MD



**Figure 1. Spartan IAE Spacecraft**



**Figure 2. Spartan IAE with Antenna Inflated**



**Figure 3. Spartan IAE Mission**

## **Jettison System Design Requirements & Constraints**

### Physical & Structural Accommodation

The jettison system has to serve as the structural interface between the Spartan carrier and the IAE canister. The characteristics of both items were fixed prior to the design of the jettison system. The jettison system has to provide an adequate load path with sufficient margins to allow for large uncertainties in the loading environment. A 22.86-cm (9-in) diameter footprint was determined to be available to accommodate each of the four jettison system posts, which are the interfaces between the IAE and the Spartan carrier.

### Jettison Performance

The system must separate the IAE from the spacecraft with low tipoff rates and with a proper separation velocity profile. Low tipoff rates are necessary to ensure that 1) the spacecraft and the jettisoned antenna do not come into contact during separation, and 2) the carrier spacecraft is stable for retrieval by the Shuttle. Contact between the parts in relative motion could potentially prevent successful separation. Spacecraft body rates must be within the attitude control system capability to null them. The separation velocity profile must be sufficient to separate the spacecraft and the antenna without imparting forces that could buckle the inflated antenna. A buckled antenna could become entangled with the spacecraft. Failure to meet these requirements could create a situation in which retrieval by the Shuttle would be impossible.

### Flight Safety

Inadvertent actuation of the jettison system, while either in the Shuttle bay or in close proximity to the Shuttle, is considered a catastrophic hazard to the Shuttle crew. Key to a successful jettison system was a design which provides adequate control of the hazard when integrated with the Spartan systems that control it.

## Overall Jettison System Design

Preliminary design studies led to the selection of a pyrotechnically initiated Marman band system with coil springs providing the separation forces. The configuration of the Spartan carrier and the IAE dictated that four discrete attach points be simultaneously separated. The Marman band design provides both the high structural load carrying capacity and the required simultaneous separation action. A Marman band design was judged to be a reliable and inexpensive approach due to both its inherent simplicity and GSFC's extensive experience with Marman band separation systems. The major components of the jettison system design are the Marman band clamp/joint assembly, the pyrotechnic bolt cutter, the pushrod/spring assembly, and the structural posts (Figure 4).

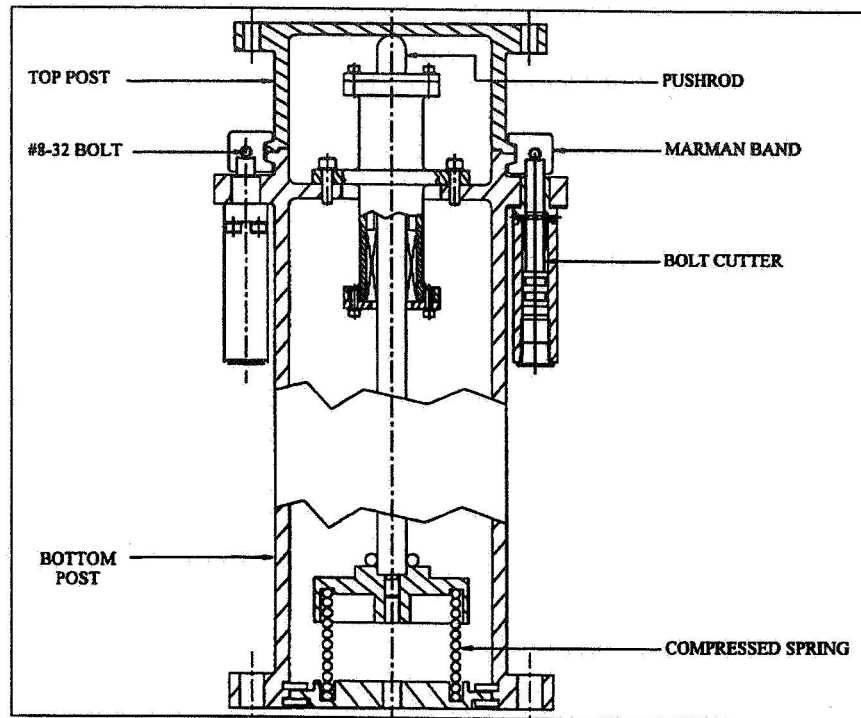
A spacecraft mass properties summary and the structural design limit load factors are given in Tables 1 and 2, respectively. These parameters, along with the relatively small clearances between the jettisoned antenna assembly and the carrier spacecraft, drove the detailed design and testing of the jettison system.

TABLE 1 SPARTAN IAE STRUCTURAL DESIGN LIMIT LOAD FACTORS				TABLE 2 SPARTAN IAE MASS PROPERTIES SUMMARY			
	X Axis	Y Axis	Z Axis		WEIGHT (kg)	C.G. (X,Y,Z cm)	Ixx Iyy Izz (kg.-m <sup>2</sup> )
TRANSLATIONAL, g	± 4.5	± 3.5	± 9.8	Carrier Spacecraft	847	63,-58,48	184, 150, 175
ROTATIONAL, rad/sec <sup>2</sup>	± 26.2	± 65.2	± 33.7	IAE (inflated)	329	76,-38, 836	47370, 47954, 4161

## Marman Band Design

The first Marman band design iteration for the IAE jettison posts consisted of a standard strip and shoe band, which could use either a guillotine cutter or an explosive bolt to release the band. Since the Shuttle program is sensitive to any kind of debris produced near a recoverable payload, the Marman band also required a catcher assembly. Due to the limited area in which the band had to fit and the correspondingly small size of the band and catcher components, the strip and shoe band design was abandoned. It was felt that a less costly and complicated design could be achieved by using a solid segmented aluminum band and a modular bolt cutter assembly which was mounted to the post and would be reusable after each firing. Similar band designs had been flown in the past by GSFC on numerous sounding rocket missions. This new smaller diameter band would incorporate many of the design features of the old sounding rocket bands.

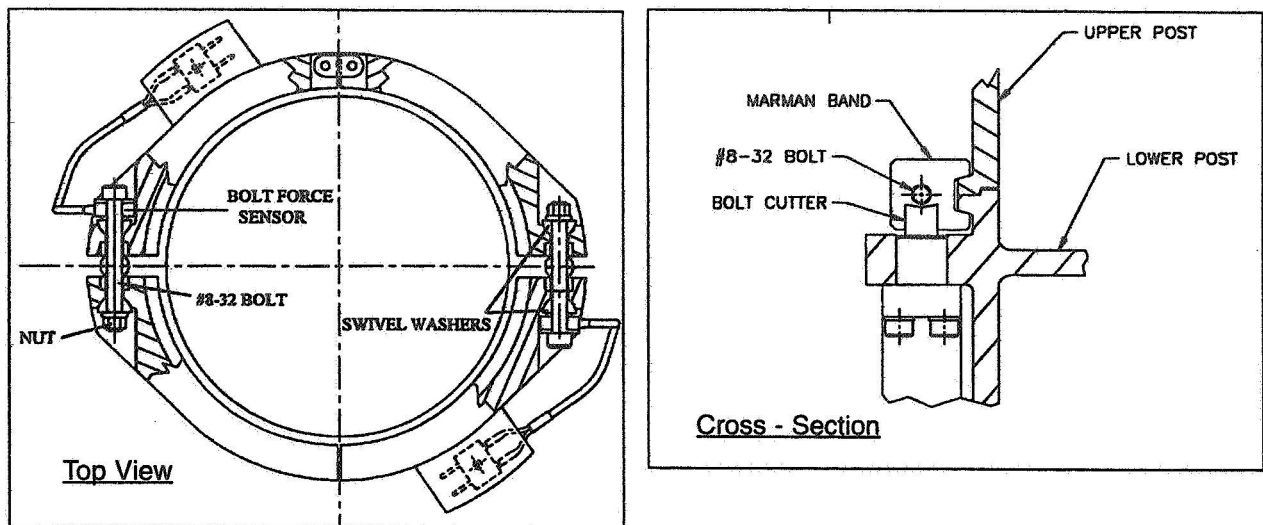
Preliminary sizing of the post diameter, band diameter, and band separation bolt diameter were performed with design calculations using a conservative weight estimate of 363 kg (800 lbm) for the ejectable portion of the IAE and the loads in Table 1. A detailed discussion of both the methods used to size the Marman band and the correlation between the design analysis and the static pull test results are presented later in the paper.



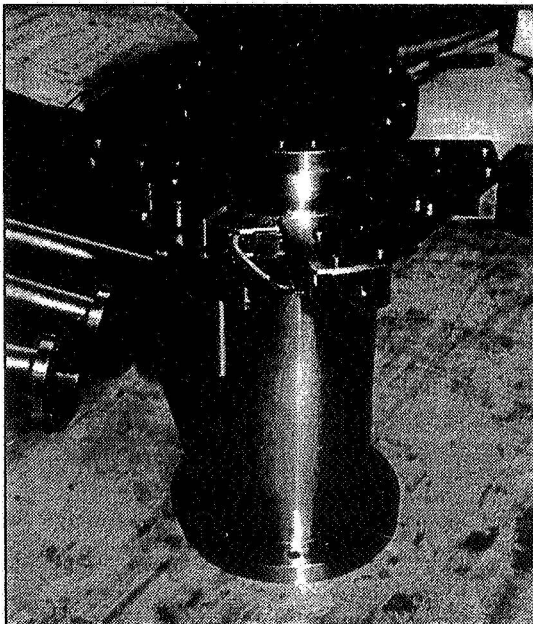
**Figure 4. IAE Jettison Post**

After determining the preliminary post loads from the design calculations, a mounting post and a solid segment Marman band were designed to fit within the available space. The IAE jettison post bands are constructed of a solid 7075-T73 aluminum ring, which has been cut into four equal segments. Each half of a band is linked and pinned together to create a flexible interface. The band halves interface to the post flanges with a 15° ramp angle and are pre-loaded with two #8-32 bolts, which rigidly clamp the top and bottom posts together (Figure 5). To preclude any type of bolt bending, the #8-32 bolts were seated into a bathtub-type fitting interface on hardened stainless steel swivel washers. Pre-load forces on the #8-32 bolts are provided by a bolt force sensor under the head of each separation bolt. Surface preparation of the bands consisted of hard anodizing the band segments and applying Braycote 601 to the band/flange interface before each installation.

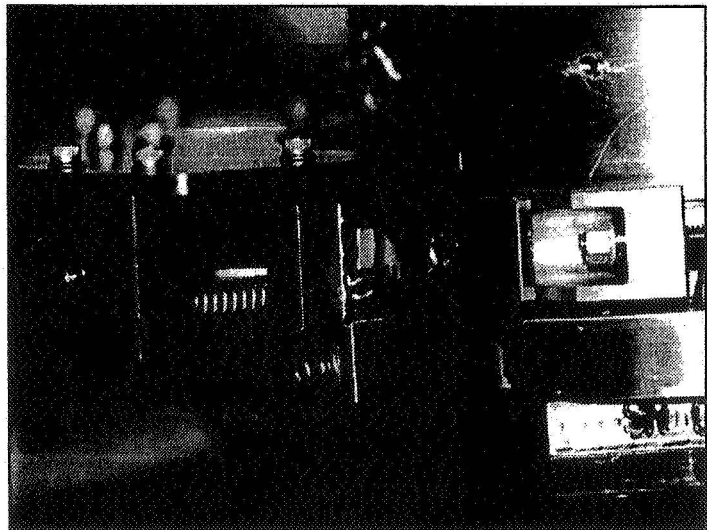
After the separation bolts are cut by the bolt cutters, the band jumps off the interface flange and is retained by four catcher brackets, mounted to the bottom post. Each catcher bracket is connected to the band by a set of tension springs, which firmly hold the band to the bracket during the rest of the Spartan IAE mission and also during re-entry and landing of the Shuttle. Figure 6 shows the fully assembled jettison post.



**Figure 5. Solid Segment Marman Band**



Spartan 207/IAE Jettison Post



Close-up of the Marman Band Interface

**Figure 6. Jettison Post Photos**



## Marman Band Analysis

A large number of different methods and formulas have been developed over the years to determine the required preload on a Marman band to prevent gapping at the ejection flange interface [3,4,5,6]. For this analysis, the following conservative relationship, which has been successfully used at GSFC in the past, was used [4]:

$$\begin{aligned} W &= W_{axial} + W_{moment} \\ W_{axial} &= \frac{F_{axial}}{\pi D} \\ W_{moment} &= \frac{4M}{\pi D^2} \\ \text{Bolt Preload} &= \frac{WD (\tan \beta - \mu)}{(1 + \mu \tan \beta)} \end{aligned}$$

where:  $W$  = Line load around the band circumference  
 $F$  = Maximum axial load at ejection interface { $F = 21617 \text{ N}$  (4860 lbf)}  
 $M$  = Maximum moment at ejection interface { $M = 1175 \text{ N-m}$  (10,400 ft-lbf)}  
 $D$  = Outside diameter of ejection interface flange {10.9 cm (4.3 in)}  
 $b$  = Flange/band ramp angle (15°)  
 $\mu$  = Coefficient of friction (normally between 0.0 and 0.10)

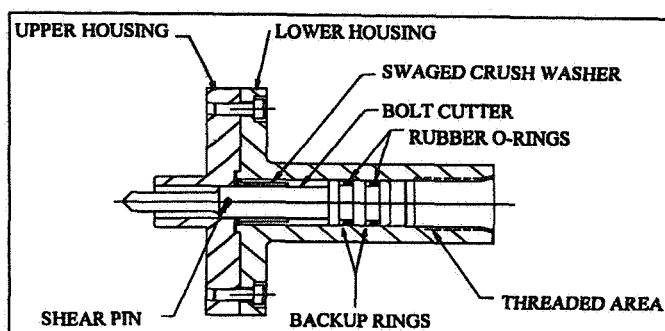
A detailed flight loads analysis yielded the loads listed above. A coefficient of friction of 0.08 was assumed, and a required preload of 3781 N (850 lbf) was calculated. The application of a 1.4 factor of safety and a small allowance for measurement uncertainty resulted in a final bolt preload specification of 5782 N (1300 lbf), with a corresponding line load of 2856 N/cm (1631 lbf/in), which was higher than the preliminary sizing calculation. The only required change in the hardware to accommodate the higher loads was the screening and re-certification of the separation bolts to a higher level.

Comparison of this Marman band line load with the line loads of other Marman band designs [6] will show that this design can develop significantly higher line loads than most designs. This is possible because of the solid segment band strength and the small diameter and large wall thickness of the ejection post. On almost any other type of band design, these large line loads would almost certainly cause potential ring rolling problems at the flange interface. Even with the very stiff interface rings of this design, this large line load was a concern and was monitored during the pull test.

## Bolt Cutter Design

Release of the bands occurs when either one of a pair of redundant bolt cutters is actuated on each post. The bolt cutter assemblies are mounted to the bottom post and consist of an upper and lower housing, a bolt cutter blade, a crush washer, and a pressure cartridge. When the separation bolt is cut by the bolt cutter blade, the cutting force transferred by the blade is reacted by the band. This type of system can only be used in combination with a small separation bolt diameter (#8-32 or less will produce

a small cutting force) and a band which is rigid enough to react this cutting force back into the post flanges without adversely affecting the separation dynamics of the band. The bolt cutter is shown in Figure 7. This design has been successfully used on numerous sounding rocket missions.



**Figure 7. Bolt Cutter Assembly**

Due to some of the previously mentioned limitations of this bolt cutter design, its acceptability for other applications will be limited; however, for this particular use, it has a number of desirable features. The upper and lower housings are made of high strength 15-5 stainless steel and can be disassembled, cleaned, and re-used after each firing. Due to the small amount of cutting force required, even the bolt cutter blades were re-used during functional testing after being re-sharpened. The modular design also allowed the bolt cutter assembly to be removed from the system without having to remove the band. The bolt cutter has proven to be simple to use, inexpensive, and very reliable.

### **Pressure Cartridge**

A Horex pressure cartridge, manufactured by Quantic Industries, was chosen to actuate the bolt cutter assembly. The cartridge is a fairly typical single bridge wire, 1.0-A "no-fire" and 4.0-A "all-fire" pressure cartridge. One of the primary reasons for choosing this cartridge is its previous use for the Hitchhiker program, and it had been qualified for flight on the Shuttle by GSFC.

The design and testing requirements for Shuttle pyrotechnics were reviewed and applied to this application. Shuttle pyrotechnic requirements are contained in NSTS 8060 Space Shuttle System Pyrotechnic Specification [7].

During the manufacturing and testing of the cartridges at Quantic, it was discovered that the Maximum Operating Pressure (MOP) of the bolt cutter assembly was high enough to yield the threads and o-ring cross-section of the CRES 302 pressure cartridge housing during the hydrostatic proof testing. Fortunately, for this application, the cartridge was significantly overcharged, so that the propellant charge could be reduced to achieve a pressure below the yield point of the cartridge body and still easily cut through the #8-32 bolt. This MOP proof test requirement in NSTS 8060 is very conservative when considering that the pressure load profile produced by a pressure cartridge firing is a very short transient load instead of the static pressure

load specified in the requirements. For this reason, it is strongly recommended that high pressure bolt cutter applications which must meet NSTS 8060 consider a higher strength housing material (Inconel 718 is common).

### **Spring/Pushrod Design**

After the bands are cut, the IAE is pushed away from the Spartan Service Module by four independent compression springs, located in each of the post assemblies. Each spring is guided by a pushrod, which rides in a linear bearing housing (Figure 4). The linear bearing housing and the pushrod provide a tightly controlled and guided stroke for the springs; however, the IAE and the Spartan Service Module are free to rotate with respect to each other during the jettison sequence. The spring design requirement was to provide enough force to push the inflated portion of the experiment away from the Spartan Service Module without buckling the struts of the antenna or without imparting angular rates into the Service Module greater than those allowed by the Spartan Attitude Control System. To verify the spring design, a dynamic analysis of the jettison sequence and of the subsequent velocity and rotational rates of the IAE and Spartan Service Module with respect to each other was performed. From the results of the dynamic analysis, it was found that a spring rate of 15 N/cm (8.5 lbf/in), with a stroke of 10.9 cm (4.3 in), would meet the desired requirements and also provide a separation velocity of approximately 0.93 m/s (25 in/s) between the Spartan Service Module and the inflated antenna.

### **Jettison System Dynamic Modeling and Simulation**

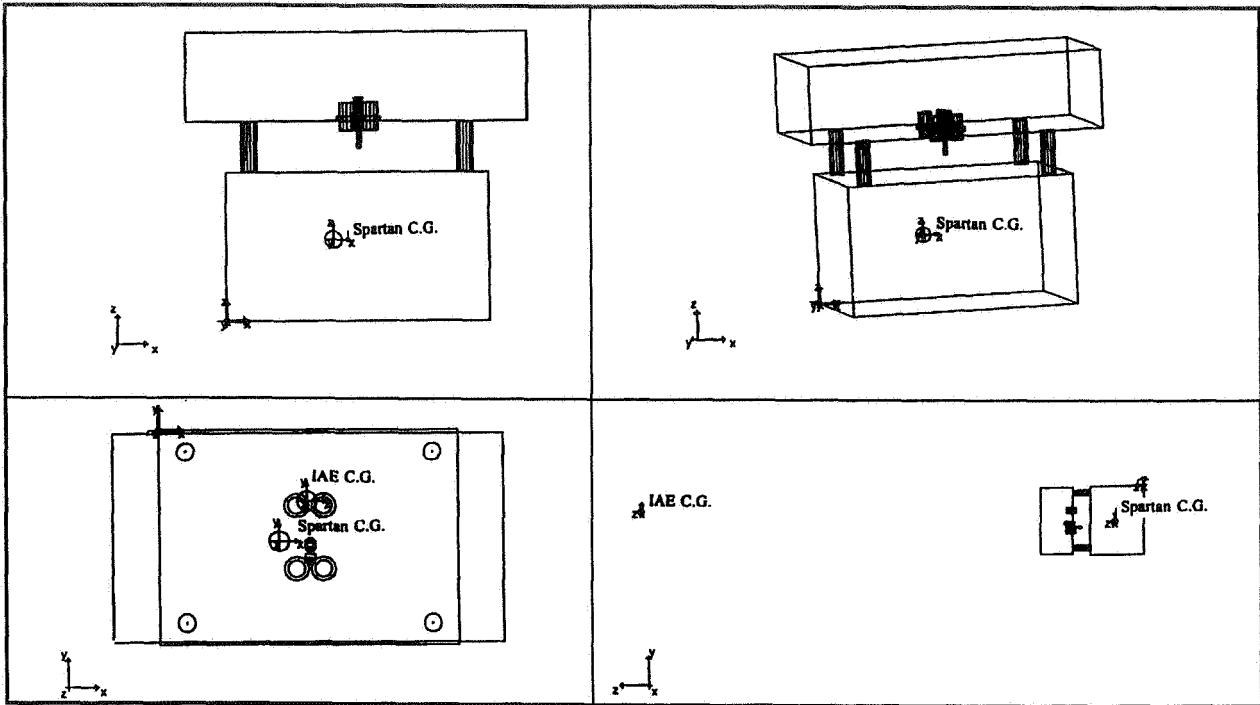
#### **Dynamic Analysis Overview**

A dynamic simulation was required in order to understand quantitatively the relative motion between the Spartan carrier spacecraft and the IAE during the jettison. This was necessary to ensure that there will be no contact between the Spartan and the IAE, that the angular rate imparted to the Spartan spacecraft will be acceptable, and that the IAE struts will not buckle. The results of the dynamic analysis were used to develop specifications for the spring rates and minimum clearances between components.

A three-dimensional, rigid-body simulation of the jettison event for both the deployed and stowed IAE was performed using Automated Dynamic Analysis of Mechanical Systems (ADAMS) software. The center of gravity (CG) displacement time histories were the output from ADAMS and mapped to NASTRAN grid geometry, so that the minimal clearance between the critical IAE and Spartan geometry could be conveniently tracked at discrete locations. Parametric studies, involving variation of the plunger spring rates by  $\pm 10\%$  and variation of the IAE CG location in the XY-plane, were included. The effect of the flexible IAE struts on the jettison event was also examined and found to be similar to the rigid simulations; therefore, only the rigid simulations are presented.

A total of twelve rigid body simulations were performed: three for the deployed and nine for the stowed configuration. The deployed cases consisted of nominal CG and plunger spring rates, along with two additional cases in which the CG and spring rates

were adjusted to produce maximum rotations about the X and Y axes. The stowed cases consisted of a nominal CG configuration, along with eight additional cases in which the CG was varied within the footprint of the four jettison posts.



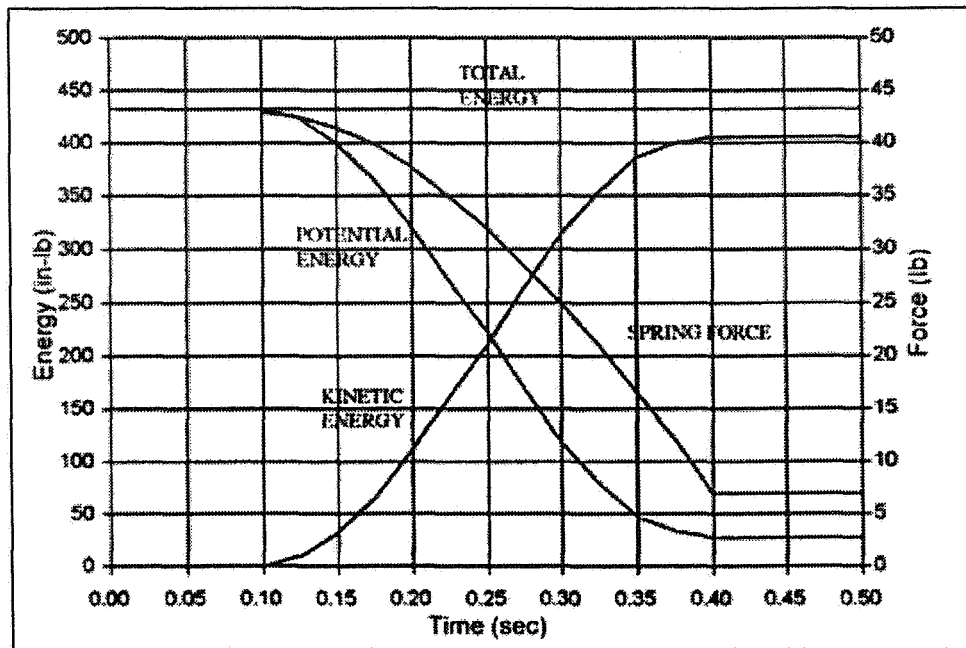
**Figure 8. Wireframe Rendering of ADAMS Model for Deployed Configuration**

#### Dynamic Models and Analysis Procedure

The nominal deployed model consists of rigid masses located at the Spartan and IAE CGs. Table 2 contains the nominal mass properties for both the Spartan and IAE. Figure 8 shows a wireframe rendering of the deployed ADAMS model. The IAE CG is shown in the lower two figures, but not in the top two figures, because it is far above the main spacecraft body in the deployed configuration. The Spartan CG is located in the interior of the lower box. The spring housings, ejector housing, and camera are located at the bottom center of the upper box, which houses the stowed IAE antenna. An overhead view of these components is found in the lower left-hand figure. The four cylinders separating the Spartan and the IAE, shown in the upper right-hand figure, represent the jettison posts.

The jettison simulations were performed over a 0.75-second interval with a time step of 0.005 seconds. The IAE and Spartan CG displacements and Euler angles were the outputs from ADAMS for each configuration. The CG information was then mapped to NASTRAN model grid geometry, and the minimum clearance was calculated. The IAE and Spartan CG rates were also tracked. Using the CG rates, jettison spring displacements, and mass properties of the system, an energy check was performed on the deployed nominal run. At each of the 100 time steps, from 0.00 to 0.50 seconds, the potential energy in the springs and the kinetic energy of the IAE and Spartan were

calculated. The sum of the energies remained constant throughout the analysis. Figure 9 shows plots of the potential, kinetic, and total energy in the system, as well as a typical jettison spring force profile.



**Figure 9. System Energy for Nominal Deployed Configuration**

#### Dynamic Analysis Results

Table 3 summarizes the results of the rigid body simulations. A positive clearance was obtained for all simulations, with a minimum clearance of 0.23 cm (0.09 in) for a worst-case stowed configuration. Also, the angular rate predicted for the Spartan is well within the ACS bounds, and the forces imparted to the IAE were found to be well within the allowable buckling for the struts. Therefore, the results of the analysis show that all the requirements for successful jettison have been satisfied, thus validating the jettison system design and allowing the specification of final spring rates.

#### Jettison Post Functional Testing

A great deal of important information was learned about the characteristics of a solid segment band during the initial functional testing of the Engineering Test Unit jettison post. As with any Marman band, it is very important to achieve consistent repeatability when installing and pre-loading the band. This was achieved here by using a detailed installation procedure and incremental monitoring of the bolt force with the bolt force sensors, the torque values, and the gap between the cutter blade and the bathtub fitting on the band. On a couple of occasions, when one of these values began to stray outside of previous average values, the band was disassembled only to find a small amount of debris on the interface or a rotational misalignment of the band with respect to the cutter assembly.

<b>Table 3 - Results of Jettison Simulations for the Deployed and Stowed Rigid IAE</b>								
	Minimum clearance (in)	Steady State Translational Velocity (in/sec)		Maximum Angular Rates (deg/sec)				
		IAE	Spartan	IAE		Spartan		
		Z	Z	Rx	Ry	Rx	Ry	
Deployed: Nominal	0.24	17.54	-6.81	-0.031	-0.004	-0.624	6.125	
Max Theta-X	0.25	17.54	-6.81	0.083	-0.004	1.088	6.159	
Max Theta-Y	0.06	17.37	-6.74	-0.033	0.169	-0.624	9.409	
Stowed: Nominal	0.40	17.74	-6.82	0.25	-5.10	-0.66	5.67	
CG (worst case)	0.09	14.57	-5.58	-0.13	20.81	-0.45	10.88	
* All minimum clearances are between the spring housings and the inflation panel.								

During the first single bolt cutter functional test, two problems with the system were discovered. The first problem had to do with the flexibility of the band. Although the first functional test was successful, which is to say that a single bolt was cut, the band was released, and the top post was ejected. It was obvious that the band was not as flexible as we would like and that there was potential for it to become hung up on the top post or in some way interfere with the ejection sequence. A simple solution to this problem was implemented by attaching a slider mechanism to the band, thus allowing the springs of the catcher assembly to move relative to the band during release. This provided more flexibility to the system and let the band move further from the post flanges after release.

The second problem had to do with bolt cutter blade and how it was cutting through the #8-32 separation bolt. In the past, on similar solid segment sounding rocket bands, a heat-treated 4140 alloy steel cutting blade, with a cutting angle of 90°, was used to cut through a single or double #6-32 separation bolt interface. Increasing the bolt diameter by 0.076 cm (0.030 in), to a #8-32, for this system was not perceived as a problem. During the first functional tests, however, it was found that this combination of bolt diameter, bolt material, cutter angle, and cutter material caused the bolt to fail on two planes instead of one. This produced a very consistent 0.25-cm (0.10-in) long bolt section to be punched out. The creation of debris raises safety concerns on Shuttle payloads, thus this was a potentially serious problem.

Close examination of the bolt failure planes clearly showed signs of shear failure across both planes. A comparison of the hardness of the cutter material and the bolt material showed very similar values of about 40 Rc. From this information, in combination with the large cutter angle (90°) and the deformation observed on the sharp point of the cutter, it was concluded that the cutter angle was too large and the cutter material was not hard enough to achieve the initial cutting depth required to fail the bolt on a single plane. To solve this problem, a new cutter blade was designed with a smaller cutting angle of 60° and made of a high strength/hardness alloy steel,

called AeroMet 100. AeroMet 100 combines high strength and hardness properties (50–54 Rc) with good ductility values and corrosion resistance. To achieve these properties, a costly and involved heat treating process must be performed; however, for our application, this turned out to be a very successful choice. The AeroMet 100 cuts through the bolt cleanly on a single plane and is so tough that, during functional testing, the cutters are being re-used after each firing after only a small amount of re-grinding on the sharp edge. Figure 10 shows magnified photos of the bolt cross-sections before and after the cutter modification.

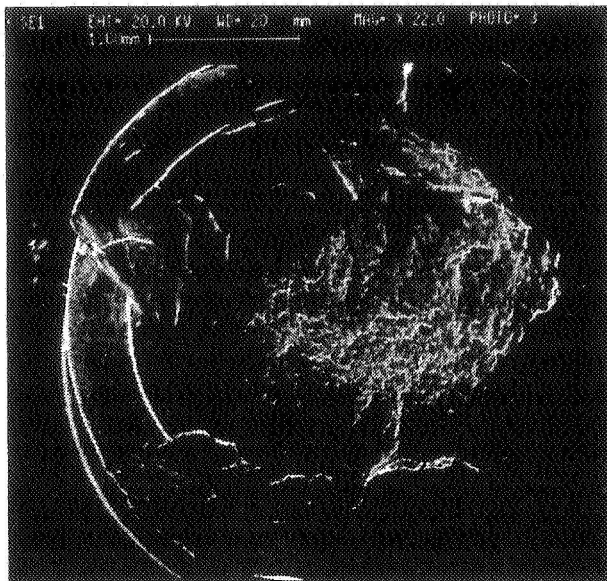
### **Jettison Post Static Load Pull Testing**

The post was subjected to two pulls initially, both at an angle of 64° and a force of 33805 N (7600 lbf). The first pull was across one of the band bolts, and the other pull was across one of the Marman band links. These two angled pulls qualified the post to the Spartan design load levels, with the additional factor of 1.4. Following the second test, the post was removed and taken to another site to be functionally tested. After the functional test, the post was re-assembled and returned to the test site and pulled two additional times. These final pulls were overload tests to see if the band could be forced to gap with either a horizontal or vertical pull force. Data from these last two pull tests provides insight into the strength of the post/band interface. The pulls are summarized below:

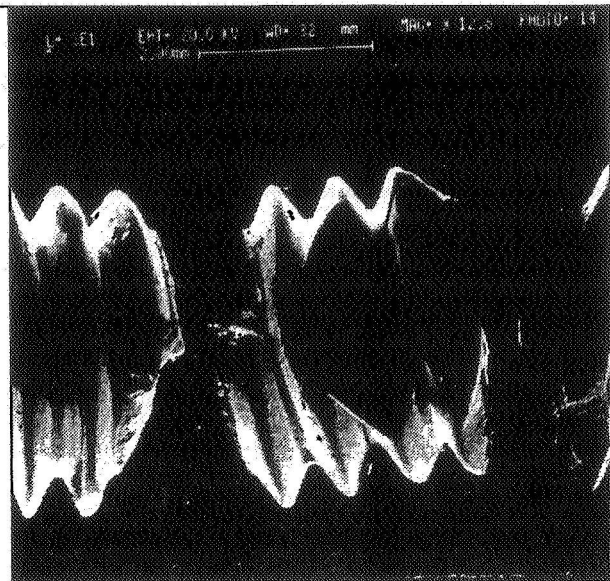
- Test 1 - Pull at an angle of 64° with a force of 33805 N (7600 lbf) across band bolt #2.
- Test 2 - Pull at an angle of 64° with a force of 33805 N (7600 lbf) across one of the links.
- Test 3 - Pull vertically until the band interface gaps.
- Test 4 - Pull horizontally until the band interface gaps.

Based on the results from the first two qualification pulls, it was determined that the Marman band interface did not gap. Figure 11 shows the stress readings at three locations (gages #1, #2, and #3 are inside the post at the flange; gages #4, #5, and #6 are on top of the Marman band; and gages #7, #8, and #9 are on the back face of the Marman band) as a function of the pull load. Figure 12 shows the bolt forces over the same load increments. Previous testing of Marman bands at GSFC has shown that, when gapping occurs at the band interface, the clamping strain energy associated with the bolt pre-load was relieved, and the Marman band and bolts began to take the entire load. This was displayed by a marked increase in the bolt loads, as well as increased hoop stresses in the band. Neither of these phenomena occurred in the first two tests for the IAE jettison post. As an additional indicator of gapping, LVDTs were added at the band interface to measure any sudden change in deflection which might occur during the test. Again, the data showed negligible changes for the first two qualification pulls. Also, strain gauges located on the inside surface of the post diameter at the ejection/ flange interface showed fairly low stresses, which removed any worries of ring rolling occurring at the flanges due to the large line load in the band (Figure 11).

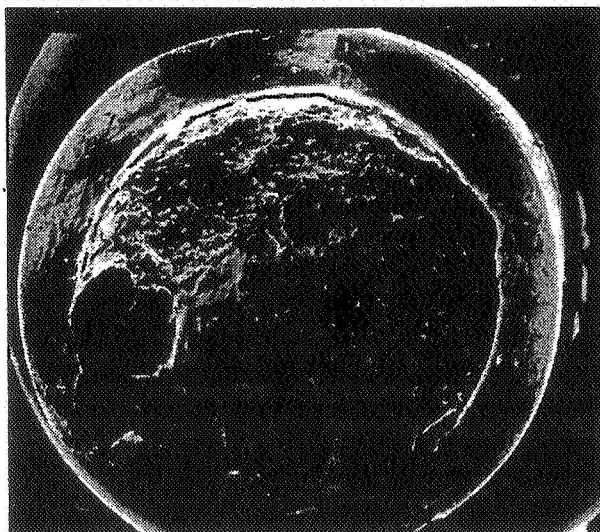




Cross section created by original cutter blade



Bolt debris created by original cutter blade (note three sections)



Cross section created by redesigned cutter blade

**Figure 10. Magnified Photos of Cut Separation Bolts**



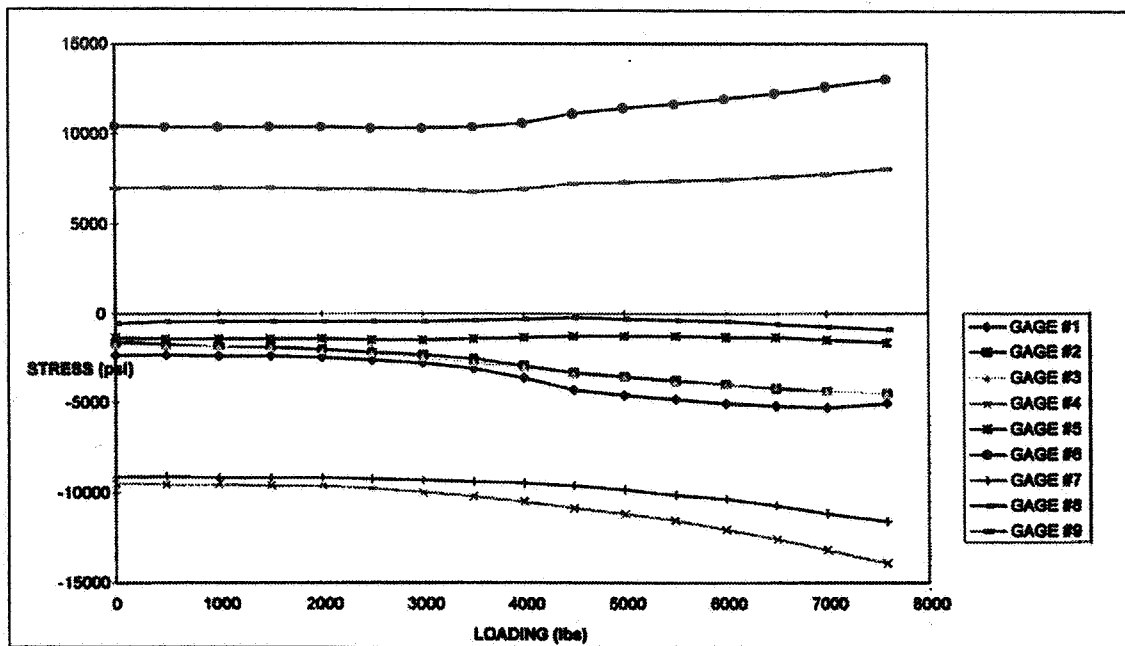


Figure 11. Stress Data Pull Test #1

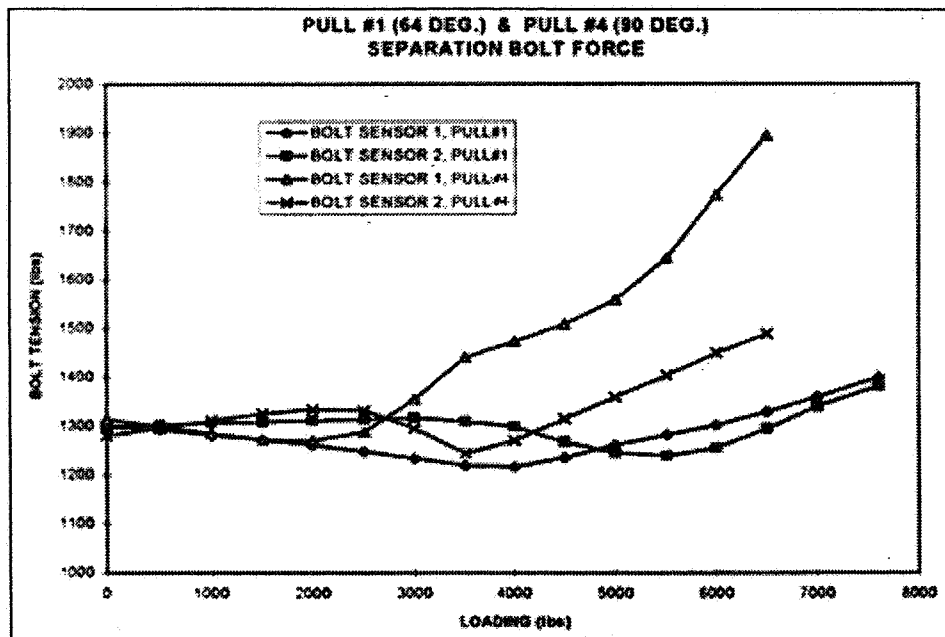


Figure 12. Bolt Force Data Pull Test #1

The most interesting results from the two overload tests occurred in the horizontal pull of test 4. Test 4 applied up to a 3853-N-m (34125-in-lbf) bending moment at the Marman band interface by pulling at 90° to the axis of the post with a load of 28912 N (6500 lbf). This is equivalent to a moment load which was three times higher than the maximum moment produced using the design limit loads. The purpose of this test was to determine at what bending load the post would either gap or reach the maximum allowable bolt force sensor readings. Based on the test plan, the loading stopped

when the bolt loads reached 8006 N (1800 lbf), which is the proof load level of the separation bolts. At this level, the stress and bolt force sensor data still did not conclusively suggest any gapping (Figure 12).

The results of the pull testing showed that the solid segment band is very strong and showed good correlation between analytical predictions and the measured bolt force and band hoop stress. Also, the results of test 4 showed that the frictional interface between the post flanges was not broken, even with a shear load of 28912 N (6500 lbf). This was a direct and positive result of the high line load in the band. The two functional tests performed after the pull tests were successful.

The results of the static pull tests were also used to specify a variable cross-section beam representation of the jettison posts in the spacecraft finite element model. The stiffness properties of the post, above and below the band interface, were determined using deflection data from the pull test. In this way, the flexibility of the Marman band joint was taken into account in the finite element model.

### **Simulated Deployment Testing of the Jettison System**

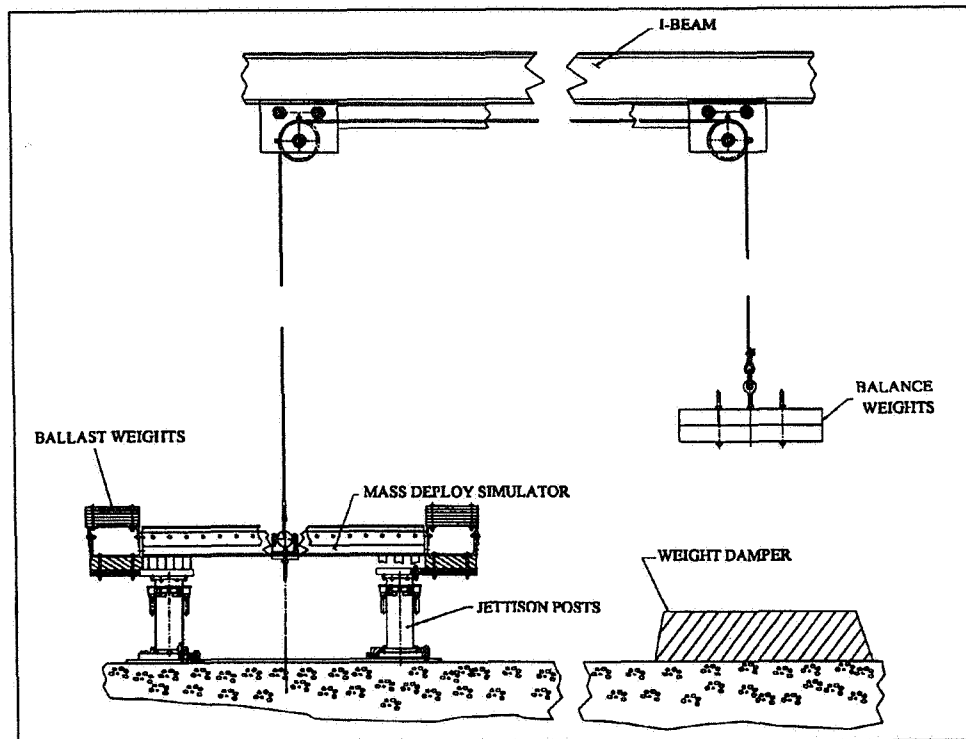
To test functionally the ejection system (all four jettison posts together) before flight, a Mass Deployment Simulator (MDS) was designed to simulate both the mass and the interface between the posts and the ejectable portion of the payload. This includes the actual flight electrical connections between the inflation panel and the experiment. These connectors are designed as rack and panel, spring-loaded, zero-force disconnect connectors. In addition to simulating the mass of the experiment under zero-g, the MDS is capable of enveloping a wide range of X-Y CGs and introducing a simulated thermal deflection in two of the jettison posts.

The simulator consists of a frame and weight assembly, which equals the weight of the ejectable portion of the IAE payload. To offset the effect of gravity, a balance weight is connected with wire rope across pulleys to the MDS (Figure 13). The X-Y CG of the MDS is adjustable by moving ballast weights and shifting the lift point accordingly. The lifting ball can be adjusted 7.6 cm (3 in) in the Z direction to account for the shifting/stacking of the ballast weights. Together, they provide the capability of testing the ejection system under a wide range of CG locations. Four tests using the MDS were planned. In all cases, only one pressure cartridge per post was planned to be fired.

Test 1 - CG located at the center of the post pattern with no IAE electrical connectors included.

Test 2 - CG located at the center of the post pattern with the IAE electrical connectors mounted in the system.

- Test 3 -CG located at the nominal IAE deployed location with an additional offset of 25% and the IAE electrical connectors mounted in the system.
- Test 4 - CG. located 100% off the nominal IAE deployed location, two posts with a simulated thermal deflection of 0.10 in, and the IAE electrical connectors mounted in the system with an undersized spring force.



**Figure 13. Mass Deploy Simulator**

As of the writing of this paper, the first three of the four tests using the MDS have been performed. In each test, the jettison posts have performed nominally without a single anomaly or problem. Due to budget and schedule constraints, the last test will most likely not be performed; however, the results of the first three tests have given us a high degree of confidence in the design approach.

## **Conclusion**

The Spartan IAE mission is manifested on STS-77 in May of 1996. The jettison system has been subjected to extensive testing and evaluation with highly successful results. It has proven that the use of multiple small Marman band clamps to separate large objects in space is a viable design approach. Furthermore, the combination of a strong solid segment band with a modular reusable bolt cutter assembly has shown, for this application, to be inexpensive, reliable, and able to carry the high structural load levels required by the Shuttle.

## References

- 1) NASA GSFC, "Spartan Capabilities Statement", SP515, 1993
- 2) Freeland, R.E., and Bilyeu, G, "Development Of Flight Hardware For A Large, Inflatable-Deployable Antenna Experiment", IAF Paper 95-1.5.0., October 1995.
- 3) Altpater J., "Stress Analysis of TDRSS Solar Array Jettison U Band Clamp Assembly", General Electric Astronautics PIR # U-1R43-LSID-804, 8/1/79, NASA GSFC 740 CM #SSPP-REF-016.
- 4) Mayor J.O., "Marman Clamp Design", NASA GSFC Memorandum dated 4/5/91, NASA GSFC 740 CM #SSPP-REF-016.
- 5) Patterson, P., GAS Carrier Ejection System (CES) Structural Analysis, Swales & Associates Report #TR-92-047, 9/28/92.
- 6) Astrotech Space Operations, Inc., GOES-IJK Separation System Study, 2/12/87, NASA GSFC 740 CM #SSPP-REF-016.

517-18

## Mars Pathfinder Rover Egress Deployable Ramp Assembly

Brian R. Spence\* and Lee F. Sword\*\*

50445  
125131  
✓

### Abstract

The Mars Pathfinder Program is a NASA Discovery Mission, led by the Jet Propulsion Laboratory, to launch and place a small planetary Rover for exploration on the Martian surface. To enable safe and successful egress of the Rover vehicle from the spacecraft, a pair of flight-qualified, deployable ramp assemblies have been developed. This paper focuses on the unique, lightweight deployable ramp assemblies. A brief mission overview and key design requirements are discussed. Design and development activities leading to qualification and flight systems are presented.

### Mission Overview

The Mars Pathfinder Program is a NASA Discovery Mission, led by the Jet Propulsion Laboratory, to launch and place a small planetary Rover, dubbed Sojourner, for exploration on the Martian surface. To enable safe and successful egress of the Rover vehicle from the spacecraft, a pair of flight-qualified, lightweight deployable ramp assemblies are utilized. Figure 1 depicts an artist rendition of the Mars Pathfinder spacecraft, Rover, and its deployable ramp assemblies, as they would appear on Mars.

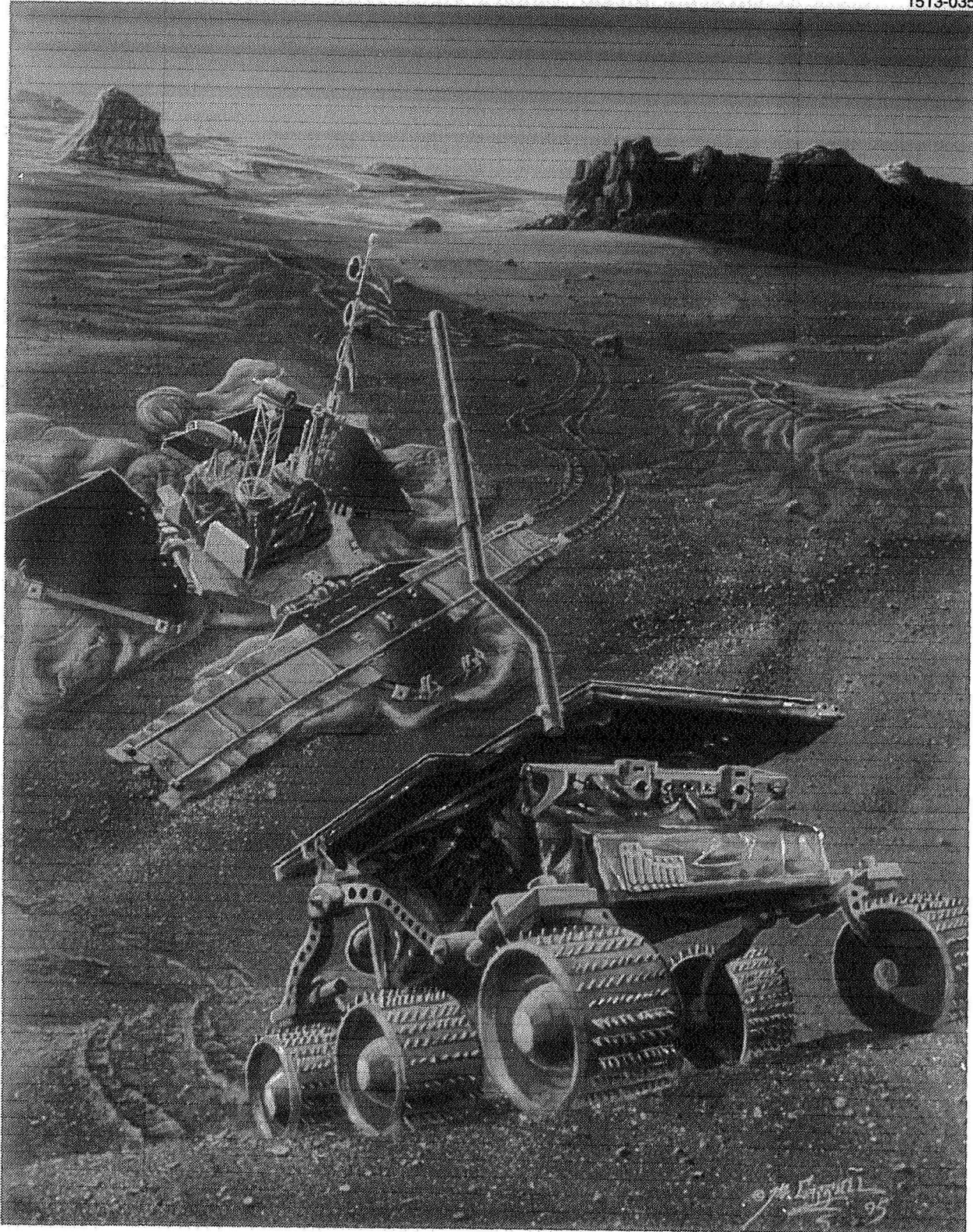
The Mars Pathfinder spacecraft is scheduled for launch in December, 1996, for a subsequent rendezvous with Mars in July, 1997. During final descent to Mars, large inflatable airbags will be pressurized to encapsulate the spacecraft and reduce the overall landing impact with the Martian surface. Once landing has been achieved, the airbags will be deflated and retracted to allow for the opening of three spacecraft petals. Each petal is populated with a complement of solar cells, which provide spacecraft power once they are completely opened and exposed to sunlight.

The Rover vehicle and the deployable ramp assemblies are stowed to one of these petals during the entire journey to Mars. After the airbags have been completely retracted, the two ramp assemblies are deployed by severing two circumferentially wrapped tie-down cables with pyrotechnic cutters. Once deployed, the ramp assemblies provide a safe and successful Rover egress path from the spacecraft to the Martian surface.

---

\* Astro Aerospace Corporation, Carpinteria, CA

\*\* Jet Propulsion Laboratory, Pasadena, CA



**Figure 1. Mars Pathfinder Spacecraft,  
Rover and Deployable Ramp Assemblies.**

## Key Design Requirements

Design requirements of space hardware for interplanetary mission applications are generally much more demanding than typical Earth-orbit applications. The deployable ramp assembly had many of its own unique requirements, ranging from operability, loading, stowed and deployed envelopes, weight, schedule, and cost. A listing of the key design requirements are shown in Table 1.

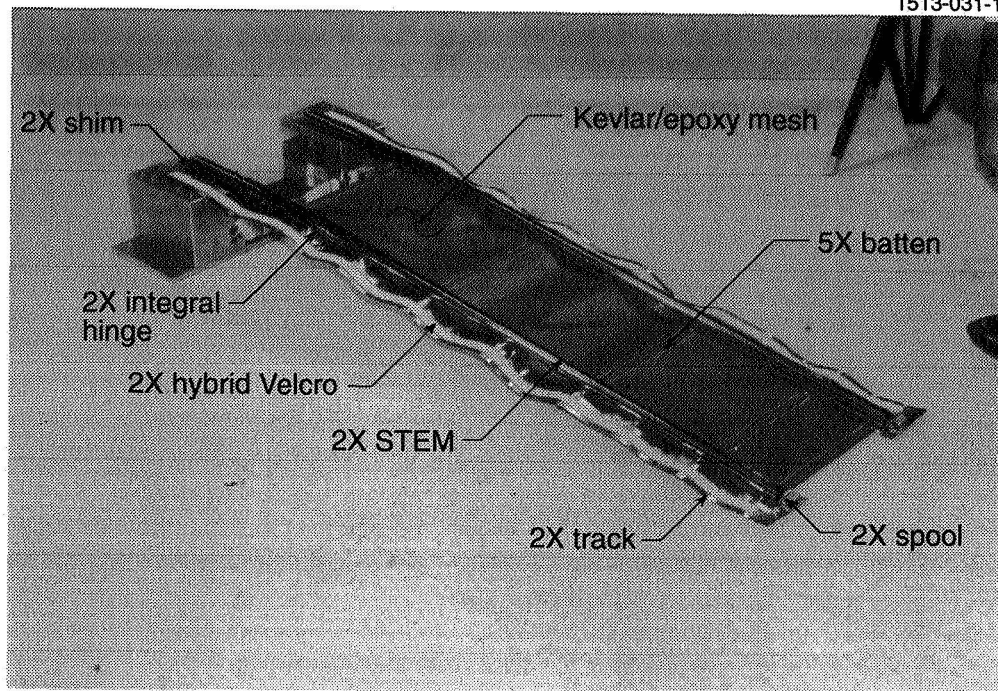
**Table 1: Key Design Requirements**

Programmatic:	1. Better, faster, cheaper
Operability:	<ol style="list-style-type: none"><li>1. Provide reliable deployment at +50°C to -140°C.</li><li>2. Provide reliable deployment at a <math>\pm 30^\circ</math> inclination to the local horizontal in all orientations.</li><li>3. Design capability for multiple deployments.</li><li>4. Provide guiding features for Rover vehicle during egress.</li></ol>
Loading:	<ol style="list-style-type: none"><li>1. Sustain a 66-g level centrifuge loading for a duration of 1 minute in each of the three orthogonal axes.</li><li>2. Sustain a low-level random vibration launch spectrum.</li><li>3. Support a Rover weight of 12.5 kg (27.55 lb) at ramp mid-span without buckling while simply supported at ends.</li><li>4. Provide ramp buckling in a cantilevered condition when Rover is translated between 1/3 and 2/3 of its distance down the ramp.</li></ol>
Envelope:	<ol style="list-style-type: none"><li>1. Stowed package to fit within a constrained compact trapezoidal volume.</li><li>2. Minimal deployed footprint which does not obscure petal-mounted solar cells.</li></ol>
Weight:	1. Ramp assembly weight $\leq 1000$ g (2.20 lb)
Schedule:	1. Eight-month design, development, production, and test of one qualification unit, two flight units, and one flight spare unit.

## Flight System Description

The Mars Pathfinder Rover Egress Subsystem consists of two deployable ramp assemblies: one fore and one aft of the translation direction (Figure 1). When deployed, the ramp assemblies measure approximately 136 cm (53.5 inches) in length by 42 cm (16.5 inches) wide and allow for safe and successful Rover egress. Figure 2 depicts the ramp assembly in the deployed configuration.





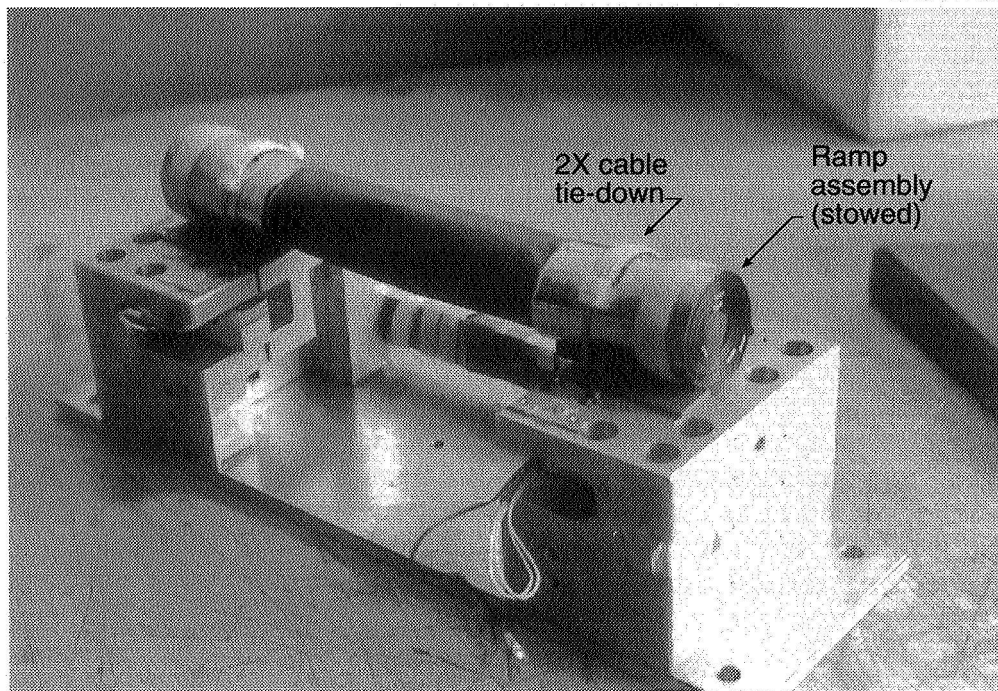
**Figure 2. Deployed Ramp Assembly.**

The flight deployable ramp assembly consists of two nested pairs of 2.18-cm (0.86-inch) diameter Astro STEM™ (Storable Tubular Extendible Member) stainless steel elements, which together provide the required strength, stiffness, and deployment force. Five aluminum alloy battens are attached to each STEM™ element along their lengths to maintain precise separation between elements, thus enabling the Rover to straddle them safely during translation. During egress, the Rover utilizes the outboard surface of each STEM™ element as an inboard curb for guiding purposes. Thin stainless steel tracks, located on the outboard side of each element, provide for a Rover wheel rolling surface. The tracks are attached to the STEM™ elements and battens by screws and rivets, respectively. When attached, the tracks play a large role in reacting all in-plane shear loads. A lightweight Kevlar/epoxy open-weave mesh completely covers the mid-span of the ramp over most of its entire length. The Kevlar/epoxy mesh helps prevent excess airbag material and other potential hazards from protruding significantly above the translation plane, where possible impediment to Rover egress could result. The Kevlar/epoxy mesh is attached and sandwiched between the elements and track and pocketed for restraint at each batten. A cylindrical spool is mechanically attached to the outboard tip of each track and centered in-line with each STEM™ element. The spools assist the initial stowage process during roll-up of the ramp assembly. The inboard end of each STEM™ element is fastened to a shim, which provide the mechanical interface with the spacecraft petal. Continuous strips of stainless steel/nylon hybrid Velcro™ are adhered to the outer sides of the top and bottom surfaces of the tracks. The hybrid Velcro™ provides kinematic coordination and control during deployment.





**Figure 3. Stowage Process.**



**Figure 4. Stowed Ramp Assembly.**

When stowed, each ramp assembly is rolled up in a compact cylindrical envelope of approximately 7.62 cm (3.0 inches) in diameter by 42 cm (16.5 inches) in length. Figure 3 depicts the stowage roll-up process. The cylindrical package is tied down to the spacecraft petal structure with two cables located on each side of the roll. Figure 4 depicts the ramp assembly in the stowed configuration. The cable tie-downs circumferentially preload the stowed package against the spacecraft petal for launch. Deployment is initialized by the simultaneous severing of the two preloaded cables with pyrotechnic cable cutters. Immediately after cable severance, the ramp unfurls to its deployed position in less than 1 second. The entire deployment sequence is shown in Figure 5.

## **Discussion**

### The Proposal Phase

This program proved to be much more involved than a routine design and development exercise of what was originally deemed as a simple deployable structure. As part of the initial proposal effort, Astro successfully produced and tested, albeit to less stringent requirements, a breadboard demonstration model in an effort to mitigate any perceived program risk. The breadboard unit appeared to satisfy the majority of requirements and was envisioned to require only slight modifications to fulfill compliance. However, as will be presented, what worked so well as a breadboard model eventually required some significant modifications in the design and manufacture to completely satisfy all the requirements.

In total, four development units were built and tested until an acceptable flight design was produced. The breadboard model, developed for proposal purposes, was literally thrown together in a matter of hours and assembled with bits of hardware salvaged throughout the shop. Items, such as used STEM™ elements, aluminum mesh screen, and soft rivets were integrated with large manufacturing tolerances. Unlike the qualification and flight units, the breadboard model had only one STEM™ element per side. At the time of the proposal, it was felt that this configuration could potentially satisfy the buckling/deflection requirements with or without slight modification. The model underwent many successful deployments under a variety of conditions prior to contract award and had lived beyond expectations. As a result, the breadboard model laid the basis for qualification design.

### Breadboard to Qualification

Once the program was underway, it was evident that the breadboard configuration, with one STEM™ element per side, was not going to meet the simply supported and cantilevered deflection loading requirements. Therefore, for the development unit design, an additional STEM™ element was added to each side of the ramp assembly. The incorporation of two elements per side was not perceived to be a concern but turned out to create some major difficulties.

1513-000b



**Figure 5. Deployment Sequence (Controlled and Coordinated).**

The addition of another STEM™ element to the design resulted in three rigid items (the inner STEM™ element, the outer STEM™ element, and the track) that needed to be tightly rolled on top of one another to create a compact stowed package. The additional STEM™ element was integrated into the design without allowing for mechanical compliance between the individual elements and track.

When the first development unit was produced and subsequently rolled up to its stowed configuration, it did not conform into a neatly oriented nested roll. Inspection showed that each element was not in intimate contact with one another. Rather, there were diametric discontinuities on practically every wrap, thus resulting in localized deformation along the elements near each rivet attachment point. Figure 6 shows an end view of the development unit stowed package with diametric discontinuities.

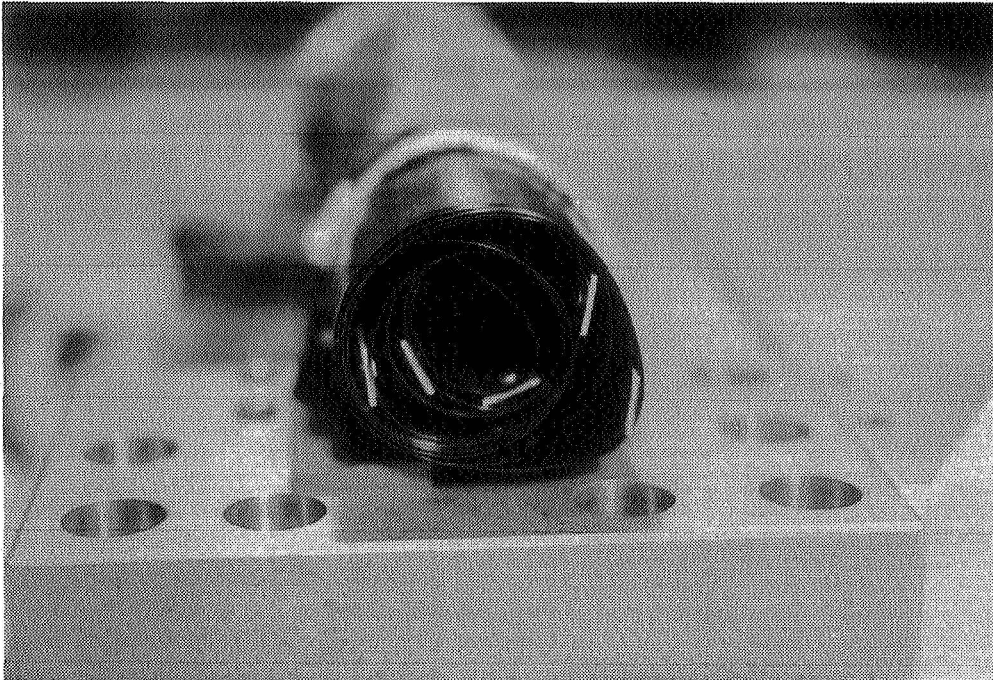
During the stowage procedure, it was evident from the physical effort required that the nested STEM™ elements were constraining each other for position. As a result, some rivets at discrete attachment points were totally or partially sheared, and some elements had elongated notches in need of mechanical compliance. Because the nested components being rolled up had no functional features to provide any mechanical compliance, damage to the ramp assembly resulted after every stowage and deployment cycle. With no built-in mechanical compliance, the STEM™ elements could only withstand approximately four to five cycles before needing replacement. In some instances, the STEM™ elements were so damaged that they experienced local deformation, tearing, and loss of spring force in critical regions, thus contributing to unacceptable deployments.

To alleviate the interference problem, elongated slot features were ultimately machined into each STEM™ element at the attachment points. The track incorporated a wave between attachment points to provide additional length to allow for diametric compliance between all the nested components. The unit was re-assembled, then subsequently stowed. Inspection of the stowed package yielded a tightly wrapped, uniform roll with elements nested in intimate contact with one another, as shown in Figure 7. Subsequent designs, incorporating mechanical compliance features, yielded no component damage and produced the ability for the hardware to sustain multiple deployments.

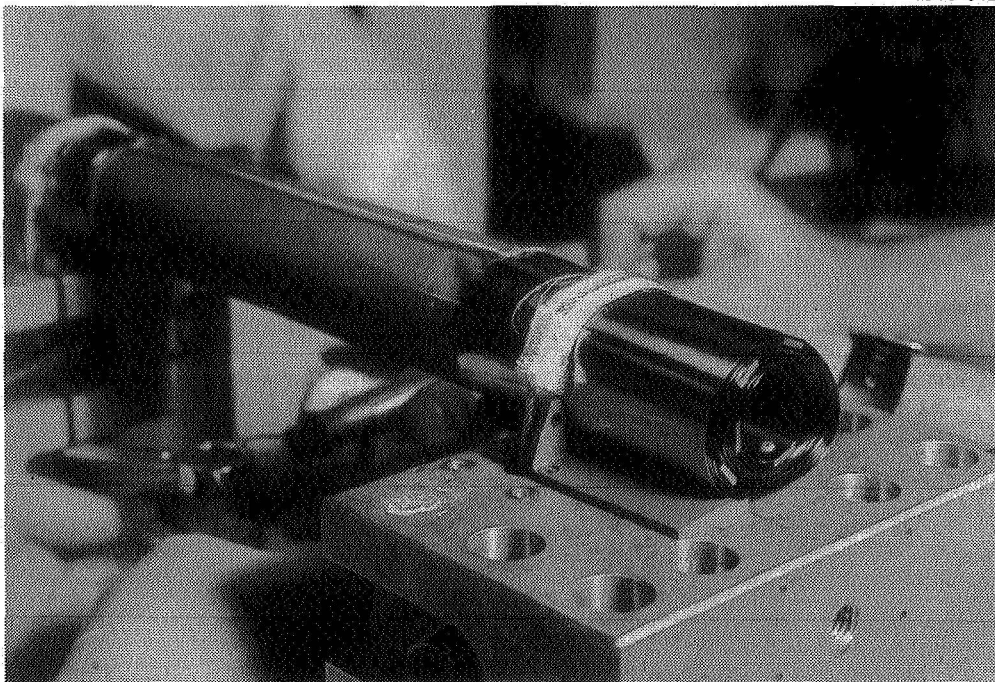
#### Complex Deployment Kinematics

Because of the “better, faster, cheaper” characteristics of this program, time and efficiency were of the essence. In the infancy stages of the program, prior to any real engineering layout work, a mechanical interface was agreed upon. As a result, the allotted stowed envelope turned out to be much more difficult to meet, once engineering and testing activities were underway. To fit within the envelope, the ramp assembly, particularly the STEM™ elements, had to be rolled up to a much tighter diameter than was comfortable. The smaller stowed diameter in the development unit resulted in more stored energy in the stowed configuration than its breadboard model predecessor.





**Figure 6. Development Unit Stowed Package with Wrap Discontinuities.**



**Figure 7. Development Unit Stowed Package with Uniform Nested Wrap.**

To meet the stringent 66-g centrifuge loading requirement, a 1112-N (250-lb) cable preload was needed to provide sufficient preload between rolls, so that the unit would not telescope outward. The high cable preload would bring a new element into the design. When the cables were preloaded to 1112 N (250 lb), an appreciable compression of the stowed cylindrical roll was noticed. In the stowed configuration, the ramp assembly behaved as a soft spring which had been compressed with 1112 N (250 lb) of circumferential preload. Upon release of the preloaded cable, it was determined from video that the initial deployment trajectory was vertically upward to a height of approximately 25.4 to 30.5 cm (10 to 12 inches). Additional tests were performed to determine the effect of varying cable preload on the initial deployment trajectory. Test results indicated that cable preload was playing a large role in influencing the initial deployment trajectory. Video was instrumental in this program for revealing the complex deployment kinematics of the ramp assembly. The video showed that, during this initial deployment sequence, the ramp assembly was allowed to swell and unfurl before the STEM™ elements could become straightened to effectively force deployment in the desired direction. In some cases, non-compliant deployments resulted with sometimes catastrophic results, such as folding back upon itself and potentially trapping the Rover (Figure 8).

The first two development units experienced erratic deployment characteristics with sometimes unacceptable results due to the inherent complex kinematic deployment behavior. Figure 9 shows an uncontrolled and uncoordinated deployment sequence of one early development unit. The uncontrolled and uncoordinated deployment, in itself, contributed to noticeable damage to the STEM™ elements and ultimately deteriorated their lives. Acceptable deployments and initial vertical trajectory were a function of cable preload and STEM™ element damage.

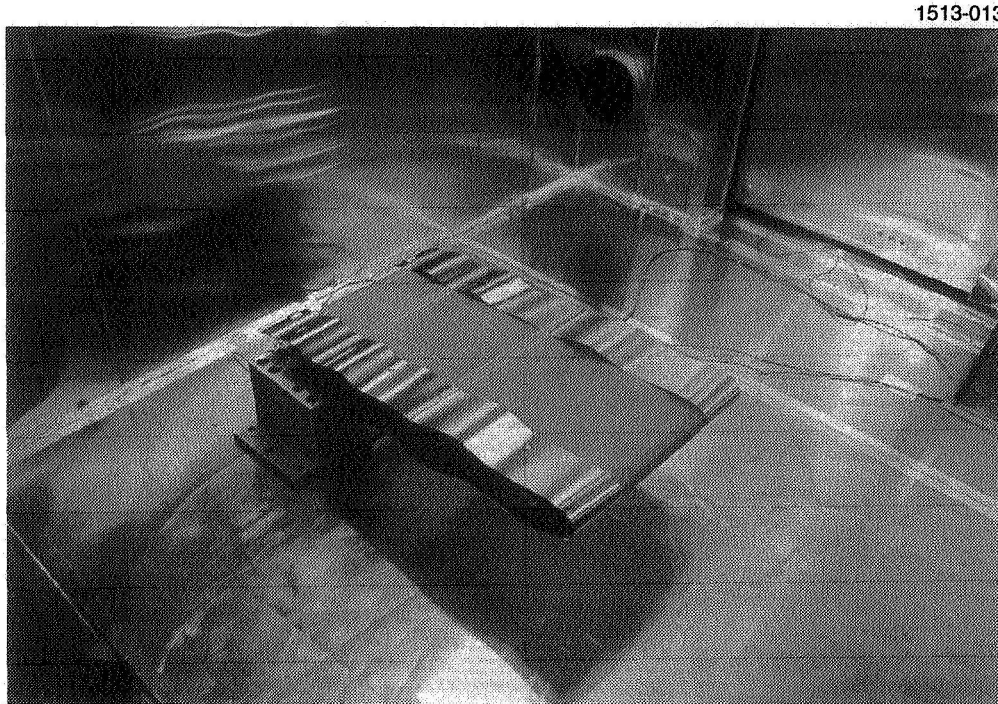
#### Controlling and Coordinating Deployment Kinematics

It was evident from the number of unacceptable deployments that we were not experiencing deployment repeatability that would be necessary to satisfy program requirements. Ideal deployment kinematics of the ramp assembly would allow for the unfurling and swelling of STEM™ elements to be at a slow rate, such that they would have the opportunity to straighten at a faster rate than the unrolling process. In effect, the deployment would be controlled and coordinated. This would allow for the unit to be literally unrolled in a linear fashion from one end to the other, a characteristic which was deeply wanted by everyone involved with the program.

To promote deployment control, coordination, and reliability, thin continuous strips of Velcro™ fastener were attached to each side of the track. The continuous Velcro™ strip was sized with sufficient peel strength to reduce the unrolling rate. During deployment, this would allow the STEM™ elements to straighten immediately after being unrolled, while the remainder of the roll would remain essentially self-contained.

The addition of Velcro™ to the design provided much-needed deployment control, coordination, and damping features. The next development unit produced was outfitted with continuous Velcro™ strips. When deployed, the unit exhibited a truly perfect deployment. Video, depicting this deployment, showed that the Velcro™ attachment effectively reduced the unrolling rate and enabled a fully controlled and

coordinated linear deployment. In simple descriptive terms, this deployment would be analogous to rolling out a carpet while holding the beginning end fixed. Figure 5 shows a ramp assembly deployment sequence with Velcro™ used to control deployment (note the linear deployment direction).



**Figure 8. Unacceptable Deployment of Development Unit.**

The controlled deployments that we were now experiencing led to a dramatic hardware reliability increase. The STEM™ elements were no longer being subjected to violent deployments and, as a result, were not being deteriorated. The incorporation of Velcro™ as a deployment coordination and control device allowed for one development unit to be subjected to over 40 deployment/stowage sequences with no major degradation.

#### Satisfying Deployment at Temperature and Inclination Extremes

Once the Velcro™ was shown to be an acceptable solution, new challenges emerged in satisfying deployment at temperature and inclination extremes. The driving requirement was to provide acceptable deployments at -140°C and at a 30° inclination at ambient conditions. Once the Velcro™ was incorporated into the design, satisfying the longitudinal 66-g centrifuge loading was no longer a problem, and the 1112-N (250-lbf) cable preload was no longer necessary. In the stowed configuration, the Velcro™ provided sufficient shear load capability between wraps, thus effectively eliminating any potential telescoping movement of the stowed package.



1513-000a

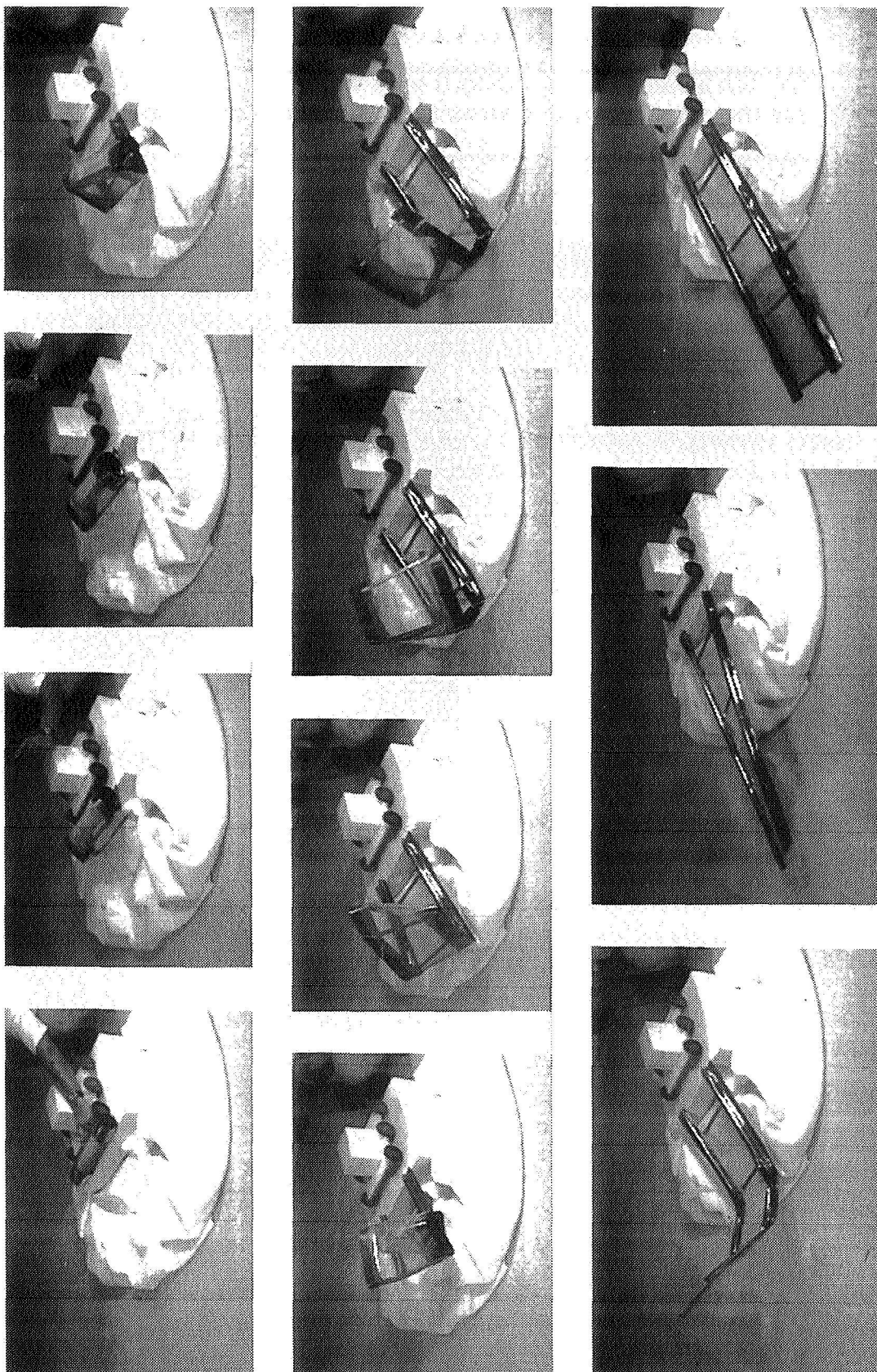


Figure 9. Uncontrolled and Uncoordinated Deployment Sequence.

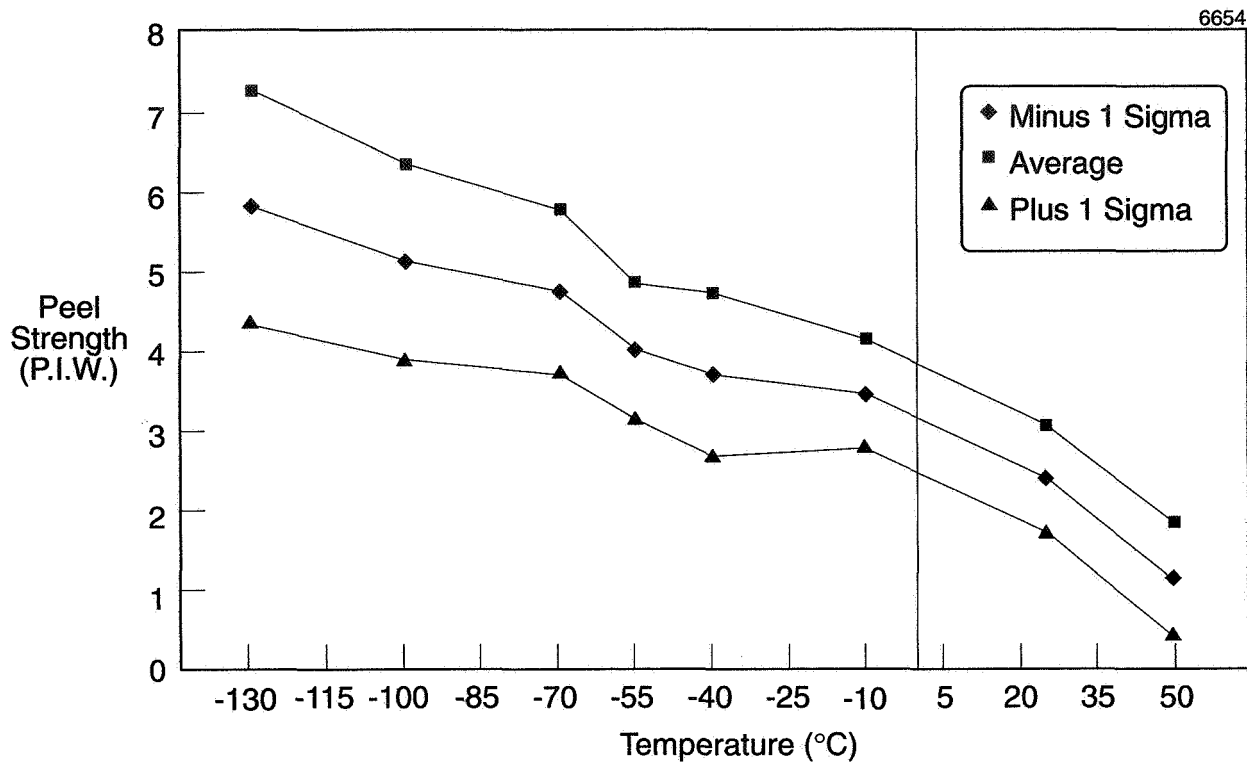


The development unit, integrated with nylon Velcro™ material, underwent an entire qualification test sequence. The unit satisfied the ambient 30° inclination deployment test but failed to deploy when subjected to -140°C. During this cold test, the unit remained motionless until the temperature was elevated to approximately -40°C. It appeared that the peel strength of nylon Velcro™ was exhibiting large temperature sensitivity. The Velcro™ strip was then reduced in width to lower its peel load capability, and the two governing deployment tests were performed again. When the unit was subjected to the ambient 30° inclination test, an acceptable deployment was performed, but it was evident that the reduction in peel strength resulted in a much higher deployment speed, with signs of uncontrolled kinematics reappearing. When subjected to the -140°C deployment test, the unit again failed to deploy, even with the reduced Velcro™ width. Only until the temperature was elevated to around -40°C did the unit finally overcome the peel strength and deploy. Removal of any more Velcro™ to satisfy the cold test was simply not an option, since doing so would not satisfy the ambient 30° inclination deployment test. Rudimentary coupon tests revealed that the nylon Velcro™ material was experiencing a glass transition phenomenon which was resulting in peak peel strengths almost five times higher at low temperatures. The -40°C deployment temperature was unacceptable for the customer, since it would have imposed significant operational impacts to the mission. Because the -140°C deployment condition could not be compromised, an alternative temperature insensitive material, exhibiting similar characteristics as nylon Velcro™, needed to be found to satisfy all the deployment requirements.

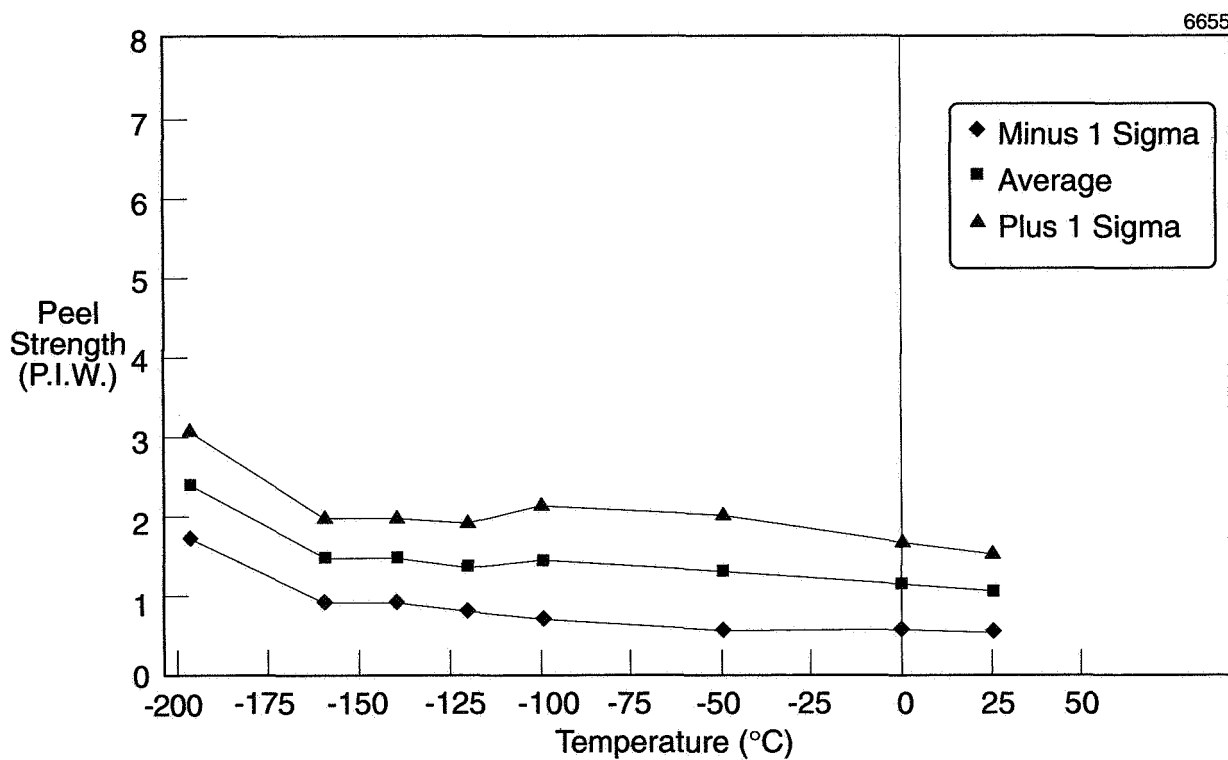
Elaborate coupon testing, performed by JPL, confirmed that nylon Velcro™ was indeed experiencing a wide range of peel strengths, not only as a function of temperature, but also as functions of humidity and rate of peel. Figure 10 shows nylon Velcro™ peel strength as a function of temperature. The JPL test data showed that nylon Velcro™ would not satisfy the deployment requirements. Program efforts focused on finding an alternative fastening system, which behaved similar to nylon Velcro, but provided roughly the same peel strengths at ambient and -140°C conditions.

The JPL testing program characterized many different combinations of Velcro™ attachment types in an effort to yield a temperature-insensitive design. Test results indicated that the ideal Velcro™ attachment candidate consisted of a nylon loop with a stainless steel hook material. This combination was termed a hybrid Velcro™ which exhibited many of the desired characteristics needed. The stainless steel hooks, as opposed to nylon, allowed for a temperature-insensitive fastener. The nylon loops, as opposed to steel, provided greater attachment areas for hook engagement. Figure 11 shows hybrid Velcro™ peel strength as a function of temperature.

With full characterization complete, the hybrid Velcro™ was then integrated into the design. The development unit was then subjected again to the complete qualification test sequence. The hybrid Velcro™ performed flawlessly during qualification testing and proved to be the desired temperature-insensitive fastener.



**Figure 10. Nylon Velcro Peel Strength vs. Temperature.**



**Figure 11. Hybrid Velcro Peel Strength vs. Temperature.**

### Flight Production Phase

Because of the many lessons learned during the program development phase, flight production and acceptance testing proceeded in a routine and uninterrupted manner. The hardware was being built, manufactured, integrated, and tested effortlessly with no anomalies. Approximately halfway through the flight hardware phase, a major concern developed, which had not been thoroughly tested. There was some uncertainty about whether the design could actually satisfy some of the buckling/deflection loading requirements necessary to support the Rover when tilted off-axis at 30°. In particular, the torsional stiffness of the ramp assembly was in question. It had never been characterized, and there was some doubt as to whether its stiffness could counteract and support an inclined Rover at a dramatic change in center of gravity. There was much speculation on what the behavior would be when the ramp was tilted  $\pm 30^\circ$  off-axis while a Rover translated across it. To fully characterize the behavior, translation tests were performed with a simulated Rover vehicle. The vehicle was set up to exhibit a similar wheel base and center of gravity as the flight design. A number of off-axis translation tests were performed, all of which resulted in catastrophic results. The further the Rover translated outboard, the greater the torsional twist of the ramp became, and the more the Rover center of gravity was offset. Eventually, when the Rover reached the outermost end of the ramp, the torsional twist was so large that the Rover could not remain stable and turned over on its side. The tests revealed that even though the hardware satisfied all qualification and acceptance testing, it could not provide successful Rover egress when tilted 30° off-axis. The requirement could not be waived, and the ramp assembly behavior, when exposed to this scenario, could potentially jeopardize the entire Mars Pathfinder mission.

To eliminate this torsional stiffness problem, an integral hinge was incorporated near the root of the ramp of each STEM™ element. The hinges were designed in such a manner that the ramp would deflect in a cantilevered condition under its own weight until the outboard tip was eventually supported by contact with the ground. This feature allowed the ramp to never reach an appreciable torsional deflection during Rover egress. In effect, the Rover could never be tilted too much off-axis to over-center itself. In all translation cases, the ramp provided the Rover an ability to maintain a low center of gravity and promote stability. Subsequent testing of the integral hinges resulted in safe and successful Rover egress at all deployment conditions. The hinges were ultimately incorporated into the flight design, and all acceptance testing and program requirements were satisfied. Figure 2 shows the final flight ramp assembly configuration with integral hinges.

## Conclusions and Lessons Learned

The development and qualification of the deployable ramp assemblies for the Mars Pathfinder program provided many exciting design challenges. This program represented the new “better, faster, cheaper” way that NASA is striving to do business. As with any flight program, there were many valuable lessons that were learned during this program, along with many constraints that were involved in meeting the “better, faster, cheaper” agency goals. Lessons learned during this program are summarized in the ensuing paragraphs.

1. Peel strength behavior of Velcro™-fastening systems is greatly dependent upon operating temperature, humidity, and rate of peel. Perform sufficient testing to characterize pertinent properties of Velcro™ in an effort to gain a thorough understanding of its behavior prior to implementation into a flight design. Ensure that your design can accommodate both high and low peel strength ranges, which are inherent with Velcro™-type materials.
2. Hybrid Velcro™ material, with nylon loop and stainless steel hook, is the least temperature-sensitive Velcro™ combination available. The hybrid system produces similar peel strengths over broad temperature ranges.
3. Mechanical interfaces should not be negotiated until sufficient layout work has been performed. Doing otherwise may cause unnecessary constraints during design.
4. Flat elements, which lie in contact with one another and are pinned at discrete points, need to incorporate slot features at their attachment points to allow for diametric conformance when wrapped together in a cylindrical roll.
5. Every effort should be made to document deployment testing with video to capture any complex kinematics which are not completely understood.
6. Sufficient coupon and development testing should be performed to mitigate risk prior to incorporation into design.

## Mars Pathfinder Lander Deployment Mechanisms

Greg R. Gillis-Smith\*

518-37  
50446  
125132 ✓  
P 18

### Abstract

The Mars Pathfinder Lander employs numerous mechanisms, as well as autonomous mechanical functions, during its Entry, Descent and Landing (EDL) Sequence. This is the first US lander of its kind, since it is unguided and airbag-protected for hard landing using airbags, instead of retro rockets, to soft land. The arrival condition, location, and orientation of the Lander will only be known by the computer on the Lander. The Lander will then autonomously perform the appropriate sequence to retract the airbags, right itself, and open, such that the Lander is nearly level with no airbag material covering the solar cells. This function uses two different types of mechanisms — the Airbag Retraction Actuators and the Lander Petal Actuators — which are designed for the high torque, low temperature, dirty environment and for limited life application. The development of these actuators involved investigating low temperature lubrication, Electrical Discharge Machining (EDM) to cut gears, and gear design for limited life use.

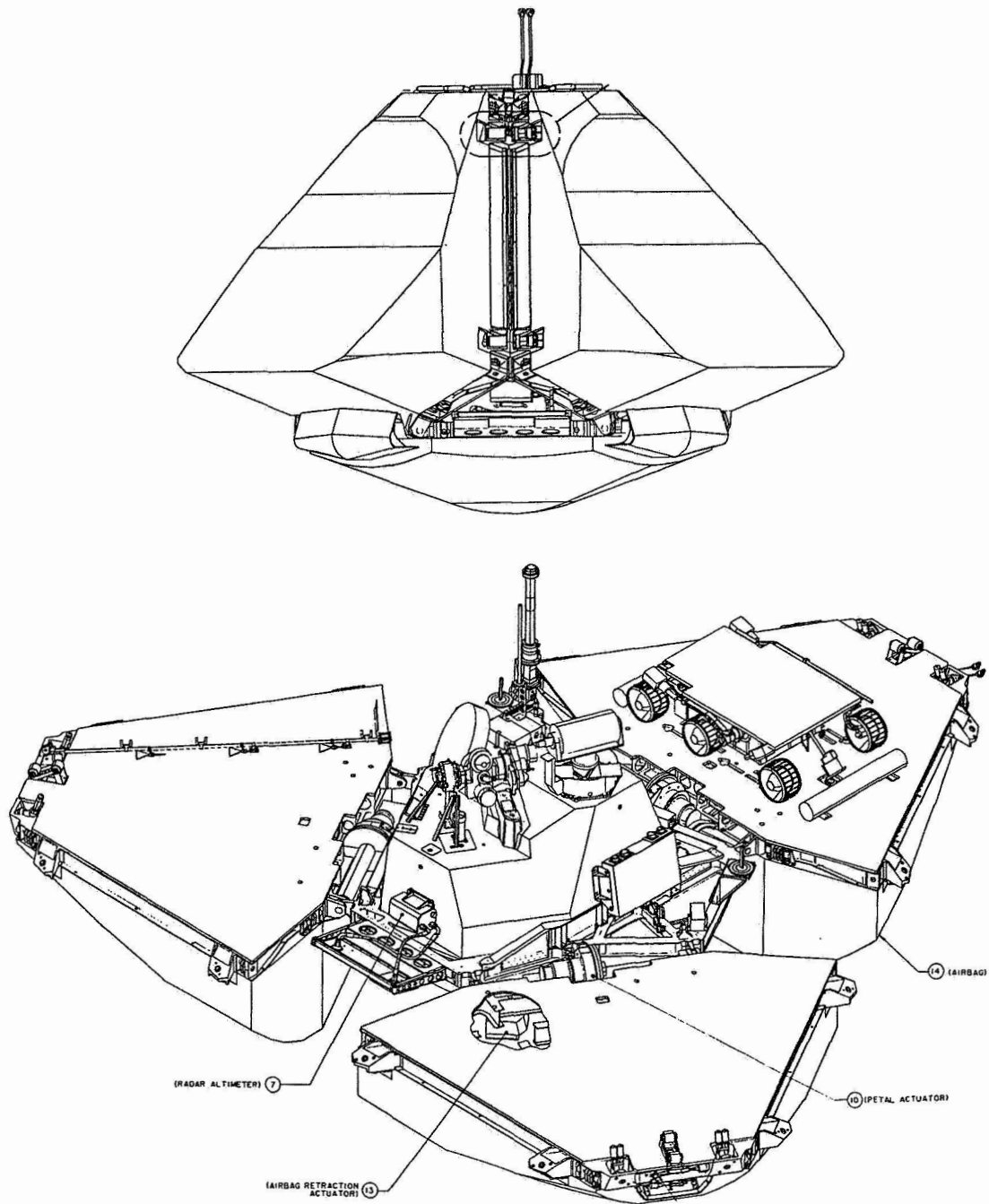
### Summary

The complex EDL sequence begins with a cruise stage separation at 8500 km altitude and 6100 m/s (13,645 mph or Mach 18 at 1 atm). After the deployment of a parachute and the descent of the Lander on a 20-m long bridle, the airbags inflate seconds before RAD firing and bridle separation. The Lander strikes the surface at roughly 22 m/s (50 mph), 35 minutes after cruise stage separation. After bouncing as high as a nine-story building and continuing to bounce for one to fifteen minutes, the Lander should come to rest somewhere in the Ares Vallis in southern Chryse Planitia on Mars on July 4, 1997. The airbags will be covering the outside surfaces of the Lander and may be either intact and partially inflated or ripped and deflated.

Upon coming to rest, the Lander must autonomously determine its attitude and condition and perform the actions required of the Airbag Retraction Actuators (ARA) and Lander Petal Actuators (LPA) to flip the Lander over, if needed, and open upright on the planet surface. The Mars Pathfinder Lander Retraction and Deployment Sequence was developed to solve some challenging and diverse technical requirements. The Lander is a tetrahedron, roughly one meter in diameter. It consists of a triangular base petal with three similar triangular side petals (Figure 1). Each of the four petals is protected during impact with Mars by a large 6-lobed airbag made of Vectran fabric (similar to Kevlar). The final resting state of the Lander is random, but it will most likely come to rest on the rocky surface with one of the four petals down. At this point, the airbags are slightly limp and draping over the petals.

---

\* Spacecraft Mechanisms Engineering, Jet Propulsion Laboratory, Pasadena, CA



**Figure 1 Mars Pathfinder Lander Stowed and Deployed**

## Sequence

Since the antenna used to communicate with Earth is located inside the closed Lander, the sequence must be completely autonomous and able to respond to the unknown landing configuration. Not only must it not give up or get into a dead end or infinite loop, but it must also be simple enough to be tested. This was accomplished by first determining the orientation (out of three basic configurations) of the Lander: base-down, side-down (any one of three), or nose-down. Figure 2 shows the flow chart of the Sequence. Each of these conditions requires a specific sequence to retract and deploy optimally. However, if the accelerometers or motor encoder telemetry should ever fail, the sequence must still enable the Lander to get upright and open. This is done by retracting all bags and deploying all petals. This results favorably, but the bag material sometimes covers parts of the solar cells. Nominally, for a side-down condition, the Airbag Retraction Actuators retract the three of the four bags on which the Lander is not resting. In doing so, the retraction cables, inside the bags, act like drawstrings to open vent patches and cinch the bags simultaneously. Five retraction cables, each about 5.7 m (224 inches) long, are retracted onto a spool inside the ARA. After the bags are retracted, the Lander again senses the gravity vector and begins to open the bottom petal first by turning on the appropriate Lander Petal Actuator; the other two petals follow. This is done to minimize the moment of the flipped mass and to protect the science payload. The final state is having all four petals coplanar, thus allowing the camera to take pictures, the communication link with Earth to be established, and the Rover to drive off the petal. Lander leveling is possible, if required.

The least likely orientation is having the Lander balanced on the top of the tetrahedron. This orientation is remarkably stable on level ground and creates a great challenge to move the center of mass over the pivot point. This is actually achieved with the use of the airbags. The airbag on the petal toward which the Lander is leaning remains unretracted, while the other bags are retracted to bring them closer to the Lander c.g. The two petals opposite the unretracted bag are opened only by 20°, so they are orthogonal to the base petal, hence the tallest they can be. The final bag is then retracted. The drag force of the bag is usually sufficient to pull the Lander onto its side, thus initiating the sequence to re-start using the side-down option.

Testing of the Sequence was performed on a full-scale, Mars-simulated terrain at ambient temperatures and also in a vacuum chamber at Mars temperature and pressure (-100°C and 8 Torr) without rocks or terrain. It was found that, even at Earth-weight, the Sequence was successful every time under normal and nominal worst-case conditions; only manually created "impossible situations" would result in failure.

# JPL Mars Pathfinder CONTROL FLOW FOR AIRBAG RETRACTION & PETAL DEPLOYMENT V2.2.2

Designed by G. R. Gillis-Smith 8/4/95  
Re-Entered by R. Manning 11/9/95  
Version 2.2 updated by G. Gillis-Smith, Brad Swenson & RM12/29/95  
Version 2.2.1 clarification RMM & GG-S 1/15/96  
Version 2.2.2 clarification RMM & GG-S 1/16/96

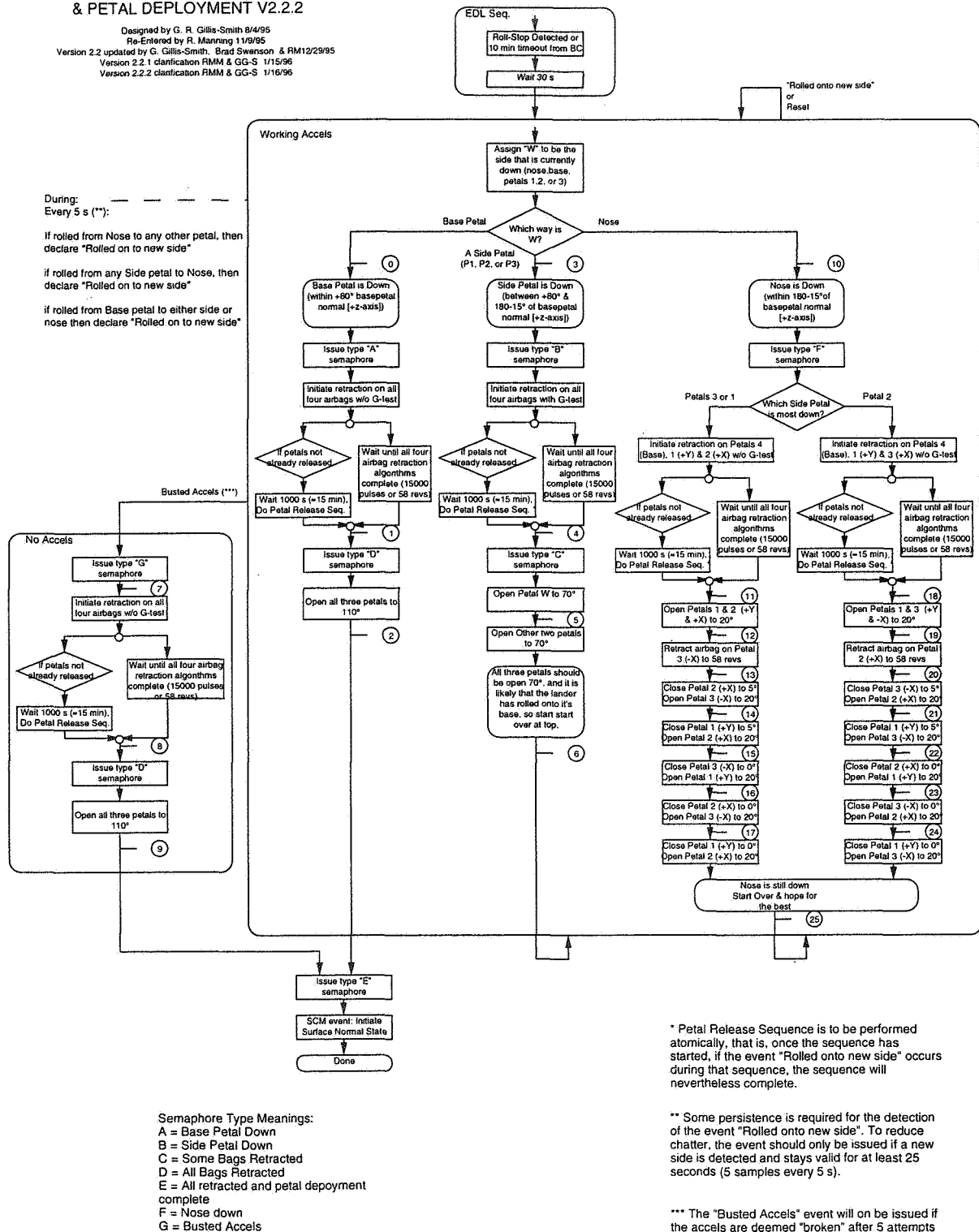
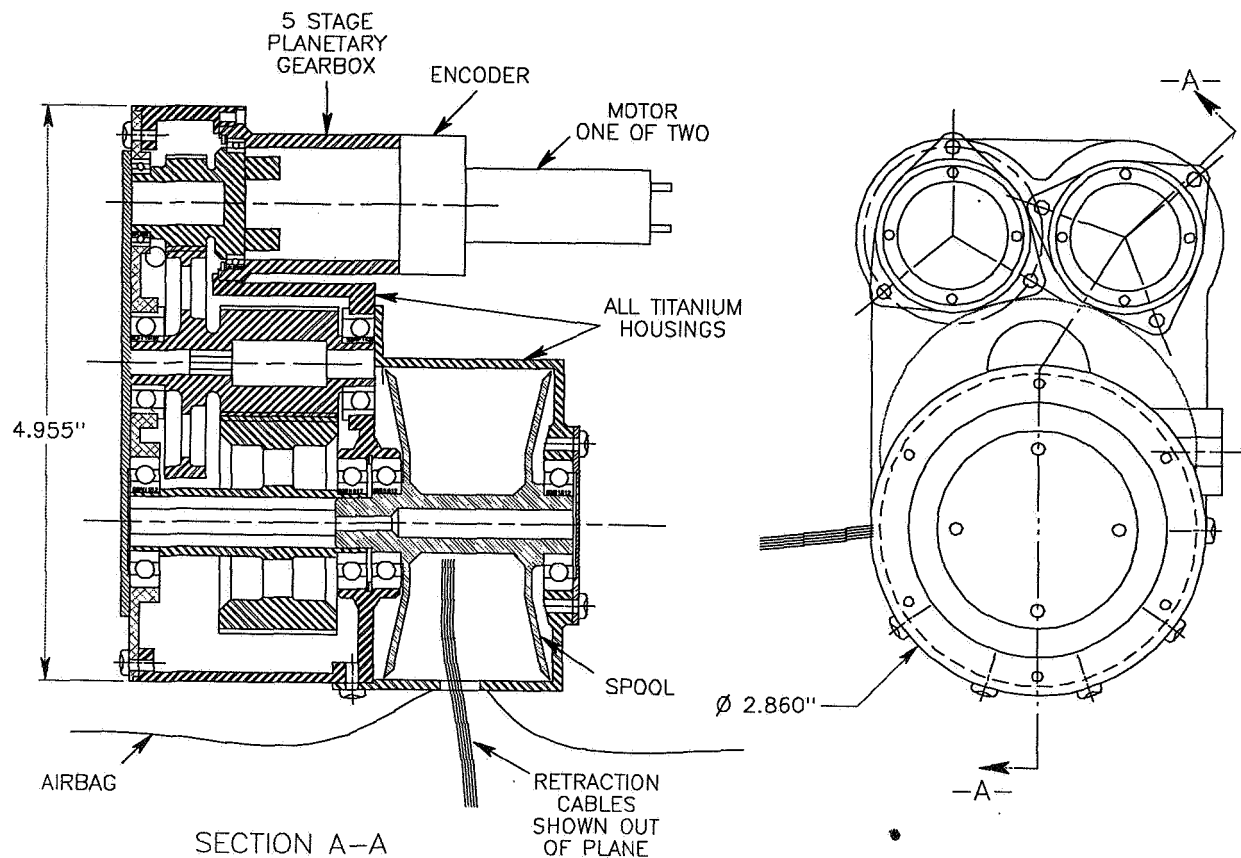


Figure 2 Airbag Retraction and Petal Deployment Sequence Flow Chart



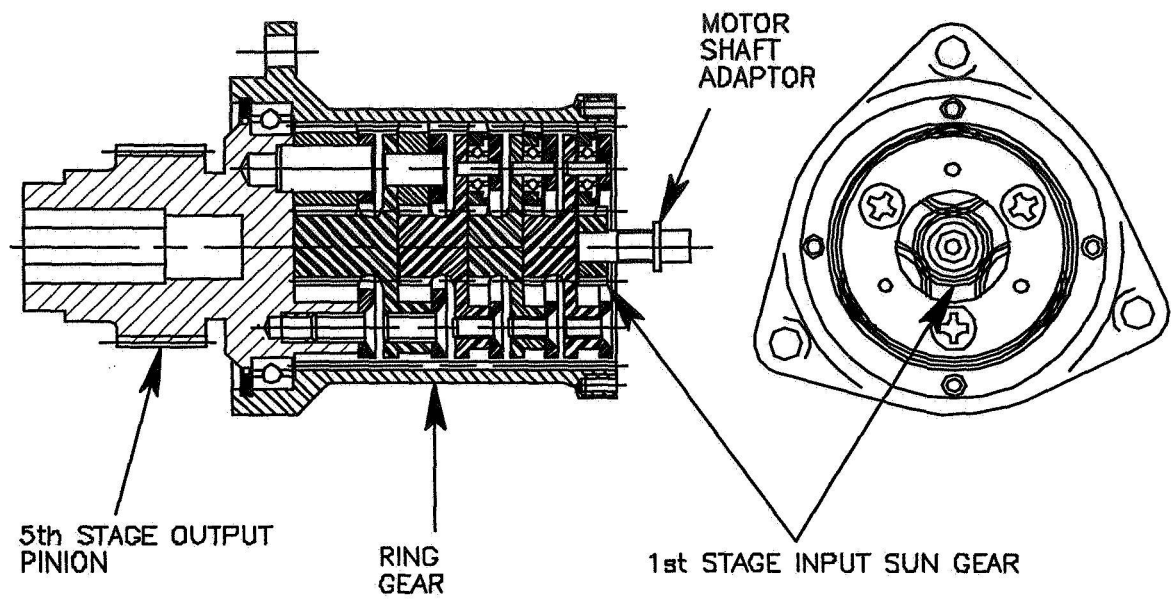
## Airbag Retraction Actuator

The Airbag Retraction Actuator is a robust winching mechanism used to retract the four large airbags on the Mars Pathfinder Lander and requires a maximum pulling force of about 1550 N (350 lb), with a 2:1 torque margin, to retract the bags completely. The primary design criterion for the actuator was a high-torque, compact, and lightweight design. It employs two DC brush Maxon motors to drive 1550:1 five-stage planetary gearboxes, which both drive a single cluster spur gear, which drives a secondary spur gear and spool assembly, thus resulting in an end-to-end 8277:1 gear ratio (Figure 3).

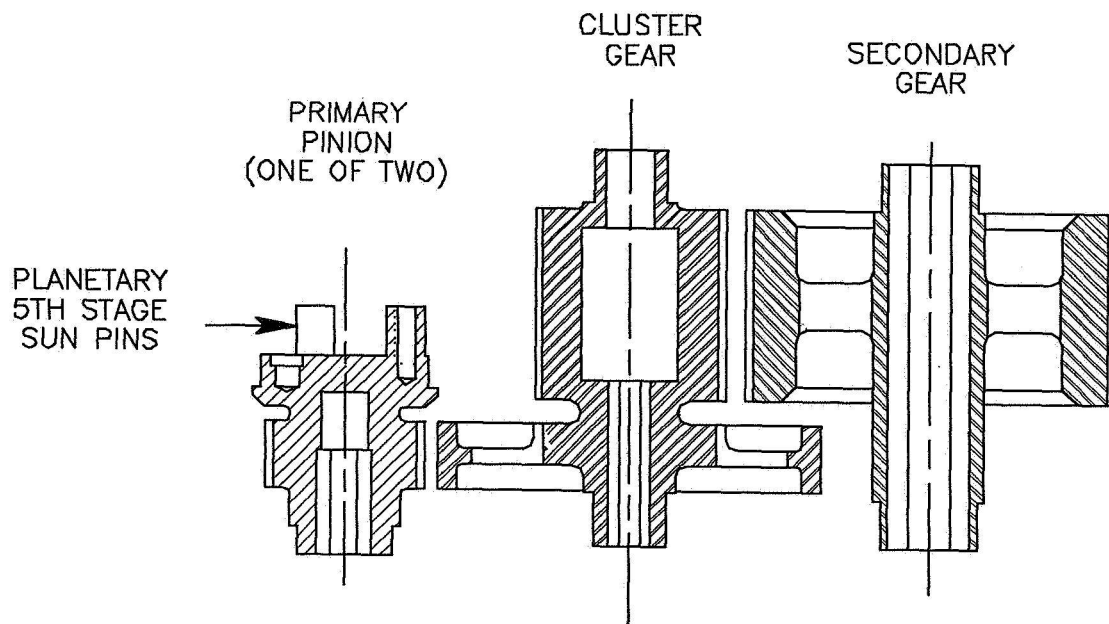


**Figure 3 Airbag Retraction Actuator**

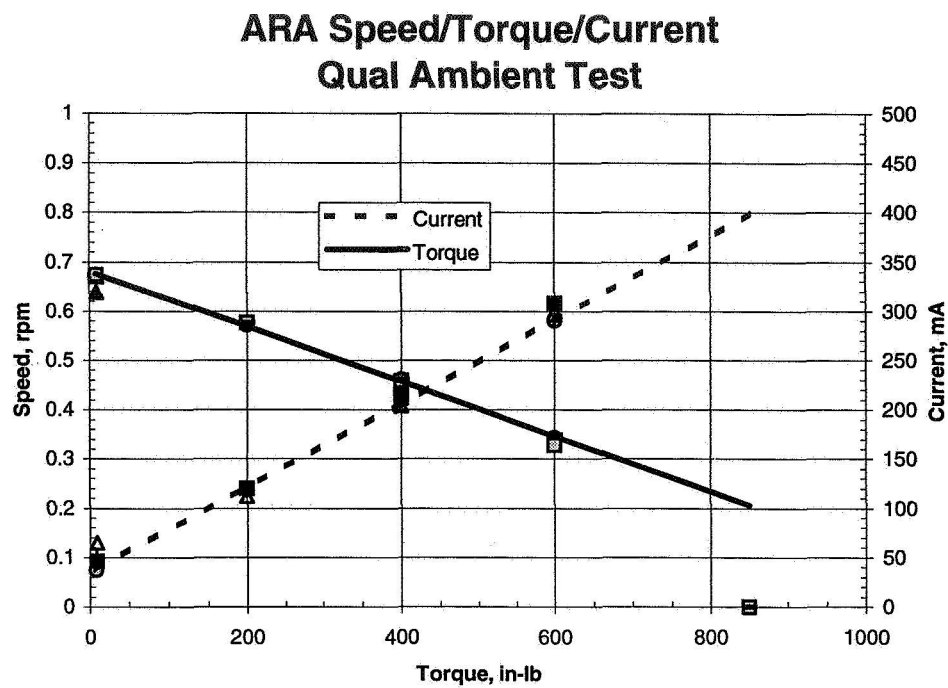
Each motor has a stall torque near 15.8 mN-m (2.24 in-oz). Located between the planetary gearbox and one of the two motors in each actuator, an optical encoder records motor revolutions and hence the length of cable retracted. The five-stage planetary gearbox was designed, such that the ring gear and output can be customized and used in any other actuator (Figure 4). This gearbox was used in the gimbal of the Imager for Mars Pathfinder and will be used in a robotic arm of a 1998 Mars lander mission. For the ARA, the fifth-stage planet carrier is a bearing-supported pinion gear that drives the cluster gear. The final output stall torque of each motor/gearbox is about 11.3 N-m (100 in-lb). The total output stall torque of the ARA is about 96 N-m (850 in-lb) at temperature (Figure 6).



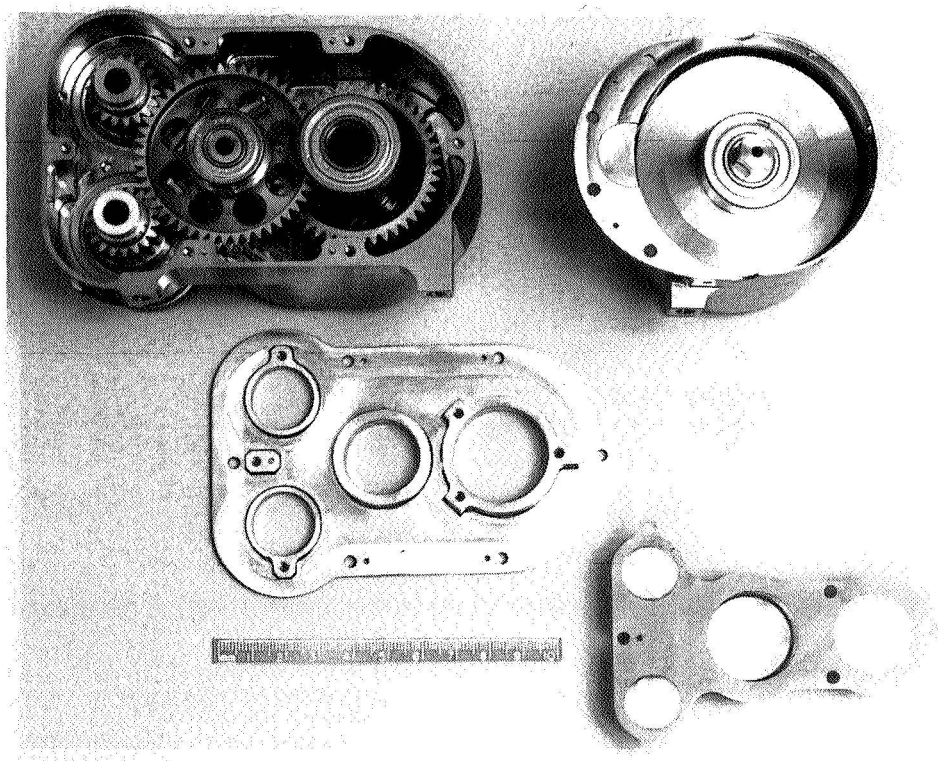
**Figure 4 ARA Five-Stage Planetary Gearbox**



**Figure 5 ARA Gears**



**Figure 6 ARA Speed/Torque Curve**



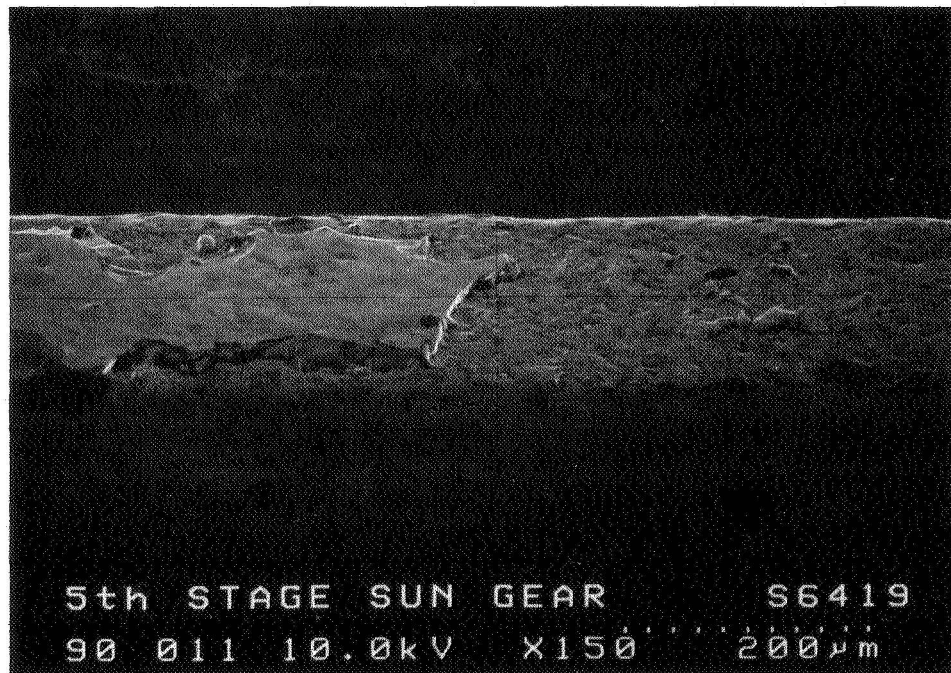
**Figure 7 ARA Assembly**



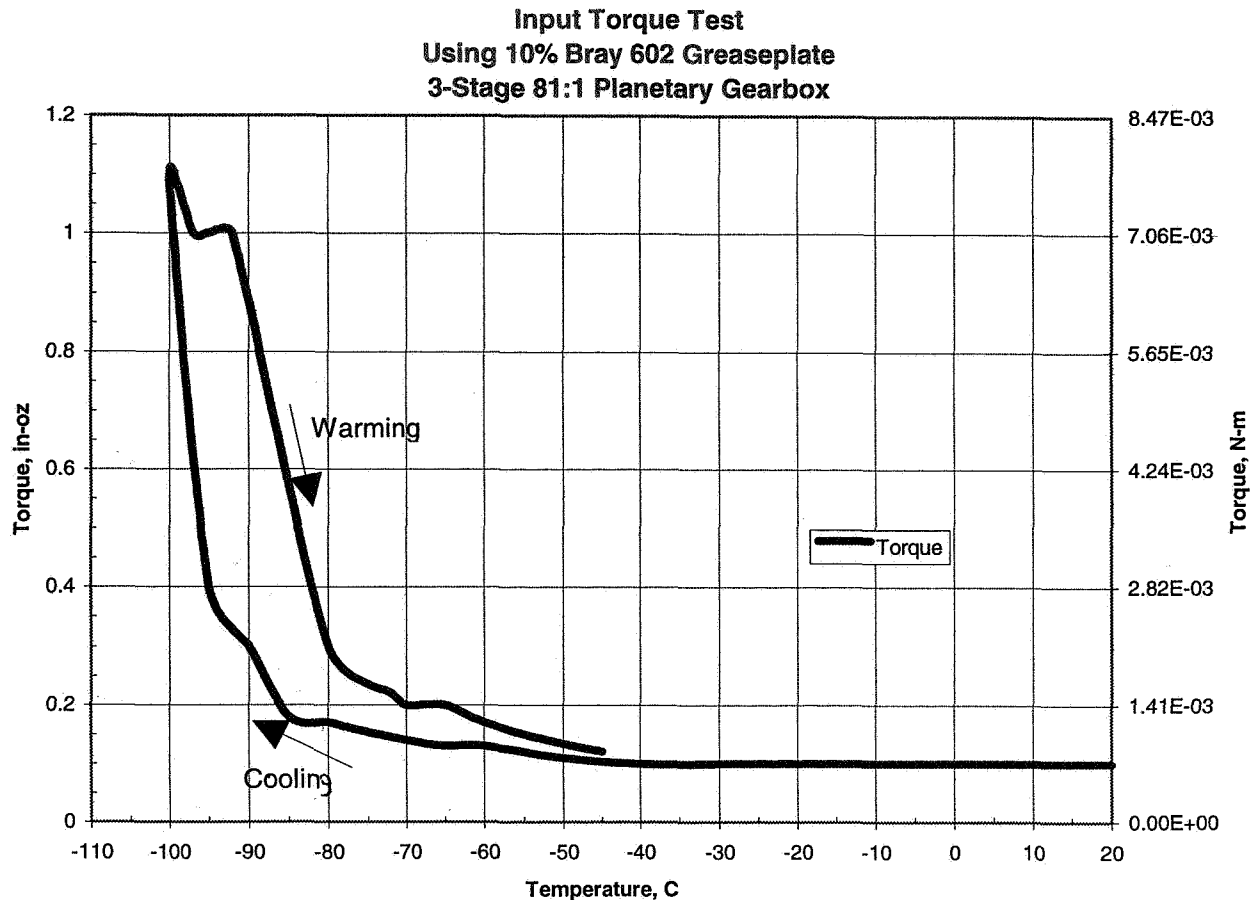
**Figure 8 Airbag Retraction Actuator Exploded View**

## Nedox Plating on Gears and Bray 604 Grease Breakdown

The 5-stage planetary gearbox was designed and built by American Technology Consortium, who made the first two prototypes with Nedox-plated ring gear and planets. Nedox is an electroless nickel/Teflon matrix, known for its great wear properties. Since Bray grease 604, which contains Bray oil 814, has superior low temperature performance and was being used at low temperature in Mars Pathfinder Rover Actuators, it was used in the two prototype gearboxes. When testing the first prototype, the performance degraded and became more erratic. It was later determined that the hard Nedox coating had suffered sub-surface delamination on the last two stages and that the Bray had turned into a hard, tar-like substance (Figure 9). Studying the cause of Bray breakdown included researching both the Lewis Acids phenomenon and the impact of nickel particles in the gearbox. "Braycote 604 may be adversely affected by Lewis Acids, such as aluminum chloride, at elevated temperatures. Rubbing surfaces of aluminum, magnesium, or titanium alloy may react with Braycote 604 causing thermal degradation to the lubricant [2]." Lewis Acids act as catalysts to cause a breakdown of the oil in Bray grease, even at low contact pressures. It was found that the 814 oil in the Bray grease was not robust enough for the high contact loads at the asperity level and that the Nedox particles probably added to the high local loading. High contact loads cause rapid oil breakdown, thus producing identical results to a breakdown catalyzed by Lewis Acids. Visually, one cannot differentiate between mechanical grease breakdown and one catalyzed by Lewis Acids at lower loads. By eliminating the Nedox plating and choosing Bray 602, the gearbox experienced no degradation after repeated heavy testing at temperature. Bray 602 was selected because it is basically Bray 600, which contains Bray oil 815Z, with molydisulfide added for extra load-carrying ability and lubricity. It has similar low temperature torque properties as Bray 601.



**Figure 9 Nedox Failure on Tip of Gear Tooth**



**Figure 10 Grease Viscosity**

Low temperature testing of Bray 602 grease

In order to determine the effects of low temperature on Bray 602, a quick test was done on three of the five stages of the ARA primary gearbox. The gearbox was cleaned and then grease-plated, using a 10% grease, 90% Freon TF solution, and mounted in a cold box with the primary stage open to the top. The primary sun gear was pressed onto a long insulating shaft, driven by a torque watch. The temperature was slowly dropped, and the torque required to turn the input sun gear was recorded (Figure 10). The hysteresis in the torque plot is believed to be due to temperature lag in the grease at the center of the gearbox. It could safely be assumed that the knee in the curve for this grease is about  $-75^{\circ}\text{C}$  to  $-80^{\circ}\text{C}$ , with almost no change in drag effects from ambient to  $-75^{\circ}\text{C}$  but with 10-fold increases from  $-75^{\circ}\text{C}$  to  $-95^{\circ}\text{C}$ . This test determined that the lowest acceptable, flight-allowable temperature limit is  $-75^{\circ}\text{C}$ , thus requiring heaters to maintain a safe temperature of  $-55^{\circ}\text{C}$ .

### EDM used to fabricate gears out of maraging steel

Using a new technology that makes the ARA interesting, the gears were produced by the wire and sinker Electrical Discharge Machining (EDM) process. This allows for infinite adjustment of gear tooth form and shape without the need for custom hobs, shapers, or new master gears for each new tooth form. This technology was first explored because the loading application was quite high and would require a tough material. The selected material, Maraging Vascomax C300, is usually heat-treated after final machining to obtain a yield strength greater than 2000 MPa (290 ksi), as well as good toughness properties. The challenges include both material shrinkage during heat treatment, thus deforming the gear, and required material strength beyond the capabilities of normal hob and shaper processes. With EDM, the material can be heat-treated prior to cutting the gear forms and final machining, thus allowing the part to have a perfect, as-cut gear tooth. Concerns of a re-cast layer that would weaken the tooth contact surfaces have been investigated. McLaren Formula 1 racing team uses EDM to manufacture their transmission gears in order to customize each gearbox for each race. However, they only use a set of gears once and then dispose of them.

In using EDM to machine the spur gears, it is important to have very accurate tooling to produce a gear with excellent form and surface properties. The ARA gears were designed to have an optimized tooth form for high load carrying capability for a limited life at peak loads. If the output gear were designed for infinite life, the face width would have been more than 10 cm for a 2.54-cm pitch diameter. These diameters were reduced to a 23.29-mm (0.917-in) PD and a face width of only 2.54 cm (1 in), but the tooth form was modified and had a 25° pressure angle. Instead of fabricating custom hobs, shapers, and master gears, EDM was selected to make these custom gears. A company was selected for their experience in high-precision EDM, but they had never before made gears. Using software written to produce gear forms, the gear data was entered, and a test gear was wire cut. This test gear was sent to a facility to analyze tooth form, surface condition, and tooth thickness. They found that the held tolerances were those of an AGMA class 10 gear, but one tooth was thicker than the rest. After researching both the EDM gear form software and the tooling used, it was discovered that the tool was not symmetric. After correcting the tooling, the flight gears were made. A second challenge was then apparent: only two of the four gears could be made using wire EDM; the other two had to be done with a sinker electrode. The electrodes were cut on the wire EDM machine, thus allowing for wire thickness offset. Premium grade, fine-grain graphite electrodes, one roughing followed by two finish, were used to produce gears of exceptional form and surface, with tolerances of an AGMA class 10 gear.

The re-cast layer is the outermost surface, which has been re-melted and weakened by the heat of the cutting process. The concern about the re-cast layer was addressed, and it was found that the type of power supply and the way the part is cut “reduced the recast to an almost inconsequential degree [1].” Additionally, electrolysis has been found to be a contributing factor in weakening parts made by EDM. The type of power supply used to cut the ARA gears is called an AE (Anti-Electrolysis) supply, a proprietary system of Mitsubishi. A DC power supply used in EDM has good machining speed, but electrolysis is high and produces more heat in the workpiece, thus causing more thermal damage. Using an AC power supply can improve the surface finish and



integrity, but the speed is half that of the DC system. In each AC cycle, one pulse chemically removes ions from the workpiece, and the pulse of opposite polarity removes less material but does not remove ions by electrolysis. "Even though (the) surface finishes are improved, we still have an electrolytically damaged workpiece, however lessened. This can be in the form of cobalt depletion, rust, oxidation, hydrogen embrittlement, etc. [1]" An AE generator capitalizes on the benefits of DC and AC systems but eliminates the disadvantages. The AC signal is rectified, such that all of the negative pulses are made positive. This creates a machining process that is fast and produces parts which are stronger and have improved surface finishes. In the case of the ARA gears, the microfinish was measured to be better than 24 rms. The inspection data for a 48-tooth gear, cut with wire EDM, and an 18-tooth gear, made with a sinker electrode, shows the variance from perfect tooth form. The average variance is 0.007 mm (0.00028 in) for the wire-cut and 0.013 mm (0.0005 in) for the sinker. It was also found that there was about 0.007 mm (0.00027 in) of taper on the sinker-made gears. These tolerances are roughly equivalent to an AGMA class 10 gear.

One other benefit of using EDM to machine the gears was that they were wire cut with an internal hex bore, since the cores of the gears needed to be lightened (Figure 7). This facilitated dyno testing, since a hex shaft adapter could be placed into any of the gears during actuation to speed/torque test the actuator at any of its stages.

### **Lander Petal Actuator**

The Lander Petal Actuator (LPA) is a large, 5.7-kg (12.5-lb), high-torque, mission-critical mechanism used to flip over and open the 330-kg lander. The LPA primary design criterion was ultra high torque (12,000 in-lb) in a small package with minimal mass (Figures 11, 14). Output speed was a secondary requirement, since the time for both retraction and deployment needed to be less than two hours. Electronic-commutated, brushless DC motors (Figure 12) were selected because of their high torque and even higher reliability; in addition, one was already being developed for another project. The motor has a 0.14-N-m (20-in-oz) output stall torque, which drives a three-stage 49.3:1 spur gearhead, driving a 4:1 internal spur gearset inside the LPA. This outputs through a detent clutch to a 160:1 S-tooth harmonic drive, limited by a maximum (ratchet) torque of 1580 N-m (14,000 in-lb). Torque is transmitted to one hinge per petal by a titanium tube with square drive holes in each end. The output speed of this 31552:1 actuator is about 40 min/rev. The LPA operating temperature is -40°C to +35°C and was tested to -55°C and +55°C, with little change in speed/torque characteristics (Figure 13). This correlated with results of the ARA primary gearbox test, which found that the Bray 602 viscous drag characteristics behave linearly down to -75°C. Kapton film heaters were incorporated into the LPA flight design to maintain actuator temperature above -40°C.

#### Detent Clutch

The clutch is driven continuously between the input to the wave generator and the housing when the actuator is powered. The purpose was to create enough backdrive torque to support the weight of the lander when the actuator is turned off. It uses four opposing pairs of small compression springs, pressing on rollers that ride on the internal surface of a toothed ring gear. The advantage of this clutch is its torque limiting



performance, which is fairly independent of vacuum and temperature conditions. The running torque is slightly lower than the breakaway torque of about 1.36 N-m (12 in-lb).

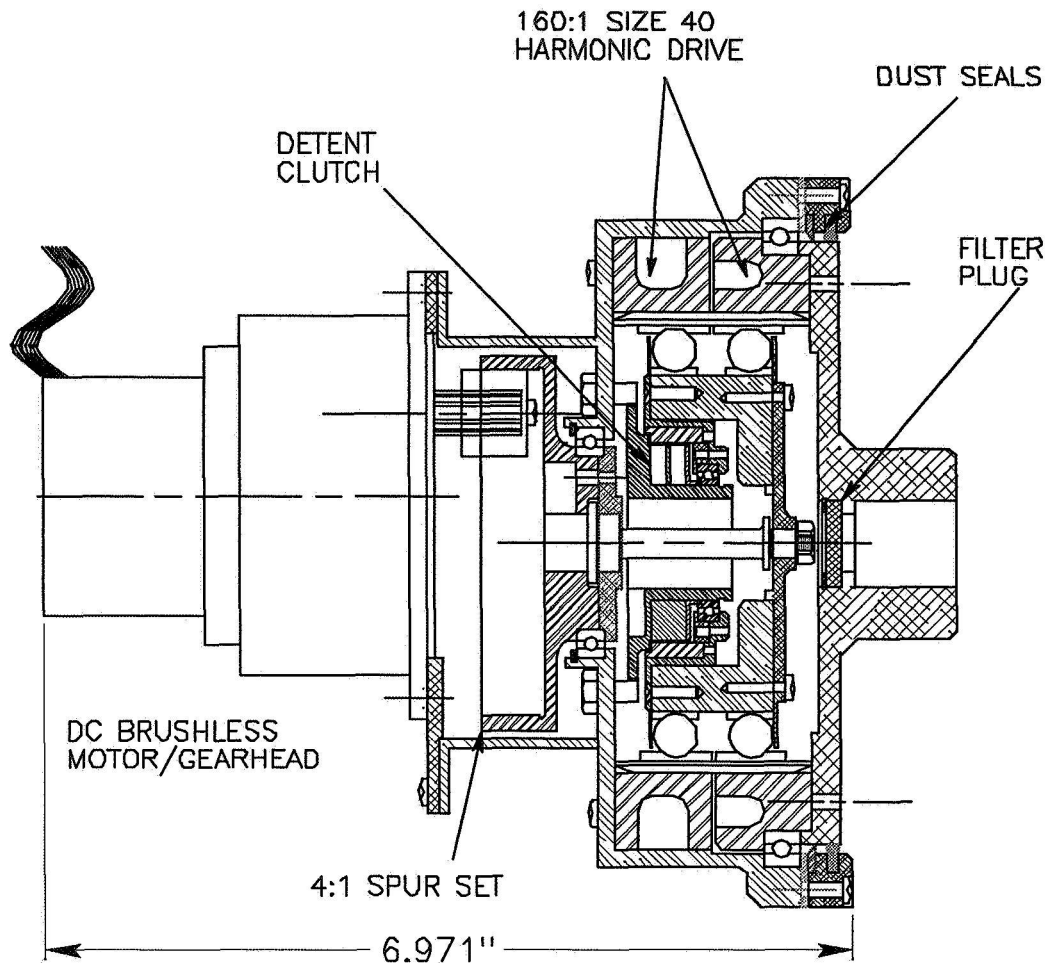


Figure 11 Lander Petal Actuator

#### Dust Protection

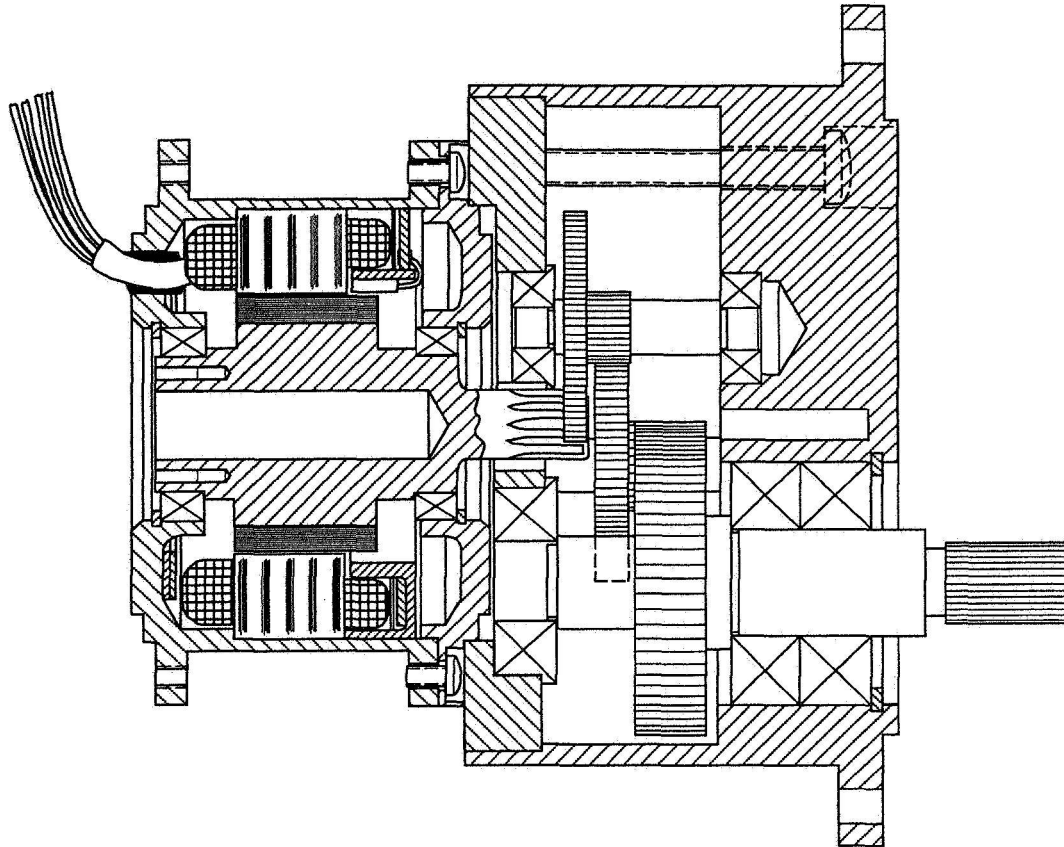
Several protective measures had to be implemented to keep the abrasive Martian dirt out of the actuator. The dust seals use both an outer felt seal and an inner Vespel wiper. The actuator must vent upon launch and refill upon landing, so a porous metal plug was incorporated into the drive hub to allow air passage without dirt (Figure 11).

#### Harmonic Drive

The S-tooth form harmonic drive is able to transmit more torque than the standard tooth form because of greater tooth contact area (Table 1). The new S-tooth enabled the use of the lighter and smaller size 40. Through dyno testing, it was found that the size 40 Harmonic would generally ratchet the flex spline gears before the motor would stall. This is undesirable but was deemed acceptable because the torque output would be limited to the value necessary to lift the Lander. These actuators were dyno tested by attaching the actuator to a 0.61-m (24-in) diameter pulley, 4 m high on a static test tower, that lifts stacks of steel weights. Cold operation was achieved by first filling a

purged Styrofoam box with liquid nitrogen and cold nitrogen gas and then re-warming with a gas heater.

The circular splines exhibited acceptable performance after lightening from 1.02 kg (2.25 lb) to roughly .68 kg (1.5 lb), much to the amazement of the Harmonic vendor. The wave generator was hollowed out to make room for the detent clutch and allow the actuator to be much more compact.



**Figure 12 DC Brushless Motor/Gearbox**

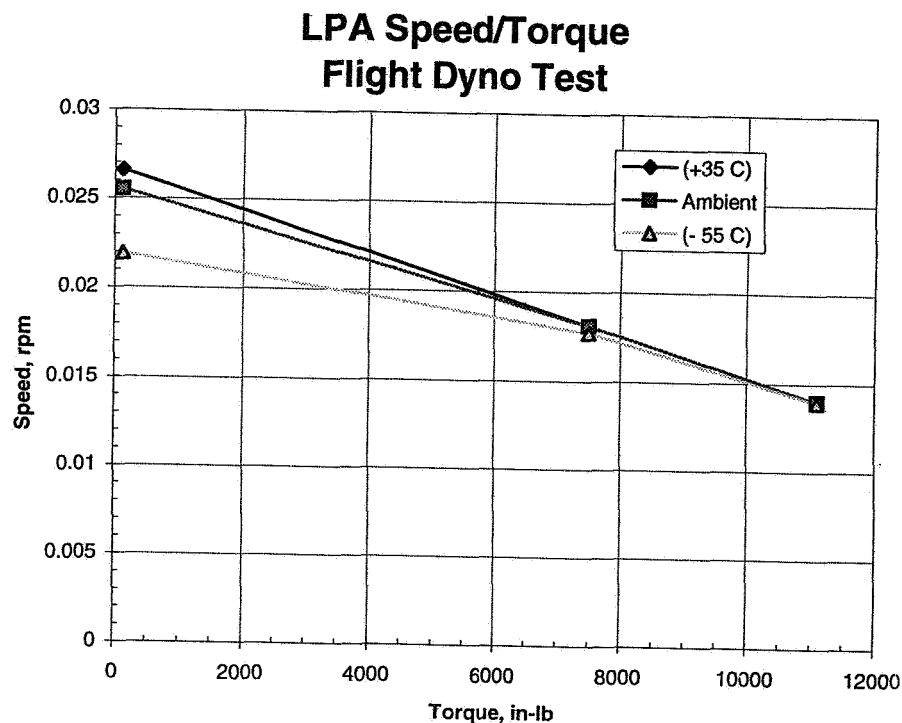
**Table 1 Comparison of Tooth Form Torque Capability**

Catalog Rating	Size 40 Standard	Size 50 Standard	Size 40 S-Tooth
Ratchet Limit	745 N-m 6600 in-lb	1410 N-m 12,490 in-lb	1580 N-m* 14,000 in-lb
Momentary Peak Limit	Ratchet Limited	Ratchet Limited	1370 N-m 12,150 in-lb
Mass (unlightened)	3.0 kg	6.0 kg	3.0 kg

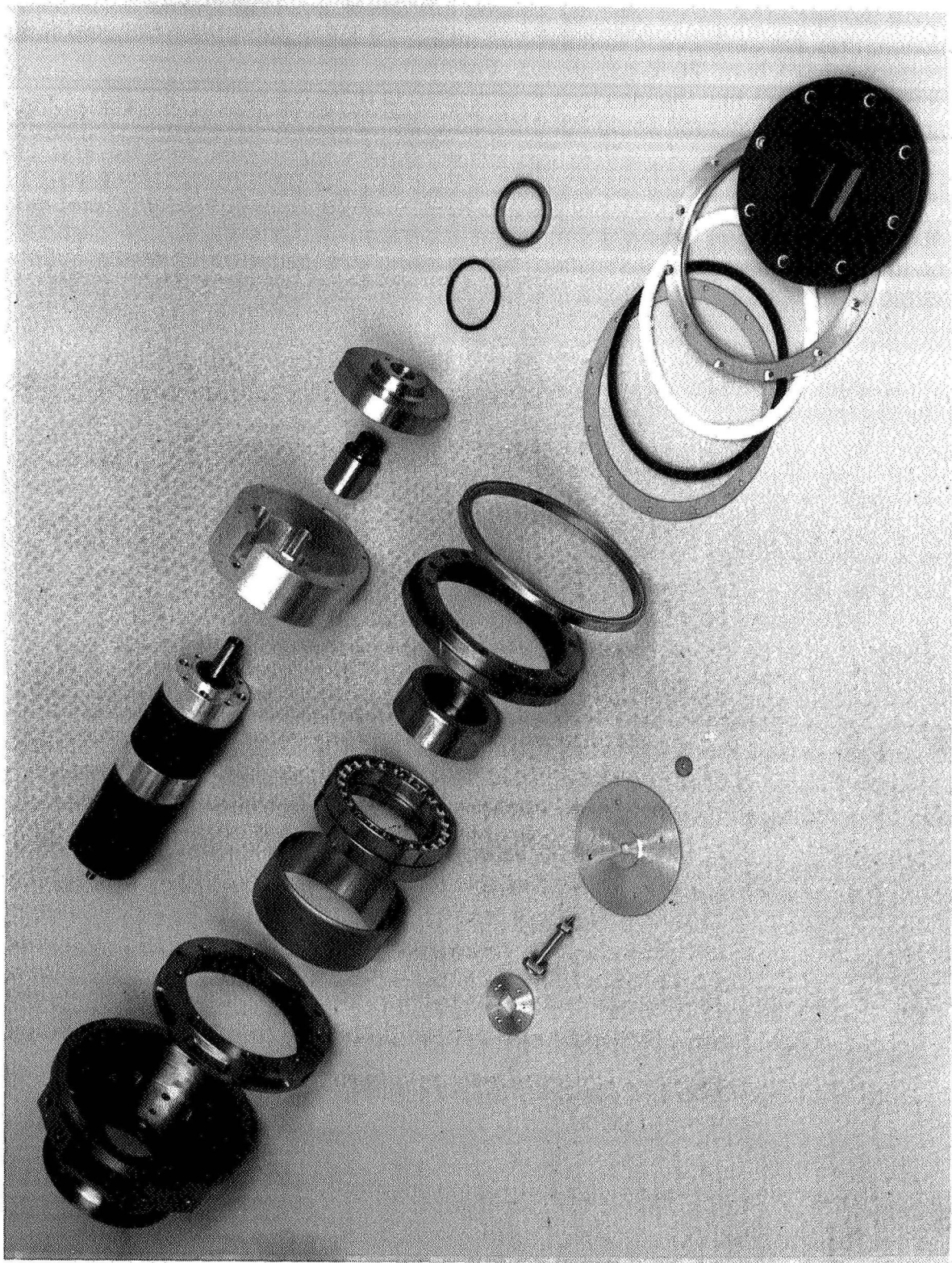
\* Tested value

### Low Temperature Application of Harmonic Gears

Since the harmonic gears are only 30-45% efficient due to their characteristic sliding friction, they are sensitive to temperature effects on lubricant. The LPA motor only produces 0.141 N-m (20 in-oz) at stall. For another application on Mars Pathfinder, a similar motor with half the stall torque was used to drive a size 10 harmonic drive directly, but this actuator would not run below -50°C. The lubricant was changed to a very light grease plate of the Bray 604 low temperature grease, thus correcting the cold operation problems. In comparison, the LPA, with 800 times the input torque applied to a size 40 harmonic gear that was filled to 10-20% of the Bray 601, had no problems to -100°C. The obvious lesson is that, when using smaller, lightweight, low-torque motors, the torque needs to be “preamplified” before being transmitted to the less efficient harmonic gear.



**Figure 13 LPA Speed/Torque Curve**



**Figure 14 Lander Petal Actuator Exploded View  
(with test motor and no clutch)**

## Conclusions

The mechanical failure of the Nedox causes us to conclude, once again, that gears under any significant load should not be plated with a hard material. Sub-surface delamination occurs due to the "ceramic-coated banana" condition. Repeated loading and deformation of the gear teeth cause the hard, non-wearing coating to flake off, thus becoming "ground-up razor blades" in the gearbox. For small, lower-torque gearboxes, this proves to be catastrophic.

Bray grease, such as 604 that uses the Brayco 814 oil, is susceptible to mechanical breakdown under moderate loads, especially in conjunction with particles that cause high loading and heat at the asperity level. Greases, such as 600, 601 (with rust preventative), and 602 (with molydisulfide), that use the Brayco 815Z oil are more robust for contact loads but should still avoid high loading or particulate contamination.

Bray 602 tends to be fairly linear in viscosity from ambient temperatures down to  $-75^{\circ}\text{C}$  but has geometric increases in viscosity, and hence torque loss, below  $-75^{\circ}\text{C}$ .

Electric Discharge Machining (EDM) is an acceptable machining technique for gears, provided that the surface has not been adversely impacted by the process. It appears that the AE power supply enables the EDM process to produce stronger parts with better surface finishes. At this time, until more life testing is possible, it would be prudent to use gears made with the EDM process for limited life applications.

Due to the high startup drag torque of harmonic gears, it is imperative to use other types of gears to "preamplify" the torque before it is transmitted to the harmonic.

Some DC brush motors may be used reliably in a space environment, but they must be free of grease lubrication at low temperatures. Extensive dyno tests on one type of small, DC brush motor proved reliable operation to  $-75^{\circ}\text{C}$ , provided that all of the grease was cleaned out.

## Acknowledgments

The research described in this paper was performed by the Jet Propulsion Laboratory, California Institute of Technology, under a contract with the National Aeronautics and Space Administration. We also wish to thank D. Peterczak and J. Sprunk, from American Technology Consortium, who designed and fabricated our ARA primary gearboxes, Ernest "Bodie" Bodensieck who designed the ARA gears, and the precision EDM machining specialists at Maroney Company.

## References

1. Guitrau, E. "EDM and Electrolysis." E & M Engineering. 1995.
2. Castrol, Inc. Specialty Products Division. Product bulletin Braycote 604. 1991.



# Reliability and Testing

Werner Auer\*

519-38

50447

125133

9 12

## Abstract

Reliability and its interdependence with testing are important topics for development and manufacturing of successful products. This generally accepted fact is not only a technical statement, but must be also seen in the light of "Human Factors." While the background for this paper is the experience gained with electromechanical/electronic space products, including control and system considerations, it is believed that the content could be also of interest for other fields.

## Introduction

The consideration of the interdependence of reliability and testing is an important subject for the success of development and production. The background for this paper is the experience gained with electromechanical/electronic space products, including control and system investigation. Besides "Technical Necessities," the "Human Factors" have to be treated. Some examples of the positive or negative influence are given.

## Reliability

Reliability can be described as the property of a product to fulfill the intended task and duty in a given environment for a defined duration with a certain probability of success. Reliability has to be therefore an inherent quality of a product which can be - and for space products, has to be - proven by appropriate testing. The required reliability has to be a major design driver from the very beginning, the first ideas and feasibility studies. This work has to also include investigations in to how the quality, reliability, and the performance of the intended product can be determined and measured. Mostly, the already available equipment for measurements, testing and production as well as design aids and experience, are points of main consideration. The same is true for proven processes for design and production.

Reliability calculations have to accompany design and development. The results of those calculations may lead to a preferred design. But caution is necessary whether the reliability numbers assumed can be realized with the available technology, parts and other resources. Already existing lists of acceptable materials, parts, subunits, software programs and so on, and of qualified vendors should be obeyed. For those elements, there are also proven reliability and life numbers available. A formal quality assurance approach with written procedures and instructions is most helpful for achieving reliability. All relevant methods and steps described there should be implemented regularly in the course of development and production phases.

---

\* TWB Wiesenbach/Heidelberg, formerly TELDIX, Heidelberg, Germany



A good definition of the work to be done with specifications demanding the necessary things only (with reasonable margins) are important for quality and schedule. The most experienced people should establish the concerned documents. Quick changes introduced after discovery of a disadvantage should be avoided. Reliability needs to scrutinize all aspects of a change. This is important throughout all phases of a program. Hardware and software must be treated equally from the standpoint of quality and reliability.

Cost and schedule restrictions may limit the efforts towards reliability. Therefore, proven principles or even existing design approaches should be used as much as possible in an actual program. Basic research and alternate design investigations should be studied independent of flight programs with less pressure on schedule but with clear aims.

It is also important that the group, working on a certain product, has the necessary knowledge of the system in which this product is used. Generally, this reduces interface problems and aids the definition and improvement of meaningful specifications. It is also speeding up a development process and is a source of motivation. In this context, interface questions must be thoroughly considered and defined. The validity and strictness of interfaces must be continuously discussed and checked by testing in early phases of a development. This is especially important in connection with subcontractors that work outside of the company or even abroad. Formal controls are inevitable. A responsible person has to overlook in a competent way both sides of an interface.

Important subcontractors have to be incorporated in quality and reliability efforts from the very beginning. In many cases, education measures have to be taken. If subcontractors have their own quality assurance system, this has to be checked in the sense of compatibility.

If there are doubts in the quality of sections of a product, technological samples, thoroughly investigated and tested, are a help to improve certain capabilities early in a program or to avoid the initially planned technology in the further development.

Often "small things" are overlooked: a wire which is not secured, a too high or too low torque applied for fastening a screw. The most ingenious design is endangered by these inconsequential items.

Providing redundancies is not always a help in achieving reliability. Switch-over units from the primary to the redundant system and back, may be of the single point failure category. In hot redundancies - primary and redundant systems work in parallel - the testing needs special attention and a high degree of knowledge.

Besides the philosophy of redundancies, the considerations of alternative and/or down-graded modes of operation can be fruitful. With the advent of high telemetry transmission rates and powerful ground-based computers, for instance, control loops may be even closed via the ground control (of course taking into calculation the "dead time" of transmissions - already in the development phase).



In many cases, reliability and life of a product have a certain dependence to each other. This statement is valid for products that exhibit a random failure behavior. In contrast, other products have a certain life expectancy due to wear-out, to fatigue processes, to evaporation, and so on. Some products show, in addition, a non-failure period, a time span, in which no failure should occur, a property that could be important to improve reliability decisively.

An important advice is: start with a concept as simple as possible. When arriving at detailed problems, every approach will demand the full capability of the personnel. Normally, a simple approach is also an elegant one that is good for the pride of all involved. Here are some examples for electromechanical/electronic devices for the principles just mentioned:

- Elimination of caging devices where conceivable (avoiding of single point failures, often at the very beginning of a mission). Instead, damping of main resonances, limitation of the excursions of oscillations, and similar methods should be developed.

- Suspensions and passive actuation can be often combined; a bearing may also act as a spring and vice versa.

- Preference of drive systems that require no additional bearing suspension. If redundant driving is required, two motors/windings on one axis should be applied. (No mechanical switch-over.)

- Selection of drive principles that promise straightforward control, e.g., position drives instead of torque drives if better suited.

- Definition of favorable mechanical/electronic interfaces, in view of separate testing capabilities of mechanics and electronics.

- Preparation of modular concepts to facilitate development, production, quality control and testing. The utilization of proven modules or derivatives of such modules enhance credibility of an approach.

- Selection of materials based not only on mass and strength but also on machinability, handling precautions, thermal characteristics, surface treatment properties etc.

- Utilization of lubrication schemes that work essentially independent of acceleration levels and directions as well as under air pressure or vacuum.

- Optimization of reliability by avoiding single point failure possibilities. Redundancy switch-over should be passive, if conceivable.

- Valid testability is a must in consideration of any approach for designing a product.

Of course, this list can be carried on, depending on the product to be discussed.

In this context, it should be borne in mind that there is a natural pride of "own designs," "own ways" which is essential for motivation. But especially here, a constructive criticism should be not excluded. Fair comparisons with other designs, different approaches, and alternative ways are very helpful.

Also the effect of a "patent philosophy" can hinder the search for the optimal solution. This is true for both aspects: other companies have patents or applied for patents that complicate the development, especially if this situation is not known at the beginning of a work, or a co-worker in your company has made an invention that he tries to realize (also for reasons of financial benefits), even if it is not the best solution.

Friendliness to each other must not lead to hiding of problem areas and keeping secret of incidents. Those should be honored who have the courage to say unpleasant truths - in time and in a friendly way.

A climate of confidence, but also of sound criticism and reasonable competition between ministries, agencies, companies, institutes and so forth is important. Political considerations should be excluded as much as possible. Technical and scientific problems have to be tackled on the grounds of natural laws and not by investigation of the opinion of higher ranking people, inside or outside the company.

Dedicated, educated, well trained, experienced, motivated and co-operative people are of utmost importance through all levels of a hierarchy in the course of the design, development, production and testing phases. Clear responsibilities, added by strict documentation and control are most important prerequisites for reliability.

## **Testing**

Quality and reliability are no substitutes for testing. Testing is no substitute for quality and reliability. Both have to go hand in hand to reach the goal providing a quality product according to specifications.

Meaningful testing has to accompany a program in all phases: feasibility studies, design, development, qualification and manufacturing. Tests must be carefully planned and performed, the test results documented.

Testing represents also a significant part of the costs of a program, but the proof of reliability - or sometimes the contrary - is essential for the success of a mission.

In many cases, designing of a product seems to be a clear sequence of efforts but valid testing can be very complex. It is no problem to invent irrelevant tests, to misinterpret results, to fail to recognize the significance of an event, and to overtest or to undertest. Inadequate testing may even obscure weak points in a design instead of bringing them to light. Too long and too severe testing may reduce reliability and life of a product, which is of course not intended.

The purpose of testing, realized in a test program, must be to prove the product's specified performance under a predicted environment. In addition, the reliability over the required life time has to be demonstrated (mostly in combination with justified

calculations). No aspect must be overlooked. Therefore, a test program has to be considered as an equally important part of a development, a qualification and a production process.

To achieve the intended purpose of a test program, a certain formality is indispensable. This includes written detailed instructions, the co-operation of independent and experienced quality assurance and quality control people, and written fail/success criteria. The strictness, formality and severity of the tests have to increase with the phases of a program from feasibility tests to qualification, acceptance, and life tests.

It is essential to employ experienced people who are able to bear the involved responsibility and to set the levels and the sequence of testing. Wrong judgment concerning test specification can result in both, damage of the product and schedule problems (besides cost overshoots). Adequate test facilities and experienced engineers are prerequisites for valid testing.

The above considerations are valid for the following categories of tests:

- Development Tests (probably also Feasibility Tests)

- Qualification Tests

- Acceptance Tests

- Refurbishment Tests and Differential Tests

- Life Tests, both Real Time or Accelerated

#### Development Tests

These tests are performed usually by design and development engineers to prove the validity of design approaches and the technologies involved. Parts and subassembly tests could be performed if deemed necessary. Therefore, these tests are not formal, but very useful to develop test procedures for later formal tests, to make quality control and quality assurance people acquainted with the actual development, and to test - in a later development phase - with more mature models, the ability to meet qualification specifications. In certain cases, such a pre-qualification tested model is utilized for a life test to gain as early as possible additional information on the long-term behavior. Of course, adequate written reporting is necessary as reference for later formal testing.

With the growing complexity of satellites, the Electro-Magnetic-Compatibility (EMC) has become of utmost importance. Therefore, strict testing and well-understood improvements to the necessary level (with suitable margins) are required in the course of the development phase. Deficiencies that would be detected in later phases only could force basic changes in a design with a result of time delays and cost problems.

#### Qualification Test

This test is crucial to the success of a project. The objectives of a qualification shall be to prove that a model built according to the established manufacturing documentation

meets all specifications and requirements in the full range of the expected environment - with reasonable margins. The results of functional tests before, after, or - if appropriate - during, the exposure to environmental conditions must be within prescribed limits. The sequence of tests should be similar to that in an actual mission: first vibration, acoustic noise and shock tests, then thermal (vacuum) tests. Often mechanisms and the associated electronics have to meet different specifications, which must be obeyed in test set-ups.

Qualification by similarity with an already qualified device is often regarded as being acceptable. If the main argument is time and money saving, one should be especially cautious. In mechanical units, even minor changes may cause catastrophic results. Even another cleaning process, another preload of bearings, or "identical parts" supplied by another vendor must be carefully considered to avoid unexpected failures. Therefore, the qualification by similarity of mechanisms should be the exception and only adopted in fully justified cases.

For electronic units, qualification by similarity is a more valid approach. For instance, the fixation of printed circuit boards or the use of special housing configurations are examples for acceptable cases.

A passed qualification test becomes the coronation of a successful development and the final demonstration of its reliability, quality and integrity. Such a test must be carried out with rigorous formality and obstinate strictness under the control of co-workers of the product assurance system. The participation of representatives of the customer at qualification tests underlines further the significance.

Depending on the general philosophy or the special situation, a qualification model may be either stripped and examined thoroughly for whether the tests have done any harm to the qualification model, or used as a formal life test model, or refurbished to a flight model (for instance by exchanging bearings with subsequent acceptance testing).

Of course, a formal qualification report must be established.

### Acceptance Test

While the qualification test demonstrates the quality, reliability and suitability of a design, acceptance testing should prove the quality and integrity of an individual flight model, built to the production specifications and procedures.

Main objectives of this test are therefore:

Demonstration in an integral way that the tested model is free of workmanship errors.

Proof that the tested model complies with the manufacturing and quality control processes, the functional performance requirements, the dimensional, weight and interface specifications.

This test should be performed under the maximum predicted operational levels (in some cases with small margins) concerning environment. Like the qualification test, acceptance testing must be carried out in a strict formal way according to written instructions under the responsibility of quality assurance people and often under supervision of representatives of the customer. A formal acceptance test report must be provided in which all important observations and deviations have to be noted. This report has to serve during a mission as the main reference if anomalies should occur.

#### Refurbishment Tests and Differential Tests

Refurbishment tests are essentially formal acceptance tests that are carried out on models, built to flight standard after their qualification testing, repair, replacement of parts and long storage, to prove the flight worthiness.

Differential tests are performed on already acceptance tested flight models if it has - for instance - become necessary to introduce minor changes into performance specifications, to marginally change the mechanical interface and so on.

After careful consideration, a differential test comprises a certain part of an acceptance test only. The results of those tests have to be documented as an appendix to the acceptance test report of the unit already formally acceptance tested.

#### Life Tests, Real Time or Accelerated

Life tests on themselves are no proof of reliability, quality and life. They make sense only, if before, by life calculations, adequate applying of proven technologies, taking into account experience gained with similar equipment, and other considerations, a basis for such a life test has been established. This becomes clearer if one is aware of the fact that a life test with one or some life test models will give no insight in the statistical behavior: If one would try to prove that a design has a life of 10 years with 99% probability, he would need in the order of 1000 life test models to get an answer with 10% accuracy. Nobody has the money and the time to work this way. And if such a test would fail, the money and the time would be lost with the result only that the developed design does not meet the life requirement.

Therefore, a life test can be a proof only for the fact that there is no basic life limiting effect present in a design. (Of course the psychological aspects of positive results of a life test should be not underestimated.)

Life testing, both real time or accelerated, needs careful consideration and planning. A certain formality and control has to take place. Life test models have to be representative concerning the life determining and life limiting features. This needs careful judgment.

While real-time life test planning is mostly straightforward, the establishing of accelerated life test procedures needs a profound knowledge of the test item and the mission conditions to define acceleration factors, modes of operation, and so on. For instance, a truly representative accelerated life test with a liquid lubrication system is not possible, because acceleration factors for temperature and speed cannot be defined.

Typical application for accelerated life testing are units with dry lubrication that are activated non-continuously. Here the silent periods between actuations can be shortened nearly to zero. For instance, the time interval between the steps including the transient time of a solar array drive can be eliminated. Here acceleration factors of up to two orders of magnitude could result and could be used with a convincing justification of the validity.

#### Single Tests to be Performed within the above Test Categories

The following single tests could be part of the above named test categories. (It should be mentioned at the very beginning that not necessarily all these single tests have to be performed in any case. Thorough considerations should aid reasonable decisions.)

#### Functional and Performance Tests

##### Mechanical Environmental Tests

- Static Load and Constant Acceleration

- Acoustic

- Sinusoidal Vibration

- Random Vibration

- Shock

##### Thermal respectively Thermal Vacuum Tests

##### Storage Tests

##### EMC (Electro-Magnetic Compatibility) Tests

#### Functional and Performance Tests

These tests comprise measurements of mass, dimensions, electrical properties, redundancy switch-overs, safety provisions, different operational modes and so on. The results should meet the specifications and requirements. They are a reference for the comparison of properties before and after exposure to environmental conditions.

#### Mechanical Environmental Test

Static load and constant acceleration tests are necessary when mechanisms should bear loads, as instruments and solar generators, even if unloading (caging) devices are used. If vibration tests are harder than static load tests, the latter could be deleted.

Acoustic tests are especially recommended when the test items are mounted at the outside of a satellite's skin and large surfaces - acting as "microphones" - are involved.

Sinusoidal vibrations with low levels are an important development tool for detecting resonances and their damping, investigation of interactions, and so on. Here,

overtesting could easily occur, therefore caution is necessary. In qualification testing, a frequency sweep could be important as proof for integrity.

Random vibration tests are decisive for proving the quality and integrity of a unit. Spectral density functions and levels must be carefully chosen to avoid unnecessary overtesting.

Shock testing should simulate the insensitivity against shocks emanating, for instance, from pyrotechnic devices. On a case to case basis, it must be decided whether vibration tests are more severe and, as a consequence, these tests could be deleted.

Thermal and thermal vacuum tests are the most important ones concerning performance during a mission. Thermal tests in a normal atmosphere are often sufficient for equipment with a hermetic housing. But at least for qualification, thermal vacuum testing should be mandatory. Especially for simulating eclipse situations, the introduction of thermal gradients could be important for searching weak points in a design as well as detecting errors in manufacturing. Often tests with rapid gradients of temperature changes - while the equipment is in operation - are touchstones for quality, reliability and integrity. Non-operation tests at temperatures exceeding the operational range could be necessary to demonstrate functional survival.

Storage tests must be subdivided into short term and long term storage tests. Short term storage tests should generally simulate the sequence of satellite launch and unit cold start. This is done best by storing the equipment after subjecting it to vibration testing at a defined low temperature for a certain time interval with subsequent cold start. Normally these tests could be the first step in a thermal or thermal vacuum test.

Long-term storage tests could be necessary for equipment that could be dormant for long periods of a mission. For instance, a redundant unit checked out in orbit should work properly on switch-on also near the end of a mission. The definition of such a test needs much experience and a profound knowledge of the equipment. Careful consideration of acceleration possibilities is necessary to finish this test in a time span fitting with the program. Good candidates for a storage test are qualification models if not needed for life testing. The acceleration methods and factors depend on the probable failure mode. For instance, if cold welding in a bearing would be the suspicion, a high storage temperature under vacuum with perhaps some micro vibrations could be employed.

EMC-tests become more and more important with the growing complexity of satellites. Well-educated and experienced people with adequate test equipment must be provided to perform valid testing. Such specialists should also influence the design and the packaging of electronic equipment, the shielding of motors and so on from the very beginning to save cost and time.

#### Test Program and Test Sequence

The **Table for Tests** explains best which tests are recommended and which are mandatory. The tests are also indicated in the sequence to be followed in each of the categories.

It should be stressed here again that formal testing under control of quality assurance and according to written procedures is obligatory for qualification, acceptance and refurbishment testing. This cannot be overemphasized. Test reports must be complete showing incidents and how they were dealt with, not only the "nice portions" of a test. Clear success and failure criteria must be established **and** followed.

### Test Facilities

The careful preparation of testing with continued improving measures and the performance of the tests strictly according to the plans and procedures must find its counterpart in excellent testing facilities, continuously and strictly maintained and controlled by quality assurance according to written standards and procedures. Conscientious, dedicated and experienced engineers must run such facilities with indefatigable discipline. The importance of test facilities which are beyond each doubt of their top condition cannot be overestimated. The control by quality assurance people should be not regarded as an unavoidable burden, but as a help of a totally independent but most interested authority to achieve and guarantee excellent quality. Out-of-company test facilities have to be monitored, too by experts of the own company and often also by those of customers. Quality products need quality testing facilities!

### **Conclusion**

It was not possible to treat all aspects of this complex subject in a short paper. Of course, the pronunciation of the different facets is characterized by the personal experience both enjoyed and suffered.

It is hoped that the interrelation between Reliability and Testing has become clearer by presenting this paper. Reliability cannot be tested into a product but is an inherent quality characteristic. Formal testing is the final significant proof of quality and reliability.

Dedicated, educated, well-trained, experienced, responsible and motivated people are the main key to quality and to reliability.

### **References**

1. Coutinho, John de S. "Advanced Systems Development Management." Robert E. Krieger Publishing Company, Malabar, Florida 1984
2. Briscoe, H. M. "A Rationale for the Testing of Space Mechanisms". First European Space & Tribology Symposium, Neuchâtel, Switzerland 1983
3. Rapp, D. "The Influence of Five Years of Storage on the Operational Readiness of a Satellite." Second Tribology Workshop, Risley, UK 1980
4. Wertz, James R. "Spacecraft Attitude Determination and Control." D. Reidel Publishing Company, Boston USA 1984



**Table for Tests**

Tests and their Sequence	Test Category				
	Dev. Test	Qual. Test	Accept. Test	Refurb. Test	Life Test
Functional Test	M	M	M	M	
Performance Test	R	M	M	M	M
EMC-Test	M	M			
Static Load Test	R	M	M	M	M
Acoustic Test	R	M			
Sinusoidal Vibration Test	M	M			
Random Vibration Test	M	M	M	M	M
Shock Test	R	M			
Performance Test	R	M	M	M	M
Storage Short Term Test	R	M	M	M	M
Thermal Vac. Perf. Test	R	M	M	M	M
Duration Test					M
Performance Test					M
Strip	R				R

*Legend: M: Mandatory, if applicable; R: Recommended*



## Development of a Hermetically Sealed Brushless DC Motor for a J-T Cryocooler

Edwin Joscelyn\*, Irwin Hochler\*, Andrew Ferri\*, Heinz Rott\*, and Ted Soukaris\*

### Abstract

This development was sponsored by Ball Aerospace for the Cryogenic On-Orbit Long-Life Active Refrigerator (COOLLAR) program. The cryocooler is designed to cool objects to 65° K and operate in space for at least 7 years. The system also imports minimal impact to the spacecraft in terms of vibration and heat.

The basic Joule-Thompson cycle involves compressing a working fluid, nitrogen in this case, at near-constant temperature from 17.2 KPa to 6.89 MPa. The nitrogen is then expanded through a Joule-Thompson valve. The pure nitrogen gas must be kept clean; therefore, any contamination from motor organic materials must be eliminated. This requirement drove the design towards sealing of the motor within a titanium housing without sacrificing motor performance. It is estimated that an unsealed motor would have contributed 1.65 g of contaminants, due to the organic insulation and potting materials, over the 7-year life. This paper describes the motor electrical and mechanical design, as well as the sealing difficulties encountered, along with their solutions.

### Introduction

The COOLLAR drive system consists of a motor, tachometer, synchro, and the drive electronics. Aeroflex's responsibility was for the motor design and the synchro integration. The other components were supplied by Ball Aerospace. A photograph of the motor and synchro assembly together with the rotor is shown in Figure 1.

The motor is a three-phase permanent magnet torque motor, which is driven by a sinusoidal current source. The current source is derived from the system synchro. In order to meet the allowable inertial disturbances generated by the drive system, the torque ripple spectrum under all operating conditions should be within the limits shown in Figure 2. The disturbance torques are generated by the harmonics of the motor torque constants and the synchro outputs, and by slot lock. The commutation torque ripple is zero if the motor torque constants and the synchro outputs are mathematical sine waves; therefore, to maintain the commutation ripple within acceptable levels, the harmonics have to be carefully controlled. The slot lock torque ripple is minimized by the slot/pole combination and rotor skewing. The motor operates at 12.5 to 44 rad/s at a torque load up to approximately 10.6 N-m. The specification for the motor is as follows:

---

\* Aeroflex Laboratories Inc., Farmingdale, New York

$K_{t \text{ phase}}$  ..... 76 (+/- 4) N-m/amp  
 $R_{\text{Phase}}$  ..... 0.151 ( $\pm 0.014$ ) ohms  
 Poles ..... 16  
 Phases ..... 3 (not interconnected, open delta)  
 O.D. .... 0.177 m maximum  
 Length ..... 0.081 m

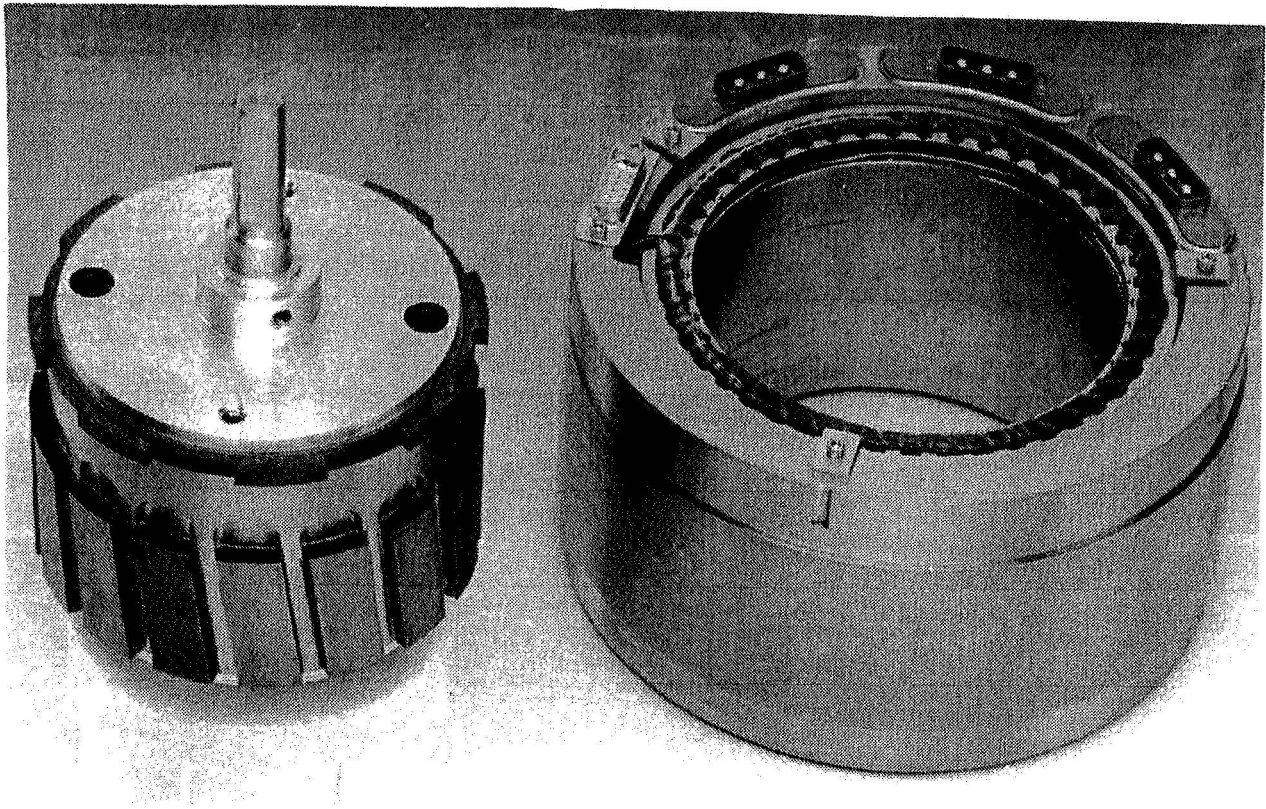


Figure 1 Motor/Synchro Photograph

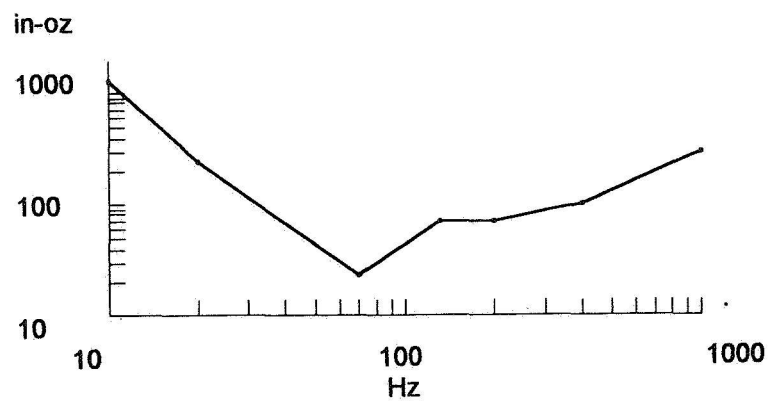


Figure 2 Allowable Torque Ripple Spectrum

## Motor Design

There are a variety of slot/pole configurations which will give a sinusoidal back EMF waveform (and therefore a sinusoidal  $K_t$ ). A convenient arrangement, as shown by Hendershot [1], is a 2.25 slot/pole ratio with a  $15^\circ$  pole angle for a 16-pole skewed rotor. The stator has 36 slots.

The first order of business was to determine the torque capability of this configuration for the physical size allowed. Finite Element Analysis (FEA) was used to determine the flux density in the air gap so that conventional Lorentz force calculations could be made. The FEA technique also allows the rotor to be displaced by a small angle where the change in energy is used to calculate torque using the principle of virtual work.

The maximum length that the physical constraints allow is a stack of 0.043 m. The maximum diameter of the rotor is 0.113 m. The physical air gap is 0.41 mm, and the magnetic air gap is 0.66 mm, which allows room for the titanium shell which seals the motor from the nitrogen. An FEA equipotential line plot, generated by the magnets with a single phase winding excited, is shown in Figure 3.

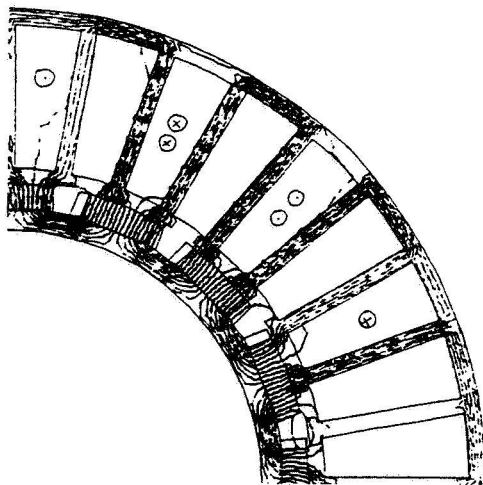


Figure 3 Magnetic FEA Model

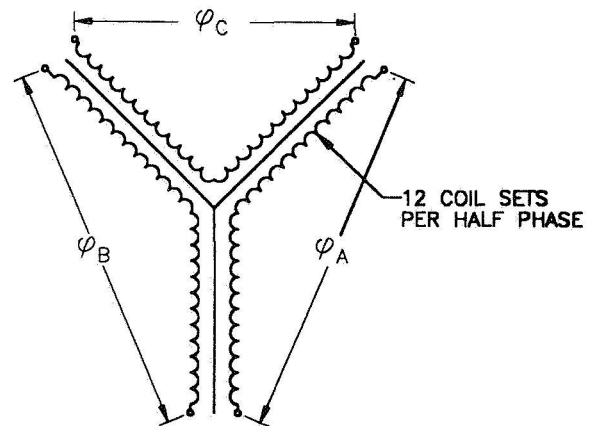


Figure 4 Winding Diagram

From the FEA, the resultant flux density in the air gap is  $1.05 \text{ W/m}^2$ . In order to affect an unconnected winding, yet preserve the sinusoidal waveform given by a wye winding, the motor was wound as shown in Figure 4.

Each of the 24 coils which form a single phase has 6 turns of wire. This gives an effective length of 12.7 m per phase. This calculates to a  $K_t$  of 0.362 N-m/amp for 1/2 phase, using the Lorentz method. For a sinusoidal waveform, the  $K_t$  for a leg-to-leg winding (making 1 phase in our winding scheme) is 1.5 times the 1/2 phase value, or 0.54 N-m/amp. Subtracting a 6% loss due to a 1 slot skew gives a 0.51 N-m/amp torque constant prediction.

Using FEA to generate a predicted torque constant via the virtual work principle, the rotor was displaced  $2^\circ$  with the change in energy divided by the angle yielding torque. The FEA results for this model is 0.050 Joules/0.0349 radians = 1.43 N-m. Multiplying by 4, since only 1/4 of the model is analyzed, and dividing by the 10 A used in the analysis gives a  $K_t = 0.57$  N-m/amp. Skewing reduces  $K_t$  to 0.536 N-m/amp. Both of these predictions, 0.511 N-m/amp and 0.536 N-m/amp were close, since the actual performance result was 0.515 N-m/amp. The motor resistance was 0.143 ohms.

## Mechanical Considerations

The system design requires that the motor be a "plug-in" unit (i.e. the specially designed hermetic connectors need precise alignment with the housing outer dimensions). This, in turn, requires that the lamination stack be dimensionally concentric to locate centrally within the titanium housing. The lamination material is vanadium permendur because the winding area had to be maximized, due to the densely packed 32-filar winding needed to achieve the required low resistance. Lamination manufacturers were not willing to hold the tolerances required to allow precise stacking after heat treatment because this metal tends to buckle and move. This problem was solved by laminating heat-treated sheets to the 0.043-m dimension and using EDM techniques to cut the finished lamination stack. The edges were remarkably clean with the dimensions precise to 0.025-mm tolerances.

The next problem was the titanium shell design. It was recognized that attempting to machine the inner diameter to 0.254 mm thick would have been a problem. Either the extremely thin part would wrinkle during machining, or the wall could distort due to the insertion and bonding of the stator. Another concern was where to make the seams for electron beam welding of the final seal. The approach was to pre-machine the inner diameter with a thick wall, install and bond the stator, and machine the inner diameter to the thin wall required. Figure 5 shows a cross-section diagram of the motor. The seam to be electron beam welded is indicated.

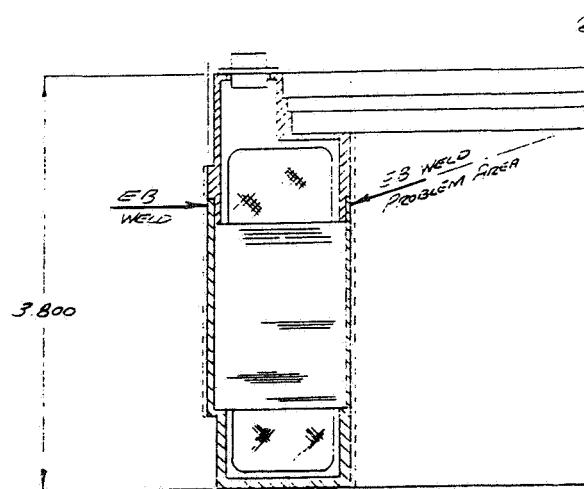
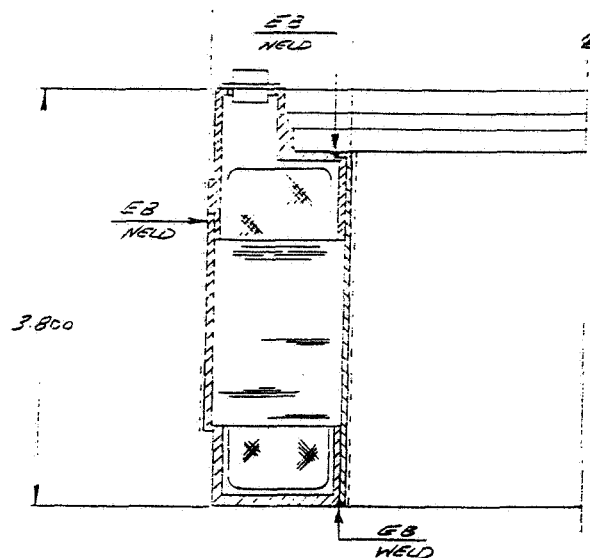


Figure 5 Initial Seam Configuration

## Electron Beam Welding

Titanium is particularly well-suited for electron beam welding. Initial attempts at welding, however, were disastrous. The weld was difficult for the welder to approach from the inside, and the material burned through, thus leaving holes in the seam. The beam could not burn through to the appropriate depth without melting excessive surrounding material which, in turn, caused the holes. Even though earlier test sections, which were flat representations of the overlapping interface, were successfully welded, it became obvious, after several attempts, that the design approach needed to be changed. The new approach is reflected in Figure 6.



**Figure 6 Final Seam Configuration**

This approach eliminated the thin-wall sections where the weld was to occur. This design allowed easy access to the welder, and the thicker cross-sections allowed the beam to penetrate and weld properly. The inner cylinder was still initially pre-machined with a thicker cross-section and machined after welding.

The connector design was a custom hermetic seal with three pins for each phase (one for case ground). The connectors were fixed relative to the outer diameter for the "plug-in" interface and electron beam welded to the top of the motor. Because of the flat, thick surface, electron beam welding was not a problem in this area.

## Motor Losses Due to the Titanium

A concern is the magnitude of eddy current losses due to the titanium. Eddy currents are proportional to the magnetic frequency squared, the length of the eddy current path squared, the flux density squared, and the material volume. The eddy currents are inversely proportional to the material resistivity. Calculating the power [2]:

$$P_{\text{eddy}} = \pi^2 f^2 \tau^2 \beta^2 \nu / 6\rho$$

where (all MKS units)  $f$  is the magnetic reversal frequency,  $\tau$  is the stack length,  $\beta$  is the flux density,  $\nu$  is the volume of titanium, and  $\rho$  is the resistivity for the motor rotating at 40 rad/s, gives a power loss of 17.3 watts. The flux distribution in the material is sinusoidal and does not cover the entire volume at all times with maximum value. More appropriately, the value above is reduced by the 75% magnet coverage and the average for a squared sine wave, which is 0.5. This gives a theoretical power loss of 6.4 watts.

The actual power loss was measured by taking the difference between the motor drag torque at 40 rad/s housed and unhoused. The power loss due to the 0.254-mm layer of titanium was measured as 6 watts.

## Conclusions

“Clean” motors can be manufactured in this manner. The losses were only 1.4% of the peak operating power for this motor. Smaller motors operating at faster speeds can be made with thinner internal wall thicknesses. Applications that require motors placed near optical elements would be natural for this technology. Step motors which place objects in and out of optical paths, such as filter wheels, would also benefit from this approach. The COOLLAR drive system has been tested at Ball Aerospace with superlative performance results.

## References

1. Hendershot, J.R. “Design of Brushless Permanent-Magnet Motors.” Magna Physics Corp., Publishing Division, (1990), pp103.
2. E.E. Staff, MIT. “Magnetic Circuits and Transformers.” John Wiley (1943), pp136-137.



521-37  
50449  
125135 ✓

## The Design, Development and Qualification of a Lightweight Antenna Pointing Mechanism

M. Shmulevitz\* and A. Halsband\*

### Abstract

This paper describes the design, development, and qualification of a new lightweight and compact Antenna Pointing Mechanism (APM). The APM was specially designed to meet the stringent mass, envelope, and environmental requirements of OFFEQ experimental satellite. During the development phase, some problems were encountered with the brushless DC motors, slip ring contact resistance, and bearing drag torque. All of these problems were resolved, and two APM units have been operating successfully in orbit since April, 1995.

### Introduction

Data link between OFFEQ experimental satellite and ground control is provided by two redundant APM units. The strict and demanding requirements for minimum mass and envelope enhanced a unique design approach featuring a lightweight (1.8 kg) and compact (150-mm flange diameter x 220-mm length) antenna pointing mechanism.

Although the APM housings and shafts were manufactured from aluminum alloy, the overall system design allows a large temperature range (-30°C to +60°C) without any active thermal control. Based on a gimbal (pitch over yaw) arrangement, the mechanism has hard-preloaded ball bearings and aluminum gears lubricated with sputtered MoS<sub>2</sub>. The APM is designed for LEO applications and configured to minimize effects of monatomic oxygen erosion on the tribological elements. Electrical transfer (command & power) to the elevation axis is achieved by a compact slip ring unit, and RF feed to the antenna is accomplished via two miniature rotary joints. The APM has been tested in thermal vacuum conditions to a 4-year equivalent life in orbit. Its overall pointing accuracy is 1°, and the average power consumption is 2 watts.

During the development phase, some problems were encountered with the brushless DC motors, slip ring unit, and bearing drag torque. Changing the materials in the motor resolved the cracks and cuts that formed in the windings. The slip ring unit exhibited increased electrical resistance after exposure to laboratory air. Rotation for a only few revolutions restored normal conditions. In order to reduce blocking effects, the APM bearings contain toroid ball separators and "loose" conformity races. However, this approach did not eliminate the increase of drag torque encountered during the life test. Also, it has been found that a dependency, which was stabilized at an acceptable torque margin, exists between APM mode of operation and drag torque.

---

\* Israel Aircraft Industries / MBT, Yehud, Israel

## APM Description

The APM (Figures 1 and 2) provides more than a full hemispherical coverage due to its capability to rotate continuously in the azimuth axis and to its  $0^{\circ}$ - $115^{\circ}$  rotation range in the elevation axis. The APM azimuth axis consists of a rotating inner housing that is simply supported by a pair of bearings: the large bearing is fixed, and the small bearing floats with respect to the stationary housing. The bearings used for this application were 440C stainless steel, precision (ABEC 7) angular-contact ball bearings (bore diameters 58.73 mm and 19.05 mm, respectively) with double rows of balls, preloaded back-to-back, and protected by two metal shields. Only the grooves were dry-lubricated with sputtered  $\text{MoS}_2$ , and ball separators were toroid rings made of Duroid.

The rotating assembly is driven by a brushless DC motor via a stainless steel spur gear that meshes with a gear made of aluminum alloy and lubricated with sputtered  $\text{MoS}_2$  (same for all other gears in the mechanism). The servo control feedback is provided by a resolver and aluminum gear mesh. To enable the continuous azimuth rotation, electrical and RF transfers to the elevation axis are achieved by a slip ring unit and rotary joint, respectively.

The elevation axis of the APM consists of two rotating arms: one is axially fixed, and the other arm floats axially with respect to the inner housing. A brushless DC motor drives the axially fixed arm, whereas the elevation resolver (not seen in the cross-section of Figure 2) is driven by the floating arm via an aluminum gear mesh. RF transfer to the antenna is accomplished with the elevation rotary joint and coaxial cables. The hold down and release mechanism, attached to the antenna backside tip, provides the stowage and release capability. The antenna itself consists of a printed circuit board made of Duroid and is bonded to a honeycomb sandwich with high-modulus, graphite-epoxy face sheets.

## Design Philosophy

The APM design approach focused on one main objective: to minimize the APM mass, yet withstand all other requirements, as defined in Table 1. A compact design and selection of proper materials were considered the method to obtain the design goals.

The selection of materials started with titanium alloy as the first choice for the APM shaft and housing material. It has the advantage of a coefficient of thermal expansion (CTE) that closely matches the selected 440C stainless steel bearing material and a good stiffness-to-weight ratio. However, careful examination of the APM mass budget revealed that, with titanium alloy, the allocated overall mass will be exceeded. Beryllium and other exotic materials were considered unfavorable due to fabrication problems, availability, and price. Aluminum alloy (7075-T7351) was the second choice to be checked. With respect to APM mass budget and stiffness-to-weight ratio, aluminum alloy is a good choice. But with the big difference in CTE between aluminum alloy and 440C stainless steel, this solution seemed unacceptable.

Nevertheless, a thorough investigation has been carried out and, with the assistance of the European Space Tribology Laboratory (ESTL) computer prediction, bearing frictional torque and contact stress were analyzed as a function of different bearing fits and thermal strains. The results showed that, although there is a large increase in bearing frictional torque and contact stress, the obtained values are still acceptable. The nominal frictional torque of the whole system was specified to be 10% of motor stall torque at ambient conditions, and the servo control was designed to accommodate the large change in friction torque. The most significant result of this analysis was the understanding of mechanism performance as a function of thermal gradients. With a hard preloaded back-to-back bearing arrangement and aluminum shaft and housing, bearing torque and contact stress increase rapidly when the outer bearing race temperature is lower than the inner race temperature. The opposite will occur if the outer bearing race temperature is higher than the inner race temperature. In that case, for only a 10°C temperature gradient, the bearings will be off-loaded (i.e., no preload). System design of OFFEQ satellite required direct installation (i.e., no booms) of the APM to the OFFEQ plate at the nadir side. Thermal analysis showed that, for most cases, the APM outer housing, which is attached to OFFEQ plate, will have higher temperatures with respect to the inner housing (shaft), which points to space. Therefore, the tendency is that thermal gradients will reduce bearing preload and friction torque. The worst condition will be an isothermal case with no gradients. In addition, tolerance analysis showed that, with a clearance fit and bearings off-loaded, the pointing accuracy and stiffness will not be adversely affected.

A considerable amount of work has been taken by our subcontractor to develop the rotary joint. The critical parameter of the rotary joint is the ability of the bearings to conduct the heat dissipated in the rotating section of the co-axial line to the housing. The thermal conductance of a ball bearing in vacuum is proportional to the axial and radial load, the size of the bearing, and the number and diameter of balls. A face-to-face bearing arrangement has been used to ensure that bearing thermal conductance increases when the temperature of the shaft rises above that of the housing. Also, a compliant spacer was used to compensate for the change in preload due to thermal gradients. To improve the thermal conductivity, all metallic parts, except for the bearings, were made from aluminum or beryllium copper.

## Testing

The design and location of the APM antenna impose a large static imbalance with respect to the APM elevation and azimuth axes. In order to simulate correctly APM performance in orbit and to eliminate all G effects, the antenna has been replaced by a dummy payload for all functional and thermal vacuum tests. This dummy payload has the same inertial load and stiffness as the antenna, and its center of gravity coincides with the APM axes. The APM qualification model has been subjected to the following tests:

Functional tests - These tests have been performed during the various stages of APM qualification. They include static and dynamic pointing accuracy check, torque threshold at different angular positions, dynamic check, and RF test. Dynamic check was executed by operating the APM at a typical tracking mode for seven minutes. Current and voltage consumption were monitored, and system tracking error was derived by comparison of command versus resolver position.

Vibration tests - Vibrations were conducted with the APM stowed in the launch configuration. Three types of vibration tests were carried out: sine vibration (10g sinusoidal up to 200 Hz), random vibration (12.5 Grms up to 2000 Hz, 3 min per axis), and acoustic test (142 dB overall noise level, 3-min duration). The APM was also subjected to three shocks of 50g for 11 ms in each axis direction.

Thermal vacuum cycling - This test was conducted by exposing the APM to eight temperature cycles between -40°C to +60°C at a vacuum level of  $10^{-6}$  Torr. At each of the temperature extremes, functional tests were carried out.

Thermal vacuum life test - This was an accelerated test divided into two phases. At phase 1, temperature condition was +23°C, whereas temperature condition was -20°C in phase 2 (vacuum was  $10^{-6}$  Torr). In each phase of the test, the APM was operated in a typical tracking mode maneuver for seven minutes, then for two minutes. All the obtained data was processed and statistically analyzed. Having completed this basic cycle (7 minutes operation + 2 minutes processing), repeated cycles, to an equivalent life of two years in orbit, were carried out automatically by special software.

## **Problems Resolved**

### Slip ring contact resistance

During functional testing of the APM (vacuum, ambient temperature), unexpected dither behavior of the elevation axis was observed. Failure investigation revealed an excessive increase of contact resistance in the slip ring signal tracks (in the magnitude of hundreds and thousands of ohms). A short run-in (even two revolutions) was found to be sufficient to restore the slip ring contact resistance to its normal values. Yet, our main concern was the cause of slip ring contamination. It was believed that MoS<sub>2</sub> particles from the APM gears contaminated the slip ring, since MoS<sub>2</sub> has the property of semiconductor resistance.

A contamination barrier was introduced into the APM to prevent particles from falling on the slip ring tracks. However, dither behavior of the elevation axis still occurred whenever the APM was operated (in vacuum) after exposure to laboratory air. In addition, high contact resistance was also found in the slip ring power tracks, thus showing that at least 8 contact points are being contaminated simultaneously, and that did not seem reasonable. Further investigation with the slip ring manufacturer revealed that oxidation of the slip ring galvanic deposit may occur in air. It was also suggested that, for future application and new orders of slip rings, the galvatronics shall be coated with a 0.2- $\mu$ m Au-Co layer, called DUOR, which acts as a dry lubricant and corrosion protection. Finally, it was decided that at the beginning of life in orbit, the APM will undergo a short run-in as a "cleaning process."

### Brushless DC motor

During life testing at  $-20^{\circ}\text{C}$ , a serious problem arose with the brushless DC motor. The phenomenon was a large increase in the input voltage without any change in the input current. Checking motor resistance revealed that the resistance is doubled, which indicates that there is a cut in the motor windings. It should be stated that this type of motor was a qualified item with space heritage.

The brushless DC motor basically consists of a ring-shaped stator with molded windings, a permanent magnet rotor without windings, and an inductive pick-off. A review of stator materials and manufacturing procedures revealed that cracks are usually formed in the epoxy resin, which is used for the impregnation of the windings. In addition, stress analysis showed that a cut will occur with a crack size of 0.02 mm. The failed motor was disassembled from the APM and dismantled into parts. Then, by thorough inspection of the stator, a cut beneath a crack of 0.04-mm width was found.

Subsequent efforts were taken by our vendor to qualify stators with various epoxy resins and to improve an insulation disc. These stators were subjected to endurance thermal tests, including 72 thermal shocks between  $-55^{\circ}\text{C}$  to  $+115^{\circ}\text{C}$  for a dwell time of 1 hour and transfer in 7 seconds. It was found that a rigid insulation disc of titanium alloy and scotchcast 281 epoxy resin gives the best results. Consequently, all motors were repaired to include these modifications.

### Drag torque

APM drag torque is composed of its bearing, slip ring, rotary joint, and resolver torques. The most sensitive items that contribute to the overall drag torque are the bearings. In order to reduce blocking effects, the selected bearings contain toroid ball separators and "loose" conformity (56%) inner and outer races. During phase 1 of the life test at  $+23^{\circ}\text{C}$ , APM voltage consumption, which is related to the drag torque, increased from 18 PWM to 28 PWM, where it was stabilized. The stall torque of the motor is 200 PWM, and therefore torque margin is high. The notch (Figure 3) is a result of a one-day intermission in the test. It indicates that the system has a relaxation property when not operated, but this phenomena is not well understood.

During phase 2 of the life test at  $-20^{\circ}\text{C}$ , APM voltage and current consumption were considerably higher due to the thermal strain effects. Azimuth axis voltage consumption increased from 30 PWM to about 50 PWM, where it was stabilized at an acceptable torque margin. Performing a short run-in of the system showed that the overall drag torque was reduced. This behavior is attributed to the spread of debris piling and the "release" of cage wind up.

## **Conclusions**

The design, development, and testing approaches were verified with the successful operation of two APM units in orbit. Satellite telemetry shows good correlation between the drag torque obtained during ground testing and the drag torque in orbit. Moreover, checking the drag torque with respect to the temperature of the OFFEQ plate indicates that the two APM units are exposed to thermal gradients that reduce the bearing preload and torque. It is of vital importance to consider the thermal environment and temperature during the conceptual design of any mechanism. Finally, although developed specifically for the OFFEQ satellite, the APM is a versatile design that may be adapted to other gimbal applications.

## **Acknowledgment**

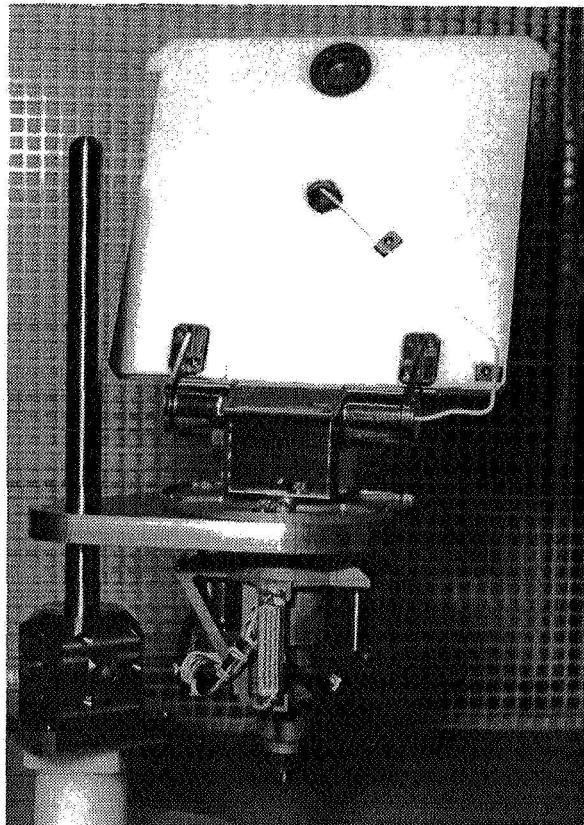
The authors wish to thank Dr. Rob Rowntree of ESTL for his consulting concerning the analysis of bearing frictional torque, contact stress, and tribology design. We also wish to thank the SAGEM team for their collaboration in solving the problem with the brushless DC motor and Eli Levy and Dov Varbin of MBT for their contribution to the development of the electronics and servo control.

## **References**

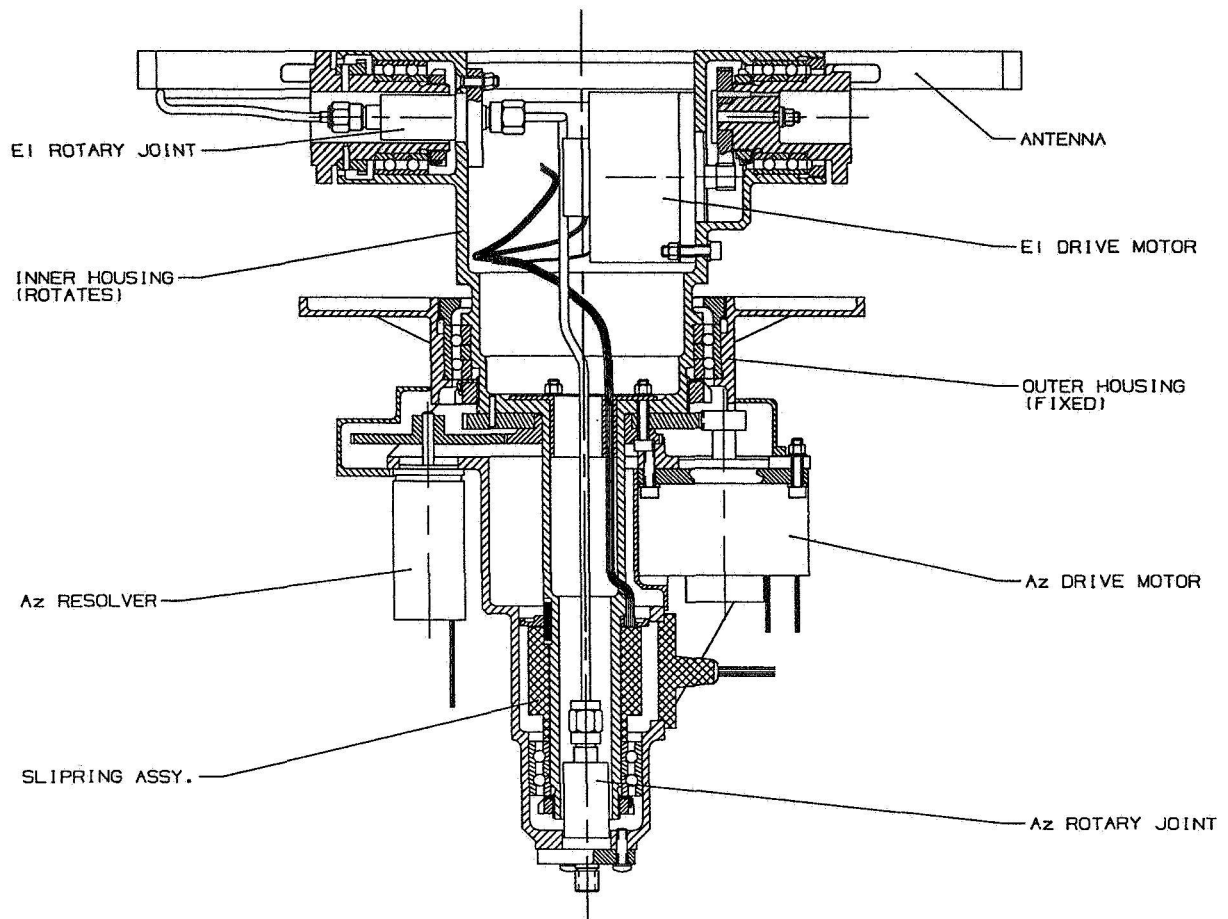
1. T. A. Harris, Rolling Bearing Analysis, John Wiley and Sons, Inc., 1984.
2. S. H. Loewenthal, "Two Gimbal Bearing Case Studies: Some lessons learned," NASA 22nd Aerospace Mechanisms Symposium, May 1988, pp. 253-269.
3. ESTL, Tribology for Spacecraft, Course Notes.

**Table 1. Main Requirements and Capabilities**

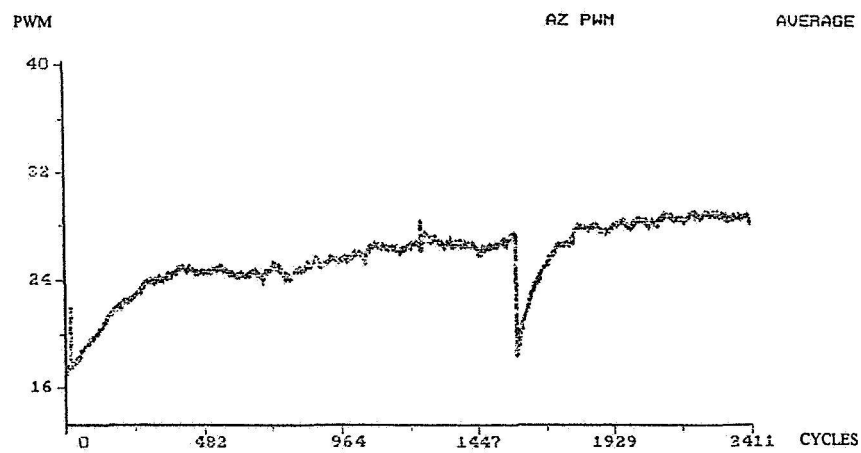
Parameter		Requirement	Capability
Mass (payload excluded)	[Kg]	<2	1.8
Azimuth rotation	[deg]	$\pm 180$	360 cont.
Elevation rotation	[deg]	0 - 115	0 - 115
Total pointing accuracy	[deg]	1.8	1.0
Max. angular acceleration	[deg/sec <sup>2</sup> ]	10	10
Max. angular velocity	[deg/sec]	10	10
Eigenfrequency	[Hz]	>50	250
Torsion stiffness	[N-m/rad]	>400	6500
Torque margin		>3.0	>5.5
Operating temperature	[°C]		
Maximum		+50	+60
Minimum		-20	-30
Mode of operation	(tracking mode)	Intermittent	Obtained
Life	[years]	>2	4



**Figure 1. APM Qualification Model**



**Figure 2. APM Cross Section**



**Figure 3. Life Test - Phase 1, Voltage Consumption Summary**



## EVA Assembly and Release of Highly Loaded Bolts

Jim Olmstead\* and Paul Barker\*

522-37  
50450 ✓  
125136 ✓

### Abstract

The modification of a multi-jackbolt mechanism, Superbolt™<sup>1</sup>, for on-orbit release of highly loaded bolts is described. Preload and release test data demonstrate that modification of a commercial product produced a solution for the deployment of the Space Station Remote Manipulator System (SSRMS) that was less expensive, faster, and lighter than other alternatives. Using the Superbolt design, virtually unlimited bolt loads can be applied or released with a standard wrench.

### Introduction

Using highly loaded bolts for the assembly or deployment of structures in space has been limited due to torque, force, weight, shock loads, power, and/or space restrictions. Heavy torque- and force-multiplying mechanisms can be used, but they must be stored when not in use. Alternative methods of preload release include explosives, shape memory metals, and spools. Each of these methods carries a cost in terms of functional redundancy, safety considerations, and fragment/debris containment, especially for large, highly loaded bolts. When Extra Vehicular Activity (EVA) is available, a space-qualified, multi-jack bolt mechanism, Superbolt™, is simpler.

### Requirements for the SSRMS Tie-Down Release System

During launch, the double-folded, SPAR-designed SSRMS is secured to a modified British Aerospace Space Lab Pallet by eight 19-mm (3/4 in) rods that are 1.15 m (45 in) in length (Figure 1). These rods are stretched over 3.8 mm (0.150 in) by an 80-kN (18000-lbf) preload. They may contain up to 100 kN (22500 lbf) during launch. During SSRMS on-orbit deployment, the rods must be unloaded and stored by an astronaut, preferably using standard EVA wrenches with less than 34 N-m (25 ft-lbf) of torque. Other desirable features are that the release mechanism requires little EVA time, is compact, easy to store, light, simple, and requires minimum development.

### What is a Superbolt™?

A Superbolt™ is a patented multi-jackbolt nut that generates high loads using low torques and standard hand tools. About the same size as a conventional nut, Superbolts™ are popular for civil and industrial applications. SPAR's SSRMS application of Superbolt™ technology, illustrated in Figure 2, will be an aerospace first.

\* SPAR Aerospace Limited, Space Systems Division, Brampton, Ontario, Canada

<sup>1</sup> Superbolt is a registered trademark and patented system of Superbolt, Inc. of Carnegie, PA.

## **Principle of Operation of the Superbolt™**

The torque required to preload a bolt is roughly proportional to its diameter. SPAR's engineering model (EM) Superbolt™ circumvents this by using three very strong 8-mm (5/16-in) jackbolts to tension a larger 19-mm (3/4-in) rod. The combination of three jackbolts, that are 2.4 times smaller in diameter than the rods, results in approximately 7.2 times lower torque requirements. A further torque reduction results from the jackbolt small end bearing area, which absorbs much less torque than a conventional bolt head.

## **Proof of Concept**

SPAR originally developed a force-multiplier mechanism for the simultaneous release of a pair of preloaded rods. This heavy, precise mechanism had an intricate set-up procedure and required removal and storage after deployment of the SSRMS. A weight reduction analysis resulted in its immediate replacement with the small, simple, and proven Superbolt™. Two commercial grade Superbolts™ were quickly tested on a tie-down test bed, built to test the original force-multiplier mechanism. The required rod tension was achieved with a torque significantly less than the 34-N-m (25-ft-lbf) EVA torque limit.

## **Engineering Model (EM)**

Shortly after the successful breadboard test, an EVA-compatible, space-qualified Superbolt™ was designed, in cooperation with Superbolt, Inc. Modifications made were:

### **General**

- 1) Use of stress corrosion cracking-resistant materials.
- 2) Prevention of galling by using dissimilar materials at each interface.
- 3) Generation of drawing conforming to DOD-STD-100, including references to controlled processes, such as non-destructive testing.

### **Jackbolts**

- 1) Use of 19-mm (7/16-in) EVA jackbolt heads.
- 2) Use of 260-ksi MP35N to reduce jackbolt diameter and thus required torque.
- 3) Lubrication of jackbolts with space-qualified Lubeco 905 lubricant.

### **Nut**

- 1) Increase of nut diameter for greater EVA jackbolt access.
- 2) Integration of a tether loop into the nut.
- 3) Increase of nut height to meet fracture requirements.

Note that in order to measure torques accurately, the EM bolts did not have any locking features. To prevent loosening during the high vibration of launch, the flight jackbolts will each have a polyester film locking pellet on the thread. The above modifications were checked for compliance with Space Station requirements by performing finite element, fracture, and thermal on-orbit touch temperature analysis.

## EM Test Results

Rods and EM Superbolts™, fabricated by Superbolt, Inc., were tested in the tie-down test bed. Rod tension and bending were measured with strain gauges. Jackbolts were torqued with a torque wrench in sequence by one turn per bolt per sequence. This procedure was used to tighten and loosen the jackbolts. During test, the jackbolts were tightened and untightened several times, up to 3.5, 4.0, and 4.5 jackbolt turns. These roughly represent 90-, 100-, and 115-kN (20,000-, 22500-, and 25500-lbf) rod loads, respectively. Generally, the thread coefficient of friction decreased with both jackbolt load and test number (Figure 4). As a final test, the Superbolt™ was loaded to over 130 kN (29600 lbf). The ends of the jackbolts mushroomed slightly and indented the thrust washer. The apparent coefficient of friction increased about 30% but was still very low. This increase may have been due to plastic deformation of the washer and/or lubricant failure. Although the bolt load was 50% greater than required, a harder washer and/or a thicker lubricant is suggested to increase the bolting system capacity. Test results for torque versus preload and release are shown in Figure 5. The Superbolt™ torques were about 10 times less for assembly and release than for an equivalent 19-mm (3/4-in) bolt. The number of jackbolt turns versus preload and the bending in the tie-down bolt due to loosening of one jack bolt were also obtained from test. Briefly, the results were:

Assembly torque	@ 80 kN (18000 lbf)	15.0 N-m (11. ft-lbf)
Release torque	@ 87 kN (19500 lbf)	10.2 N-m (7.5 ft-lbf)
Total energy released		170. N-m (125 ft-lbf)
Jackbolt turns to release		4.9 turns

The release torque was less than one third of the available 34-N-m (25-ft-lbf) continuous EVA torque and less than a quarter of the maximum available 54-N-m (40-ft-lbf) momentary EVA torque. To prevent excessive bending in the preloaded rods, only two turns per jackbolt per sequence during untorquing were allowed. Neutral buoyancy simulation tests, performed at Marshall Space Flight Center, confirmed the Superbolt™ accessibility for release and the feasibility of storing the bolts prior to their return to Earth. Timelines have been developed for the Superbolt™ release tasks and are within the EVA time allowances for the mission. In fact, actual Superbolt™ EVA time is comparable to the previous force-multiplying mechanism because the Superbolt™ can be undone with standard EVA tools, and its compact size does not require separate storage from the rods.

## Flight Hardware

The flight hardware was built by SPAR under license from Superbolt, Inc. SPAR's experience with space-related requirements and quality assurance made this the most effective solution.

## Summary

Design, analysis and verification of the SSRMS Superbolt™ has been performed. The Superbolt™ allows release of 110-kN (25000-lbf) bolt loads while using less than a third of the available on-orbit torque. The application of the Superbolt™ concept for the assembly and release of highly loaded bolts in space demonstrates that adaptations of proven commercial products are viable alternatives to unique, complex designs.

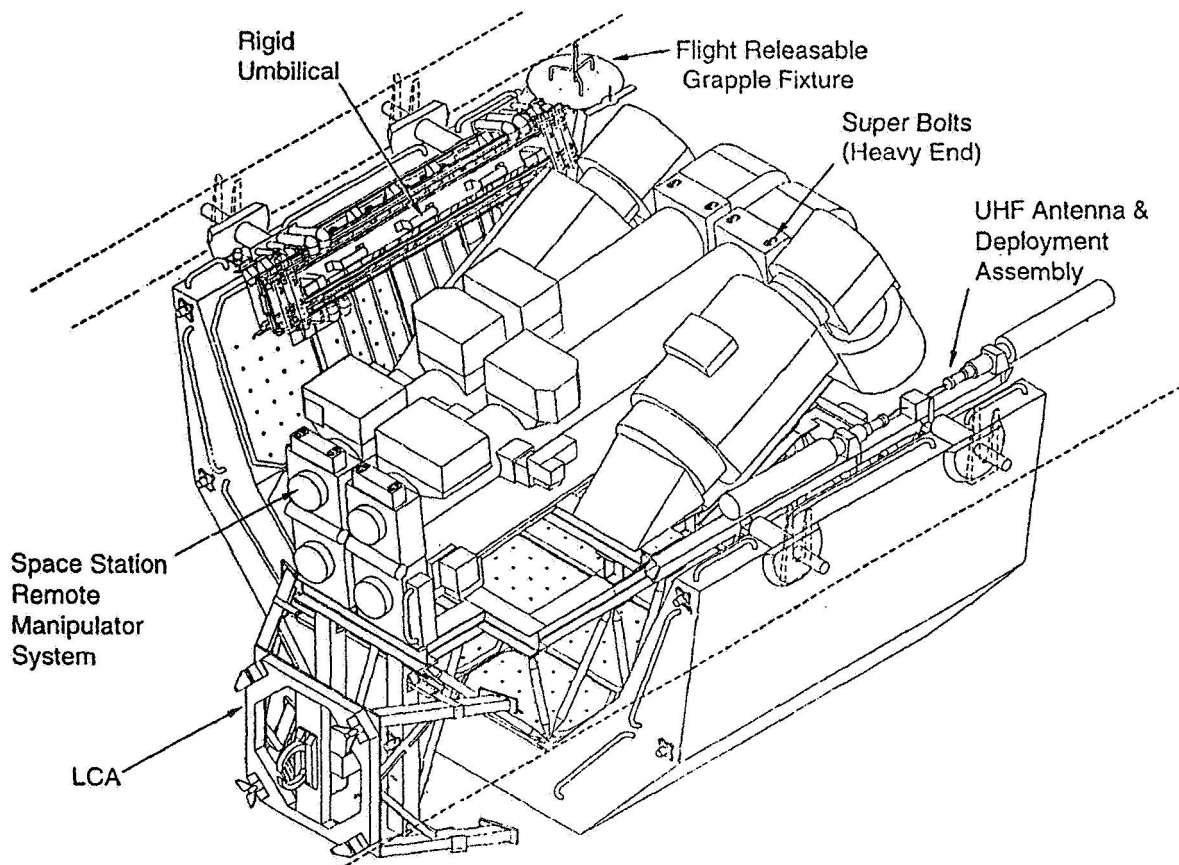
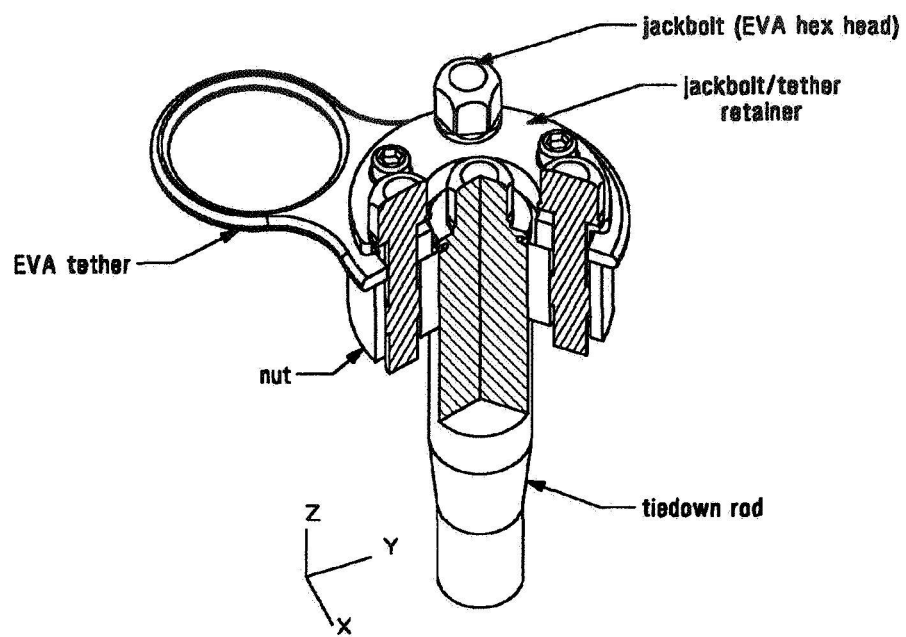
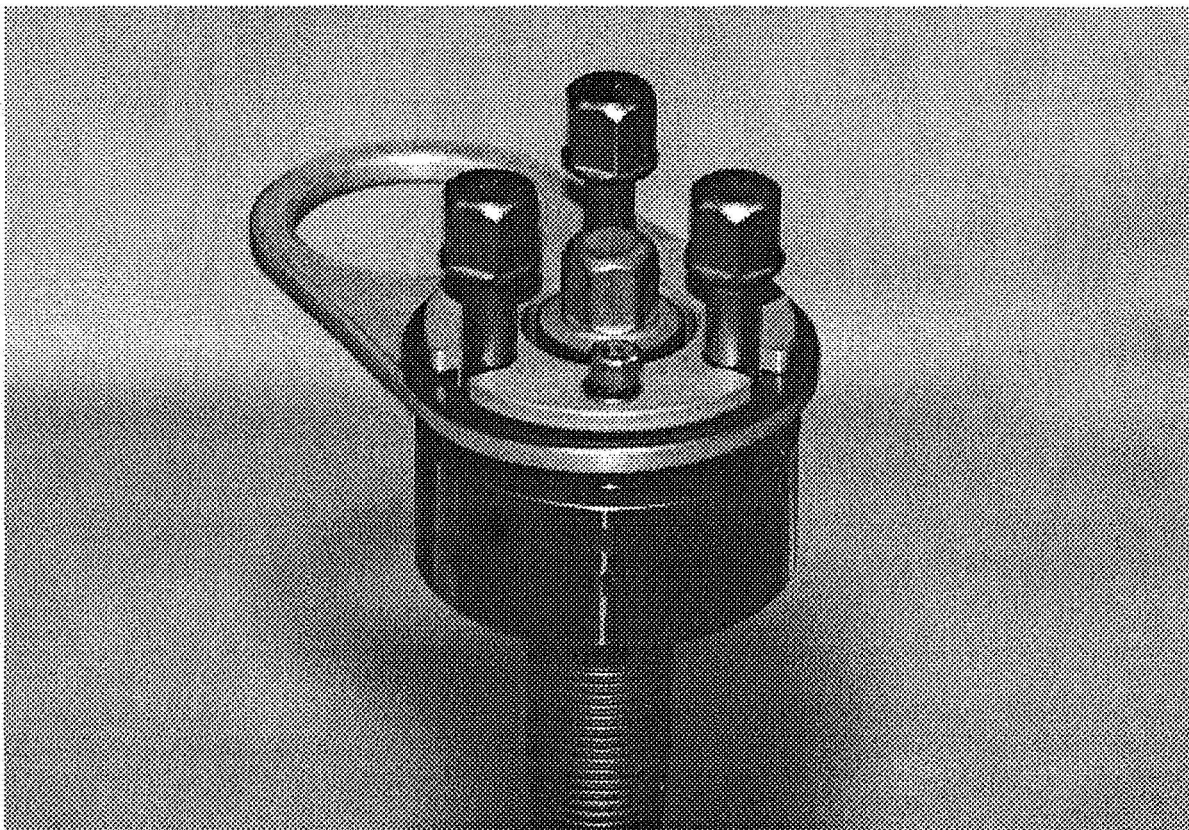


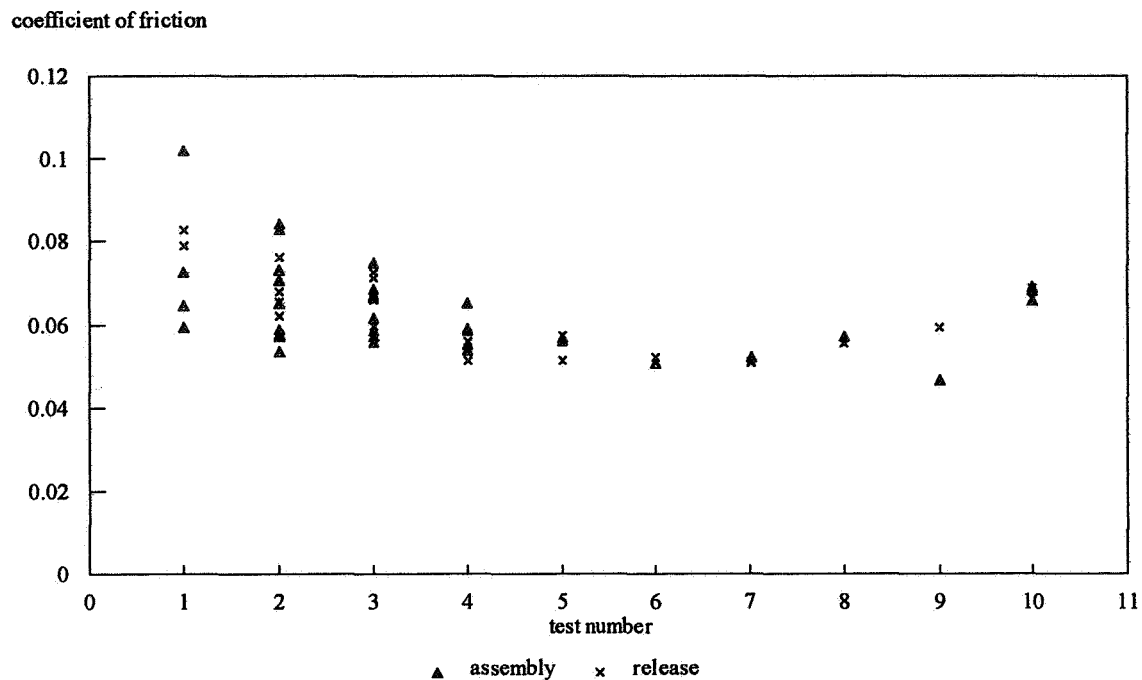
Figure 1. SSRMS Launch Configuration



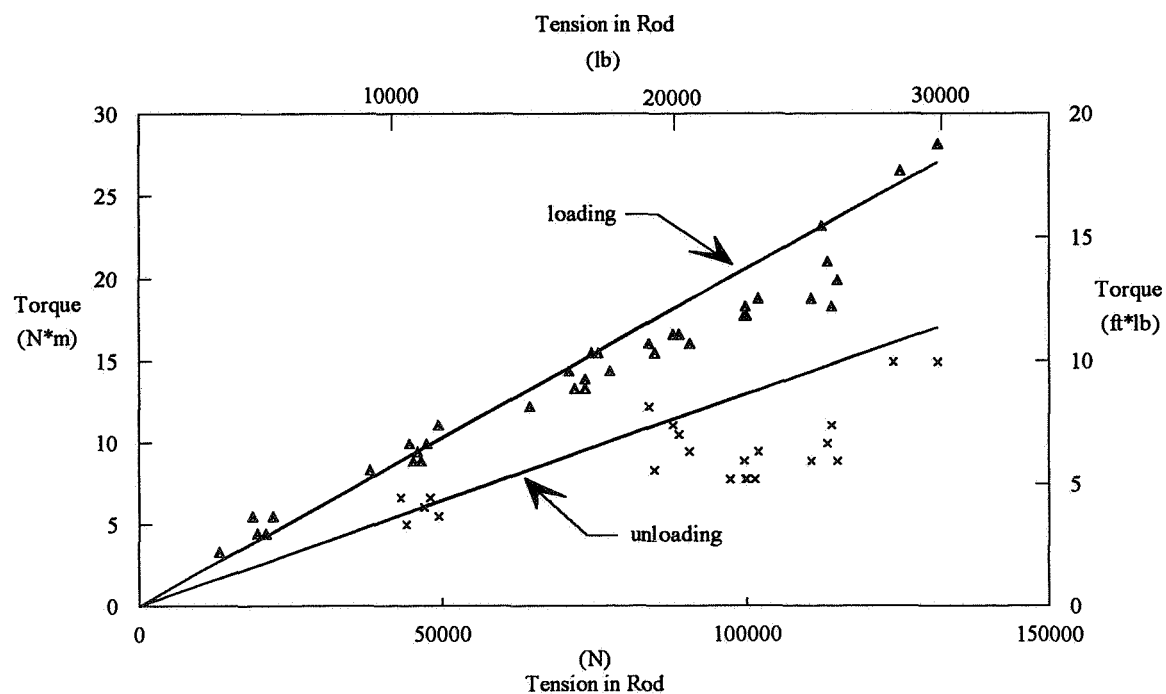
**Figure 2. Superbolt Detail**



**Figure 3. Flight Superbolt**



**Figure 4. Friction vs Test Number**



**Figure 5. Torque vs Preload**

# Remote Manual Operator for Space Station Intermodule Ventilation Valve

James R. Guyaux, PE\*

## Abstract

The Remote Manual Operator (RMO) is a mechanism used for manual operation of the Space Station Intermodule Ventilation (IMV) valve and for visual indication of valve position. The IMV is a butterfly-type valve, located in the ventilation or air circulation ducts of the Space Station, and is used to interconnect or isolate the various compartments. The IMV valve is normally operated by an electric motor-driven actuator under computer or astronaut control, but it can also be operated manually with the RMO. The IMV valve RMO consists of a handle with a deployment linkage, a gear-driven flexible shaft, and a linkage to disengage the electric motor actuator during manual operation. It also provides visual indication of valve position. The IMV valve RMO is currently being prepared for qualification testing.

## Introduction

The IMV valve RMO has often been described as "just a handle", but in fact it has several stringent, and sometimes conflicting, requirements and constraints that have made it into a rather sophisticated and complex mechanism. The IMV valve RMO consists of several interrelated mechanisms in one unit. These different mechanisms are used to deploy and stow the RMO handle, to actuate the IMV valve, to disengage the electric motor-driven actuator, and to provide visual valve position indication.

## Requirements and Constraints Driving the Design

The requirements imposed on the IMV RMO are the reasons for its existence, but some of them contributed substantially to the resulting complexity of this mechanism. As with requirements, constraints caused the mechanism to be more complex. Constraints are sometimes described as the designer's friend, but some were anything but friendly.

### Requirements

The RMO must provide for manual operation by either an EVA-suited astronaut or a regular clothed astronaut functioning in a zero-gravity environment. The EVA suit is bulky, and an astronaut can exert only limited force when restricted by the EVA suit and/or zero gravity. The RMO should rotate in the "logical" direction — i.e., clockwise to open the valve and counterclockwise to close the valve. It should also require a limited angle of rotation to avoid excess motion and ambiguity. In addition to providing visual indication of valve position without consumption of additional electric power and with minimal increase in IMV electric power use, the RMO must be visible in low light. The RMO must stow flush with or below the surface of the close-out panel. In addition, it should have a good "feel" or adequate stiffness to give confidence in both actuation

---

\* AlliedSignal Aerospace, Tempe, Arizona

and position indication. This also requires any detents to be adequately positive, but not “too” positive. The RMO must withstand the push-off loads imposed by an astronaut moving around the Space Station.

### Constraints

The IMV valve is located in the duct work and behind close-out paneling, thus preventing convenient or direct access to the valve and its actuator. The IMV valves are used in pairs — one located on each side of each hatch. This requires both “right-hand” and “left-hand” installations of both the IMV valve and the RMO. The logical location for the RMO is on the close-out panel as close as possible to the IMV valve. In the end cone of a module, this area is very crowded. This requires the RMO to be as compact as possible, especially in the stowed position. The available location puts the RMOs very close to the hatch track. A limited number of spare RMO and IMV units will be carried on the Space Station, and any spare must be useable in any location.

### **Detailed Description Of The Mechanisms**

The IMV RMO is actually several different mechanisms closely connected together. Each has its own purpose and unique characteristics. Making them work together in minimum space was the real challenge of this design.

#### Deployment and stowage, inverted slider-crank mechanism

To go from the stowed to deployed position, the RMO handle pivots on its handle mount and rotates about an axis parallel to the surface of the close-out panel. A spring-loaded detent mechanism holds the handle in either the stowed or deployed position. This presented some problems since the detent must be stiff enough to keep the handle stowed during launch vibration and yet permit deployment by an astronaut under zero-gravity conditions.

The RMO handle mount rises out of its housing by approximately 4.3 cm (1.7 in) during deployment. This allows the handle to rotate over the hatch track with adequate clearance for the astronaut’s fingers. Although this rising action is needed in only half of the installations since only the right-hand installation needs to rotate over the hatch track (in the left-hand installation, the rotation is away from the track), it is provided in all units for commonality. This rising action is accomplished with an inverted slider-crank mechanism driven by a pinion and sector gear. The pinion is part of the rotating handle and rotates with the handle about a pivot axis on the handle mount. The pinion engages a sector gear that is the crank of the slider-crank. The sector and crank also pivot on an axis on the handle mount. The handle mount is the slider. A connecting link connects the moving end of the sector gear/crank and a [pivot] connected to the hub. The hub is “ground,” or a fixed point, with respect to the deployment mechanism.

In more detail, as viewed from the side (Figure 1), the handle rotates counterclockwise approximately 147° from the stowed position to the deployed position. The pinion, which is directly connected to the handle, makes this same rotation about the handle pivot axis, which is fixed to the handle mount. The sector, which is part of the crank of the crank-and-slider linkage, is engaged with the pinion and rotates approximately 79° clockwise about an axis that is also fixed to the handle mount. The gear ratio between



the handle/pinion and sector-crank is 15:28. The other end of the sector-crank is pinned to the upper end of the connecting link. The lower end of the connecting link is pinned to a bracket attached to the hub. The hub is the fixed link, and the handle mount is the slider of this inverted crank-and-slider mechanism.

Stowage is just the reverse of deployment. The handle is rotated about the pinion axis, the pinion rotates the sector-crank which now pulls up on the connecting link, and the handle mount slides back down to its stowed position.

#### Valve actuation, geared flexible shaft

With the handle deployed, the astronaut can rotate the handle, handle mount, sector-crank, connecting link, etc., as a unit to actuate the IMV valve. The bracket, which connects the connecting link to the hub, also acts as a key to transmit torque from the handle mount to the hub. A gear, attached to the hub, engages a pinion which drives a flexible shaft. The gear-to-pinion ratio is 3:1 (i.e., the flexible shaft turns three times as fast as the handle). This speed-up makes the relatively small-diameter flexible shaft appear three times as stiff in torsion and reduces the torque that it is required to transmit.

#### Actuator motor and gear train disengagement, flexible shaft as push link

The IMV valve electric motor driven actuator has a high reduction ratio and is therefore hard to back-drive. This makes it necessary to disengage the motor and gear train of the actuator to permit manual operation. As the RMO handle is deployed, the handle mount slides up relative to the hub and the RMO housing. A U-shaped link, attached to the lower end of the handle mount and prevented from rotating by guides attached to the housing, pushes upward on two rocker arms pivoted on the housing. The other ends of these rocker arms push downward on a yoke that, in turn, pushes on a flange on the flexible shaft core. This exerts an axial force on the flexible shaft core, making it act as a compression link.

At the IMV valve actuator, the core of the flexible shaft pushes on a pin extending through the input pinion of the right-angle gear set. The pin pushes on a rocker link that moves the face gear clutch out of engagement. This disengages the motor and gear train from the actuator output shaft and allows the RMO to turn the actuator output shaft without back-driving the gear train and motor.

This disengagement of the electric motor driven actuator by RMO deployment also has the effect of defeating any automatic or electrical remote control of the IMV. This is a good news/bad news situation. It keeps the deployed handle from flailing about unexpectedly, but it also prevents the IMV valve from working normally if the RMO is inadvertently left in the deployed position.

#### Visual position indication. RMO always turns with valve

Whether the RMO handle is deployed or stowed, it remains connected to the valve by the flexible shaft and rotates whenever the valve moves and through twice the angle the valve moves. A pointer, attached to the RMO hub, points to legend marks on the flange of the RMO housing to indicate valve position. The pointer is in the plane of the RMO housing flange to permit viewing from a wide angle without confusion.

#### Overload protection, flexible shaft as torsion spring

The RMO must withstand an astronaut "push-off" load of up to 222 N (50 lbf) in any direction. If this load is imposed horizontally with the handle deployed and in a direction that would further open an open valve or further close a closed valve, it imposes torque that is a potentially damaging overload on the IMV valve actuator. There are positive limit stops in the IMV actuator at both extremes of travel that establish the fully open and fully closed valve positions. Positive rotation stops in the RMO limit handle travel to approximately 25° beyond the actuator stops with the flexible shaft allowed to deflect torsionally. This over-travel is sufficient to allow for tolerances and to ensure that the RMO or the actuator can always move the valve to either the open or closed position, as defined by the actuator limit stops, and is small enough to keep the torque below damaging levels. The torque is limited by the torsional stiffness or spring rate of the flexible shaft.

If this "push-off" load is imposed in a direction that would open a closed valve or close an open valve, it is permitted to do so. If the "push-off" load is in the direction to further deploy the deployed RMO handle, the handle and mechanism are strong enough to sustain it.

#### Rigging, common units used in different locations

To achieve the commonality requirement (i.e., that an IMV valve and a RMO be useable in either the "right-hand" or "left-hand" installation), some special "rigging" is required at installation. The upper portion of the IMV valve actuator can be rotated around the valve shaft to make the flexible shaft connection face either "right" or "left." Six clamp screws must be loosened, and the upper gear housing must be rotated into proper position before the RMO flexible shaft is connected to the actuator. After the RMO flexible shaft is connected, the upper gear housing can be rotated a small amount in either direction until the visual position indicator pointer matches up to the legend marks. Tightening the six clamp screws finishes the "rigging."

## **Lessons Learned**

### Work with customer to define requirements as early as possible.

Well into this program, the specific requirements were not clearly defined. The customer was not completely sure what was needed, and early specifications for the IMV only indicated that it “provide for manual operation.” Only after many conversations with the customer and several visits to the customer’s facility were the real requirements established.

### Build development or prototype hardware early.

The proper detent stiffness was not determined until after hardware was built. The original detent was much too stiff, and the detent ball made deep grooves in the hardened detent cam. This problem had not been predicted by calculations. A larger diameter detent ball and softer spring solved the problem.

Several parts had “rattle” or lost motion, thus resulting in damage during early vibration tests. Some re-design was necessary to constrain all the parts and avoid vibration-induced damage. The RMO does not experience much vibration in service, but the in-transit or launch vibration is quite severe.

## **Conclusion**

The IMV valve RMO started out to be “just a handle,” but its stringent, and sometimes conflicting, requirements and constraints resulted in a rather sophisticated and complex mechanism. We tried to avoid or reduce this complexity, but complexity appears necessary for the RMO to accomplish its functions.

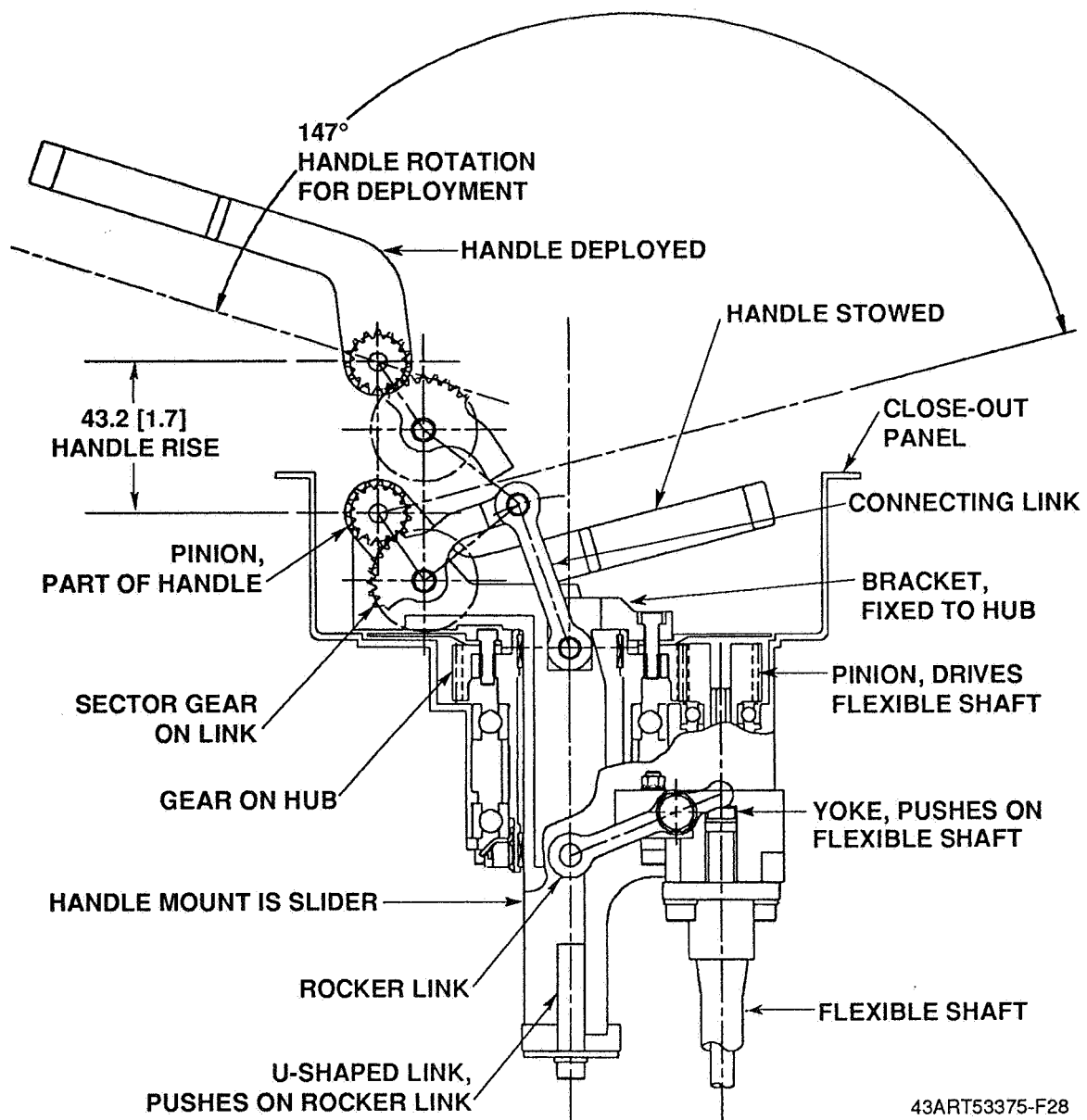


Figure 1. Side View of Remote Manual Operator Mechanism

## Miniature Rotary Actuator

R. A. Fink and R. C. Ellis\*

S24-37 ✓  
50452  
12 5138  
p6

### Abstract

The trend toward smaller satellites has challenged component manufacturers to reduce the size, weight, and cost of their products while maintaining high performance. Both a new stepper motor and a new harmonic drive were developed to meet this need. The resulting actuator embodies small angle stepper technology usually reserved for larger units and incorporates an integral approach to harmonic drive design. By product simplifications, costs were significantly reduced over prior designs.

### Introduction

Design and fabrication of a new miniature actuator presented a number of challenges. As the unit size is reduced, manufacturing tolerances must be tightened to maintain the same relative precision and performance that customers expect. A new product generally evolves from a fresh look at existing technology with improvements based on changing needs. Development must also consider that the customers for smaller satellites are insisting on lower cost. New concepts in design would be required to simplify the hardware while maintaining or improving quality. Both the motor and harmonic drive designs were analyzed with these goals.

This paper addresses the development of a new motor in the first section. The second section discusses the harmonic drive design and the third section reports the results of the complete actuator. There were a number of problems and lessons learned at each step of the development. Final optimization depended on the close cooperation of the motor and harmonic drive manufacturers.

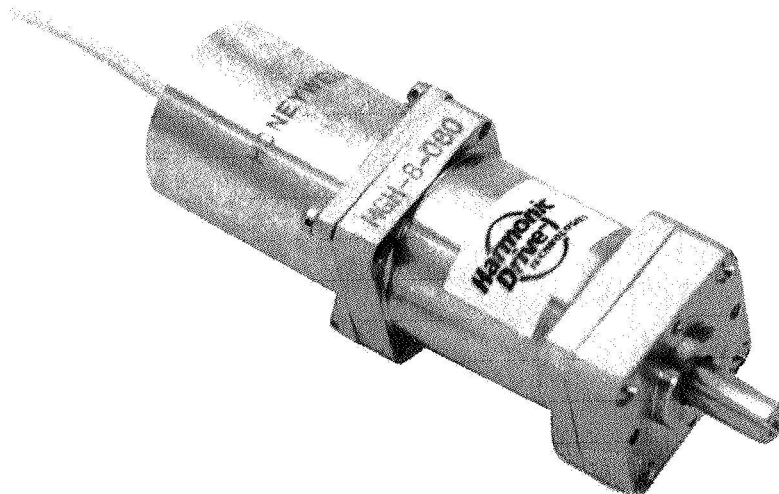
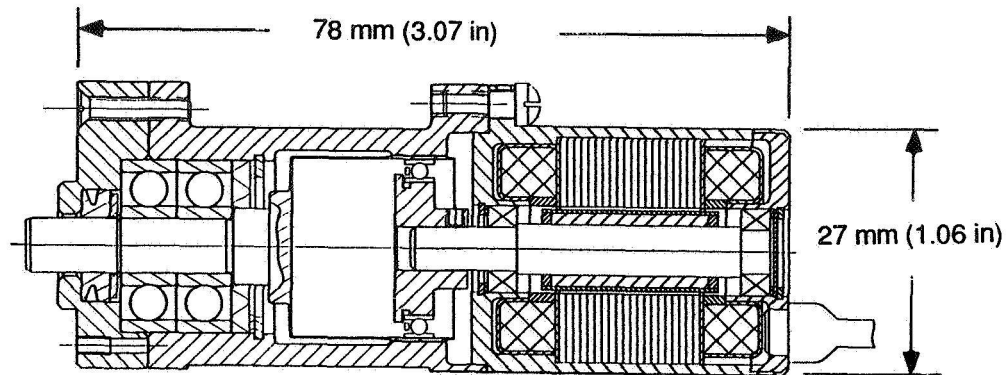


Figure 1

\* Honeywell Electro Components, Durham, NC

44965231-  
25 2



**Figure 2**

## Stepper Motor

The motor design developed on this project combines a large number of poles (12) in a small size 11 package. This results in a smaller step angle (15 degrees), a higher step rate, and more torque than conventional permanent magnet stepper motors of the same size. The motor maintains the same inertia as 2 pole motors of the same size. The motor was also designed to have the same resistance as many previous 2-pole, 90-degree stepper designs used on numerous space programs, ensuring that the input power and thermal considerations remain unchanged. This motor technology has been used in a larger diameter for a 2 phase unipolar, 2-degree stepper to drive a two-axis antenna pointing mechanism for a commercial satellite.

## Motor Test Results

The motors were tested for basic parameters; resistance, inductance, etc., then subjected to running tests. Table 1 summarizes the test data. Powered data is at 24 volts. The maximum start-stop rate was measured by slowly increasing the step rate until the unit would not consistently start and recording the highest rate it would always start. The maximum slew rate was measured by powering the motor and gradually increasing the step rate until the motor stopped. The highest rate that the unit would always run was recorded.

**Table 1, Summary of Motor Test Data**

Parameter	Expected	S/N 1	S/N 2
Winding Resistance ( $\Omega$ )	72	71.3	73.1
Inductance (mH)	20	20.5	21.8
Max. Start-stop Rate (pps)	900	911, 988	1000, 956
Max. Slew Rate (pps)	2000	2100, 2082	2104, 2128
Rated Torque at 400 pps (mN•m)	10.6 (in-oz)	12.2	11.3
Stall Torque (mN•m)	14 (2 in-oz)	15.2	14
Detent Torque (mN•m)	3.5 (0.5 in-oz)	1.4 - 5.6	1.4 - 5.6
Drag Torque: coulomb (mN•m)	1.4 (0.2 in-oz)	2	0.7
viscous (mN•m/rad/s)	0.0014	0.001	0.0019
Weight (kg)	-	0.114 (4 oz)	0.114

The detent torque was measured by back driving the unexcited motor at two degrees per second through a rotary torque transducer and recording the torque on a strip chart. The drag torque was measured in a similar fashion except at five speeds from approximately 60 to 380  $\text{rad/s}$  (600 to 3600 RPM). The drag torque was separated into coulomb and viscous components using a simple linear regression.

### Lessons Learned, Motor

The engineering model motors built on this project performed as expected except the detent torque showed significantly more variation over the 24 detent null positions than desired or expected as shown in Figure 3. This variation was originally attributed to distortion of the magnetic laminations due to the prototype nature of the hardware machining. The cause was, in fact, a design anomaly which caused most of these variations. A careful analysis of the magnetic circuit revealed the importance of using critical proportions between elements of the circuit. Once this fact was determined, we designed a two-degree, two-phase motor using the same principles developed on this project while being careful to maintain the proper proportions in the magnet circuit. Figure 4 shows how the detent torque variations were minimized on this 2 degree step angle design.

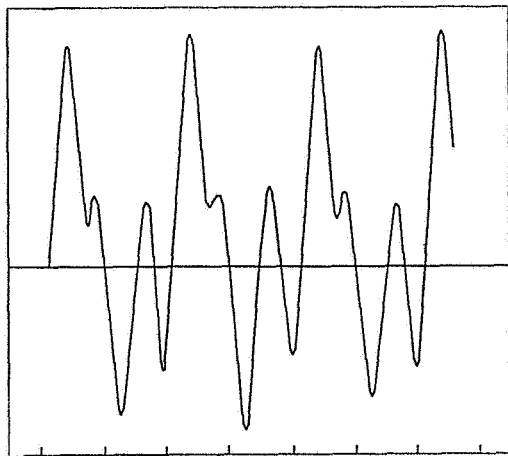


Figure 3

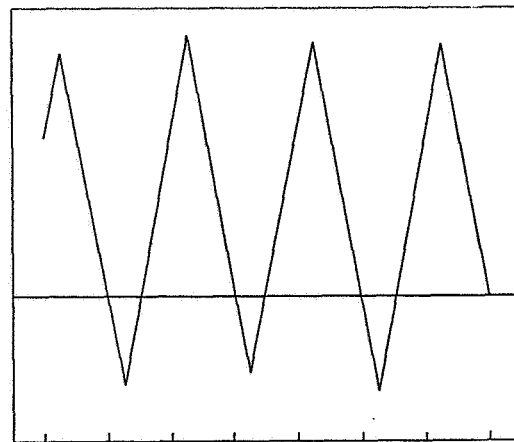


Figure 4

### Harmonic Drive

#### Principle of Operation

As with all harmonic drives, the MGH 8 operates by rotating an elliptical-shaped wave generator within the flexspline causing a one tooth displacement with the circular spline. This displacement results in a high ratio between the input and output stages. The harmonic drive gearing in the MGH provides zero backlash, high positional accuracy, high torsional stiffness and a torque rating equal to conventional units twice its size.

### Description of Design

The MGH 8 is a miniature gearhead with an integral harmonic drive having a 20 mm (0.8 inch) pitch diameter. It has an 80:1 ratio achieved by using very fine gear teeth (200 diametral pitch). The harmonic drive is designed to complement mechanical and performance characteristics of the stepper while incorporating new concepts. It has the same outer diameter and permits direct mounting of the motor. Several unique features improve reliability and structural simplicity. Materials and lubricants are spacecraft rated.

Integration of the harmonic drive components with the housing, bearings and shaft results in an elegant design with minimum parts count. The output shaft is integral to the flexspline. It is supported by two preloaded bearings (MPB SSR-1960 series) and includes an oil seal on the output shaft. The circular spline is machined integral with the gearhead housing, providing maximum miniaturization with minimum weight. The wave generator is mounted directly to the motor shaft, eliminating the need for the typical Oldham coupling.

### **Test Results, Harmonic Drive**

Performance (see Table 2) maintained the high standards expected of a harmonic drive. The maximum torque rating comfortably exceeded the maximum motor stall torque, providing a 3:1 margin. Torsional stiffness, while high, was less than expected (see lessons learned). Positional accuracy was consistent with the reduced size.

**Table 2**

Torsional Stiffness (N•m/rad)		270 (2400 in-lb/rad)
Positional Accuracy (arc sec)		±185
Maximum output torque (N•m)		3.4 (30 in-lb)
Rated output torque (N•m)		1.6 (14 in-lb)
Shaft side load rating (N)	static	220 (50 lb)
	dynamic	67 (15 lb)

### **Lessons Learned, Harmonic Drive**

#### Circular Spline

Although machining the circular spline directly into the housing has benefits in size and weight, it caused a deburring problem. Burrs created from shaping the teeth in the circular spline housing were difficult to remove. There were three reasons for the problem: a) the very small, 200 pitch gear teeth; b) the annealed 304L material; and c) the configuration of the gear blank.

Nothing could be done about the very small 200 pitch gear teeth required to produce the 80:1 ratio. The deburring problem was addressed by: a) redesigning the gear blank to provide more clearance for the shaper cutter at the end of the cutter stroke and b) changing the housing/circular spline material from 304L stainless steel to a more free machining 303 grade. This will require further investigation since 303 is not recommended for spacecraft applications.



### Torsional Stiffness

The design goal for torsional stiffness was 360 N•m/rad (3200 in-lb/rad). The measured torsional stiffness of the MGH gearheads was 270 N•m/rad (2400 in-lb/rad). The original specification of 360 N•m/rad was calculated for the harmonic drive components and did not include the output shaft. The MGH is being offered as a complete gearhead with an integral output shaft. Therefore, the torsional stiffness value must include the shaft stiffness as well as the harmonic drive gear stiffness, and results in a lower value than the original design goal. This points out the need to calculate all contributors to stiffness even if they seem to be insignificant.

### **Integrated Actuator Assembly**

Two stepper motors were assembled to harmonic drives and tested for critical performance characteristics. Motor testing showed good torque output at extremely high stepping rates. Computer analysis of the complete actuator showed that the maximum step rate would be reduced to about half of the rate of the motor alone. This was confirmed during test and was especially discouraging based on the high rate achieved for the motor (see lessons learned). Further development was indicated and is now in process.

The actuator design was tailored for several applications. It could be used as umbilical disconnect mechanisms and cover actuators as well as caging and deployment mechanisms. With the addition of power transfer capability (cable drum or slip rings), it could be used for a small solar array drive. Also under consideration is the use as antenna pointing mechanisms for small Low Earth Orbit satellites. The small step angle ( $0.1875^\circ$ ) may make this practical.

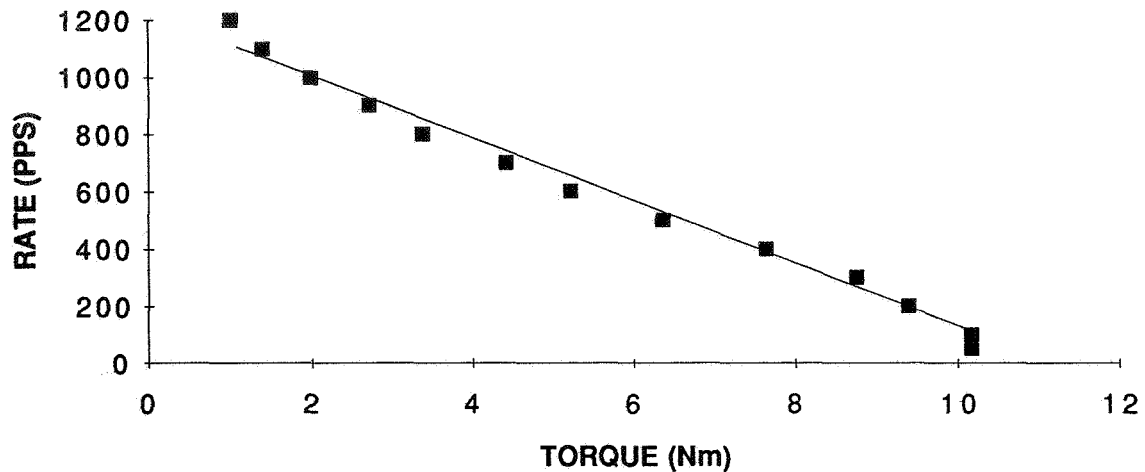
Cost projections of the new miniature actuator show that the design simplifications reduced cost to approximately half that of more conventional designs.

### **Test Results, Integrated Actuator**

Two actuators were tested and exhibited similar performance except for a low speed torsional resonance in only one unit (see lessons learned). As expected, the stepping rate was reduced due to the inertia of the input wave generator, but the starting rate exceeded 500 pulses per second without pulse rate ramping. Output torque was exceptionally high for the unit size and weight. Detent torque is a function of the motor magnetic detent.

**Table 3**

Rated Torque (N•m @ 400 pps)	0.56 (5 in-lb)
Stall Torque (N•m minimum)	1.1 (10 in-lb)
Detent Torque (N•m minimum)	0.17 (1.5 in-lb)
Slew Speed (pulses per second)	1500
Step Angle (degrees)	0.1875
Weight (kg)	0.25 (8.5 oz)



**Figure 5**

## **Lessons Learned, Integrated Actuator**

### Input inertia

The wave generator inertia limited the motor step rate to approximately half of the no-load motor rate. All stepper and servo motors are sensitive to load inertia. To decrease the inertia, the wave generator plug to which the wave generator bearing is assembled was changed from stainless steel to aluminum. This change halved the input inertia from  $2.36 \text{ g}\cdot\text{cm}^2$  ( $0.013 \text{ oz}\cdot\text{in}^2$ ) to  $1.21 \text{ g}\cdot\text{cm}^2$  ( $0.0066 \text{ oz}\cdot\text{in}^2$ ). The MGH gearhead was performance tested with both the steel and the aluminum plug. There were no measurable differences in the harmonic drive characteristics with the two different materials but high speed performance would be significantly improved. Further testing is scheduled and results should be available at the symposium.

### Torsional resonance

One of the two development actuators exhibited a torsional resonance at step rates below 100 pps and performance was seriously degraded. Disassembly of the two harmonic drives revealed that the problem unit had a low torsional stiffness. This explained a low input drag and the resonance. The inertia of the test equipment load contributed to the resonance. It was realized that improved fitting tolerances would be required for production harmonic drives. This problem points out one of the major pitfalls in the use of stepper motors for driving inertia loads. They often become unstable at certain resonant frequencies. Any system that uses a stepper (with or without a harmonic drive) should be carefully analyzed for torsional stability over the full range of step rates expected.

## **Conclusions**

While some design optimization is still needed, the development of this miniature, high-performance, low cost actuator would not have been possible without the mutual cooperation of the motor and harmonic drive manufacturers. There were no revolutionary design breakthroughs, just evolutionary adaptation of existing concepts to changing requirements.

525-37  
50453  
125139 ✓  
pg

## Mir Environmental Effects Payload Handrail Clamp/Pointing Device

Stephen J. Hughes\*

### Abstract

The Mir Environmental Effects Payload (MEEP) consists of four International Space Station Alpha (ISSA) Risk mitigation experiments to be transported and deployed in a common carrier. This carrier is to be transported to the Mir Space Station aboard the Space Shuttle and deployed during a US Extravehicular Activity (EVA) on the handrails of the Mir Docking Module (DM). This paper describes the design of the handrail clamp/ pointing device used by the astronauts to attach the carrier to the station.

### Introduction

In an effort to increase the probability of success and the overall safety of ISSA, the National Aeronautics and Space Administration (NASA) ISSA office requested proposals for a series of risk mitigation experiments. NASA Langley Research Center (LaRC) proposed a universal carrier to be deployed on the Mir Space Station as an exposure facility. Four different researchers expressed an interest in having experiments deployed in the carrier. Two were micrometeoroid and debris experiments: Orbital Debris Collector, an experiment that uses a material called aerogel to capture the hyper velocity particles; and Polished Plate Micrometeoroid and Debris, an experiment in which the impact craters in witness plates are analyzed to validate statistical models of debris at station altitudes. The remaining two experiments are materials exposure and contamination experiments: Passive Optical Sample Array (POSA), an experiment to study the effects of the contaminants that surround a working space station on optical coatings and various other "space-rated" materials; and POSA II, a similar experiment to POSA, with different material samples and an additional requirement to experience atomic oxygen effects as well. After negotiations with the Russian Space Agency (RSC), an agreement was reached — the experiments could be deployed on the DM that was being delivered by the Space Shuttle (STS) to Mir, and the units could be deployed with a US EVA. To preclude modification to the Russian-manufactured DM, the decision was reached to mount the experiments to handrails on the DM with an EVA-deployable clamping mechanism. Each of the four experiments had different viewing requirements. Two of the experiments required ram/wake viewing, which required Mir flight orientation data. This data was difficult to ascertain, and with the compressed schedule, time was not available to wait for resolution of the flight orientation. Consequently, it was necessary to develop a pointing device with a great deal of flexibility.

---

\* NASA Langley Research Center, Hampton, VA

## The Handrail Clamp/Pointer

One generic device was developed to mount each of the four payloads. Each device had two mechanisms: one to clamp on the handrail, and one to point the payload. A simple over-center mechanism was chosen for the handrail clamp, and an adjustable preload ball and socket was chosen for the pointer. Since the items were being designed for space flight, materials were selected that would not outgas. The POSA experiment set even more stringent guidelines for outgassing than normal STS guidelines and, as a result, did not allow the mechanisms to be lubricated. Also, dissimilar materials were chosen to prevent "cold welding".

### The Handrail Clamp

On the DM, several straight sections of handrail were available for clamping. Initially, RSC agreed to provide several 1000-N clamps, shown in documents from joint Johnson Spaceflight Center (JSC)/RSC EVA requirements working groups. After several unsuccessful attempts to acquire these clamps, the decision was made to develop the clamps in-house. The 1000-N clamping force was chosen as a design point. Only rough external dimensions were available on the RSC clamps, so it was not possible to simply manufacture a duplicate. An entirely new clamp had to be designed (Figure 1). Experience has shown that "simple works best" when designing tools for use during EVA, so an over-center mechanism was chosen to provide the clamping action. The cross-section of the handrail was given as 25 mm square with a tolerance of  $\pm 1$  mm. The wall thickness was shown to be 2 mm, with no tolerance given. An analysis was performed to verify that this clamping force would not damage the handrail. A problem arose in providing a consistent clamping force with the 2-mm variation in handrail external dimensions. The variation of the handrail dimension would probably be less than the given tolerance over the width of the clamp, but the clamp had to allow for the tolerances shown on the drawings since the actual handrail was not available for measurements at the time of the design. Using a stack of disk springs, a spring-loaded button was developed to provide a consistent load for any handrail with external dimensions within the tolerance range. To make the clamp more stable and decrease the concentrated load on the handrail, the clamp incorporated three load points. A simple four-bar linkage was used to provide three uniform over-center motions with one actuation lever. Roller bearings were used at the over-center contact points to provide a lower, more consistent actuation force and to prevent unnecessary damage to the handrail. A spring-loaded lock (lever lock) was provided for the clamp lever to prevent the lever from being inadvertently knocked back over-center. For additional safety, a capture plate with a simple push lock (capture plate lock) was provided to keep the payload attached to the handrail in the event the clamp became unlocked while on orbit. Since the clamp was being designed for free-floating EVA, the mechanism had to be designed for one-handed operation. There were also several general design requirements for EVA tool design: big actuating levers to facilitate EVA-gloved operation, sharp corner/edge guidelines, and a maximum 120-N actuation pulse [1].

### The Pointer

The pointer employs a ball in a spring-loaded socket and relies on friction to provide the locking torque (Figure 2). To prevent accidental overloading of the handrail, the

pointer had to provide a torque-limiting feature, which allowed the payload to slip in the socket in the event of an inadvertent kick load (550 N, 125 lb). Locking torque of the ball and socket was driven by two items: ball diameter, which determines the moment arm at which the friction force acts; and spring force, which determines the magnitude of the friction force. Because the pointer device mounted atop the clamp body, the external dimensions of the clamp body limited the maximum ball diameter. Disk springs stacks were again used to provide the spring force on the socket. A lead screw controlled the spring stack compression, thus providing an adjustable spring load. A locking knob (similar in operation to a knob in the EVA tools catalogue [2]) was provided to control the position of the lead screw. The lock was needed to prevent the lead screw from backing out once the preload position was achieved. The spring rate and screw pitch were sized per the following requirements: maximum hand-applied torque, 4.5 N-m; maximum on-orbit acceleration (station reboost or shuttle docking), 0.06 g. This acceleration value was found in a presentation that was the best source of information available at the time of design development. Later, after the pointer design was in fabrication, another document [3] became available that showed a 0.5 g requirement for Mir payloads, with a first mode below 20 Hz. This new requirement caused an order of magnitude increase in the spring force. The higher spring rate was achieved by rearranging the disk spring stacking sequence. The increased locking torque required to maintain pointing at 0.5 g acceleration did not exceed the break-away torque value that satisfied the kick load constraint. The increased spring rate did, however, drive the knob actuation torque well beyond an acceptable range. As a result, a 7/16-inch hexagonal protrusion was added to the knob, thus allowing the use of an EVA contingency tool to tighten the knob.

## Testing and Development

By late December, 1994, it was apparent that the Russian handrail clamps would not be available for MEEP. Therefore, design and manufacturing of in-house hardware began in earnest. By April 17, 1995, one high fidelity proto-flight unit of all the MEEP hardware (experiment container, handrail clamp, and an STS payload bay sidewall carrier) was delivered to the JSC Weightless Environment Training Facility (WETF) for crew evaluation. In general, the eight astronauts who trained with the hardware were satisfied with the overall performance of the hardware. Three requests for changes that affected the handrail clamp/pointer device were made: to shorten the handrail clamp lever; to modify the method of attachment of the experiment container to the pointer; and to modify the bayonet fitting that interfaced with the astronaut mini-workstation, thereby facilitating simultaneous transport of the two devices. These requests were incorporated into a new proto-flight unit that was delivered to JSC for a manned thermal vacuum test on June 29, 1995. The test was conducted at  $-80^{\circ}\text{C}$  and  $10^{-3}$  Pa. The handrail clamp performed flawlessly, but the pointer developed an interference that prevented the ball from moving freely. The unit was returned to LaRC for disassembly and inspection. The designed clearance that provided for thermal growth mismatch was substantially reduced by manufacturing inaccuracies. As a result, the body of the pointer had pinched the ball at the cold test temperatures. In order to meet the delivery schedule to JSC, dimensional verification was not performed, and, as a consequence, the inaccuracy was not discovered. The problem was corrected with the use of shims. By August 1, 1995, all four flight units were

delivered to Kennedy Space Center for a fit check with the Russian DM and the application of final flight markings. The devices were once again returned to LaRC to have those flight markings engraved and painted with a special ultra-low outgassing black ceramic paint (RM 550 IB). A second WETF unit was manufactured along with the flight units. Both WETF units were delivered to JSC to assist with mission timeline testing and continued crew training. The flight units were delivered to SpaceHab December 15, 1995, to be packed in soft stowage in the SpaceHab Module.

## **References**

1. Extra Vehicular Activity (EVA) Hardware Generic Design Requirements Document, JSC-26626
2. EVA Tools and Equipment Reference Book, JSC-20466 Rev B
3. Hardware General Design Standards and Test Requirements, US/R-002, Dec. 1994

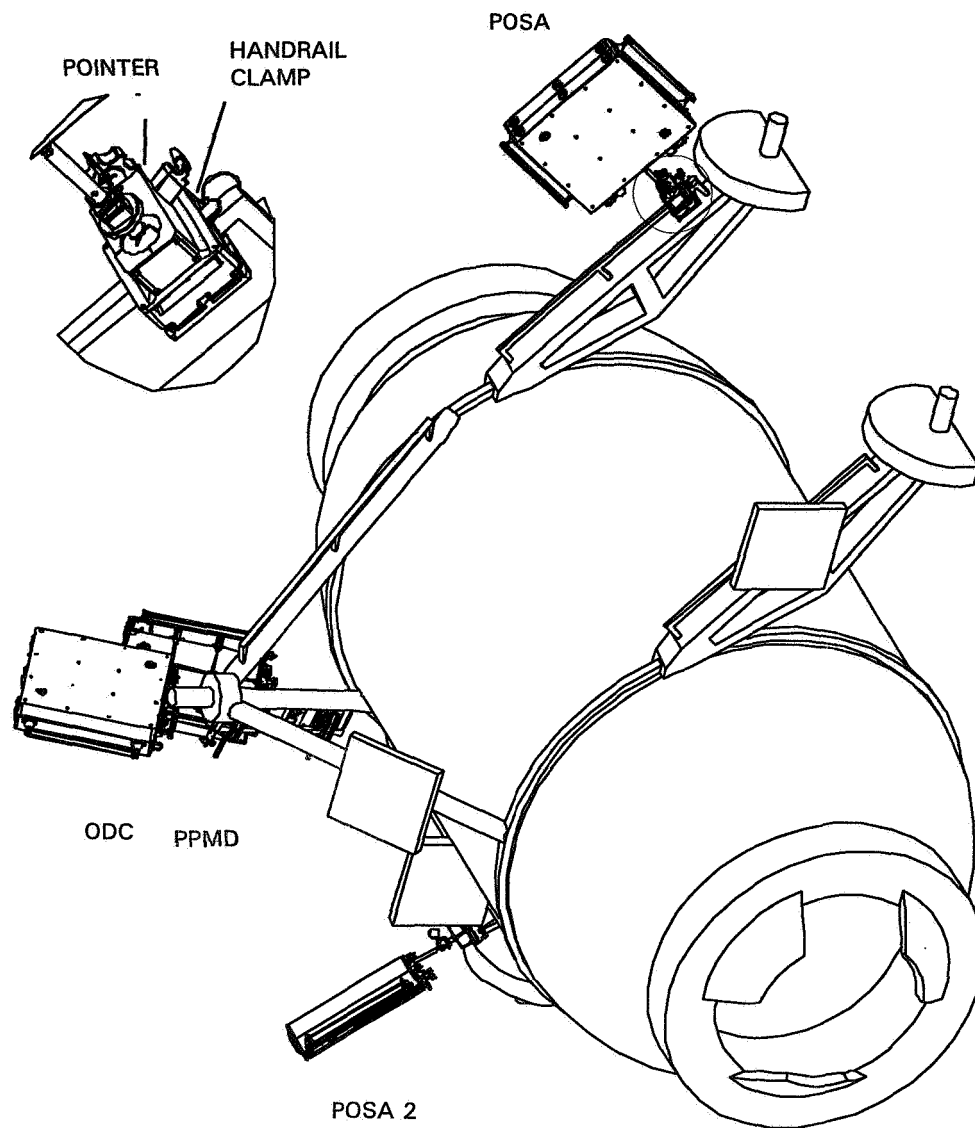


FIGURE 1. MEPP DEPLOYED ON DOCKING MODULE

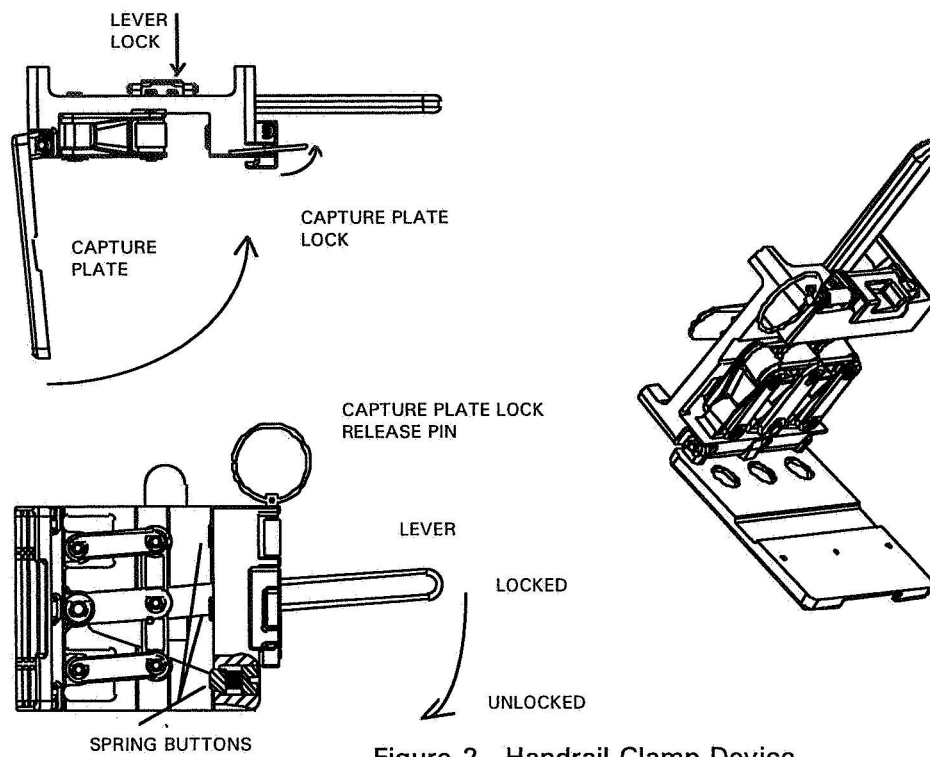


Figure 2. Handrail Clamp Device

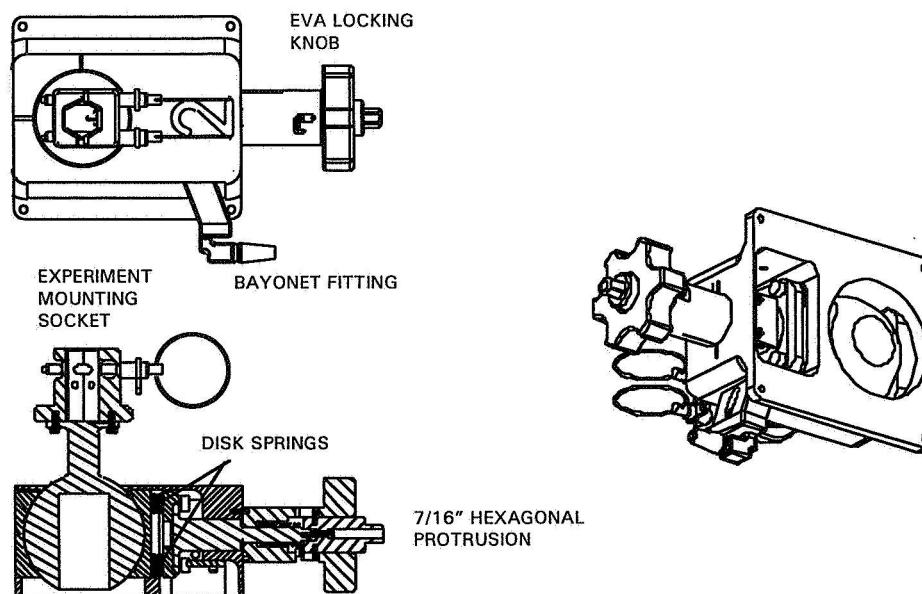


Figure 3. Pointer Device



526-37  
50454  
125140  
P

**A Computer Controlled Power Tool  
for the Servicing of the Hubble Space Telescope**

Paul W. Richards<sup>\*</sup>, Carl Konkel<sup>\*\*</sup>, Chris Smith<sup>\*\*</sup>,  
Lee Brown<sup>+</sup> and Ken Wagner<sup>\*</sup>

## **Abstract**

The Hubble Space Telescope (HST) Pistol Grip Tool (PGT) is a self-contained, micro-processor controlled, battery-powered, 3/8-inch-drive hand-held tool (Figure 1). The PGT is also a non-powered ratchet wrench. This tool will be used by astronauts during Extravehicular Activity (EVA) to apply torque to the HST and HST Servicing Support Equipment mechanical interfaces and fasteners. Numerous torque, speed, and turn or angle limits are programmed into the PGT for use during various missions. Batteries are replaceable during ground operations, Intravehicular Activities, and EVAs.

## **Introduction**

Before each HST Servicing Mission the PGT is programmed via an RS-422 or RS-232 interface. Fourteen torque settings and three speed settings can be programmed for each mission. A specific number of turns or angle can also be programmed with each torque setting. The programmed torque range is 2.7 - 33.9 N•m (2.0 - 25.0 ft•lbf); the programmed speed range is 0.5 - 6.3 rad/s (5.0 - 60.0 rpm), and the available turn settings are 0.01 - 999.99 rotations or 1 - 1000 deg. Other programmable variables include stall time, sleep time, auto off time, torque thresholds, and angle thresholds. Integral to the PGT is a Multisetting Torque Limiter (MTL), which is a mechanical device for protecting hardware from the application of excessive torque. The MTL has 6 settings that are ground re-configurable before each mission. The MTL torque range is 1.4 - 67.8 N•m (1.0 - 50.0 ft•lbf).

## **Overview**

The PGT is grouped into Functional Subsystems and physical Assembly Modules. The five Functional Subsystems are: Mechanical, Electrical, Battery, Software, and Operator Interfaces. There are five Assembly Modules: MTL, Power Train, Main Housing, Electronics Module, and Battery Module. A cutaway view of the PGT can be seen in Figure 2.

A modular design simplifies assembly and maintenance and can be utilized during troubleshooting by exchanging modules with other PGT units. Each module can be installed and removed as a separate subassembly. All modules are fastened to the

---

<sup>\*</sup> NASA, Goddard Space Flight Center, Greenbelt, MD

<sup>\*\*</sup> Orbital Sciences Corporation, Greenbelt, MD

<sup>+</sup> Swales and Associates, Inc., Beltsville, MD

Main Housing directly or through another module. The Battery Module is secured within the Main Housing battery shroud using a locking mechanism.

## **Functional Subsystems**

### Mechanical Subsystem

The Mechanical Subsystem provides the necessary mechanisms and structure needed to apply output torque. The Assembly Modules with a majority of components from the Mechanical Subsystem include the MTL, Power Train, and Main Housing.

### Electrical Subsystem

The Electrical Subsystem provides the analog and digital functions as well as the platform required for software and computer control. This fault-tolerant, re-programmable electronic subsystem consists of the Electronics Module as well as the ON/OFF circuit breaker, the A/B mode switch, and the DC/DC converter. The challenge was to package this motor control system, along with a 25-measurement signal conditioning system, an 8-channel/10-bit data recording system, and a reliable power supply into a volume of 245 cm<sup>3</sup> (15 cubic inches). This challenge was met using proven state-of-the-art electronic design and assembly techniques, including an all-digital control scheme, multi-function microcontroller, off-the-shelf hybrid microcircuits, programmable logic, and two-sided surface mount technology.

### Battery Subsystem

The Battery Subsystem which provides the power for the PGT consists of the self-contained Battery Module. The requirements for the Battery Subsystem were to maintain at least 28V with a 1A continuous current for the electronics and 8.25A pulse current discharge for the motor. As a goal, sufficient capacity for an entire 6 hour EVA was desired. These requirements also have to be met at the worst-case thermal conditions for the HST Servicing mission.

Selecting the proper battery technology and cell size to meet these requirements yet keeping the battery small enough for an astronaut to translate with the PGT was a difficult process. Four technologies; Nickel-Cadmium (NiCd), Nickel-Metal-Hydride (NiMH), Lithium-Ion (Lilon), and Silver-Zinc (AgZn), were identified as potential PGT Battery technologies. Of the four candidates, Lilon cells possess the highest combination of cell voltage and volumetric energy density. The PGT Battery Module will be the first space qualified Lilon battery.

The Software of the PGT computer implements three major functions; Servo-System, Fault Detection, Data Collection. The Servo-System is a closed loop feedback system which limits the torque, speed and the angle output of the PGT. The control is based upon Proportional and Integral control algorithm using pulse width modulation and the knowledge of the native motor speed/torque curve. The software will allow the motor to function at the lesser of three conditions; programmed torque, programmed speed, or the maximum output based upon the native speed/torque curve. The computer system also collects and stores fault data, diagnostic data, and performance data. The various faults that can be detected are Software, Temperature, Current,

Voltage, and Torque. The fault history is stored in non-volatile memory to allow for trouble shooting during development, testing, and use.

### Operator Interfaces

The Operator Interface Subsystem provides the means for all necessary operator input and provides visual feedback through markings, an alphanumeric display, and status and warning light emitting diodes (LEDs). The operator selects the configuration of the PGT through various switches and collars. The selection collars include the MTL Torque collar, Ratchet collar, Programmed Torque collar, and the Speed collar. The Speed collar also has a CAL setting which tests the LEDs, the Alphanumeric Display and calibrates the torque transducer. The switches include the ON/OFF circuit breaker, the A/B Mode switch, and the trigger.

Configuration, performance, and fault information is shown to the operator via the LEDs and Alphanumeric Display. The LEDs consist of the POWER (green), FAULT (red), and TORQUE (green/red). The Alphanumeric Display shows the programmed torque, programmed speed, direction, actual peak torque, and actual cumulative rotation since the last configuration change. Fault messages are also presented to the operator in the Alphanumeric Display.

### **Assembly Modules**

#### Multisetting Torque Limiter (MTL)

The MTL, located at the forward end of the PGT rotates with the output shaft. There are six torque settings which are ground re-configurable before each mission. The MTL torque range is 1.4 - 67.8 N•m (1.0 - 50.0 ft•lbf). Each setting increases the torque of the previous setting by 1.4 - 20.3 N•m (1.0 - 15.0 ft•lbf). The highest value implemented will be 41.3 N•m (30.5 ft•lbf), which is the maximum design limit of the PGT in the manual mode. The torque settings are selected by the operator by unlocking the thumb switch and rotating the MTL torque selector collar. The thumb switch prevents inadvertent reconfiguration of the MTL.

#### Power Train

The PGT Power Train consists of the motor, gearing, and torque transducer, and ratchet/clutch mechanism. The PGT motor is a 28V, four pole, brushless dc motor. The motor uses samarium cobalt magnets on the rotor and employs hall effect sensor commutation. The gearing is a 2-stage planetary gear set with a reduction ration of 110:1.

The operator selects the motorized or manual mode of the output shaft by rotating the ratchet collar and aligning the visual indicator with the desired setting. There are three settings: Ratchet Clockwise (RCW), Motorized (MTR), and Ratchet Counterclockwise (RCCW). In the MTR setting a clutch is engaged and the motor output shaft is connected through the MTL which to the PGT output shaft. In the RCW and RCCW settings the clutch is disengaged and either the clockwise or counter-clockwise ratchet pawl is engaged. When in either the RCW or RCCW settings, the load path is through the ratchet pawl to the Main Housing. There is also a hall effect sensor electrical inhibit, which allows motorized operation in the MTR mode, but inhibits motorized

operation in the RCW and RCCW mode. This inhibit prevents motor operation during inadvertent contact with the trigger.

### Main Housing

The Main Housing consists of the Collar/Switch Subassembly, and a two-piece housing, which consists of the Power Train housing, the handle and trigger and the battery shroud. The Collar/Switch Subassembly contains the Speed collar, Torque collar, ON/OFF circuit breaker switch, A/B mode switch, and the DC/DC Converter.

### Electronics Module

The Electronics Module consists of an analog circuit board and a digital circuit board mounted in an aluminum housing. The major components of these boards are a 87C196KD microcontroller, a Clock Oscillator, Memory Address Latches, EEPROM, a Erasable Programmable Logic Device (EPLD) EMP5130, 82C55 port expander, DAC-8412 quad digital to analog converter, Strain-gauge Torque Transducer signal conditioning circuit, temperature (Motor, Battery and Motor-drive Hybrid) signal conditioning circuits, Hardware Torque Warning Circuit, Latch-up current-limiting circuits, and a Motor Drive Hybrid circuit.

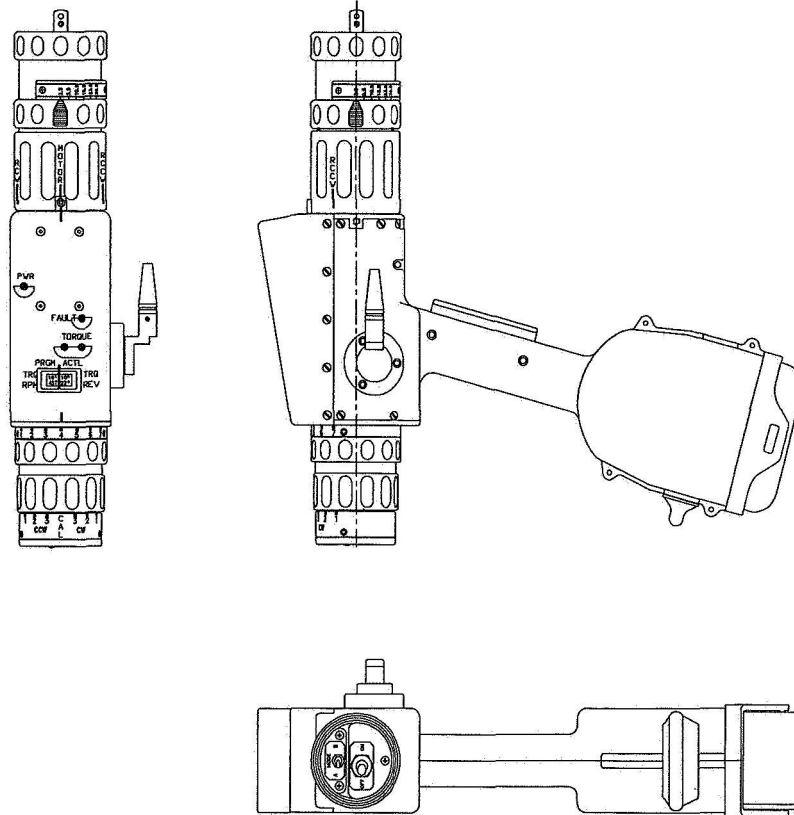
### Battery Module

Each PGT Battery Module contains ten Lilon cells connected in series to create a 41V open circuit and a 36V nominal closed circuit battery. The battery design was optimized to approximately 2.4 A•hr capacity using modified C sized cell. The cell pack is then packaged into a nickel-plated aluminum housing. A cover is fastened on top to form the battery module. On one end of the module is a rectangular sub-miniature connector which provides an interface to the tool for positive and negative power lines. A 10A fuse on the negative line provides over-current protection in the event of a short in the tool. The battery modules and the battery shroud are keyed with alignment grooves to prevent incorrect insertion.

The battery module design includes a temperature sensor to sense battery/cell temperature. If battery temperature increases to above nominal level, the Alphanumeric Display will indicate a high battery temperature warning to the user. If battery temperature increases and approaches an unsafe level, a software command is given to remove power using the circuit breaker.

### Conclusion

The application of satellite mechanism technology and design methods was critical in the production of a compact, ergonomic power tool which meets the accuracy, reliability, and safety requirements for the HST Second Servicing Mission.



**Figure 1**  
**Pistol Grip Tool**  
**External View**

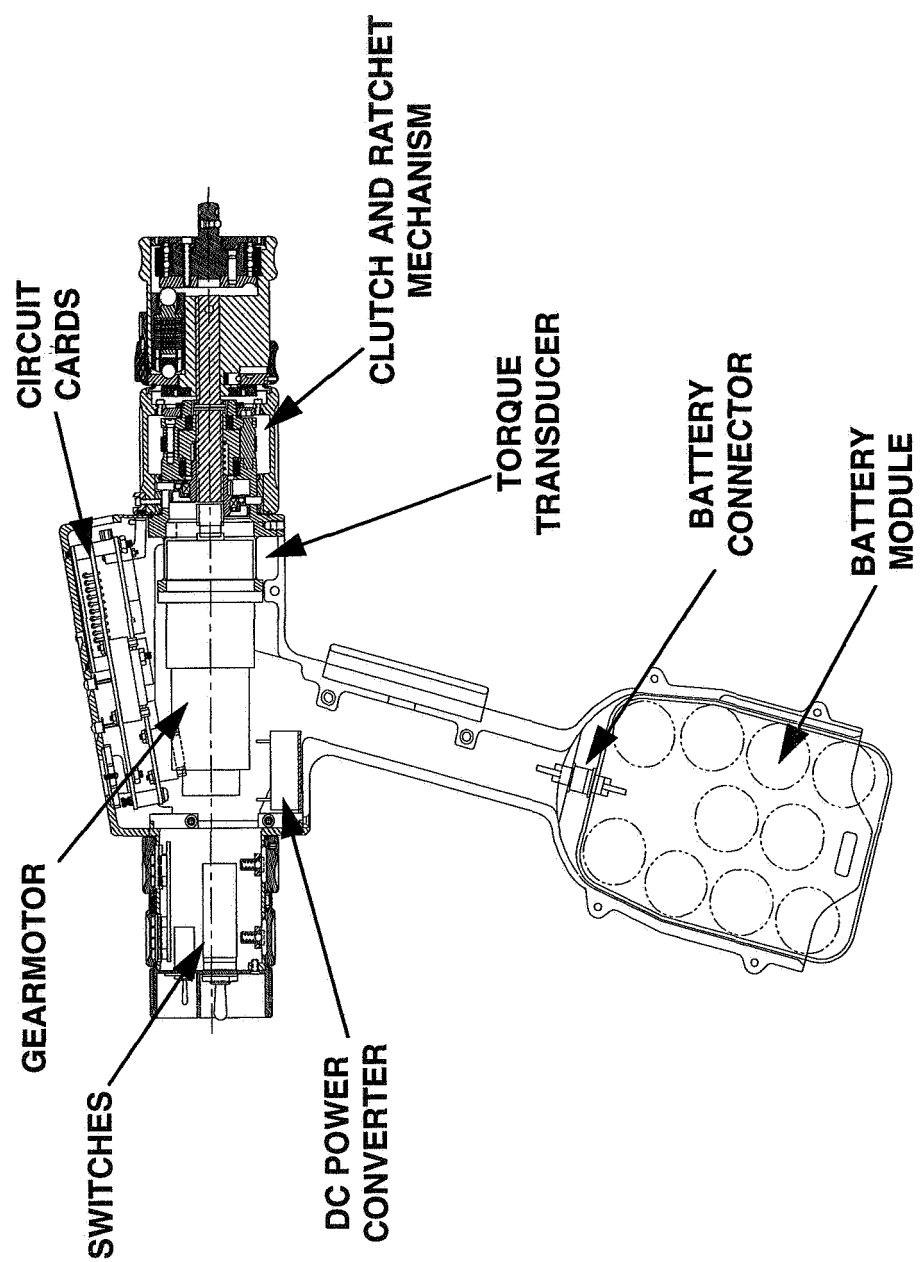


Figure 2  
Pistol Grip Tool  
Cutaway View

# 537-37 50455 125141 P ✓

## Umbilical Mechanism Assembly for the International Space Station

A. Ali Mandvi\*

### Abstract

Mechanisms for engaging and disengaging electrical and fluid line connectors are required to be operated repeatedly in hazardous or remote locations on space station, nuclear reactors, toxic chemical and undersea environments. Such mechanisms may require shields to protect the mating faces of the connectors when connectors are not engaged and move these shields out of the way during connector engagement. It is desirable to provide a force-transmitting structure to react the force required to engage or disengage the connectors. It is also desirable that the mechanism for moving the connectors and shields is reliable, simple, and the structure as lightweight as possible.

With these basic requirements, an Umbilical Mechanism Assembly (UMA) was originally designed for the Space Station Freedom and now being utilized for the International Space Station.

### Introduction

The Umbilical Mechanism Assembly (UMA) consisting of an active half and a passive half provides the capability to remotely engage electrical umbilical connectors on various space station subsystems.

One of these subsystem is the Mobile Transporter (MT). The MT provides the capability of moving the Mobile Remote Servicer (MRS) and payloads to discrete locations along the station truss for assembly and maintenance operations. The UMA will be used to connect the electrical power umbilical from the truss segments to the MRS.

This paper is written to provide an overview of the UMA and describes its features and capabilities. Kinematics of the mechanisms and details of various assemblies are provided. Criteria for calculating the actuation load is defined. Results and lessons learned from the development test are addressed.

### Summary

The UMA automatically connects and disconnects electrical umbilical contacts while shielding the electrical connectors from debris. The mechanism reacts mating and demating loads internally, without additional supporting structures. The mechanism is designed for service in outer space, where its shields would protect against micro meteoroids, debris, and ultraviolet radiation.

---

\* McDonnell Douglas Aerospace, Huntington Beach, CA

The mechanism consists of an active and a passive assembly. It can accommodate an initial linear misalignment of 6.35 mm (0.25 in) and an angular misalignment of 2° between the active and passive assemblies.

All functions -- extension of the plug, mating, and movement of the debris shield -- are actuated by a single drive mechanism with redundant motors. An override feature in the drive train allows manual operation in case of motor failure.

## **UMA Features and Capabilities**

Key features and capabilities of the UMA are as follows:

- Remotely connect umbilical connectors for the transfer of power and data for multiple applications on International Space Station
- Accommodate an initial linear misalignment of 6.35 mm (0.25 in) and angular misalignment of 2° between the active and passive assemblies
- Provide capability for on-orbit replacement
- Envelope of the active half is 29.21 x 34.29 x 35.56 cm (11.5 x 13.5 x 14 in) and passive half is 26.92 x 28.70 x 17.78 cm (10.6 x 11.3 x 7.0 in)
- Connector mating force of 1112 N (250 lbf) minimum
- Design life cycles - 5000
- Capability provided for Extravehicular Activity backup
- Male and female connectors are protected from external debris
- Weight of active half is 32.0 kg (70.4 lb) and passive half is 6.7 kg (14.7 lb)
- Electrically single failure tolerant
- Mechanically zero failure tolerant and designed to minimum risk
- Operate in vacuum in a temperature range of -78.9 to 60 °C (-110 to +140 °F) environment
- Withstand launch on the Space Shuttle in an acoustic vibration environment of 13 grms in a frequency range of 25 to 2000 hertz

## **Design Factors**

The mechanical components of the UMA were analyzed for structural strength to meet the following Space Station requirements:

### **Safety factors**

On-orbit	Limit = 1.1 x maximum design load
	Ultimate = 1.5 x maximum design load
Launch	Limit = 1.0 x maximum design load
	Ultimate = 1.4 x maximum design load

The UMA is designed to withstand ultimate load of 5671 N (1275 lbf) connector mating load.



## UMA Description

The UMA shown in Figure 1, is a lightweight and reliable mechanism that provides for automatic mating and demating of a pair of connectors.

The electrical connector (receptacle) lies within a passive assembly while an electrical connector (plug) lies on a movable carrier in an active assembly. Major components of the UMA active and passive assemblies are shown in Figure 2 and Figure 3, respectively. A motor-driven mechanism translates the carrier down on two Acme drive screws to mate the connectors. As the carrier moves down, it rotates a pair of pivoting covers at the lower end of the active half, moving them out of the way of the carrier. As the covers pivot down, receptacle and plug respectively on the movable members and on the passive half engage (see Figure 4). Mating and demating forces are reacted between the passive half housing and active half housing through the movable covers, which avoids the need for an additional rigid connecting structure.

The movable covers not only transmit mating and demating forces, but also provide coarse alignment of the connectors prior to mating. A pair of shield on the passive half cover the lower connector prior to mating. The lower connector is mounted on four stacks of Belleville washers allowing shift and tilt to align the connectors as they mate. A manual override mechanism is provided on the UMA active half to operate the mechanism in case of motor failure.

A set of launch restraint mechanism on each side of the active half secures the active half body against the substructure during the launch environment and until in position on orbit. The restraints are released (single function) during the initial actuation of the active half.

The active half is powered by functionally redundant Integrated Motor Controller Actuator (IMCA) and controlled through a MIL-STD-1553 data bus. The IMCA is commanded to actuate the UMA and engage the plug with the receptacle when the UMA active half is within the engagement envelope of the passive half. Another command to the IMCA retracts the connector carrier and uncouples the connector.

## Kinematics

The mating sequence is shown in Figure 5 and consists of the following steps:

- a) Upon receipt of an electrical signal through the data bus, the IMCA drives a gear train that turns the drive screws and begins to extend the connector carrier of the active half.
- b) A cam surface on the carrier begins to open the debris shield doors of the active half. As these doors approach the end travel, they engage the passive half housing through four probe/drogue interfaces.
- c) The carrier continues to extend and contacts strikers on a set of linkages that open the passive half debris shields. The operation is completed as the pins in the male

electrical connector are inserted into the sockets in the receptacle on the passive half.

- d) Redundant position sensing through limit switches is incorporated to stop the connector carrier at predetermined engage and disengage positions. In case of limit switch failure the IMCA motor control software will turn off the motor when a predetermined turn-count is reached. A hard stop is also provided at either extreme position and the motor torque is limited so that contact with the hard stop cannot induce motor burn-out or cause mechanical failure of any UMA component.

## **UMA Assembly Details**

### **Structural Compliance System**

The active half is suspended on the primary structure on four helical springs. These springs deflect in the axial and or lateral directions and allow the active half to achieve structural compliance with the rigidly mounted passive half.

### **Carrier Cam Operation and Interaction with the Debris Shields**

The carrier contains the electrical plug and translates up and down on two drive screws. Each drive screw is attached on the active half body in a gimbal bearing at the upper end and on a thrust bearing at the lower end.

On each side of the carrier there are two 'L' shaped cam profiles shown in Figure 6. These cams operate a set of debris shield doors. While translating downwards, the carrier (prior to engaging the electrical connectors) contacts debris shields linkage on the passive half and opens them. As the carrier translates downward on the drive screws, the doors gradually open drogues on each door and engage with probes on the passive half. The cams also transmit sufficient force to align the active half with the passive half as the probes seat in the drogues. The probe and drogue interaction subsequently provide the load reacting link between the active and passive half when the pins in the plug are inserted into the receptacle in the passive half.

The electrical receptacle is attached on the passive half on four stacks of Belleville disk springs shown in Figure 3. These spring stacks allow the receptacle to shift sideways and tilt slightly to achieve final alignment with the plug and limit the pin insertion load on the plug.

### **Power Train**

The drive screws are single start, 1.27 cm (0.5 in) in diameter and have 3.94 threads per centimeter (10 threads per inch) pitch. These screws are operated from a gear box having 8.3:1 reduction from the motor input through three spur gear meshes. The gears are design per American Gear Manufacturer's Association (AGMA) class 10 specification and are made from Nitraolloy 135 M. The gear teeth surface is nitrided for wear resistance to Rockwell hardness 30-36. For corrosion protection, the gears are cadmium plated. Everlube 620 dry film lubricant is used for lubrication. Each gear is mounted in a set of sealed ball bearings.

### Launch Restraint System

Two launch restraint mechanisms shown in Figure 7 are attached on each side of the active half to secure it against the substructure during the launch environment.

Each launch restraint system consists of a spring loaded pivoting housing and a set of restraint pins connected on a bellcrank linkage system. In the launch configuration the pins are engaged in the pivoting housing while the bellcrank is in contact with the carrier and the linkage system is in the overcenter position. As the carrier moves downward, the bellcrank linkage system pulls the restraint pins out of the housing, the housing pivots away from the guides and the active half is then able to achieve compliance with the passive half.

### **Actuation Loads**

The UMA mechanism requires less than 6 in-lb of actuation torque to provide a minimum connector preload of 1112 N (250 lb). The actuation system provides more than 100% torque margin relative to the torque available from the actuator [(2.05 N•m) (18 in•lbf)].

The efficiency of the drive screw is a critical parameter in sizing the UMA actuator and the structure. The actuator was sized for worst case load with the worst case drive train efficiency. The efficiency of the screw threads varies with the coefficient of friction and the thread geometry. The mechanism structure was sized to withstand a jamb condition with the highest actuation torque at the greatest drive train efficiency.

The overall efficiency of the screw is based on the following relationship (derivation is found in Appendix I) and the friction versus efficiency is shown in Figure 8.

$$F = \frac{Eff_s}{1 + Eff_s \cdot (r_t \cdot \mu) \cdot 2\pi/L} \cdot \tau_{app} \cdot 2\pi/L \quad (1)$$

Loading efficiency is based on coefficient of friction of 0.2 and 0.5 and from the above figure it is found to be between 0.114 and 0.244 (2)

### Actuator Loads at Gearbox inputs

The best and worst case efficiencies of the gearbox are based on 1% to 3% efficiency loss per stage. This results in an overall efficiency of between 91% to 97%.

The UMA actuation loads come from three sources, namely alignment load, passive half cover actuation load, and load from connector seating/preloading. The largest being the connector seating/preloading load of 1112 N (250 lb).

Each isolator spring has a spring rate of 4378 N/m (25 lb/in) and may deflect as much as 1.27 cm (0.5 in), therefore, the alignment load is:

$$4 \cdot 0.0127 \text{ m} \cdot 4378 \text{ N/m} = 222.4 \text{ N (50 lb)} \quad (3)$$

The torque required to achieve alignment with these springs was found to be insignificant with respect to the torque required for connector seating/preloading. Similarly the torque required to actuate the passive half debris shields was also found to be insignificant.

The mechanical advantage and efficiency of each stage of the drive train and the efficiency of the drive screw were taken into account for developing the actuator torque. The maximum drive screw torque required (with low screw efficiency) is based on the following relationship:

$$T = \frac{P \cdot L}{2 \cdot \pi \cdot \text{Eff}} \quad (4)$$

$$\frac{1112 \cdot 0.00254}{2 \cdot \pi \cdot 0.114} = 3.945 \text{ N}\cdot\text{m} \text{ (34.9 in}\cdot\text{lb)} \quad (5)$$

Where:

T = Actuator torque

P = Maximum load for connector seating/preload

Eff = Worst-case screw efficiency (0.114)

L = screw pitch

The maximum actuation torque is further reduced by 8.3:1 gear ratio, but slightly increased by the worst case gear train efficiency (91%). Therefore, the actuation torque is:

$$\frac{3.945}{8.3 \cdot 0.91} = 0.4325 \text{ N}\cdot\text{m} \text{ (4.62 in}\cdot\text{lb)} \quad (6)$$

The UMA drive train efficiency can vary over a range of more than two to one. This compounded by the torque limit tolerance of 10% of the actuator and results in the possibility that as much as 3736.5 N (840 lbf) can be transmitted to one of the nuts under some mechanism jamb conditions. Therefore, the UMA components are sized to withstand this jamb load.

## Development Test

Development test was planned in the early phase of the design to characterizing and verifying the performance of the UMA, but also to gain information and experience on as many elements of the design as possible. Initial testing began on July 1, 1991

Primary objectives of the test were to:

- Evaluate performance characteristics at ambient and cold vacuum environments
- Demonstrate cycle performance equal to twice the space station life
- Demonstrate launch survivability in a space shuttle random vibration environment

As the test progressed, provisions were made to assess/observe additional aspects of the tests to achieve maximum return from the program. Specifically, a separate test was conducted to select a suitable dry film lubricant on the drive screws.

### Test Results

Development testing was completed in June 1993. All objectives of the test were met.

1. The structural compliance capability was verified at both ambient and cold temperature thermal vacuum environments. During performance testing the connectors were successfully mated with all possible worst case out-of-alignment conditions between the active and passive halves.
2. Completed over 11,000 life cycles which represented twice the on-orbit estimated operations.
3. During the initial performance test it was found that the Everlube 620 dry film was wearing off the drive screws and galling the threads.
4. During vibration testing the launch restraints prematurely actuated due to inadvertent movement of the carrier.
5. The original suspension springs were found to be very stiff and caused excessive distortion of the passive half structure.

### Lessons Learned and Design Refinements

The following modifications were incorporated to resolve deficiencies noted in items 3, 4 and 5 of the above results

1. Everlube dry film lubricant on the drive screws was replaced with Tiolube which was found to provide better performance in a separate test. The installation of the drive screw was also modified with thrust bearings on the lower end and gimbal bearings at the upper end of each drive screw. The UMA mechanism with the new dry film lubricant and bearings was retested during the life cycle test. Test showed that the reported wearing and galling problem was corrected and reduction in the motor torque was achieved.
2. To prevent premature movement of the carrier in the random vibration environment, four spring-loaded plungers on the active half were installed to interface with detents on the carrier (Figure 6). This arrangement was successfully retested without any anomalies.
3. The suspension springs were replaced with more compliant springs and subsequent tests did not show any significant distortion of the passive half structure.

## Conclusion

The UMA meets all performance requirements. The design of the UMA is mature and the flight hardware is in final fabrication while the qualification testing is expected to be completed in September 1996. The mechanism will be qualified to operate on orbit in a thermal vacuum environment. This mechanism can be used in various other applications for umbilical connections of electrical, data, video, fiber optics or fluid lines.

## Acknowledgment

This work was performed under contract HX3200 Boeing Defense & Space Group, Houston TX.

## References

- 1) UMA, Structural Integrity Report, MDC95H0423
- 2) Umbilical Mechanism Analysis Report, MDC 93H0428
- 3) UMA, Configuration Item Specification, SP-M-601

## Appendix I

The expression for drive screw nut force for a given torque across the screw threads is:

$$F = Eff_s \cdot \tau_s \cdot 2\pi/L$$

Where the thread efficiency is given by:

$$Eff_s = \frac{\cos(\alpha) - \mu \cdot L/(\pi \cdot D_m)}{\cos(\alpha) + \mu \cdot \pi \cdot D_m/L}$$

given:

$\alpha$  = Angle

$\mu$  = coefficient of friction

$L$  = Screw Lead, inches per thread

$D_m$  = Diametral Mean of the screw

$\tau_s$  = Torque across screw threads

For a perfectly efficient ten threads per inch screw, the relationship between nut force and the torque across the screw threads is:

$$F = Eff_s \cdot \tau_s \cdot 2\pi/L = 1.0 \cdot \tau_s \cdot 2\pi \cdot 10$$

However, the ten threads per inch UMA Acme Screws operate between 12% and 25% power transmission efficiency due to thread and thrust bearing friction. At this low efficiency, the screw is irreversible.

Including the thrust bearing friction effects into the overall efficiency factor complicates the equations slightly. However, it can be seen from the results that in the screw efficiency regime that we operate in that the overall efficiency is insensitive to bearing friction.

The thrust bearing friction torque is proportional to axial force on the screw.

$$\tau_f = r_t \cdot \mu_t \cdot F$$

Where the applied torque is the sum of both the torque applied at the nut and the thrust bearing friction torque.

$$F = Eff_s \cdot (\tau_{app} - \tau_f) \cdot 2\pi / L$$

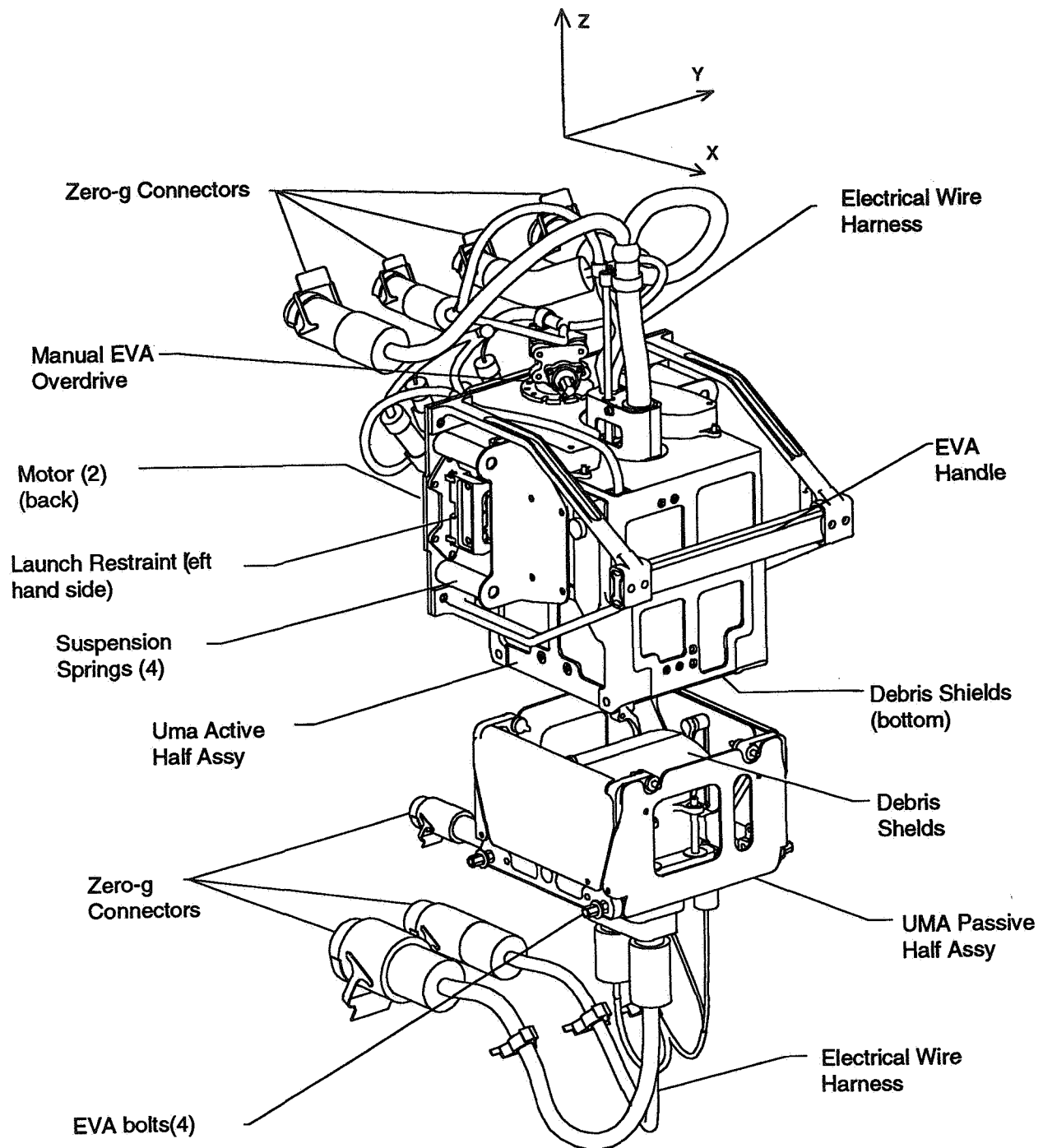
$$F = Eff_s \cdot (\tau_{app} - r_t \cdot \mu_t \cdot F) \cdot 2\pi / L$$

Solving for F

$$F = \frac{Eff_s \cdot \tau_{app} \cdot 2\pi / L}{1 + Eff_s \cdot (r_t \cdot \mu) \cdot 2\pi / L}$$

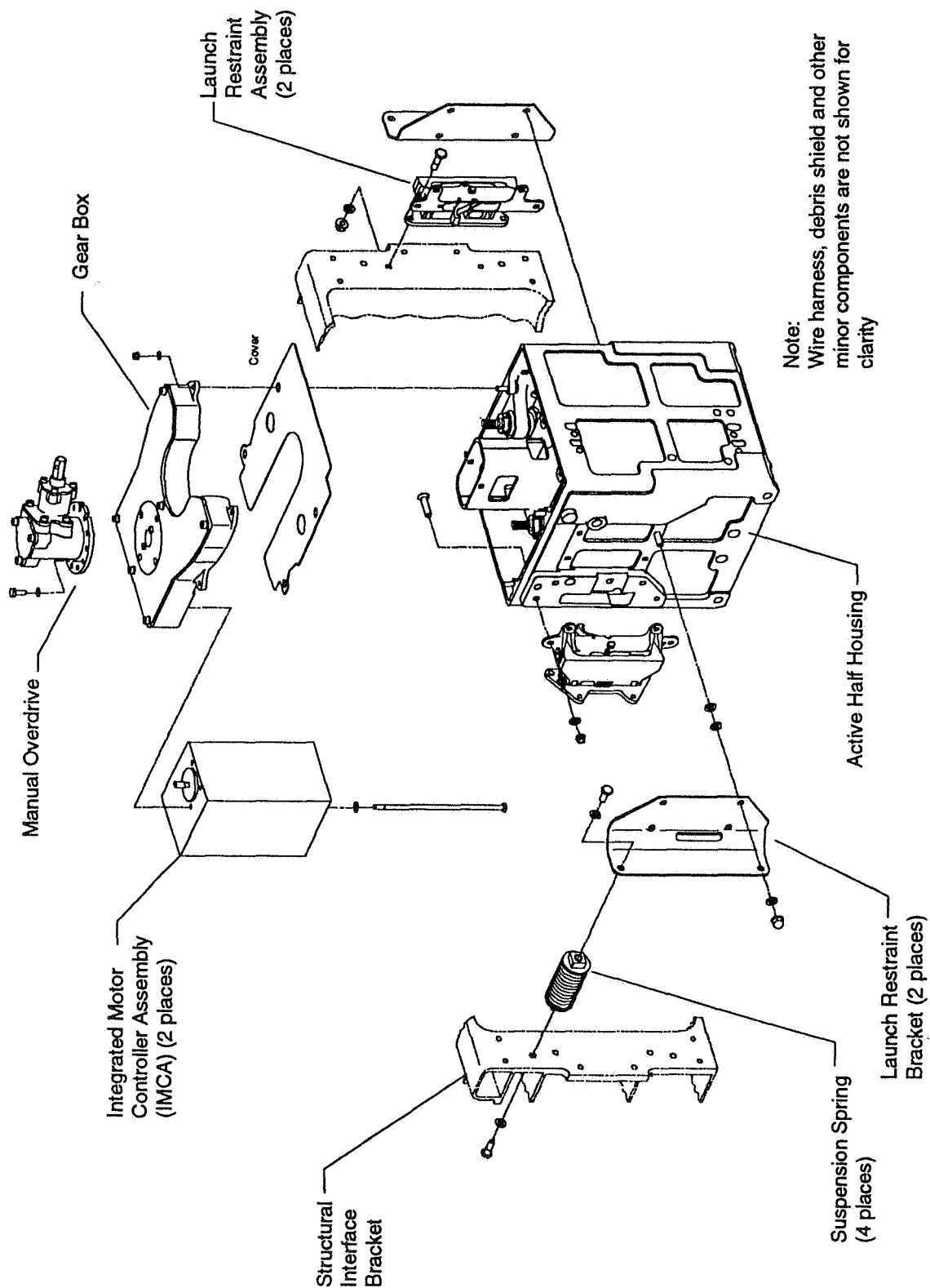
Arranging the equation screw efficiency as a function of coefficient of friction is

$$F = \frac{Eff_s}{1 + Eff_s \cdot (r_t \cdot \mu) \cdot 2\pi / L} \cdot \tau_{app} \cdot 2\pi / L$$



**Figure 1**  
**Umbilical Mechanism Assembly (UMA)**  
**Active and Passive Halves**





**Figure 2**  
Components of UMA Active Half

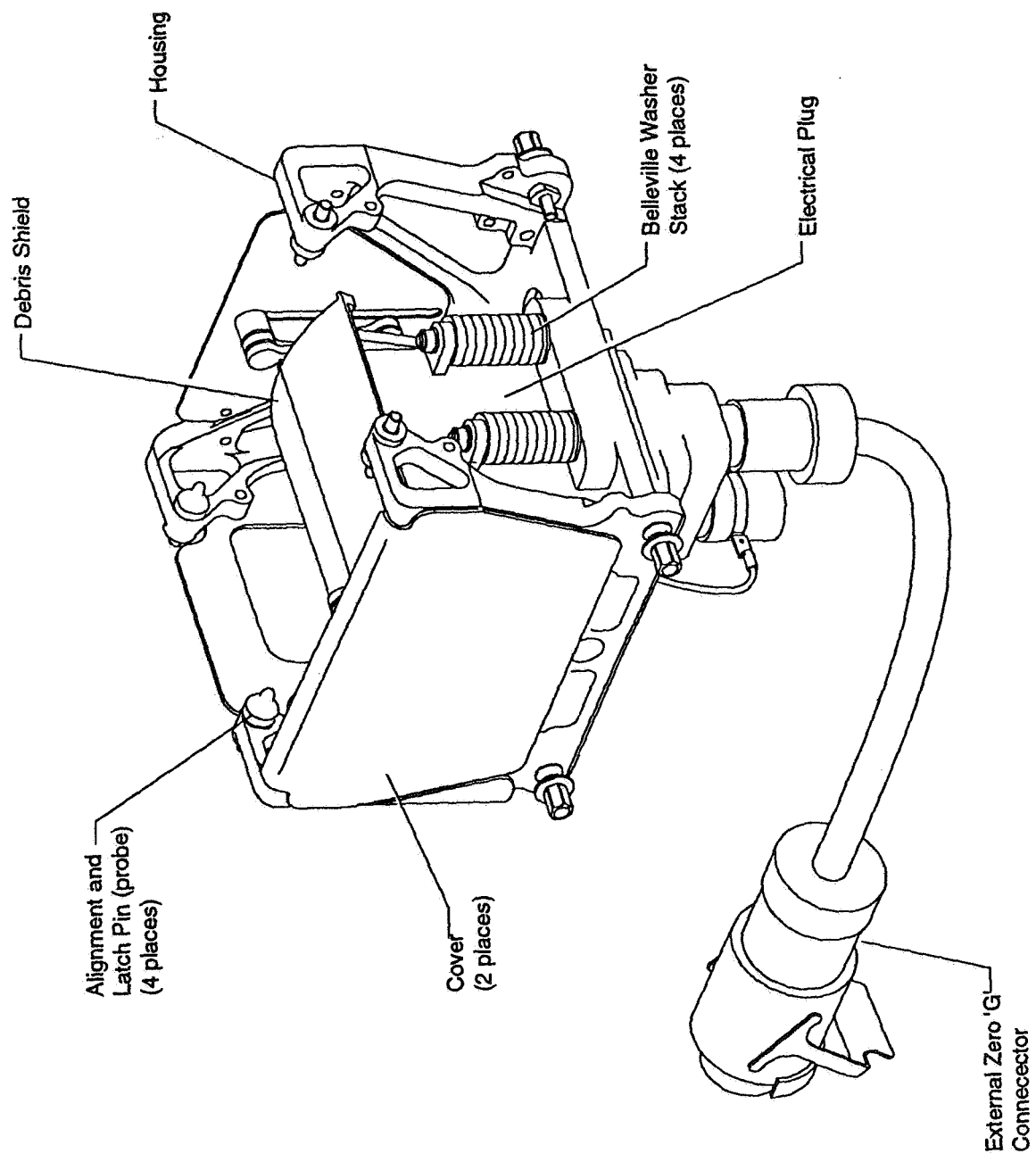
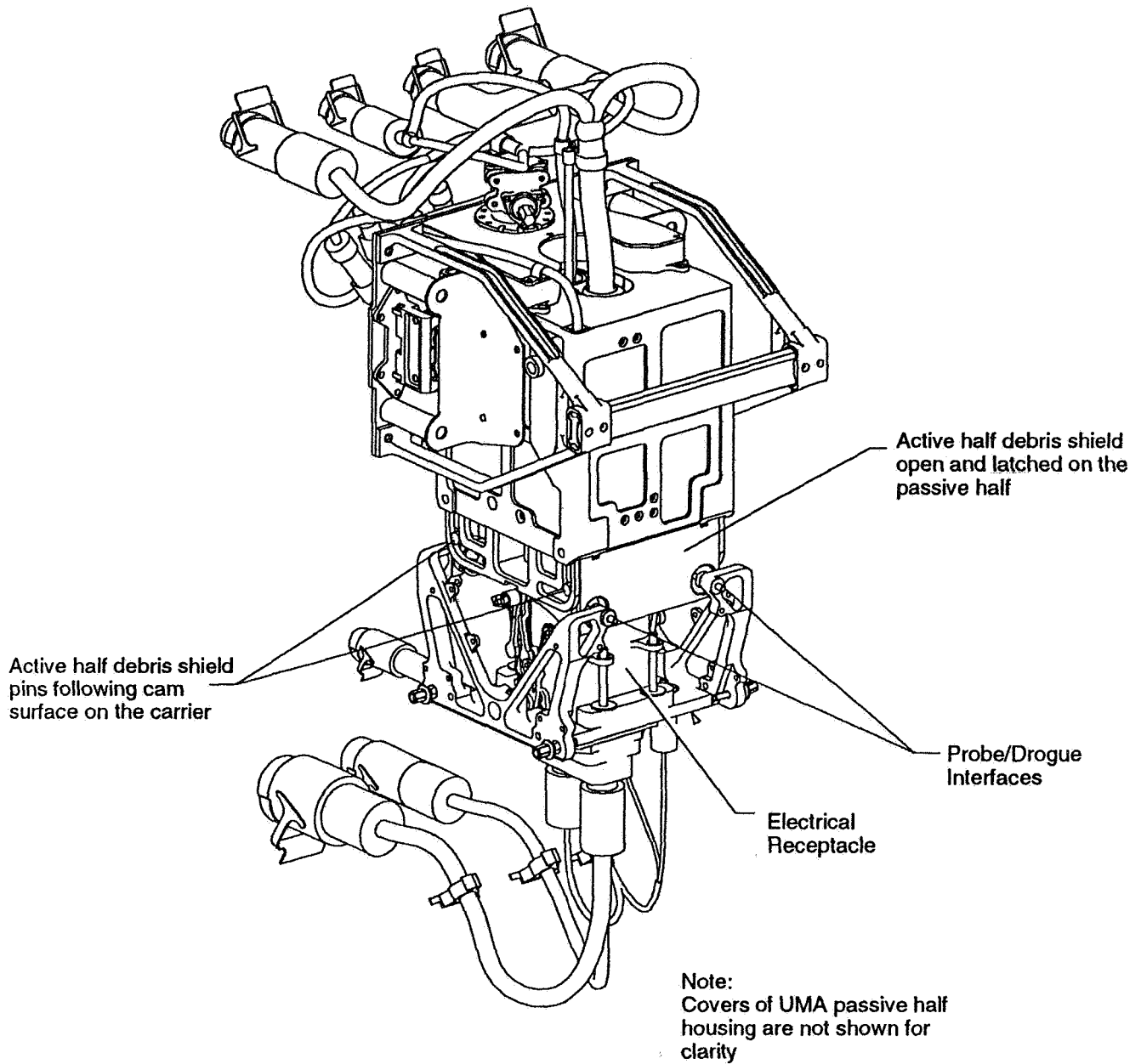
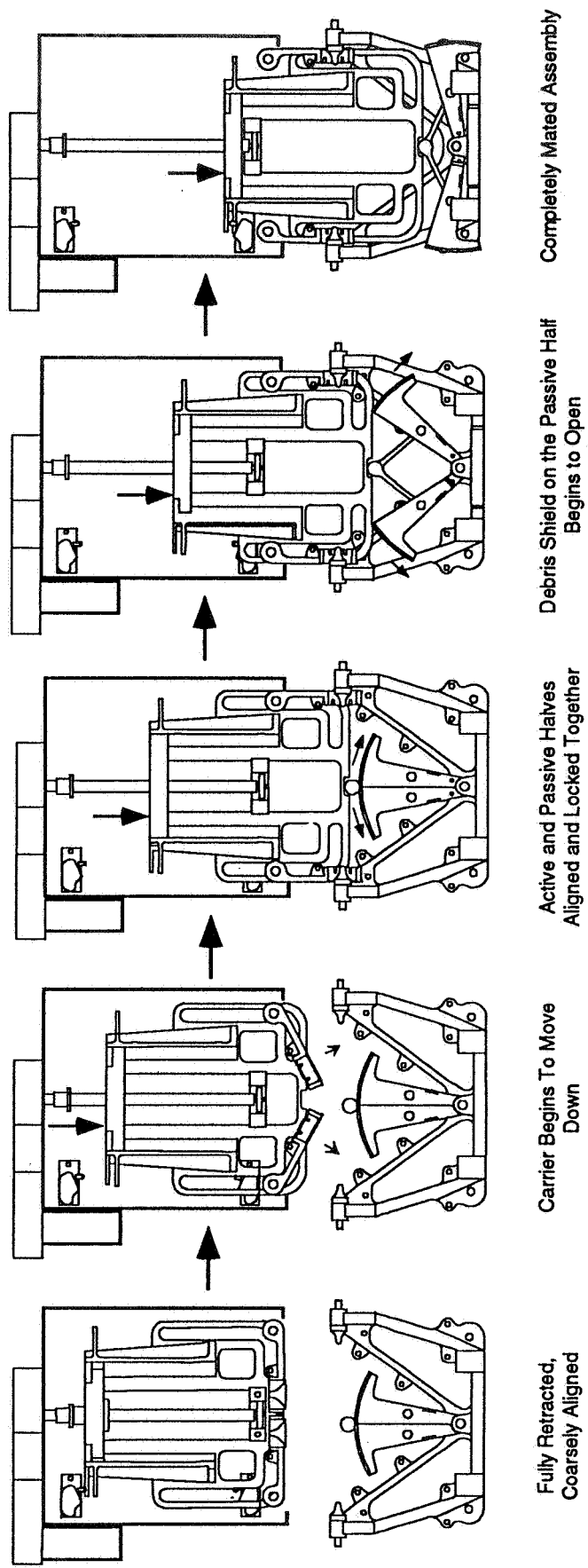


Figure 3  
Component Details of UMA Passive Half

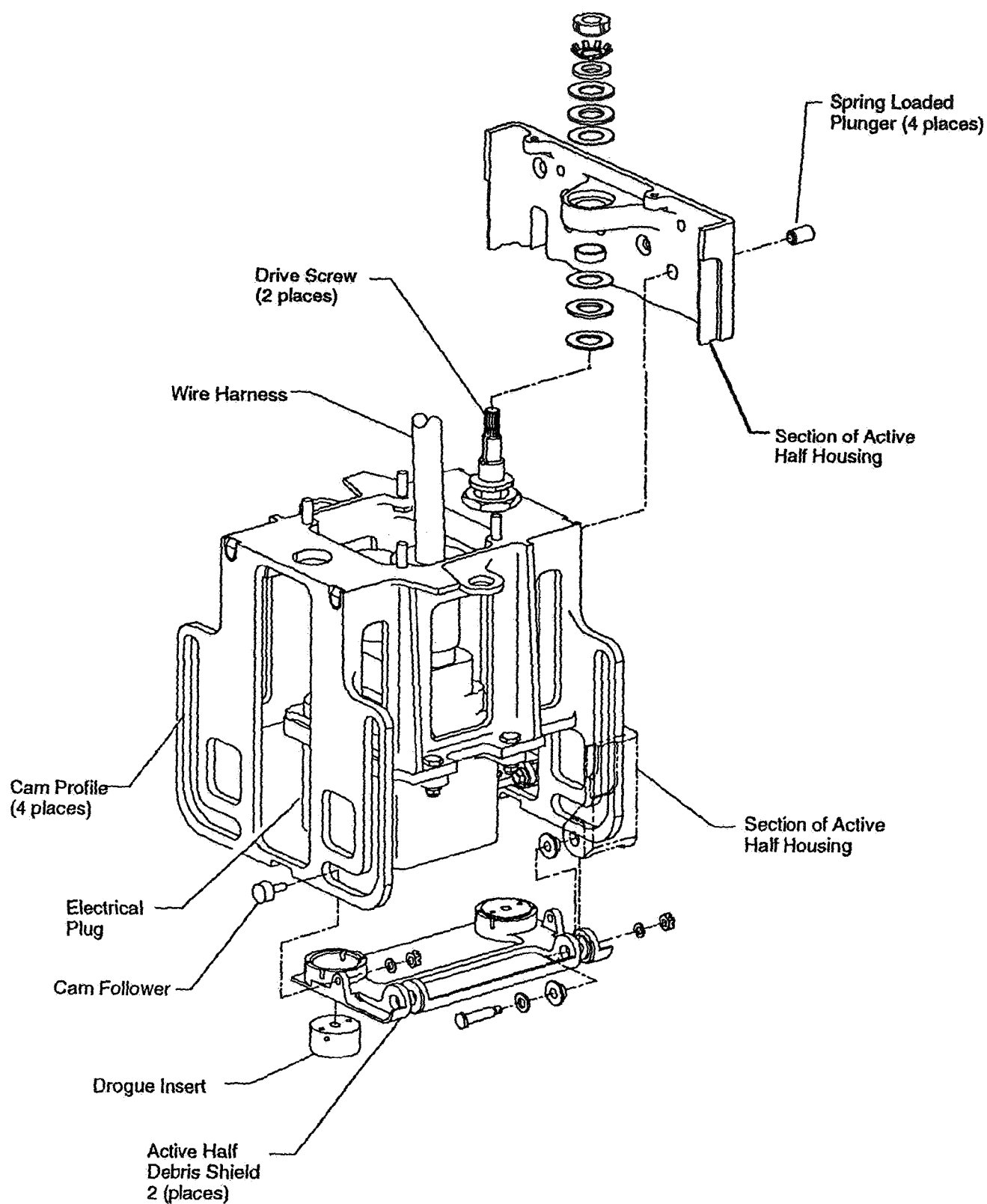


**Figure 4**  
**UMA active and passive halves in latched configuration**



Note:  
Electrical plug/receptacle and other  
details are not shown for clarity

Figure 5  
Mating Sequence



**Figure 6**  
**Carrier Assembly**

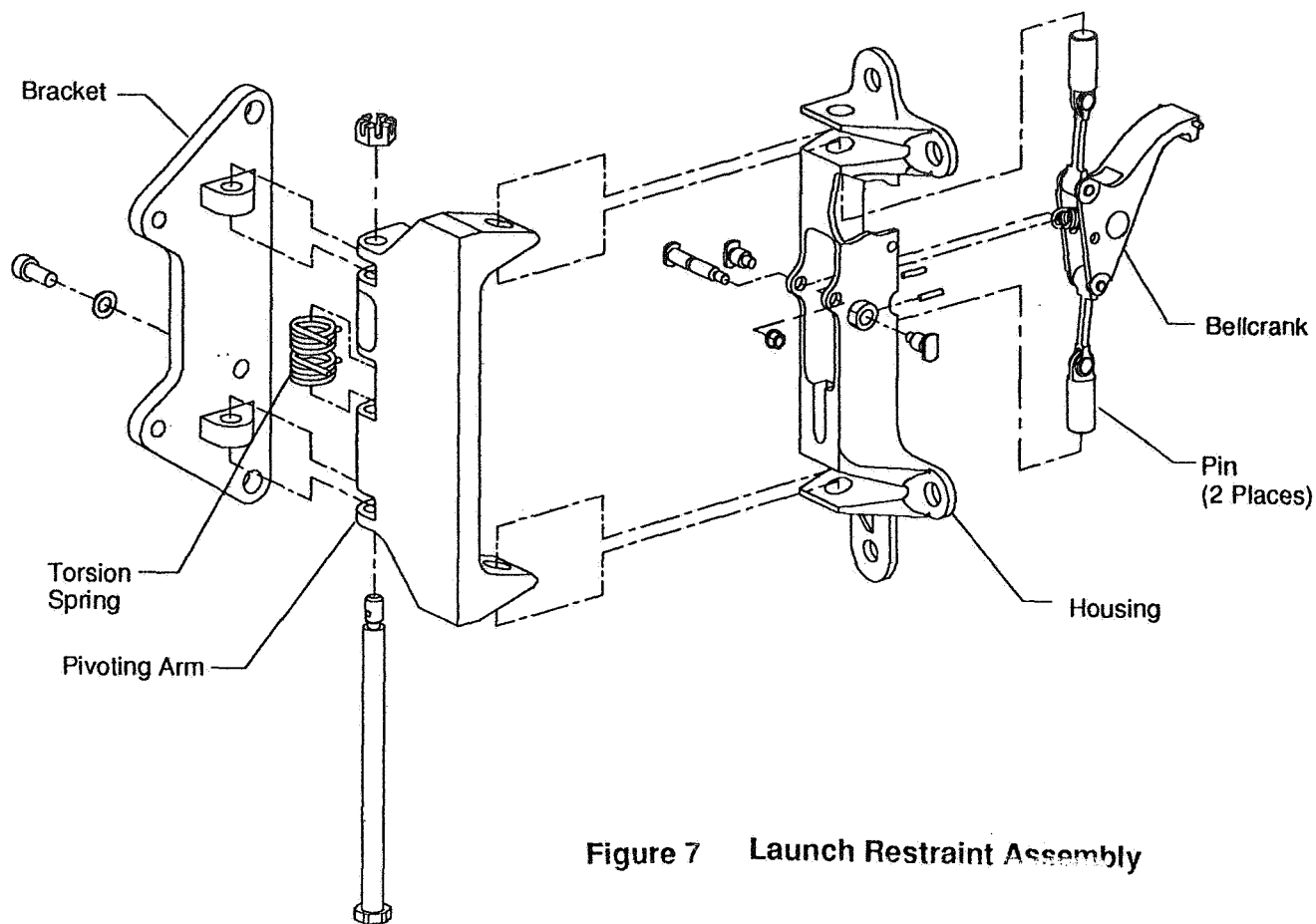


Figure 7 Launch Restraint Assembly

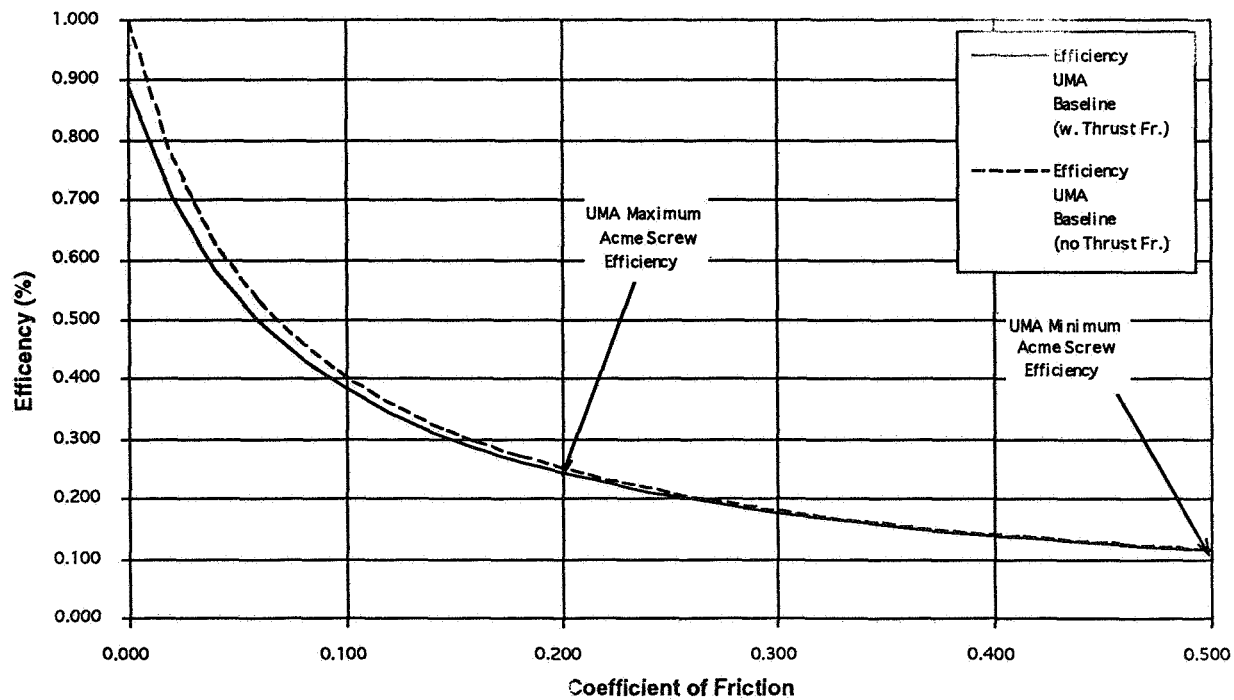


Figure 8 UMA Drive Screw Efficiency

528-18  
50456  
125142 ✓  
10  
P

## Magnetic Docking Aid for Orbiter to ISS Docking

William C. Schneider\*, Kornel Nagy\*, John A. Schliesing\*

### Abstract

The present docking system for the Orbiter uses mechanical capture latches that are actuated by contact forces. The forces are generated when the two approaching masses collide at the docking mechanism. There is always a trade-off between having high enough momentum to effect capture and low enough momentum to avoid structural overload or unacceptable angular displacements. The use of the present docking system includes a contact thrusting maneuver that causes high docking loads to be induced into Space Station.

A magnetic docking aid has been developed to reduce the loads during docking. The magnetic docking aid is comprised of two extendible booms that are attached adjacent to the docking structure with electromagnets attached on the end of each boom. On the mating vehicle, two steel plates are attached. As the Orbiter approaches Space Station, the booms are extended, and the magnets attach to the steel plates on the mating vehicle. The capture latches on the docking system are actuated (without thrusting), by slowly driving the extendible booms to the stowed position, thus reacting the load into the booms. This results in a docking event that has lower loads induced into Space Station structure.

This method also greatly simplifies the Station berthing tasks, since the Shuttle Remote Manipulation System (SRMS) arm need only place the element to be berthed on the magnets (no load required), rather than firing the Reaction Control System (RCS) jets to provide the required force for capture latch actuation.

The Magnetic Docking Aid was developed and undergone development testing on a six degree-of-freedom (6 DOF) system at JSC.

### Introduction

The present docking system, based on the early Russian version of the Apollo-Soyuz electro-mechanical docking mechanism, has been successfully used to dock the Space Shuttle Orbiter to the Russian Space Station Mir. A similar docking system will be used to dock to the International Space Station (ISS). The docking mechanism is located on the top of the external airlock in the Orbiter payload bay (Figure 1). Figure 2 shows the overall view of the magnetic docking aid installation on the docking system. The docking mechanism consists of the capture compliance and attenuation system, the capture latch system, the extend retract system, the structural latching system, and the separation system. The system provides the guide, capture ring with 6 DOF for capture compliance and attenuation stroke, and it is made up of a series of ball screws and interconnecting differentials to achieve the 6 DOF. The guide and capture rings are suspended by three sets of ball screws and nut combinations,

---

\* NASA, Johnson Space Center, Structures and Mechanics Division

equally spaced around the ring. The screws are linked at the guide ring with an interconnecting gear to provide coordinated roll and translation motions of the capture ring. The ball nut pairs are kinematically linked together at the base and attached to a universal joint. Each ball nut pair provides a torque input to the differential mechanism. The three interconnecting differentials ensure dependent movement of ball nut pairs to provide coordinated pitch-yaw motion of the capture ring. The three springs and three dampers, geared into the ball screw rotation, provide roll and shear motion damping, and their two differential centering springs and three high energy dampers provide pitch and yaw motion damping. Three additional springs reduce the impact shock loading to the differentials. Final output from the differentials, connecting to the spring, is "slip clutched" for axial force load limiting. The docking mechanism is shown schematically in Figure 3, and Figure 4 shows one set of ball screws and differentials.

The docking mechanism uses mechanical capture latches that are actuated by contact forces, generated when the two approaching masses collide at the docking mechanism. There is always a trade-off between having high enough momentum to effect capture and low enough momentum to avoid structural overload or unacceptable angular displacements. On the first visit to Russia, it was very clear that the capture ring was extremely stiff in shear or lateral motion. Subsequent test verified that the characteristics of the docking mechanism were unacceptable, and it would not allow the planned docking with the Space Shuttle by simply impacting at the docking mechanism. An operational method was developed, such that thrusting the nose of the Orbiter just at contact would make the ring comply without moving the Shuttle Orbiter and would achieve capture most of the time. However, the loads were rather high. It is precisely this reason that the concept of using a magnetic docking aid was invented. An extendible boom mechanism is attached to the side of the docking mechanism at the airlock interface, whereby it is extended with electro-magnetic power. The astronaut would perform the docking as he would normally, except that he would simply press an actuator, instead of thrusting the Shuttle, thus slowly withdrawing both the extendible boom mechanism and the magnet, which had been attached to the opposite side. This action then gently pulls the two vehicles into compliance with the mechanism, without creating high loads. This paper describes the integration of well-known devices into a system in such a fashion as to greatly minimize the induced docking loads.

### **Magnetic Docking Aid Description**

The magnetic docking aid is implemented with a minimum of additional hardware. The following components are added to the existing docking hardware:

- Two extendible booms that are attached on the airlock support structure, next to the active half of the docking mechanism in the Orbiter payload bay. Figure 5 shows the location of these booms. The extendible booms used in the development testing are bi-stem actuators, manufactured by Astro Aerospace Corp. In the stowed position, the stems are coiled on two opposing spools in the base of the boom. The boom is deployed and retracted with a DC motor, which drives the spools to extend and retract the stems. Electromagnets are



mounted on the end of each boom. The electromagnets are powered by cables that are coiled on the outside of the booms and easily extend when the booms are deployed.

- The mating steel plates are mounted on brackets next to the passive half of the docking mechanism on the ISS Pressurized Mating Adapter (PMA). Figure 6 shows the location of the steel plates.
- The control switches for the magnetic docking aid are mounted in the docking system control panel, located in the aft flight deck panel.
- The Orbiter docking approach, with the current docking targets and the current contact conditions, is used for docking with the magnetic docking aid, except no post contact thrusting is required.

Docking with the magnetic docking aid is accomplished with the following sequence:

1. As the Orbiter approaches Space Station, the booms are extended to a distance such that the magnets contact and attach to the steel plates on the mating vehicle when the petals on the active and passive capture rings are nested. Any relative motion, either closing or laterally, will only cause low loads, since the extendible boom will backdrive to give low compression loads and will deform easily (low lateral stiffness) for lateral motion.
2. The capture ring is extended simultaneously while the extendible booms are being retracted.
3. The latches on the docking system capture ring are then engaged (without post contact thrusting), by reacting the load into the extendible booms in tension. The load required to actuate the capture latches is approximately 156 N (35 lb) and is totally reacted by the extendible boom magnets (not by accelerating the structural mass). The need for continuing dynamic analysis, year after year, is eliminated because the latches are activated statically and the loads are internally reacted.
4. Once the capture latches are engaged, the power to the electromagnets is turned off, and the booms are retracted.
5. The remaining portion of the docking is the same as the current docking sequence. The capture ring is driven to the retracted position, thus pulling the Orbiter and space station together, actuating the structural latches, compressing the seals, and forming the structural attachment to complete the docking sequence. This results in a docking event that has lower loads into the Space Station structure.

The magnetic docking aid greatly simplifies the ISS berthing tasks as well. The SRMS arm is used to place the element to be berthed near the berthing interface. The magnets, on the end of the extended booms, attach to the steel plates on the mating interface. The booms are then retracted (with the SRMS in an inactive mode), thus enabling berthing without the need for firing the RCS jets to provide the required force for capture latch actuation.

## **Docking Loads Using the Magnetic Docking Aid**

Docking loads were computed for the magnetic docking aid system by using the Ring-Finger Docking Dynamics simulation (RFDD), developed by personnel in the Structures and Mechanics Division of NASA-JSC.

There are 4 major components to the docking loads analysis:

1. Statistical initial contact conditions model
2. RFDD simulation using the Androgynous Peripheral Assembling System (APAS)
3. ISS elastic-body modal analysis/critical structural loads model
4. SRMS/APAS/SRMS berthing model for two ISS stage assembly events

The statistical contact model, describing contact conditions, hardware mounting errors, and the time delay of the post-contact thrust firing initiation, are used to generate the initial contact condition for docking (typically 200 to 300 cases are generated for the Monte Carlo statistical loads analysis approach).

The RFDD simulation, using the APAS dynamic docking mechanism simulation model, is used to calculate system capture performance and interface loads. The APAS docking mechanism analysis model used in this study was developed by NASA personnel. The APAS docking mechanism model was verified through correlation with the 6-DOF test conducted in Moscow.

The ISS elastic-body/structural loads model is used to calculate docking interface loads and critical internal structural loads throughout the space station.

### **APAS Docking Mechanism Simulation Model**

A high-fidelity simulation model of the APAS docking mechanism has been developed by Johnson Space Center. The APAS is the most mechanically complicated docking mechanism simulated by Johnson Space Center to the present. Figure 3 shows a schematic view of the APAS. Previous major JSC-modeled docking mechanisms included:

1. Apollo Ring and Cone docking mechanism — a USA Apollo design concept similar to APAS
2. Apollo Probe/Drogue docking mechanism
3. The USA-designed and manufactured docking mechanism for the Apollo/Soyuz Test Project
4. USA-designed Orbiter/SSF docking mechanisms.

The mechanism math model simulates the significant dynamic and kinematic characteristics of the docking mechanism, including the following:

- Ball-screw actuator/shock attenuators.
- Interconnecting gear train between ball-screw pairs at the guide ring.

- Interconnecting gears and torque-rods between ball-screw pairs at the base.
- 3 interconnected differential and centering springs mechanisms.
- 3 lateral, motion-limiting spring mechanisms and rate dampers.
- Preloaded, axial motion spring mechanism at the output of the differentials for connection to the slip clutch/motor drive mechanism.
- Clutch/motor drive mechanism.
- Time-delayed, post-capture activated rotational dampers.
- Capture latch load vector depression resistance.
- Docking interface capture latch tolerance criteria.
- Ball-screw and differential mechanism-constrained dynamics.
- APAS friction, flexibility, and hysteresis characteristics.
- Contact dynamics between the internal petal guides/rings, including sliding friction.
- Orbiter and ISS rigid-body mass properties and geometry.
- Orbiter RCS Post Contact Thrust (PCT) capture latch maneuver.
- Fully coupled APAS/docking vehicle elastic response dynamics (for both Orbiter and ISS).

### **Correlation of the RFDD Simulation Model with Test Data**

The RFDD simulation model was fully correlated with the 6 DOF test in Moscow for capture latching performance and interface loads. This correlation included developmental docking hardware at nominal temperature and qualification hardware at nominal -30°C and -50°C. The correlation is excellent for the total test program. Typical correlation results are shown in Figures 7 and 8.

Figure 7 shows the correlation between RFDD simulation results and the 6 DOF Qual. hardware test number 1.5 results. This test simulated a closing velocity of 3 cm/s (0.1 fps), an Orbiter yaw of 4°, and a PCT delay of 2.0 seconds after initial contact. Figure 8 shows the correlation between RFDD simulation results and the 6 DOF Phase 2A -50°C test data results. This test simulated a post contact thrust firing before contact with a resulting closing velocity of 15 cm/s (0.5 fps) at initial contact. The fully correlated RFDD simulation was then modified to simulate the Magnetic Docking Aid system and used to develop system characteristics for the Magnetic Docking Aid concept.

### **Magnetic/Extendible Boom Simulation Model**

A model of the extendible boom/magnetic assemblies has been developed and added to the RFDD/APAS docking simulation. The following features have been included in the mathematical simulation model in RFDD:

- Extendible boom and magnet physical characteristics
- Number of extendible booms used

- Extendible boom base and extended magnet positions
- Engagement logic and locking magnet to engagement plate at initial contact
- Extendible boom pull down delay from time of engagement
- Extendible boom retraction to APAS ring capture latching phase
- Magnetic release delay from time of ring capture latch
- Boom and magnet loads characteristics
- Magnet/servo-motor logic and pull down characteristics
- Extendible boom backdrive and tension loads
- Extendible boom beam shear loads.

### **Point Design Results for the Magnetic Docking Aid System**

In Figure 9, the results of three RFDD simulations are plotted on the same curve. Each simulations had the same initial conditions, but the first simulation had no MDAS and used a PCT to effect capture latching, while the other two simulations used the MDAS to effect capture latching. The docking vehicle had a relative twist attitude (Orbiter yaw error) of  $4.0^\circ$  between the vehicles. The dual-boom case, where two booms were assumed to be engaged, resulted in a peak compressive load of 1757 N (395 lb), as compared to the PCT case, which resulted in a peak compressive load of 8585 N (1930 lb). The third case represented one failed boom engagement and one engaged boom, which pulled together at a slower rate with a resulting peak load of 1521 N (342 lb). The tension loads in the booms during the pull down for the dual boom simulation are shown in Figure 10. The tension load for a single pull down boom, assuming the other boom did not engage, is shown in Figure 11. The net pull load of the single boom is slightly less than that of the dual booms, thus resulting in a longer time to capture and release the booms (6.2 seconds vs. 10.8 seconds ).

### **Docking Vehicle Load Relief Using the Magnetic Docking Aid System**

A load study without PCT was assumed to be equivalent to using the Magnetic Docking Aid System, since the impact velocity without PCT is the same as when using the Magnetic Docking Aid system. Vehicle loads have been determined for the STS-74 mission, with and without PCT, to understand the load relief of the Magnetic Docking Aid system. The STS-74 mission is very similar to the ISS mission and is a good indicator of benefit. The load cases include the RCS plume flex body dynamics that occur during the approach. The initial contact conditions are based on a Monte Carlo statistical analysis, including 232 load cases generated from the NASA statistical initial contact condition model. These cases were corrected for missing simulator error sources (i.e., thermal deflections and instrument misalignment). The results are given in Table 1, where the Percentage Reduction Using MDAS column shows significant load reduction when using the MDAS.

## **Design of Magnet/Striker Plate Footprint**

A study was conducted to determine the dimensions of the striker plate footprint required for the electromagnets. Supplied by the Rendezvous and Prox-Ops working Group, contact conditions from the 232 cases were used to represent 3- $\sigma$  initial contact conditions. This data was modified to include thermal distortion and instrument alignment accuracy. The data represents misalignment at first docking hardware contact. This is conservative, since the natural dynamics of conic docking petal contact geometry would reduce the interface misalignment. Magnetic engagement footprints were computed for parametric variation of radius (R) to MDAS from the APAS centerline and height (H) of the magnet. The magnet/striker plate footprint can be interpreted from the plot of magnet position at initial contact (Figure 12). The resulting footprint of 25 cm by 30 cm (10 in by 12 in) is based on data from this figure and accounts for the diameter of the magnet.

## **Docking Loads Results and Conclusions**

Dynamic simulation of the Magnetic Docking Aid system has been conducted for a large range of initial contact conditions. The vehicle interface loads, using the Magnet Docking Aid system, are much smaller than when using the PCT maneuver. Time to capture latch the docking rings is less than 20 seconds. The Magnetic Docking Aid method of capture latching achieves its design goals, thus greatly reducing loads and lifetime concerns throughout the Space Station. The MDAS removes the requirement for PCT by quick magnetic engagement of the ISS and retraction with significant velocity to effect the capture latches. Studies were conducted to determine the system sensitivity if one of the two magnetic booms failed to engage its respective strike plate. It was found that the failure of only one Magnetic Docking Aid did not adversely affect the docking capture latching operations or vehicle dynamics.

## **Development Testing**

A mock-up was designed and built for development testing of the Magnetic Docking Aid. Figure 13 shows the development test hardware setup.

Tests were performed in the structures laboratory at the Johnson Space Center with 4° pitch, 4° roll, and 3.8 cm (1.5 in) lateral misalignment. Various misalignment combinations were performed. The results showed that capture was achieved in all cases using the Magnetic Docking Aid. A test run was performed without the Magnetic Docking Aid, and the hardware did not consistently latch.

Tests were also performed using the 6 DOF facility and STS-71 station/shuttle inertial properties. The initial conditions were 0.1 ft/sec axial velocity, 4.6 cm (1.8 in) lateral misalignment, 3° pitch and 3° roll misalignment. Tests were performed with one and two magnets attached. Positive capture was achieved for the test cases with engaged magnets.

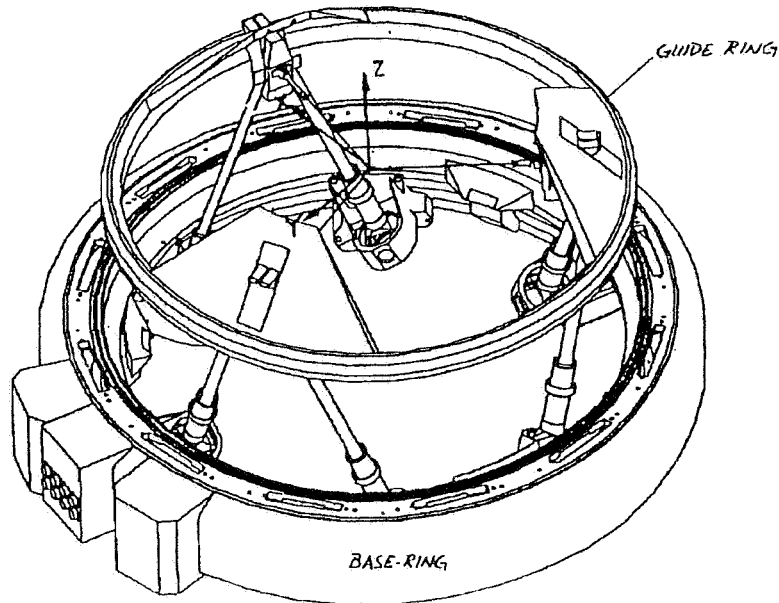
## Summary

In summary, the Magnetic Docking Aid has been designed, analyzed, and tested and shown to meet the objective of allowing two large spacecraft to be gently docked, without the characteristically high induced loads.

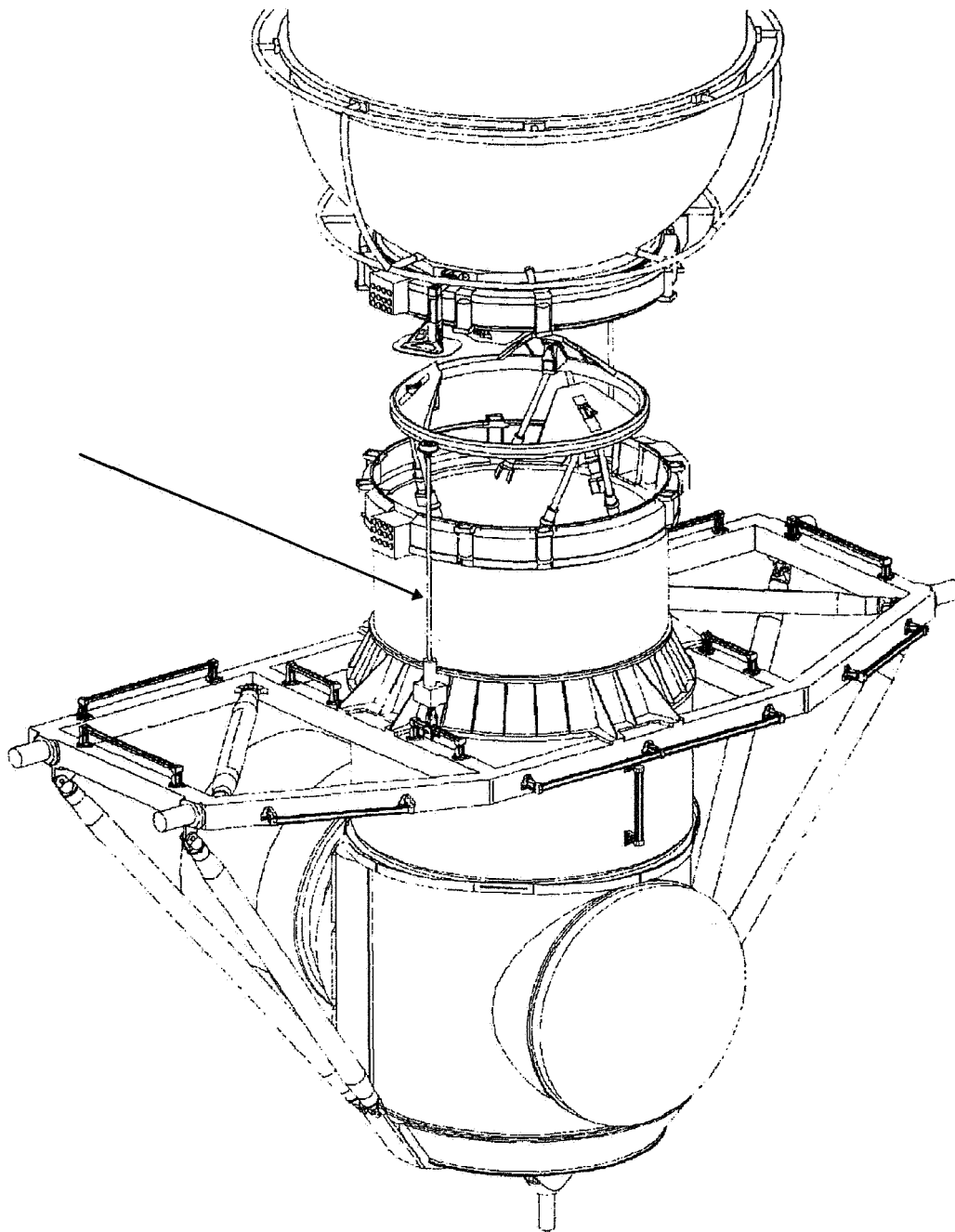
**Table 1**  
**Docking Vehicle Load Relief**  
**Using the Magnetic Docking Aid System (MDAS)**

Load Indicator	Load Type	Peak Load Using PCT	Peak LM Using PCT	Reduction Using MDAS
Priroda-BM	Axial	305.80 kg	3.27	-33.7%
Kristal-DM	Bending	463.40 kg	1.08	-61.7%
Kvant SP2	My	32.57 kg-m	3.07	-12.7%
Kvant SP1	Shear	11.50 kg	4.35	-48.9%
HGA	My	72.92 kg-m	1.51	-69.7%
EEU	Shear	15.71 kg	3.18	-31.0%
Kvant SP2	Bending	36.42 kg	2.75	-52.8%
Progress-BM	My	1612.00 kg-m	3.10	-41.5%
Kristal-DM	My	461.29 kg-m	1.08	-68.2%
Kvant-2 SP2	My	113.01 kg-m	3.45	-65.2%
Kristal-DM	My	1927.00 kg-m	2.59	-35.1%

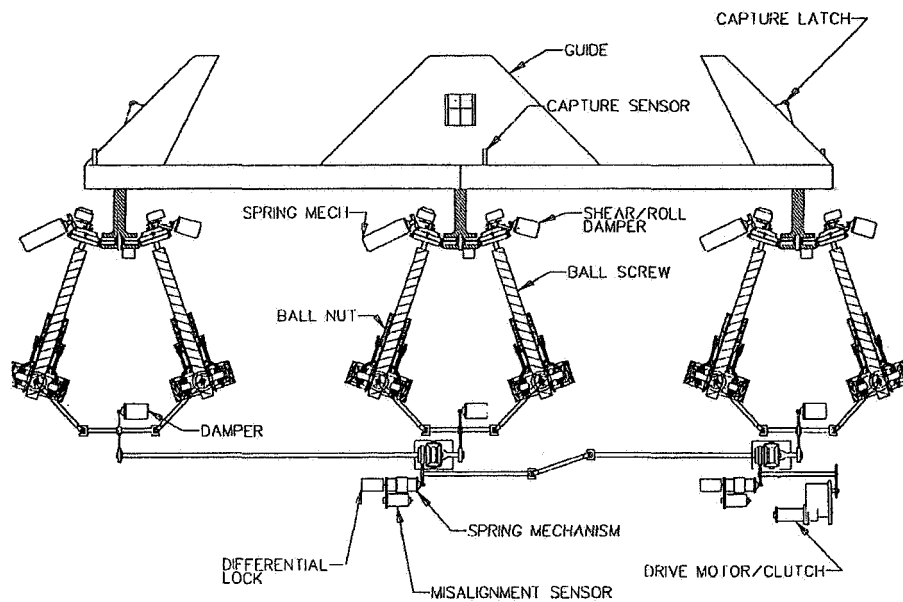
- Critical peak Load Margin (LM) results with and without PCT.
- Loads without PCT represents using the Magnetic Docking Aid



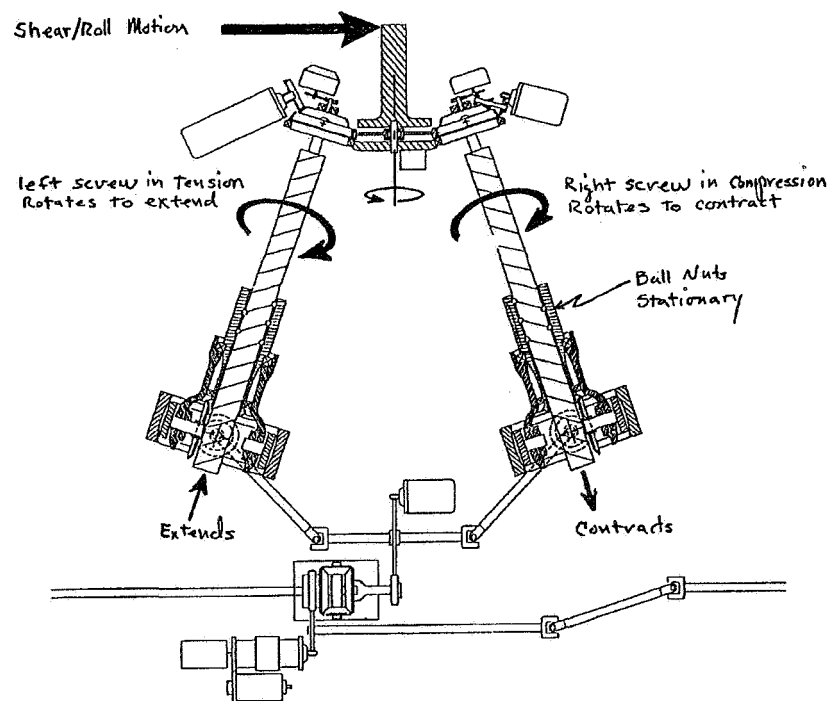
**Figure 1 Docking Mechanism**



**Figure 2 Magnetic Docking Aid Installation on airlock**

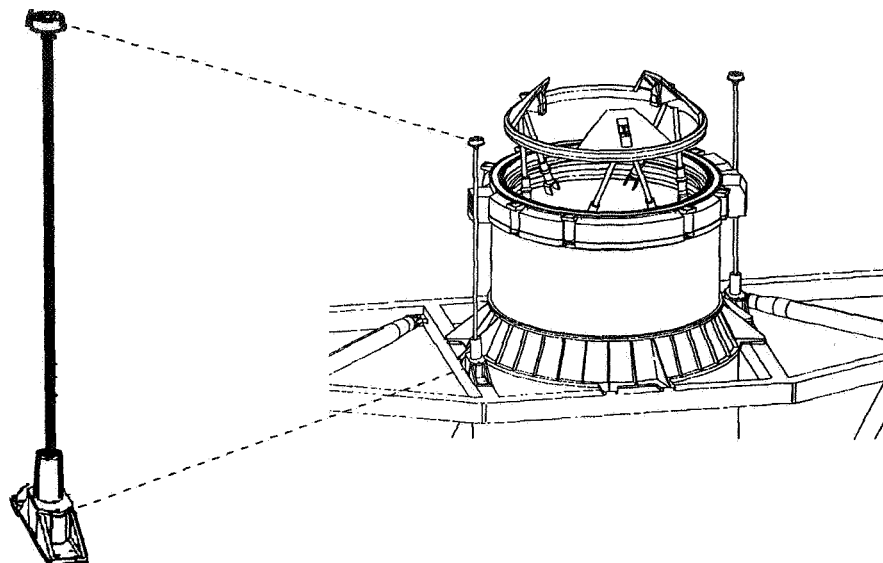


**Figure 3 APAS Docking Mechanism Schematic**

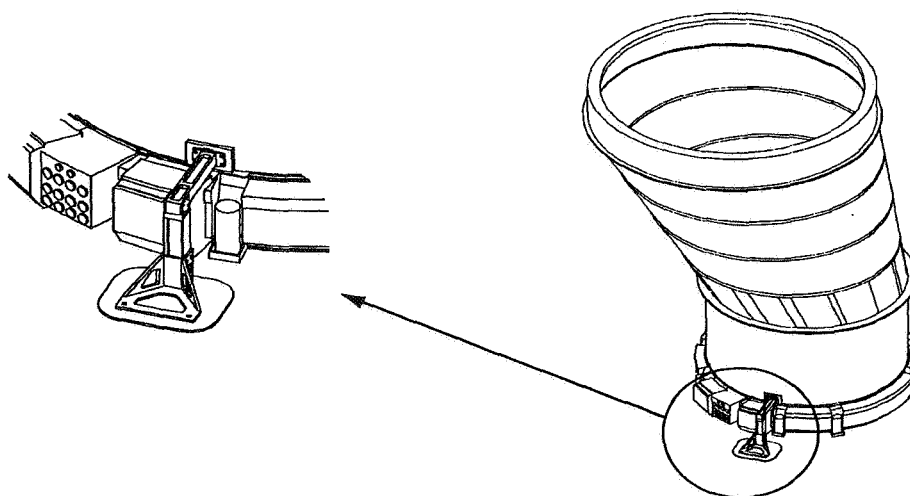


**Figure 4 Ball Screw and Differential set**





**Figure 5 Extendible booms on airlock structure**



**Figure 6. Steel plate mounting on PMA for ISS**

Test Correlation (Qual,P2): Nominal Temperature  
APAS Q1M1, testing case tc1\_5, qual1.5-nom.dat

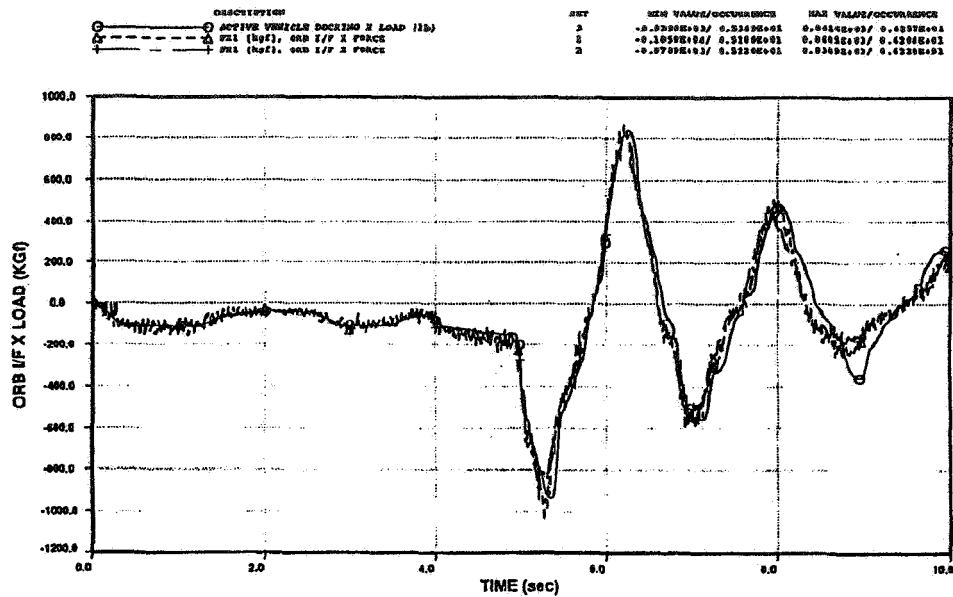


Figure 7. RFDD Math Model/ Qual 1.5 Test Data Correlation  
(IC's: PCT at 2.s, Vz=0.1 ,Yaw=4 degrees)

Test Correlation (PHASE 2A,P2): -50c temperature  
APAS Q1M1, testing case tc17\_1a, qual17.1a-50c.dat

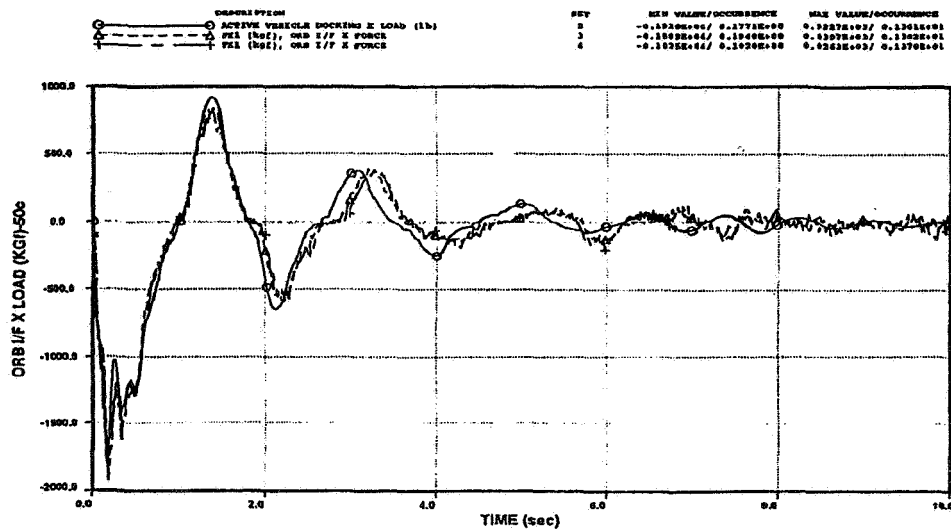
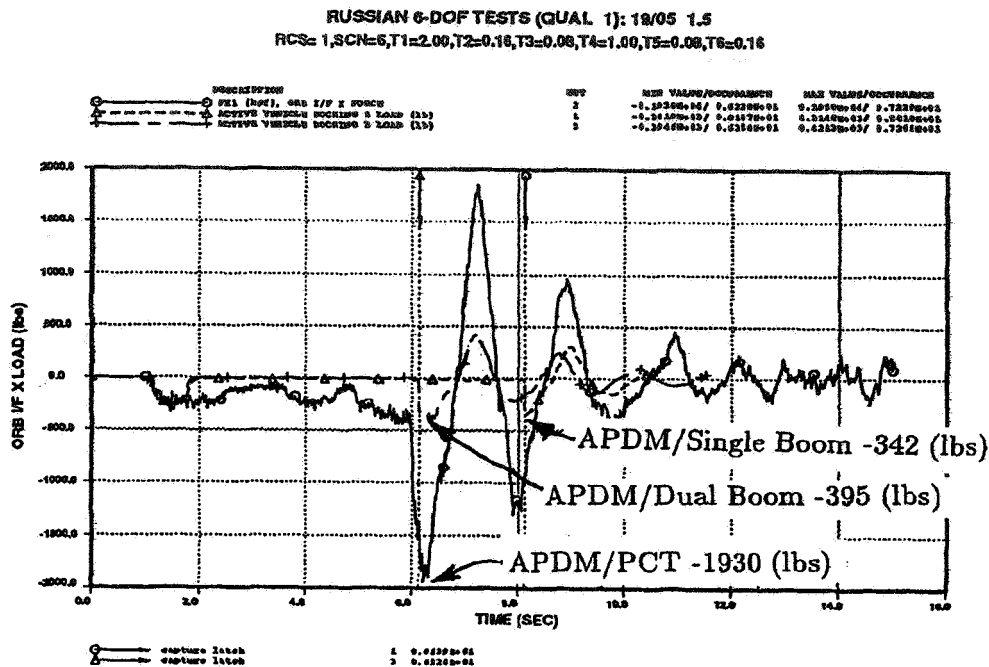
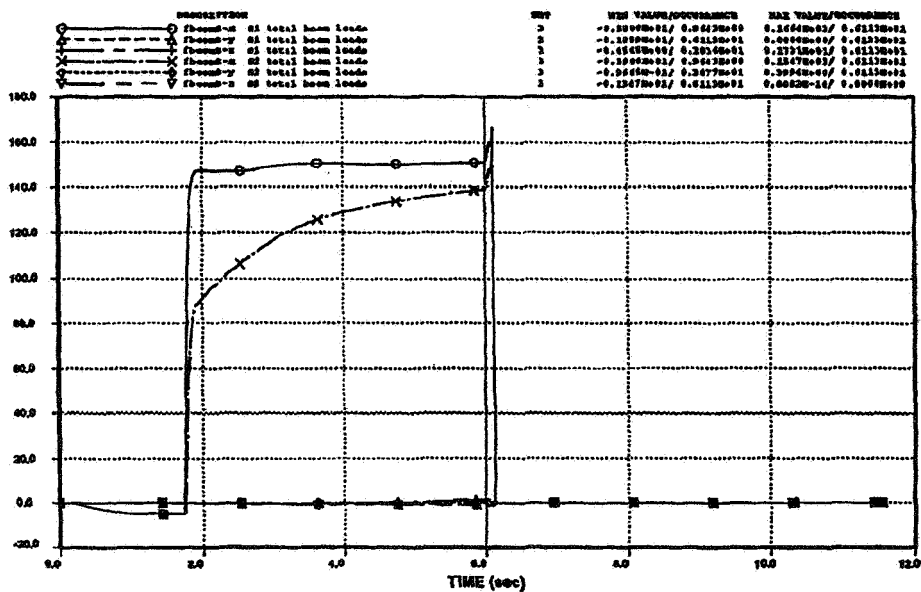


Figure 8. RFDD Math Model/ Phase 2A -50 degrees c Test Data Correlation  
(IC's: PCT before contact, Vz=0.5)



**Figure 9. Boom/ Magnet Design Case (Qual 1.5 - nom.dat),  
Comparison plots between Qual, Single, and Dual Booms**

Shuttle/Mlr, magload03.dat, apas m1m1.1  
Dual Boom, Roll=4, Mix=0, Vel Boom =6ips



**Figure 10. Boom Pull Down Loads for Design Case (Dual Boom)**

Shuttle/Mir, magload04.dat, spas m1m1.1  
Single boom, Roll=4, Miss=0, Vel Boom =0ips

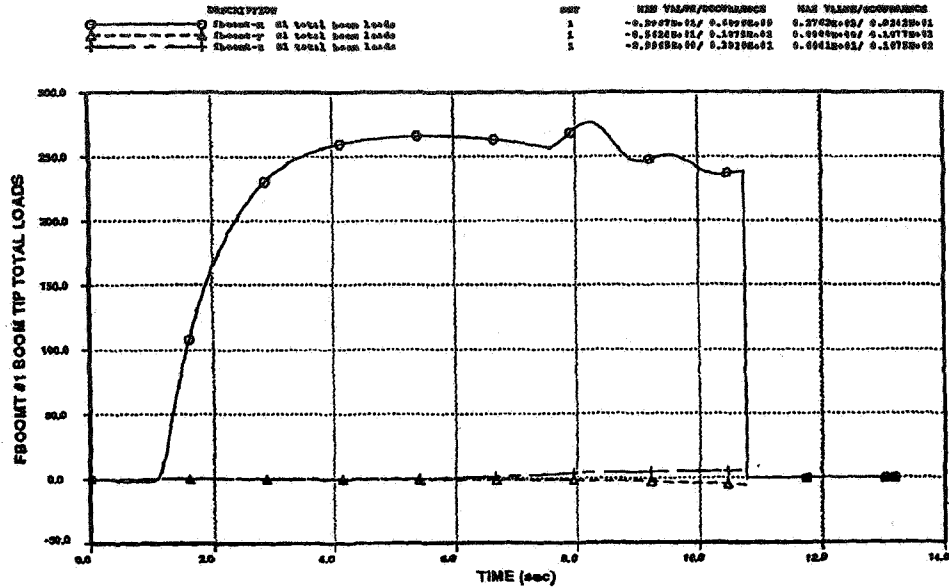


Figure 11. Boom Pull Down Loads for Design Case (Single Boom)

SES CONTACT CONDITIONS (232 cases)  
MAGNET study, parameters: H=1, R=4

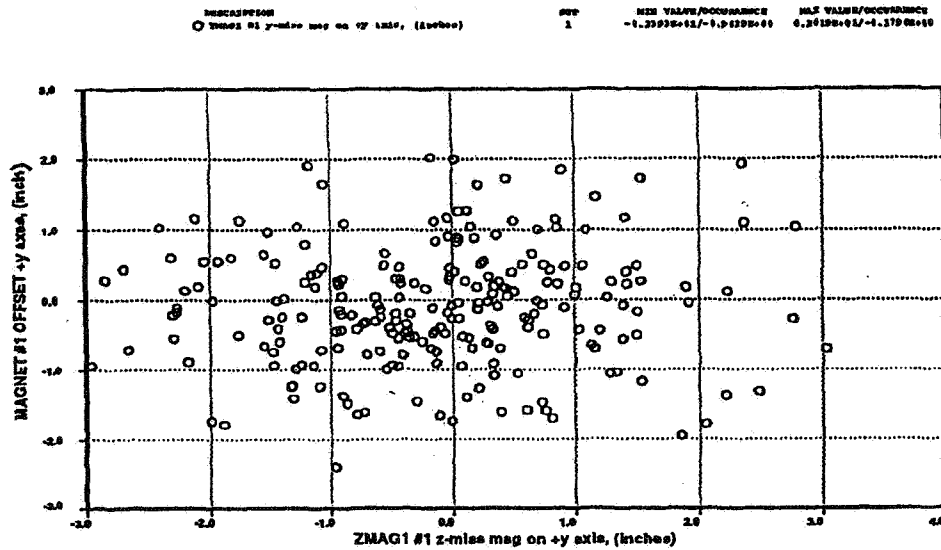
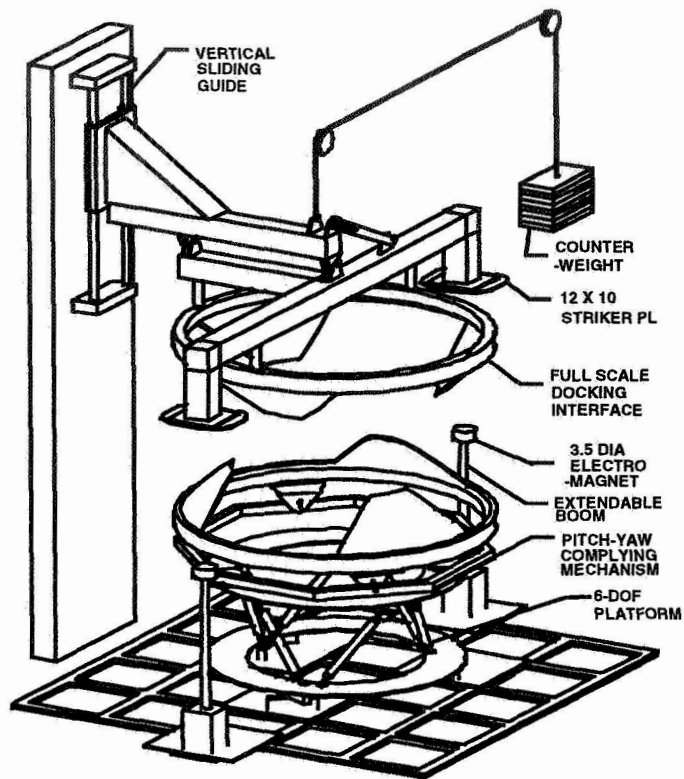


Figure 12. Design of Magnet/ Striker Plate Footprint



**Figure 13 Development Test Hardware Installation**



529-37  
50457  
125143  
p 16

# The Micro Conical System: Lessons Learned from a Successful EVA/Robot-Compatible Mechanism

Mark Gittleman, P.E.\* and Alistair Johnston\*

## Abstract

The Micro Conical System (MCS<sup>1</sup>, Figure 1) is a three-part, multi-purpose mechanical interface system used for acquiring and manipulating masses on-orbit by either extra-vehicular activity (EVA) or telerobotic means. The three components of the system are the micro conical fitting (MCF), the EVA micro conical tool (EMCT), and the Robot Micro Conical Tool (RMCT). The MCS was developed and refined over a four-year period. This period culminated with the delivery of 358 Class I and Class II micro conical fittings for the International Space Station and with its first use in space to handle a 1272 kg (2800 lbm) Spartan satellite (11,000 times greater than the MCF mass) during an EVA aboard STS-63 in February, 1995. The micro conical system is the first successful EVA/robot-compatible mechanism to be demonstrated in the external environment aboard the U.S. Space Shuttle.

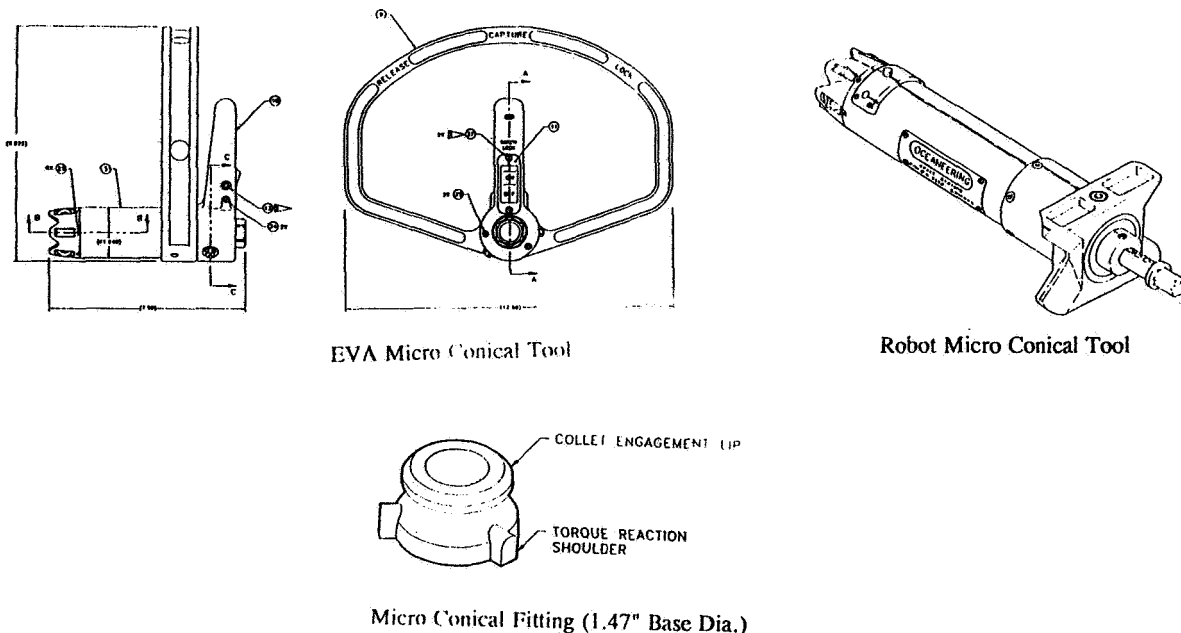


Figure 1. Micro Conical System

\* Oceaneering Space Systems, Houston, TX

<sup>1</sup> U.S. Patent No. 5,320,395

## Introduction and Background

The International Space Station (ISS) will be maintained primarily through the exchange of new on-orbit replaceable units (ORUs) for expired ORUs. The micro conical fitting is designed to be the primary interface to grasp ORUs and to provide the local torque reaction needed for turning the heads of the ORU retention bolts. These bolt heads are typically located in the center of the MCF. The MCS is capable of handling ORUs up to 1272 kg (2800 lbm ) and is rated for use on the ISS for ORUs up to 600 kg (1320 lbm). The micro conical fitting is an ISS standard interface.

The micro conical system was derived by combining the space station operational drivers with Oceaneering's unique experience in developing tools and interfaces for use underwater by telerobotic systems and commercial divers. Like many undersea structures, the space station will be maintained by both telerobotic work systems and direct human intervention (EVA crew).

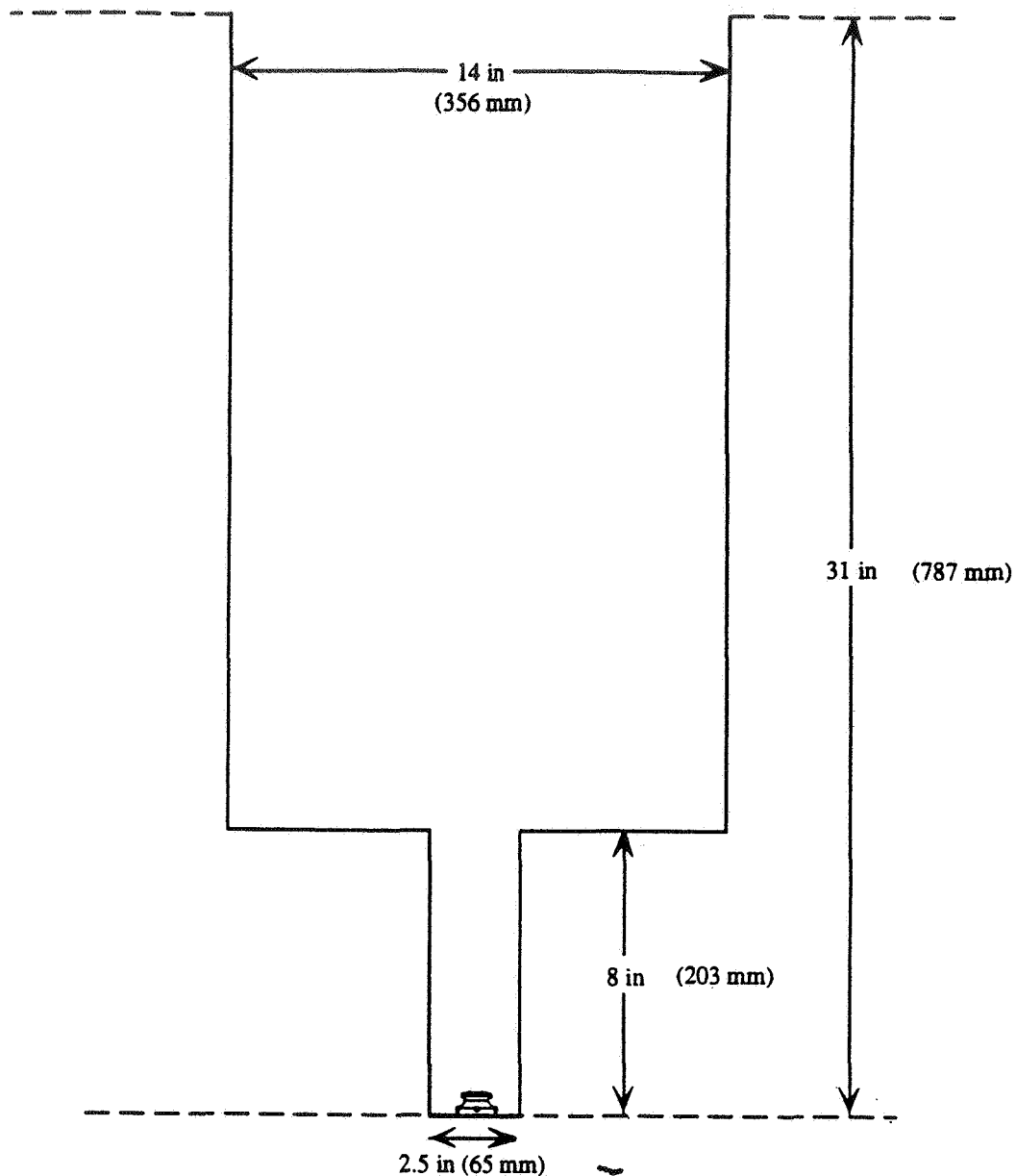
The most successful approach to coaxing useful work from telerobotic systems underwater has been to use them primarily as tool delivery systems. This approach encourages the use of standard interfaces and of smart tools that have a front end common to both the human (diver or astronaut) and the telerobot. Importantly, this approach also allows tools to be adapted to the capabilities of the work system (human or telerobot), and the telerobotic systems to be designed to the simplicity level needed for reliable operations. Experience has shown that making a mechanical system simple enough for a telerobot to use will also improve its human compatibility.

The primary operational drivers for MCS development were the extreme volume and envelope requirements needed to accept the alternate space station standard tool and interface system. (The alternate system consists of the H-handle, micro interface, and the end-effector of the Special Purpose Dexterous Manipulator, or SPDM. The SPDM end-effector is called the ORU Tool Change Out Mechanism, or OTCM). Whereas the micro/OTCM combination requires an approach envelope of at least 35.5 cm (14 in) in diameter, the MCS approach envelope diameter is only 5.6 cm (2.2 in, Figure 2).

The micro conical system is unique in several ways:

- 1) From the outset, it was designed to be compatible with both EVA astronauts and space telerobotic systems. Testing and development were performed in parallel.
- 2) It is based on the lessons learned through twenty years of underwater work with both telerobots and commercial divers. These lessons drove a system that consists of a single interface and two tools: one for the astronaut, and one for the robot. However, the two tools have a common front end, which is used to grasp the fitting, and vary primarily in the means of actuation.





**Figure 2. MCS Approach Envelope**

- 3) The MCS is quite compact and lightweight: the fitting weighs only 0.11 kg (0.24 lbf), and the EVA tool weighs only 2.63 kg (5.8 lbf). Despite its size, the fitting is rated to  $\pm 227$  kg ( $\pm 500$  lbf, shear and axial) and  $\pm 184$  N-m ( $\pm 250$  ft-lbf, bending and torsion). The tool is rated to input loads of 76 N-m (167 ft-lbf) in torque and bending and 85 kg (187 lbf) in shear and axial loading (these numbers do not include safety factors used in the actual testing).

- 4) The MCS provides a high misalignment, latching soft dock. Thus, even when the tool is misaligned by up to  $\pm 7^\circ$  with respect to the vertical axis, the collets will still latch to the lip of the fitting, hence providing a loose connection that can only be broken by deliberate motion of the collect actuator to the release position. In normal operations, the collets are moved from the soft dock position to hard dock or release either by an EVA actuator lever or by rotary input from the telerobotic system end-effector.

## Micro Conical System Concept Development

From the start, the MCS was intended to be an integrated EVA/telerobot-compatible ORU handling system. It originally included an EVA tool, a robot tool, and two fittings: the conical and the micro conical. In the initial concept, the two powered tools featured a common front end and gear box/motor combination that could be grasped and used by either work system (EVA or telerobot). The tool, known as the multi-purpose torque tool (MPTT), could also interface with both the micro conical fitting and the larger conical fitting. From earlier design experience with underwater tools and interfaces, OSS understood that the fittings and tools had to be designed together.

The initial geometry of the micro conical fitting included a ramping lip, or groove, designed to accept detent pins. This feature evolved into the flat lip at the top of the final design. The MPTT design, therefore, included a set of three spring loaded pins that interfaced with the MCF at the ramping lip. The pins were designed to spring into the MCF geometry and provide a detent soft dock with the proper axial force. They were then locked into place by a spring-loaded locking ring.

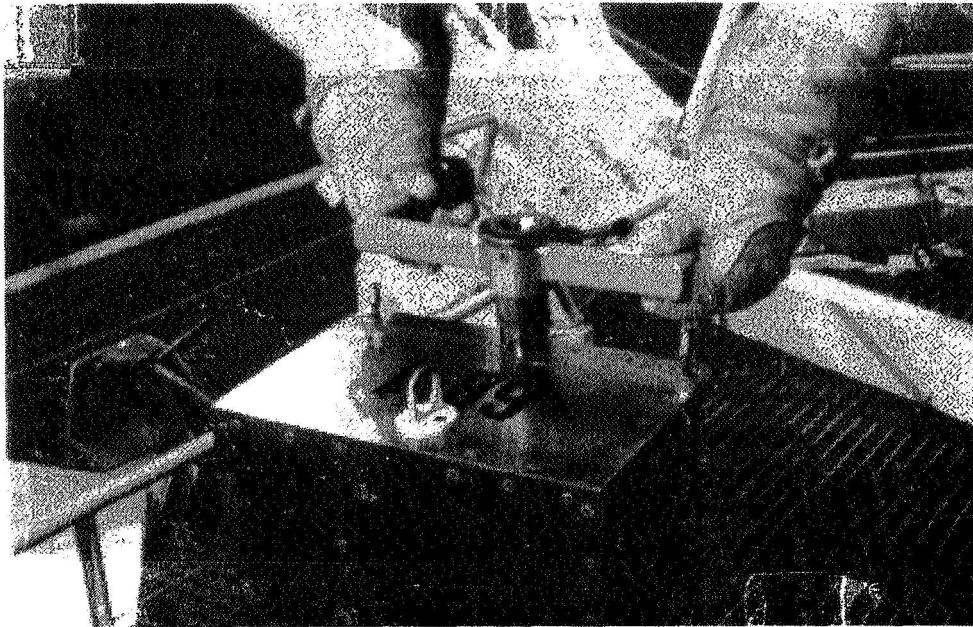
Initial testing of the system took place in 1990-1991 in both the Johnson Space Center (JSC) Weightless Environment Training Facility (WETF) and the OSS Robotic Test and Integration Laboratory (RTAIL). RTAIL testing showed that teleoperators had difficulty in pinpointing the occurrence of soft dock. Telerobotic testing also showed that:

- the pin/groove geometry resulted in very high stress concentrations at the pin/groove interface, resulting in frequent MCF galling
- soft dock should be achievable from a highly misaligned position
- a latching soft dock would be preferred to a detent.

From testing the MPTT and related EVA/robot-compatible hardware in the WETF, astronauts also indicated a preference for a latching soft dock ("soft latch") over a spring detent. In a soft latch, spring-biased latches, or collets, on the tool engage a complementary geometry, or "lip," on the passive interface and "latch." In this condition, the two parts are mated but may still have some relative motion.

When the collets are moved firmly against the lip, pre-loaded, and then locked in place, the tool is considered "hard docked" to the interface and ready for further use (as a torque reaction point and/or for ORU handling).

In 1991, Space Station requirements drove OSS to abandon the conical fitting and MPTT and to concentrate on developing the micro conical system. The first EVA proof-of-concept micro conical tool (Figure 3) was completed in December, 1991, and tested extensively in the JSC WETF and in NASA's parabolic flight airplane, the KC-135.



**Figure 3. EVA Proof-of-Concept Micro conical Tool**

This proof-of-concept tool and the re-designed MCF incorporated all of the geometric features and lessons learned, as described above. The six collets on the tool tip interfaced with the underside of the flat lip at the top of the MCF. The castellations on the end of the tool tip interfaced with the torque reaction pins located at 120° increments about the circumference of the MCF (these castellations also provided six discrete tool-to-fitting orientations).

In use, as the collets are pushed over the top of the MCF and past the edge of the lip, they move outward and then inward, providing both a soft latch and a visual status indicator to the user. As the handle at the rear of the tool is rotated clockwise, the internal collet carrier rides up a cam, thereby moving the collets upward and inward until they are seated firmly against the fitting. At this point, the user has established a rigid connection, or hard dock, between the fitting and tool.

Although this tool and fitting combination worked quite well, OSS identified several technical issues to be improved in the next generation:

- The collets were too narrow and not strong enough to take the desired load range.
- The separate status indicators incorporated into the collet geometry were unnecessary because they were redundant, and they needlessly raised the cost and compromised the structural integrity of the collets.
- A single cam slot could not take the desired load, so an additional slot was added.

Based on the success of the first EMCT, OSS was directed by NASA to develop the first proof-of-concept RMCT. The design was reviewed and approved in June 1992. The resulting product (Figure 4) is still in use by the NASA Robotic Systems Evaluation Laboratory and is currently being used to test and verify robotic hardware for the ISS<sup>2</sup>. This design incorporated the lessons learned in the RTAIL and WETF and used the same internal mechanisms as the EMCT, but with collets of increased size and strength.

The actuation of the RMCT is necessarily different from the EMCT. Instead of the manual rotary actuator of the EMCT, the RMCT uses rotary input from the telerobot end-effector, the OTCM (Figure 5). The OTCM is expected to provide torque output incrementally up to 37 N-m (50 ft-lbf) in either direction. It can also extend and retract approximately 7 cm (2.78 in)<sup>3</sup>. The 7/16" hex head, located at the rear of the RMCT, drives one of two internal splines and is turned by the OTCM. In the driver-retracted position, the hex head interface drives the RMCT collets inward or outward. When the extend function is actuated, the OTCM torque driver pushes the hex interface outward, disengages one spline, engages another, and forces the RMCT torque driver to a position approximately flush with the tip of the tool. This second spline is part of the RMCT torque driver, so when torque is applied by the OTCM to the hex head in this position, the torque is passed directly to the RMCT torque driver, which can be used to engage or disengage an ORU retention bolt. Collet position status (release, soft latch ready, or hard dock) is provided by mechanical visual indicators located near the tool tip, within the field of view of some proposed OTCM cameras.

The RMCT/MCF interface was recently tested by NASA for its stiffness and misalignment characteristics. The results of those tests are as follows<sup>4</sup>:

	Load/Torque	Moment Arm	Test Load	Average Stiffness
Axial	454 kg (1000 lbf)	n/a	454 kg (1000 lbf)	95365 kg/cm (82,600 lbf/in)
Bending	34 N-m (550 in-lbf)	24 cm (9.45 in)	27 kg (60 lbf)	1634 N-m/rad (26,600 in-lbf/rad)
Torsion	55 N-m (900 in-lbf)	7.62 cm (3 in)	136 kg (300 lbf)	2820 N-m/rad (45,900 in-lbf/rad)

In each case, neither the MCF nor the RMCT yielded.

<sup>2</sup> Large 6B Avionics Box Orbital Replaceable Unit Robotic Compatibility Evaluation, Test Procedures, JSC-33331, October 1995 & Large 6B Avionics Box Orbital Replaceable Unit Robotic Compatibility Evaluation, Test Plan, JSC-33327

<sup>3</sup> ORU/Tool Changeout Mechanism Subsystem Specification, SPA- SS-SG-1027

<sup>4</sup> Robotic Track Task Robot Micro Conical Tool Characterization Test Report, JSC-33311, April, 1995

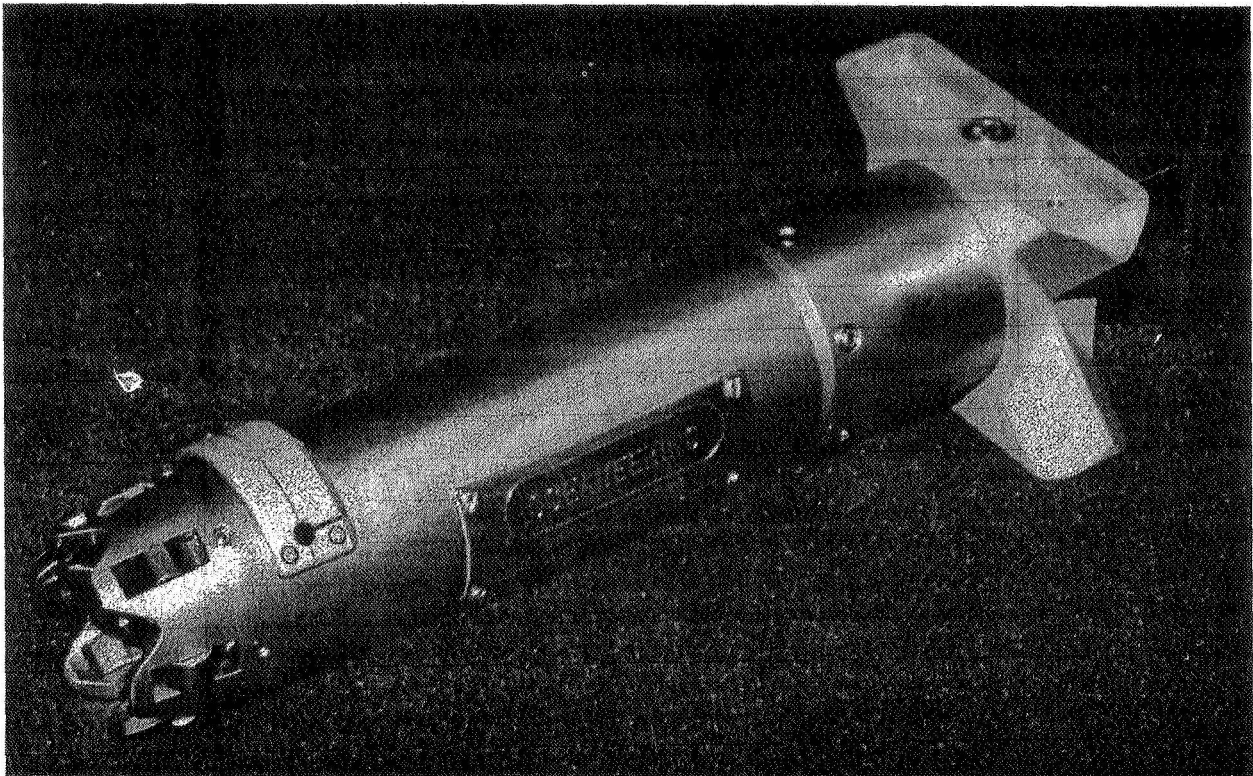


Figure 4. Proof-of-Concept RMCT

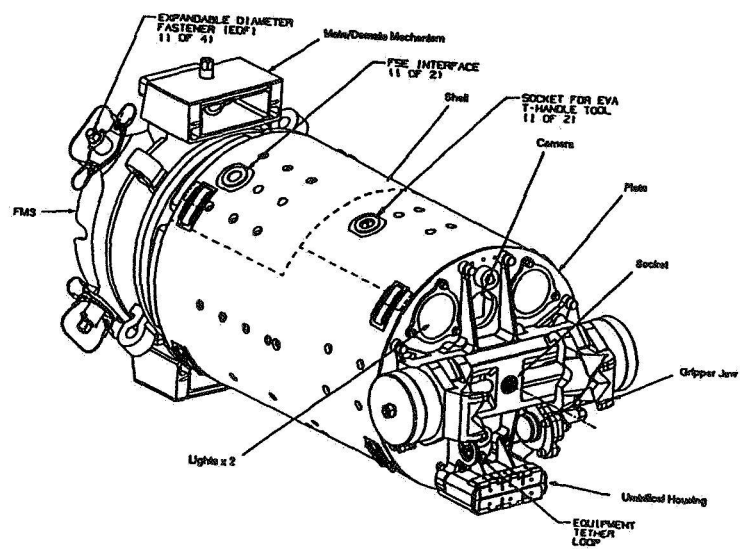


Figure 5. OTCM

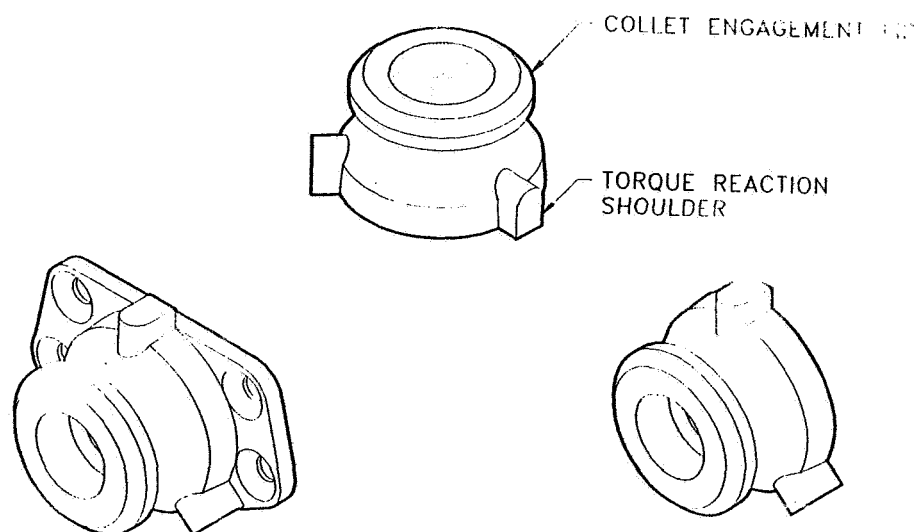
The success of the RMCT design led the MCS design team to conclude that the larger collets should be incorporated into the next, and final, revision of the EMCT. The design team also questioned the use of press-fit pins, since the torque reaction shoulders for the MCF. The issues of assembly costs, reliability of the press fit in the thermal environment of space, and the ability of the design to react high torsional loads, led OSS to design the single-piece MCF that was ultimately flight-qualified.

In August, 1993, OSS signed a contract with McDonnell-Douglas Aerospace to complete development, flight certification, and manufacturing of the MCF and EMCT for ISS.

### **Micro Conical Fitting (MCF) Detailed Engineering**

The MCF was designed as an EVA/robot-compatible handling interface for on-orbit manipulation of ORUs. As such, its design requirements encompassed limits of 227 kg (500 lbf) in axial and shear loading and 184 N-m (250 ft-lbf) in torsion and bending. In addition, the MCF has an operating temperature range of -93 to +82°C (-200° to +180°F) and an on-orbit lifetime of 30 years.

OSS designed three types of the MCF to satisfy all identified uses on the ISS: the 3/4" through hole, the counterbore, and the flanged fitting (Figure 6). All three configurations have an identical external geometry around the lip and torque reaction pin areas to allow grasping by either micro conical tool. The 3/4" through hole and counterbore MCFs are attached from their rear face using six 1/4-28" UNJF screws. The flanged MCF is attached using four No. 10 screws through the front flange face.



**Figure 6. MCF Types**

OSS performed preliminary analyses on the MCF to approximate the local stresses adjacent to the underside lip area and to determine the material properties required for the development test articles. Two development test articles were fabricated, one from CRES Custom 455 and one from MP35N.

OSS performed early development testing using an Instron machine to verify the results of the preliminary analyses. The development test units were subjected to the on-orbit loading forces of 184 N-m (250 ft-lbf) in torsion, 227 kg (550 lbf) in axial compression and tension, and a combined loading of 227 kg (550 lbf) in shear and 184 N-m (250 ft-lbf) in bending. Each test unit was instrumented with four rosette strain gauges positioned 90° apart on the inner surface of the through hole to allow for future correlation of stresses with the detailed FEA model. In order to simulate the loads applied by the micro conical tool tip, OSS fabricated a test jig that housed six beryllium copper collets, using preliminary material selected for the RMCT and EMCT collets. The MCF test units withstood all nominal loading conditions without any evidence of yield or failure.

During an unscheduled test when the MCF test units were subjected to a maximum of 6342 N-m (8600 ft-lbf), the collets of the tool test jig yielded. Although no yielding was observed at the MCF lip, there was substantial compressive plastic deformation from the tool tip on the upper surface of the torque reaction shoulders.

#### Fracture Analyses

The MCFs do not satisfy NASA ISS requirements for a non-fracture critical component. In particular, the momentum of a nominal ORU release from failure of a fitting would exceed the requirements of a non-hazardous released part during zero gravity flight. Additionally, the crew or robot limit load would induce maximum tensile stress in the flange or lip area of the part and exceed 30% of the ultimate strength of the MCF material (CRES Custom 455, condition H1000).

The fracture mechanics analyses were therefore tailored to verify that the configuration of the MCF in the lip area of the fracture critical zone had an adequate life expectancy. The standard crack sizes listed in SSP 30558<sup>5</sup> were assumed to be in the worst-case location and orientation on the part. Based on the worst-case stress distribution, conservative fatigue spectra were applied to verify part survival for a minimum of four service lifetimes.

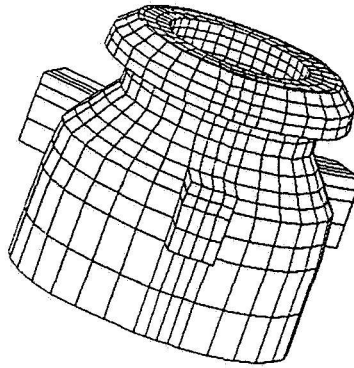
An iterative process of fracture mechanics analyses and different types of non-destructive evaluations were performed to determine the proper sensitivity of inspection. Liquid penetrant inspection (per MIL-STD-6866, Type II, Sensitivity 3) was selected and implemented. Under these circumstances, electropolishing becomes a requirement and is used to remove smear or masking materials from mechanically disturbed surfaces induced by the fabrication processes.

---

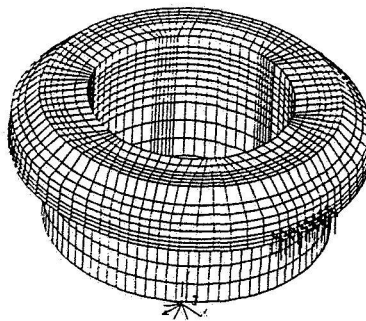
<sup>5</sup> Fracture Control Requirements for Space Station

### Finite Element Analyses

The finite element analysis examined the static strength and the structural non-linearity where the tool collets come into contact with the MCF lip. Figure 7 shows a coarsely meshed model resembling the development test article. The model was constructed from eight-node, hexahedral elements over the entire part. Even though the mesh size was fairly coarse, it was sufficient to verify that the area of greatest concern for stress was the re-entrant fillet radius of the collet engagement lip. After having identified the zone of highest stress, the model (Figure 8) was constructed. It has a very fine mesh in the lip area and extends to the bottom of the cylindrical portion adjacent to the conical part of the MCF body.



**Figure 7. MCF Coarse Mesh Model**



**Figure 8. MCF Lip Fine Mesh Model**

The model is fully constrained over the bottom cross-section of the cylinder. This model was used for all finite element stress calculations.



In order to determine the collet loads applied to the previous model, it was necessary to construct a spring model of the MCT with representative stiffness elements of the internal components. These loading conditions were then applied to the fine mesh model of the MCF lip area. To determine the margin of safety at the fillet radius of the lip, the calculated stresses were combined with factors of safety (1.10 on yield and 1.50 on ultimate), a 1.15 fitting factor, and a 0.95 reduction of material strength (due to operating temperature range). The minimum margin of safety was determined to be 0.269.

Only the enveloping crew-induced loads were considered during the analysis of the Space Station MCFs. Prior to the first use of the MCFs on STS-63 as a handling interface for the Spartan payload, OSS performed additional analyses unique to this mission. Identifying a remote possibility that the EMCT might not release from the MCF, OSS analyzed the vibrational loads that would be imparted to the MCF by the tool in case of re-entry with the tool still attached to the Spartan and in the payload bay. This analysis showed that re-entry loads were enveloped by the crew-induced loads.

### **EVA Micro Conical Tool (MCT) Detailed Engineering**

The EVA micro conical tool interfaces with all three types of the MCF. The specification loads for the tool design were derived from the maximum crew-induced, on-orbit load of 85 kg (187 lbf) applied at any point on the tool. Like the MCF, the tool was designed for an operating temperature range of -93°C to +82°C (-200°F to +180°F), but with an on-orbit lifetime of only 10 years (due to a change in the International Space Station design life). The primary operational design requirements were the highly misaligned soft latch and the automatic spring back to capture-ready mode for the actuation lever.

Materials selection for the MCT addressed structural considerations under the applied limit loads, the potential for galling of the internal components during operation under load, and the possibility of cold welding of the MCT to the MCF under prolonged thermal cycling.

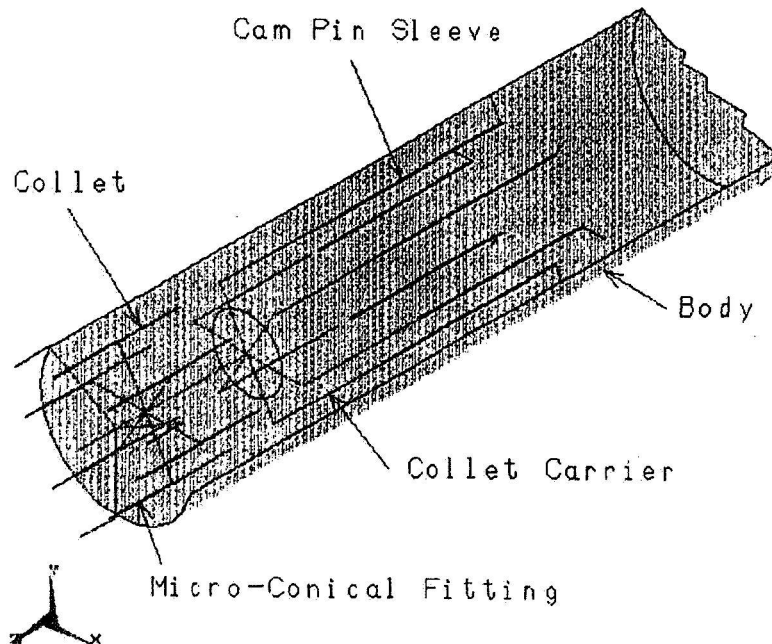
To determine the individual loads imparted by each tool collet to the MCF in the worst-case loading configuration, preliminary analysis on the MCT was performed using the spring model from the MCF finite element analysis. It was assumed that the areas of concern in the tool tip would be the collets and their pivot pins.

Two development tools were produced for testing in the WETF and aboard the KC-135 aircraft.

### **EMCT Fracture and Loads Analysis**

The EMCT does not satisfy the requirements for non-fracture critical assemblies. Specifically, the EMCT is designed to function as a portable ORU handle, allowing the crew to manipulate large payloads without extra tethers. Due to the potential risk of a released mass during zero-gravity operations, this use of the EMCT results in an operational configuration where the tool becomes a Criticality I hazard. For each

piece part that is identified as fracture critical, the highest stress associated with each fracture-sensitive area was analyzed. Appropriate stress concentration factors were applied. Standard crack sizes for liquid penetrant NDE (identified in JSC 22267A) were used on the fracture-critical components. Conservative fatigue spectra, based on the worst-case stress distribution, were applied to each part for verification of part survival during four service lifetimes (a service lifetime consists of three missions that include up to four EVA uses followed by a contingency landing). All fracture-critical parts were inspected using liquid penetrant methods (per MIL-STD-6866, Type I, Sensitivity 3). Additionally, all fracture-critical parts were either electropolished (for CRES alloys) or etched (for aluminum alloys) to remove residual surface smearing prior to NDE inspections.



**Figure 9. MCT Spring Model**

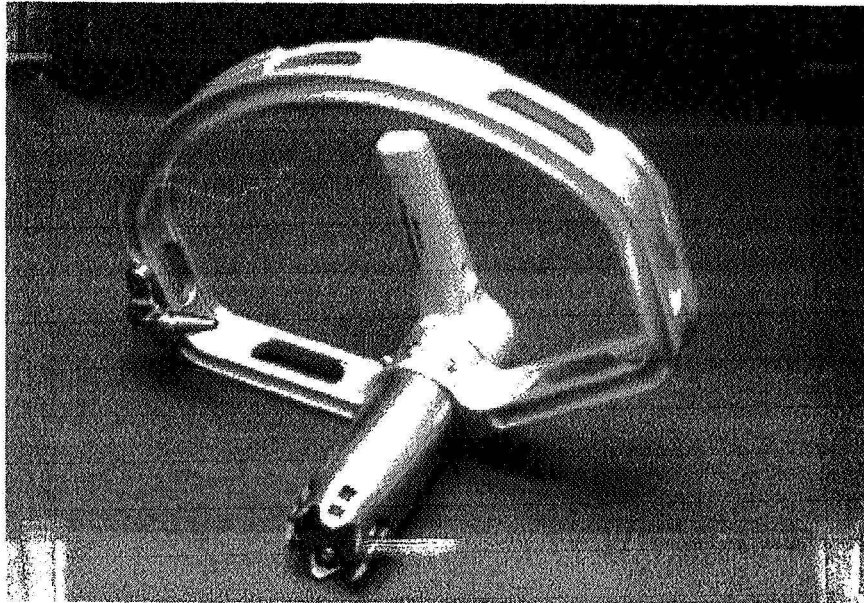
The spring model of the MCT (Figure 9) was used to derive the worst-case stresses in each load-bearing component. The outer barrel of the MCT is represented by shell elements. Gap/contact elements were placed between the MCT collets and the MCF lip at six equidistant locations and between the MCT tool tip and MCF torque reaction shoulders at three equidistant locations. As the loading was applied to the model in various directions, some gap elements made contact while others opened up.

Because the mechanical elements in the load path were not accessible for instrumentation during testing, this approach was the only feasible way to determine the state of the surface contacts under the various loading conditions.

A total of 96 different external loading conditions were applied to the spring model to generate individual component stresses. To determine the margin of safety at the fillet radius of the lip, the calculated stresses were combined with factors of safety (1.10 on yield and 1.50 on ultimate), a 1.15 fitting factor, and a 0.95 reduction of material strength (due to operating temperature range).

The Failure Modes & Effects analysis performed on the STS-63 EMCT identified only one critical failure where the EMCT could not be released from the MCF even after engaging the contingency release mechanism. To disposition this potential failure, structural analysis was performed on both the EMCT and MCF to prove that a failed tool could withstand the vibrational loads encountered during re-entry.

The MCT (Figure 10) was successfully used on STS-63 to manipulate the Spartan payload. This was the first on-orbit demonstration of the EMCT and MCF. It proved that a carefully designed mechanical system with an interface mass of only .11 kg could be used to handle satellites as much as 11000 times the interface mass (the Spartan satellite weighed 1270 kg).



**Figure 10. STS-63 MCT  
Micro Conical System Certification**

### Micro Conical Fitting(MCF) Certification

The 3/4" through hole and counterbore MCF designs were certified for space flight at NASA JSC. Certification was accomplished by test for the loading configurations and life cycle and by inspection for the workmanship and mass properties.

The loads tests were conducted at the NASA ES Structures Test Laboratory and used limits loads of 227 kg (550 lbf) and 184 N-m (250 ft-lbf). A fitting factor was applied to all limit loads. Factors of safety of 1.1 were applied for yield loads, and 1.5 were applied for ultimate loads. In order to test for the environmental requirements of -93°C to +82°C (-200°F to +180°F), the applied loads were increased by an additional 6% to account for the reduced load-carrying capacity of Custom 455 stainless steel at +82°C (+180°F, MIL-HBK-5<sup>6</sup>).

As required in the Specification Control Document governing the certification requirements for the MCF, the loads were applied in the following order for each load condition: limit load, yield load, ultimate load. The load conditions were:

- axial tension
- axial compression
- torsion
- bending with simultaneous shear.

After static testing was completed, a cyclic test was performed to verify the 6000-cycle service life. A test jig, consisting of a functional tool tip, was used to grapple the MCF and then hard dock. These functions were controlled by hydraulic actuators that drove the tool tip onto the MCF to the soft dock state, hard docked the tool tip, released the collets, and withdrew the tool tip away from the MCF.

### Micro Conical Tool (MCT) Certification

The STS-63 version of the EMCT was certified for space flight in March, 1995. As with the MCF, load tests were conducted at the NASA ES Structures Test Laboratory. Applied to three positions along the EMCT handle, load tests were performed at only 1.1 times the limit load of 85 kg (187 lbf). All installation and actuation forces, including contingency release, were verified to be within their specification for temperatures ranges of -93°C to +82°C (-200°F to +250°F). Life cycle testing was limited to 200 cycles for certification on this specific mission.

## **Conclusions**

The success of the micro conical system as an EVA/robot-compatible mechanism can be attributed to the basic approach of the design team. In particular, the team understood that:

- the basic design must be driven primarily by operational considerations
- a mechanism designed for one work system, then modified for the other, will please neither; therefore, development must be as an integrated system
- EVA and telerobot operations testing should be conducted in parallel
- the lessons learned from the testing must be used

---

<sup>6</sup> Metallic Material and Elements for Aerospace Vehicles Structures

- a very small, axisymmetric fitting with appropriate load paths and compatible tooling is capable of handling satellites or other masses as much as 11,000 times the mass of the fitting
- a latching soft dock is a useful capability for both astronauts and telerobots
- a common EVA/robot interface and front-end-of-tool-design, with differing crew and robot actuation and handling interfaces, is as viable an approach to on-orbit tools as it is to underwater tools
- human/robot-compatible tools and interfaces will become an enabling approach to space exploration and work.

Designing a mechanical system for both EVA and robotic compatibility need not increase the size, cost, or complexity of the "basic" system. Furthermore, as long as human compatibility requirements and capabilities are considered from the outset, designing a tool and interface system to the limited capabilities of a telerobot can actually enhance the human compatibility of the system: "if the robot can do it, it should be easy for the astronaut."

If a mechanism is made for human use, operations are the key. After the basic operations and configuration have been determined through iterative testing, then the detailed design can take place. The micro conical system proves that mechanisms can be equally compatible with humans and telerobots, and that operational constraints can be used to create reliable, simple, and strong mechanical systems.



## NASA Space Shuttle Lightweight Seat

Chris Hansen\*, Wayne Jermstad\*, James Lewis\* and Todd Colangelo\*\*

### Abstract

The Space Shuttle Lightweight Seat - Mission Specialist (LWS-MS) is a crew seat for the mission specialists who fly aboard the Space Shuttle. The LWS-MS is a lightweight replacement for the mission specialist seats currently flown on the Shuttle. Using state-of-the-art analysis techniques, a team of NASA and Lockheed engineers from the Johnson Space Center (JSC) designed a seat that met the more stringent requirements demanded of the new seats by the Shuttle program, and reduced the weight of the seats by 52%.

This paper describes the design approach used in developing the seat and the unique requirements of the seat itself. The paper also discusses the techniques that the engineers used to improve the safety and reliability of the seat, and to reduce its weight. The techniques used include a heavy emphasis on design optimization, analysis, and a simplified design.

### Introduction

The Lightweight Seat project was performed in-house by civil servants and contractor personnel at JSC. The LWS-MS project became a reality after it was determined that significant weight savings, as well as safety improvements, could be realized if the present seats flown on the Space Shuttle were redesigned using state-of-the-art engineering technologies. The seat itself is a mechanism that must be capable of detaching from the floor of the orbiter and folding into a small volume. The seat is shown in Figure 1 in its installed configuration. Figure 2 shows the seat in its stowed configuration. The fact that the seat itself is a mechanism rather than a static structure improves the seat's safety by giving flexibility to the structure and allowing the seat to withstand significant floor deformations during a crash event. The seat is also an example of a new emphasis in the aerospace community towards less complex designs. This approach improves reliability, decreases cost and manufacturing times, and in the case of the Lightweight Seat, reduces weight, the primary goal of the LWS-MS project. Within the seat itself, there are several unique mechanisms that perform multiple functions.

Several unique requirements made the LWS-MS design challenging. The main requirement was a dramatic reduction in weight. To make the project economically feasible, a weight reduction of 45% had to be achieved. The weight savings was necessitated by a need to reduce the weight of the entire Shuttle to support the heavy First Element launch of the Space Station in 1997. Removing weight in the crew compartment was of even greater importance due to its location far forward of the

\* NASA - Johnson Space Center, Houston, TX

\*\* Lockheed Martin Engineering and Sciences, Houston, TX

Shuttle's center of gravity. Weight removed from the crew compartment has the magnified effect of allowing ballast weight to be removed from the aft end of the Shuttle, allowing an even greater weight savings.

In addition to weight, several safety improvements (relative to the current crew seats) were to be made to the LWS-MS. The seat was to be subjected to a military and FAA requirement known as floor warping. The seat structure had to be capable of tolerating significant floor deformations being applied to the seat's attach points while undergoing its expected external loading. For external loading, the seat had to withstand a statically applied 20-g load, which is the crash environment specified by the Shuttle program. Using a 95th percentile crew member and equipment, with a mass of 142 kg (313 lb), led to an external load being applied to the seat of 27.8 kN (6260 lb) as well as inertial loads from the seat mass itself. The high loading conditions meant that the seat had to be strong, but the seat also had to be flexible enough to avoid subjecting the seat to high, concentrated loads during the enforced displacements demanded by floor warping. The floor warping requirement was instituted by the FAA after crash investigations determined that many seats designed for aircraft were very strong, yet because of their high stiffness were breaking free of the floor in actual crashes where the floor structure was deformed, resulting in occupant deaths. The floor warping requirement ensured that designers made their seats flexible enough to avoid this dangerous situation. The FAA also began requiring that aircraft seats undergo dynamic crash testing, similar to the auto industry. The FAA felt that the crash environment could not be simulated adequately with a statically applied load environment. The LWS-MS team felt that the new crew seat should also be subjected to a dynamic crash test in recognition of the FAA's recommendations.

## **Design Philosophy**

Because the requirements for designing seats demand high strength and high flexibility, commercial seat designers use a "design by test" philosophy. Seats are designed and subjected to crash tests, redesigned and re-tested until a satisfactory design is found. This process is expensive and requires the use of a crash test facility. It also does not adequately address the issue of variance in material properties. If a seat has unusually high material property values, its chances of passing a given test are increased. If the test is passed and the seat design is accepted, many of the production units may have significantly lower strength than the qualification unit. In addition, it is not practical to test to all worst-case conditions. There may be more than twenty load cases that are relevant to the seat structure, and it would be very expensive to test all cases. Therefore, our team used a method which ensures that the seat is capable of withstanding all load environments, using specified minimum material property allowables. These factors led the LWS-MS team to use state-of-the-art analysis techniques to drive the seat design. The knowledge of structural analysis and the computer infrastructure at NASA allowed the engineers to develop complex mathematical models to predict the behavior of the seat during all load environments, including the static applied loads, enforced displacements due to floor warping, and the dynamic crash environment. Using these tools, the design of the seat could be tested and optimized using the analysis models, saving the cost of expensive prototype testing, and ensuring that the final seat design would be capable of meeting



its strength and flexibility requirements. The plan was not to neglect testing, but rather to use testing as a verification tool to assure that the math models were behaving properly. Once this was assured, the math models could be used to perform detailed studies of the seat without the risk of damaging expensive prototype units. With this philosophy in mind, a detailed analysis program was instituted at the beginning of the program. The analysis was used to drive the design and find design solutions that could meet the demanding requirements.

Another of the seat requirements that made the design of the seat more complicated was its on-orbit folding. The seat had to be easily removable from the floor and stowable in a small volume to allow more room for crew operations on the flight deck and the mid deck. This meant that the seat itself had to be a mechanism. A quick-disconnect floor fitting had to be designed as well as the seat folding mechanism. These mechanisms also had to be modeled analytically since they were a major contribution to the flexibility of the seat. The challenge was to utilize the mechanisms' joint flexibility to help tolerate floor warping, utilize their structural strength to carry high crash loads, and yet make them simple enough to be manufactured and maintained at a low cost.

## **Design Overview**

The LWS-MS was designed to be removable and collapsible from the Space Shuttle mid deck and flight deck floors to facilitate on-orbit stowage. To accomplish on-orbit stowage, a quick disconnect floor fitting was designed. The quick disconnect floor fitting is located at the base of each leg. The floor fitting and spherical floor stud are shown in Figure 3. Because the seat had to tolerate significant floor deformations, it was undesirable to have a rigid connection at the seat to floor interface. The spherical joint in the orbiter floor fitting prevents large bending moments from being transferred to the seat legs, allowing the necessary flexibility and stiffness required to handle the crash loads as well as floor warping. The floor fitting assembly contains a housing that slips around the spherical floor stud, a retaining collar which slides down to capture the stud, and a spring loaded button that holds the collar in place. If the button is depressed, the collar can slide upwards, allowing the floor fitting to slide off of the spherical stud. The button slides into a detent which keeps the collar from sliding down into the locked position until the fittings are placed back on the floor studs. When locked onto the spherical floor stud, each floor fitting can tolerate a combination of 10° floor rotation in the pitch and roll axes.

Once the legs are released from the floor they can be folded under the seat pan for stowage. The rear legs fold forward, allowing the floor fittings to engage dummy studs, locking the legs in the folded position. Both front legs fold inward with the right leg having a lower pivot point, allowing the left leg to be folded and held captive by the right leg when in the folded configuration. Both legs are then held in place with a Velcro strap attached to the seat pan.

Another feature designed into the seat is an adjustable and removable headrest, shown in Figure 4. To accommodate the range in height of the crew members, the

headrest needed to be adjustable. The headrest is a single, machined piece which uses two posts that are inserted into the top of the seat back. The adjustment feature comes from a series of holes in the side of the right post. These holes can be engaged by a spring-loaded pin that is actuated from the side of the seat. This design also accommodates stowage, allowing the headrest to be removed from the top of the seat and inserted into the seat back, reducing the stored volume.

An operational requirement which drove the seat design was that the seat back had to be adjustable between a 2° forward launch position and a 10° back landing position, relative to a vertical reference plane. One of the primary load paths between the seat back and the floor attach points are two struts, shown in Figure 5, which connect the seat back to the seat pan. These struts are also used to accomplish the seat back angle changes. The upper end of the struts are attached to “sliders” which are captive in a track located on the side of the seat back. The sliders, shown in detail in Figure 7, are held in place within the track by spring-loaded, adjustable latches. In the launch position, the latches engage a hole in the slider, preventing the slider from moving within the track and thereby locking the seat back in place. When the latch is actuated, the sliders are free to slide below the latches to a hard stop. The latches move back into position and block the slider from traveling upward, locking the seat back in place at a different angle. The mechanism is shown in cross-section, describing the two positions, in Figure 9. To accommodate stowage, the latches can be actuated and the sliders moved past them upward in the track to the folded position where they are locked in place by smaller retention locks at the top of the track, shown in Figures 4 and 10. Once released from the retention locks, the sliders can move down in the tracks and the seat back can be returned to its launch or landing position.

The seat back folding mechanism consists of three main components. Titanium struts with rod-end bearings at each end are fixed at the lower end to the seat pan and connected at the upper end to the slider which allows rotation of the seat back. A latch mechanism consisting of a spring-loaded latch fixes the slider within the lower track and can be actuated by a cable and controller. An aluminum upper track acts as a guide for the slider when moving between the stowed position and the lower track which houses the latch mechanisms.

The strut is a solid, fixed-length rod with swaged bearings, shown in Figure 6. One of the main design drivers for the strut was clearance between the seats. Weight could have been saved if a hollow thin-walled tube had been used for the strut, however the diameter would have been larger, violating clearance constraints. To save weight the strut was fabricated from titanium, saving 0.23 kg (0.5 lb) per strut compared to previous stainless steel struts.

The latch mechanism, shown globally in Figures 5 and 8, consists of a latch which is held captive inside the lower track housing by a cap screw through a slot that limits latch travel. The latch is positively loaded outward with a captive compression spring. A small rod affixed to the back end of the latch runs down the middle of the compression spring and through the spring housing bracket that is attached with the same cap screw to the lower track housing. The two latch mechanisms (one on each

side of the seat) are tied together in the middle of the seat back with a 4-sided pivoting lever arm. It is designed to be adjustable so that any rotation of the lever arm actuates both latches simultaneously. However, one of the main design challenges with this device was ensuring that both sides of the seat and latch mechanisms would act together when sliding or latching. To address this problem, the latch mechanism was designed to be adjustable using laminated shims and a set screw, shown in detail in Figure 9. The seat is assembled using a nominal shim thickness above and below the latch. Once the seat is together, the seat back is rotated to the latched position and the sliders are monitored as they latch. If the two sides do not latch properly, the shims are adjusted until both sides act together. This method adjusts the slider when the seat back is in the forward, or launch, position. A set screw at the bottom of the lower track completes the necessary adjustments, controlling the gap size which sets the slider location in the 10° back, or landing, position.

The aluminum upper tracks, shown in Figure 10, are designed to allow translation of the sliders along the side of the seat back, allowing the seat to fold. No significant loading occurs through the upper track so weight and cost savings are gained by using a lower strength, lighter material like aluminum. The lower end of the upper track is inset into the upper end of the lower track to aid in alignment and to ensure a smooth transition between the two.

## Analysis

### Finite Element Modeling

Many detailed finite element models have been used to design and analyze the LWS-MS. These models consist of detailed local models used to predict stresses and deformations in local areas where large models are inefficient. There is also a large, global finite element model (FEM) of the entire seat primary structure. This non-linear model was used to analyze the seat structure as a system and to determine critical loads and load paths, as well as post-yielding behavior of the seat structure and the effects of this behavior on the seat's structural performance. The global model has roots back to the beginning of the LWS program. When the LWS-MS concept was developed, a simple finite element model using beam and plate elements was created to verify that the seat design had potential as a solution to the aggressive requirements of the project. As the project proceeded, detailed upgrades were made to the model to increase its fidelity and to reflect the design changes that occurred as the project progressed. The final global model was verified through several static and dynamic load tests performed specifically to verify the accuracy of the global model. The global FEM, shown in Figure 11, is an accurate representation of the stiffness of the seat. Non-linear solution sequences are used to account for material non-linearities as well as geometric non-linearities due to the large deformations created by the enforced displacements from floor warping at the floor interface. The global FEM was created using SDRC's I-DEAS finite element modeling software. The model was then solved using MSC's NASTRAN finite element code.

The global FEM also demonstrates the ability to structurally model mechanisms. In those design tasks that require a mechanism to tolerate high stresses during

operation, several finite element modeling tools exist, such as NASTRAN, which can greatly facilitate design and optimization. Joint stiffness, material non-linear behavior, and large displacement solutions can be used to develop design concepts before any actual units are manufactured. This design approach saves time, money, and lowers the chance of having a mechanical failure later in the program.

#### Dynamic Crash Analysis

Dynamic analysis of the seat and its occupant was performed to predict and even design the type of dynamic loading the seat and occupant would experience during a crash. By performing this analysis during the seat design process, the amount of dynamic crash testing required to develop the LWS-MS was significantly reduced when compared to conventional design approaches.

The analysis uses the Dynamic Analysis and Design Software (DADS) package by Computer Aided Design Software, Incorporated. DADS was chosen over other multi-body simulation codes because of its ability to incorporate flexible-body information from NASTRAN. Custom code written by NASA JSC was added to the DADS software to model the seat restraint system, and to model contact between the occupant and the seat. The equations of motion are solved using a modal formulation. The large mass technique is used to input an acceleration profile to the base of the seat.

The occupant is modeled as a group of fifteen rigid bodies which are connected at fourteen joints. The body mass properties and joint locations are the same as the Wright Patterson Air Force Base Articulated Total Body model of a 50% Hybrid II crash test dummy. Additional mass was added to account for the equipment worn by the orbiter crew. The model is shown in two configurations in Figures 12 and 13. Figure 12 shows the model in its initial state, at simulation time of 0.0 milliseconds. Figure 13 shows the model at the end of its dynamic analysis run at a simulation time of 200.0 milliseconds.

The harness is modeled as cables running over frictionless pulleys. The cables have a nonlinear load deflection curve which was determined using test data. A series of crash tests using a rigid boilerplate seat was conducted at the Federal Aviation Administration's Civil Aeromedical Institute (CAMI) in Oklahoma City. In these tests a 50% Hybrid II crash test dummy was fitted with the LWS-MS restraint system. These tests provided data to characterize the restraint system.

The seat mass and stiffness is represented in the DADS model. Alter statements are used in MSC/NASTRAN to output the mass matrix, stiffness matrix, and the first six eigenmodes of the LWS global finite element model. Modal transient analysis of the seat alone was performed using MSC/NASTRAN to determine that the first six eigenmodes were sufficient to represent the seat response. The NASTRAN analysis also was used to verify the DADS flexible model of the seat alone.

The dynamic analysis and the CAMI boilerplate tests showed the potential for strut loads in excess of those resulting from static analysis. The strut and mechanism were beefed up accordingly. The LWS-MS successfully passed its dynamic testing and the

DADS model shows good correlation with test data for both low and high level input tests.

## Testing

While analysis played an important and comprehensive role in the design of the LWS-MS, a detailed testing program was incorporated to verify and insure the structural integrity of the LWS-MS, as well as correlate the many math models used in the LWS program. Several small tests were performed on I-Beam cross sections to verify the ability of the NASTRAN models to predict crippling failures in the material plastic region. These tests demonstrated excellent correlation with the NASTRAN models.

An ultimate static load test was performed on the seat, using hydraulic actuators to apply loads at the seat belt attach locations. The total load distribution between the shoulder strap and the lap belts had been characterized during CAMI boilerplate tests, and was used to simulate the loads which would be applied during a crash. The seat was loaded to an equivalent 20-g static load. Deflection gages, strain gages, and load cells at the seat/floor attach points were used to characterize the seat's structural load paths and verify the global FEM. Pre-test predictions of all the deflection and strain gages as well as the load cells were made using the global FEM. Real-time data was taken during the test and predictions were compared to actual values at every 10% load step. Model correlation was excellent, achieving deviations of less than 10% from predictions. No post-test model corrections were needed.

Dynamic crash testing of the LWS-MS was performed at the Federal Aviation Administration's Civil Aeromedical Institute (CAMI) in Oklahoma City. While the seat was being designed, a series of tests were done using the restraint system and a rigid seat. These tests aided in the characterization of the restraint system for dynamic analysis. A low level dynamic test (7g input) was performed on the second qualification unit. The purpose of this test was to verify the math model of the seat and occupant. Finally a high level dynamic test (16g input) was performed on the third qualification unit. The purpose of this test was to produce loads at the floor equivalent to the floor's design strength. All tests were passed successfully.

The seat also had to pass vibration and cycle testing to insure that it could survive certification to 100 Shuttle missions, a project requirement. A flight-like qualification unit was subjected to a vibration environment of 6.5  $g_{rms}$  for 48 minutes on each of its three axes. Since the seat is to be flown with crew members attached, the vibration tests were done using an anthropomorphically correct test dummy wearing a launch and entry suit.

The mechanisms on the seat, including the floor fittings, seat back folding mechanism, and headrest were subjected to life cycle tests which simulated their use over the life of the seats.

## Conclusions

The Lightweight Seat - Mission Specialist is scheduled to fly aboard the Space Shuttle in February of 1997 for the second Hubble Telescope servicing mission and continue to fly afterwards for the life of the shuttle program. The final weight of the LWS-MS was measured at 22.62 kg (49.87 lb), 4.99 kg (11 lb) under the design goal, and a weight savings of 52% over the original shuttle mission specialist seats. There were several lessons learned on this project:

1. Mechanisms can be used to solve a variety of problems related not only to movement and transfer of forces, but also to solve flexibility problems. The flexibility inherent in mechanisms helped the LWS meet a structural flexibility requirement which greatly improved the safety of the seat design.
2. Investing a large amount of time in performing analysis early in a program can save time and money later by taking the mystery out of testing and avoiding costly failures and redesigns. If a mechanism or structure can be well understood in the early stages of a design, many of the potential problems can be found before the design is even complete.
3. The analysis tools available commercially for evaluating mechanisms and structures are very capable and can solve many classes of mechanism problems.
4. Designing simple mechanisms leads to fewer number of parts and can dramatically increase the reliability of your system. With fewer and less complex mechanisms, design, analysis, and testing efforts can be spent on optimization problems such as reducing weight, cost, and manufacturing time.
5. Involving designers, analysts, manufacturers, and customers early in the project, even as early as the conceptual design phase, can solve many potential problems before they become expensive later in the design process. The success of LWS project is the direct result of a serious commitment by the LWS team to this philosophy.

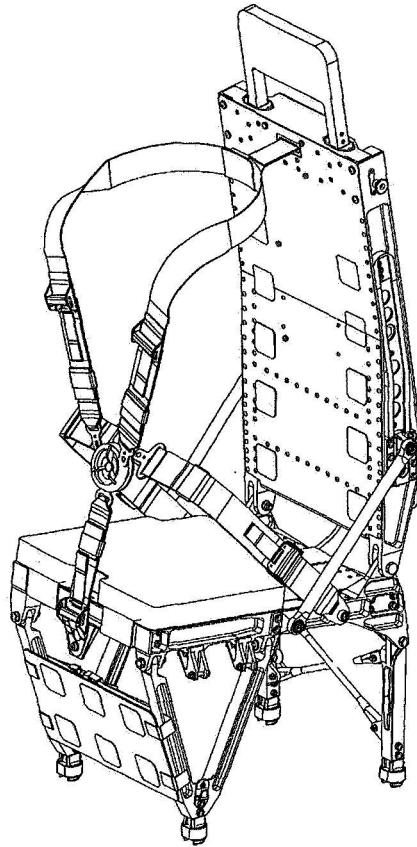
## References

1. JSC-26731, *Program Requirements Document for the Orbiter Lightweight Seats - Mission Specialist (LWS-MS)*. NASA JSC, Houston, Texas, November 1994
2. JSC-26919, *Structural Integrity Verification Plan for the Orbiter Lightweight Seats - Mission Specialist (LWS-MS)*. NASA JSC, Houston, Texas, September 1995
3. JSC-26918, *Certification Plan for the Orbiter Lightweight Seats - Mission Specialist (LWS-MS)*. NASA JSC, Houston, Texas, August 1995

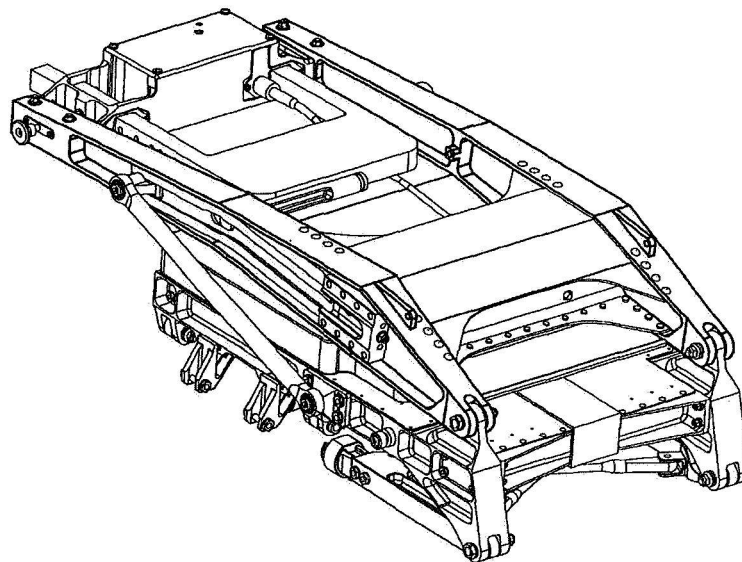
4. *The Development of Dynamic Performance Standards for Civil Aircraft Seats*, Stephen Soltis, William Nissley, Federal Aviation Administration, U.S. Department of Transportation, 1990

### **Acknowledgments**

The authors would like to thank the Lightweight Seat team for making this project successful and contributing many dedicated hours toward reaching our goals and making a lighter and safer crew seat. We would also like to thank the Federal Aviation Administration for the generous use of their expertise and their test facilities at the Civil Aeromedical Institute in Oklahoma City.

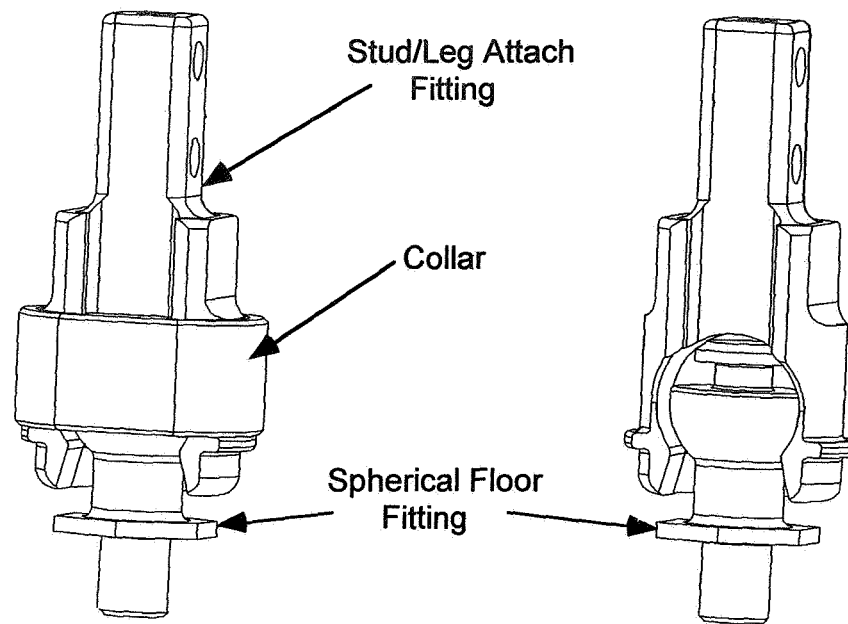


**Figure 1. Lightweight Seat - Installed Configuration**

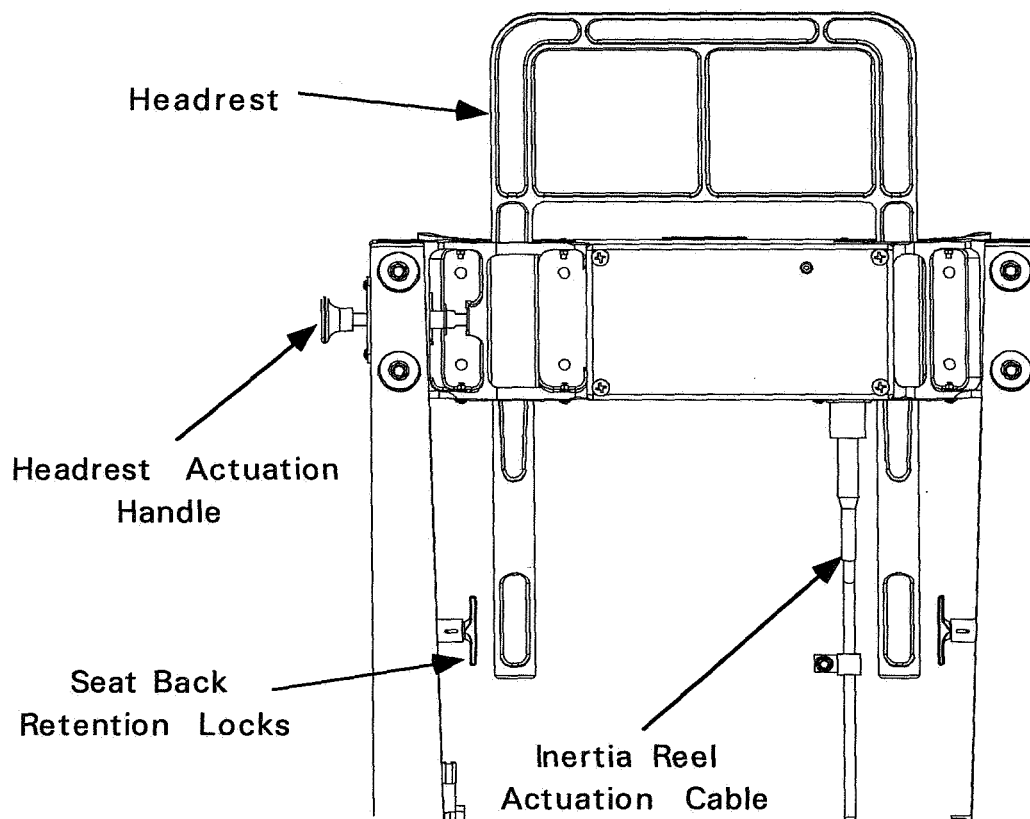


**Figure 2. Lightweight Seat - Stowed Configuration**

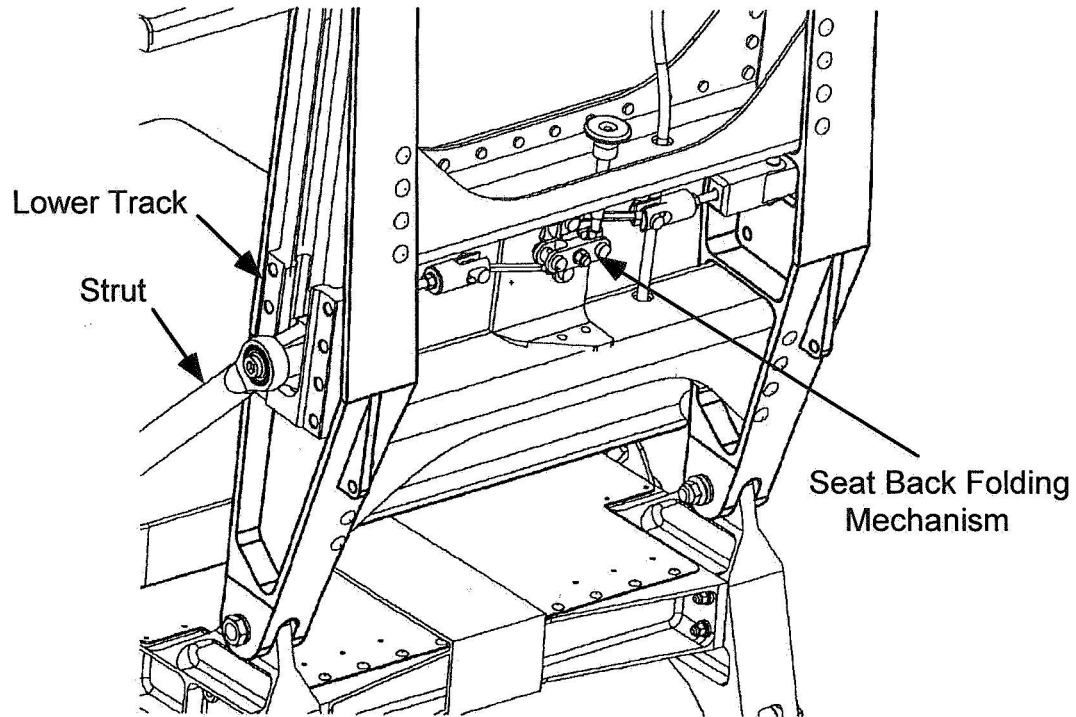




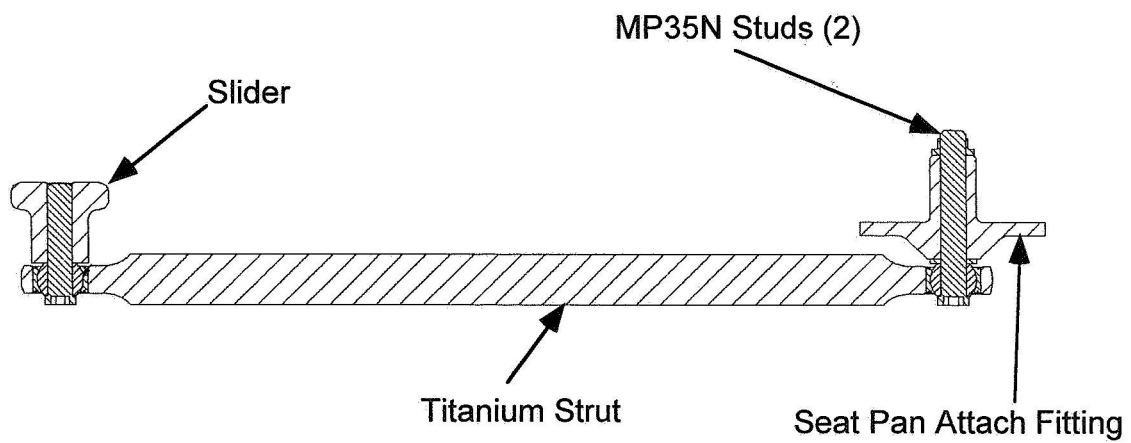
**Figure 3. Floor Fitting**



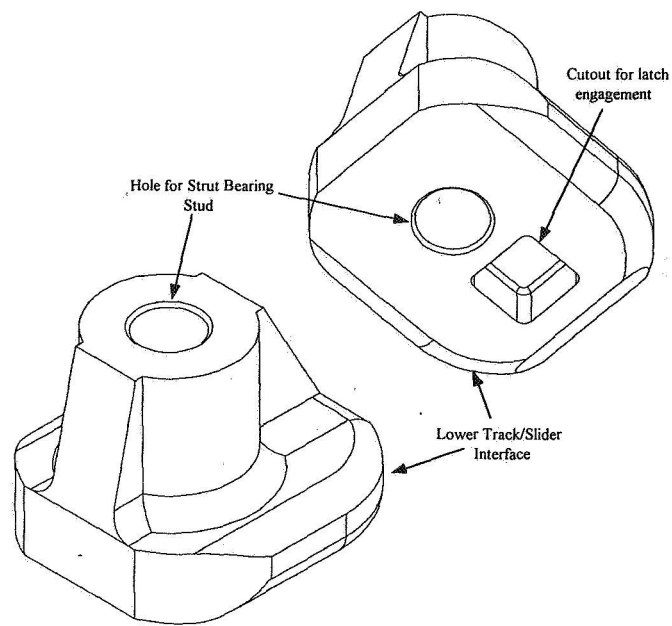
**Figure 4. Headrest Mechanism**



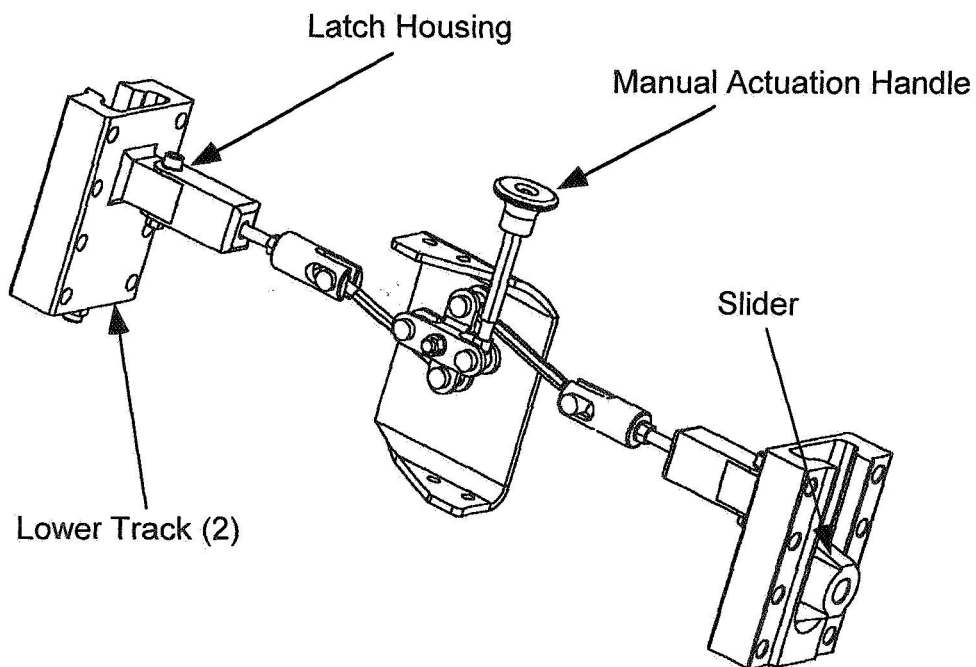
**Figure 5. Seat Back Folding Mechanism**



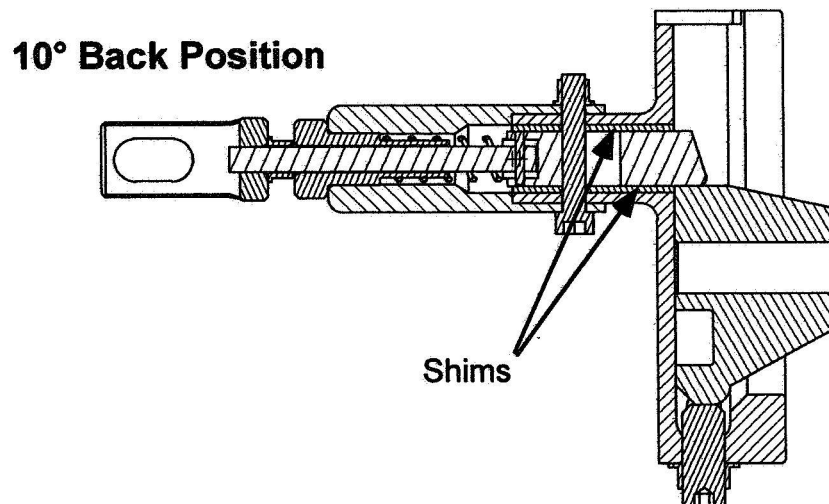
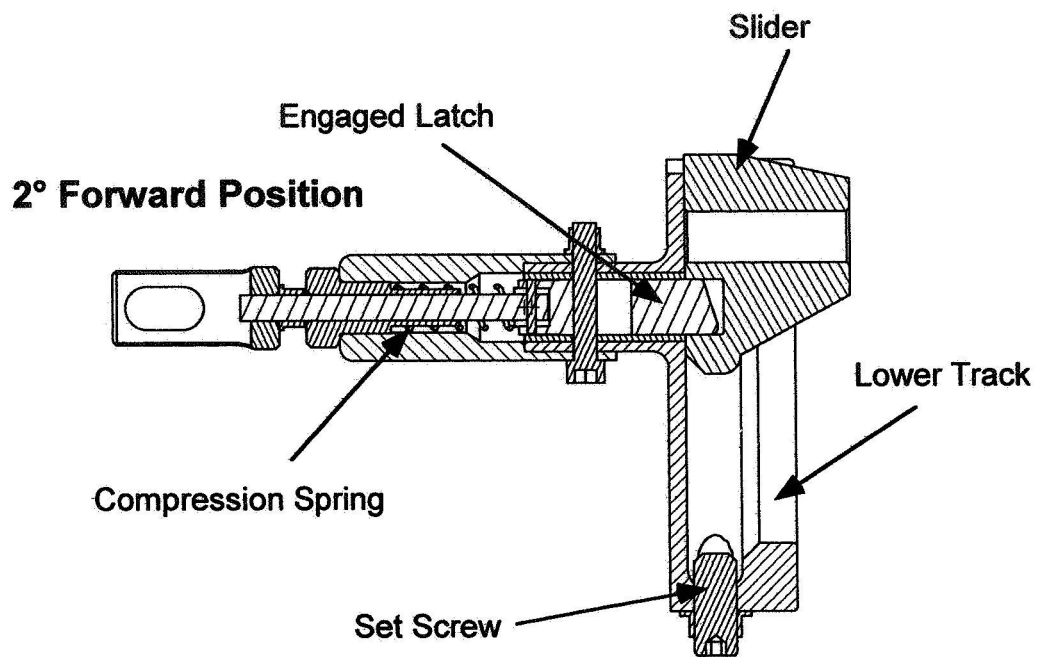
**Figure 6. Titanium Strut and Slider**



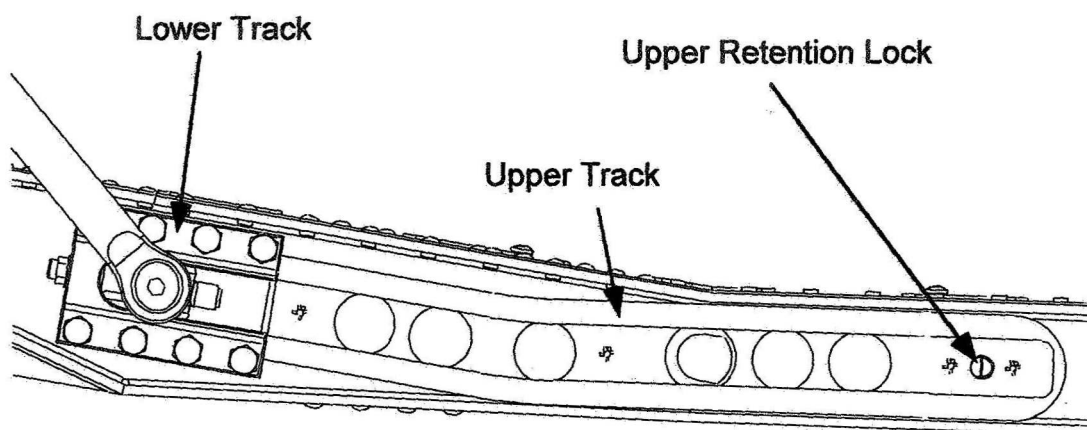
**Figure 7. Slider**



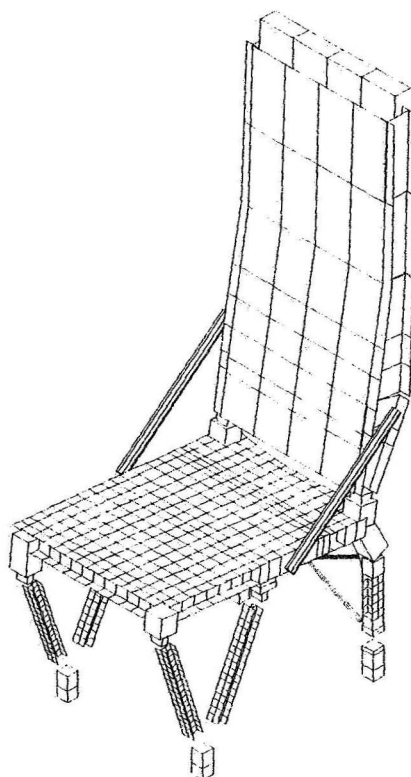
**Figure 8. Seat Back Actuation Mechanism**



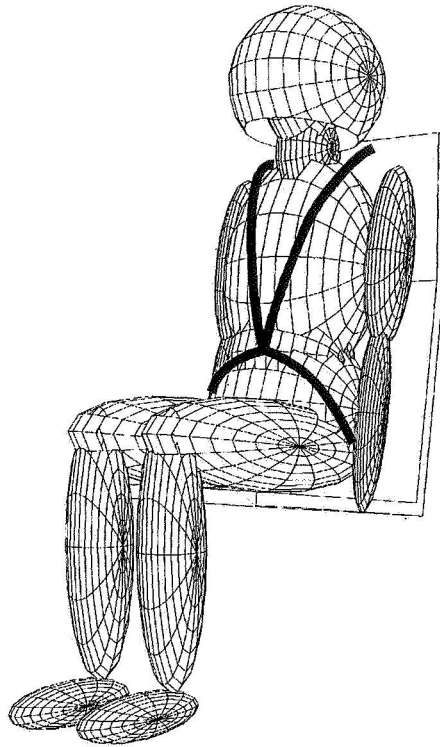
**Figure 9. Lower Track Housing and Latch Cross Sectional Views - 2 Seat Back Angle Positions**



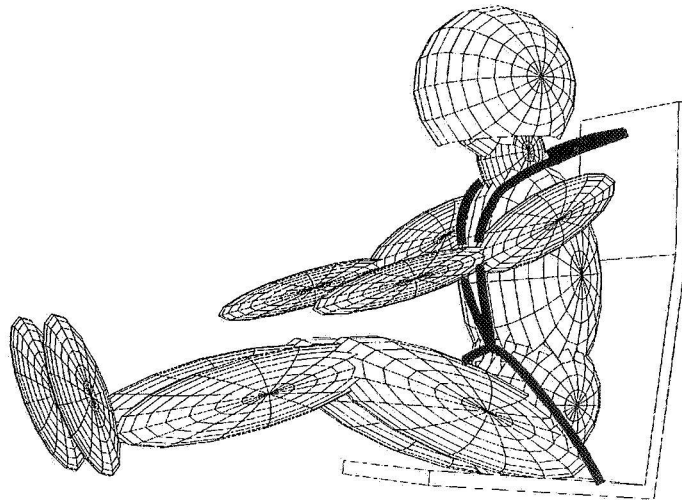
**Figure 10. Upper Track**



**Figure 11. Global Finite Element Model of the Lightweight Seat**



**Figure 12. DADS Model at Initial Time Step - 0.0 milliseconds**



**Figure 13. DADS Model at Final Time Step - 200.0 milliseconds**

REPORT DOCUMENTATION PAGE			Form Approved OMB No. 0704-0188	
Public reporting burden for this collection of information is estimated to average 1 hour per response, including the time for reviewing instructions, searching existing data sources, gathering and maintaining the data needed, and completing and reviewing the collection of information. Send comments regarding this burden estimate or any other aspect of this collection of information, including suggestions for reducing this burden, to Washington Headquarters Services, Directorate for Information Operations and Reports, 1215 Jefferson Davis Highway, Suite 1204, Arlington, VA 22202-4302, and to the Office of Management and Budget, Paperwork Reduction Project (0704-0188), Washington, DC 20503.				
1. AGENCY USE ONLY (Leave blank)	2. REPORT DATE May 1996	3. REPORT TYPE AND DATES COVERED Conference Publication		
4. TITLE AND SUBTITLE 30th Aerospace Mechanisms Symposium		5. FUNDING NUMBERS		
6. AUTHOR(S) Obie H. Bradley, Jr. and John F. Rogers, Compilers				
7. PERFORMING ORGANIZATION NAME(S) AND ADDRESS(ES)  NASA Langley Research Center Hampton, VA 23681-0001		8. PERFORMING ORGANIZATION REPORT NUMBER  L-17569		
9. SPONSORING/MONITORING AGENCY NAME(S) AND ADDRESS(ES)  National Aeronautics and Space Administration Washington, DC 20546-0001		10. SPONSORING/MONITORING AGENCY REPORT NUMBER  NASA CP-3328		
11. SUPPLEMENTARY NOTES Cosponsor: Lockheed Martin Missiles and Space Company, Inc., Sunnyvale, CA 94088 Conference Coordinator: Obie H. Bradley, Jr., Internal Operations Group, 804-864-7040, Langley Research Center, Hampton, VA				
12a. DISTRIBUTION/AVAILABILITY STATEMENT  Unclassified-Unlimited Subject Category 15		12b. DISTRIBUTION CODE		
13. ABSTRACT (Maximum 200 words)  The proceedings of the 30th Aerospace Mechanisms Symposium are reported. NASA Langley Research Center hosted the proceedings held at the Radisson Hotel in Hampton, Virginia on May 15-17, 1996, and Lockheed Martin Missiles and Space Company, Inc. cosponsored the symposium.  Technological areas covered include bearings and tribology; pointing, solar array, and deployment mechanisms; orbiter/space station; and other mechanisms for spacecraft.				
14. SUBJECT TERMS Spacecraft components; Solar array deployment; Pointing, deployment, bearings; Tribology			15. NUMBER OF PAGES 408	
			16. PRICE CODE A18	
17. SECURITY CLASSIFICATION OF REPORT Unclassified	18. SECURITY CLASSIFICATION OF THIS PAGE Unclassified	19. SECURITY CLASSIFICATION OF ABSTRACT Unclassified	20. LIMITATION OF ABSTRACT	